Technische Universität Kaiserslautern

Fachbereich Chemie

Time-resolved pump-probe action spectroscopy on isolated organic dyes and supramolecular photocatalysts

Am Fachbereich Chemie der Technischen Universität Kaiserslautern genehmigte

Dissertation

(D386)

zur Erlangung des akademischen Grades „Doktor der Naturwissenschaften"

vorgelegt von

Dipl.-Chem. Dimitri Imanbaew

Betreuer: PD Dr. C. Riehn

Tag der wissenschaftlichen Aussprache: 07.07.2017

Technische Universität Kaiserslautern

Die vorliegende Arbeit wurde im Zeitraum von Oktober 2013 bis Juni 2017 im Fachbereich Chemie der Technischen Universität Kaiserslautern unter der Betreuung von PD Dr. C. Riehn angefertigt.

Datum des Antrages auf Eröffnung des Promotionsverfahrens: 11.01.2017

Promotionskomission:

Vorsitzender: Prof. Dr. W. R. Thiel

1. Berichterstatter: PD Dr. C. Riehn

2. Berichterstatter: Prof. Dr. G. Niedner-Schatteburg

„Versuchen ist der erste Schritt zum Versagen.“

Homer Simpson

Content

1 Introduction

The ultimate goal of chemical physics is to unravel events that bring about chemistry, that is to answer the fundamental question of how a molecular system proceeds on its way from reactants to products. The corresponding underlying processes, *e.g.* vibrational motions, responsible for the formation and breaking of chemical bonds, charge and energy transfer happen very often incomprehensibly fast, down to the femtosecond (fs) timescale. These processes are of utmost importance for the mode of operation in both natural and artificial molecular assemblies. For example, the isomerization of the retinal chromophore in rhodopsin, a fundamental step in vision, proceeds within tens to hundreds femtoseconds,[1-5] whereas energy and charge transfer in artificial light harvesting assemblies used for efficient conversion of solar energy into storable forms, take place on a pico- to femtosecond timescale.[6-10]

To monitor these events, a technique with ultrafast time-resolution has to be employed. Hence, the investigation of rapid processes are the domain of ultrafast, time-resolved spectroscopy, often based on a pump-probe scheme, pioneered by Zewail *et al.* in 1985,[11-12] which lead to the development of numerous experimental methods, such as fs up-conversion for ultrafast fluorescence lifetimes,[13-14] time-resolved photoelectron[15] or transient absorption (TA) spectroscopy.[16] The general scheme in pump-probe experiments is using an ultrashort laser pulse to optically excite a molecular ensemble to a particular vibrational or electronic state and subsequently interrogate the evolution of the created excited state population in time with a second laser pulse. For electronically excited states, often, excited state absorption (or stimulated emission) to a higher (or lower) lying electronic state is measured to monitor the excited state population. Due to the spectral broadness of Fourier-transform limited, ultrashort laser pulses, wave-packet formation by coherent excitation of several vibronic/rovibronic states may also be observed, providing additional information on structure and coupling of excited states.[17-18]

Condensed phase investigations, although often much closer to the native environment of a reacting molecular system, have a severe drawback, owing to the abundance of species possibly present in solution. The influence of the surrounding solvent, counter-ions, protonation equilibria, and contaminants may obscure mechanistic steps or affect

properties of the target molecule dramatically. Additionally, experimental results are difficult to benchmark with quantum chemical calculations. Besides the often higher computational costs involved, the solute environment affects energies and intensities of electronic transitions in absorption spectra and the possible presence of other unidentifiable absorbing species may alter experimental results. These obstacles can be circumvented combining optical spectroscopy with mass spectrometric detection in the gas phase, allowing mass selective preparation of a target ion ensemble, whose intrinsic properties are then decoupled from its surrounding. At the same time the burden on quantum chemical calculations is alleviated.

Condensed phase spectroscopic methods for population analysis are based on the absorption of light by molecules of interest according to the Beer-Lambert Law. This applies equally to ultrafast fs spectroscopy on ensembles in the condensed phase, which is usually analyzed by monitoring changes in optical density (ΔOD in TA spectroscopy). In most cases the same is not applicable to gas phase studies, as the optical density *in vacuo* is usually not high enough to detect attenuation of an incident light beam by absorption. Thus, an action spectroscopy scheme is employed, recording the yield of product molecules (fragments, isomers) as a result to photoexcitation. Time-resolution is introduced to UV/Vis photofragmentation by monitoring the time delay dependent fragmentation enhancement, resulting from additional probe pulse absorption by a pump-selected ensemble. In this thesis, a detection scheme was employed first realized by Jouvet *et al.*, combining a fs laser system with electrospray ionization (ESI)[19-22] for target ion ensemble preparation and time-of-flight (TOF)[23-24] mass spectrometric detection.[25-26] Weinkauf *et al.* extended this approach to commercially available quadrupole ion trap mass spectrometers, however, never used the technique to its full potential, restricting themselves to only a few studies.[27-28]

The following work aims to fathom the capabilities of an improved experimental setup for time-resolved pump-probe photofragmentation action spectroscopy, combining a tunable ultrafast laser source with quadrupole ion trap mass spectrometry. The method is applied to cationic and anionic molecular systems, with regard to detection of electronically excited state dynamics as well as vibrational and rotational wave-packet dynamics.

One focus of this thesis is placed on the electronic excited state dynamics fluorescein dyes. Fluorescein represents one of the most popular categories of dyes in biochemistry. Owing to its high molar absorptivity and fluorescence quantum yield,[29] fluorescein based markers are often used in fluorescence labeling[30-31] or as probes for *e.g.* redox cycles in living cells[32] and sensors of various metal ions or other small molecules.[33] Applicability in biochemistry as a fluorescence marker requires functionalization to allow for conjugation to biomolecules, which may have detrimental effects on its luminescence properties.[34] Additionally, depending on the pH-value and the functional groups, fluorescein dyes can appear in several charge states and prototropic forms[29] in a relatively narrow pH-range, encumbering spectroscopic studies on the excited state properties of a specific charge state in solution. The employed spectroscopic gas phase method shall shed some light on the charge state and substituent dependent excited state properties of fluorescein and some selected derivatives.

Secondly, the excited state dynamics of a model carbocyanine dye are presented. Cyanines are a class of synthetic organic dyes, consisting of two terminal, tertiary/quaternary amine groups (or heteroaromatic moieties) linked by a chain of odd-numbered, conjugated carbon atoms. Owing to their remarkable absorption and luminescence properties, cyanines are used in various industrial applications[35-36] and in biomedical imaging as *e.g.* staining agents[37-40] or fluorescence markers.[41-46] Their absorption/emission properties can be easily modified by increasing the chain length in the polymethine backbone, enabling absorption/emission of light from the high frequency visible, up to the near infrared region.[46-47] Additionally, cyanines are popular model systems for studying photoinduced isomerization, which can be photoinduced via the excited state.[48-58] Cyanines are intrinsically charged, thus they qualify for mass spectrometric detection schemes without altering their inherent electronic properties.

Lastly, a major focus of this thesis was assessing the capabilities of the utilized experimental setup and method for the study of charge transfer dynamics in supramolecular catalysts for photocatalytic hydrogen generation. In cooperation with the research group of Prof. S. Rau (Universität Ulm), three heterodinuclear complexes were investigated, two of which have already been extensively studied in solution by TA[59-62] and thus used as a benchmark for the experimental setup. The third complex is based on a novel bridging ligand, which binds to the catalytic metal center via an N-

heterocyclic carbene, promising higher structural integrity. The ever increasing demand in sustainable energy resources calls for the optimization of catalytic methods for solar energy conversion into storable forms, such as hydrogen.[9, 63-67] From these investigations, structure-property correlations shall be drawn, which may aid in the optimization of future photocatalysts based on theory derived rational design.[68-74]

1.1 References

[1]   A. G. Doukas, M. R. Junnarkar, R. R. Alfano, R. H. Callender, T. Kakitani, B. Honig, *"FLUORESCENCE QUANTUM YIELD OF VISUAL PIGMENTS: EVIDENCE FOR SUBPICOSECOND ISOMERIZATION RATES"*, *Proc. Natl. Acad. Sci.* **1984**, *81*, 4790-4794.

[2]   R. Schoenlein, L. Peteanu, R. Mathies, C. Shank, *"THE FIRST STEP IN VISION: FEMTOSECOND ISOMERIZATION OF RHODOPSIN"*, *Science* **1991**, *254*, 412-415.

[3]   M. Taiji, K. Bryl, M. Nakagawa, M. Tsuda, T. Kobayashi, *"FEMTOSECOND STUDIES OF PRIMARY PHOTOPROCESSES IN OCTOPUSS RHODOPSIN"*, *Photochem. Photobiol.* **1992**, *56*, 1003-1011.

[4]   L. A. Peteanu, R. W. Schoenlein, Q. Wang, R. A. Mathies, C. V. Shank, *"THE FIRST STEP IN VISION OCCURS IN FEMTOSECONDS: COMPLETE BLUE AND RED SPECTRAL STUDIES"*, *Proc. Natl. Acad. Sci.* **1993**, *90*, 11762-11766.

[5]   Q. Wang, R. W. Schoenlein, L. A. Peteanu, R. A. Mathies, C. V. Shank,*"VIBRATIONALLY COHERENT PHOTOCHEMISTRY IN THE FEMTOSECOND PRIMARY EVENT OF VISION"*, *Science* **1994**, 422-422.

[6]   Y. Kobuke, *"ARTIFICIAL LIGHT-HARVESTING SYSTEMS BY USE OF METAL COORDINATION"*, *Eur. J. Inorg. Chem.* **2006**, *2006*, 2333-2351.

[7]   P. D. Frischmann, K. Mahata, F. Wurthner, *"POWERING THE FUTURE OF MOLECULAR ARTIFICIAL PHOTOSYNTHESIS WITH LIGHT-HARVESTING METALLOSUPRAMOLECULAR DYE ASSEMBLIES"*, *Chem. Soc. Rev.* **2013**, *42*, 1847-1870.

[8]   M. R. Wasielewski, *"PHOTOINDUCED ELECTRON TRANSFER IN SUPRAMOLECULAR SYSTEMS FOR ARTIFICIAL PHOTOSYNTHESIS"*, *Chem. Rev.* **1992**, *92*, 435-461.

[9]   D. Gust, T. A. Moore, A. L. Moore, *"MOLECULAR MIMICRY OF PHOTOSYNTHETIC ENERGY AND ELECTRON TRANSFER"*, *Acc. Chem. Res.* **1993**, *26*, 198-205.

[10]   T. J. Meyer, *"CHEMICAL APPROACHES TO ARTIFICIAL PHOTOSYNTHESIS"*, *Acc. Chem. Res.* **1989**, *22*, 163-170.

[11]   J. L. Knee, L. R. Khundkar, A. H. Zewail, *"PICOSECOND MONITORING OF A CHEMICAL REACTION IN MOLECULAR BEAMS: PHOTOFRAGMENTATION OF R−I→R‡+I"*, *J. Chem. Phys.* **1985**, *83*, 1996-1998.

[12]   N. F. Scherer, J. L. Knee, D. D. Smith, A. H. Zewail, *"FEMTOSECOND PHOTOFRAGMENT SPECTROSCOPY: THE REACTION ICN → CN + I"*, *J. Phys. Chem.* **1985**, *89*, 5141-5143.

[13]   H. Chosrowjan, S. Taniguchi, F. Tanaka, *"ULTRAFAST FLUORESCENCE UPCONVERSION TECHNIQUE AND ITS APPLICATIONS TO PROTEINS"*, *FEBS J.* **2015**, *282*, 3003-3015.

[14]   J. Xu, J. R. Knutson, *"ULTRAFAST FLUORESCENCE SPECTROSCOPY VIA UPCONVERSION: APPLICATIONS TO BIOPHYSICS"*, *Methods Enzymol.* **2008**, *450*, 159-183.

[15]   A. Stolow, A. E. Bragg, D. M. Neumark, *"FEMTOSECOND TIME-RESOLVED PHOTOELECTRON SPECTROSCOPY"*, *Chem. Rev.* **2004**, *104*, 1719-1758.

[16]   R. Berera, R. van Grondelle, J. T. M. Kennis, *"ULTRAFAST TRANSIENT ABSORPTION SPECTROSCOPY: PRINCIPLES AND APPLICATION TO PHOTOSYNTHETIC SYSTEMS"*, *Photosynth. Res.* **2009**, *101*, 105-118.

[17] M. Gruebele, A. H. Zewail, *"Femtosecond wave packet spectroscopy: Coherences, the potential, and structural determination"*, *J. Chem. Phys.* **1993**, *98*, 883-902.

[18] B. M. Garraway, K. A. Suominen, *"Wave-packet dynamics: new physics and chemistry in femto-time"*, *Rep. Prog. Phys.* **1995**, *58*, 365.

[19] J. Fenn, M. Mann, C. Meng, S. Wong, C. Whitehouse, *"Electrospray ionization for mass spectrometry of large biomolecules"*, *Science* **1989**, *246*, 64-71.

[20] J. B. Fenn, *"Electrospray Wings for Molecular Elephants (Nobel Lecture)"*, *Angew. Chem. Int. Ed.* **2003**, *42*, 3871-3894.

[21] J. B. Fenn, M. Mann, C. K. Meng, S. F. Wong, C. M. Whitehouse, *"Electrospray ionization–principles and practice"*, *Mass Spectrom. Rev.* **1990**, *9*, 37-70.

[22] M. Yamashita, J. B. Fenn, *"Electrospray ion source. Another variation on the free-jet theme"*, *J. Phys. Chem.* **1984**, *88*, 4451-4459.

[23] N. Mirsaleh-Kohan, W. D. Robertson, R. N. Compton, *"Electron ionization time-of-flight mass spectrometry: Historical review and current applications"*, *Mass Spectrom. Rev.* **2008**, *27*, 237-285.

[24] U. Boesl, *"Time-of-flight mass spectrometry: Introduction to the basics"*, *Mass Spectrom. Rev.* **2017**, *36*, 86-109.

[25] H. Kang, C. Dedonder-Lardeux, C. Jouvet, G. Grégoire, C. Desfrançois, J. P. Schermann, M. Barat, A. Fayeton, *"Control of Bond-Cleaving Reactions of Free Protonated Tryptophan Ion by Femtosecond Laser Pulses"*, *J. Phys. Chem. A* **2005**, *109*, 2417-2420.

[26] H. Kang, C. Jouvet, C. Dedonder-Lardeux, S. Martrenchard, C. Charrière, G. Grégoire, C. Desfrançois, J. P. Schermann, M. Barat, J. A. Fayeton, *"Photoinduced processes in protonated tryptamine"*, *J. Chem. Phys.* **2005**, *122*, 084307.

[27] D. Nolting, T. Schultz, I. V. Hertel, R. Weinkauf, *"Excited state dynamics and fragmentation channels of the protonated dipeptide H2N-Leu-Trp-COOH"*, *Phys. Chem. Chem. Phys.* **2006**, *8*, 5247-5254.

[28] D. Nolting, R. Weinkauf, I. V. Hertel, T. Schultz, *"Excited-State Relaxation of Protonated Adenine"*, *Chem. Phys. Chem.* **2007**, *8*, 751-755.

[29] R. Sjöback, J. Nygren, M. Kubista, *"Absorption and fluorescence properties of fluorescein"*, *Spectrochim. Acta Mol. Biomol. Spectrosc.* **1995**, *51*, L7-L21.

[30] L. D. Lavis, T.-Y. Chao, R. T. Raines, *"Fluorogenic Label for Biomolecular Imaging"*, *ACS Chem. Biol.* **2006**, *1*, 252-260.

[31] L. D. Lavis, R. T. Raines, *"Bright Ideas for Chemical Biology"*, *ACS Chem. Biol.* **2008**, *3*, 142-155.

[32] E. W. Miller, S. X. Bian, C. J. Chang, *"A Fluorescent Sensor for Imaging Reversible Redox Cycles in Living Cells"*, *J. Am. Chem. Soc.* **2007**, *129*, 3458-3459.

[33] X. Li, X. Gao, W. Shi, H. Ma, *"Design Strategies for Water-Soluble Small Molecular Chromogenic and Fluorogenic Probes"*, *Chem. Rev.* **2014**, *114*, 590-659.

[34] X.-F. Zhang, J. Zhang, L. Liu, *"Fluorescence Properties of Twenty Fluorescein Derivatives: Lifetime, Quantum Yield, Absorption and Emission Spectra"*, *J. Fluoresc.* **2014**, *24*, 819-826.

[35] *"Industrial Dyes: Chemistry, Properties, Applications"*, Editor: K. Hunger, Wiley-VCH, **2003**.

[36] R. W. Sabnis, *"Handbook of Biological Dyes and Stains: Synthesis and Industrial Applications"*, Wiley, Pfizer Inc., Madison NJ, **2010**.

[37] A. Kitaguchi, N. Yamaguchi, M. Nasu, *"Simultaneous enumeration of viable Enterobacteriaceae and Pseudomonas spp. within three hours by multicolor fluorescence in situ hybridization with vital staining"*, *J. Microbiol. Methods* **2006**, *65*, 623-627.

[38] J. A. Kiernan, *"Histochemistry of Staining Methods for Normal and Degenerating Myelin in the Central and Peripheral Nervous Systems"*, *J. Histotechnol.* **2007**, *30*, 87-106.

[39] M. Eriksson, H. J. Karlsson, G. Westman, B. Åkerman, *"Groove-binding unsymmetrical cyanine dyes for staining of DNA: dissociation rates in free solution and electrophoresis gels"*, *Nucleic Acids Res.* **2003**, *31*, 6235-6242.

[40] J. A. Kiernan, *"Chromoxane cyanine R. II. Staining of animal tissues by the dye and its iron complexes"*, *J. Microsc.* **1984**, *134*, 25-39.

[41] G. Patonay, J. Salon, J. Sowell, L. Strekowski, *"Noncovalent Labeling of Biomolecules with Red and Near-Infrared Dyes"*, *Molecules* **2004**, *9*, 40.

[42] H. Yu, J. Chao, D. Patek, R. Mujumdar, S. Mujumdar, A. S. Waggoner, *"Cyanine dye dUTP analogs for enzymatic labeling of DNA probes"*, *Nucleic Acids Res.* **1994**, *22*, 3226-3232.

[43] J. Rao, A. Dragulescu-Andrasi, H. Yao, *"Fluorescence imaging in vivo: recent advances"*, *Curr. Opin. Biotechnol.* **2007**, *18*, 17-25.

[44] M. Fernandez-Suarez, A. Y. Ting, *"Fluorescent probes for super-resolution imaging in living cells"*, *Nat Rev Mol Cell Biol* **2008**, *9*, 929-943.

[45] M. S. T. Gonçalves, *"Fluorescent Labeling of Biomolecules with Organic Probes"*, *Chem. Rev.* **2009**, *109*, 190-212.

[46] S. Luo, E. Zhang, Y. Su, T. Cheng, C. Shi, *"A review of NIR dyes in cancer targeting and imaging"*, *Biomaterials* **2011**, *32*, 7127-7138.

[47] A. Mishra, R. K. Behera, P. K. Behera, B. K. Mishra, G. B. Behera, *"Cyanines during the 1990s: A Review"*, *Chem. Rev.* **2000**, *100*, 1973-2012.

[48] Z. Wei, T. Nakamura, S. Takeuchi, T. Tahara, *"Tracking of the Nuclear Wavepacket Motion in Cyanine Photoisomerization by Ultrafast Pump–Dump–Probe Spectroscopy"*, *J. Am. Chem. Soc.* **2011**, *133*, 8205-8210.

[49] J. Rodríguez, D. Scherlis, D. Estrin, P. F. Aramendía, R. M. Negri, *"AM1 Study of the Ground and Excited State Potential Energy Surfaces of Symmetric Carbocyanines"*, *J. Phys. Chem. A* **1997**, *101*, 6998-7006.

[50] G. Ponterini, F. Momicchioli, *"Trans-cis photoisomerization mechanism of carbocyanines: experimental check of theoretical models"*, *Chem. Phys.* **1991**, *151*, 111-126.

[51] J. Kabatc, J. Pączkowski, *"The photophysical and photochemical properties of the oxacarbocyanine and thiacarbocyanine dyes"*, *Dyes and Pigments* **2004**, *61*, 1-16.

[52] S. Ghelli, G. Ponterini, *"Identification of the photoisomers of two carbocyanines by 1H NMR spectroscopy"*, *J. Mol. Struct.* **1995**, *355*, 193-200.

[53] B. Dietzek, A. N. Tarnovsky, A. Yartsev, *"Visualizing overdamped wavepacket motion: Excited-state isomerization of pseudocyanine in viscous solvents"*, *Chem. Phys.* **2009**, *357*, 54-62.

[54] B. Dietzek, B. Brüggemann, T. Pascher, A. Yartsev, *"Pump-Shaped Dump Optimal Control Reveals the Nuclear Reaction Pathway of Isomerization of a Photoexcited Cyanine Dye"*, *J. Am. Chem. Soc.* **2007**, *129*, 13014-13021.

[55] M. M. Bishop, J. D. Roscioli, S. Ghosh, J. J. Mueller, N. C. Shepherd, W. F. Beck, *"Vibrationally Coherent Preparation of the Transition State for Photoisomerization of the Cyanine Dye Cy5 in Water"*, *J.Phys. Chem. B* **2015**, *119*, 6905-6915.

[56] I. Baraldi, A. Carnevali, F. Momicchioli, G. Ponterini, *"Electronic spectra and trans—cis photoisomerism of carbocyanines. A theoretical (CS INDO CI) and experimental study"*, *Spectrochim. Act. Mol. Spectrosc.* **1993**, *49*, 471-495.

[57]   P. F. Aramendia, R. M. Negri, E. S. Roman, *"Temperature Dependence of Fluorescence and Photoisomerization in Symmetric Carbocyanines.Influence of Medium Viscosity and Molecular Structure"*, *J. Phys. Chem.* **1994**, *98*, 3165-3173.

[58]   B. D. Adamson, N. J. A. Coughlan, G. da Silva, E. J. Bieske, *"Photoisomerization Action Spectroscopy of the Carbocyanine Dye DTC+ in the Gas Phase"*, *J. Phys. Chem. A* **2013**, *117*, 13319-13325.

[59]   M. Wächtler, J. Guthmuller, S. Kupfer, M. Maiuri, D. Brida, J. Popp, S. Rau, G. Cerullo, B. Dietzek, *"Ultrafast Intramolecular Relaxation and Wave-Packet Motion in a Ruthenium-Based Supramolecular Photocatalyst"*, *Chem. Eur. J.* **2015**, *21*, 7668-7674.

[60]   M. G. Pfeffer, B. Schäfer, G. Smolentsev, J. Uhlig, E. Nazarenko, J. Guthmuller, C. Kuhnt, M. Wächtler, B. Dietzek, V. Sundström, S. Rau, *"Palladium versus Platinum: The Metal in the Catalytic Center of a Molecular Photocatalyst Determines the Mechanism of the Hydrogen Production with Visible Light"*, *Angew. Chem. Int. Ed.* **2015**, *54*, 5044-5048.

[61]   S. Tschierlei, M. Presselt, C. Kuhnt, A. Yartsev, T. Pascher, V. Sundström, M. Karnahl, M. Schwalbe, B. Schäfer, S. Rau, M. Schmitt, B. Dietzek, J. Popp, *"Photophysics of an Intramolecular Hydrogen-Evolving Ru–Pd Photocatalyst"*, *Chem. Eur. J.* **2009**, *15*, 7678-7688.

[62]   C. Kuhnt, M. Karnahl, S. Tschierlei, K. Griebenow, M. Schmitt, B. Schafer, S. Krieck, H. Gorls, S. Rau, B. Dietzek, J. Popp, *"Substitution-controlled ultrafast excited-state processes in Ru-dppz-derivatives"*, *Phys. Chem. Chem. Phys.* **2010**, *12*, 1357-1368.

[63]   N. S. Lewis, D. G. Nocera, *"Powering the planet: Chemical challenges in solar energy utilization"*, *Proc. Natl. Acad. Sci.* **2006**, *103*, 15729-15735.

[64]   D. Gust, T. A. Moore, A. L. Moore, *"Realizing artificial photosynthesis"*, *Faraday Discuss.* **2012**, *155*, 9-26.

[65]   Y. Tachibana, L. Vayssieres, J. R. Durrant, *"Artificial photosynthesis for solar water-splitting"*, *Nat Photon* **2012**, *6*, 511-518.

[66]   S. Dahl, I. Chorkendorff, *"Solar-fuel generation: Towards practical implementation"*, *Nat. Mater.* **2012**, *11*, 100-101.

[67]   J. A. Turner, *"A Realizable Renewable Energy Future"*, *Science* **1999**, *285*, 687-689.

[68]   G. Ajayakumar, M. Kobayashi, S. Masaoka, K. Sakai, *"Light-induced charge separation and photocatalytic hydrogen evolution from water using RuIIPtII-based molecular devices: Effects of introducing additional donor and/or acceptor sites"*, *Dalton Trans.* **2011**, *40*, 3955-3966.

[69]   G. W. Brudvig, J. N. H. Reek, K. Sakai, L. Spiccia, L. Sun, *"Catalytic Systems for Water Splitting"*, *ChemPlusChem* **2016**, *81*, 1017-1019.

[70]   S. Masaoka, Y. Mukawa, K. Sakai, *"Frontier orbital engineering of photo-hydrogen-evolving molecular devices: a clear relationship between the H2-evolving activity and the energy level of the LUMO"*, *Dalton Trans.* **2010**, *39*, 5868-5876.

[71]   H. Ozawa, M. Kobayashi, B. Balan, S. Masaoka, K. Sakai, *"Photo-Hydrogen-Evolving Molecular Catalysts Consisting of Polypyridyl Ruthenium(II) Photosensitizers and Platinum(II) Catalysts: Insights into the Reaction Mechanism"*, *Chem. Asian J.* **2010**, *5*, 1860-1869.

[72]   H. Ozawa, K. Sakai, *"Photo-hydrogen-evolving molecular devices driving visible-light-induced water reduction into molecular hydrogen: structure-activity relationship and reaction mechanism"*, *Chem. Commun.* **2011**, *47*, 2227-2242.

[73]   A. R. Parent, K. Sakai, *"Progress in Base-Metal Water Oxidation Catalysis"*, *ChemSusChem* **2014**, *7*, 2070-2080.

[74]   C. V. Suneesh, B. Balan, H. Ozawa, Y. Nakamura, T. Katayama, M. Muramatsu, Y. Nagasawa, H. Miyasaka, K. Sakai, *"Mechanistic studies of photoinduced intramolecular and intermolecular electron transfer processes in RuPt-centred photo-hydrogen-evolving molecular devices"*, *Phys. Chem. Chem. Phys.* **2014**, *16*, 1607-1616.

2 Experimental setup and methods

2.1 Experimental setup

Figure 1 depicts a scheme of the experimental setup used in this thesis to perform transient pump-probe photofragmentation (tPF) experiments on isolated molecular ions in the gas phase. For this purpose a modified electrospray ionization (ESI) quadruple ion trap (QIT) mass spectrometer (amaZon Speed, Bruker Daltonics) was combined with a commercial femtosecond (fs) Ti^{3+}:sapphire oscillator/amplifier laser system (Wyvern 1000™, KMLabs). Two optical parametric amplifiers (OPA) of white light continuum (TOPAS-C, LightConversion) were used as a source for pump and probe laser pulses of tunable wavelength (240-2500 nm). A more detailed description of the individual components will be given in the following sections.
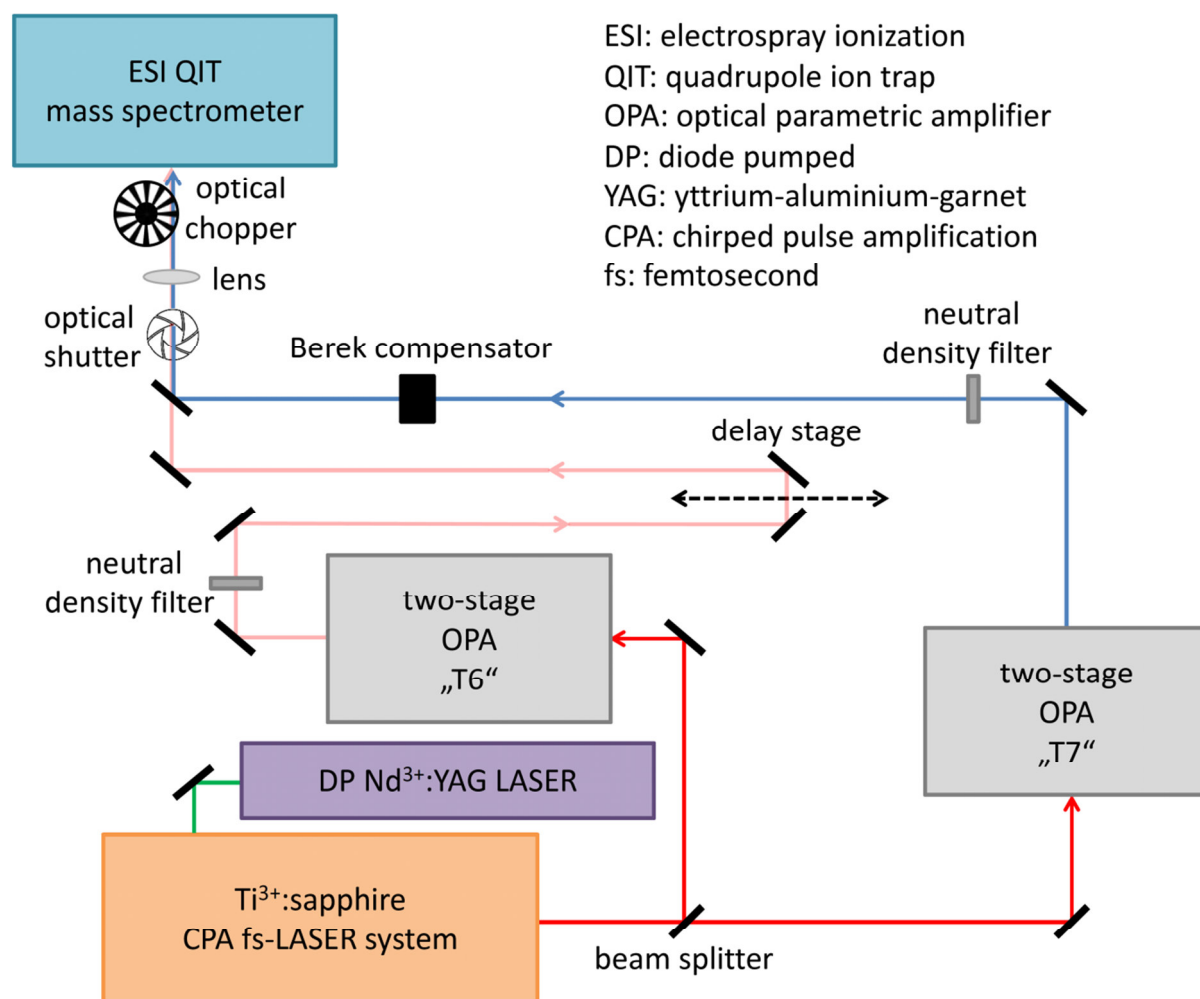
Figure 1 Schematic experimental setup used for tPF experiments.

2.2 Electrospray ionization quadrupole ion trap mass spectrometer

2.2.1 Transferring ions into the gas phase: electrospray ionization

Electrospray ionization (ESI)[1-2] allows for the transfer of dissolved ions into the gas phase and is, like the matrix assisted laser desorption ionization (MALDI),[3] considered to be a soft ionization technique, *i.e.* excessive fragmentation of the molecules is prevented. This characteristic made it popular among biologists for the mass spectrometric study and characterization of thermally labile macromolecules.[4-6] The principle of the ESI method was proposed by Dole *et al.* in the late 1960s[7] and improved upon by Fenn *et al.*, who was awarded the noble prize in 2002 for the development of the first applications in 1984.[1-2, 8-10] The extensive review of the ESI process over the last decades is a testament to its importance not only for biological applications, but for the mass spectrometric and spectroscopic community in general.[11-15]
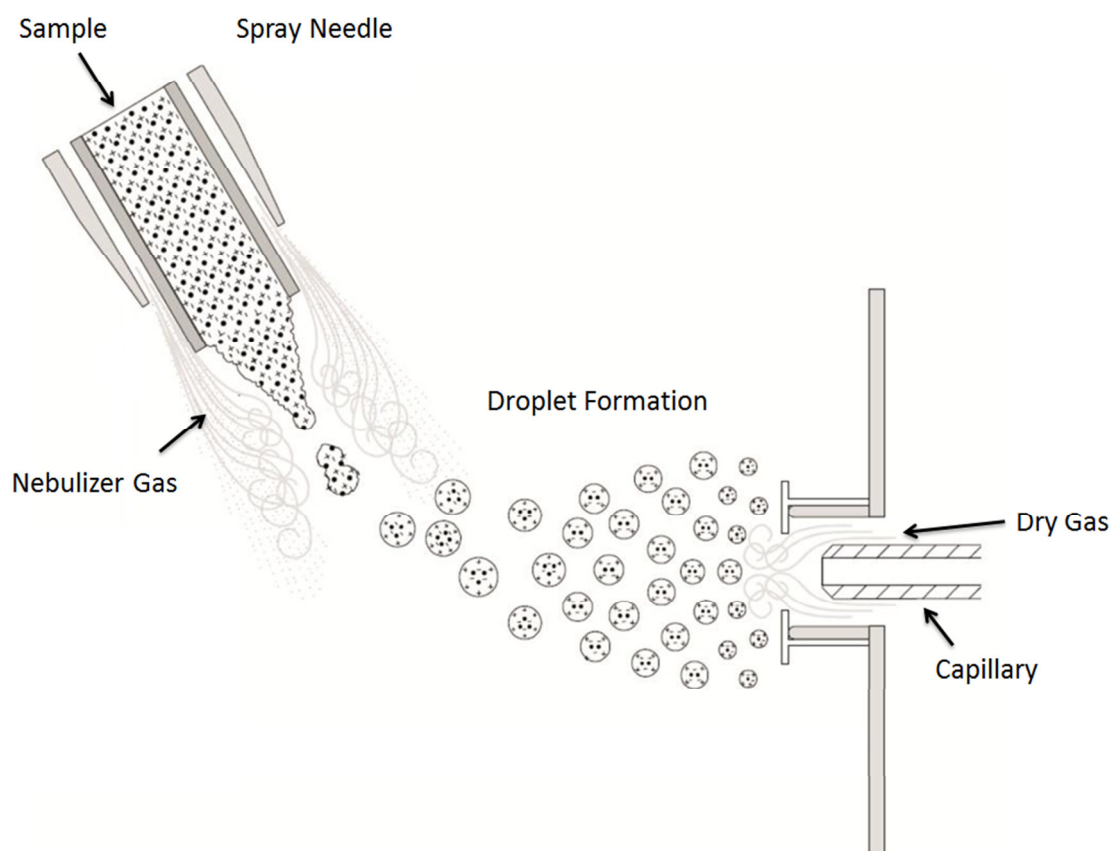
Figure 2 Schematic depiction of the ESI process. Adapted from Ref. [16].

ESI can be roughly subdivided into two processes: firstly, the nebulization of the sample solution and secondly the desolvation of the analyte ions prior to transfer into the vacuum system of the mass spectrometer (Figure 2). The sample solution is infused into the spray chamber through a grounded spray needle mounted inside a tube from which a continuous flow of heated nebulizer gas (*e.g.* nitrogen) streams. A combination of strong shear forces generated by the stream of nebulizing gas at the tip of the spray needle and the field gradient between the capillary (held at typically 2-6 kV) and the needle draws out the sample (in a so-called Taylor cone) and disperses the solution into droplets. Depending on the electrostatic field, ions of preferentially either positive or negative polarity are attracted to the droplet surface, resulting in a fine spray of charged droplets inside the spray chamber – hence the name electrospray. Prior to entering the vacuum chamber of the mass spectrometer through the capillary (typically a glass capillary with metal coated ends) the remaining solvent has to be removed to lay bare the ions. Therefore, the droplets are met by a counterflow of neutral, heated drying gas (*e.g.* nitrogen) evaporating the remaining solvent shell, further reducing the droplet size, and consequently forcing the surface charges in close proximity. The charge density increases at the surface until the repulsive Coulomb force overcomes surface tension, at which point the droplets disperse into smaller ones; commonly referred to as "Coulomb Explosion".[17] This mechanism repeats itself, until only bare ions are left (Charge Residue Mechanism).[7, 18-19] An alternative theory postulates that ions are directly emitted into the gas phase from the droplets, as soon as the electric field generated by the surface charge density is high enough to overcome surface tension (Ion Evaporation Model).[19-21] The ease with which emission from the surface takes place is dictated by the solvation enthalpy of the ions. Both methods are generally accepted for describing the ion formation process, however, the exact mechanism is a topic of debate.[19, 22] For effective desolvation and ionization, the right choice of a solvent is of utmost importance. Solvents that have a lower surface tension, lower heat capacity and dielectric constant like methanol and acetonitrile benefit the ESI process.

2.2.2 Storing and analyzing ions in the gas phase: quadrupole ion trap

The quadrupole ion trap (QIT) is based on the work of Paul and Steinwedel,[23] hence it is commonly referred to as "Paul trap". Ions can be accumulated over a variable time, isolated and fragmented via collision induced dissociation (CID). The basic layout of the trap consists of two end cap electrodes (entrance and exit cap) enclosing a ring electrode (Figure 3)

1. Entrance Cap
2. Exit Cap
3. Ring Electrode
4. Ion Cloud / Helium

Ions entering trap

Ions ejected to detector
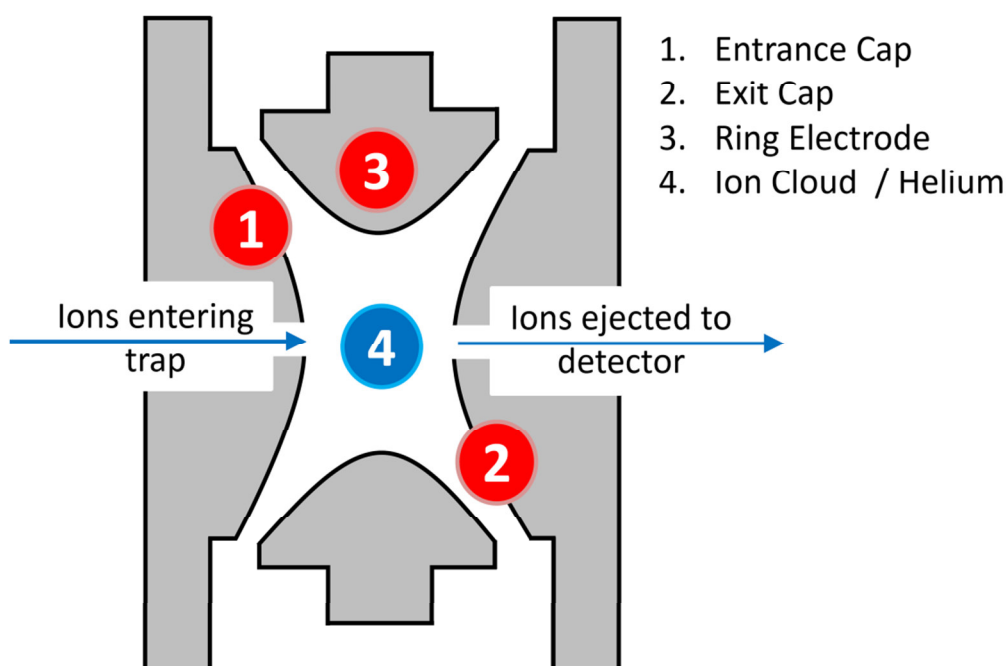
Figure 3 Schematic layout of a quadrupole ion trap.

Ions enter the trap through a hole in the entrance cap and are decelerated by collision with a damping gas (typically helium) present at a constant partial pressure ($\sim 3 \cdot 10^{-7}$ mbar). The interplay between an alternating potential (RF) applied to the ring electrode and a direct potential (DC) applied to the end caps creates a three-dimensional field, trapping the decelerated ions on oscillating trajectories. The movement of an ion in such a field can be mathematically described by the Mathieu equations.[24] Depending on the amplitudes of the applied potentials only ions of a certain mass to charge ratio (m/z) range are trapped on stable orbits (shaded area of the diagram in Figure 4), whereas ions outside the stable region of the Mathieu diagram are lost due to collision with the walls of the trap.
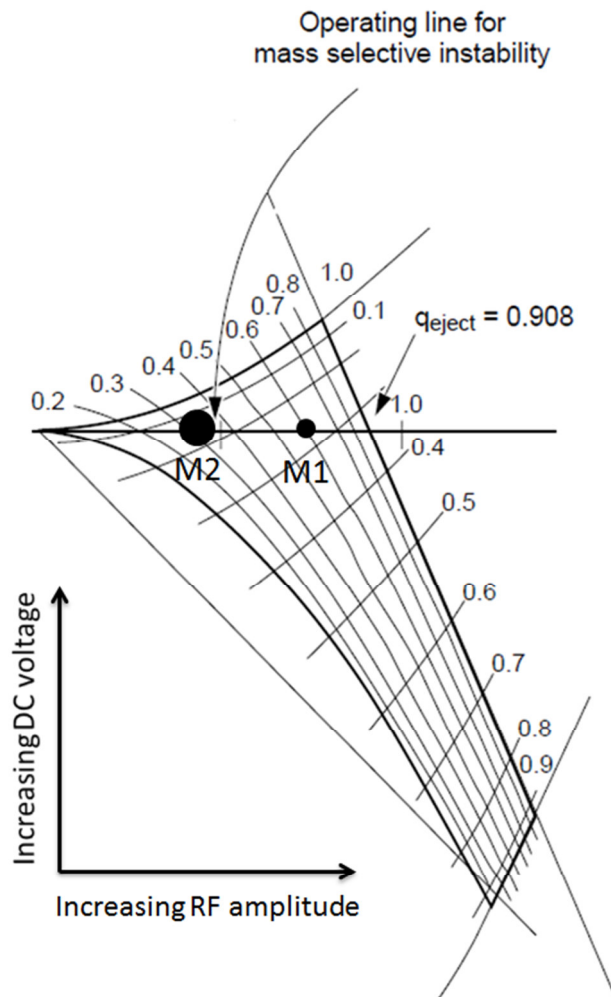
Figure 4 Mathieu stability diagram for a quadrupole ion trap.[25]

In the amaZon series of QIT mass spectrometers, mass analysis is performed by a stepwise increase of the RF amplitude, driving ions (of increasing m/z ratio) to the stability limit, at which point they are ejected from the trap through a hole in the exit cap, hitting a detector. The ion signal intensity is recorded in dependence of the RF voltage, which is then converted into a mass spectrum.

2.2.3 Bruker amaZon Speed mass spectrometer

In this thesis, a modified Bruker Daltonics amaZon Speed mass spectrometer was used (Figure 5).
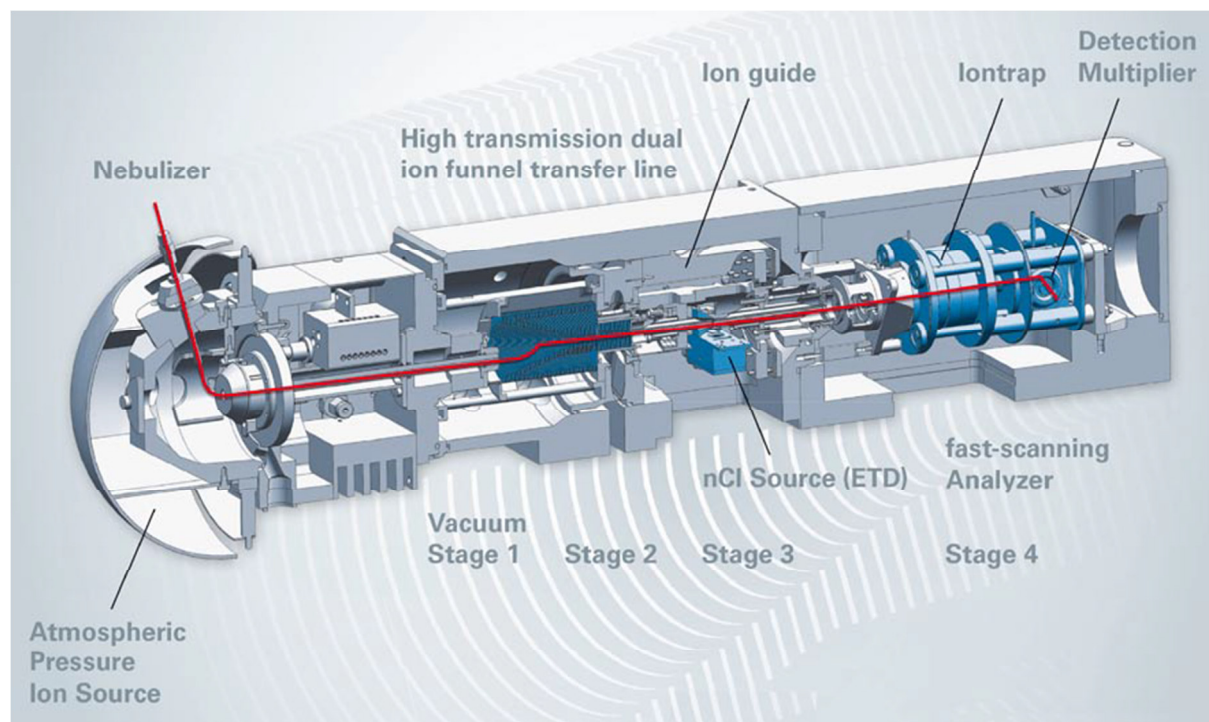
Figure 5 Scheme of an amaZon series mass spectrometer (Bruker Daltonics).[25]

The ions are formed in the ESI source (Apollo II) at atmospheric pressure, transferred and expand from the end of the transfer capillary into the first vacuum stage (~1 mbar), at which point the desolvated ions are accelerated towards a dual funnel transfer line, installed off axis with respect to the ion beam (stage 1 and 2). This particular setup serves two purposes: firstly, the dual funnel focuses the divergent ion beam, which enters the vacuum stage at a wide solid angle, due to gas expansion of the carrier gas into the vacuum chamber. Secondly, the off-axis alignment of the funnel prevents neutral molecules (mainly solute molecules) from entering the next vacuum stage by collision with the ring electrodes, reducing gas load in the subsequent stages. The ions are guided through the third vacuum stage by a high-precision multipole and are afterwards focused into the ion trap (stage 4), in which they are accumulated, stored and mass analyzed.

The amaZon Speed mass spectrometer was modified for gas phase laser spectroscopy in cooperation with Bruker Daltonics. For this purpose, the top of the vacuum chamber cover was fitted with two openings for the laser beam and additionally with a breadboard for mounting of optical elements to guide the laser beam into the high vacuum stage housing the ion trap. The openings were capped with fused silica windows, tightened by viton seals. Furthermore, two holes (∅=2 mm) were drilled on opposite ends of the ring electrode, perpendicular to the ion beam axis, creating an optical path through the ion trap center. Additionally, two mirrors were mounted beneath the trap at a 45° angle to guide the beams (Figure 6) out of the mass spectrometer.
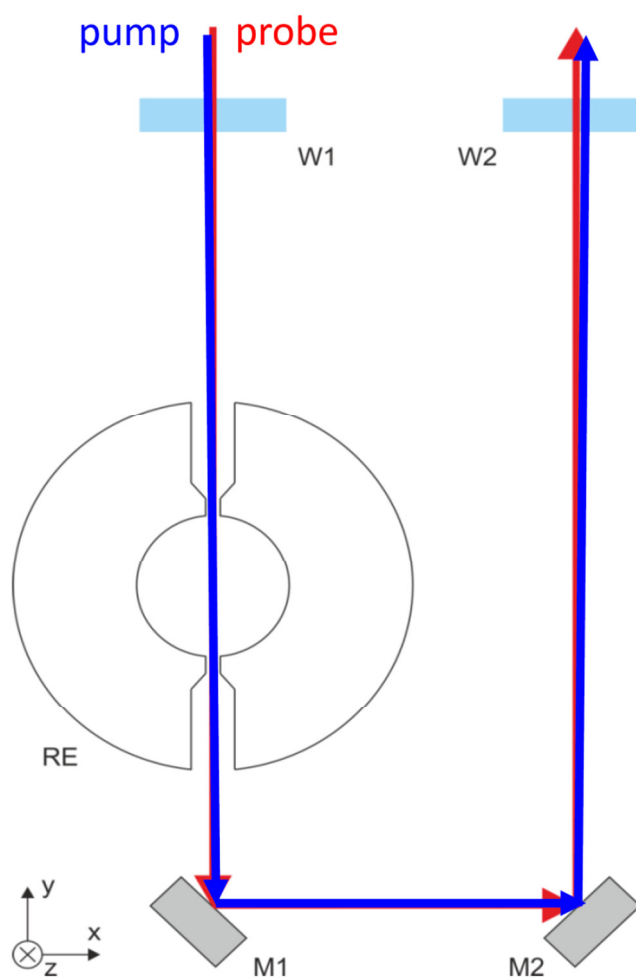
Figure 6 Schematic beam path through the modified ring electrode (RE) of the ion trap. Pump and probe beams enter and leave the vacuum chamber through two fused silica windows (W1 and W2). The mirrors M1 and M2 act as a retroreflector and guide the beam out of the mass spectrometer. Adapted from Ref. [26].

The outgoing laser pulses are directed onto an ultrafast photodiode to visualize the passing probe pulse train on an oscilloscope. This is used in order to monitor and control the phase shift of the optical chopper for a manual synchronization of the laser amplifier triggered optical chopper and the duty cycle of the mass spectrometer.

An optical shutter was installed to prevent laser pulses from passing the trap outside the designated fragmentation time window specified in the mass spectrometer control software (BrukerTrapControl 7.0). The trigger signal for the shutter was fed to the shutter controller from the mass spectrometer's auxiliary interface.

Apart from ion trap modifications, an inlet line for neutral gases was added to the mass spectrometer (Figure 7 and Figure 8). It was mainly used to leak a definite amount of neutral furan vapor in a semi-controllable manner into the high vacuum chamber. This allowed for estimating the temporal resolution at a given pump-probe wavelength combination by recording the ultrafast multiple-photon ionization of furan, which is equivalent to the cross correlation function (ccf) of the laser pulses.[27-28]
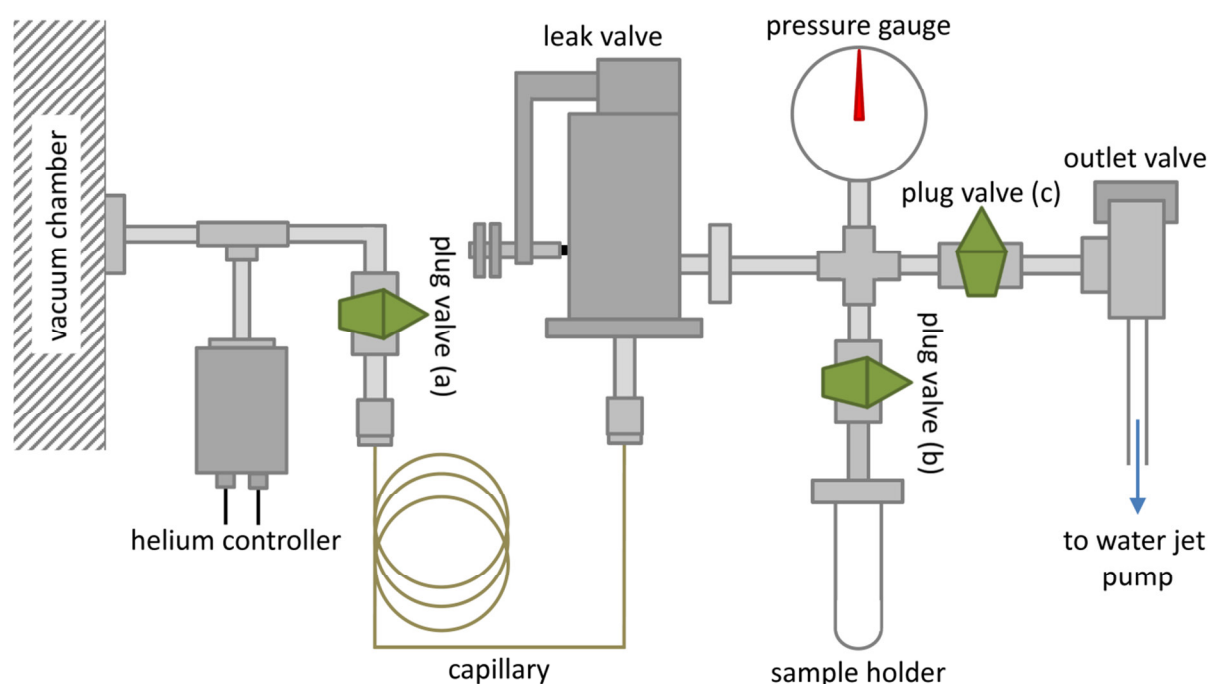
Figure 7 Scheme of the neutral gas inlet line added to the amaZon Speed mass spectrometer. Adapted from Ref. [29].

A union tee was mounted to the high vacuum chamber (stage 4) of the mass spectrometer, which allowed admixture of furan to the helium buffer gas, introduced via the helium controller to the trap. The furan vapor pressure was reduced by means of an ultrahigh vacuum leak valve in combination with a PEEK (polyether ether ketone) capillary.
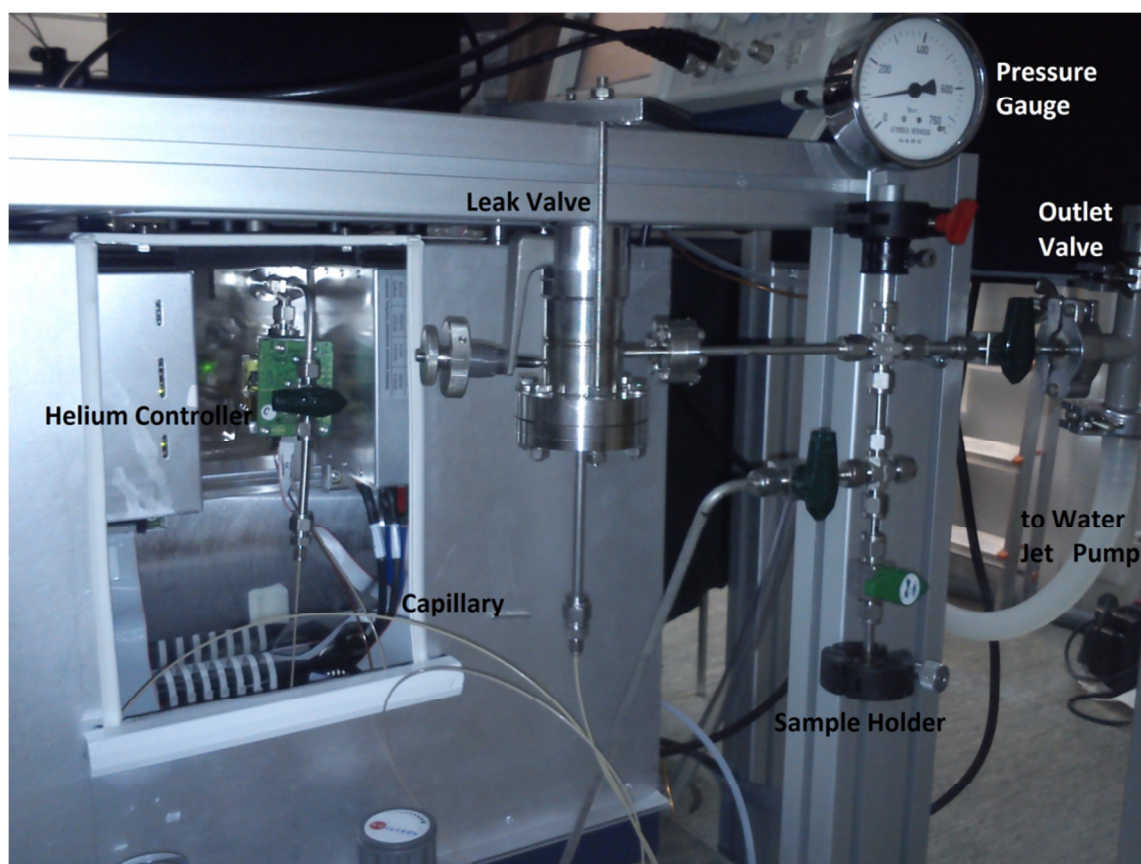
Figure 8 Gas inlet line for neutral gases.[29]

Furan was introduced using the following procedure:[29] With the leak valve closed, a small amount of furan is placed inside the sample holder. After freezing the sample with liquid nitrogen, plug valves (b) and (c) are opened and the volume evacuated by a water jet pump. Closing valve (c) and melting the furan inside the holder loads the volume before the leak valve with the neutral gas at its vapor pressure (~700 mbar at 21 °C). The leak valve is then opened to introduce a definite amount of furan into the vacuum chamber, which is monitored within the operating software of the mass spectrometer. A partial pressure of 2-3·10^{-7} mbar of furan is sufficient to produce a satisfactory cross-correlation signal over a wide spectral range of the pump pulse.

2.3 Chirped pulse amplification femtosecond LASER system: the Wyvern 1000™

2.3.1 A source for femtosecond laser pulses: mode-locked Ti³⁺:sapphire laser

With the advent of reliable and stable titanium-doped solid-state lasers in 1986,[30] dye lasers have been largely replaced as a source for ultrashort laser pulses. The gain medium in such a solid-state laser consists of sapphire (monocrystalline Al_2O_3) doped with Ti^{3+} ions. Sapphire serves as an excellent crystal lattice, due to its thermal conductivity properties, reducing thermal lensing effects. Ti^{3+} as a dopant has a very large gain bandwidth, *i.e.* the frequency range for which optical amplification in a gain medium can occur, resulting in a large number of optical frequency modes oscillating within the resonator (Figure 9); a prerequisite for generation of ultrashort laser pulses by frequency mode-locking.
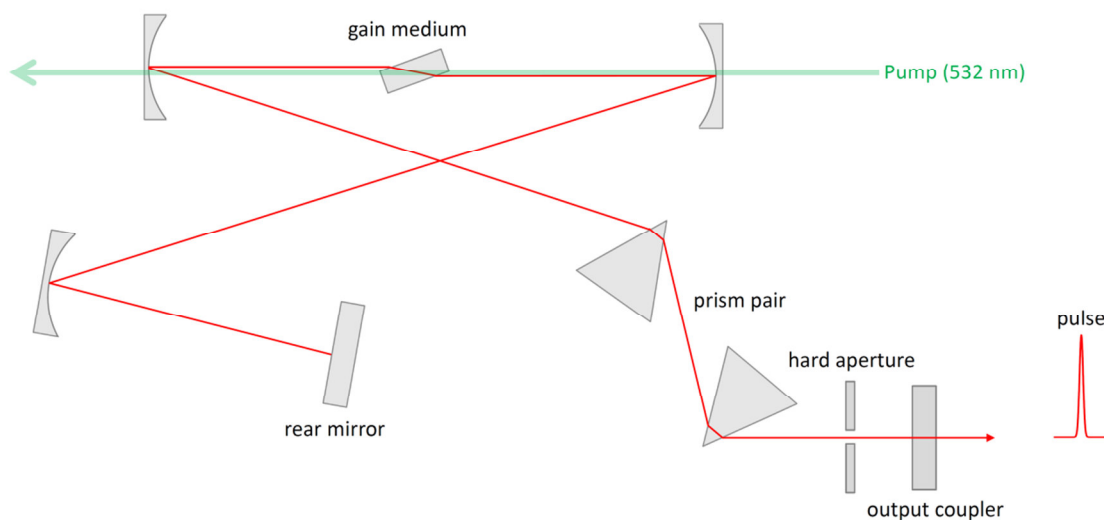
Figure 9 Schematic resonator setup of a passively mode-locked fs solid-state laser.

The gain medium is a Ti^{3+}:sapphire crystal, which is often pumped by a diode pumped solid state (DPSS) Nd^{3+}:YAG laser (YAG: yttrium-aluminium garnet). The resonator consists of the gain medium placed between an output coupler mirror (a partially reflective mirror) and a rear mirror. Typically a prism pair is placed in the optical path to counteract chromatic dispersion, causing *i.e.* pulse broadening, introduced by the gain medium and other optical components. The mode of operation of such a resonator is then as follows: a large bandwidth of optical frequencies is emitted by the pumped gain

medium, which oscillate within the resonator. If these (longitudinal) modes exhibit a fixed phase relationship, the electric fields of all frequency components add up constructively to a maximum of the total field strength in regular time-intervals, and destructively in between these temporal positions (Figure 10).
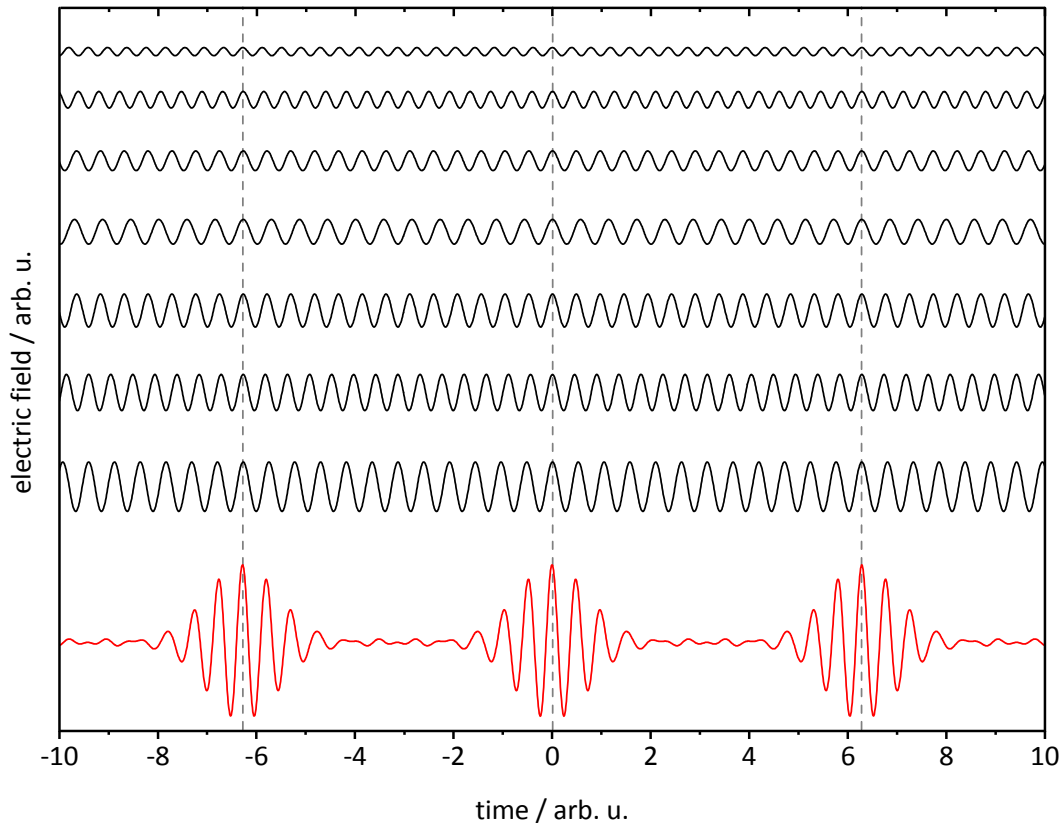
Figure 10 Constructive interference of several longitudinal modes with different frequencies and fixed phases leads to the formation of periodic pulses in the time-domain.

Each time the pulse "circulating" in the resonator hits the output coupler, a pulse is emitted from the oscillator. The length of the resonator not only dictates the number of oscillating longitudinal modes, but also the repetition rate (typically 80-100 MHz) at which the oscillator emits. For good pulse stability, it is crucial that only modes with a fixed phase relationship are allowed to oscillate within the resonator, whereas modes with random phases are suppressed. In passively mode-locked oscillators, mode suppression is achieved by means of *e.g.* a saturable absorber, which may also serve as the rear mirror of the resonator (SESAM: semiconductor saturable absorber mirror). The mode of operation involves absorption saturation of the SESAM by the leading edge of the pulse, thus temporarily reducing the losses experienced by the pulse. From Figure 10, it is clear that only modes with a fixed phase add up constructively to high

total electric field strengths, saturating the absorber, whereas modes with a random phase experience high losses at the SESAM.

A different technique for passive mode-locking, which is used in the Wyvern 1000™, involves self-focusing in the gain medium. Self-focusing is based on the Kerr effect and occurs due to nonlinear response of a medium traversed by intense light. Simply put, the refractive index n of a non-linear medium (with the non-linear refractive index n_2) is dependent on the intensity I of the propagating light according to $n = n_0 + n_2 \cdot I$, with n_0 being the ordinary refractive index. Thus high optical intensities lead to tighter focusing and a better overlap of high intensity modes (*i.e.* mode-locked modes) with the pump laser inside the gain medium, increasing the rate of stimulated emission of these modes (soft aperture operation). Additionally, a physical aperture can be placed inside the resonator to "peel off" off-phase modes, which are thus not, or only weakly focused, resulting in higher losses (hard aperture operation).[31-32]

2.3.2 Chirped pulse amplification

Ultrashort pulses can exhibit very high optical peak intensities when amplified, even at moderate pulse energy. This may lead to non-linear effects in the amplifying gain medium, causing various pulse distortions, such as optical and temporal broadening or, in the worst case, dealing damage to optical elements, including the gain medium itself. This is avoided by temporally stretching the pulses (introducing a "chirp"), thus reducing peak power, prior to amplification. The pulses are chirped at a strongly dispersive medium (a grating pair), *i.e.* the spectral components of the pulse are retarded with respect to each other, meaning that the instantaneous frequency of pulse is time-dependent. In an up-chirped pulse, for example, the instantaneous frequency rises, *i.e.* the low frequency components of a pulse are at the leading edge, whereas the higher frequency modes arrive later (Figure 11).
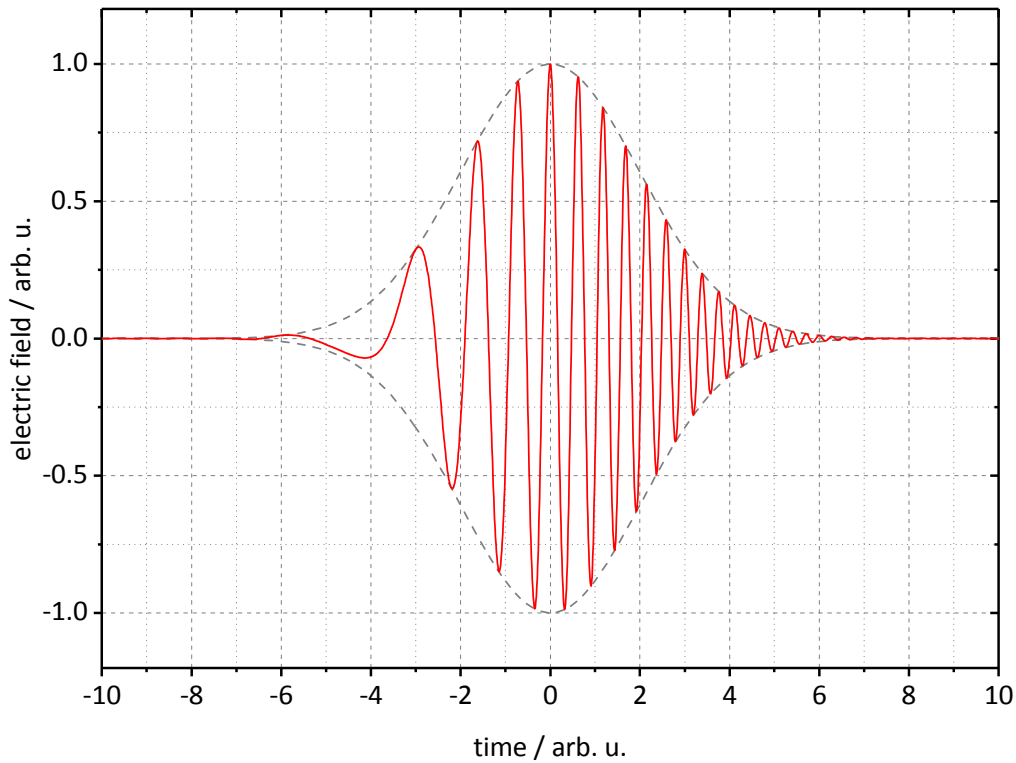
Figure 11 Example for a linearly up-chirped pulse, *i.e.* the instantaneous frequency increases in time.

The temporally stretched pulse is seeded into an optical resonator, containing the amplifier gain medium (Ti^{3+}:sapphire). By use of an electro-optical switch (usually a combination of a Pockels Cell (PC), a quarter-wave plate ($\lambda/4$) and a thin film polarizer (TFP)), a single pulse is trapped in the resonator for a designated amount of time, undergoing several round trips in the resonator, while being strongly amplified within the gain medium, which is pumped separately by a high-power frequency doubled Nd^{3+}:YAG laser. Afterwards, the optical switch releases the amplified pulse, which is subsequently temporally compressed in a dispersive compressor (again a grating pair), counteracting the chirp introduced in the stretcher. The chirped pulse amplification (CPA) scheme is illustrated in Figure 12.
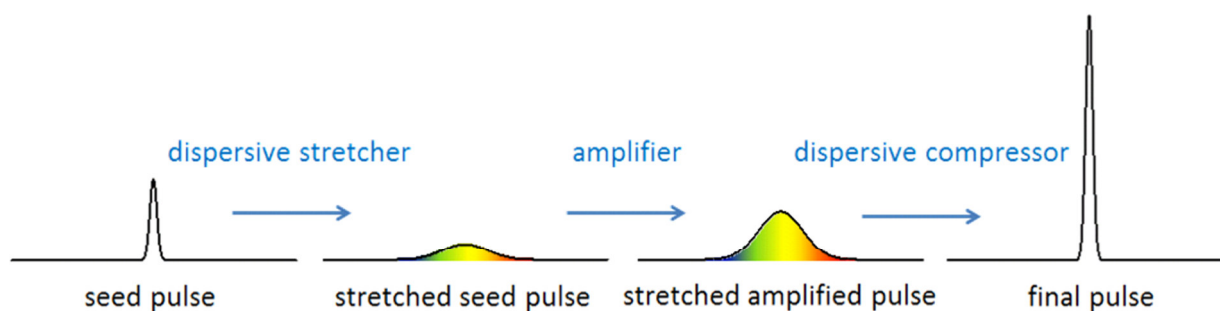
Figure 12 CPA scheme for the amplification of ultrashort laser pulses.

In this thesis, an fs oscillator and single stage regenerative amplifier laser system (Wyvern 1000™ series, KMLabs) was used for pulse generation and amplification. In this particular setup, the amplification crystal is cryogenically cooled (to -230 °C), reducing pulse distortion effects and the risk of damaging the amplifier gain medium. This allows for the generation of ~50 fs pulses with energies of up to 4.0 mJ at a central wavelength of ~780 nm and a set repetition rate of approximately 1 kHz. In the following, a rough amplifier scheme (Figure 13) and description of the mode of operation is presented.

The seed pulses are generated in the oscillator by passive mode-locking of the resonator modes emitted from the laser gain medium (Ti^{3+}:sapphire), which is pumped by a frequency doubled, diode pumped Nd^{3+}:YAG laser (Opus 532). At every round trip a part of the mode-locked pulse, oscillating between the rear-mirror (O-RM) and the output coupler (OC), is emitted and directed (passing over M1) into the stretcher. The combination of several broadband mirrors and a grating (S-G) introduces a chirp, stretching the seed pulse in time and concomitantly lowering the beam plane. The pulse leaves the stretcher in the opposite direction to the incoming pulse at lowered altitude. It is picked up by M1 and directed into the amplifier stage via M2. High voltage is applied to the PC, which then serves as a quarter-wave plate and, in combination with another quarter wave plate ($\lambda/4$), rotates the plane of polarization of a single incoming seed pulse from vertical to horizontal. The change in polarization prevents the pulse from passing the thin film polarizer (TFP1), trapping the pulse inside the amplifier resonator cavity consisting of A-RM1 and A-RM2. The trapped seed pulse oscillates in the resonator, passing the amplifier crystal (Ti^{3+}:Sapphire, AC), contained in an evacuated cryo-cell and pumped by a second diode pumped (DP) frequency doubled Nd^{3+}:YAG laser (LDP-200 MQG). After several round trips, the plane of polarization is rotated (by switching off the PC), allowing the amplified pulse to pass TFP1 and leave the amplifier resonator via M2. The pulse passes the Faraday rotator and is reflected at a second thin film polarizer (TFP2) towards the compressor, passing over M3. In the compressor, a grating pair (C-G1 and C-G2) counteracts the chirp initially introduced in the stretcher. The roof mirror (M4) lowers the altitude of the beam plane, allowing M3 to pick up the amplified pulse and guide it out of the amplifier.

Figure 13 Scheme of the Wyvern 1000™ fs-laser system consisting of a Ti³⁺:sapphire oscillator and cryogenic Ti³⁺:sapphire regenerative ultrafast amplifier.

The output from the amplifier was split at two beam splitters in effectively three arms, according to the scheme in Figure 14.
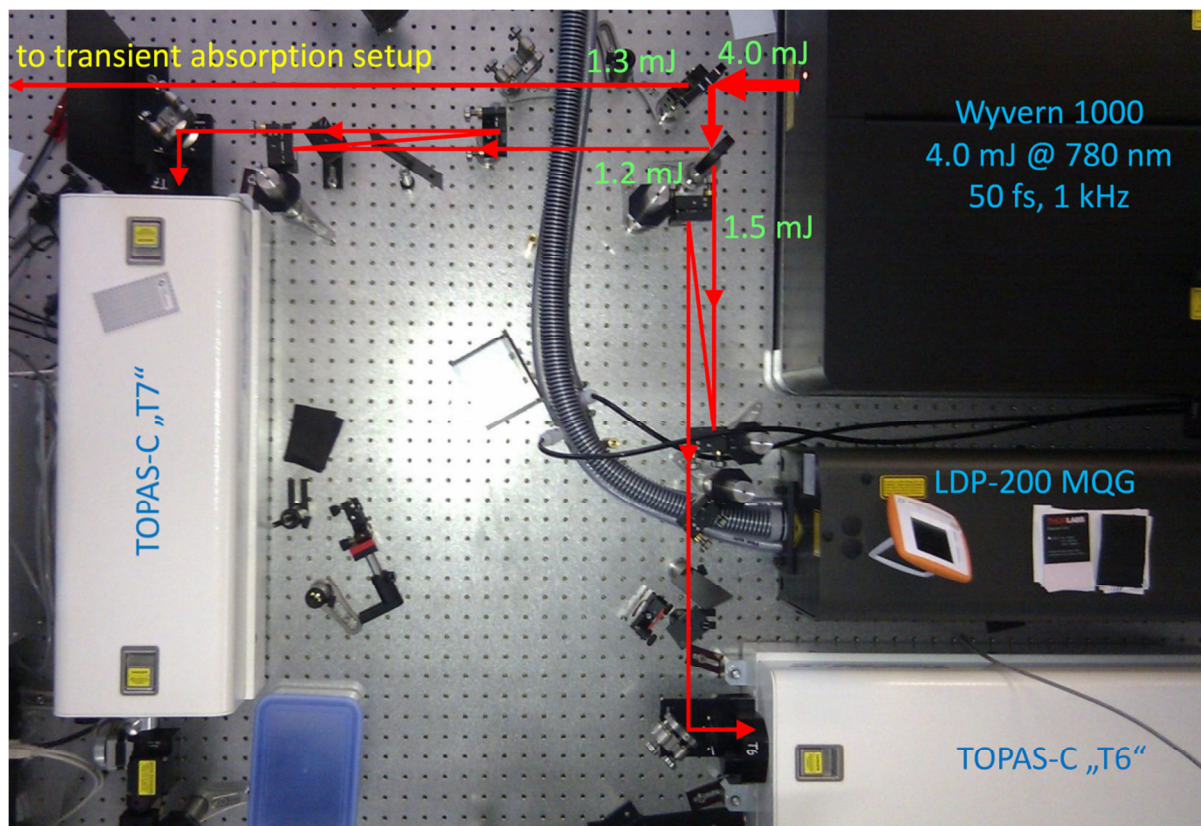
Figure 14 Scheme depicting the splitting of the amplifier output beam into three arms using two sequenced beam splitters.

One of the arms (1.3 mJ) was used for whit light continuum (WLC) generation in liquid phase transient absorption (TA) spectroscopy, which is of no relevance for this thesis. The other arms (1.2 mJ and 1.5 mJ) were directed to the OPA systems (TOPAS-C T6 and T7) for pump and probe pulse generation in tPF experiments. Schematic layout and mode of operation of the TOPAS-C systems will be briefly described in the following (Figure 15).

BS: beam splitter
WLG: white-light continuum generator
NC: non-linear crystal
D: beam dump
DM: dichroic mirror
DS: delay stage

① pump from amplifier
② pump pre-amplification stage
③ pump amplification stage
④ seed white-light generation
⑤ white-light continuum (WLC)
⑥ pump WLC amplification
⑦ pre-amplified signal
⑧ residual pump + signal + idler
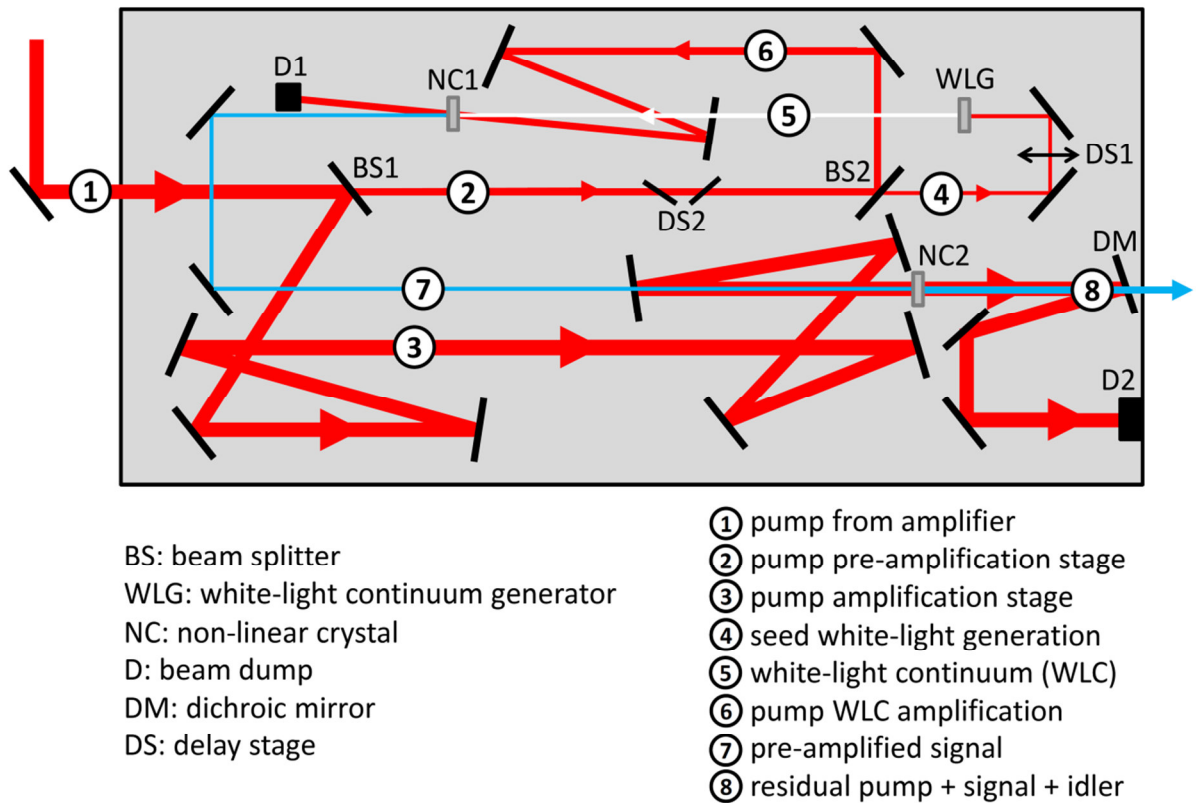
Figure 15 Schematic layout of the TOPAS-C system for optical parametric amplification of white-light continuum. Widening and collimating optical elements were omitted for clarity.

The pump beam from the amplifier (1) is steered into the TOPAS-C and split at the first beam splitter (BS1) into a low energy (2) and high energy (3) beam. The transmitted beam (2), ~30-70 µJ of energy, hits a second beam splitter (BS2) producing a low energy beam (4), which is focused on a sapphire plate (WLG) to generate white-light continuum (5), and a beam (6) of higher energy (80% of the 30-70 µJ) used for pre-amplification of the white-light. (5) is temporally stretched and intersected with (6) non-collinearly in the non-linear crystal (NC1), generating a signal and an idler beam. The idler and residual (6) are dumped (D1), whereas the pre-amplified signal (7) is collimated and overlapped with the bulk of the initial pump beam (3) in a second non-linear crystal (NC2). The residual pump (3) is either reflected at a dichroic mirror and dumped (D2) or used together with the generated signal and idler beams (8) in subsequent frequency mixing stages.

The wavelength of the signal beam (7) generated in the pre-amplifier corresponds to the WLC (5) wavelength overlapped with the pre-amplifier pump (6) in NC1 and is controlled by changing the delay of the WLC with respect to the pump via a delay stage

(DS1). Additionally, NC1 is rotated for best phase matching of the intersected white-light and the pump. The delay between the pre-amplified idler (7) and the pump of the amplifier stage (3) is controlled by a second delay stage (DS2) consisting of two Brewster angled plates, affecting the intensity of the signal and idler beams generated in NC2. Rotation of NC2 dictates parametric amplification in NC2. By changing the positions of NC1 and NC2 in combination with the two delay stages (DS1 and DS2), the effectively generated signal and idler beams (in NC2) cover a wavelength range of 1140-1620 nm and 1520-2500 nm, respectively. The tuning range is extended by two external frequency mixers (converters) located at the output of the TOPAS-C systems. Beta-barium borate (BBO) crystals of type I phase matching are used for second harmonic (SH) or fourth harmonic (FH) generation of the signal and idler waves and the SH of the sum frequencies (SF) generated from the pump in combination with either the idler (I) or the signal (S) beam. Sum frequencies are obtained by mixing the pump with the idler (SFI) in a BBO crystal of type I phase matching or mixing the signal with the pump in a BBO crystal of type II phase matching. The accessible wavelength ranges by various combinations of the output waves are summarized in Table 1.

Table 1 Accessible wavelength ranges by sum frequency (SF) and higher harmonic (second harmonic SH, fourth harmonic FH) generation of the signal (S) and idler (I) waves in combination with the residual pump beam from the amplifier.

wave	wavelength range / nm
S	1520-2500
I	1140-1620
SHI	795-1160
SHS	570-810
SFI	525-580
SFS	472-527
FHI	400-485
FHS	285-400
SHSFI	262.5-287.5
SHSFS	236-263.5

A pair of wavelength separators we attached in sequence to the last mixer stage to filter residual radiation passing the mixers from the desired pulse wavelength. These separators only operate in a limited wavelength range and have to be exchanged to match the desired output wavelength (Table 2 and Figure 16).
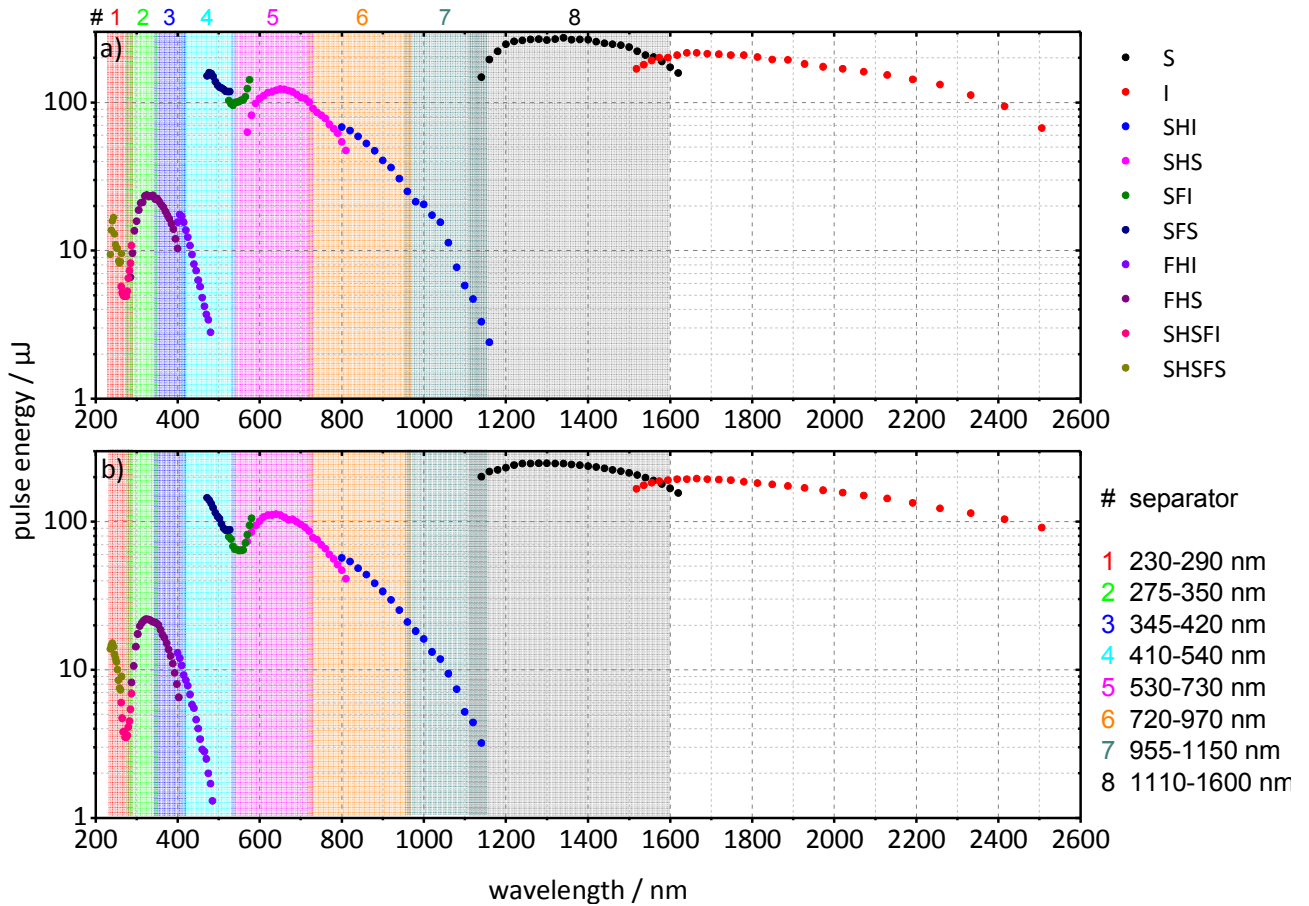
Figure 16 Wavelength dependent pulse energies (measured after separators) of the waves generated in TOPAS T6 **(a)** and T7 **(b)**. Colored areas denote the wavelength range of the utilized wavelength separators.

2.4 Experimental methods

2.4.1 UV/Vis photofragmentation

Laser induced fragmentation in combination with mass spectrometry is a versatile tool to perform structural investigations on ionic systems under isolation. The major appeal of a gas phase approach is the ability to mass select the desired species and additionally the lack of a solvent environment, making theoretical modeling less costly. The fragmentation of ions by laser irradiation at fixed frequencies (either using infrared (IR) or ultraviolet (UV) light sources) is an attractive alternative to the commonly applied collision induced dissociation (CID), especially in setups where collisional gas cannot be used[33] or fails to produce a comprehensive fragmentation pattern, due to kinetic limitation of the fragmentation process, such as in sequencing of larger oligopeptides.[34] In addition, the tunability of laser systems allows for recording of photodissociation action spectra, analogous to absorption spectra in solution, by monitoring the fragmentation as a function of photon energy, *i.e.* photon wavelength.

Gas phase fragmentation pathways may differ depending on the excitation method. In CID, excitation occurs via collision of the electrostatically-accelerated ionic system with a quasi-stationary neutral buffer gas. Upon collision, energy is transferred to the internal heat bath of the target molecule until energy buildup exceeds the dissociation threshold and the molecule undergoes fragmentation. Usually, the energy is introduced into the molecule by low energy collisions (with small neutral molecules as background gas, such as helium), resulting in a slow energy buildup, so that molecules have time to rearrange and explore the lowest fragmentation pathways (slow heating).[35] A similar process takes place by infrared-multiple photon dissociation (IRMPD), for which consecutive (non-coherent) absorption of typically several IR photons is necessary to result in fragmentation of molecules.[36-37] UV/Vis photoexcitation, on the other hand, instantaneously transfers a large amount of energy to the molecule by absorption of a single photon ("fast heating") (Figure 17).[38]
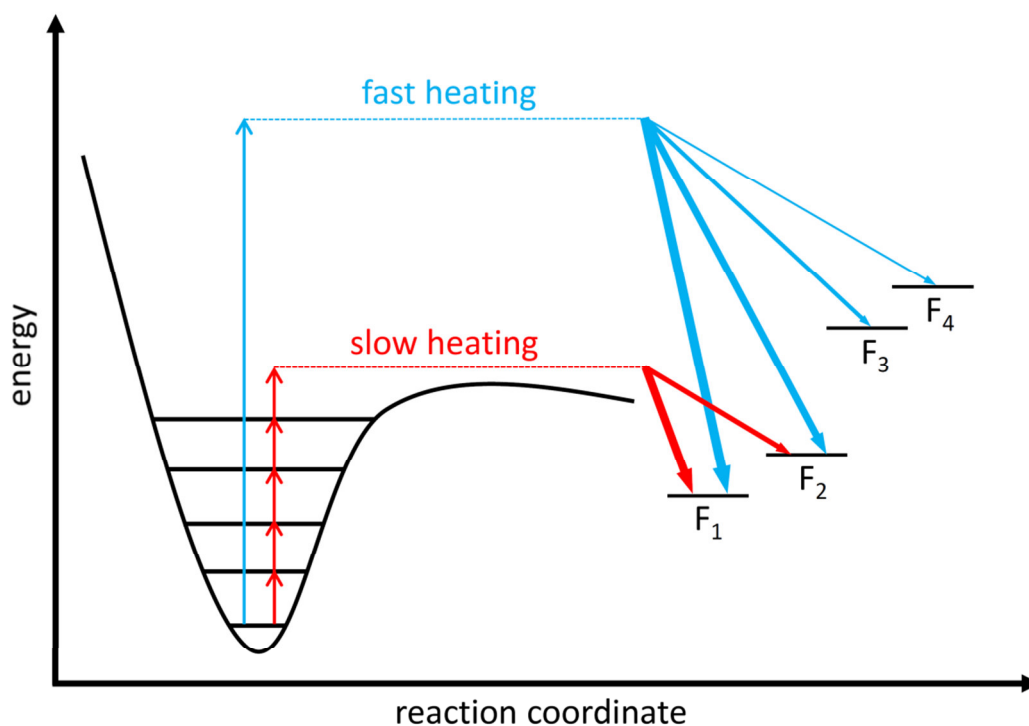
Figure 17 Scheme depicting fragment ion formation by UV/Vis PF (blue, "fast heating") and CID or IRMPD (red, slow heating). Boldness of arrows denotes relative fragment ion intensities formed upon the respective dissociation process. For a slow heating process, usually only lowest energy fragment products (*e.g.* F_1 and F_2) are formed, whereas in a fast heating process additional fragment channels above the dissociation threshold may be accessed (*e.g.* F_3 and F_4). Adapted from Ref. [38].

In contrast to CID and IRMPD, UV/Vis PF may occur either barrierlessly from an excited state or indirectly from the ground state. In the former case the molecule is excited to a repulsive excited state potential from which it dissociates rapidly (Figure 18a).[39] Thus fragment products may be observed, exclusive to a dissociative coordinate of the respective excited state. Indirect dissociation, on the other hand, occurs if the ions are excited to a bound electronic excited state (Figure 18b). Depending on the potential barrier, the ions may still fragment from the excited state directly; although less likely, if coupling to the ground state is efficient. Otherwise, the ions undergo internal conversion (IC) to a highly vibrationally excited (hot) ground state from which dissociation takes place. Coupling of the excited state to the ground state dictates the internal energy stored in specific internal degrees of freedom, and thus the rate of fragmentation for the respective channel, influencing the intensities of occurring fragment ion signals. If the internal energy after photoexcitation and subsequent IC does not exceed the dissociation barrier, a second photon may be absorbed,[40] although possibly with

reduced probability, as the Franck-Condon factors are typically smaller for non-resonant transition from a hot ground state to the excited state. A possible multiple-photon process for UV/Vis dissociation can be identified by measuring the dependence of fragmentation on the laser pulse energy. Although fragmentation by non-coherent multiple-UV/Vis-photon absorption is conceivable, it should generally result in a lower fragmentation yield than for one-photon PF (as discussed above).

From extensive comparison of UV/Vis PF to CID fragmentation patterns in this thesis, the dominating process is believed to be indirect fragmentation from a hot ground state. This can be an issue for recording of one-color PF spectra, as fragmentation from the ground state proceeds with a rate on the same order at which collisions with the helium buffer gas take place (µs-ms), resulting in thermalization of hot ions, and thus signal suppression in PF spectra. Fragmentation upon longer wavelength excitation is especially prone to collisional quenching, due to an inherently lower internal energy imparted to the ions.
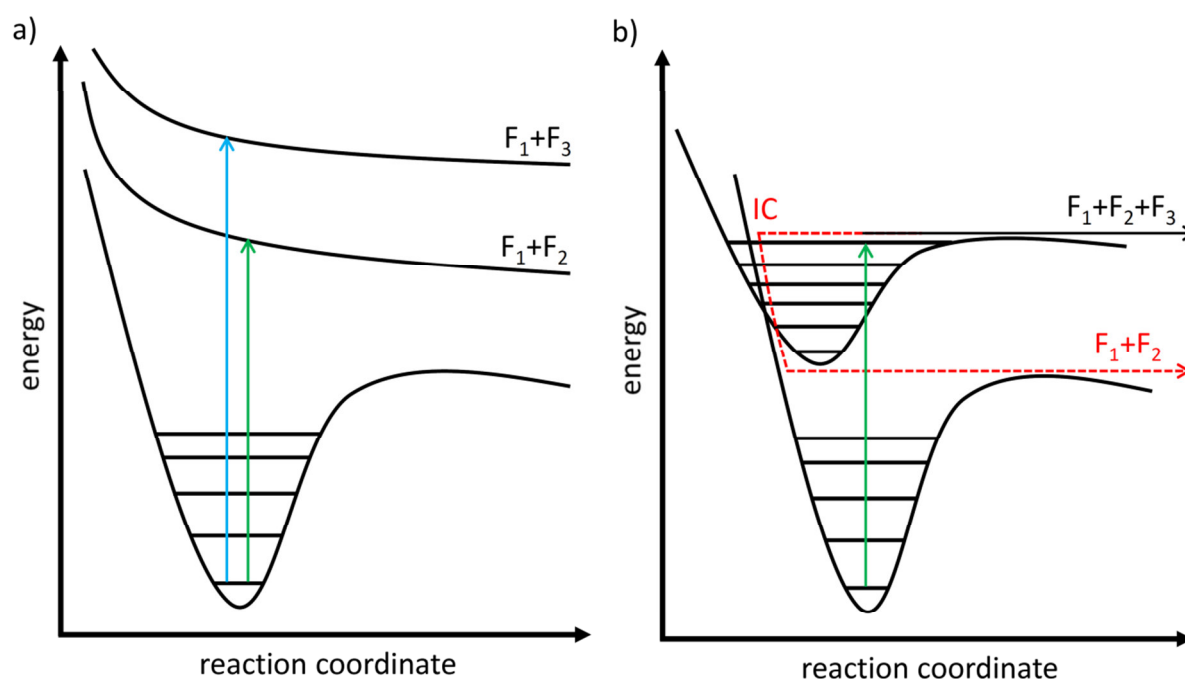
Figure 18 Scheme depicting fragment ion formation by UV/Vis PF from a repulsive excited state **(a)** and a bound excited state **(b)**. From a bound state, the target ion either dissociates directly or after IC to the hot ground state. Depending on the dissociation barrier in the excited state, the former or the latter process may prevail, resulting in different fragment ions observed.

2.4.2 Time-resolved UV/Vis photofragmentation

Monitoring the evolution of fragment ion formation in time is an extension to photo-induced dissociation, which is realized by a pump-probe scheme. The advent of ultrafast lasers paved the way for time-resolved spectroscopy on the timescale of chemical reactions (femtochemistry) pioneered by A. H. Zewail (Nobel prize in chemistry in 1999).[41] In these early experiments a pump-probe scheme was employed to study photodynamics of small, neutral molecules in the gas phase by multiple-photon-ionization on the pico- and femtosecond timescale.[42-43] The molecules were excited to a higher electronic state by a pump laser and subsequently ionized from the excited state by probe photon absorption. Although the photoionization scheme is common in pump-probe spectroscopy, it is generally not applicable to cationic species, as the higher ionization potentials of cations are difficult to overcome. Hence a different detection scheme is employed, monitoring the fragmentation efficiency as a function of pump-probe delay. This particular scheme was first realized by Jouvet *et al.* in their studies on protonated tryptamine[44] and tryptophan[45] with time-of-flight (TOF) detection of fragment ions, and later expanded to commercially available ion trap mass spectrometers by Weinkauf *et al.*[27-28]

The transient pump-probe PF (tPF) method is based on interrogating the population of a resonantly excited (pump step) molecular ensemble, *e.g.* excited into the first electronic excited state S_1, by probe photon absorption, inducing a subsequent transition to higher lying electronic states ($S_n \leftarrow S_1$), which is accompanied by an increase in fragmentation yield. As discussed for the steady-state case, the molecules do not necessarily fragment directly from the respective S_n state, but later-on after IC from a highly vibrationally excited ground state. In ion trap setups, fragmentation from the ground state takes place in competition to collisional quenching with the helium buffer gas on a µs-ms time scale, depending on the partial pressure.[46] The increase in fragmentation rate and yield stems from the increase in internal energy of molecules after pump+probe excitation with respect to pump-only excitation. Noteworthy, the probe process is not necessarily controlled to be resonant and assumed to be of multi-photonic character, thus its underlying transitions to higher-lying electronic states are in general unknown. However, when the molecular system undergoes electronic relaxation processes (*e.g.* IC or intersystem crossing, ISC) the cross section of the probe pulse is altered between the

different states, usually resulting in a decreased absorption cross section upon formation of lower lying electronic states. This is attributed to three effects: 1) a dilution of population, due to population of several vibronic states, 2) a loss of propensity, *i.e.* Franck-Condon overlap, for these vibronic states towards higher-lying electronic states, and 3) the multiple-photon character of the probe absorption process, which makes transitions from lower electronic states less likely. Figure 19 depicts a simplified tPF scheme for an arbitrary system, in which IC is the only relaxation channel after photoexcitation.
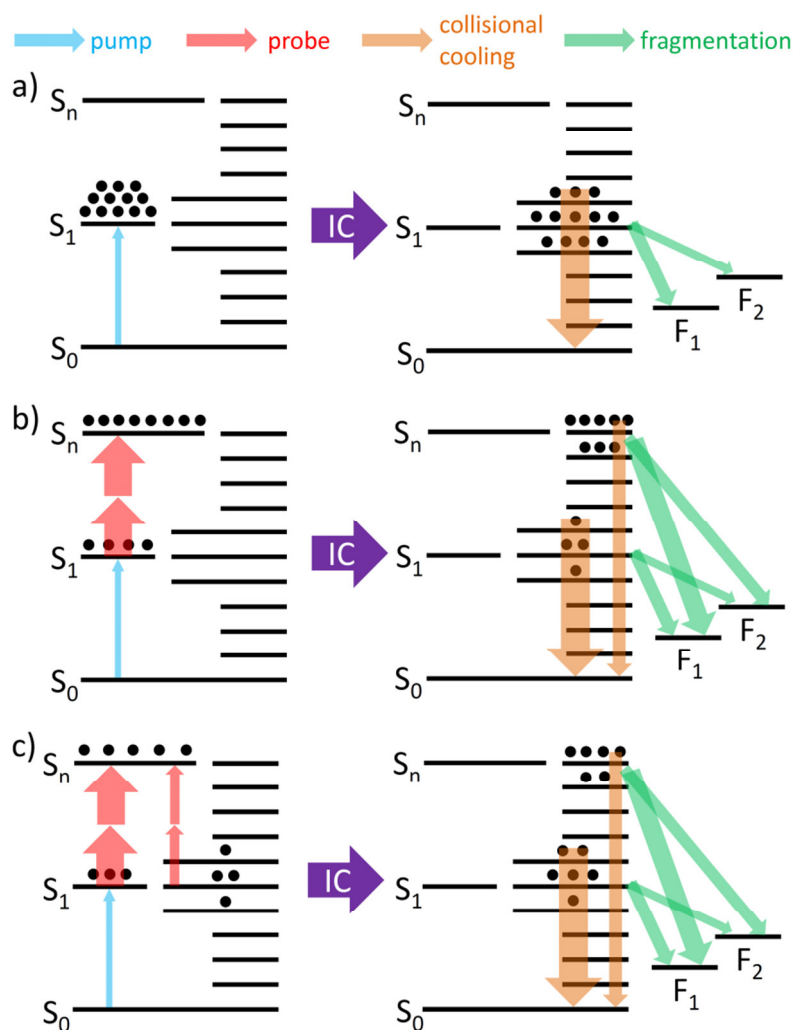
Figure 19 tPF detection scheme. Arrow colors denote different radiative/non-radiative processes, whereas boldness represents the process rates (bolder arrows indicate higher rates or higher probabilities). Dots represent ion population in the respective electronic/vibrational state. For the sake of clarity, vibrational states of the excited states are not illustrated. Ion population is depicted for three cases: **(a)** negative pump-probe delay, *i.e.* probe arrives prior to resonant pump-excitation, **(b)** coherent pump-probe excitation at zero time delay and **(c)** positive pump-probe delay, *i.e.* probe arrives after pump-excitation.

In case a), the ion population is excited resonantly to the S_1 electronic state and decays via IC to the hot ground state S_0 by coupling to vibronic states from which the excited ions fragment, forming two different fragment products (F_1 and F_2). The relative fragmentation yields depend on the internal energy, with F_2 exhibiting a higher barrier for fragmentation. Fragmentation proceeds on a longer timescale (µs-ms) than the electronic decay (ps) and is in competition with thermalization of the hot ions by collisional quenching. No excitation to higher electronic states (S_n) by probe photon absorption takes place. In case b) a majority of the pump-excited ion population is elevated to a higher lying electronic state S_n, by (multiple-)probe-photon absorption. IC takes place from either the S_1 or the S_n state, resulting in two populations in S_0 with distinctly different internal energies. The "hotter" population is less susceptible to collisional deactivation, thus higher total fragmentation yields are observed with respect to pump-only excitation (at the same pump energy). Case c) depicts a scenario, in which the probe pulses arrive sometime after excitation with pump-photons, so that the system had time to partially relax; in this case to the S_0 state. Only the ions in the S_1 state have a relatively high cross section for multiple-photon absorption of the probe photons, whereas ions in the hot S_0 state are less likely to absorb probe photons (ion population is "diluted" over several vibrational states, exhibiting smaller Franck-Condon overlap). Compared to b) the ion population in the "hotter" S_0 state is smaller. Hence the total fragmentation yield is also lower. With increasing pump-probe delay, the effective ion population in the S_n state diminishes, further reducing the fragmentation yield. The delay dependent fragment ion intensities thus map the lifetime of the S_1 state. The fragment signal evolution sketched for a simple, arbitrary case in Figure 19 can be applied to any system, which may exhibit various relaxation channels of the excited state population.

Although the detection scheme is akin to the one employed by Jouvet *et al.* and Weinkauf *et al.*, the experimental setup utilized in this thesis has a major advantage over the referenced setups, as the OPA systems allow for tuning of the pump and probe pulses in a broad spectral range individually, not relying on the fundamental (~800 nm) of a Ti^{3+}:sapphire laser and its higher harmonics for generation of suitable laser pulses. Thus a wider assortment of molecules can be investigated, such as organic dyes with extensive π-systems or charge transfer processes in transition metal complexes, which require pump wavelengths in the visible region.

2.4.3 Standard measurement procedures and data processing

Mass spectra and CID mass spectra were recorded in enhanced resolution mode (8100 m/z /s at a mass resolution of 0.2 fwhm / m/z). The mass range was adjusted to the respective compound under study; however, the lower boundary was typically left at m/z 50. Sample solutions were prepared at a concentration of $5 \cdot 10^{-7}$ to $5 \cdot 10^{-6}$ mol/L and continuously infused into the spraying chamber by a Hamilton® syringe and a syringe pump at a set flow rate of 120 µL/h. The temperature of the nitrogen drying gas was set to 180 °C at a flow rate of 4-5 L/min. Nebulizer pressure and needle potential were adjusted to yield the highest and most stable precursor ion signal. Typical values were 5 psi (345 mbar) and 4.4 kV for the pressure and needle potential, respectively. The "target mass" option within the instrument software was used to tune the transfer parameters. The "target mass" was in general set to the m/z ratio of the compound under investigation. Accumulation time of the ions was adjusted so as not to exceed a total ion count of ~ 1-$1.5 \cdot 10^{5}$. The helium buffer gas partial pressure inside the trap was approximately $3 \cdot 10^{-3}$ mbar. The mass spectrometer was controlled by the BrukerTrapControl 7.0 software and data analysis was performed using BrukerDataAnalysis 4.0.

PF and tPF measurements were performed using the modified Bruker Daltonics amaZon Speed ion trap mass spectrometer in ultrascan mode (32.500 m/z /s at a mass resolution of 0.4 fwhm / m/z). Two non-collinear parametric amplifiers of white-light continuum (TOPAS-C, Light Conversion) pumped by a CPA ultrafast regenerative amplifier (Wyvern 1000™, KMLabs, 4 µJ, 780 nm, Δt=50 fs, controlled by Dragon Master V3.00 software) provided a source of tunable radiation in the UV/Vis and NIR region in order to record static (multiple-photon) PF and tPF spectra. The output from the T7 was used for generation of pump pulses (UV/Vis) in both static and transient experiments, whereas the T6 provided exclusively probe pulses in the near infrared (NIR) region (1200 nm).

Steady-state (multiple-photon) PF spectra were obtained by recording the PF mass spectra at an individual set wavelength one at a time. The output wavelength of the T7 was set by the WinTOPAS v3.2.35 software, checked using an AvaSpec USB high resolution fiber optics spectrometer (ULS3648, Avantes) and, if necessary, corrected by adjusting the Delay2 in the WinTOPAS software. Pulse energies (1-2µJ) were kept

constant across the whole recorded spectral range. For this purpose, the energies at a given wavelength were monitored on an energy meter (Vega, Ophir) equipped with a pyroelectric sensor, and attenuated using a neutral density filter to the desired pulse energy, prior to recording the fragment spectrum. The mass spectrometer was operated with the BrukerIonTrap 7.0 software in ultrascan mode, averaging ten cycles for a single mass spectrum. Accumulation time was set appropriately so that the ion count did not exceed a value of $1\text{-}1.5\cdot10^5$. If not stated otherwise, the fragmentation time was set to 150 ms, which, in combination with the 981 Hz repetition rate of the amplifier, amounted to ~150 laser pulses per ion cloud. The fragment mass spectra were recorded for at least 2 minutes for a set wavelength. The procedure was repeated for each set wavelength in the recorded spectral region, spacing the data points equidistantly with a step size of 3-5 nm. Parent ion and fragment ion intensities were extracted as ion chromatograms from the mass spectra by using a home-made VisualBasic script.[26] The total fragment ion yield $Y(\lambda)$ at a given wavelength λ was calculated according to $Y(\lambda)=\sum F_i/[(\sum F_i+\sum P_j)\cdot\lambda]$, where F_i and P_j are the fragment and parent ion intensities, respectively. Division by the numerical value of λ was performed to account for different photon energies at constant laser pulse fluence.

Measurements of the fragment ion yield dependence on the pump pulse energy were performed analogously. For a set wavelength, consecutive PF mass spectra were recorded at increasingly higher pulse energies. Fragment ion chromatograms were extracted and processed according to the procedure described above. Energy E dependence of the fragmentation yield Y was evaluated applying a polynomial fit function ($Y = A \cdot E^n$), where n is an estimate for the number of photons needed to induce fragmentation.[47]

tPF spectra were recorded by resonant (one-photon) excitation of the isolated ions using the output from TOPAS-C T7 (usually in the visible region) and subsequent time-delayed probing by non-resonant (multiple-)photon (1200 nm) absorption of the photoselected ion ensemble. Pump intensities were, if applicable, usually kept as low as possible to avoid multiple-photon excitation. If not stated otherwise, the initial repetition rate (981 Hz) of the pump and probe pulse trains was reduced to 327 Hz by an optical chopper, resulting in irradiation of a single ion cloud with ~50 pump-probe pairs. The mutual polarization plane orientation of the linearly polarized pump and

probe beams was adjusted by rotating the polarization plane of the pump with respect to the (vertically polarized) probe pulses using a Berek polarization compensator. The retardation for a selected pump pulse wavelength was adjusted accordingly by tilting the compensator plate, so that the compensator functioned as a λ/2-waveplate, allowing for easy control of the polarization plane orientation by rotation of the Berek compensator. The probe pulses were continuously delayed in time with respect to pump pulses by means of a silver retroreflector mounted on a single axis delay stage (M-531.DD, PI). The DC motor controller (C-863.11 Mercury, PI) operating the delay stage was controlled using the PIMikroMove Software. The pump and probe pulses were spatially overlapped and focused onto the ion cloud inside the trap with a f=50 cm lens. Pointing of the beams was adjusted for maximum PF yield at zero time delay (t_0). The time-delay was continuously scanned (from negative to positive pump-probe delay) at constant scan speed, which was adjusted for equidistant steps between each data point of typically 4 ps (for a total time delay of 1.6 ns), 2 ps (total delay of 800 ps), 100 fs (total delay of 40 ps) and 20 fs step size for total delays shorter than 40 ps. Each scan took 10 min to complete and was repeated 12-15 times, depending on signal quality. Fragment ion chromatograms were extracted from the raw data using a VisualBasic script,[26] which was run in the BrukerDataAnalysis 4.0 software. The yields Y_i of the individual fragment ion channels were evaluated according to $Y_i = F_i/[(\sum F_i + \sum P_j)]$ (F_i: intensity fragment i and P_j: intensity parent j) and additionally converted from the internal time-scale of the mass spectrometer to a pump-probe delay dependency with a template file developed in LibreOffice Calc. The so obtained kinetic traces were averaged over all repeated scans for every single fragment ion channel and either summed up (total fragment yield) or subjected to a fitting routine individually.

To evaluate the system response at any given pump-probe wavelength combination, the cross correlation function (ccf) was determined by measuring the pump-probe dependent multiple-photon ionization of neutral furan inside the ion trap with the same step size and at the same scan speed used in the respective experiment.[27-28] For that purpose, furan at a partial pressure of ~1-3·10^{-7} mbar was introduced into the trap according to the procedure described above. The overlap of the pump and probe pulse electric fields give a rise to a quasi-instantaneous, short-lived ion signal resulting from laser induced electron detachment from neutral furan molecules, which are then detected mass spectrometrically. Time-zero and the temporal resolution were estimated

from the center and the fwhm of the Gaussian ion signal (Figure 20), respectively and used in fitting of the kinetic traces.
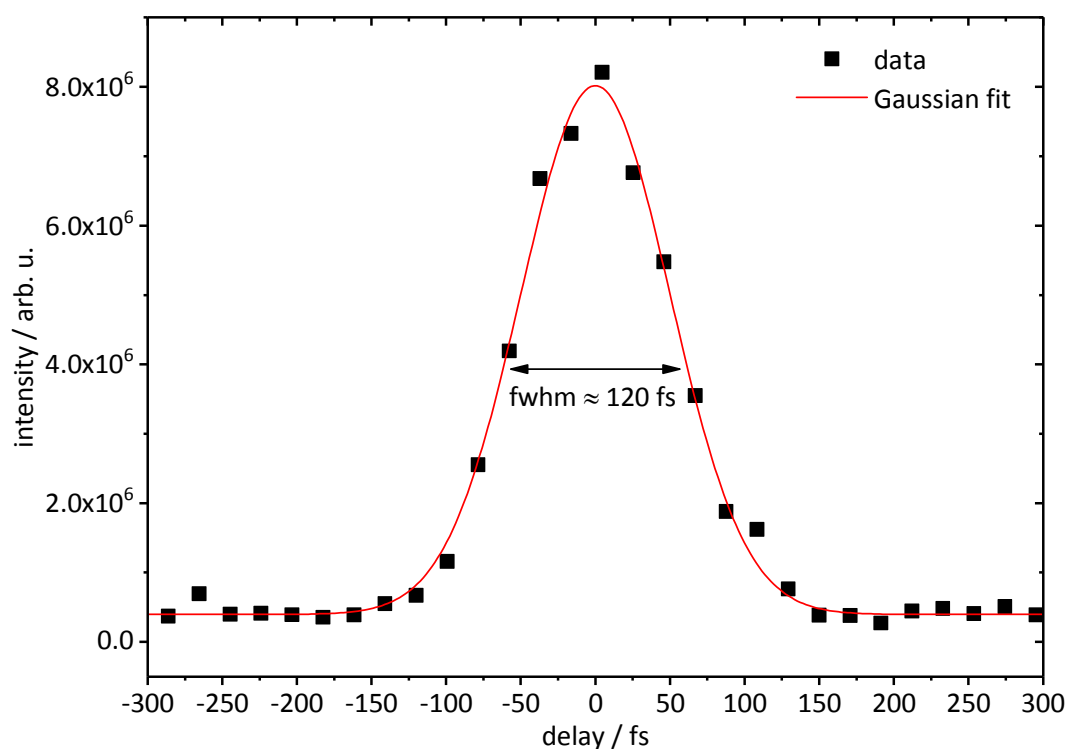
Figure 20 Temporal resolution estimated from a Gaussian approximation of the cross correlation measured by coherent (multiple-)pump+probe photoionization of neutral furan; shown examplatorily for a wavelength combination of: λ_{pump}=400 nm + λ_{probe}=1200 nm.

Transient fragment spectra were usually fitted by a convolution of a sum of exponentials augmented with the system response obtained from the laser pulse cross correlation according to $S(t)=\sum_i A_i(exp(-t/\tau_i)*g(t,t_0,t_p))$ (τ_i decay time constants, t_0: time zero, t_p: fwhm of ccf), using Origin 9.0G or a fitting software[48] based on the MINUIT optimization package.[49] Sinusoidally modulated transients were evaluated with Origin 9.0G or an open source software (DecayFit)[50] running within the MATLAB (R2013a) environment.

2.5 Computational methods

2.5.1 Density functional theory

Density function theory (DFT) is a quantum chemical method for modeling the electronic ground state properties of many-body systems from the spatially dependent electron density. Since 1970s it was mainly used for calculations to determine solid state

physics, and deemed not accurate enough for calculations in quantum chemistry. However, with better refinement of the approximations used to model exchange and correlations interactions it became more popular among theoretical chemists, due to its relatively low computational costs.

The foundation of DFT is the Hohenberg-Kohn-Theorem,[51] claiming that for a given electron-density $n(\boldsymbol{r})$, the potential $v(\boldsymbol{r})$, which produced said density, is uniquely defined, *i.e.* if $n(\boldsymbol{r})$ is known, $v(\boldsymbol{r})$ and also the Hamiltonian $\hat{H}$ is known. Thus, any observable of a system can be derived from the density alone. The beauty of this approach lies within the Kohn-Sham formalism, stating that the density of a system of N interacting fermions can be calculated as the density of an auxiliary system of non-interacting fermions. In first approximation, the electrons are treated separately. Hence, instead of solving the Schrödinger equation of an N particle system as a whole, a set of N orthonormal one-electron-Schrödinger equations are solved, also known as Kohn-Sham equations:

$$\left(-\frac{1}{2}\nabla^2 + v_{eff}(\boldsymbol{r})\right)\varphi_j(\boldsymbol{r}) = \epsilon_j\varphi_j(\boldsymbol{r}) \tag{1}$$

With ϵ_j being the energy eigenvalue of the corresponding Kohn-Sham orbital $\varphi_j(\boldsymbol{r})$.

The density of the system is then obtained by

$$n(\boldsymbol{r}) = \sum_{j=1}^{N}\left|\varphi_j(\boldsymbol{r})\right|^2 \tag{2}$$

and the effective single-electron potential $v_{eff}(\boldsymbol{r})$ is written as

$$v_{eff}(\boldsymbol{r}) = v_{ext}(\boldsymbol{r}) + \int \frac{n(\boldsymbol{r}')}{|\boldsymbol{r}-\boldsymbol{r}'|}d^3r' + v_{XC}(\boldsymbol{r}) \tag{3}$$

The first term is the external potential $v_{ext}(\boldsymbol{r})$ exerted by the atom core(s), the second term (the so-called Hartree term) describes the electron-electron Coulomb repulsion and $v_{XC}(\boldsymbol{r})$ is the exchange-correlation potential, which treats the many-particle interactions. From the definition of the effective potential $v_{eff}(\boldsymbol{r})$, two main conclusions can be drawn. Firstly, since the effective potential depends on the density $n(\boldsymbol{r})$ and is

also necessary to calculate the density in the first place (from the Kohn-Sham functions), the eigenvalue problem has to be solved iteratively.

Secondly, although the N electron system was initially conceived as a system of N non-interacting particles, the many particle interactions cannot be disregarded. Thus the Kohn-Sham-formalism only shifted the problem of treating many-body systems to the exchange-correlation (XC) term. The major concern is now that the exact functionals for exchange and correlation are not known and must be approximated. One way to do so is the local density approximation (LDA), in which the density at a local point is assumed to be uniform (electron gas). An improvement to this formalism is the generalized gradient approximation (GGA), which, in addition, incorporates the local change in density, *i.e.* the density gradient. Today, hybrid functionals, such as B3LYP,[52-53] have become very popular, which include a varying degree of exact exchange calculated according to the Hartree-Fock-formalism.

2.5.2 Time-dependent density functional theory

Time-dependent density functional theory (TD-DFT) extends the idea behind DFT. The foundation of TD-DFT is the Runge-Gross-Theorem,[54] which proved (analogous to the Hohenberg-Kohn-Theorem for a static system) that all observables of a interacting many-body system, evolving from an initial (true) state ψ_0, can be extracted from the density $n(\boldsymbol{r}, t)$ of a non-interacting (Kohn-Sham) system of fermions starting in an initial state Φ_0. The proof of the Runge-Gross-Theorem is more involved than the Hohenberg-Kohn-Theorem, since the time-dependent effective potential at a given time is dependent on the densities at all previous times. Detailed explanation of the theory can be found in *e.g.* Ref. [55].

Suffice to say is that, analogous to DFT, the time-dependent density can be obtained according to

$$n(\boldsymbol{r},t) = \sum_{j=1}^{N} \left|\varphi_j(\boldsymbol{r},t)\right|^2 \tag{4}$$

with a set of N orthonormal $\varphi_j(\boldsymbol{r},t)$ orbitals obeying the time-dependent Kohn-Sham equation

$$\left(-\frac{1}{2}\nabla^2 + v_{eff}(\boldsymbol{r},t)\right)\varphi_j(\boldsymbol{r},t) = i\frac{\partial}{\partial t}\varphi_j(\boldsymbol{r},t) \tag{5}$$

Analogous to the potential of a Kohn-Sham system in the ground state, $v_{eff}(\boldsymbol{r},t)$ is split into three terms:

$$v_{eff}[n;\Phi_0](\boldsymbol{r},t) = v_{ext}[n;\Psi_0](\boldsymbol{r},t) + \int \frac{n(\boldsymbol{r}',t)}{|\boldsymbol{r}-\boldsymbol{r}'|}d^3r' + v_{XC}[n;\Psi_0,\Phi_0](\boldsymbol{r},t) \tag{6}$$

With the first term, $v_{ext}[n;\Psi_0](\boldsymbol{r},t)$, being the external time-dependent field, the second the time-dependent Hartree potential and the third the XC potential. Again, the XC potential has to be approximated as s functional of the density and, in contrast to DFT, also as a functional of the true initial state Ψ_0 and the Kohn-Sham initial state Φ_0.

Within this work, geometry optimizations and vibrational frequency calculations were performed on the DFT level of theory, whereas for calculations of vertical transition energies TD-DFT was employed. Calculations were managed and monitored using mainly the Extensible Computational Chemistry Environment (ECCE)[56] interface running the Gaussian 09 program package.[57] Individual use of basis sets and functionals will be specified within each chapter. Calculations were gratefully performed on the computing clusters of the TU Kaiserslautern, which are under supervision of the theoretical research group of Prof. Dr. C. van Wüllen.

2.6 References

[1] J. Fenn, M. Mann, C. Meng, S. Wong, C. Whitehouse, *"ELECTROSPRAY IONIZATION FOR MASS SPECTROMETRY OF LARGE BIOMOLECULES"*, *Science* **1989**, *246*, 64-71.

[2] J. B. Fenn, M. Mann, C. K. Meng, S. F. Wong, C. M. Whitehouse, *"ELECTROSPRAY IONIZATION–PRINCIPLES AND PRACTICE"*, *Mass Spectrom. Rev.* **1990**, *9*, 37-70.

[3] M. Karas, D. Bachmann, U. Bahr, F. Hillenkamp, *"MATRIX-ASSISTED ULTRAVIOLET LASER DESORPTION OF NON-VOLATILE COMPOUNDS"*, *Int. J. Mass Spectrom. Ion Processes* **1987**, *78*, 53-68.

[4] R. D. Smith, J. A. Loo, C. G. Edmonds, C. J. Barinaga, H. R. Udseth, *"NEW DEVELOPMENTS IN BIOCHEMICAL MASS SPECTROMETRY: ELECTROSPRAY IONIZATION"*, *Anal. Chem.* **1990**, *62*, 882-899.

[5] M. Mann, *"ELECTROSPRAY: ITS POTENTIAL AND LIMITATIONS AS AN IONIZATION METHOD FOR BIOMOLECULES"*, *Org. Mass Spectrom.* **1990**, *25*, 575-587.

[6] K. Breuker, M. Jin, X. Han, H. Jiang, F. W. McLafferty, *"TOP-DOWN IDENTIFICATION AND CHARACTERIZATION OF BIOMOLECULES BY MASS SPECTROMETRY"*, *J. Am. Soc. Mass. Spectrom.* **2008**, *19*, 1045-1053.

[7] M. Dole, L. L. Mack, R. L. Hines, R. C. Mobley, L. D. Ferguson, M. B. Alice, *"MOLECULAR BEAMS OF MACROIONS"*, *J. Chem. Phys.* **1968**, *49*, 2240-2249.

[8] J. B. Fenn, *"ELECTROSPRAY WINGS FOR MOLECULAR ELEPHANTS (NOBEL LECTURE)"*, *Angew. Chem. Int. Ed.* **2003**, *42*, 3871-3894.

[9] M. Mann, C. K. Meng, J. B. Fenn, *"INTERPRETING MASS SPECTRA OF MULTIPLY CHARGED IONS"*, *Anal. Chem.* **1989**, *61*, 1702-1708.

[10] M. Yamashita, J. B. Fenn, *"ELECTROSPRAY ION SOURCE. ANOTHER VARIATION ON THE FREE-JET THEME"*, *J. Phys. Chem.* **1984**, *88*, 4451-4459.

[11] J. F. d. l. Mora, G. J. Van Berkel, C. G. Enke, R. B. Cole, M. Martinez-Sanchez, J. B. Fenn, *"ELECTROCHEMICAL PROCESSES IN ELECTROSPRAY IONIZATION MASS SPECTROMETRY"*, *J. Mass Spectrom.* **2000**, *35*, 939-952.

[12] N. B. Cech, C. G. Enke, *"PRACTICAL IMPLICATIONS OF SOME RECENT STUDIES IN ELECTROSPRAY IONIZATION FUNDAMENTALS"*, *Mass Spectrom. Rev.* **2001**, *20*, 362-387.

[13] T. C. Rohner, N. Lion, H. H. Girault, *"ELECTROCHEMICAL AND THEORETICAL ASPECTS OF ELECTROSPRAY IONISATION"*, *Phys. Chem. Chem. Phys.* **2004**, *6*, 3056-3068.

[14] A. P. Synder, *Biochemical and biotechnological applications of electrospray ionization mass spectrometry, Vol. 619*, American Chemical Society, **1996**.

[15] H. D. Dewald, *"ELECTROSPRAY IONIZATION MASS SPECTROMETRY: FUNDAMENTALS, INSTRUMENTATION AND APPLICATIONS (ED. COLE, RICHARD B.)"*, *J. Chem. Educ.* **1999**, *76*, 33.

[16] *"ELECTROSPRAY IONIZATION FUNDAMENTALS"*, *BDAL Training Document*.

[17] M. Cloupeau, B. Prunet-Foch, *"ELECTROSTATIC SPRAYING OF LIQUIDS: MAIN FUNCTIONING MODES"*, *J. Electrostat.* **1990**, *25*, 165-184.

[18] G. Schmelzeisen-Redeker, L. Bütfering, F. W. Röllgen, *"DESOLVATION OF IONS AND MOLECULES IN THERMOSPRAY MASS SPECTROMETRY"*, *Int. J. Mass Spectrom. Ion Processes* **1989**, *90*, 139-150.

[19] P. Kebarle, M. Peschke, *"ON THE MECHANISMS BY WHICH THE CHARGED DROPLETS PRODUCED BY ELECTROSPRAY LEAD TO GAS PHASE IONS"*, *Anal. Chim. Acta* **2000**, *406*, 11-35.

[20] J. V. Iribarne, B. A. Thomson, *"ON THE EVAPORATION OF SMALL IONS FROM CHARGED DROPLETS"*, *J. Chem. Phys.* **1976**, *64*, 2287-2294.

[21] B. A. Thomson, J. V. Iribarne, *"FIELD INDUCED ION EVAPORATION FROM LIQUID SURFACES AT ATMOSPHERIC PRESSURE"*, *J. Chem. Phys.* **1979**, *71*, 4451-4463.

[22] S. Banerjee, S. Mazumdar, *"Electrospray Ionization Mass Spectrometry: A Technique to Access the Information beyond the Molecular Weight of the Analyte"*, *Int. J.Anal. Chem.* **2012**, *2012*, 40.

[23] W. Paul, H. Steinwedel, in *Z.Naturforsch. A* **1953**, *8*, 448.

[24] N. W. McLachlan, *"Theory and application of Mathieu functions"*, New York, Dover Publications, **1964**.

[25] BDaltonics, *"amaZon Series User Manual"*, **2009**.

[26] F. Menges, doctoral thesis, TU Kaiserslautern **2013**.

[27] D. Nolting, T. Schultz, I. V. Hertel, R. Weinkauf, *"Excited state dynamics and fragmentation channels of the protonated dipeptide H2N-Leu-Trp-COOH"*, *Phys. Cchem. Chem. Phys.* **2006**, *8*, 5247-5254.

[28] D. Nolting, R. Weinkauf, I. V. Hertel, T. Schultz, *"Excited-State Relaxation of Protonated Adenine"*, *Chem. Phys. Chem.* **2007**, *8*, 751-755.

[29] D. Imanbaew, diploma thesis, TU Kaiserslautern **2013**.

[30] P. F. Moulton, *"Spectroscopic and laser characteristics of Ti:Al2O3"*, *J. Opt. Soc. Am. B* **1986**, *3*, 125-133.

[31] T. Brabec, P. F. Curley, C. Spielmann, E. Wintner, A. J. Schmidt, *"Hard-aperture Kerr-lens mode locking"*, *J. Opt. Soc. Am. B* **1993**, *10*, 1029-1034.

[32] T. Brabec, C. Spielmann, P. F. Curley, F. Krausz, *"Kerr lens mode locking"*, *Opt. Lett.* **1992**, *17*, 1292-1294.

[33] D. P. Little, J. P. Speir, M. W. Senko, P. B. O'Connor, F. W. McLafferty, *"Infrared Multiphoton Dissociation of Large Multiply Charged Ions for Biomolecule Sequencing"*, *Anal. Chem.* **1994**, *66*, 2809-2815.

[34] J. Mitchell Wells, S. A. McLuckey, *"Methods in Enzymology"*, Academic Press, **2005**, *402*, 148-185.

[35] S. A. McLuckey, D. E. Goeringer, *"SPECIAL FEATURE:TUTORIAL Slow Heating Methods in Tandem Mass Spectrometry"*, *J. Mass Spectrom.* **1997**, *32*, 461-474.

[36] T. D. Fridgen, *"Infrared consequence spectroscopy of gaseous protonated and metal ion cationized complexes"*, *Mass Spectrom. Rev.* **2009**, *28*, 586-607.

[37] J. R. Eyler, *"Infrared multiple photon dissociation spectroscopy of ions in Penning traps"*, *Mass Spectrom. Rev.* **2009**, *28*, 448-467.

[38] J. C. Marcum, doctoral thesis, University of Colorado, **2011**.

[39] R. Bersohn, A. H. Zewail, *"Time Dependent Absorption of Fragments During Dissociation"*, *Ber. Bunsenges. Physik. Chem.* **1988**, *92*, 373-378.

[40] M. W. Forbes, R. A. Jockusch, *"Gas-Phase Fluorescence Excitation and Emission Spectroscopy of Three Xanthene Dyes (Rhodamine 575, Rhodamine 590 and Rhodamine 6G) in a Quadrupole Ion Trap Mass Spectrometer"*, *J. Am. Soc. Mass. Spectrom.* **2011**, *22*, 93-109.

[41] A. H. Zewail, *"Femtochemistry: Atomic-Scale Dynamics of the Chemical Bond Using Ultrafast Lasers (Nobel Lecture)"*, *Angew. Chem. Int. Ed.* **2000**, *39*, 2586-2631.

[42] J. L. Knee, L. R. Khundkar, A. H. Zewail, *"Picosecond monitoring of a chemical reaction in molecular beams: Photofragmentation of R–I→R‡+I"*, *J. Chem. Phys.* **1985**, *83*, 1996-1998.

[43] N. F. Scherer, J. L. Knee, D. D. Smith, A. H. Zewail, *"Femtosecond Photofragment Spectroscopy: The Reaction ICN → CN + I"*, *J. Phys. Chem.* **1985**, *89*, 5141-5143.

[44] H. Kang, C. Jouvet, C. Dedonder-Lardeux, S. Martrenchard, C. Charrière, G. Grégoire, C. Desfrançois, J. P. Schermann, M. Barat, J. A. Fayeton, *"Photoinduced processes in protonated tryptamine"*, *J. Chem. Phys.* **2005**, *122*, 084307.

[45] H. Kang, C. Dedonder-Lardeux, C. Jouvet, G. Grégoire, C. Desfrançois, J. P. Schermann, M. Barat, A. Fayeton, *"Control of Bond-Cleaving Reactions of Free*

PROTONATED TRYPTOPHAN ION BY FEMTOSECOND LASER PULSES", *J. Phys. Chem. A* **2005**, *109*, 2417-2420.

[46] P. Remes, G. Glish, *"PRACTICAL ASPECTS OF TRAPPED ION MASS SPECTROMETRY", Volume IV*, CRC Press, **2010**, 739-767.

[47] J. D. Bhawalkar, G. S. He, P. N. Prasad, *"NONLINEAR MULTIPHOTON PROCESSES IN ORGANIC AND POLYMERIC MATERIALS"*, *Rep. Prog. Phys.* **1996**, *59*, 1041.

[48] M. Kunitski, Fitting Program PP2Color, Goethe University, Frankfurt, **2009**.

[49] F. James, M. Roos, MINUIT Computer Code, Program D-506, Cern Program Library, **1977**.

[50] S. Preus, *"DECAYFIT - FLUORESCENCE ANALYSIS SOFTWARE 1.3"*.

[51] P. Hohenberg, W. Kohn, *"INHOMOGENEOUS ELECTRON GAS"*, *Phys. Rev.* **1964**, *136*, B864-B871.

[52] A. D. Becke, *"DENSITY-FUNCTIONAL THERMOCHEMISTRY. III. THE ROLE OF EXACT EXCHANGE"*, *J. Chem. Phys.* **1993**, *98*, 5648-5652.

[53] C. Lee, W. Yang, R. G. Parr, *"DEVELOPMENT OF THE COLLE-SALVETTI CORRELATION-ENERGY FORMULA INTO A FUNCTIONAL OF THE ELECTRON DENSITY"*, *Phys. Rev. B* **1988**, *37*, 785-789.

[54] E. Runge, E. K. U. Gross, *"DENSITY-FUNCTIONAL THEORY FOR TIME-DEPENDENT SYSTEMS"*, *Phys. Rev. Lett.* **1984**, *52*, 997-1000.

[55] M. A. L. Marques, N. T. Maitra, F. M. S. Nogueira, E. K. U. Gross, A. Rubio, *"FUNDAMENTALS OF TIME-DEPENDENT DENSITY FUNCTIONAL THEORY"*, Springer, **2012**.

[56] G. Black, K. Schuchardt, D. Gracio, B. Palmer, in *Computational Science — ICCS 2003: International Conference, Melbourne, Australia and St. Petersburg, Russia, June 2–4, 2003 Proceedings, Part IV* (Eds.: P. M. A. Sloot, D. Abramson, A. V. Bogdanov, Y. E. Gorbachev, J. J. Dongarra, A. Y. Zomaya), Springer Berlin Heidelberg, Berlin, Heidelberg, **2003**, pp. 122-131.

[57] M. J. Frisch, G. W. Trucks, H. B. Schlegel, G. E. Scuseria, M. A. Robb, J. R. Cheeseman, G. Scalmani, V. Barone, B. Mennucci, G. A. Petersson, H. Nakatsuji, M. Caricato, X. Li, H. P. Hratchian, A. F. Izmaylov, J. Bloino, G. Zheng, J. L. Sonnenberg, M. Hada, M. Ehara, K. Toyota, R. Fukuda, J. Hasegawa, M. Ishida, T. Nakajima, Y. Honda, O. Kitao, H. Nakai, T. Vreven, J. A. Montgomery Jr., J. E. Peralta, F. Ogliaro, M. J. Bearpark, J. Heyd, E. N. Brothers, K. N. Kudin, V. N. Staroverov, R. Kobayashi, J. Normand, K. Raghavachari, A. P. Rendell, J. C. Burant, S. S. Iyengar, J. Tomasi, M. Cossi, N. Rega, N. J. Millam, M. Klene, J. E. Knox, J. B. Cross, V. Bakken, C. Adamo, J. Jaramillo, R. Gomperts, R. E. Stratmann, O. Yazyev, A. J. Austin, R. Cammi, C. Pomelli, J. W. Ochterski, R. L. Martin, K. Morokuma, V. G. Zakrzewski, G. A. Voth, P. Salvador, J. J. Dannenberg, S. Dapprich, A. D. Daniels, Ö. Farkas, J. B. Foresman, J. V. Ortiz, J. Cioslowski, D. J. Fox, Gaussian, Inc., Wallingford, CT, USA, **2009**.

3 Rotational and vibrational dynamics of deprotonated and protonated fluorescein studied by time-resolved photofragmentation in an ion trap

Dimitri Imanbaew[1], Maxim F. Gelin[3], and Christoph Riehn[1],[2]

[1]*Fachbereich Chemie, Technische Universität Kaiserslautern, Erwin-Schrödinger-Str. 52-54, 67663 Kaiserslautern, Germany*

[2]*Landesforschungszentrum OPTIMAS, Erwin-Schrödinger-Str. 46, 67663 Kaiserslautern, Germany*

[3]*Fakultät für Chemie, TU München, Lichtenbergstraße 4, 85747 Garching, Germany*

3.1 Preamble

The following work has been published in the online journal *Structural Dynamics*. The experimental work, data processing and evaluation, as well as structural and energetic calculations were performed by me. Simulations of the transient anisotropy data and theoretical considerations thereof were provided by Maxim. F. Gelin (TU München). The initial draft of the manuscript was written by me and revised by Christoph Riehn.

Full Reference to the publication:

3.2 Abstract

Excited state dynamics of deprotonated and protonated fluorescein were investigated by polarization dependent femtosecond time-resolved pump-probe photofragmentation in a 3D ion trap. Transients of deprotonated fluorescein exhibit vibrational wave-packet dynamics with weak polarization dependence. Transients of protonated fluorescein show only effects of molecular alignment and rotational dephasing. The time resolved rotational anisotropy of protonated fluorescein is simulated by dynamics of the calculated orientational correlation function. The observed differences between deprotonated and protonated fluorescein are ascribed to their different higher lying electronically excited-states and corresponding structures. This is partially supported by time-dependent density functional theory calculations of the excited state structures.

3.3 Introduction

Fluorescein **[FL]** and its derivatives represent one of the most popular categories of dyes in biochemistry. Due to their high molar absorptivity and fluorescence yield,[1] fluorescein based markers are often used in fluorescence labeling[2-3] or as probes for *e.g.* redox cycles in living cells[4] and sensing of various metals ions or other small molecules.[5] In solution, **[FL]** appears pH-dependent in up to four charge states/prototropic forms (dianion **[FL-2H]**$^{2-}$, monoanion **[FL-H]**$^-$ as a phenolate or carboxylate, neutral **[FL]** and cation **[FL+H]**$^+$) exhibiting specific absorption and emission characteristics.[1] **FL** is easily chemically linked to biopolymers and therefore used in (steady-state) fluorescence anisotropy measurements,[6-8] with the goal to improve microscopic fluorescence imaging[7-10] and study the dynamics of protein-folding[11] or conformational rearrangements by time-resolved fluorescence anisotropy (TR-FA).[12-14] The importance of the latter applications, their perspective for Förster resonance energy transfer (FRET) studies[15-17] and furthermore the search for insight into the influence of solvation on the different charge states has sparked interest in gas phase studies coupled with mass spectrometric or fluorescence detection.[18-21] In addition, recently, it was convincingly demonstrated that a gas phase analogue to TR-FA is possible by implementation of a femtosecond (fs) time-resolved photodetachment anisotropy (TR-PA) scheme.[22] In that report rotational and vibrational wave-packet

dynamics were observed for **[FL-H]**⁻ by velocity-map imaging detection of photoelectrons.

In the present study we extend these experiments by employing the complementary method of linearly polarized fs transient photofragmentation (tPF) in an ion trap, which allows us to investigate the dynamics of the monoanionic phenolate **[FL-H]**⁻ and the cationic fluorescein species **[FL+H]**⁺ (Scheme 1). We present first results obtained by this technique and discuss differences with respect to the molecular structures of the involved electronically excited states of **[FL-H]**⁻ and **[FL+H]**⁺, as well as the utilized detection schemes (TR-PA vs. tPF) in studies of **[FL-H]**⁻.
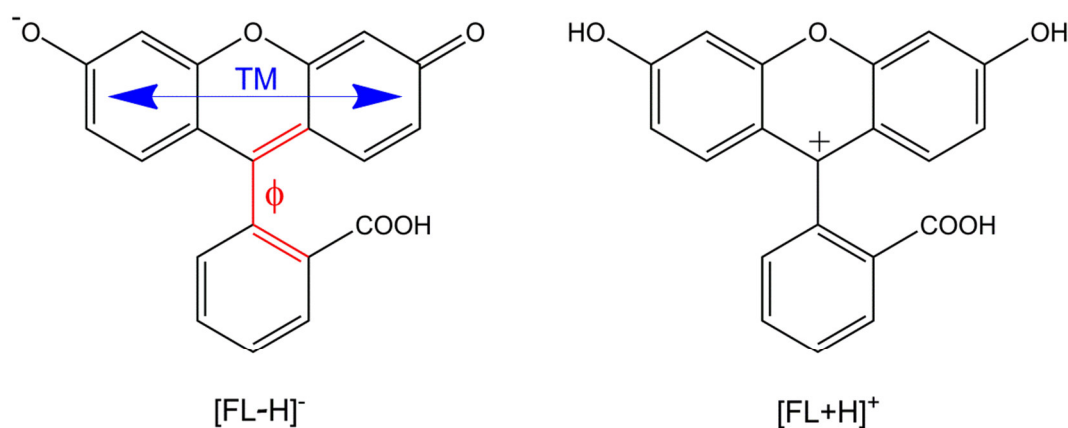
Scheme 1 Schematic structure of phenolate **[FL-H]**⁻ (left) and **[FL+H]**⁺ (right). TM and φ denote the transition dipole moment for the $S_1 \leftarrow S_0$ transition of **[FL-H]**⁻ and the dihedral angle of the torsional coordinate of the benzoic acid ring vs. the xanthene unit, respectively.

3.4 Experimental setup and calculations

The disodium salt of **FL** and methanol of LC-MS grade were purchased from Sigma-Aldrich and used without further purification. Time-resolved and polarization-dependent photofragmentation (PF) experiments were conducted using a modified Paul-type quadrupole ion trap mass spectrometer (amaZon speed, Bruker Daltonics) in combination with a Ti:sapphire oscillator and amplifier system (Wyvern 1000™, KMLabs).[23] Briefly, **[FL-H]**⁻ and **[FL+H]**⁺ were generated by electrospray ionization (ESI) of a methanolic solution of the **FL** salt (c=5·10⁻⁶ M) in negative and positive ion mode, respectively. For the study of **[FL+H]**⁺ a small amount of formic acid (1 vol-%) was added to the sample solution in order to increase the cation signal. The sample

solution was continuously infused by a syringe pump at a flow rate of 120 µL/h. Nitrogen as drying gas was set to a flow rate of 4 L/min at 180°C. The nebulizer pressure was set to 5 psi (345 mbar).

The fs laser pulses were generated in a cryogenic ultrafast regenerative laser amplifier system delivering 50 fs pulses at ~1 kHz repetition rate (central wavelength of ~785 nm). The pulse train was split to pump two optical parametric amplifiers of white light continuum (TOPAS-C, Light Conversion) for generating pump and probe pulses of tunable wavelength (240-2500 nm). Temporal delay between pump (520 nm, 0.3 µJ; 425 nm, 0.8 µJ) and probe pulses (1200 nm, 150 µJ) was controlled via an optical delay line. Pump and probe pulses were spatially overlapped quasi-collinearly by focusing into the center of the Paul ion trap with a lens (f=50 cm). The beam diameter in the ion trap was estimated to be ~1 mm using the knife-edge technique. The relative polarization of pump and probe pulses was controlled by a Berek compensator in the pump path. The initial ~1 kHz repetition rate was reduced to ~330 Hz by an optical chopper. Each isolated portion of ions was irradiated by 50 pump/probe pulse pairs.

The tPF signals were recorded as extracted ion chromatograms while continuously varying the delay between the pump and probe pulses. Evaluation of the transient signals was performed as $F_i/(F_i+P_j)$, where F_i and P_j are the sums of the intensities of fragment and parent ion signals, respectively. To evaluate the temporal resolution at a given pump/probe wavelength combination, we recorded the multi-photon ionization signal of neutral furan in the ion trap as a function of time delay between the pump and probe pulses.[24] The obtained signal represents an intensity cross correlation function (ccf) of the pump and probe laser pulses. The instrumental system response was then estimated from the fwhm of the resulting Gaussian-shaped photoionization signal. A typical value for the fwhm of the ccf at 520 nm (pump)/1200 nm (probe) [425 nm/1200 nm] is ~110 fs [~135 fs].

Time-resolved experiments with polarization-sensitive detection reveal reorientation of transition dipole moments and relaxation of the optically induced anisotropy in real time, both in liquid phase[25] and in the gas phase.[26] The signals obtained from our polarization dependent tPF experiments arise from the same phenomena, as observed in TR-PA measurements. We therefore used the same method of analysis to disentangle

rotational from population dynamics, as described and applied successfully in Ref. [22]. Briefly, this analysis originates from TR-FA and is implemented by measuring transient signals at parallel and perpendicular relative linear laser polarization. This method allows us to calculate an isotropic signal $S(t)$ unfettered by rotational dynamics, as well as an anisotropic function $r(t)$, dealing with the directionality of the probe process with respect to pump photon absorption. $S(t)$ and $r(t)$ are defined as

$$S(t) = \frac{1}{3}\left(I_{\parallel}(t) + 2I_{\perp}(t)\right) \tag{1}$$

and

$$r(t) = \frac{I_{\parallel}(t) - I_{\perp}(t)}{I_{\parallel}(t) + 2I_{\perp}(t)} \tag{2}$$

with $I_{\parallel}(t)$ and $I_{\perp}(t)$ being the signal intensities recorded at time delay t for parallel and perpendicular pump/probe polarization, respectively.

For a one photon pump+one photon probe (1+1') process, the anisotropy is determined by the standard formula (3):

$$r(t) = \frac{2}{5}\left\langle \frac{3\cos^2(\beta(t)) - 1}{2} \right\rangle = \frac{2}{5}\left\langle P_2(\mathbf{\mu}_1(0)\mathbf{\mu}_2(t)) \right\rangle \tag{3}$$

(see, e.g. the monograph by J. R. Lakowicz (3rd Ed., Springer 2006), Ch. 10, equation (10.22)). Here $cos(\beta(t)) = \mathbf{\mu}_1(0)\mathbf{\mu}_2(t)$, $\mathbf{\mu}_1$ and $\mathbf{\mu}_2$ are the unit vectors along the transition dipole moments (TMs) responsible for the transitions initiated by the pump and probe pulses, $\langle ... \rangle$ stands for rotational averaging, and $P(x)=(3x^2-1)/2$ is the second order Legendre polynomial. The time dependence of $\mathbf{\mu}_2(t)$ results from molecular rotation. Values for $r(t)$ vary from initially $r_0 = r(t=0) = +0.4$ for parallel TM orientations or $r_0 = -0.2$ for perpendicular TM orientations to the final stationary distribution $r(t_{dephas})$, where a characteristic time constant t_{dephas} is determined by the rotational constants of the molecular system.

For a (1+2') process, the anisotropy is given by a similar equation (4), which can be retrieved from Refs. [27-28]:

$$r(t) = \frac{4}{7}\left\langle P_2\left(\boldsymbol{\mu}_1(0)\boldsymbol{\mu}_2(t)\right)\right\rangle \tag{4}$$

Here we assumed that the anisotropic part of the two-photon absorption tensor is proportional to $\boldsymbol{\mu}_1 \otimes \boldsymbol{\mu}_2$, where $\boldsymbol{\mu}_2$ is a unit vector in the molecular frame. Hence, one obtains slightly different starting values of $r_0 = +4/7 \approx +0.57$ and $r_0 = -2/7 \approx -0.29$ for parallel and perpendicular TM orientations, respectively.

Single point density functional theory (DFT) and time-dependent (TD-)DFT calculations were performed at the 6-31++G(d,p) level using the ωB97XD functional[29] within the Gaussian 09 package.[30] Investigation of the ground (S_0) and first excited state (S_1) potential energy surface with respect to the dihedral angle between the xanthene and benzoic acid unit of fluorescein was performed without complete geometry optimization, as optimization of even a single excited state geometry at this level of theory is very time consuming.

3.5 Results and discussion

3.5.1 Dynamics of [FL-H]⁻

The isolated fluorescein monoanions, **[FL-H]**⁻ (m/z 331, most abundant isotope), were excited at their longest wavelength gas phase absorption maximum (520 nm, 0.3 µJ) determined in former gas phase PF studies[18-19] and subsequently probed with high intensity pulses of longer wavelength (1200 nm, 150 µJ).

The major product fragment (for both pump-only and pump-probe photoexcitation) is located at m/z 287 or 286, corresponding to a loss of CO_2 (-44 Da) or HCO_2 (-45 Da) originating most likely from the benzoic acid moiety (Figure 1, for a difference mass spectrum *cf.* Figure S1a).

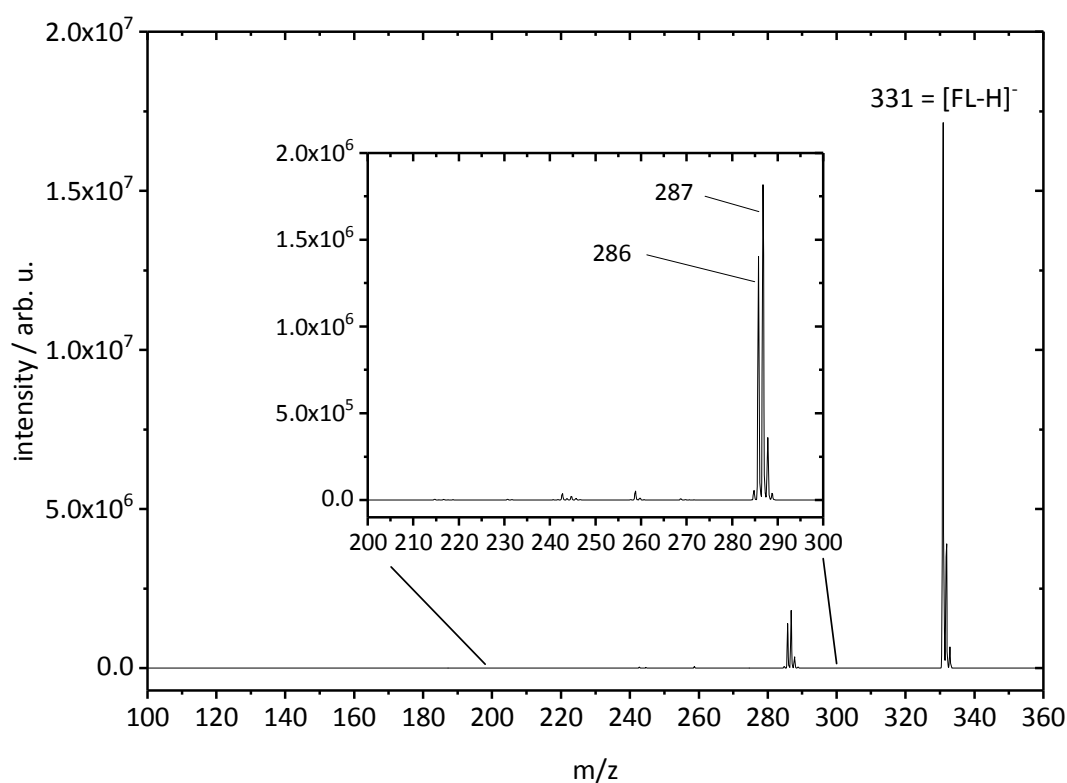**Figure 1** Mass spectrum depicting the formation of fragment ions after pump-probe photoexcitation of isolated **[FL-H]**⁻ (m/z 331, most abundant isotope).

As the fragmentation behavior is dominated by only one product ion, which is formed after loss of CO_2 or HCO_2, one can assume an efficient energy transfer from the initially excited xanthene unit to the adjacent benzoic acid moiety. Irradiation with both pump

and probe laser pulses (at sub-picosecond or picosecond delay) does not lead to other additional fragmentation products but enhances the fragmentation efficiency by a factor of ~30 (Figure S2) compared to fragmentation observed at negative delay (probe-pump) or by pump-only photoexcitation (Figure 2). This signal enhancement is a prerequisite for recording tPF spectra as reported previously[23-24, 31-33] and contains information on the dynamics of the involved electronically excited states.

We performed measurements on the laser power dependence of the **[FL-H]⁻** fragmentation yield for the related pump-only fragmentation and confirmed that this process is based on a multiple-photon absorption (Figure S3a).[19] Since the bond dissociation enthalpy for C-COOH of benzoic acid is ~430 kJ/mol,[34] it is conceivable that at least two photons at 520 nm (~230 kJ/mol) are necessary for generating the observed fragment ions. However, we assume that the contribution of multiple-photon-pump+probe PF to the time-resolved signal is negligible in our experiments, as the laser intensity used (0.3 μJ) is very low and pump-only excitation under these conditions leads to barely noticeable fragmentation (compared to pump-probe excitation; Figure S2). In accordance with the documented fragmentation behavior of **[FL-H]⁻** in the literature,[19] we did not observe a large contribution of a possible photodetachment (PD) loss channel. Since PD leads to neutral species, their contribution to the total fragment yield is difficult to assess by ion trap methods. We note that from the difference mass spectrum (Figure S1a) one would obtain ~25 % of the parent ion loss that cannot be accounted for by the accompanying fragment ion signal increase. This could be attributed to a PD channel. However, the absolute ion signal intensities are subject to significant fluctuations of ~10 % for the parent ion and ~5 % for the main fragment ion, so that a quantitative analysis of the PD yield from our data is not meaningful. Nevertheless, recently the time-resolved PD of **[FL-H]⁻** was studied employing 495 nm (~242 kJ/mol) pump / 400 nm (~300 kJ/mol) probe laser pulses.[22] The photoelectron yield under those excitation conditions was not given, but it is known (from studies on *e.g.* the chromophore of the green fluorescent protein)[35] that at higher photon energies PD may prevail over possible nuclear fragmentation processes. Taking these observations into account, we assume that in our case the pump (520 nm) + probe (1200 nm) signal stems from (1+2') excitation, resulting in a total excitation energy of ~430 kJ/mol, which enables fragmentation but does not lead to a large PD yield.

Figure 2 depicts the fragment ion yield as a function of time delay for parallel and perpendicular relative polarization of the pump and probe laser pulses.
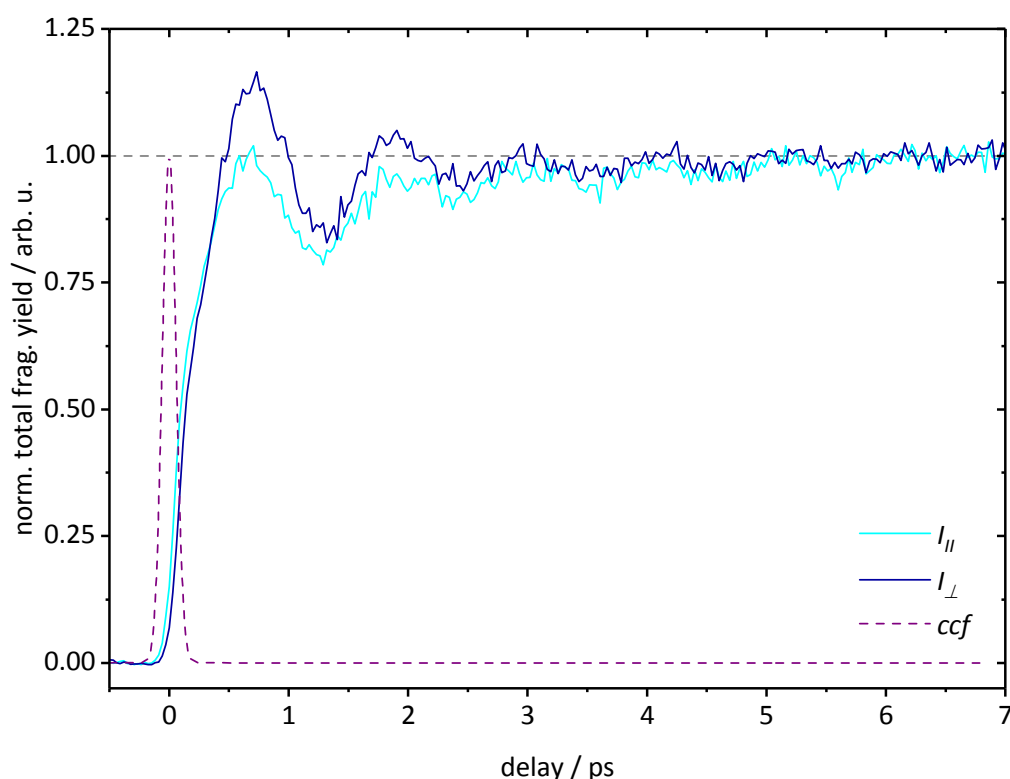
Figure 2 Normalized total fragmentation efficiency of **[FL-H]**⁻ as a function of pump-probe delay depending on the relative polarization between pump and probe pulses; λ_{pump}=520 nm (0.3 µJ) and λ_{probe}=1200 nm (150 µJ).

Signal intensities were background corrected and normalized to unity at long time delay for better comparison of the initial signal rise at time-zero and shortly afterwards. Both transients exhibit an initial rise, much slower (~700 fs from zero to signal maximum) than the estimated system response of ~110 fs (*cf.* section *3.4*) However, at short time delay (0.5–4 ps), the signal recorded for perpendicular laser polarization has higher intensity than the signal recorded for parallel polarization. At longer time delay, both signals are buried in noise and virtually coincide (note: this is also true for the raw data, which is not shown and discussed here). Furthermore, both traces are sinusoidally modulated with a period of ~1 ps. This modulation disappears within ~6 ps. A similar dependence of a transient signal on the relative polarization orientation between pump (495 nm) and probe (400 nm) pulses, as well as a strong modulation was observed for **[FL-H]**⁻ in the gas-phase applying TR-PA.[22] In TR-PA experiments, however, the total photoelectron signal intensity exhibited 1) a stronger dependence on the relative laser

polarization, 2) the trace for parallel pump-probe polarization featured a higher intensity (compared to the signal at perpendicular polarization) and 3) the oscillatory component (of similar frequency) disappeared on a shorter timescale (within ~3 ps).

The isotropic signal function $S(t)$ and the anisotropy function $r(t)$ calculated from our tPF data (Figure 2) according to equations (1) and (2) are shown in Figure 3.
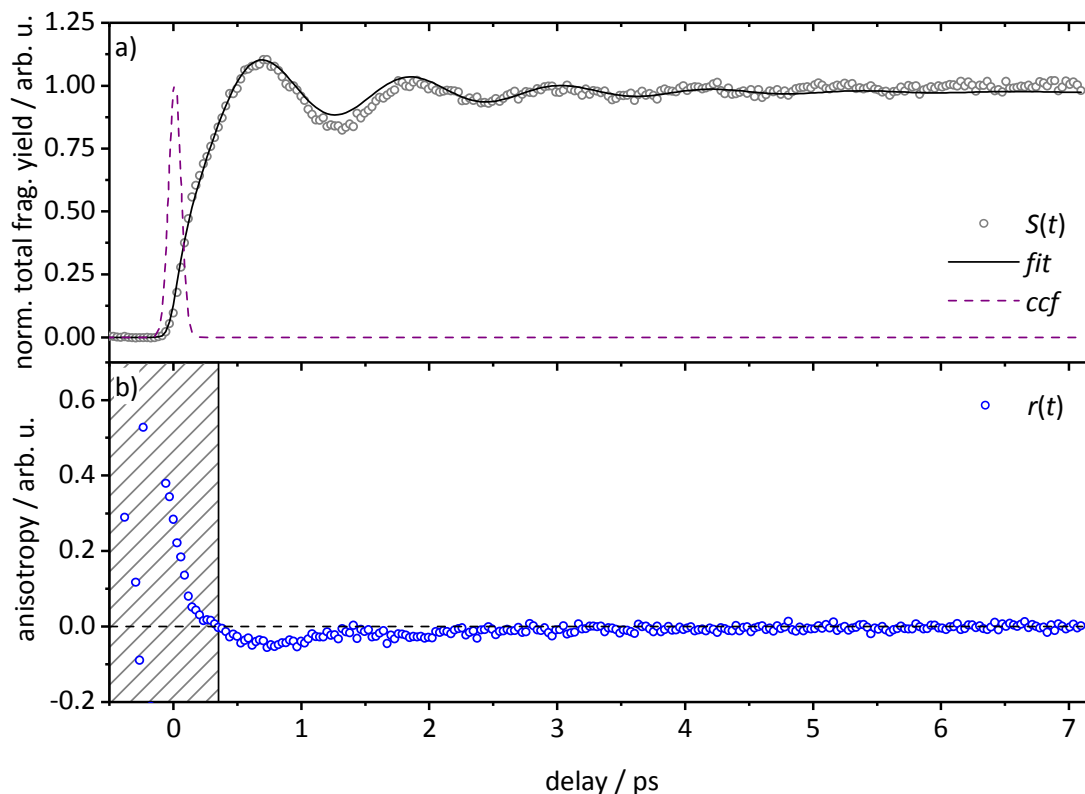
Figure 3 (a) Time-resolved isotropic signal function $S(t)$ exhibiting the formation of a long lived S_1 state superpositioned with vibrational wave-packet dynamics and **(b)** time-resolved anisotropy function $r(t)$ for analysis of rotational dephasing of **[FL-H]⁻**; $S(t)$ and $r(t)$ were calculated from equation (1) and (2), respectively.

Based on this decomposition analysis, as described in section *3.4,* the trace in Figure 3a depicts only the population dynamics of excited **[FL-H]⁻**, *i.e.* the preparation of a long lived (no decay was observed for a delay time of up to 800 ps) electronically excited (S_1) state and the concurrent formation of a vibrational wave-packet, modulating the step-like transient signal. By fitting this transient to a convolution of a Gaussian with an exponentially decaying sinusoidal modulation $(1+b \cdot sin(\omega \cdot t+\varphi) \cdot exp(-t/\tau))$, the oscillation period is found to be $2\pi/\omega=T=1.2$ ps, corresponding to a vibrational frequency of

$28\,cm^{-1}$, which compares nicely to the reported frequency of $32\,cm^{-1}$ from TR-PA experiments.[22]

The anisotropy function $r(t)$ of a freely rotating ensemble of molecules should exhibit the dephasing of a rotational wave-packet formed upon photoselection by coherent excitation of ions ($S_1 \leftarrow S_0$) that are aligned parallel with their TMs to the pump laser polarization. Specifically, the TM for **[FL-H]**$^-$ is oriented along the long axis of the xanthene moiety (here: the x-axis, Scheme 1). The linearly polarized probe laser then samples these excited molecules by further excitation ($S_n \leftarrow S_1$) to higher electronically excited states from which fragmentation occurs directly or after subsequent internal conversion (IC) and energy redistribution to other states. The dephasing dynamics that determines the decay of the anisotropy function $r(t)$ from its initial value r_0 to the final stationary value is determined by the temperature T of the ensemble (width of the rotational energy distribution or a number of states forming the rotational wave-packet) and the frequencies of rotational motions of molecules perpendicular to the alignment axis, which are specified by the rotational constants or the corresponding moments of inertia. The time for reaching the minimum anisotropy value can be approximated by $t_{dephas}=(I_B/k_BT)^{1/2}$,[36] which yields $t_{dephas} \approx 3\,ps$ for fluorescein at $300\,K$, as recently determined in Ref. [22].

However, the experimentally determined anisotropy function for **[FL-H]**$^-$ (Figure 3b) by tPF does not point to a successful detection of a strong molecular alignment. Firstly, the initial anisotropy r_0 is not unambiguously obtained from our experimental data. Secondly, the difference in the signal for perpendicular and parallel pump-probe polarization is small. The former difficulty stems from the nearly identical and fast rise of both signals close to time zero. One should also note that the two traces for perpendicular and parallel pump-probe polarization have been measured consecutively so that we cannot exclude a slight temporal shift (~40 fs) between the transients. This uncertainty in absolute position and thus delay time could lead to strong variations for the anisotropy function in the rising part of the signal. We therefore neglect the values for $r(t)$ calculated in this early part of the transient (shaded area in Figure 3b) and analyze only the data with $t_{delay} \geq 300$ fs. Nonetheless, a dependence on the relative laser polarization is clearly present in the data at hand, with the trace for perpendicular orientation being larger than the trace for parallel orientation (Figure 2). Moreover, the

trace recorded at magic angle relative polarization lies in its intensity between the two former scans (*cf.* Figure S4). Furthermore, the difference between the two traces vanishes with increasing time delay (at ~4-6 ps). The function $r(t)$ starts with small negative values (-0.05 to -0.1), which indicates perpendicularly polarized pump-probe transitions. However, theoretical (initial) values for pure transitions of that type (r_0(*perpendicular,* 1+2')=-0.29) are not matched. Based on the data presented it is also difficult to estimate reliably an approximate dephasing time, as the initial anisotropy r_0 could not be determined and the S/N for this data is not sufficient for a more detailed analysis. These results are different compared with the rotational dynamics for **[FL-H]⁻** as obtained by TR-PA recently, which clearly point to a strong molecular alignment.[22]

3.5.2 Dynamics of [FL+H]⁺

As our mass spectrometric setup allows for studies on both negatively and positively charged ions, we were also able to investigate and directly compare the dynamics of the related protonated fluorescein cations **[FL+H]⁺** to the already discussed monoanions. This exemplifies an advantage of our ion trap gas phase approach since the separate photophysical study of **[FL+H]⁺** in solution is strongly hampered by the influence of protonation equilibria.[1]

[FL+H]⁺ ions were excited by pump laser pulses at the absorption maximum of their $S_1{\leftarrow}S_0$ transition (425 nm, 0.8 μJ) as documented in the literature[18-19] and subsequently probed with high intensity pulses of longer wavelength (1200 nm, 150 μJ). The pump-probe PF mass spectrum (Figure 4, for a difference mass spectrum *cf.* Figure S1b) of isolated **[FL+H]⁺** (m/z 333, most abundant isotope) provides evidence for a more complex fragmentation behavior than observed for **[FL-H]⁻**.
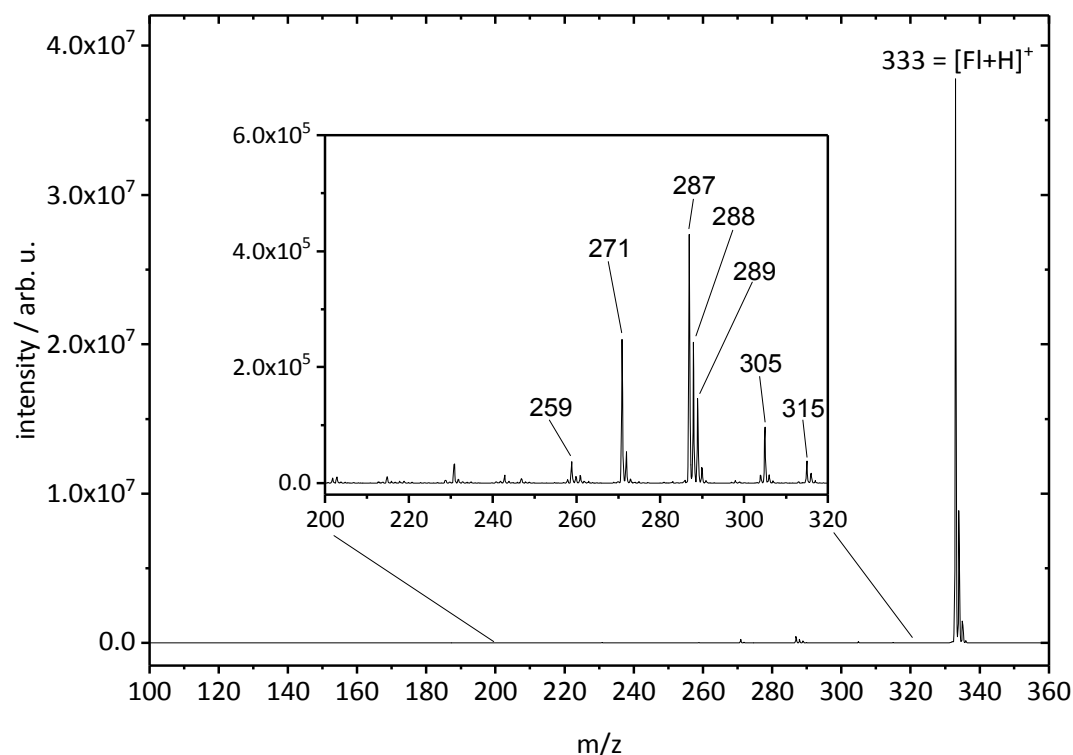
Figure 4 Mass spectrum depicting the formation of fragment ions after pump-probe photoexcitation of isolated **[FL+H]⁺** (m/z 333, most abundant isotope).

Prominent identified fragment ions are: m/z 315 (neutral loss of H_2O); m/z 305 (neutral loss of CO); m/z 271 (neutral loss of H_2O and HCOOH (formic acid)) apart from the main (~60% of the total fragmentation signal) product ion at m/z 287, corresponding to a loss of HCOOH, most likely from the benzoic acid moiety. This fragmentation pattern was noted before in Ref. [18-19] and also observed in IR multiple-photon dissociation (IRMPD) experiments.[20] Furthermore, **[FL+H]⁺** exhibits a much lower fragmentation yield than **[FL-H]⁻**, even when applying higher pump photon energy and intensity for photoexcitation (425 nm vs. 520 nm excitation wavelength and an intensity of 0.8 µJ vs. 0.3 µJ, respectively). Measurement of the intensity dependence of the one-color (pump-only) PF yield clearly suggests a two-photon absorption process prior to fragmentation of **[FL+H]⁺** (Figure S3b). This is understandable upon consideration of the C-COOH bond dissociation enthalpy (~430 kJ/mol for benzoic acid)[34] vs. the pump photon energy (425 nm; ~280 kJ/mol). Based on the much lower fragmentation yield (compared to **[FL-H]⁻**), we infer that this bond enthalpy is either higher for **[FL+H]⁺** or energy transfer from the excited xanthene unit to the benzoic acid ring is less efficient than for **[FL-H]⁻**.

Thus, we assume that additional dissociation channels are accessible producing a complex fragment pattern.

Interestingly, very similar fragmentation pattern were reported for both **[FL+H]$^+$** and **[FL-H]$^-$** in IRMPD experiments.[20] This points, for both excitation schemes (nanosecond IRMPD and fs UV/Vis), toward dissociation starting from highly vibrationally excited electronic ground states. However, the photonic excitation mechanisms in both cases are evidently different. Whereas the generally accepted mechanism of IRMPD is based on consecutive absorption and fast vibrational redistribution steps (usually within ps to ns),[37] we have to assume for fs two-photon UV PF a fast resonant absorption of two photons within one femtosecond laser pulse of ~100 fs width. This is based on the assumption that collisional cooling in the ion trap takes place in between the laser pulses (millisecond time scale). Consequently there is not enough time for energy redistribution between absorption of these photons, unless it proceeds on a sub-100 fs timescale. Subsequent internal conversion leads to highly vibrationally excited states from which eventually fragmentation takes place.

Figure 5 depicts the total fragment ion yield of **[FL+H]⁺** as a function of time delay for parallel and perpendicular pump-probe polarization.
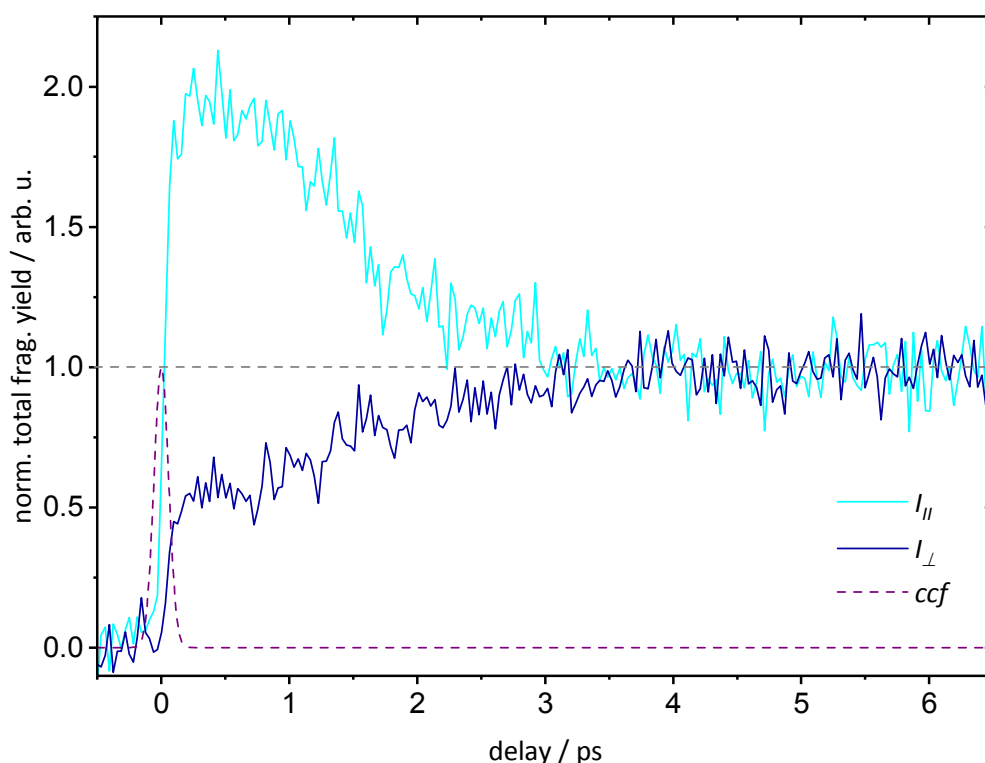
Figure 5 Normalized total fragmentation efficiency of **[FL+H]⁺** as a function of pump-probe delay depending on the relative polarization between pump and probe pulses; λ_{pump}=425 nm (0.8 µJ) and λ_{probe}=1200 nm (150 µJ).

The data were background corrected and the signal was normalized to unity at long time delay, as already described for measurements on **[FL-H]⁻**. Comparing the results obtained for **[FL-H]⁻** and **[FL+H]⁺**, the difference is striking. First and foremost, the transients of **[FL+H]⁺** show a strong dependence on the relative laser polarization, with the transient for parallel polarized pump and probe pulses exhibiting a much stronger signal at short time delay compared to the trace for perpendicular polarization. Both polarization traces approach a constant signal value (equivalent to the magic angle signal level) after a time delay of ~3 ps. Secondly, the initial rise time of the transient signal for both traces is much shorter (~250 fs) than obtained for **[FL-H]⁻**. Lastly, no periodic modulation of the signal can be observed.

For further analysis, the isotropic signal $S(t)$ (Figure 6a) and anisotropy signal $r(t)$ (Figure 6b) were calculated from the data shown in Figure 5.
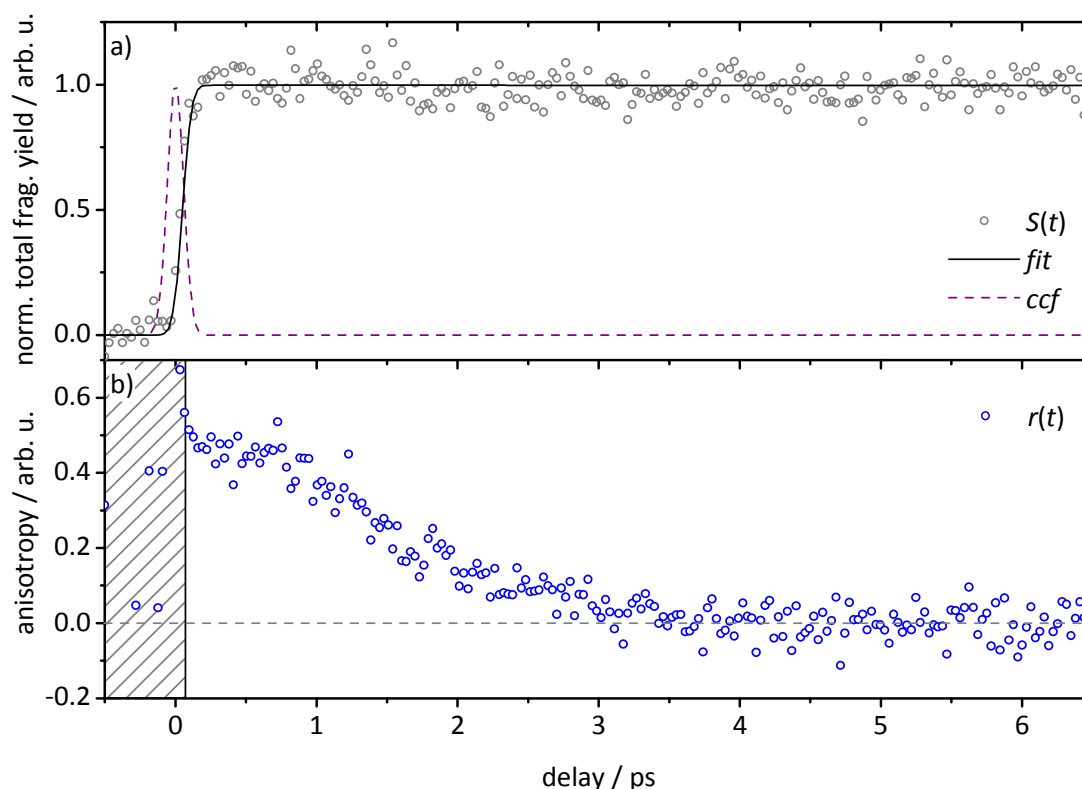
Figure 6 (a) Time-resolved isotropic signal function $S(t)$ exhibiting the formation of a long lived S_1 state and **(b)** time-resolved anisotropy function $r(t)$ for the analysis of rotational dephasing of **[FL+H]$^+$**; $S(t)$ and $r(t)$ were calculated from equation (1) and (2), respectively.

By removing the contribution of rotational dephasing from the transient, it is revealed that the transient signal of **[FL+H]$^+$** shows no ultrafast dynamics besides rapid formation of a long lived state (similar to **[FL-H]$^-$**, no notable decay was observed for a time delay of up to 800 ps). Furthermore, no oscillatory component and thus vibrational coherence can be discerned from the calculated isotropic signal.

From the calculated anisotropy function $r(t)$ one can distinguish two notable features: firstly, the anisotropy is lost after ~3 ps, as the function reaches its minimum value. Secondly, the anisotropy has an initial value of $r_0 \approx +0.5$. A value for r_0 exceeding +0.4 in fluorescence anisotropy investigations is usually indicative of a multiple-photon excitation process, reaching a maximum of 0.57 and 0.67 for a two photon absorption and three photon absorption process, respectively (assuming a parallel orientation of the transition dipole moments for excitation and probing).[38-40] According to equation (4), for example, the value of $r_0 \approx +0.5$ can be recovered assuming $r_0=(4/7)P_2(\mu_1\mu_2)=0.5$, which yields an angle of $\approx 17°$ between μ_1 and μ_2. Given that the calculated rotational

constants for the electronic ground states of **[FL+H]⁺** and **[FL-H]⁻** differ only by 1-4 % (*cf.* Figure S5 and Table S1), one can estimate that the characteristic rotational decay times are very similar. Moreover, we estimate that the changes of the rotational constants by electronic excitation will be on the same order of magnitude, so that in the following we use only the ground state constants for analysis. For **[FL+H]⁺** the calculated ground state rotational constants are: A=0.2285 GHz, B=0.2229 GHz and C=0.1384 GHz, resulting in the following moments of inertia: $I_A=I_x=3.673\cdot10^{-44}$ kg m², $I_B=I_y=3.765\cdot10^{-44}$ kg m² and $I_C=I_z=6.064\cdot10^{-44}$ kg m². Thus, t_{dephas} at 300 K is estimated to ~3 ps, as discussed for **[FL-H]⁻** (see *3.5.1*).

In order to model the dynamics of the rotational anisotropy, *i.e.* rotational dephasing time, in more detail we have simulated the time-resolved orientational correlation function for different TM orientations, assuming parallel polarization for both pump and probe steps ($\boldsymbol{\mu}_1=\boldsymbol{\mu}_2$). After scaling for the maximum value, our simulation reproduces the experimental $r(t)$ trace nicely (Figure 7), assuming that the TMs are parallel to the axis of the smallest moment of inertia. The theoretical basis for the simulations and their input parameters, *i.e.* orientation of TM, moments of inertia and temperature, are given as supplementary material (*cf. 3.8.4*; see also Ref. [41]).
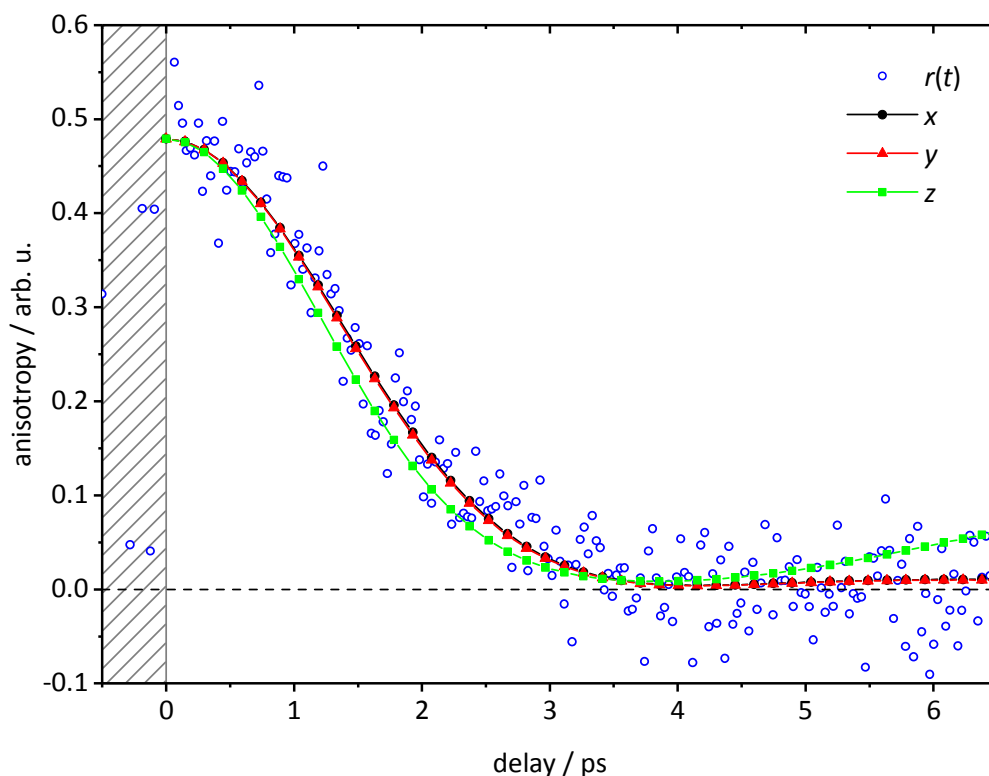
Figure 7 Time-resolved anisotropy $r(t)$ exhibiting rotational dephasing of **[FL+H]⁺**. Black dots, red triangles, and green squares represent $r(t)$ simulated for TMs $\boldsymbol{\mu}_1=\boldsymbol{\mu}_2$ directed along the axis of the smallest (x), intermediate (y) and largest (z) moment of inertia, respectively. Blue circles show experimental $r(t)$ from Figure 6a.

3.5.3 Comparison and discussion

Comparing the presented experimental results for the ultrafast dynamics of the ion-trapped and isolated deprotonated fluorescein **[FL-H]⁻** and protonated fluorescein **[FL+H]⁺** the following points are remarkable: 1) **[FL-H]⁻** exhibits upon electronic excitation strong vibrational coherences in its tPF trace whereas **[FL+H]⁺** does not display this behavior, 2) **[FL-H]⁻** exhibits only a weak anisotropy pointing towards perpendicularly oriented pump-probe transitions, whereas **[FL+H]⁺** shows a clear and strong alignment based on parallel oriented pump-probe transitions with a characteristic rotational dephasing time. Dephasing for **[FL+H]⁺** can be successfully modeled employing the ion ensemble temperature and the relevant molecular rotational constants (moments of inertia). Furthermore, 3) in comparison of our results for **[FL-H]⁻** to the recently reported data by TR-PA[22] one can state a good agreement with respect to the observation and frequencies of the vibrational coherence (28 cm⁻¹ vs. 32 cm⁻¹). However, the results for the time-resolved anisotropy function are completely different.

Only weak anisotropy for our employed PF scheme was found, but strong anisotropy and rotational dephasing was obtained for photoelectron detection.[22] How can we rationalize this drastic difference in ultrafast dynamics and anisotropy of these two isoelectronic molecular systems?

The occurrence of vibrational coherences upon electronic excitation, *i.e.* preparation of vibrational wave-packets in the excited state is usually connected to an inherent vibrational excitation of the electronically excited state with respect to one or several specific modes. If the ground and excited state exhibit significantly different geometries along a vibrational coordinate, coherent excitation of several similar vibrational modes in the excited state potential energy surface is possible. A vibrational wave-packet, comprised of several superimposed vibrational states with a favorable phase relation, is then launched, which oscillates with a period close to the relevant vibrational mode and finally decays by coupling to other vibrational modes. Since the vibrational timescale is usually much shorter than the rotational one, a superposition of vibrational and rotational wave-packets may be observed, as reported *e.g.* for polarized four-wave mixing spectroscopy on gaseous iodine.[42] In the case of **[FL-H]**⁻, Horke *et al.* assigned a low-frequency torsional motion of the benzoic moiety *vs.* the xanthene unit to the experimentally observed vibration of 32 cm⁻¹. The dihedral angle between both units changes from 90° in the ground state to 53° in the electronically excited state.[22] This assignment was supported by TD-DFT calculations and geometry optimization of the first electronically excited state of **[FL-H]**⁻. We have observed a similar frequency (28 cm⁻¹) for **[FL-H]**⁻ by tPF, so that its rationalization can be given on the same grounds. However, for **[FL+H]**⁺ this relaxation coordinate seems not to play a significant role. In order to support this hypothesis, we have performed single-point energy calculations (method see section *3.4*) for the transition energies of distorted ground state geometries with dihedral angles between 90° and 40° (Figure 8) which clearly show that a relaxation for **[FL-H]**⁻ is energetically possible whereas for **[FL+H]**⁺ only an increase of energy for $\varphi<90°$ was found. These theoretical results are consistent with our experimental observations.
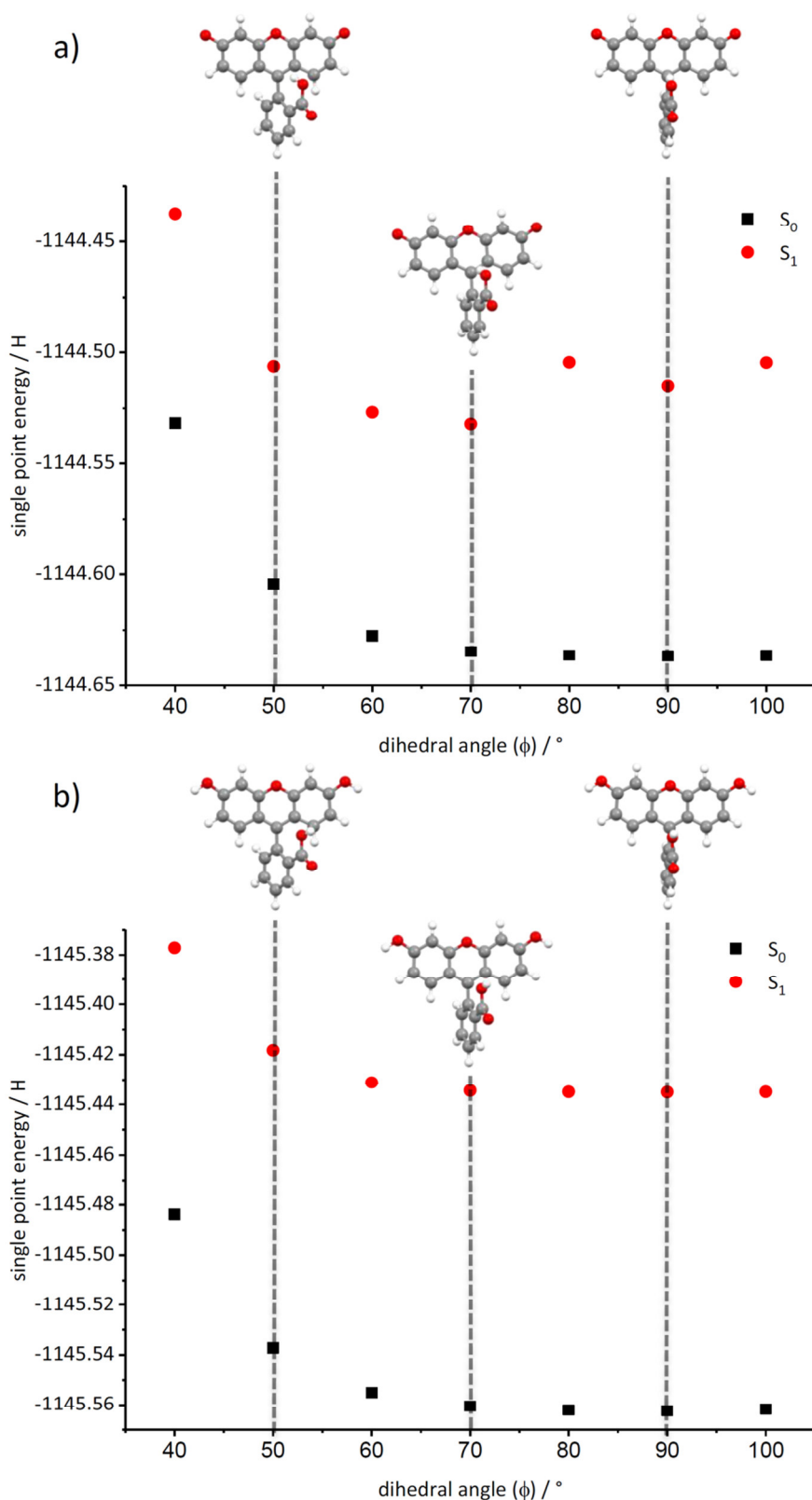
Figure 8 Calculated singlet point energies of the S_0 (black squares) and S_1 (red circles) depending on the dihedral angle φ (*cf.* Scheme 1). Calculations for **[FL-H]⁻ (a)** suggest an excited state geometry with lower energy for $\varphi<90°$ in contrast to the energetically lowest ground state geometry ($\varphi\approx90°$). For **[FL+H]⁺ (b)** the energetically lowest S_0 and S_1 geometries are obtained at a dihedral angle of $\varphi\approx90°$.

The differences in the time-resolved anisotropy function $r(t)$ obtained by tPF and TR-PA for **[FL-H]⁻** and also the differences towards the results for **[FL+H]⁺** can only be qualitatively rationalized by variations in the respective higher lying electronic states. Since the excitation (pump) wavelength for **[FL-H]⁻** was nearly the same in tPF and TR-PA experiments, the discrepancies can only originate from different probe wavelengths (2x1200 nm vs. 400 nm) and detection schemes. Most crucial for interrogating molecular alignment and thus gaining information on rotational dynamics by this pump-probe method is that the probe laser absorption is connected to a transition with a well-defined orientation of the related transition dipole moment, most desirably parallel (or perpendicular) to the pump transition. Since the number and density of electronically excited states of xanthene dyes is strongly increasing in this energy region (~4-6 eV), we assume that this condition is not generally fulfilled. However, in Ref. [22] a polarization-sensitive probe was established by detecting energy resolved electrons after time-resolved PD from anions. Similar experimental schemes for the detection of rotational wave-packets have been reported before for time-resolved photoelectron imaging of neutral molecules.[43-44] In the detection scheme that we use in our experiments, we cannot impose polarization-sensitivity due to the long timescales (μs regime) involved in the generation of photofragments and their storage in the 3D ion trap. Thus, we rely on utilization of appropriate electronic transitions for the probe laser in the molecules under study. Based on these considerations we infer that for **[FL-H]⁻** the probe laser leads to excitation of several higher lying electronically excited states with mostly perpendicular orientation of TMs, whereas for the **[FL+H]⁺** only one or a few states with parallel oriented TMs are singled out.

This discussion points towards weaknesses of the tPF method that one should be aware of: the lack of knowledge about the assignment of the probe laser excitation process and its (often) multi-photonic character. We assume that the cross section for absorption of the probe laser pulse is altered for different vibronic states, which is the basis for studying ultrafast electronic dynamics by this scheme. This could make the comparison of the dynamics of different species difficult since one cannot completely exclude "unfortunate" probe transitions with either very small cross sections or very similar cross sections for initial and final states of a process. This means that in the case of small cross sections the corresponding electronically excited states may be missed and for

similar cross sections it may not be possible to map electronic dynamics at all. We believe that both possibilities do not apply to the investigated **[FL-H]**[-] and **[FL+H]**[+] species since in both cases we observed the formation of a long-lived electronically excited state and detected some ultrafast dynamics on top of that. However, at the present status of our knowledge about the higher electronically excited states of the fluorescein molecular system and the tPF method we cannot completely rule out an explanation for the non-observation of wave-packet dynamics in **[FL+H]**[+], which is based on the assumption that in this case the probe laser cross section is not dependent on the torsional wave packet dynamics.

Taking into account these considerations, we can only qualitatively characterize the molecular electronic level structure of the molecular ionic species of interest. These qualitative rationalizations have to be supported in the future by accurate electronic structure and geometry calculations for the higher lying electronic states of **[FL-H]**[-] and **[FL+H]**[+].

Finally we note, that preliminary experiments for other fluorescein derivatives in our laboratory (e.g., 2',7'-Dichlorofluorescein, 2',7'-Difluorofluorescein, 5-Aminofluorescein and 5-Nitrofluorescein), gave very similar results for the deprotonated and protonated fluorescein species, respectively.

3.6 Summary and conclusions

In summary we have obtained by tPF the excited state vibrational and rotational dynamics of **[FL-H]**[-] and **[FL+H]**[+] in an ion trap at room temperature. Pronounced vibrational wave-packet motion was observed for **[FL-H]**[-], which is connected to the relaxation of the dihedral angle between the benzoic acid and xanthene units in the electronically excited state, as assigned before in Ref. [22]. For **[FL+H]**[+] no vibrational wave-packets were observed by tPF. Since the final state of the probe transition is not known, it cannot be completely excluded that the probe laser cross section for **[FL+H]**[+] might be insensitive to possible wave-packet dynamics in the primary excited state. However, TD-DFT calculations suggest for **[FL+H]**[+] an excited state structure similar to the ground state with a dihedral angle of 90°, so that a wave-packet could not be launched for this torsional angle.

The polarization dependence of the tPF transients for **[FL-H]**⁻ was weak and could be related to a superposition of probe transitions with perpendicularly aligned TM with respect to the xanthene unit. For **[FL+H]**⁺ a strong polarization dependence was observed and the time-resolved anisotropy function was determined. The observed rotational dephasing was interpreted by the loss of anisotropy of an **[FL+H]**⁺ ion ensemble at room temperature. The dephasing of the corresponding rotational wave-packet was successfully simulated by the time-resolved orientational correlation function. From this analysis we conclude that the probe process of **[FL+H]**⁺ consists probably of a two-photon transition with a TM aligned parallel to the xanthene unit.

In conclusion, the applied technique of fs tPF in an ion trap proves to be very valuable for the analysis of ultrafast molecular vibrational and rotational dynamics and electronically excited states of ionic dye molecules under isolated conditions. It is complementary to TR-PA since it is based on the detection of fragment ions instead of the corresponding photoelectrons (for anions) and extends this methodology towards cationic systems. The drawback of the tPF method lies in the multiphotonic character of its probe process and lack of knowledge about the related absorption cross sections and the involved higher lying electronically excited states. However, the latter deficit can also be turned into a tool for gaining information on the character of these states, as demonstrated in this work.

Acknowledgements

3.7 References

[1] R. Sjöback, J. Nygren, M. Kubista, *"Absorption and fluorescence properties of fluorescein"*, *Spectrochim. Acta Mol. Biomol.Spectrosc.* **1995**, *51*, L7-L21.

[2] L. D. Lavis, T.-Y. Chao, R. T. Raines, *"Fluorogenic Label for Biomolecular Imaging"*, *ACS Chem. Biol.* **2006**, *1*, 252-260.

[3] L. D. Lavis, R. T. Raines, *"Bright Ideas for Chemical Biology"*, *ACS Chem. Biol.* **2008**, *3*, 142-155.

[4] E. W. Miller, S. X. Bian, C. J. Chang, *"A Fluorescent Sensor for Imaging Reversible Redox Cycles in Living Cells"*, *J. Am. Chem. Soc.* **2007**, *129*, 3458-3459.

[5] X. Li, X. Gao, W. Shi, H. Ma, *"Design Strategies for Water-Soluble Small Molecular Chromogenic and Fluorogenic Probes"*, *Chem. Rev.* **2014**, *114*, 590-659.

[6] M. U. Kumke, G. Li, L. B. McGown, G. T. Walker, C. P. Linn, *"Hybridization of fluorescein-labeled DNA oligomers detected by fluorescence anisotropy with protein binding enhancement"*, *Anal. Chem.* **1995**, *67*, 3945-3951.

[7] D. M. Jameson, J. A. Ross, *"Fluorescence Polarization/Anisotropy in Diagnostics and Imaging"*, *Chem. Rev.* **2010**, *110*, 2685-2708.

[8] K. Suhling, J. Siegel, P. M. P. Lanigan, S. Lévêque-Fort, S. E. D. Webb, D. Phillips, D. M. Davis, P. M. W. French, *"Time-resolved fluorescence anisotropy imaging applied to live cells"*, *Opt. Lett.* **2004**, *29*, 584-586.

[9] M. Y. Berezin, S. Achilefu, *"Fluorescence Lifetime Measurements and Biological Imaging"*, *Chem. Rev.* **2010**, *110*, 2641-2684.

[10] M. Schäferling, *"The Art of Fluorescence Imaging with Chemical Sensors"*, *Angew. Chem. Int. Ed.* **2012**, *51*, 3532-3554.

[11] C. A. Royer, *"Probing Protein Folding and Conformational Transitions with Fluorescence"*, *Chem. Rev.* **2006**, *106*, 1769-1784.

[12] D. Allsop, L. Swanson, S. Moore, Y. Davies, A. York, O. M. A. El-Agnaf, I. Soutar, *"Fluorescence Anisotropy: A Method for Early Detection of Alzheimer b-Peptide (Ab) Aggregation"*, *Biochem. Biophys. Res. Commun.* **2001**, *285*, 58-63.

[13] B. J. Thevenin, N. Periasamy, S. B. Shohet, A. S. Verkman, *"Segmental dynamics of the cytoplasmic domain of erythrocyte band 3 determined by time-resolved fluorescence anisotropy: sensitivity to pH and ligand binding"*, *Proc. Natl. Acad. Sci. . U S A* **1994**, *91*, 1741-1745.

[14] E. Deprez, P. Tauc, H. Leh, J.-F. Mouscadet, C. Auclair, M. E. Hawkins, J.-C. Brochon, *"DNA binding induces dissociation of the multimeric form of HIV-1 integrase: A time-resolved fluorescence anisotropy study"*, *Proc. Natl. Acad. Sci.* **2001**, *98*, 10090-10095.

[15] R. M. Clegg, A. I. H. Murchie, A. Zechel, C. Carlberg, S. Diekmann, D. M. J. Lilley, *"Fluorescence resonance energy transfer analysis of the structure of the four-way DNA junction"*, *Biochem.* **1992**, *31*, 4846-4856.

[16] S. M. Riddle, K. L. Vedvik, G. T. Hanson, K. W. Vogel, *"Time-resolved fluorescence resonance energy transfer kinase assays using physiological protein substrates: Applications of terbium–fluorescein and terbium–green fluorescent protein fluorescence resonance energy transfer pairs"*, *Anal. Biochem.* **2006**, *356*, 108-116.

[17] P. S. Eis, D. P. Millar, *"Conformational distributions of a four-way DNA junction revealed by time-resolved fluorescence resonance energy transfer"*, *Biochem.* **1993**, *32*, 13852-13860.

[18] P. D. McQueen, S. Sagoo, H. Yao, R. A. Jockusch, *"On the Intrinsic Photophysics of Fluorescein"*, *Angew. Chem. Int. Ed.* **2010**, *49*, 9193-9196.

[19] H. Yao, R. A. Jockusch, *"Fluorescence and Electronic Action Spectroscopy of Mass-Selected Gas-Phase Fluorescein, 2′,7′-Dichlorofluorescein, and 2′,7′-Difluorofluorescein Ions"*, *J. Phys. Chem. A* **2013**, *117*, 1351-1359.

[20] H. Yao, J. D. Steill, J. Oomens, R. A. Jockusch, *"Infrared Multiple Photon Dissociation Action Spectroscopy and Computational Studies of Mass-Selected Gas-Phase Fluorescein and 2′,7′-Dichlorofluorescein Ions"*, *J. Phys. Chem. A* **2011**, *115*, 9739-9747.

[21] T. Tanabe, M. Saito, K. Noda, E. B. Starikov, *"Molecular structure conversion of fluorescein monoanions in an electrostatic storage ring"*, *Eur. Phys. J. D* **2012**, *66*, 163.

[22] D. A. Horke, A. S. Chatterley, J. N. Bull, J. R. R. Verlet, *"Time-Resolved Photodetachment Anisotropy: Gas-Phase Rotational and Vibrational Dynamics of the Fluorescein Anion"*, *J. Phys. Chem. Lett.* **2015**, *6*, 189-194.

[23] D. Imanbaew, Y. Nosenko, C. Kerner, K. Chevalier, F. Rupp, C. Riehn, W. R. Thiel, R. Diller, *"Excited-state dynamics of a ruthenium(II) catalyst studied by transient photofragmentation in gas phase and transient absorption in solution"*, *Chem. Phys.* **2014**, *442*, 53-61.

[24] D. Nolting, T. Schultz, I. V. Hertel, R. Weinkauf, *"Excited state dynamics and fragmentation channels of the protonated dipeptide H2N-Leu-Trp-COOH"*, *Phys. Chem. Chem. Phys.* **2006**, *8*, 5247-5254.

[25] R. M. Hochstrasser, M. A. Pereira, P. E. Share, M. J. Sarisky, Y. R. Kim, S. T. Repinec, R. J. Sension, J. R. G. Thorne, M. Iannone, R. Diller, P. A. Anfinrud, C. Han, T. Lian, B. Locke, *"Anisotropy studies of ultrafast dipole reorientations"*, *Proc. Indian. Acad. Sci. Chem. Sci.* **1991**, *103*, 351-362.

[26] P. M. Felker, A. H. Zewail, *"Purely rotational coherence effect and time-resolved sub-Doppler spectroscopy of large molecules. I. Theoretical"*, *J. Chem. Phys.* **1987**, *86*, 2460-2482.

[27] A. P. Blokhin, M. F. Gelin, I. I. Kalosha, S. A. Polubisok, V. A. Tolkachev, *"Polarized fluorescence of polyatomic fragments produced through photodissociation of polyatomic molecules in the gas phase"*, *J. Chem. Phys.* **1999**, *110*, 978-993.

[28] A. P. Blokhin, *Ser. Fiz.-Mat. Navuk* **1984**, *4*, 58-66.

[29] J.-D. Chai, M. Head-Gordon, *"Long-range corrected hybrid density functionals with damped atom-atom dispersion corrections"*, *Phys. Chem. Chem. Phys.* **2008**, *10*, 6615-6620.

[30] M. J. Frisch, G. W. Trucks, H. B. Schlegel, G. E. Scuseria, M. A. Robb, J. R. Cheeseman, G. Scalmani, V. Barone, B. Mennucci, G. A. Petersson, H. Nakatsuji, M. Caricato, X. Li, H. P. Hratchian, A. F. Izmaylov, J. Bloino, G. Zheng, J. L. Sonnenberg, M. Hada, M. Ehara, K. Toyota, R. Fukuda, J. Hasegawa, M. Ishida, T. Nakajima, Y. Honda, O. Kitao, H. Nakai, T. Vreven, J. A. Montgomery Jr., J. E. Peralta, F. Ogliaro, M. J. Bearpark, J. Heyd, E. N. Brothers, K. N. Kudin, V. N. Staroverov, R. Kobayashi, J. Normand, K. Raghavachari, A. P. Rendell, J. C. Burant, S. S. Iyengar, J. Tomasi, M. Cossi, N. Rega, N. J. Millam, M. Klene, J. E. Knox, J. B. Cross, V. Bakken, C. Adamo, J. Jaramillo, R. Gomperts, R. E. Stratmann, O. Yazyev, A. J. Austin, R. Cammi, C. Pomelli, J. W. Ochterski, R. L. Martin, K. Morokuma, V. G. Zakrzewski, G. A. Voth, P. Salvador, J. J. Dannenberg, S. Dapprich, A. D. Daniels, Ö. Farkas, J. B. Foresman, J. V. Ortiz, J. Cioslowski, D. J. Fox, Gaussian, Inc., Wallingford, CT, USA, **2009**.

[31] D. Nolting, R. Weinkauf, I. V. Hertel, T. Schultz, *"Excited-State Relaxation of Protonated Adenine"*, Chem. Phys. Chem. **2007**, *8*, 751-755.

[32] H. Kang, C. Dedonder-Lardeux, C. Jouvet, G. Grégoire, C. Desfrançois, J. P. Schermann, M. Barat, A. Fayeton, *"Control of Bond-Cleaving Reactions of Free Protonated Tryptophan Ion by Femtosecond Laser Pulses"*, J. Phys. Chem. A **2005**, *109*, 2417-2420.

[33] H. Kang, C. Jouvet, C. Dedonder-Lardeux, S. Martrenchard, C. Charrière, G. Grégoire, C. Desfrançois, J. P. Schermann, M. Barat, J. A. Fayeton, *"Photoinduced processes in protonated tryptamine"*, J. Chem. Phys. **2005**, *122*, 084307.

[34] J. Shi, X.-Y. Huang, J.-P. Wang, R. Li, *"A Theoretical Study on C−COOH Homolytic Bond Dissociation Enthalpies"*, J. Phys. Chem. A **2010**, *114*, 6263-6272.

[35] M. W. Forbes, R. A. Jockusch, *"Gas-Phase Fluorescence Excitation and Emission Spectroscopy of Three Xanthene Dyes (Rhodamine 575, Rhodamine 590 and Rhodamine 6G) in a Quadrupole Ion Trap Mass Spectrometer"*, J. Am. Soc. Mass. Spectrom. **2011**, *22*, 93-109.

[36] A. P. Blokhin, M. F. Gelin, E. V. Khoroshilov, I. V. Kryukov, A. V. Sharkov, *"Dynamics of optically induced anisotropy in an ensemble of asymmetric top molecules in the gas phase"*, Opt. Spectrosc. **2003**, *95*, 346-352.

[37] J. Roithova, *"Characterization of reaction intermediates by ion spectroscopy"*, Chem. Soc. Rev. **2012**, *41*, 547-559.

[38] A. Kawski, J. Gryczyński, Z. Gryczyński, *Z. Naturforsch. A* **1993**, *48*, 551.

[39] I. Gryczynski, H. M. Malak, S. W. Hell, J. R. Lakowicz, *"Three-photon excitation of 2,5-bis(4-biphenyl)oxazole: steady-state and time-resolved intensities and anisotropies"*, BIOMEDO **1996**, *1*, 473-480.

[40] I. Gryczynski, H. Malak, J. R. Lakowicz, *"Three-photon induced fluorescence of 2,5-diphenyloxazole with a femtosecond Ti:sapphire laser"*, Chem. Phys. Lett. **1995**, *245*, 30-35.

[41] A. P. Blokhin, M. F. Gelin, O. V. Buganov, V. A. Dubovskii, S. A. Tikhomirov, G. B. Tolstorozhev, *"Femtosecond Dynamics of Optically Induced Anisotropy of Complex Molecules in the Gas Phase"*, J. Appl. Spectrosc. **2003**, *70*, 70-78.

[42] T. Siebert, M. Schmitt, A. Vierheilig, G. Flachenecker, V. Engel, A. Materny, W. Kiefer, *"Separation of vibrational and rotational coherences with polarized femtosecond time-resolved four-wave mixing spectroscopy"*, J. Raman Spectrosc. **2000**, *31*, 25-31.

[43] A. Stolow, A. E. Bragg, D. M. Neumark, *"Femtosecond Time-Resolved Photoelectron Spectroscopy"*, Chem. Rev. **2004**, *104*, 1719-1758.

[44] T. Suzuki, *"Femtosecond Time-Resolved Photoelectron Imaging"*, Annu. Rev. Phys. Chem. **2006**, *57*, 555-592.

3.8 Supplementary material to "Rotational and vibrational dynamics of deprotonated and protonated fluorescein studied by time-resolved photofragmentation in an ion trap"

Content

3.8.1 Mass spectrometric data

Figure S1 (a) Difference mass spectrum of **[FL-H]⁻** and **(b) [FL+H]⁺** calculated by subtracting the mass spectrum recorded at negative time delay (probe-pump) from the mass spectrum at positive time delay (pump-probe); positive signals imply an increase in ion signal intensity, whereas negative signals represent a decrease in ion signal intensity. For an assignment of the mass peaks *cf.* section *3.5.1* and *3.5.2*.

3.8.2 Photofragmentation
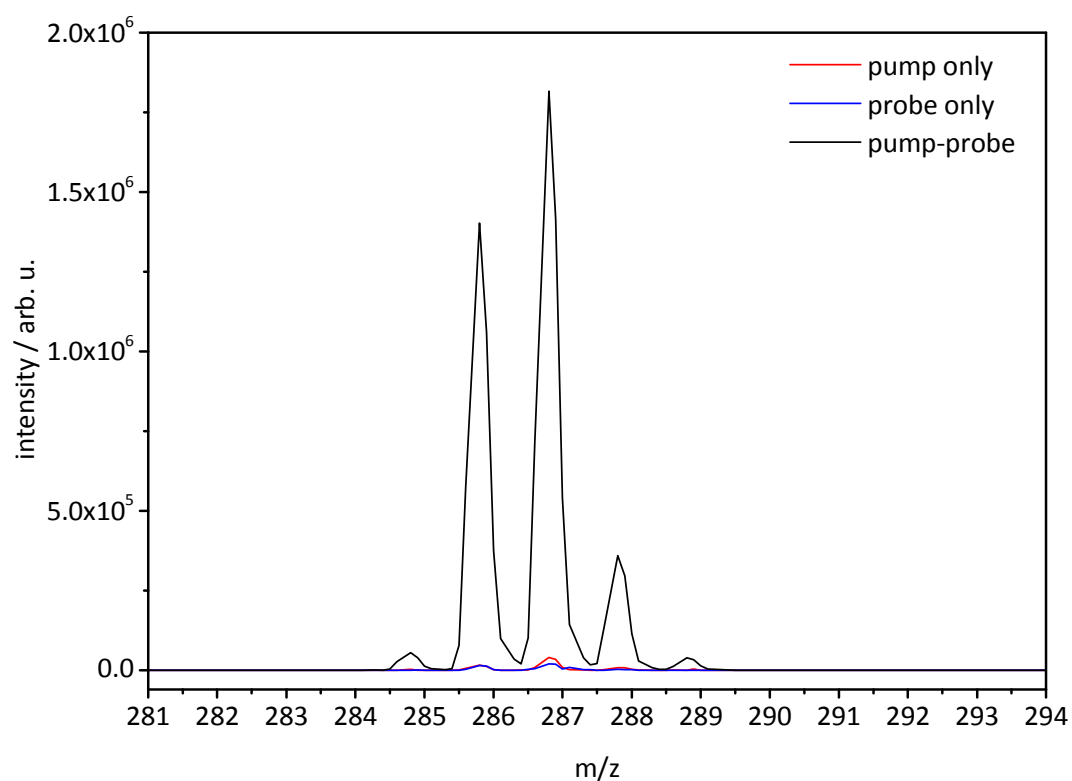
Figure S2 Fragment signal intensity (loss of CO2, HCO2) after pump only (red), probe only (blue) and coherent pump-probe photoexcitation (black) of isolated **[FL-H]$^-$**; λ_{pump}=520 nm (0.3 µJ) and λ_{probe}=1200 nm (150 µJ).
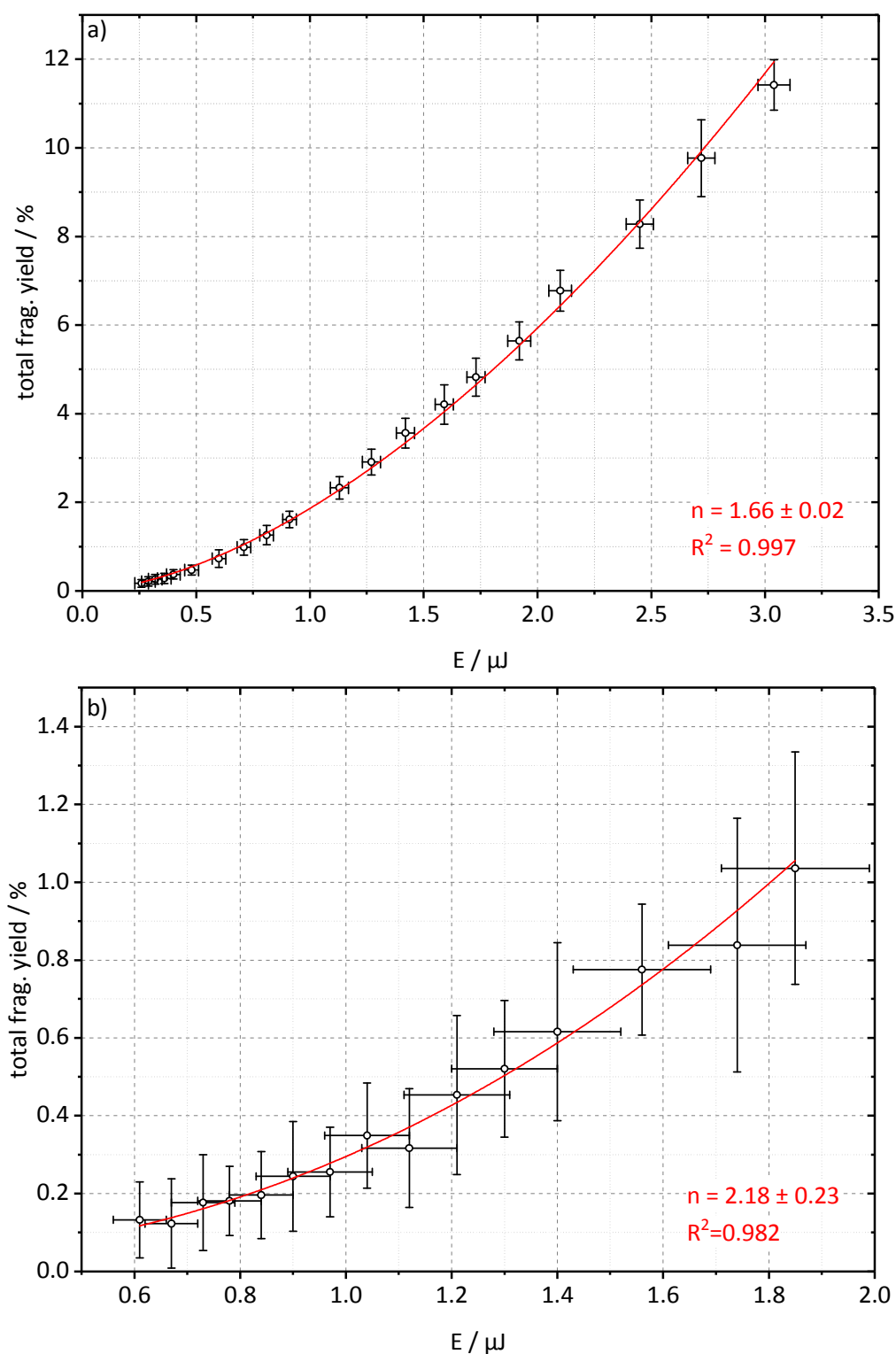
Figure S3 (a) Pulse energy E dependent total fragmentation yield Y of **[FL-H]⁻** and **(b) [FL+H]⁺** obtained by one-color photoexcitation at 520 nm and 425 nm, respectively; polynomial fits $Y = A \cdot E^n$ suggests in average a two-photon (n) absorption process for both **[FL-H]⁻** and **[FL+H]⁺**.[1]
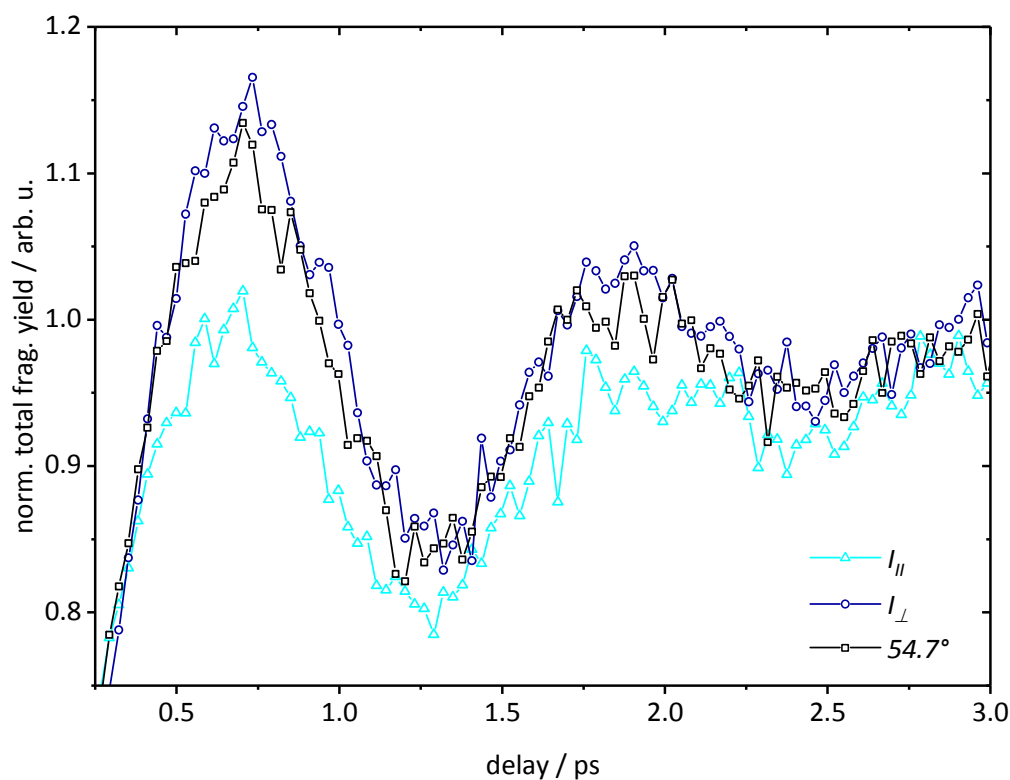
Figure S4 Transient photofragmentation traces of **[FL-H]**⁻ as a function of pump-probe delay (here shown for *Δt*=0.3–3 ps) recorded at parallel (dark blue triangles) and perpendicular (cyan circles) relative linear polarization orientation, as well as at the magic angle (black squares); λ_{pump}=520 nm (0.3 μJ) and λ_{probe}=1200 nm (150 μJ).

3.8.3 DFT calculations
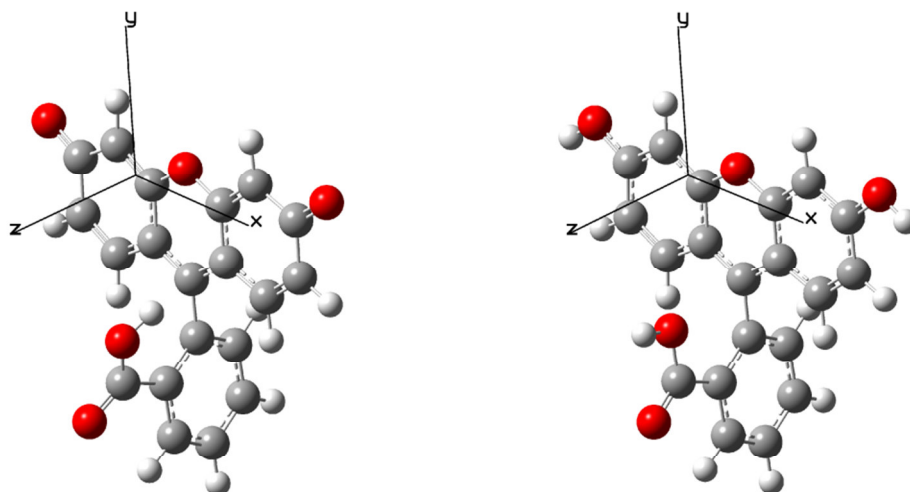
Figure S5 *Ab initio* calculated ground state geometries of **[FL-H]**$^-$ (left) and **[FL+H]**$^+$ (right). Level of theory: DFT/ωB97XD/6-31++G(d,p).

Table S1 *Ab initio* calculated ground state rotational constants and moments of inertia of **[FL-H]**$^-$ and **[FL+H]**$^+$ along the respective Cartesian axes. Level of theory: DFT/ωB97XD/6-31++G(d,p).

	[FL-H]$^-$			**[FL+H]**$^+$		
Axis i	x	y	z	x	y	z
B_i/GHz	0.2376	0.2212	0.1401	0.2285	0.2229	0.1384
I_i/10^{-44} kg·m^2	3.532	3.794	5.990	3.673	3.765	6.064

3.8.4 Calculation of the orientational correlation functions of the second rank for freely rotating asymmetric top molecules

The orientational correlation functions of equations (3) and (4) can explicitly be defined as follows:

$$
\begin{aligned}
\langle P_2(\boldsymbol{\mu}_1(0)\boldsymbol{\mu}_2(t))\rangle = & F^2_{(-2)(-2)}(t)D^2_{(-2)0}(\Omega_{\mu_a})D^{2*}_{(-2)0}(\Omega_{\mu_e}) + \\
& + F^2_{(1)(1)}(t)D^2_{(1)0}(\Omega_{\mu_a})D^{2*}_{(1)0}(\Omega_{\mu_e}) + F^2_{(-1)(-1)}(t)D^2_{(-1)0}(\Omega_{\mu_a})D^2_{(-1)0}(\Omega_{\mu_e}) + \\
& + F^2_{00}(t)D^2_{00}(\Omega_{\mu_a})D^2_{00}(\Omega_{\mu_e}) + F^2_{(2)(2)}(t)D^2_{(2)0}(\Omega_{\mu_a})D^2_{(2)0}(\Omega_{\mu_e}) + \\
& + F^2_{(2)(0)}(t)(D^2_{00}(\Omega_{\mu_a})D^2_{(2)0}(\Omega_{\mu_e}) + D^2_{(2)0}(\Omega_{\mu_a})D^2_{00}(\Omega_{\mu_e}))
\end{aligned}
\tag{S1}
$$

Here

$$
D^2_{m(\pm k)}(\Omega) = \frac{1}{\sqrt{2}}(D^2_{mk}(\Omega) \pm D^2_{m-k}(\Omega)), \; k > 0
\tag{S2}
$$

are the symmetrized Wigner's D-functions, and $\Omega_{\mu_i}(\psi_{\mu_i}, \theta_{\mu_i}, 0)$ denote the angles specifying orientations of the TMs $\boldsymbol{\mu}_1$ and $\boldsymbol{\mu}_2$ in the molecular frame.

Equation (S1) reveals that the time evolution of the orientational correlation function is governed by the six basis functions

$$
F^2_{00}(t), \; F^2_{(2)(2)}(t), \; F^2_{(2)(0)}(t), F^2_{(-2)(-2)}(t), \; F^2_{(1)(1)}(t), \; F^2_{(-1)(-1)}(t)
\tag{S3}
$$

A convenient method of the evaluation of the basis functions (S2) has been developed in Refs. [2,3]. The method employs the action-angle representation of the rotational dynamics and yields the following explicit formulas for the quantities (S3):

$$
\begin{aligned}
F^{2(\Gamma_{\pm z})}_{00}(t) = & 3\delta^2 \{ \sum_{N=-\infty}^{\infty} [(y_1 - N)^2 Q^-_{2N,0}(t) + (y_1 - 2N)^2 Q^+_{2N,1}(t)] + \\
& + 6\sum_{N=1}^{\infty} N^2 Q^-_{2N,0}(t)\} + F^{2(\Gamma_{\pm z})}_{00}(t \to \infty) ,
\end{aligned}
\tag{S4}
$$

$$
\begin{aligned}
F^{2(\Gamma_{\pm z})}_{(2)(2)}(t) = & F^{2(\Gamma_{\pm z})}_{(2)(2)}(t \to \infty) + \frac{1}{\delta^2}\{6(2+\delta^2)^2 \sum_{N=1}^{\infty} N^2 Q^-_{2N,0}(t) + \\
& + \sum_{N=-\infty}^{\infty} [(y_3(1+\delta^2) + y_4 - 2N(2+\delta^2))^2 Q^+_{2N,1}(t) + \\
& + (y_3(1+\delta^2) + y_4 - N(2+\delta^2))^2 Q^-_{2N,2}(t)]\}
\end{aligned}
\tag{S5}
$$

$$F_{(2)0}^{2(\Gamma_{\pm z})}(t) = F_{(2)0}^{2(\Gamma_{\pm z})}(t \to \infty) + \sqrt{3}\{6(2+\delta^2)\sum_{N=1}^{\infty} N^2 Q_{2N,0}^-(t) +$$

$$+ \sum_{N=-\infty}^{\infty}[((y_3(1+\delta^2)+y_4-2N(2+\delta^2))Q_{2N,1}^+(t)+$$

$$+(y_3(1+\delta^2)+y_4-N(2+\delta^2))^2 Q_{2N,2}^-(t)]\} \qquad (S6)$$

$$F_{(-2)(-2)}^{2(\Gamma_{\pm z})}(t) = (1+\delta^{-2})\{24\sum_{N=1}^{\infty} N^2 Q_{2N,0}^+(t) + \sum_{N=-\infty}^{\infty}[(y_3+y_4-4N)^2 Q_{2N,1}^-(t)+$$

$$(y_3+y_4-4N)^2 Q_{2N,2}^+(t)\} \qquad (S7)$$

$$F_{(-1)(-1)}^{2(\Gamma_{\pm z})}(t) = 6\sum_{N=0}^{\infty}(2N+1)^2 Q_{2N+1,0}^-(t) +$$

$$+ \sum_{N=-\infty}^{\infty}[(y_1+y_4-2(2N+1))^2 Q_{2N+1,1}^+(t)+(y_1+y_4-(2N+1))^2 Q_{2N+1,2}^-(t)] \qquad (S8)$$

$$F_{(1)(1)}^{2(\Gamma_{\pm z})}(t) = (1+\delta^2)\{6\sum_{N=0}^{\infty}(2N+1)^2 Q_{2N+1,0}^+(t) +$$

$$+ \sum_{N=-\infty}^{\infty}[(y_1+y_3-2(2N+1))^2 Q_{2N+1,1}^-(t)+(y_1+y_3-(2N+1))^2 Q_{2N+1,2}^+(t)]\} . \qquad (S9)$$

Here

$$F_{00}^{2(\Gamma_{\pm z})}(t \to \infty) = \frac{f_0}{2\pi}\int_{\varepsilon_0}^{1} d\varepsilon\, K b^{-3/2}(3\varepsilon^2\frac{E}{K}-1)^2 \qquad (S10)$$

$$F_{(2)(2)}^{2(\Gamma_{\pm z})}(t \to \infty) = \frac{3f_0}{2\pi}\int_{\varepsilon_0}^{1} d\varepsilon\, K b^{-3/2}((2\delta^{-2}+1)(\frac{E}{K}-1)+1-\varepsilon^2)^2 \qquad (S11)$$

$$F_{(2)0}^{2(\Gamma_{\pm z})}(t \to \infty) = \frac{\sqrt{3}f_0}{2\pi}\int_{\varepsilon_0}^{1} d\varepsilon\, K b^{-3/2}((2\delta^{-2}+1)(\frac{E}{K}-1)+1-\varepsilon^2)(3\varepsilon^2\frac{E}{K}-1) \qquad (S12)$$

are the stationary (long-time) asymptotic values of the basis functions (S3),

$$Q_{N,n}^{\pm}(t) = \frac{f_0 \pi^3}{2\delta^2} \int\limits_{\delta/\sqrt{\delta^2+1}}^{1} d\varepsilon \frac{b^{-3/2} \varepsilon^4 q^N \exp\{2n\sigma\}}{K^3 (1 + q^N \exp\{2n\sigma\})^2} P_{Nn}(t),$$ (S13)

$$P_{Nn}(t) = (1 - \beta_{Nn}^2 t^2) \exp\{-\beta_{Nn}^2 t^2 / 2\},$$ (S14)

$$\beta_{Nn} = \frac{1}{I_x \sqrt{b}} [n I_y + \frac{\varepsilon I_y (I_z - I_x)(y_4 - \pi N / 2K)}{I_z \sqrt{1 + \delta^2}}]$$ (S15)

The parameters

$$f_0 = I_y \sqrt{1 - \delta^2} \Big/ \sqrt{I_x I_z} \ , \delta^2 = I_z (I_x - I_y) / I_x (I_y - I_z),$$ (S16)

are uniquely determined by the main moments of inertia,

$$b = I_y (I_z + \varepsilon^2 (I_x - I_z)) / I_x I_z \, , q = \exp\{-\pi K' / K\},$$ (S17)

$K = K(\lambda)$ is the complete elliptic integral of the first kind,

$$K' = K(\lambda'), \lambda' = \sqrt{1 - \lambda^2} \ ,$$ (S18)

$F(u, \lambda')$ is the elliptic integral of the second kind, $E = E(\lambda)$ is the corresponding complete integral,

$$\sigma = \frac{\pi}{2K} F(u, \lambda'), u = \text{arctg}(\delta / \lambda),$$ (S19)

and $y_n = \vartheta_n'(i\sigma) / \vartheta_n(i\sigma)$ where $\vartheta_n(i\sigma)$ are the Jacobi theta functions of the complex argument.

In the above formulas, time is expressed in units of the mean rotational period $\sqrt{I_y / (kT)}$, where k is the Boltzmann constant and T is a temperature.

3.8.5 References

[1] J. D. Bhawalkar, G. S. He, P. N. Prasad, "NONLINEAR MULTIPHOTON PROCESSES IN ORGANIC AND POLYMERIC MATERIALS", *Rep. Prog. Phys.* **1996**, 59, 1041-1070.
[2] A. P. Blokhin, *Izv. AN BSSR. Ser. Fiz.-Mat.* **1986**, *2*, 70-79.
[3] A. P. Blokhin, *Izv. AN BSSR. Ser. Fiz.-Mat.* **1986**, *4*, 77.

4 Charge state dependent excited state quenching in 5-Amino- and 5-Nitrofluorescein

Dimitri Imanbaew[1], Joachim Hewer[1], Sebastian Dillinger[1], Gereon Niedner-Schatteburg[1,2], and Christoph Riehn[1,2]

[1]*Fachbereich Chemie, Technische Universität Kaiserslautern, Erwin-Schrödinger-Str. 52-54, 67663 Kaiserslautern, Germany*

[2]*Landesforschungszentrum OPTIMAS, Erwin-Schrödinger-Str. 46, 67663 Kaiserslautern, Germany*

4.1 Preamble

The following chapter is formatted as to become a manuscript for publication and has not been submitted, yet. Data acquisition, data processing and the theoretical calculations were performed by me. I received experimental support from J. Hewer and S. Dillinger for recording IRMPD spectra. The initial draft of the manuscript was written by me.

4.2 Abstract

The intrinsic photophysics of protonated and deprotonated 5-Nitro- (**[5-NF]**) and 5-Aminofluorescein (**[5-AF]**) were investigated by steady-state and transient photofragmentation spectroscopy in a 3D ion trap. Infrared multiple-photon dissociation spectroscopy revealed only for the monoanions of **[5-NF]** a strong contribution of tautomeric (phenolate, carboxylate) forms to the ion population inside the trap. The recorded gas phase absorption spectra were compared to calculations by time-dependent density functional theory (TD-DFT). Time-resolved fragment mass spectra reveal distinct differences in the excited S_1 excited state life-times on a picosecond timescale, depending sensitively on the substituent (amino-, nitro-), as well as the charge state (cationic and monoanionic). The difference in excited state dynamics was ascribed to excited state quenching by photoinduced intramolecular electron transfer (PeT). Our assumption is corroborated by the sequences of frontier orbitals obtained from DFT calculations. Additionally, the monoanionic forms of both **[5-NF]** and **[5-AF]** exhibit wave-packet dynamics. Peculiarly, the observed wave-packet dynamics are much more complicated compared to our previously reported results on unsubstituted fluorescein, requiring at least two vibrational modes for modeling the periodic modulation.

4.3 Introduction

Owing to its high absorption coefficient, bright fluorescence and high emission quantum yields,[1] fluorescein and its derivatives are used in various biochemical applications as sensors[2-5] or labels[6-9]. Often, functional groups are incorporated into the benzoic acid moiety (B) of the dye, allowing for fine-tuning of its properties such as the pK_a value and the solubility.[10] Most importantly, functionalization enables conjugation to biomolecules, necessary for spectroscopic techniques such as fluorescence imaging and fluorescence anisotropy.[11-14] These modifications, however, may drastically impact the emission properties of the dye, although the chromophore/fluorophore (xanthene moiety, X) remains chemically unaltered and almost no interaction between the phenyl ring and the fluorophore is expected. This is due to a perpendicular orientation of the sub-units, resulting in lack of π-conjugation. Nagano *et al.* demonstrated that fluorescein can be understood as a covalently linked donor-acceptor (D-A) dyad and that

fluorescence quenching may occur by intramolecular photoinduced electron transfer (PeT).[15-19] Depending on the reduction/oxidation potential, and thus the relative energies of the frontier molecular orbitals (MO) located on the donor or acceptor site (Figure 1), PeT may occur either from the photoexcited fluorophore X* (X* acting as an electron donor, d-PeT) to B or from B to X* (X* acting as an electron acceptor, a-PeT).
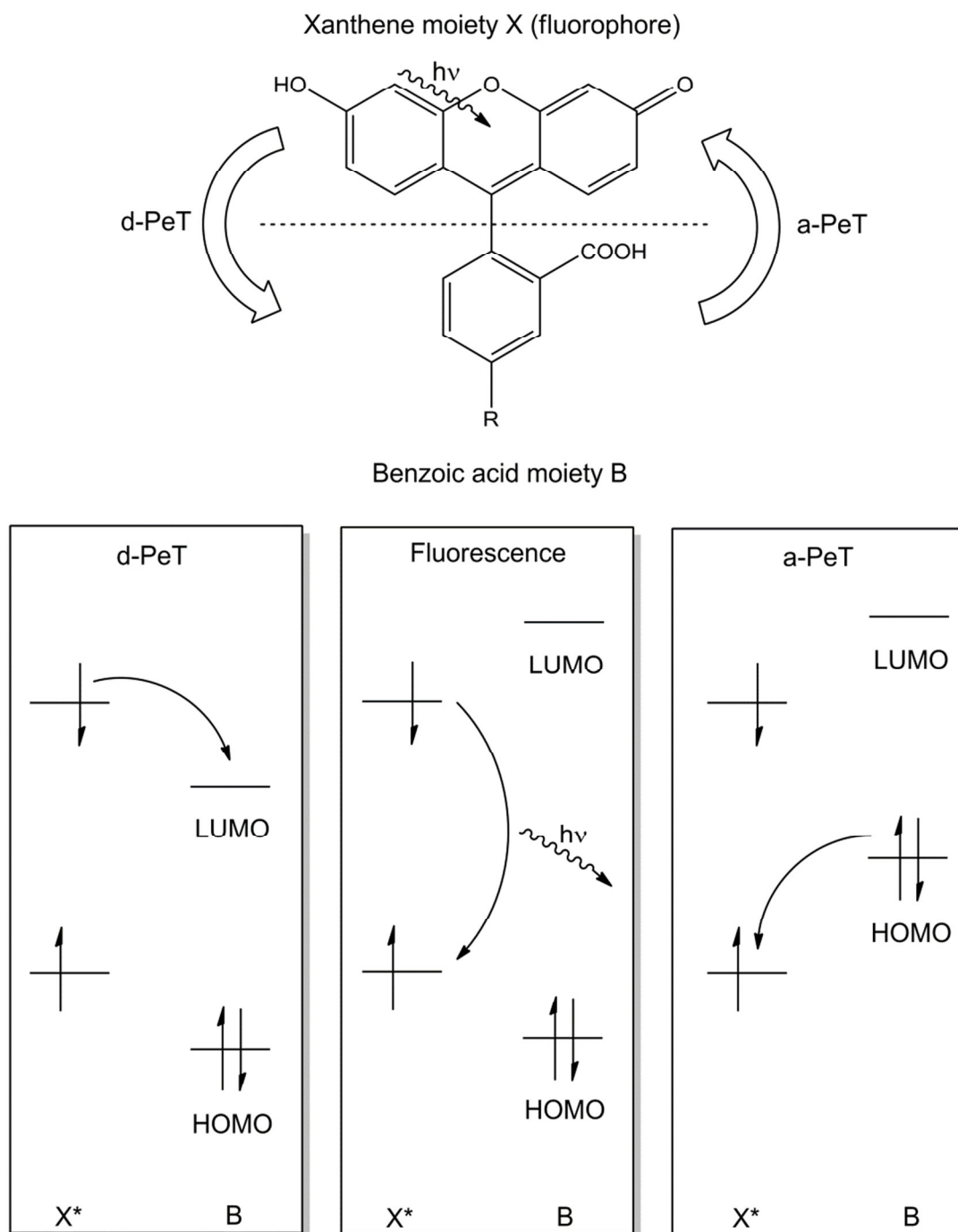
Figure 1 Schematic MO diagram depicting fluorescence quenching by photoinduced electron transfer (PeT). HOMO: highest occupied MO, LUMO: lowest unoccupied MO.

Based on this principle, Nagano *et al.* synthesized a variety of fluorescein derivatives, modulating the fluorescence properties by fine-tuning the redox potentials of the donor and acceptor moieties.[15-19] Following a similar approach for our studies, we turned our attention to two commercially available fluorescein derivatives, namely 5-Aminofluorescein **[5-AF]** and 5-Nitrofluorescein **[5-NF]**, with B bearing either an electron-donating (amino-) or electron-withdrawing (nitro-) group in *meso*-position to X. **[5-AF]** and **[5-NF]**, apart from their neutral quinoidal and lactonic forms, can appear in four charge state dependent forms (monocationic, monoanionic, as phenolate or carboxylate, and dianionic; Figure 2).
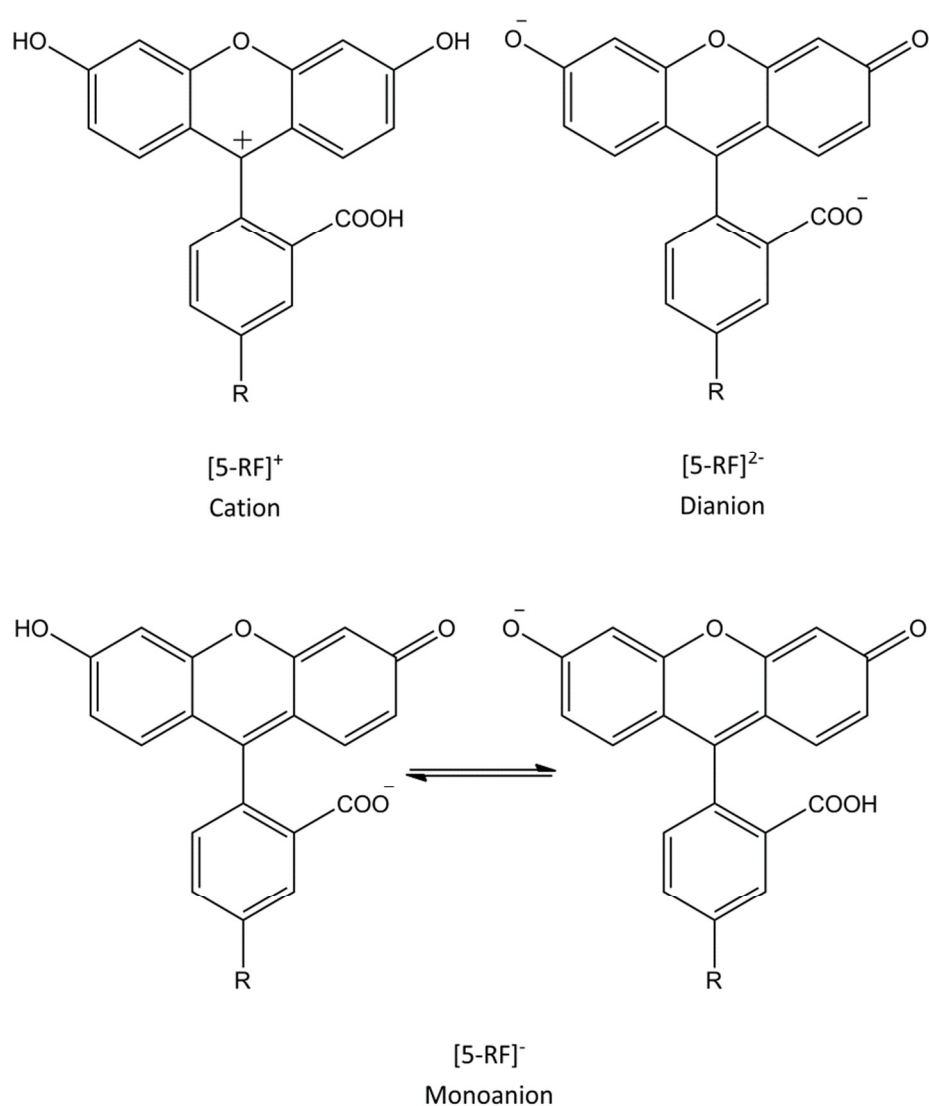
Figure 2 Schematic representation of the four charge state dependent forms of fluorescein dyes; R=NH$_2$, NO$_2$.

The absorption and emission properties of the dianions (**[5-RF]$^{2-}$**, R=A(mino), N(itro)) were previously investigated in aqueous solution and compared to the unsubstituted

fluorescein dianion **[F]$^{2-}$**.[20-21] It was found that the respective absorption and emission spectra were qualitatively very similar to **[F]$^{2-}$**, exhibiting only a small shift of the absorption and emission band maxima positions.[20-21] Substitution, however, had a profound impact on the fluorescence characteristics, dramatically decreasing the fluorescence quantum efficiency (from ~0.9 for **[F]$^{2-}$** to almost zero for **[5-AF]$^{2-}$** and **[5-NF]$^{2-}$**) and furthermore turning the mono-exponential fluorescence decay to a bi-exponential one, attributed to an additional relaxation process of the S_1 excited state by PeT.[20-21] The involvement of PeT was furthermore supported by transient experiments on **[5-NF]$^{2-}$** employing nanosecond laser flash photolysis. The occurring transient absorption signals could be unambiguously assigned to the concurrent formation of a *m*-nitrobenzoate radical anion and the cation of the X fluorophore, which was in accord with considerations based on a smaller reduction potential of *m*-nitrobenzoate (-0.92 V compared to -2.24 V for benzoate), thus resulting in an increased thermodynamic driving force for an intramolecular PeT from the X donor moiety to the *m*-nitrobenzoate.[20]

In the following, we apply pump-probe transient photofragmentation spectroscopy (tPF) in the gas phase on these two substituted fluorescein derivatives to gain unprecedented insight into the early excited state dynamics of the PeT process, influenced by the charge state of the respective species. Our assignment is corroborated by TD-DFT calculations, revealing a shift in frontier orbital energies, thus enabling PeT only in some cases. Prior to our study on electronic dynamics, we perform infrared multiple-dissociation (IRMPD) experiments to identify the ion population of the trapped molecular systems under study.

4.4 Experimental setup and calculations

Methanol of LC-MS grade was purchased from Sigma-Aldrich. Neutrals of **[5-NF]** and **[5-AF]** were purchased from TCI and electrosprayed from methanolic solutions without further purification. Steady-state PF and tPF experiments were conducted using a modified Paul-type electrospray ionization (ESI) quadrupole ion trap mass spectrometer (amaZon Speed, Bruker Daltonics) in combination with a Ti:sapphire oscillator and amplifier system (Wyvern 1000™, KMLabs). Two optical parametric amplifiers of white light continuum provided a source for tunable, ultrashort laser pulses (~100 fs) in either the UV/Vis region (pump, 240-580 nm) or the near infrared (NIR) region (probe,

1200 nm). IRMPD experiments were conducted using an amaZon SL mass spectrometer. An optical parametric oscillator/amplifier (OPO/OPA, LaserVision) pumped by a Q-switched Nd^{3+}:YAG laser (PL8000, Continuum) was used to generate tunable IR radiation in a spectra range from 2800 cm^{-1} up to 3760 cm^{-1} ($\delta\nu$=0.9 cm^{-1}, δt=7 ns). More details on the experimental setup and procedures are given in the supplement (section *4.9.1*).

Density functional theory (DFT) and time-dependent (TD-)DFT calculations were performed at the 6-31+G(d) level using the ωB97XD[22] functional within the Gaussian 09 program package.[23] This functional incorporates long-range dispersion and nonlocal Hartree-Fock exchange corrections, better suited for the theoretical modeling of molecular anions and excitations with significant contributions from transitions of charge transfer character.[24-25]

4.5 Results

4.5.1 Infrared multiple-photon dissociation

Fluorescein and its derivatives bear several functional groups, which may serve as sites for protonation. Furthermore, the carboxyl-group of the benzoic acid moiety is not rigid, resulting in a large number of possible rotamers for both the cationic and anionic species. Jockusch *et al.* performed IRMPD measurements on isolated fluorescein **[F]** and 2',7'-dichlorofluorescein ions in an ion trap. Surprisingly, they found the favored monoanionic isomer in the gas phase to be the phenolate instead of the benzoate form.[26] Introducing functional groups into the phenyl ring may change this behavior, especially in the case of **[5-NF]**-, as benzoic acid functionalized with electron withdrawing groups has typically a lower pK_a value.[27] For a first qualitative insight into the conformers that are present in the ion trap, we recorded IRMPD spectra in a frequency region of 2800-3760 cm^{-1}, which is sensitive to O-H-stretching vibrations and should allow for discrimination between tautomeric forms by comparison with theoretical IR spectra.

The geometries and respective relative Gibbs free energies of the five lowest energy conformers of **[5-AF]**- and **[5-NF]**- are shown in Figure 3. Note that for the sake of conciseness, we omitted rotamers resulting from rotation of the O-H-group at X (in Anion X and Anion X'; lactone), as the energy differences are negligible and, more

importantly, their excited state properties are expected to be indistinguishable from those of the conformers we took into account.
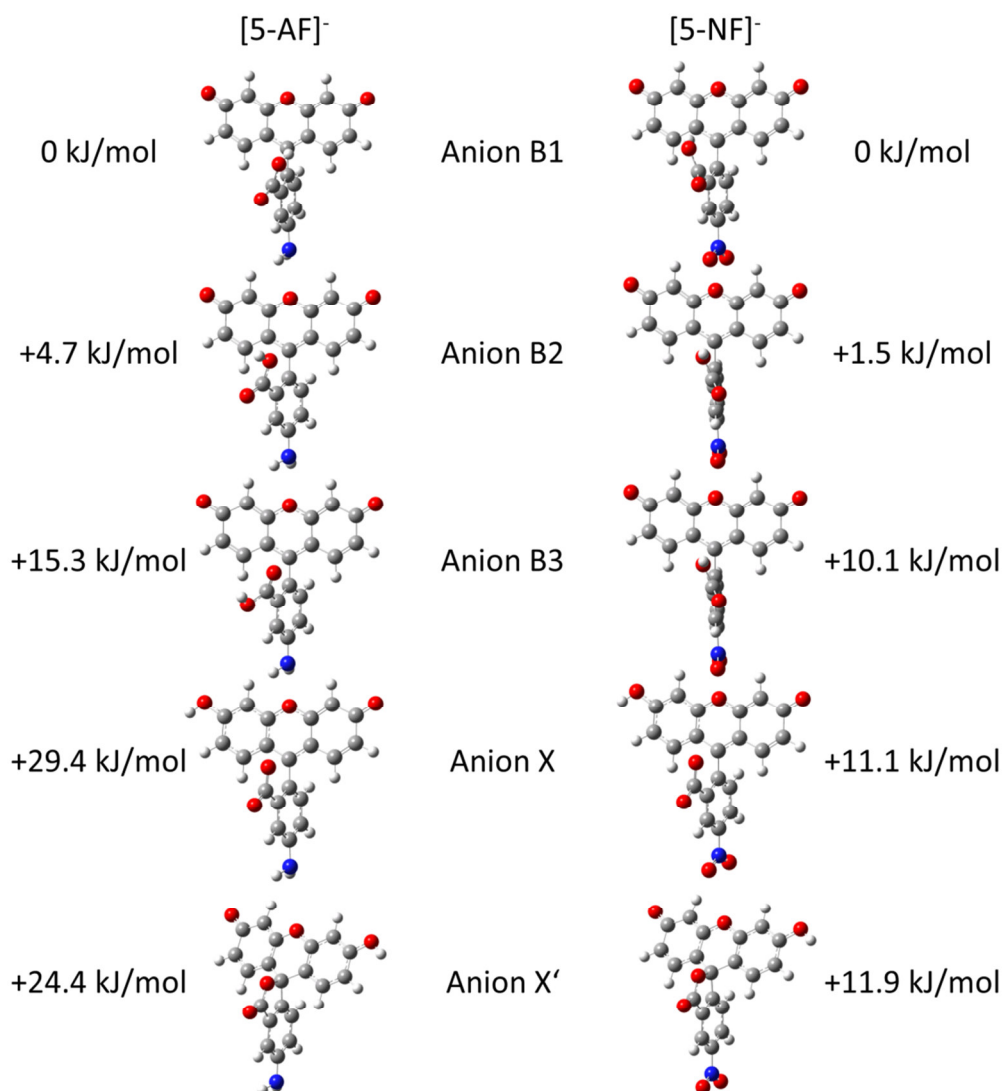
Figure 3 DFT (ωB97XD/6-31+G(d)) optimized ground state geometries and relative Gibbs free energies of the five lowest energy conformers of **[5-AF]⁻** (left) and **[5-NF]⁻** (right).

Anion B1 and Anion B2 are calculated to be the two most stable conformers at the B3LYP/6-31+G(d) level of theory for both **[5-AF]⁻** and **[5-NF]⁻**. In Anion B1, the hydrogen of the carboxylic acid group points towards the center of one of the terminal phenyl rings in X, whereas in Anion B2 the carboxylic O-H group points away from X. Anion B3 is slightly less stable for both derivatives. Another conformer would result from rotating the O-H group of Anion B3 (hydrogen pointing "downward"). However, it was not found as the structure obtained from geometry search is identical to Anion B1, which implies that a long range hydrogen-bond like interaction between the carboxylic

hydrogen and the X provides significant stabilization to this conformer. This is also suggested by the unusual orientation of the carboxylic O-H found in the geometry of Anion B1. The benzoates are predicted to be less stable, by +29.4 kJ/mol for **[5-AF]**$^-$ and (noteworthy) only +11.1 kJ/mol for **[5-NF]**$^-$, than the respective lowest energy conformer. The electron withdrawing property of the nitro-group apparently stabilizes the excess charge after deprotonation at the carboxylate site, whereas the amino substituent has the opposite effect, resulting in a less stable conformer Anion X. The lactone forms of **[5-AF]**$^-$ and **[5-NF]**$^-$ (Anion X') both exhibit relative energies (24.4 and 11.9 kJ/mol, respectively) comparable to the non-lactone form. The lactone form has a slightly skewed geometry, as the central C-atom in the xanthene ring is forced from a planar to a tetrahedral configuration, which impairs conjugation within the π-system.

IRMPD of **[5-AF]**$^-$ (m/z 346) yields only two major fragment ions at m/z 302 and 301, attributed to the loss of CO_2 and CO_2H (Figure S2), whereas for **[5-NF]**$^-$ (apart from the loss of CO_2 and CO_2H at m/z 332 and 331, respectively) additional fragmentation channels (m/z 315, 302 and 285) were observed (Figure S3). In general, it is quite difficult to unravel the fragmentation behavior of purely organic compounds and usually a thorough mechanistic study is required. At this point, we refrain from providing a definite identification of the occurring fragment ion signals. However, we would like to point out that the additional signals observed for **[5-NF]**$^-$ probably involves the nitro-substituent as a formal leaving group (resulting in *e.g.* the signal at m/z 302 and 285) whereas for **[5-AF]**$^-$, no fragment signal originates from a cleaving of the $C-NH_2$ bond in the substituted benzoic acid sub-unit. This results probably from a stronger C-N bond between the benzoic acid carbon atom and the amino nitrogen atom with respect to the $C-NO_2$ bond strength. In a recent study on the bond lengths and dissociation enthalpies in substituted benzene compounds it was found that the $C-NO_2$ bond in nitrobenzene is indeed weaker than the $C-NH_2$ bond in aniline. This was explained by a weaker hyperconjugation in nitrobenzene, due to unfavorable π-π* electrostatic repulsion[28] thus opening up additional fragmentation routes resulting in a more complex fragmentation behavior of the nitro-compound. Recording the fragment ion intensity as a function of photon energy enables us to record gas phase IR spectra. The experimental IRMPD and calculated IR spectra of **[5-AF]**$^-$ are shown in Figure 4.

Figure 4 Experimental IRMPD (top, red) and IR spectra (below, black) calculated for the five considered conformers of **[5-AF]⁻**. Calculated IR intensities are shown as sticks and broadened with 7 cm⁻¹ fwhm Lorentzian functions (black lines). A scaling factor of 0.95 was employed.

Two broad absorption bands ($\sim$3040 cm^{-1} and 3420 cm^{-1}) and a more narrow, low intensity band ($\sim$3650 cm^{-1}) can be identified in the experimental IRMPD spectrum of **[5-AF]**$^{-}$. By comparison with the calculated spectra of the respective conformers, the absorption centered at 3040 cm^{-1} (green) can be assigned to aromatic C-H stretching vibrations. The position of the intense band at $\sim$3420 cm^{-1} matches better the predicted weakened COO-H stretching vibration of Anion B1, whereas the same stretching vibration (in Anion B2 and B3) exhibits reduced calculated absorption intensity and additionally is shifted to higher energies (to $\sim$3590 cm^{-1}). The expected N-H stretching (symmetric and asymmetric) vibrations were not observed in the experimental spectrum. This is either due to them being low in intensity or the bands coincide with the absorption band at $\sim$3420 cm^{-1}, as suggested by the calculated spectrum of Anion B1. Lastly, the weak absorption band at $\sim$3650 cm^{-1} can probably be attributed to a free O-H stretching vibration, located at the X moiety, which is exclusive to Anion X and X'. Clearly, the experimental spectrum agrees best with the calculated spectrum of Anion B1. From the relative intensities of the observed absorption bands in the IRMPD spectrum, one may deduce that the population of trapped anions consists mainly of Anion B1 and probably, to a far lesser degree, of Anion X and X'. Anion B2 and B3 cannot be completely excluded, due to their low relative energies (4.7 kJ/mol and 15.3 kJ/mol, respectively). However, the frequencies of the calculated O-H stretching vibrations ($\sim$3590 cm^{-1}) do neither fit the broad, intense band (3420 cm^{-1}) nor the low intensity band (3650 cm^{-1}) observed in the experiment. A summary of the calculated vibrational frequencies and intensities is given in Table S6.
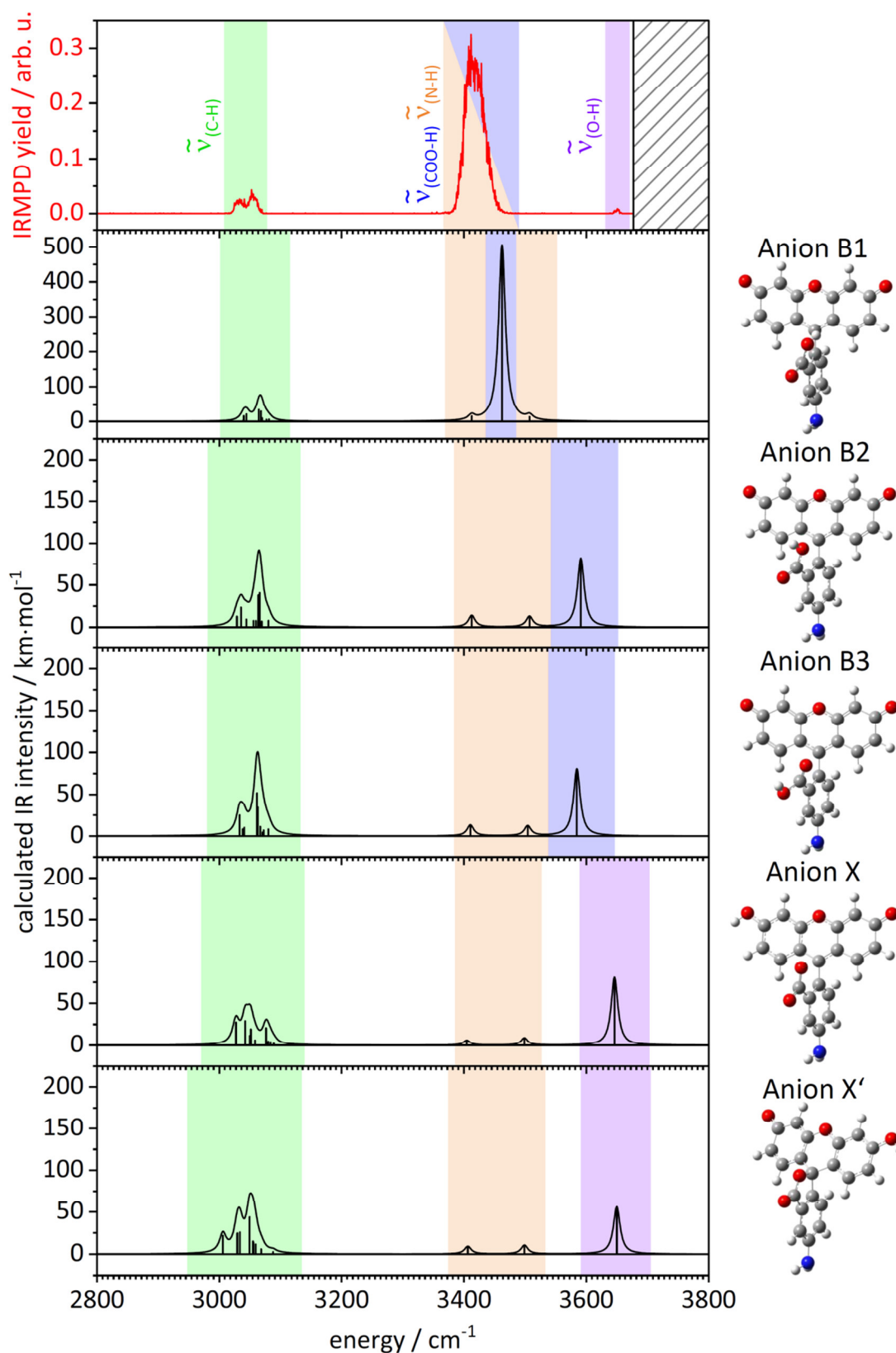
Figure 5 Experimental IRMPD (top, red) and IR spectra (below, black) calculated for the five considered conformers of **[5-NF]⁻**. Calculated IR intensities are shown as sticks and broadened with 7 cm⁻¹ fwhm Lorentzian functions (black lines). A scaling factor of 0.95 was employed.

Similar to **[5-AF]**⁻, the experimental IRMPD spectrum of **[5-NF]**⁻ (Figure 5) exhibits two broad IR bands (~3040 cm⁻¹ and ~3400 cm⁻¹) and a narrow band at ~3650 cm⁻¹, which has a drastically increased intensity compared to the absorption band of similar energy in the spectrum of **[5-AF]**⁻. Additionally, a low-intensity band in the O-H stretching region is observed at ~3570 cm⁻¹. By comparison of the experimental spectrum with the calculated spectra, it is obvious that the broad absorption at ~3400 cm⁻¹ is best described by the hydrogen bonded COO-H stretching vibration, present in Anion B1. The narrow absorption band at ~3650 cm⁻¹ agrees well with the calculated free phenolic O-H stretching vibration of Anion X and X'. Lastly, the free COO-H stretching vibrations calculated for Anion B2 and B3 coincide with the low intensity band observed at ~3570 cm⁻¹ in the experimental spectrum. The spectral comparison implies that no conformer can definitely be excluded for a complete theoretical description of the experimental spectrum. Anion B2 and B3 should, however, not be significantly populated, whereas the intense absorption bands at ~3400 cm⁻¹ and ~3650 cm⁻¹ provide strong evidence for a high contribution of Anion B1 and Anion X/X' like conformers to the ion population present under the given experimental conditions. A summary of the calculated vibrational frequencies and intensities is given in Table S7.

It is not clear as to why there is no impactful spectral evidence for Anion B2 and B3 in the experiments, although these conformers are predicted to be the two most stable structures next to the lowest energy conformer. Anion X and X', on the other hand, have calculated relative energies similar to that of Anion B3, however, the high intensity of the free O-H stretching vibration in the IRMPD spectrum implies that this tautomer contributes significantly to the ion population. It is conceivable that due to the lose nature of the carboxylic acid group, the O-H may rotate more or less freely at room temperature, allowing for interconversion between the geometries of the phenolate and thus in average a higher population of the lowest energy conformer, within the timeframe of the experiment. A change between the two tautomeric forms, on the other hand, is not possible in the gas phase, which implies that already a considerable amount of the benzoate must be present in solution and is kinetically trapped in this form during the transfer from solution to the gas phase.

In summary, the IRMPD spectra in the O-H stretching vibration region strongly point to a population of anions mainly consisting of Anion B1 like geometries in the case of **[5-AF]**⁻, whereas for **[5-NF]**⁻ both conceivable tautomers contribute equally to the ion population and thus lead to the observed spectral features in the experiment.

For the cations, only four distinct isomers were identified. Stable lactonic structures were not obtained from geometry search. Again, for the sake of convenience, we omitted rotamers resulting from rotation of the two O-H-groups at X, as their spectroscopic behavior is not expected to be drastically different. The geometries and respective relative Gibbs free energies of the four lowest energy conformers of **[5-AF]**⁺ and **[5-NF]**⁺ are presented in Figure 6.
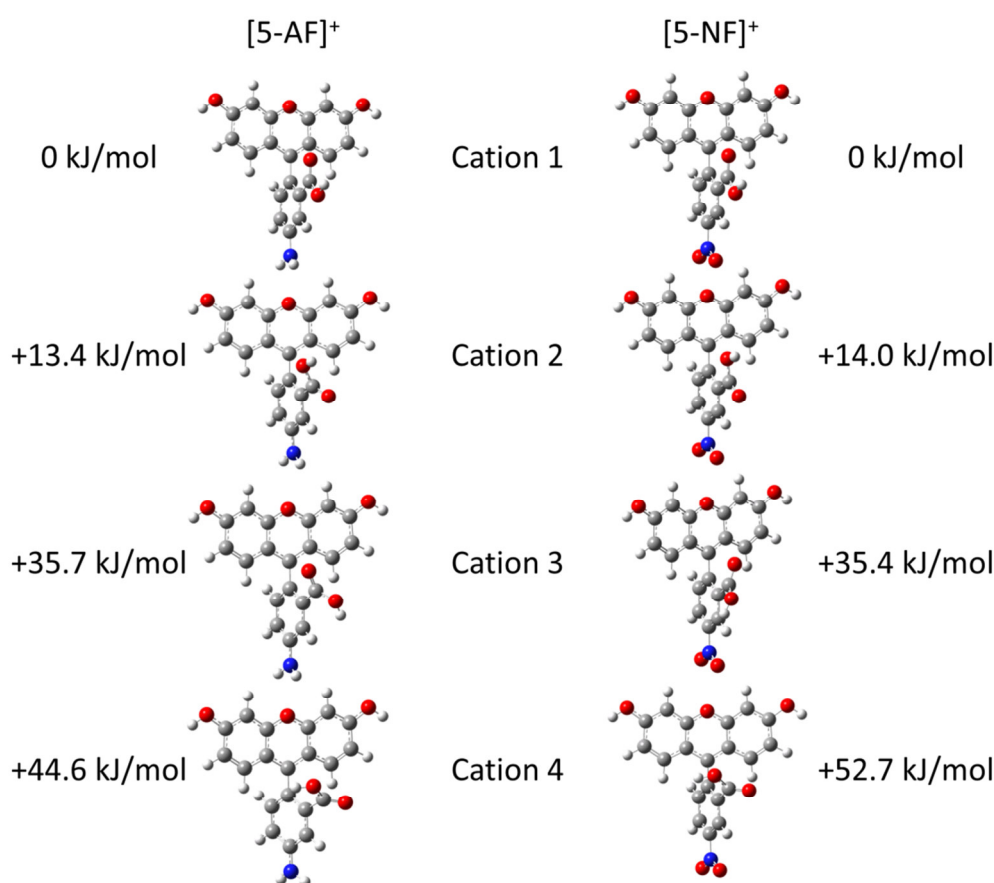
Figure 6 DFT (ωB97XD/6-31+G(d)) optimized geometries and relative Gibbs free energies of the four lowest energy conformers of **[5-AF]**⁺ and **[5-NF]**⁺.

The four lowest energy cationic conformers of **[5-AF]⁺** and **[5-NF]⁺** solely differ in the orientation of the carboxylic O-H group. In Cation 1, the hydrogen is bound to the oxygen atom farthest away from X, whereas in Cation 2 the hydrogen is in closer proximity to X. However, it points in the opposite direction, probably to minimize interaction with the increased positive charge density in the protonated fluorophore X. The geometry of Cation 3 results from rotation of the carboxylic O-H bond starting from the geometry of conformer Cation 1. The hydrogen atom, however, is not pointing straight downward, but rather out of the phenyl-ring plane to avoid the adjacent phenyl-hydrogen atom. Such a conformer was not found for the anionic species, as structure optimization starting form a similar geometry resulted in Anion B1. Surprisingly, the geometry denoted as Cation 4, which is reminiscent of the lowest energy conformer found for the anions (Anion B1), is the energetically highest conformation. The deviation from the mutual orientation of 90° between X and B (~27° and ~19° for **[5-AF]⁺** and **[5-NF]⁺**) is highest for this geometry and additionally the carboxyl group is twisted out of the phenyl-plane by >50°, avoiding a geometry in which the hydrogen atom points directly towards the xanthene unit. A summary of the changes in geometry upon structure optimization of the respective conformers is given in the supporting information section (section *4.9.2*; Table S1 and Figure S1).

The fragmentation of the cations induced by IR irradiation is quite complex compared to the respective monoanions. A similar behavior was observed by Jockusch *et al.* in their IRMPD and UV/Vis photodissociation studies on **[F]⁺** and its two halogenated derivatives.[26, 29-30] The main fragmentation channels for **[5-AF]⁺** and **[5-NF]⁺** are the loss of the carboxylic acid group (m/z 302 and 332, respectively) and additionally the concomitant loss of the respective functional group (m/z 286; -HCOOH,-NH₂ for **[5-AF]⁺**; -HCOOH,-NO₂ for **[5-NF]⁺**). The relative signal intensity of the fragment at m/z 286 is higher for **[5-NF]⁺**, indicative of a weaker bond strength between the carboxylic acid ring and the formal leaving group. The experimental IRMPD and calculated IR spectra of **[5-AF]⁺** and **[5-NF]⁺** are shown in Figure 7 and 8.
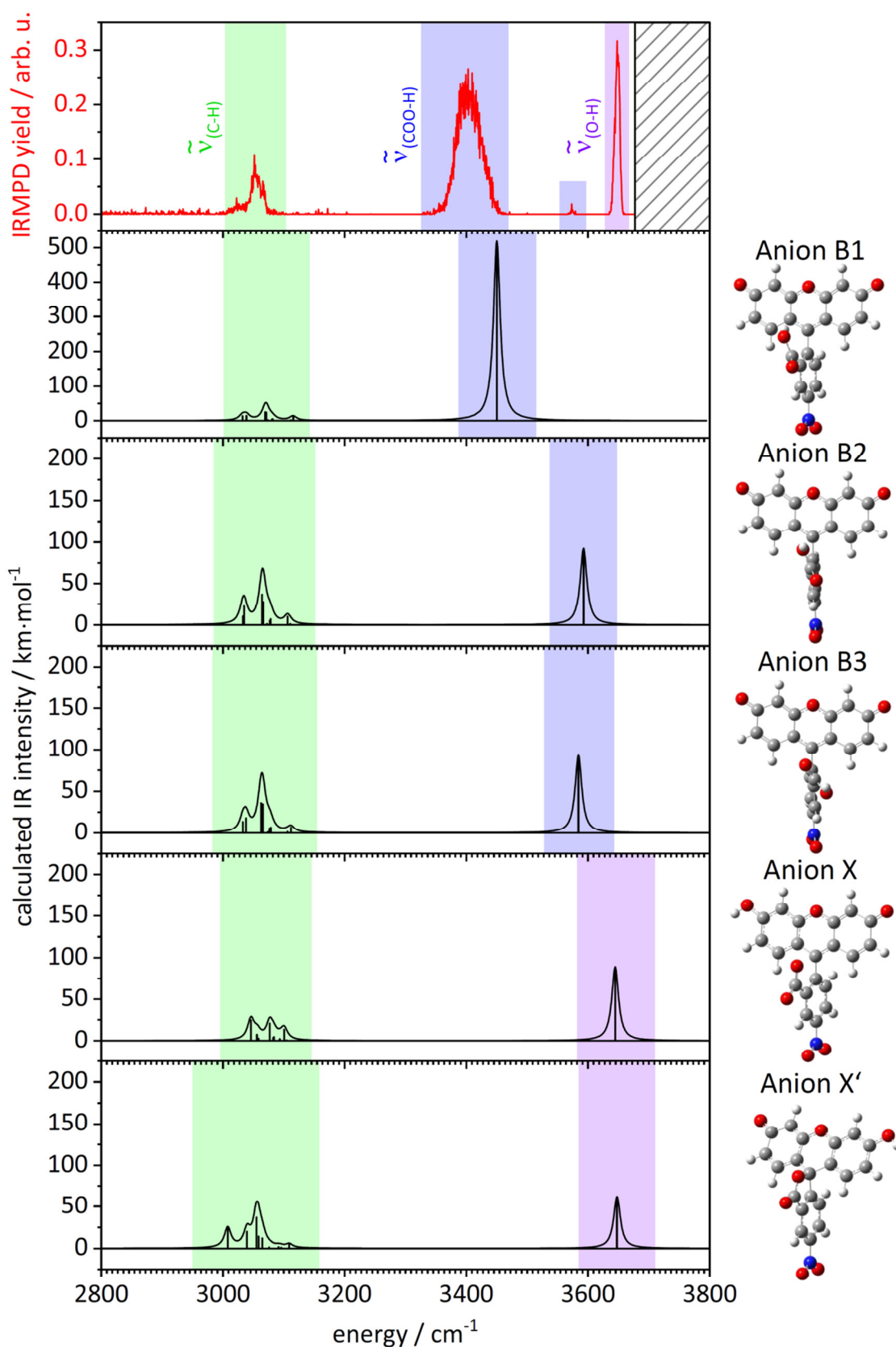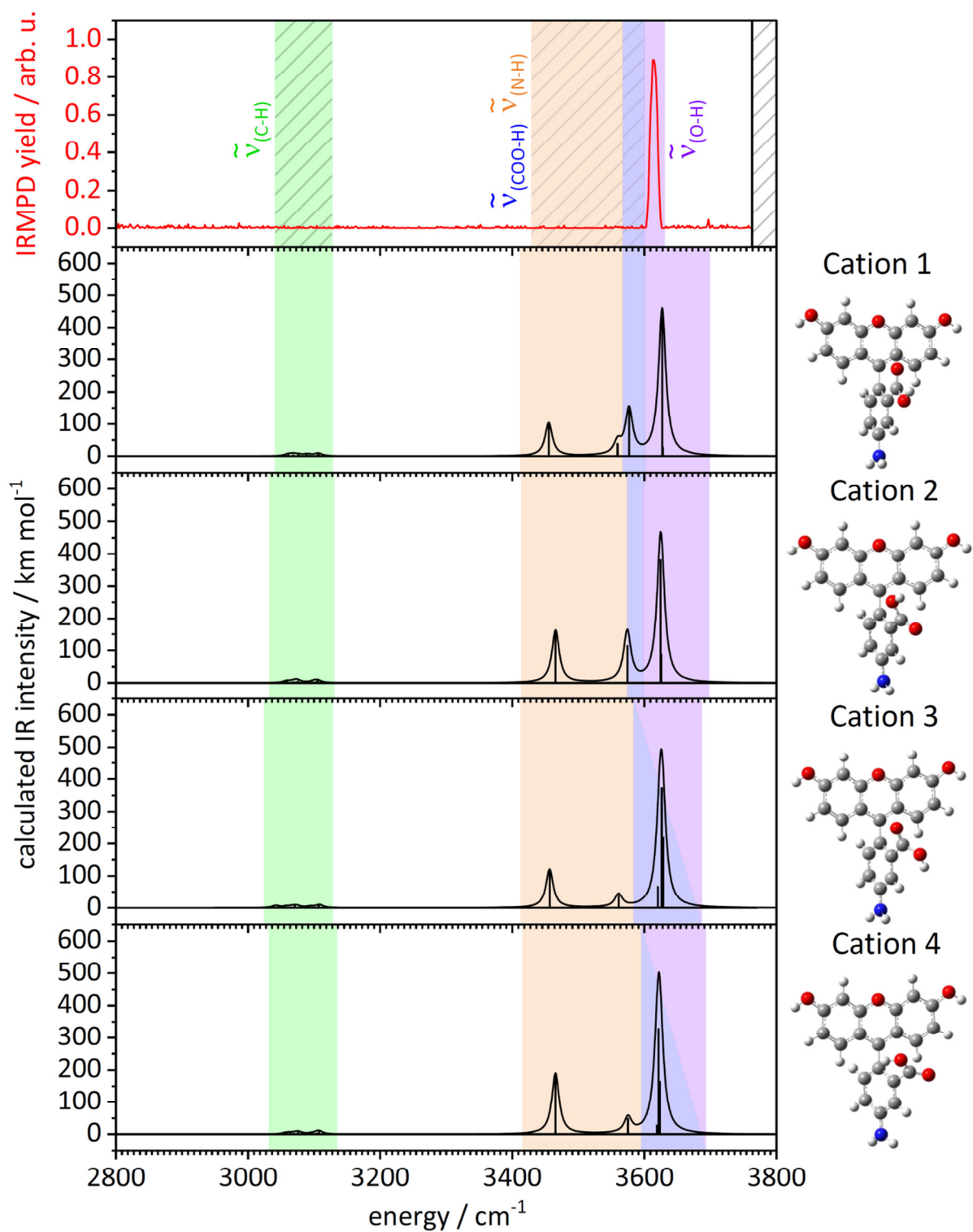
Figure 7 Experimental IRMPD (top, red) and IR spectra (below, black) calculated for the four considered conformers of **[5-AF]$^+$**. Calculated IR intensities are shown as sticks and convoluted with 7 cm^{-1} fwhm Lorentzian functions (black lines). A scaling factor of 0.95 was employed.

Figure 8 Experimental IRMPD (top, red) and IR spectra (below, black) calculated for the five considered conformers of **[5-NF]+**. Calculated IR intensities are shown as sticks and convoluted with 7 cm^{-1} fwhm Lorentzian functions (black lines). A scaling factor of 0.95 was employed.

The experimental spectra of the cations exhibit less spectroscopic features than those of the monoanions, although more IR active chromophores are present. In the IRMPD spectrum of **[5-AF]⁺** only a single narrow band at ~3610 cm⁻¹ is distinguishable, whereas in the spectrum of **[5-NF]⁺** a low intensity band at ~3560 cm⁻¹ and an intense band at ~3610 cm⁻¹ can be identified. No spectral features, which can be associated with aromatic C-H stretching vibrations, are observed for both cationic species. These, however, have a smaller calculated IR intensity for all considered conformers compared to calculated IR intensities for the anionic species (nearly an order of magnitude smaller than for **[5-AF]⁻**). Furthermore, the expected N-H stretching (symmetric and asymmetric) vibrations are not observed in the experimental spectrum of **[5-AF]⁺**. Either the absorption intensity is severely overestimated by the level of theory applied, or the bands are spectroscopically dark, due to *e.g.* a poor vibrational energy redistribution (IVR) process. The calculated IR spectra of Cation 1 and 2 are nearly indistinguishable regarding band composition and energetic spacing between the calculated vibrational modes. Although theory predicts (for Cation 1 and 2 like geometries) two separate absorption bands for the free phenolic O-H and the carboxylic O-H stretching vibration, presumably only one of those can be assigned to the single band observed in the experimental spectrum of **[5-AF]⁺**, unless the energy of the COO-H vibration is underestimated by theory. Hence it would lie closer to the free O-H vibration, merging into one absorption feature, as predicted, *e.g.* by the calculated IR spectra for Cation 3 and 4 like geometries. This, however, is questionable, as the experimental IRMPD spectrum of **[5-NF]⁺** exhibits two distinct absorption bands (~3560 cm⁻¹ and ~3610 cm⁻¹), which can be assigned either to the free xanthene O-H or the COO-H vibration, agreeing reasonably well with the calculated IR spectra for Cation 1 and Cation 2. It is thus conceivable that two separate bands (associated with either the O-H or COO-H stretching vibration) are more likely to appear in the experimental spectrum of **[5-NF]⁺**, as the electron withdrawing property of the nitro-substituent should weaken the O-H bond in the carboxylic acid group, shifting it to lower energies, with respect to the phenolic O-H vibration. In **[5-AF]⁺**, the amino-substituent possesses electron donating properties. Hence, the opposite effect is expected, *i.e.* a shift of the COO-H vibration towards higher energies and closer to the free xanthene O-H vibration. If this is indeed the case, then the level of theory applied may not be sufficient to account for such an effect. The weakening of the COO-H bond, due to hydrogen like

bonding is predicted by theory for Cation 3 and 4 like structures so that the frequency of the COO-H stretching vibration virtually coincides with the free xanthene O-H vibration. However, these two geometries have calculated relative energies of 35.7 (35.4) kJ/mol and 44.6 (52.7) kJ/mol for **[5-AF]**$^+$ (**[5-NF]**$^+$) and are hence not expected to contribute significantly. An overview over the calculated vibrational frequencies and intensities for **[5-AF]**$^+$ and **[5-NF]**$^+$ is given in Table S8 and S9, respectively.

In summary, the IRMPD spectra of the anionic compounds imply that the ion population of **[5-AF]**$^-$ consists mainly of the lowest energy isomer Anion B1, whereas for **[5-NF]**$^-$ no isomer can be definitely excluded. The relative intensities of the appearing gas phase IR bands, however, point to the coexistence of mainly Anion B1 like geometries and its tautomeric form (either Anion X or the lactonic Anion X'). The rotamers (Anion B2 and B3), although not lying significantly higher in energy, seem not to contribute significantly, unless their spectral features remain dark for a yet unknown reason.

The experimental spectra of the cations exhibit less spectral features than the spectra of the anions. The main absorption band in the calculated spectra of the isomers fits the experiment in either case, making identification of the ion population questionable. However, due to the high relative energies of Cation 3 and 4 isomers, mainly Cation 1 and 2 are expected to contribute to the ion ensemble in the trap.

4.5.2 UV/Vis photofragmentation and absorption action spectra

Upon irradiation of the isolated cationic and monoanionic forms of **5-NF** and **5-AF** with fs-laser pulses in a wavelength range from 240 nm up to 580 nm photoproducts are formed. The UV/Vis mass spectra of **[5-AF]**$^-$ and **[5-NF]**$^-$ closely resemble those from IRMPD studies, with the main fragmentation channels of **[5-AF]**$^-$ being the loss of CO_2 (44 Da)/HCO2 (45 Da) (Figure S2, Tab. S2) and for [5-NF]$^-$ additionally encompasses dehydration and probably loss of the functional nitro-group. **[5-AF]**$^+$ (Figure S3, Table S3) and **[5-NF]**$^+$ (Figure S4, Table S4), exhibit a more complex fragmentation behavior, including dehydration, decarboxylation and loss of the respective functional group. Curiously, the fragmentation mass spectra observed by IRMPD and UV/Vis photoexcitation are nearly identical for the anions with regard to the number and relative intensity of the occurring product signals, whereas in the IRMPD mass spectra of the cations, numerous additional fragment products appear at lower m/z compared to

UV/Vis PF. From the similarity of the fragmentation mass spectra recorded for the anions by IRMPD and PF, we deduce that fragmentation probably occurs in both excitation schemes from the electronic ground state. For IRMPD, this is given, as the generally accepted mechanism relies on a rapid relaxation process, *i.e.* IVR, by coupling the excited vibrational mode to the internal heat bath, thus allowing for a consecutive re-excitation of the same vibrational coordinate in the electronic ground state until internal energy buildup exceeds the dissociation threshold. For Vis-photoexcitation a similar mechanism must be invoked,[31] *i.e.* the photoexcited ions return to a highly vibrationally excited ground state by internal conversion (IC) and the retained excess energy is redistributed throughout the many vibrational modes in the molecule. If the excess energy is sufficiently large, the molecule dissociates, otherwise the cycle repeats and another photon may be absorbed, albeit at a lower probability, due to an inherent change in geometry of the hot molecule and hence less favorable Franck-Condon factors for absorption of a second photon. From one-color PF studies on the monoanions one can assume efficient IC and a subsequent IVR process to vibrational modes which are also primarily populated during relaxation in IRMPD. For the cations, the respective excited state probably couples inefficiently to the electronic ground state, spreading the excitation energy over a multitude of vibrational modes, thus we observe numerous fragment channels. Furthermore, bond dissociation energies must be higher for the cations, requiring the absorption of at least a second photon in the UV/Vis region, as suggested by the fragmentation yield dependence on the photon pulse energy (Figure S6). A similar behavior was observed for the monocationic and monoanionic forms of **[F]** and its halogenated derivatives, where the cationic form exhibited a complex fragmentation behavior and typically required higher laser pulse energies to induce fragmentation.[29-30]

Recording the fragment ion intensity as a function of photoexcitation wavelength yields the PF spectra, which we compare to theoretical absorption spectra calculated for all conformers we considered in the discussion of the IRMPD spectra (Figure 3 and 6).
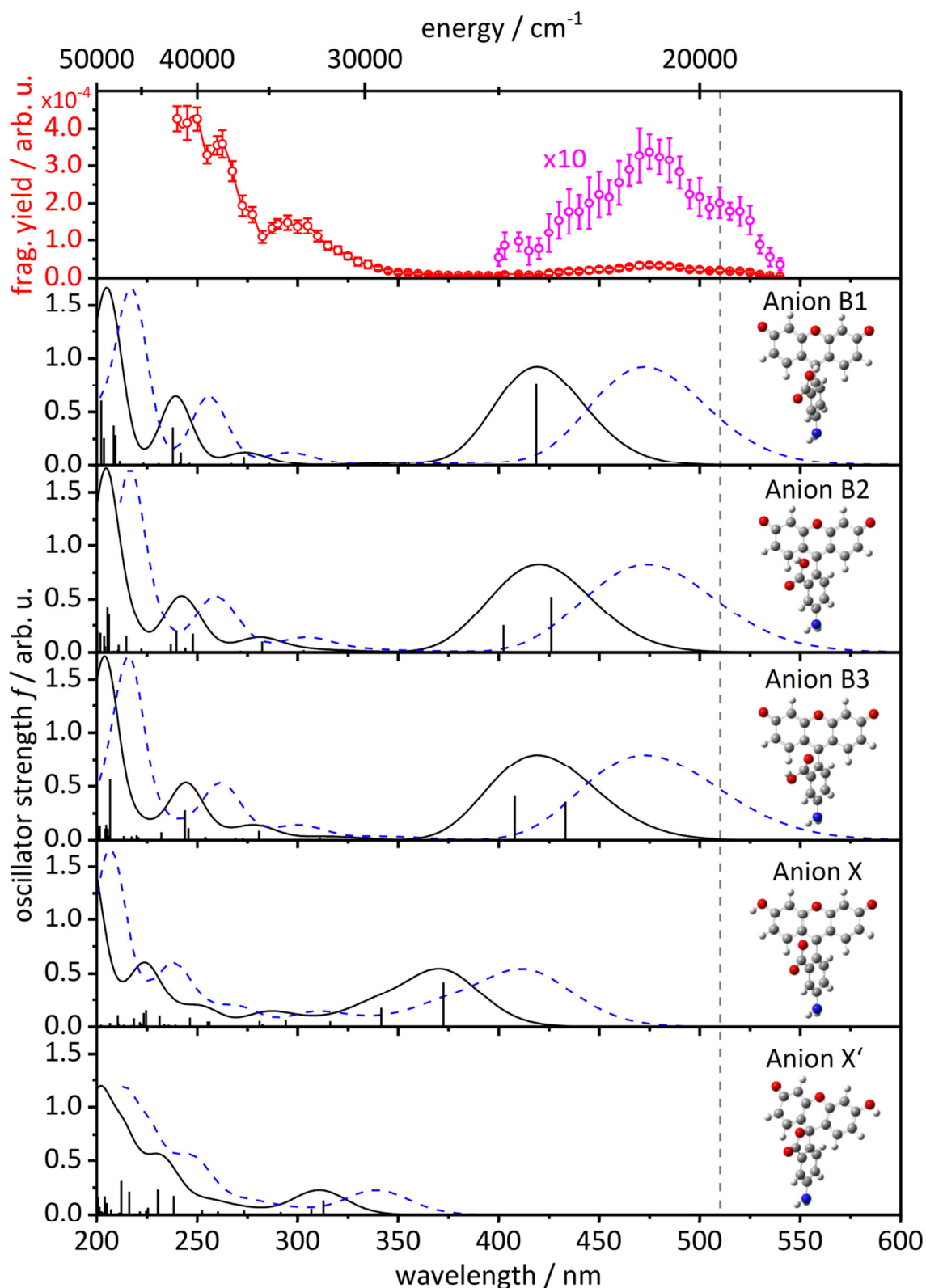
Figure 9 Experimental PF spectrum (top, red) of **[5-AF]**⁻ and linear UV/Vis spectra (below, black) calculated for the five considered conformers. Calculated UV/Vis absorption intensities are shown as sticks and convoluted with 3000 cm⁻¹ fwhm Gaussian functions (black lines). To account for errors in TD-DFT calculated transition energies, the convoluted spectra were shifted bathochromically by 3000 cm⁻¹ (blue, dashed line). Vertical dashed line denotes pump-wavelength (510 nm) used in transient experiments.

On first glance, the PF spectrum of **[5-AF]**⁻ (Figure 9) compares poorly to the calculated linear absorption spectra, with the most striking difference being the missing long wavelength absorption band predicted at ~420 nm for conformers of Anion B (1-3) like geometries. The experimental spectrum features a broad, band like structure at longer wavelengths (made clearer by magnification of the particular absorption region; Figure 9, inset), however, it is low in intensity and red-shifted by ~60 nm compared to theory. From our experience, low intensity bands in absorption action spectra are common when employing ion trap techniques, especially in the Vis region. Since the excess energy stored within the molecular system (after photoexcitation and subsequent IC) dictates the rate of fragmentation, and obviously, absorption of longer wavelength photons results in less internal energy, the rate of fragmentation for ions excited at longer wavelengths is more prone to collisional quenching with the helium buffer gas in the trap. Collisional quenching, coupled with non-linearity of the fragmentation process (Figure S6) typically results in less pronounced or even missing bands in the absorption action spectra at longer wavelengths.

After shifting the calculated absorption bands by 3000 cm⁻¹ to lower energies (in order to account for overestimation of transition energies by TD-DFT) the theoretical spectra for Anion B1-3 like geometries agrees qualitatively well with the experimental spectrum, whereas the spectra calculated for Anion X and X' have less pronounced features, are located at higher energies and thus show no similarity to the experiment. From our calculations, the low intensity band at ~300 nm is of charge transfer character (CT) from the benzoic acid to the xanthene unit (CT(B→X)), whereas the spectral region below 250 nm consists of a multitude of localized π-π*-transitions centered on either X or B, or transitions of partial CT character (for assignment *cf.* section *4.9.6*; Table S10-14 and Figure S8-12). The broad, low intensity, absorption band at 480 nm is calculated to be a purely X localized π-π*-transition (LE(X)) for Anion B1. Interestingly, the orientation of the carboxylic OH-group has a strong influence on the character of the long wavelength absorption band, turning it from a purely LE(X) excitation to a mixed LE(X) and CT transition, partially moving electron density from X to B (CT(X→B)) for geometries in which the carboxylic OH-group is pointing away from X. Apparently, the sequence of frontier orbitals depends delicately on whether the hydrogen bond-like interaction is present or absent in a particular geometry, as the LUMO for Anion B1 is localized on X whereas for B2 and B3 the LUMO is localized on B, thus affecting the

nature of the most intense, lowest energy transition. The absorption spectra calculated for the tautomer (Anion X) and lactone structure (Anion X') exhibit a profoundly different band structure with the longest wavelength absorption bands shifted to higher energies. For Anion X the S_1 state is of LE(X) character, whereas the first excited state of Anion X' with significant oscillator strength (S_2, f=0.13) is a mixed LE(X) and CT(X→B) transition. Similar to results obtained from IRMPD experiments, we cannot completely exclude (at least) a minor ion population of Anion X/X'–like structures. A summary of the TD-DFT calculated lowest lying excited states calculated for the conformers of **[5-AF]**⁻ is given in Table 1.

Table 1 Longest wavelength vertical singlet transitions calculated for various conformers of **[5-AF]**⁻ at the ground state geometry (TDDFT/ωB97XD /6-31+G(d)). Calculated central wavelengths λ are given together with corresponding values $λ_S$ obtained after bathochromically shifting the transition energies by 3000 cm⁻¹. Only transitions with an oscillator strength of f>0.1 are displayed. Contributions to electronic transitions with a weight of <10 % were omitted. See Figure S8-12 for respective frontier orbital isosurfaces.

| conformer	state	transition (weight / %)	character	λ / nm	$λ_S$ / nm	f
Anion 1	S_1	HOMO→LUMO (96)	LE(X)	419	479	0.76
Anion 2	S_1	HOMO→LUMO (64) HOMO→LUMO+1 (33)	CT(X→B) LE(X)	426	488	0.52
	S_2	HOMO→LUMO (34) HOMO→LUMO+1 (63)	CT(X→B) LE(X)	402	457	0.25
Anion 3	S_1	HOMO→LUMO (83) HOMO→LUMO+1 (13)	CT(X→B) LE(X)	433	498	0.41
	S_2	HOMO→LUMO (14) HOMO→LUMO+1 (82)	CT(X→B) LE(X)	408	465	0.41
Anion X	S_1	HOMO→LUMO (91)	LE(X)	373	420	0.42
	S_2	HOMO-2→LUMO (47) HOMO-1→LUMO (42)	CT(B→X) CT(B→X)	341	380	0.18
Anion X'	S_2	HOMO→LUMO+3 (56) HOMO→LUMO+4 (20)	LE(B)/ CT(B→X)	313	345	0.13
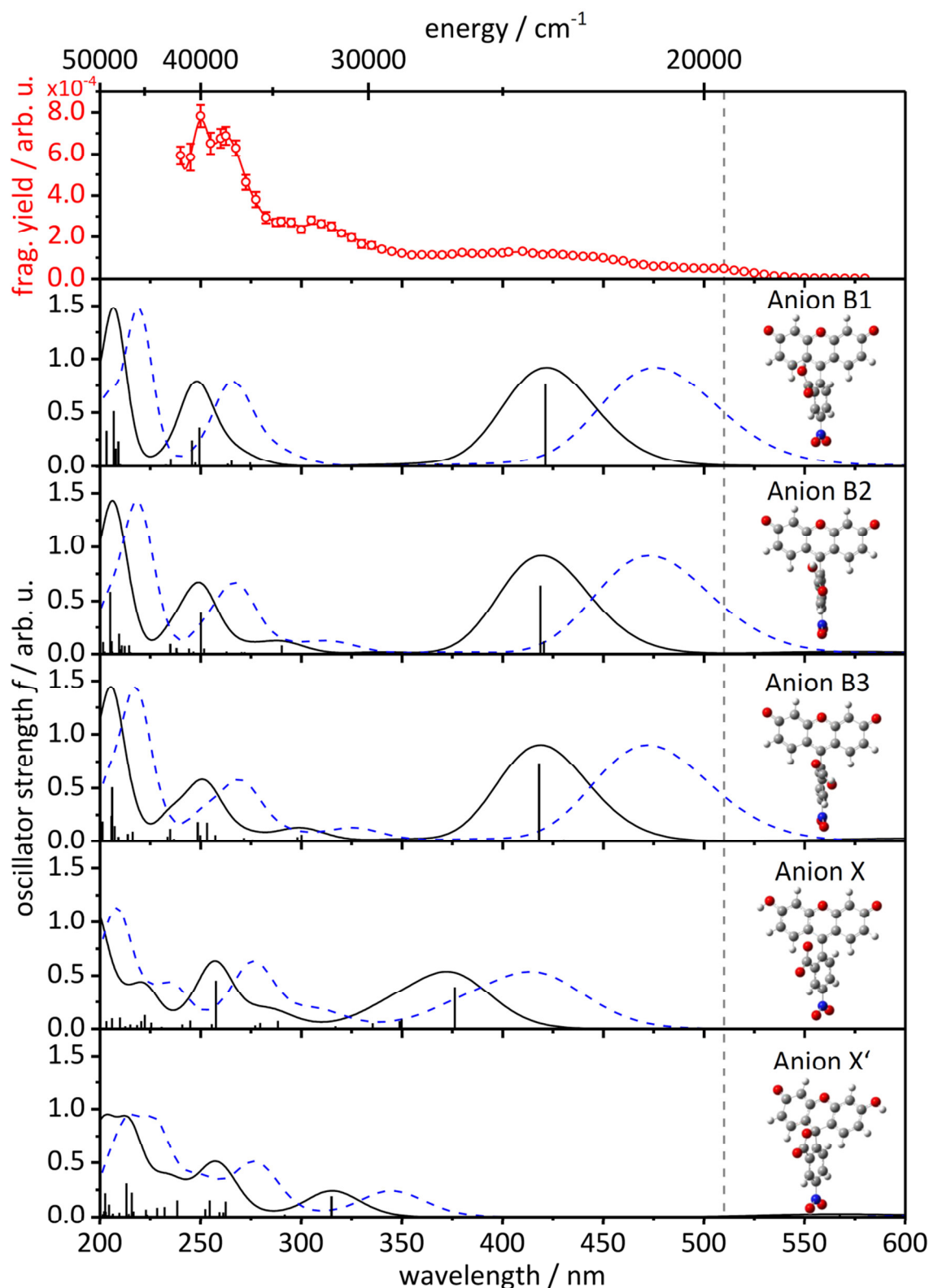
Figure 10 Experimental PF spectrum (top, red) of **[5-NF]⁻** and linear UV/Vis spectra (below, black) calculated for the five considered conformers. Calculated UV/Vis absorption intensities are shown as sticks and convoluted with 3000 cm⁻¹ fwhm Gaussian functions (black lines). To account for errors in TD-DFT calculated transition energies, the convoluted spectra were shifted bathochromically by 3000 cm⁻¹ (blue, dashed line). Vertical dashed line denotes pump-wavelength (510 nm) used in transient experiments.

The calculated absorption spectra for the conformers of **[5-NF]**⁻ compare worse to the experimental PF spectrum than in the case of **[5-AF]**⁻, even after shifting the transitions by 3000 cm⁻¹ to lower energies (Figure 10). The main difference is the increased fragmentation yield in the spectral range between 350-420 nm. In this region we observe nearly no fragmentation for **[5-AF]**⁻, thus the experimental spectrum bears closer resemblance to the theoretical spectra (Anion B1-3). We believe that **[5-NF]**⁻ also should exhibit a weak and broad long wavelength absorption band (at ~480 nm) similar to **[5-AF]**⁻, however, it is obscured by the increased fragmentation baseline. Measurements on the laser pulse energy of the fragmentation yield of **[5-NF]**⁻ (at 510 nm photon energy) hints at a lower order excitation process compared to **[5-AF]**⁻ (polynomial fit in Figure S6 implies an excitation process of n=1.24 and n=1.67 order, respectively). If this holds true for fragmentation across the recorded spectral region (240-580 nm), then it is conceivable that absorption of a single photon in a wavelength region of 350-400 nm may result in higher fragmentation than expected, even if absorption probability is low. The increased excess energy in a wavelength region of 350-400 nm (with respect to excess energy provided by absorption of a photon at *e.g.* 480 nm) results in a higher unquenched population and thus increased fragmentation. Another explanation for the broadened absorption band in the spectrum of **[5-NF]**⁻ is the coexistence of conformers with different absorption behavior. From the IRMPD spectrum of **[5-NF]**⁻ we already deduced that the trapped ion population must consist of both tautomeric forms (benzoate and phenolate). The calculated lowest energy transition (S₁) for the benzoates (Anion X/X') of **[5-NF]**⁻ is shifted to higher energies with respect to the more intense transitions calculated for Anion B1-3 conformers and strikingly coincides with the wavelength region of increased fragmentation (350-400 nm) in the experiment. A convolution of the calculated absorption spectra of Anion B1, Anion X and X' fits the experiment qualitatively well (Figure S7). As the absorption spectrum results from excitation of tautomers, we refrain from a definite assignment of the band "progression" to specific transition. However, if we compare the experimental spectrum to the calculated spectra, we may tentatively assign the longest wavelength flank (>450 nm) to a purely LE(X) excitation of the Anion B1-3 ion population and the signal in the range of 350-400 nm to excitation of the benzoate population (Anion X), which is of mixed CT(X→B), LE(B) and LE(X) character (for assignment *cf.* section *4.9.6*; Table S15-19 and Figure S13-17). A summary of the

TD-DFT calculated lowest lying excited states calculated for the considered conformers of **[5 NF]**⁻ is given in Table 2.

Table 2 Longest wavelength, vertical singlet transitions calculated for various conformers of **[5-NF]**⁻ at the ground state geometry (TDDFT/ωB97XD /6-31+G(d)). Calculated central wavelengths λ are given together with corresponding values λ_S obtained after bathochromically shifting the transition energies by 3000 cm^{-1}. Only transitions with an oscillator strength of f>0.1 are displayed. Contributions to electronic transitions with a weight of <10 % were omitted. See Figure S13-17 for respective frontier orbital isosurfaces.

| conformer	state	transition (weight / %)	character	λ / nm	λ_S / nm	f
Anion 1	S_2	HOMO→LUMO+1 (92)	LE(X)	421	482	0.76
Anion 2	S_2	HOMO→LUMO+1 (83)	CT(X→B)	420	481	0.12
	S_3	HOMO→LUMO+2 (88)	LE(X)	419	479	0.64
Anion 3	S_3	HOMO→LUMO+2 (94)	LE(X)	433	498	0.73
Anion X	S_1	HOMO→LUMO (34)	CT(X→B)	376	424	0.39
		HOMO→LUMO+1 (54)	LE(X)			
Anion X'	S_5	HOMO→LUMO+3 (78)	LE(X)	315	348	0.19
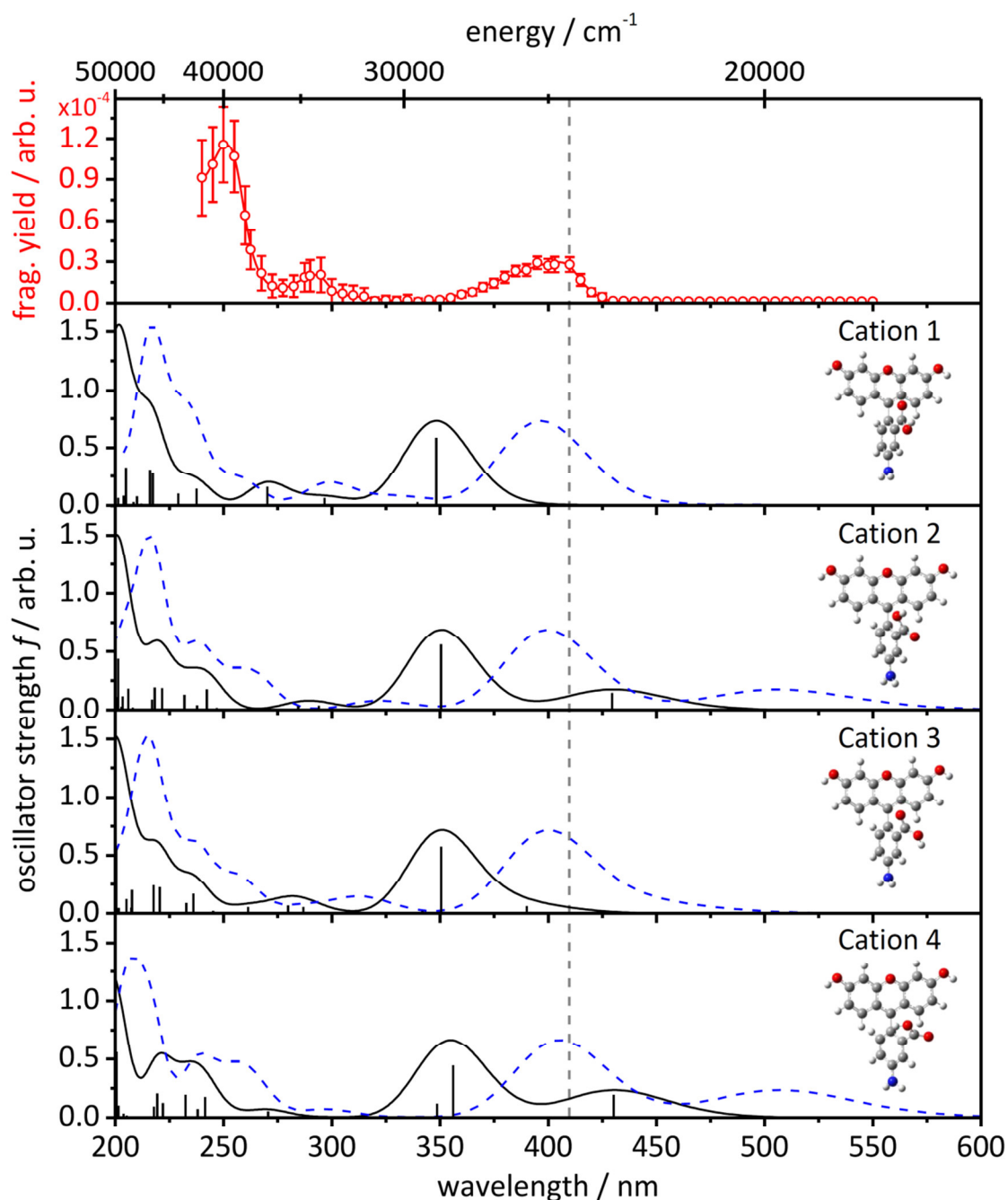
Figure 11 Experimental PF spectrum (top, red) of **[5-AF]⁺** and linear UV/Vis spectra (below, black) calculated for the five considered conformers. Calculated UV/Vis absorption intensities are shown as sticks and convoluted with 3000 cm^{-1} fwhm Gaussian functions (black lines). To account for errors in TD-DFT calculated transition energies, the convoluted spectra were shifted bathochromically by 3000 cm^{-1} (blue, dashed line). Vertical dashed line denotes pump-wavelength (410 nm) used in transient experiments.
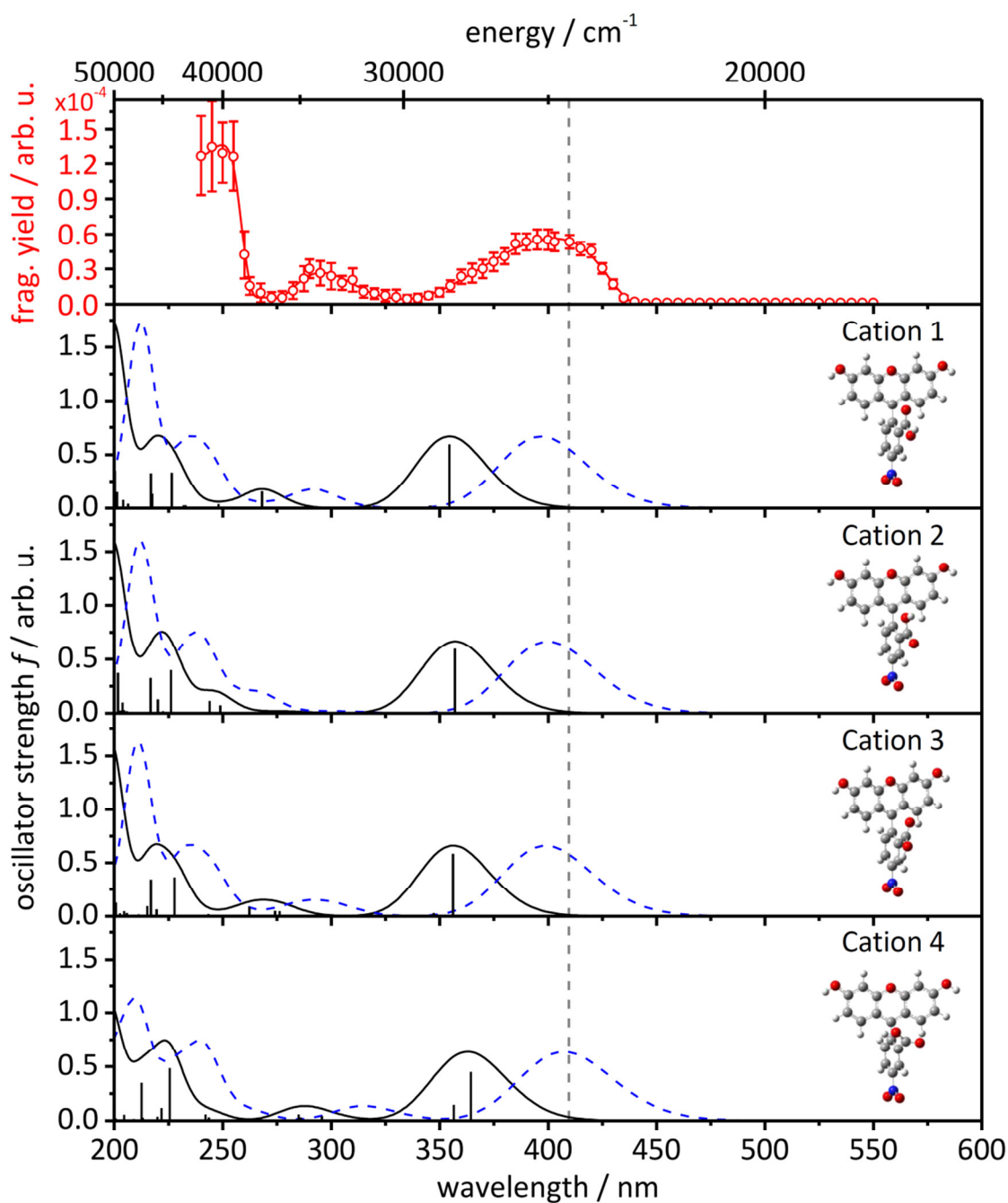
Figure 12 Experimental PF spectrum (top, red) of **[5-NF]+** and linear UV/Vis spectra (below, black) calculated for 1the five considered conformers. Calculated UV/Vis absorption intensities are shown as sticks and convoluted with 3000 cm⁻¹ fwhm Gaussian functions (black lines). To account for errors in TD-DFT calculated transition energies, the convoluted spectra were shifted bathochromically by 3000 cm⁻¹ (blue, dashed line). Vertical dashed line denotes pump-wavelength (410 nm) used in transient experiments.

Lastly we compare the experimental PF spectra of the cations to the TD-DFT calculated linear absorption spectra (Figure 11 and 12) we obtained for the considered conformers (Figure 5). The PF spectra of **[5-NF]⁺** and **[5-AF]⁺** are quite similar in shape and composition, consisting mainly of two absorption bands at ~400 nm and ~290 nm, and a broad, structureless absorption region below 250 nm. The general shape and composition of the recorded PF spectra compares surprisingly well to the calculated gas phase absorption action spectra, although fragmentation efficiency is drastically reduced compared to the anions. Similar to our calculations for the anions, TD-DFT overestimates the transitions by ~3000 cm⁻¹. Hence for a better comparison the convoluted spectra were bathochromically shifted by said value (Figure 11 and 12, dashed blue line). By comparing our experimental to the respective calculated spectra, we assign the absorption bands at ~290 nm for both **[5-NF]⁺** and **[5-AF]⁺** to CT(B→X) transitions and the region below 250 nm to a multitude of localized π-π*-transitions on either X or B moiety, or to transitions of partial CT character (for assignment *cf.* section *4.9.6*; Table S20-23/Figure S18-21 and Table S24-27/Figure S22-25 for **[5-AF]⁺** and **[5-NF]⁺**, respectively). The broad absorption bands at 400 nm in the spectra of both **[5-AF]⁺** and **[5-NF]⁺** can be assigned to LE(X) transitions. Note that this transition is calculated to be to the S_1 state for **[5-NF]⁺** and the S_2 state for **[5-AF]⁺** for all considered geometries. The calculated S_1 state transition for **[5-AF]⁺** is of CT(B→X) character. However, the intensity strongly depends on the orientation of the carboxylic OH-group, *i.e.* the oscillator strength is negligible for Cation 1 and 3, whereas for Cation 2 and 4 the oscillator strength is on the same order of magnitude as the intense $S_2 \leftarrow S_0$ transition (*e.g.* f=0.15 vs. 0.56 for the $S_1 \leftarrow S_0$ and $S_2 \leftarrow S_0$ transition of Cation 2, respectively). The corresponding band was not observed in the experimental spectrum of **[5-AF]⁺**. Either the fragmentation in this region is collisionally quenched, or the rotamers featuring a more intense $S_1 \leftarrow S_0$ transitions do not contribute significantly to the trapped ion population, which is feasible to assume (at least for Cation 4), as these exhibit quite high relative Gibbs energies of formation with respect to the lowest energy conformer (13.4 and 44.6 kJ/mol for Cation 2 and 4). A summary of the TD-DFT calculated lowest lying excited states calculated for the four conformers of **[5-AF]⁺** and **[5-NF]⁻** is given in Table 3 and Table 4, respectively.

Table 3 Longest wavelength, vertical singlet transitions calculated for various conformers of **[5-AF]⁺** at the ground state geometry (TDDFT/ωB97XD /6-31+G(d)). Calculated central wavelengths λ are given together with corresponding values λ$_S$ obtained after bathochromically shifting the transition energies by 3000 cm⁻¹. Only transitions with an oscillator strength of *f*>0.1 are displayed. Contributions to electronic transitions with a weight of <10 % were omitted. See Figure S18-21 for respective frontier orbital isosurfaces.

conformer	state	transition (weight / %)	character	λ / nm	λ$_S$ / nm	*f*
Cation 1	S$_2$	HOMO-1→LUMO (94)	LE(X)	348	389	0.58
Cation 2	S$_1$	HOMO→LUMO (94)	CT(B→X)	430	494	0.15
	S$_2$	HOMO-1→LUMO (94)	LE(X)	350	391	0.56
Cation 3	S$_2$	HOMO-1→LUMO (94)	LE(X)	351	392	0.57
Cation 4	S$_1$	HOMO→LUMO (94)	CT(B→X)	430	494	0.19
	S$_2$	HOMO-2→LUMO (16) HOMO-1→LUMO (79)	LE(X)	356	399	0.44

Table 4 Longest wavelength, vertical singlet transitions calculated for various conformers of **[5-NF]⁺** at the ground state geometry (TDDFT/ωB97XD /6-31+G(d)). Calculated central wavelengths λ are given together with corresponding values λ$_S$ obtained after bathochromically shifting the transition energies by 3000 cm⁻¹. Only transitions with an oscillator strength of *f*>0.1 are displayed. Contributions to electronic transitions with a weight of <10 % were omitted. See Figure S22-25 for respective frontier orbital isosurfaces.

conformer	state	transition (weight / %)	character	λ / nm	λ$_S$ / nm	*f*
Cation 1	S$_1$	HOMO→LUMO (95)	LE(X)	354	396	0.59
Cation 2	S$_1$	HOMO→LUMO (95)	LE(X)	357	400	0.59
Cation 3	S$_1$	HOMO→LUMO (94)	LE(X)	356	399	0.58
Cation 4	S$_1$	HOMO-1→LUMO (19) HOMO→LUMO (76)	LE(X)	364	409	0.45
	S$_2$	HOMO-1→LUMO (78) HOMO→LUMO (18)	LE(X)	357	400	0.15

In the following, the recorded time-resolved pump-probe PF spectra for the anionic and cationic species of **[5-AF]** and **[5-NF]** are presented. The trapped ions were thereby excited at their respective longest wavelength absorption band, which, according to our calculations, corresponds in each case to mainly a LE(X) transition.

4.5.3 Ultrafast electronic dynamics of [5-AF]⁻

The **[5-AF]⁻** ions were excited by pump laser pulses at the longest wavelength absorption maximum (510 nm, 0.3 μJ, *cf.* Figure 9) and subsequently probed with high energy pulses in the near NIR region (1200 nm, 120 μJ). Figure 13 depicts the fragment ion yield as a function of pump-probe delay up to a total delay of 800 ps recorded at the magic angle (54.7°).

Figure 13 Background corrected total fragmentation yield (open circles) of **[5-AF]⁻** as a function of pump-probe delay recorded for a total delay of 800 ps at the magic angle (54.7°). λ_{pump}=510 nm (0.3 μJ) and λ_{probe}=1200 nm (120 μJ). Dashed line denotes signal level subtracted to generate a residual for fitting. Inset: Fit of the residual signal **(a**, black)** is given along the fit decomposition **(b**, blue and cyan)**.

The transient rises on a sub-picosecond timescale, reaching signal maximum at a time delay of ~700 fs and stays for up to 800 ps (total pump-probe delay accessible) at this level. At shorter positive delay (0-7 ps) we furthermore observe a strong periodic modulation of the step like tPF signal, which is maintained for several oscillations within the observed timeframe. This behavior is indicative of the formation of a vibrational

wave-packet in the excited state potential well, *i.e.* the coherent excitation of several vibrational excited states of one or several vibrational modes. If these states show a favorable phase relation, a wave-packet is launched and oscillates with a period close to the frequency of the respective mode until energy redistribution by coupling to other degrees of freedom results in a decay of the modulation, *i.e.* dephasing of the wave-packet. Wave-packet dynamics has also been observed by us for the anionic form of unsubstituted fluorescein **[F]**⁻.[32] The oscillation period was found to be $2\pi/\omega$=T=1.2 ps, corresponding to a vibrational frequency of 28 cm⁻¹, which we assigned to a low frequency torsional motion of B *vs.* X, based on TD-DFT calculations and similar results reported for time-resolved photodetachment anisotropy (TR-PA) measurements by Horke *et al.*[33] In contrast to **[F]**⁻, **[5-AF]**⁻ exhibits a more complex signal modulation, which cannot be simulated by a single damped sine function. For a more convenient theoretical modeling of the periodic modulation the residual signal was used after subtracting the signal level at long time delay (dashed line, 800 ps). The resulting dataset is shown in the inset of Figure 13 together with the fit based on two damped sine functions $(A_1 \sin(\omega_1 \cdot t + \varphi_1) \cdot e^{-t/\tau_1} + A_2 \sin(\omega_2 \cdot t + \varphi_2) \cdot e^{-t/\tau_2})$. The oscillation periods T of the two components are found to be ~1.3 ps and ~1.0 ps, which correspond to a vibrational frequency of ~26 cm⁻¹ and ~33 cm⁻¹, respectively.

4.5.4 Ultrafast electronic dynamics of [5-NF]⁻

The **[5-NF]⁻** ions were excited by pump laser pulses at the longest wavelength absorption maximum (510 nm, 0.3µJ, *cf.* Figure 10) and subsequently probed with high intensity pulses in the NIR region (1200 nm, 120 µJ). Figure 14 depicts the fragment ion yield as a function of time delay up to a total delay of ∼600 ps recorded at the magic angle (54.7°).
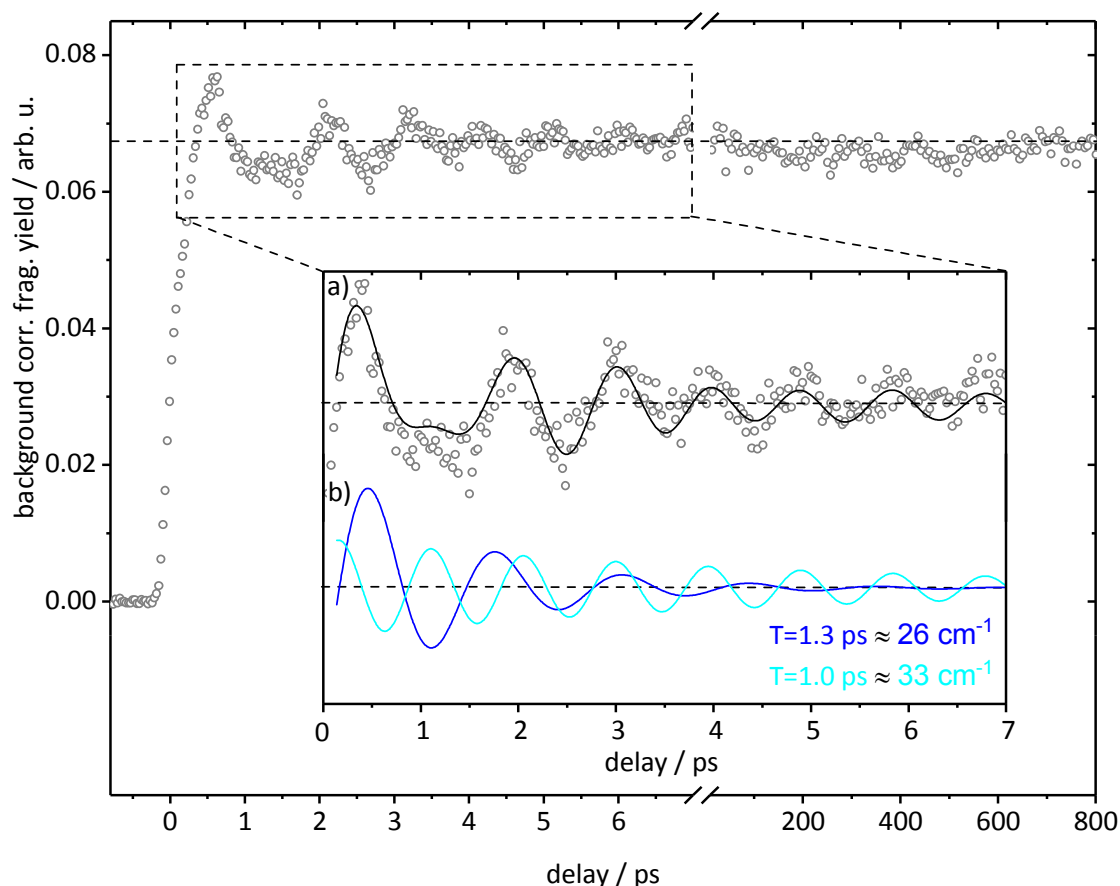

Figure 14 Background corrected total fragmentation yield (open circles) of **[5-NF]⁻** as a function of pump-probe delay recorded for a total delay of 600 ps at the magic angle (54.7°). λ_{pump}=510 nm (0.3 µJ) and λ_{probe}=1200 nm (120 µJ). Fit of the signal (black) is given along the fit decomposition (red and green) and residual (bottom). Inset: Modulated tPF signal for a shorter total time delay **(a**, open circles**)**. Dashed line denotes the background level subtracted from the signal to generate a residual for fitting. Fit of the residual signal **(b**, black**)** is given along the fit decomposition **(c**, blue and cyan**)**.

Similar to the transient recorded for **[5-AF]**⁻, the signal rises on a sub-picosecond timescale. In contrast to **[5-AF]**⁻, however, it decays to the signal level at negative pump-probe delay within ∼300 ps. This implies that the whole excited state population decayed to the ground state or to a spectroscopically dark state, *i.e.* a state with either a low absorption cross section for the probe photons or lying too low in energy so that a higher lying state (S_n) cannot be accessed by multiple-photon probe absorption. The signal decay can be satisfactorily fitted with a bi-exponential model, yielding two time constants of 13.1±0.5 ps and 76.2±5.5 ps. Furthermore, analogous to **[5-AF]**⁻, the transient signal is sinusoidally modulated, indicative of wave-packet formation, which dephases within approximately 7 ps. For further analysis, the exponentially decaying background signal was subtracted from the transient signal (Figure 14, dashed line in inset), yielding a simpler residual used for theoretical modeling. The signal was fitted applying a sum of two damped sine functions. Analogous to **[5-AF]**⁻, the oscillation periods T of the two components are found to be ∼1.4 ps and ∼1.0 ps corresponding to a vibrational frequency of ∼24 cm⁻¹ and ∼33 cm⁻¹, respectively.

4.5.5 Ultrafast electronic dynamics of [5-AF]⁺

The **[5-AF]⁺** ions were excited by pump laser pulses at the red edge of the longest wavelength absorption maximum (410 nm, 0.5µJ, *cf.* Figure 11) and subsequently probed with high intensity pulses in the NIR region (1200 nm, 120 µJ). Figure 15 depicts the fragment ion yield as a function of time delay up to a total delay of 800 ps recorded at the magic angle (54.7°).
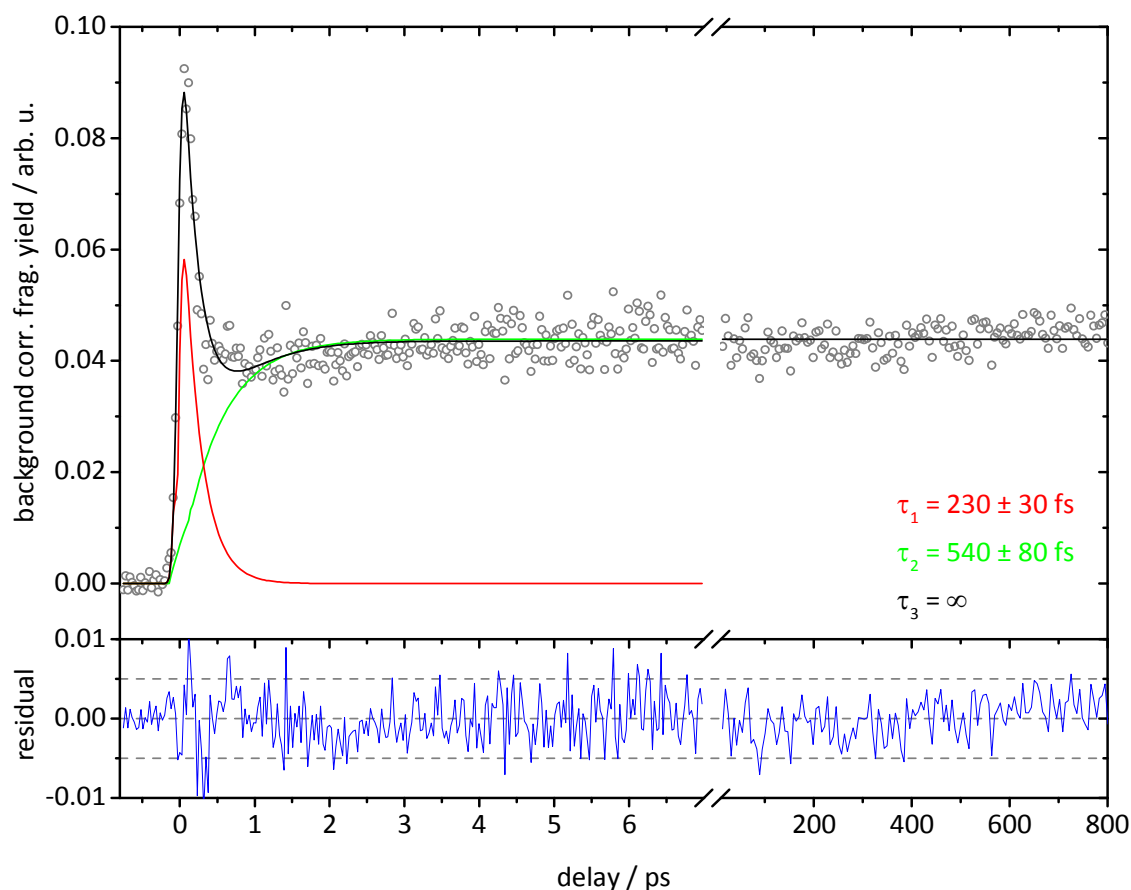
Figure 15 Background corrected total fragmentation yield (open circles) of **[5-AF]⁺** as a function of pump probe-delay recorded for a total delay of 800 ps at the magic angle (54.7°). λ_{pump}=410 nm (0.8 µJ) and λ_{probe}=1200 nm (120 µJ). Fit of the signal (black) is given along the fit decomposition (red and green) and residual (bottom).

The transient rises ultrafast on the order of the estimated system response (~120 fs). The signal then exhibits a mono-exponential decay and a concomitant signal increase within 230 fs and 540 fs, respectively. The resulting fragment ion signal intensity is maintained for up to a total delay of 800 ps, indicating the formation of a relatively long lived excited state. In contrast to the transient signal recorded for the monoanions, no signal modulation was observed at shorter pump-probe time delays.

4.5.6 Ultrafast electronic dynamics of [5-NF]+

The **[5-NF]+** ions were excited by pump laser pulses at the longest wavelength absorption maximum (410 nm, 0.5μJ, *cf.* Figure 12) and subsequently probed with high intensity pulses in the NIR region (1200 nm, 120 μJ). Figure 16 depicts the fragment ion yield as a function of time delay up to a total delay of 800 ps recorded at the magic angle (54.7°).
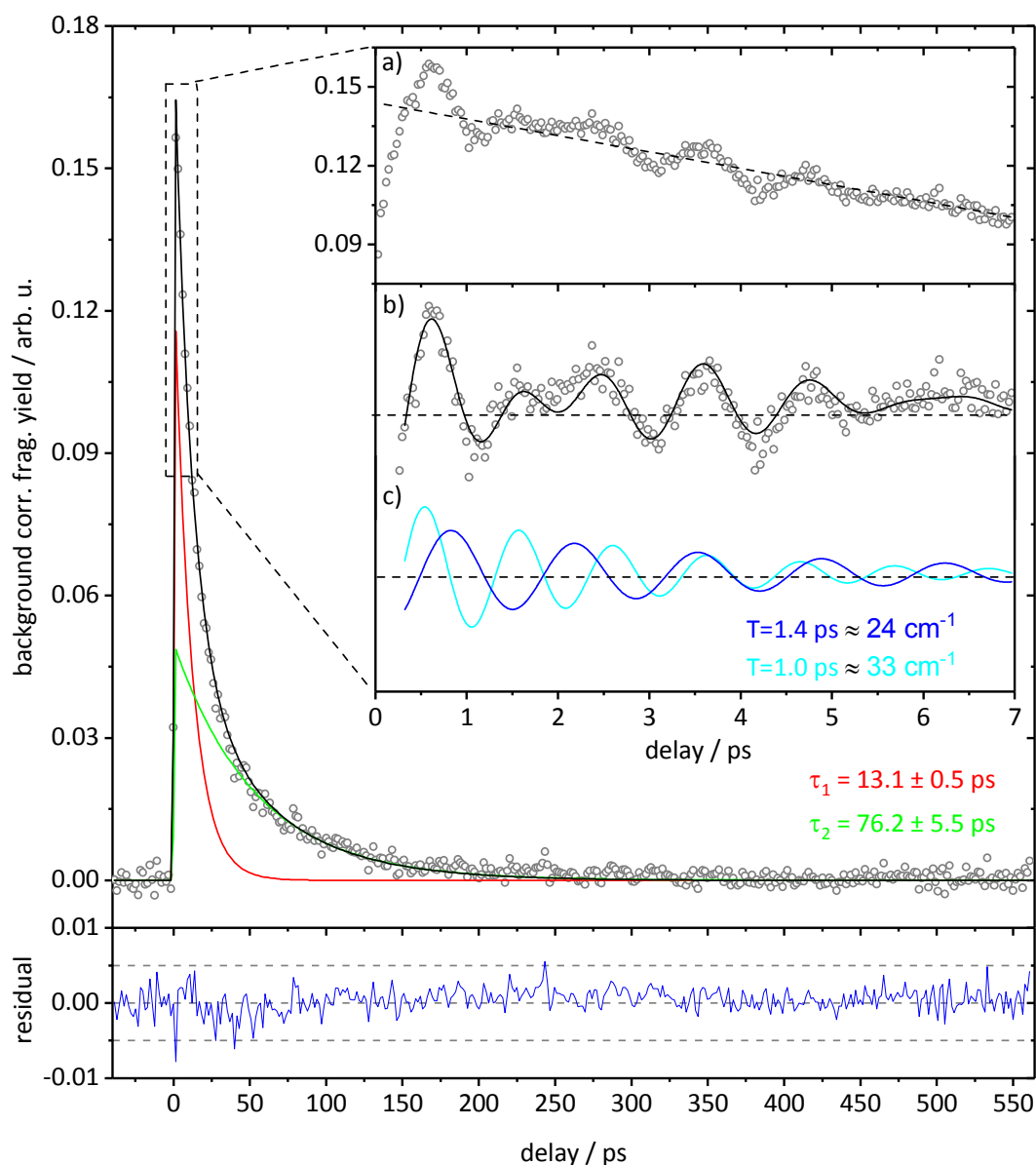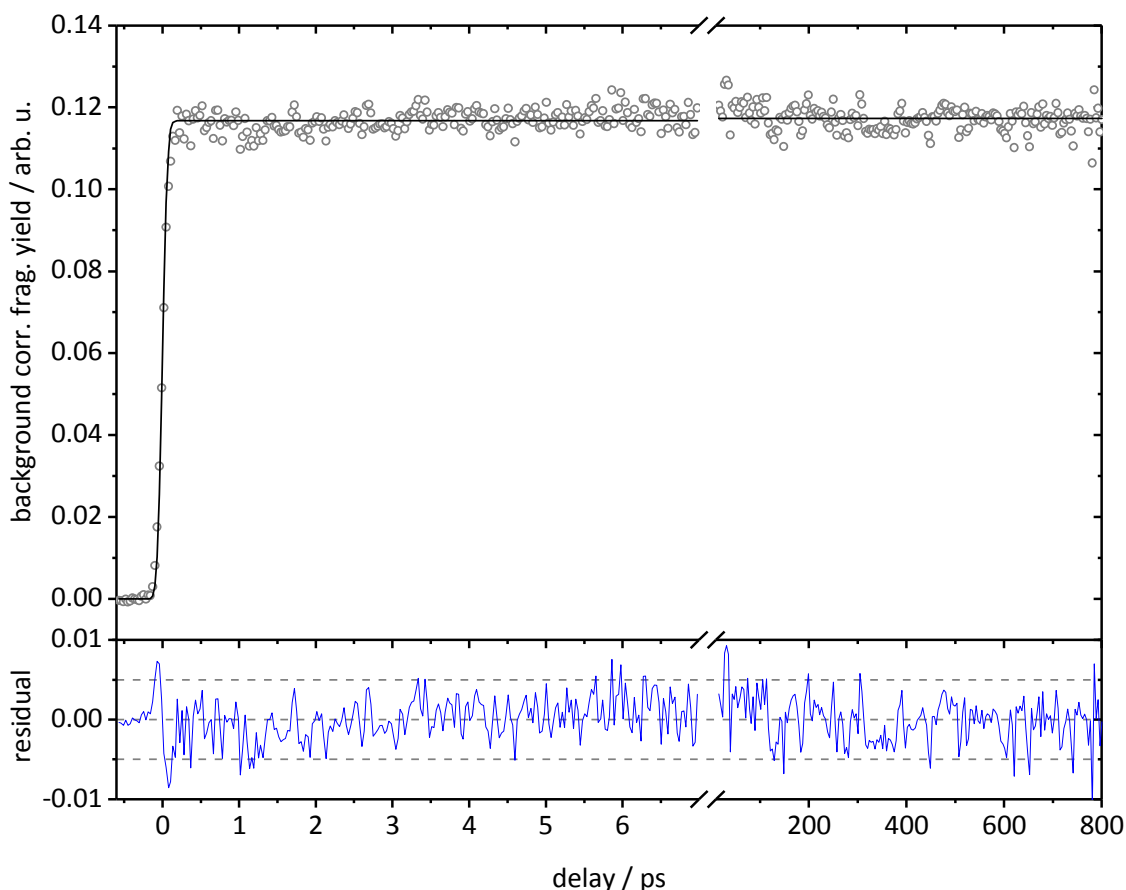

Figure 16 Background corrected total fragmentation yield (open circles) of **[5-NF]+** as a function of pump probe-delay recorded for a total delay of 800 ps at the magic angle (54.7°). λ_{pump}=410 nm (0.8 μJ) and λ_{probe}=1200 nm (120 μJ). Fit of the signal (black) is given along the fit residual (bottom).

The transient rises ultrafast on the order of the estimated system response (~120 fs). In contrast to the transient recorded for **[5-AF]+**, the signal does not show any trace of ultrafast electronic dynamics or dynamics on a longer timescale apart from the formation of a long lived state, which is similar to the behavior observed for the cation of the unsubstituted fluorescein **[F]+**.[32] Furthermore, no signal modulation was observed at shorter pump-probe delays.

4.6 Discussion

The differences in excited state dynamics of the these fluorescein derivatives are remarkable: first and foremost, only the anions exhibit wave-packet dynamics, resulting in sinusoidal modulation of the transient signals, whereas for the cations such behavior was not observed (although, at least for **[5-NF]⁺**, the S/N should be sufficient). Secondly, whether the transients exhibit ultrafast electronic dynamics depends heavily on the nature of the substituent (amino/nitro), as well as on the charge state. First we qualitatively discuss the origin of the ultrafast dynamics, keeping in mind that for fluorescein derivatives PeT is considered a viable deactivation channel.
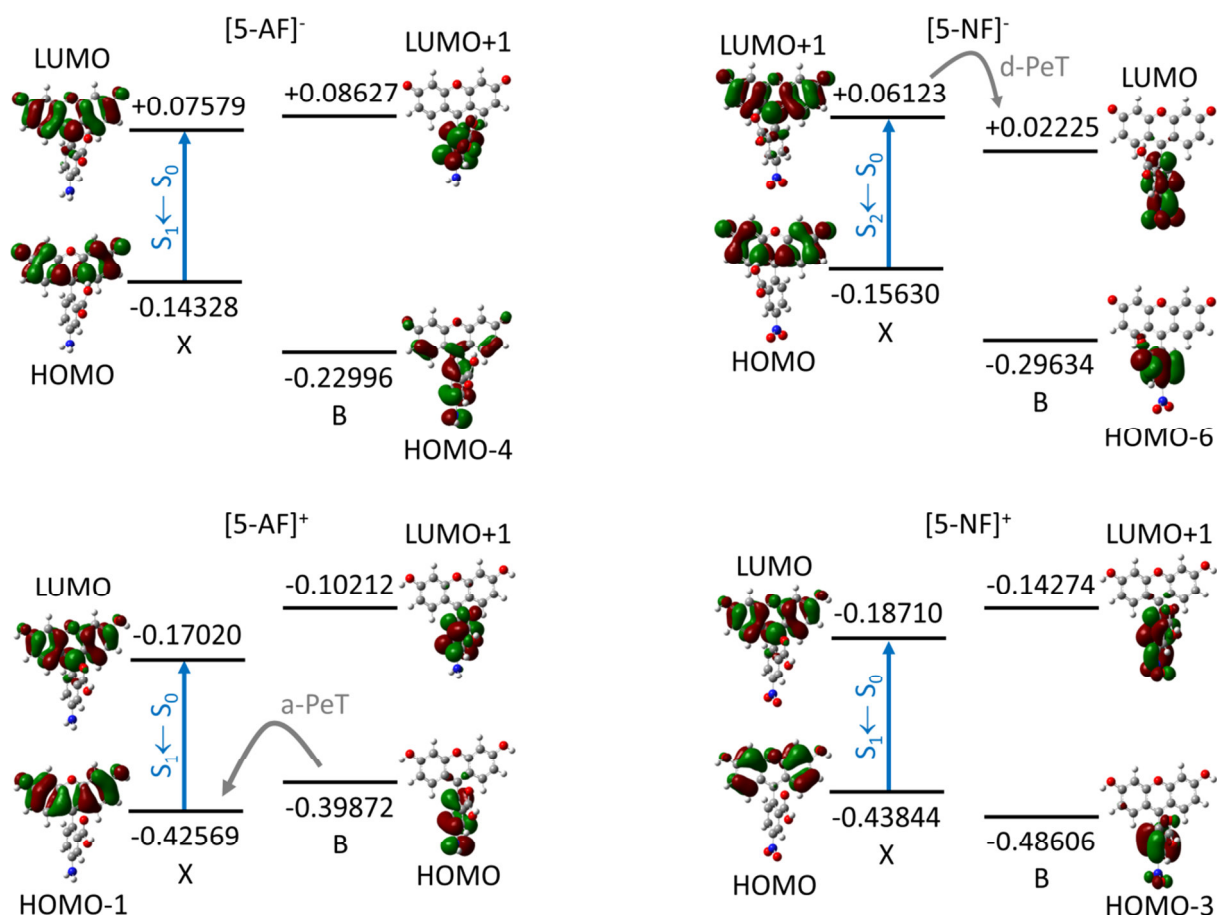
Figure 17 Sequence of highest occupied molecular orbitals (HOMO) and lowest unoccupied molecular orbitals (LUMO) centered at the xanthene (X) and benzoic acid (B) moieties calculated for the lowest energy conformers of **[5-AF]⁻**, **[5-NF]⁻**, **[5-AF]⁺** and **[5-NF]⁺**. Orbital energies are given in Hartree. Blue arrow denotes the character of the respective calculated lowest energy transition most probably excited using λ_{pump}=510 nm for the anions and λ_{pump}=410 nm for the cations (*cf.* Table 1-4).

For this purpose we take a closer look on the sequence of frontier orbitals we obtained from our DFT calculations, which are presented, for the sake of brevity, only for the respective lowest energy conformers (Cation 1 and Anion B1, respectively) in Figure 17 (*cf.* section *4.9.7*; Figure S26-29 for orbital sequences determined for the other conformers). Any differences in the sequence of orbitals obtained for the other conformers will be addressed explicitly, if needed. For **[5-AF]⁻**, the LUMO localized on X lies lower in energy than the first B centered LUMO. The first three HOMOs are located on X, followed by an orbital with significant contribution from B (HOMO-4). In the case of **[5-NF]⁻**, the order of orbitals is changed. Here the first LUMO is located on B, whereas the X-centered orbital (LUMO+1) is shifted to higher energies. The relative sequence of HOMOs, however, resembles the one found for **[5-AF]⁻**. The behavior of the LUMOs can be readily rationalized by the nature of the functional group: the amino-substituent in *meso*-position to X exerts a +*M*-effect (and +*I*-effect), increasing electron density in B, whereas the nitro-substituent has the opposite effect. Hence, for **[5-AF]⁻** the B-centered LUMO is higher in energy with respect to the X-localized LUMO, whereas for **[5-NF]⁻** the B-centered LUMO lies lower in energy. The same applies for the HOMOs. Here the electron donating property of the amino-group destabilizes the B-centered HOMO (HOMO-4), whereas the nitro-substituent has a stabilizing effect, increasing the gap between B- and X-centered HOMOs for **[5-NF]⁻**. The cations exhibit a somewhat different behavior. For **[5-AF]⁺**, the relative array of LUMOs is akin to **[5-AF]⁻**, whereas the B-centered HOMO lies higher in energy than the X-localized HOMO. The relative orbital sequence in **[5-NF]⁺** on the other hand is changed in such a way that it resembles the one calculated for **[5-AF]⁻**. This change in orbital sequences upon double protonation probably stems from a higher shift of the X-centered orbitals to lower energies, compared to the B-centered orbitals, which is not unexpected, as the site of protonation is located at the X-chromophore. According to the scheme presented in Figure 1, the orbital array in **[5-AF]⁺** should theoretically enable an a-PeT, whereas a d-PeT may take place for **[5-NF]⁻**. For the remaining systems (**[5-AF]⁻** and **[5-NF]⁺**), none of the above mentioned processes should be possible and thus no electronic dynamics associated with a PeT should be observable. Before we finally draw our conclusion, we would like to address the order of orbitals we obtained analogously for the other conformers. For the majority of conformers, our calculations yield qualitatively the same results, *i.e.* the orbital sequences obtained for the other conformers **[5-NF]⁻**, **[5-AF]⁺** and **[5-NF]⁺**

(*cf.* section *4.9.7*; Figure S26-29) closely resemble those of their respective lowest energy conformers (Figure 17). Only the orbital sequence of **[5-AF]**⁻ (Figure S26)depends on the geometry. The relative array of orbitals in the benzoate (Anion X) is the same as the one presented in Figure 17, whereas for Anion B2/3 and Anion X' geometries, the order resembles the one calculated for **[5-NF]**⁻. From this point on, we neglect both tautomeric forms (Anion X and X') of **[5-AF]**⁻ for the discussion, as firstly, IRMPD studies do not point to a high contribution of these geometries to the trapped ion population and, more importantly, even if the tautomers were present, we do not expect a significant contribution to the excited state population, as our chosen pump wavelength of 510 nm is allegedly not suited for sampling these conformers (*cf.* Figure 9). As regards the rotamers of Anion B1, although their orbital sequences should enable a d-PeT process, the excited states lowest in energy are calculated to be of significant CT(X→B) character (*cf.* Table 1), *i.e.* PeT is prevented from the start. Hence, if we consider PeT, then it is only feasible for the Anion B1 geometry of **[5-AF]**⁻.

Note that we also performed calculations using two other functionals in addition to the ωB97XD functional, which was in the focus of this study. However, B3LYP[34-35] and its long-range corrected extension cam-B3LYP[36] yielded similar results (*cf.* section *4.9.7*; Figure S30-33 and Table S28-30). A potential basis-set dependence of the orbital sequences will be addressed in a future study.

Having presented and discussed the results of our DFT calculations, we may now draw a comparison to our experiments. As already stated, theory implies that PeT is only feasible for **[5-AF]**⁺ and **[5-NF]**⁻, hence one should expect spectroscopic signature of such a process. Indeed, our experimental results fit this picture qualitatively well, as only **[5-NF]**⁻ and **[5-AF]**⁺ exhibit ultrafast electronic dynamics (*cf.* Figure 14 and 15, respectively). The involvement of PeT in the excited state "quenching" observed for functionalized fluorescein derivatives is furthermore corroborated by results from our previous study on **[F]**⁺ and **[F]**⁻, for which no sign of ultrafast dynamics was observed[32] and for which our calculations do not predict an orbital sequence rendering a PeT process possible (*cf.* section *4.9.7*; Figure S34 and Table S32).

At this point, the timescale and character of the observed dynamics shall be addressed: for **[5-NF]**⁻, the transient signal decays bi-exponentially to the base level on a picosecond timescale, whereas for **[5-AF]**⁺, the initially excited state decays within 230 fs to a

relative long-lived state, which apparently still has a significant absorption cross section for the probe photons; thus a relatively high fragment yield for up to 800 ps delay is retained. Additionally, the transient of **[5-AF]$^+$** bears signature of a second, slightly slower process (540 fs) allegedly contributing to the formation of the long lived signal. This second component may very well be simply an artifact, resulting from a slight misalignment of the Berek compensator used for polarization control, thus some polarization dependence of the signal leaks through. We reported on strong polarization dependence of the transient signals of **[F]$^+$** previously, stemming from molecular alignment and dephasing of a rotational wave-packet.[32] Another explanation would be a different electronic process, which occurs in parallel to the a-PeT. Curiously, **[5-AF]$^+$** is the only system for which calculations predict the S_1 state to be of CT(X→B) character and in addition places the B-centered LUMO higher in energy than the X-localized LUMO. Such combination would also theoretically enable a-PeT; in this case, however, the LUMO of X would act as an acceptor and the LUMO localized on B as the donor (as the electron is initially transferred to this orbital), possibly resulting in the observation of additional kinetics.

Still a couple of questions remain: firstly, why does the transient signal of **[5-NF]$^-$** exhibit bi-exponential decay? Secondly, why does the assumed PeT proceed for **[5-NF]$^-$** much slower than for **[5-AF]$^+$** and lastly, why does the signal, in contrast to **[5-AF]$^+$**, decays completely, although in both cases the excited state is "quenched" via PeT? As regards the latter question, a complete decay of the transient signal in our detection scheme does not necessarily imply IC to the ground state, but may also be indicative of relaxation to a spectroscopically dark state, *i.e.* a state which has a negligible absorption cross section for probe photons. The exact character of the state to which the population of **[5 NF]$^-$** decays is as of yet unknown to us, but based on our calculations, we may speculate that a charge separated state (formed after PeT) in which the negative charge is located on B, lies either too low in energy or has an insignificant absorption cross section for our employed probe photons so that in neither scenario a higher lying S_n state can be accessed. Hence fragmentation enhancement, which is a prerequisite for our detection scheme, is prohibited and the transient decays. Indeed, from the orbital sequence presented in Figure 17 (and Figure S26-29), it is evident that only for **[5-NF]$^-$** a charge separated state with increased electron density on B is possibly formed after photoexcitation and subsequent d-PeT, whereas the a-PeT process assumed for **[5-AF]$^+$**

transfers the electron to X and for the remaining two systems (**[5-AF]⁻** and **[5-NF]⁺**) charge separation does not take place at all. The second question addresses the difference in timescale of the PeT processes in **[5-NF]⁻** and **[5-AF]⁺**. Generally, PeT occurs faster the better the coupling between excited and charge separated state, *i.e.* the smaller the difference in geometry is. The faster dynamics observed for **[5-AF]⁺** thus implies that the change in geometry is rather small, resulting in a quasi-instantaneous electron transfer, whereas the geometry of **[5-NF]⁻** has to be distorted appropriately prior to switching to a charge separated state. An approach to estimate electron transfer rates is by Marcus Theory. However, application of the Marcus equation requires knowledge about both the excited state geometry and the geometry of the charge separated state, which we were not yet able to obtain.

The origin of the bi-exponential decay observed in the dynamics of **[5-NF]⁻** is another unclear aspect. Although our IRMPD spectra point strongly to coexistence of both benzoate and phenolate tautomers in the gas phase, we refrain from assigning one of the time constants to electronic decay of an excited Anion X/X' population, as we already established that the chosen pump wavelength in our time-resolved experiments is not suitable to sample these ions. Another explanation for the additional time constant could be the concurrent decay of an excited state population composed of rotamers of Anion B1. At least Anion B2 is calculated to be nearly isoenergetic to Anion B1 and may possibly exhibit different coupling between the locally excited and the charge separated state. Again, to prove this assumption, a more dedicated theoretical approach is required. Lastly, we cannot rule out charge recombination following charge separation as the origin for the second, slightly longer decay constant.

The final point to be addressed in our discussion is the signal modulation, which only appears in the transients of the anions. In our previous study on **[F]⁻**, we observed a sinusoidal modulation with a period of T=1.2 ps, corresponding to a vibrational frequency of ~28 cm⁻¹,[32] which compared remarkably well to the reported frequency (~32 cm⁻¹) obtained by Horke *et al.* from TR-PA experiments on **[F]⁻**.[33] For **[F]⁻**, Horke *et al.* assigned a low-frequency torsional motion of B vs. the X chromophore, supported by TD-DFT geometry optimization of the first electronically excited state of **[F]⁻**. Calculations revealed that the mutual dihedral angle between the sub-units decreases from 90° in the S₀ state to 53° in the S₁ state.[33] In our study on **[F]⁻** and **[F]⁺**, we

performed single-point energy calculations of distorted ground state geometries depending on the dihedral angle, which revealed that relaxation is energetically possible only for **[F]**⁻, agreeing with our observation of wave-packet dynamics only for this charge state.[32] We believe that the same reasoning applies for the functionalized fluorescein derivatives, thus wave-packet dynamics are only observed for the anions. However, as already mentioned above, the signal modulation is much more complex than in the case of **[F]**⁻, requiring at least two damped sine functions for modeling the modulation of the transient signals. The corresponding vibrational frequencies estimated from the period of the sines are nearly identical for **[5-AF]**⁻ and **[5-NF]**⁻ ($\tilde{v}_1$=26 cm⁻¹, $\tilde{v}_2$=35 cm⁻¹ and $\tilde{v}_1$=25 cm⁻¹, $\tilde{v}_2$=33 cm⁻¹, respectively), implying that similar vibrational modes are responsible for the signal modulation. As we lack the respective excited state geometries required for a more precise assignment of the frequencies to vibrational modes, we can for now only consult the frequencies obtained from ground state calculations and surmise that the frequencies in the excited state are not drastically altered. Ground state vibrational calculations reveal for both anions several low frequency (<100 cm⁻¹) vibrational modes, (*cf.* section *4.9.8*; Figure S35/36 and Table S33/34 for **[5-AF]**⁻/**[5-NF]**⁻), which encompass the torsional motion of B vs. X ($\tilde{v}_1$), a rocking motion of B within ($\tilde{v}_2$) or out of ($\tilde{v}_3$) the X plane, and torsional motions of the functional groups of B in combination with various skeletal modes ($\tilde{v}_4$-$\tilde{v}_6$ and $\tilde{v}_4$-$\tilde{v}_7$ for **[5-AF]**⁻ and **[5-NF]**⁻, respectively). Most interesting are the two lowest frequency modes, for which we, depending on the conformer, obtained values of $\tilde{v}_1$=15-24 cm⁻¹/ $\tilde{v}_2$=39-41 cm⁻¹ and $\tilde{v}_1$=17-24 cm⁻¹/$\tilde{v}_2$=30-32 cm⁻¹ from calculations on **[5-AF]**⁻ and **[5-NF]**⁻, respectively. These mode are expected to modulate the π-interaction of B and X and compare surprisingly well to the experimental values, implying a concurrent formation of two similar wave-packets in the excited state potentials of **[5-AF]**⁻ and **[5 NF]**⁻. However, it is not yet clear as to why the vibrational dynamics are so distinctly different to the one observed for **[F]**⁻, in which allegedly only one vibrational coordinate is coherently excited upon electronic excitation.[32] Presumably functionalization of B has a profound impact on the low-lying excited state properties of the molecular ions, although owing to a mutual perpendicular orientation of the two sub-units characteristic for fluorescein dyes, the interaction between the π-systems is expected to be minor. Note that we also observed remarkably different wave-packet dynamics for halogenated fluorescein derivatives, bearing chloro- or fluoro-substituents at the X chromophore,

implying that electronic modifications have an extraordinary impact on the coupling of vibrational modes. These findings will be addressed in a future study.

Another explanation for periodic modulation of transient signals in fs-spectroscopy is electronic coherence, *i.e.* the coherent excitation of two (or more) quasi-degenerate, strongly coupled excited states. The ensuing signal modulation is, however, generally higher in frequency and the wave-packet dephases on a much shorter fs time-scale. Additionally, our calculations do not point to the existence of excited states in the immediate vicinity of the respective excited state we sampled with our chosen pump wavelengths. Consequently, this reasoning should not apply to our experimental results, rendering vibrational wave-packet dynamics the only feasible explanation.

4.7 Conclusion

In conclusion, we presented an extensive spectroscopic gas phase study on the monoanionic and cationic forms of two fluorescein derivatives, functionalized with either an electron withdrawing nitro- or an electron donating amino-group at the benzoic acid ring. IRMPD spectra recorded for the anions point to a coexistence of tautomers in the case of the nitro-derivative, whereas the gas phase population of the amino-derivative consists most probably solely of the phenolate form, in which the acidic proton is located at the carboxylic acid group of B. The cationic ion populations consist of several rotamers, differing in the orientation of the carboxylic OH-group. However, only geometries in which the proton at the carboxylic acid group point towards X are significantly stabilized by long-range interaction with the π-system of X and thus expected to contribute to the ion population. The experimental UV/Vis PF spectra of the cations are in good agreement with TD-DFT calculated linear absorption spectra, whereas theory fails to satisfactorily reproduce the absorption properties of the anions. The most notable difference to the theoretical spectra is the high intensity, lowest energy transition absorption band, which is missing in the experimental spectra, probably due to collisional quenching of the fragmentation. The excited state dynamics following a localized excitation of the X chromophore exhibit remarkable dependence on the nature of the substituent (amino/nitro), as well as on the charge state. Excited state dynamics on a fs- and ps-timescale are only observed for **[5-AF]⁺** and **[5-NF]⁻**, respectively, and are attributed to excited state quenching by PeT. The sequence of frontier orbitals are in good accordance to our assumption, only enabling d-PeT for

[5-NF][-] and a-PeT for **[5-AF]**[+]. Additionally, the transient fragment mass signals of the anions are periodically modulated, which is indicative of vibrational wave-packet dynamics. From the period of the modulation, we determined two frequencies, which we assigned to two separate low frequency vibrational modes obtained from DFT calculations, showing good agreement with the experiment.

Acknowledgement

4.8 References

[1]   R. Sjöback, J. Nygren, M. Kubista, *"Absorption and fluorescence properties of fluorescein"*, *Spectrochimica Acta Part A: Molecular and Biomolecular Spectroscopy* **1995**, *51*, L7-L21.

[2]   E. W. Miller, S. X. Bian, C. J. Chang, *"A Fluorescent Sensor for Imaging Reversible Redox Cycles in Living Cells"*, *J. Am. Chem. Soc.* **2007**, *129*, 3458-3459.

[3]   V. V. Martin, A. Rothe, K. R. Gee, *"Fluorescent metal ion indicators based on benzoannelated crown systems: a green fluorescent indicator for intracellular sodium ions"*, *Bioorg. Med. Chem. Lett.* **2005**, *15*, 1851-1855.

[4]   S. Yoon, E. W. Miller, Q. He, P. H. Do, C. J. Chang, *"A Bright and Specific Fluorescent Sensor for Mercury in Water, Cells, and Tissue"*, *Angew. Chem. Int. Ed.* **2007**, *46*, 6658-6661.

[5]   X. Li, X. Gao, W. Shi, H. Ma, *"Design Strategies for Water-Soluble Small Molecular Chromogenic and Fluorogenic Probes"*, *Chem. Rev.* **2014**, *114*, 590-659.

[6]   L. D. Lavis, R. T. Raines, *"Bright Ideas for Chemical Biology"*, *ACS Chem. Biol.* **2008**, *3*, 142-155.

[7]   D. Jung, K. Min, J. Jung, W. Jang, Y. Kwon, *"Chemical biology-based approaches on fluorescent labeling of proteins in live cells"*, *Mol. BioSys.* **2013**, *9*, 862-872.

[8]   L. D. Lavis, T.-Y. Chao, R. T. Raines, *"Fluorogenic Label for Biomolecular Imaging"*, *ACS Chem. Biol.* **2006**, *1*, 252-260.

[9]   Michael N. Levine, Trish T. Hoang, Ronald T. Raines, *"Fluorogenic Probe for Constitutive Cellular Endocytosis"*, *Chem. Biol.* **2013**, *20*, 614-618.

[10]   D. Yousheng, L. Ming, S. Wei, W. Min, L. Shangzhong, X. L. Qing, *"Recent Progress on Synthesis of Fluorescein Probes"*, *Mini Rev. Org. Chem.* **2009**, *6*, 35-43.

[11]   C. C. Gradinaru, D. O. Marushchak, M. Samim, U. J. Krull, *"Fluorescence anisotropy: from single molecules to live cells"*, *Analyst* **2010**, *135*, 452-459.

[12]   D. M. Jameson, J. A. Ross, *"Fluorescence Polarization/Anisotropy in Diagnostics and Imaging"*, *Chem. Rev.* **2010**, *110*, 2685-2708.

[13]   J. Rao, A. Dragulescu-Andrasi, H. Yao, *"Fluorescence imaging in vivo: recent advances"*, *Curr. Opin. Biotechnol.* **2007**, *18*, 17-25.

[14]   T. Robertson, F. Bunel, M. Roberts, *"Fluorescein Derivatives in Intravital Fluorescence Imaging"*, *Cells* **2013**, *2*, 591.

[15] T. Hirano, K. Kikuchi, Y. Urano, T. Higuchi, T. Nagano, *"Highly Zinc-Selective Fluorescent Sensor Molecules Suitable for Biological Applications"*, *J. Am. Chem. Soc.* **2000**, *122*, 12399-12400.

[16] T. Kobayashi, Y. Urano, M. Kamiya, T. Ueno, H. Kojima, T. Nagano, *"Highly Activatable and Rapidly Releasable Caged Fluorescein Derivatives"*, *J. Am. Chem. Soc.* **2007**, *129*, 6696-6697.

[17] T. Miura, Y. Urano, K. Tanaka, T. Nagano, K. Ohkubo, S. Fukuzumi, *"Rational Design Principle for Modulating Fluorescence Properties of Fluorescein-Based Probes by Photoinduced Electron Transfer"*, *J. Am. Chem. Soc.* **2003**, *125*, 8666-8671.

[18] K. Tanaka, T. Miura, N. Umezawa, Y. Urano, K. Kikuchi, T. Higuchi, T. Nagano, *"Rational Design of Fluorescein-Based Fluorescence Probes. Mechanism-Based Design of a Maximum Fluorescence Probe for Singlet Oxygen"*, *J. Am. Chem. Soc.* **2001**, *123*, 2530-2536.

[19] T. Ueno, Y. Urano, K.-i. Setsukinai, H. Takakusa, H. Kojima, K. Kikuchi, K. Ohkubo, S. Fukuzumi, T. Nagano, *"Rational Principles for Modulating Fluorescence Properties of Fluorescein"*, *J. Am. Chem. Soc.* **2004**, *126*, 14079-14085.

[20] X.-F. Zhang, *"The effect of phenyl substitution on the fluorescence characteristics of fluorescein derivatives via intramolecular photoinduced electron transfer"*, *Photochem.l Photobiol. Sci.* **2010**, *9*, 1261-1268.

[21] X.-F. Zhang, J. Zhang, L. Liu, *"Fluorescence Properties of Twenty Fluorescein Derivatives: Lifetime, Quantum Yield, Absorption and Emission Spectra"*, *J. Fluoresc.* **2014**, *24*, 819-826.

[22] J.-D. Chai, M. Head-Gordon, *"Long-range corrected hybrid density functionals with damped atom-atom dispersion corrections"*, *Phys. Chem. Chem. Phys.* **2008**, *10*, 6615-6620.

[23] M. J. Frisch, G. W. Trucks, H. B. Schlegel, G. E. Scuseria, M. A. Robb, J. R. Cheeseman, G. Scalmani, V. Barone, B. Mennucci, G. A. Petersson, H. Nakatsuji, M. Caricato, X. Li, H. P. Hratchian, A. F. Izmaylov, J. Bloino, G. Zheng, J. L. Sonnenberg, M. Hada, M. Ehara, K. Toyota, R. Fukuda, J. Hasegawa, M. Ishida, T. Nakajima, Y. Honda, O. Kitao, H. Nakai, T. Vreven, J. A. Montgomery Jr., J. E. Peralta, F. Ogliaro, M. J. Bearpark, J. Heyd, E. N. Brothers, K. N. Kudin, V. N. Staroverov, R. Kobayashi, J. Normand, K. Raghavachari, A. P. Rendell, J. C. Burant, S. S. Iyengar, J. Tomasi, M. Cossi, N. Rega, N. J. Millam, M. Klene, J. E. Knox, J. B. Cross, V. Bakken, C. Adamo, J. Jaramillo, R. Gomperts, R. E. Stratmann, O. Yazyev, A. J. Austin, R. Cammi, C. Pomelli, J. W. Ochterski, R. L. Martin, K. Morokuma, V. G. Zakrzewski, G. A. Voth, P. Salvador, J. J. Dannenberg, S. Dapprich, A. D. Daniels, Ö. Farkas, J. B. Foresman, J. V. Ortiz, J. Cioslowski, D. J. Fox, Gaussian, Inc., Wallingford, CT, USA, **2009**.

[24] A. J. Cohen, P. Mori-Sánchez, W. Yang, *"Insights into Current Limitations of Density Functional Theory"*, *Science* **2008**, *321*, 792-794.

[25] F. Jensen, *"Describing Anions by Density Functional Theory: Fractional Electron Affinity"*, *J. Chem. Theory Comput.* **2010**, *6*, 2726-2735.

[26] H. Yao, J. D. Steill, J. Oomens, R. A. Jockusch, *"Infrared Multiple Photon Dissociation Action Spectroscopy and Computational Studies of Mass-Selected Gas-Phase Fluorescein and 2′,7′-Dichlorofluorescein Ions"*, *J. Phys. Chem. A* **2011**, *115*, 9739-9747.

[27] C. A. Hollingsworth, P. G. Seybold, C. M. Hadad, *"Substituent effects on the electronic structure and pKa of benzoic acid"*, *Int. J. Quantum Chem.* **2002**, *90*, 1396-1403.

[28] H. Zhang, X. Jiang, W. Wu, Y. Mo,*"Electron conjugation versus [small pi]-[small pi] repulsion in substituted benzenes: why the carbon-nitrogen bond in nitrobenzene is longer than in aniline"*, *Phys. Chem. Chem. Phys.* **2016**, *18*, 11821-11828.

[29] P. D. McQueen, S. Sagoo, H. Yao, R. A. Jockusch,*"On the Intrinsic Photophysics of Fluorescein"*, *Angew. Chem. Int. Ed.* **2010**, *49*, 9193-9196.

[30] H. Yao, R. A. Jockusch,*"Fluorescence and Electronic Action Spectroscopy of Mass-Selected Gas-Phase Fluorescein, 2′,7′-Dichlorofluorescein, and 2′,7′-Difluorofluorescein Ions"*, *J. Phys. Chem. A* **2013**, *117*, 1351-1359.

[31] M. W. Forbes, R. A. Jockusch,*"Gas-Phase Fluorescence Excitation and Emission Spectroscopy of Three Xanthene Dyes (Rhodamine 575, Rhodamine 590 and Rhodamine 6G) in a Quadrupole Ion Trap Mass Spectrometer"*, *J. Am. Soc. Mass. Spectrom.* **2011**, *22*, 93-109.

[32] D. Imanbaew, M. F. Gelin, C. Riehn,*"Rotational and vibrational dynamics in the excited electronic state of deprotonated and protonated fluorescein studied by time-resolved photofragmentation in an ion trap"*, *Struct. Dyn.* **2016**, *3*, 043211.

[33] D. A. Horke, A. S. Chatterley, J. N. Bull, J. R. R. Verlet,*"Time-Resolved Photodetachment Anisotropy: Gas-Phase Rotational and Vibrational Dynamics of the Fluorescein Anion"*, *J. Phys. Chem. Lett.* **2015**, *6*, 189-194.

[34] A. D. Becke,*"Density-functional thermochemistry. III. The role of exact exchange"*, *J. Chem. Phys.* **1993**, *98*, 5648-5652.

[35] C. Lee, W. Yang, R. G. Parr,*"Development of the Colle-Salvetti correlation-energy formula into a functional of the electron density"*, *Phys. Rev. B* **1988**, *37*, 785-789.

[36] T. Yanai, D. P. Tew, N. C. Handy,*"A new hybrid exchange–correlation functional using the Coulomb-attenuating method (CAM-B3LYP)"*, *Chem. Phys. Lett.* **2004**, *393*, 51-57.

4.9 Supplementary material to "Charge state dependent excited state quenching in 5-Amino- and 5-Nitrofluorescein"

Content

4.9.1 Experimental Procedures

4.9.2 Structural parameters from DFT optimized geometries

Figure S1 Scheme depicting change in dihedral angles upon geometry optimization

Table S1 Summary of relative change in dihedral angles upon geometry optimization

4.9.3 Mass spectrometric data

Figure S2 Fragment mass spectra of **[5-AF]**[-] by IRMPD and UV/Vis PF

Table S2 Identified fragment mass signals of **[5-AF]**[-]

Figure S3 Fragment mass spectra of **[5-NF]**[-] by IRMPD and UV/Vis PF

Table S3 Identified fragment mass signals of **[5-NF]**[-]

Figure S4 Fragment mass spectra of **[5-AF]**[+] by IRMPD and UV/Vis PF

Table S4 Identified fragment mass signals of **[5-AF]**[+]

Figure S5 Fragment mass spectra of **[5-NF]**[+] by IRMPD and UV/Vis PF

Table S5 Identified fragment mass signals of **[5-NF]**[+]

4.9.4 DFT calculated IR frequencies

Table S6 IR frequencies of **[5-AF]**[-]

Table S7 IR frequencies of **[5-NF]**[-]

Table S8 IR frequencies of **[5-AF]**[+]

Table S9 IR frequencies of **[5-NF]**[+]

4.9.5 Photofragmentation

Figure S6 Pulse energy dependent fragmentation yields by one-color photoexcitation

Figure S7 Comparison PF spectrum of **[5-NF]**⁻ with convolution of theoretical UV/Vis spectra calculated for different conformers

4.9.6 TD-DFT calculated electronic transitions

Table S10 Transitions calculated for the Anion B1 conformer of **[5-AF]**⁻

Figure S8 MO isosurfaces involved in transitions calculated for the Anion B1 conformer of **[5-AF]**⁻

Table S11 Transitions calculated for the Anion B2 conformer of **[5-AF]**⁻

Figure S9 MO isosurfaces involved in transitions calculated for the Anion B2 conformer of **[5-AF]**⁻

Table S12 Transitions calculated for the Anion B3 conformer of **[5-AF]**⁻

Figure S10 MO isosurfaces involved in transitions calculated for the Anion B3 conformer of **[5-AF]**⁻

Table S13 Transitions calculated for the Anion X conformer of **[5-AF]**⁻

Figure S11 MO isosurfaces involved in transitions calculated for the Anion X conformer of **[5-AF]**⁻

Table S14 Transitions calculated for the Anion X' conformer of **[5-AF]**⁻

Figure S12 MO isosurfaces involved in transitions calculated for the Anion X' conformer of **[5-AF]**⁻

Table S15 Transitions calculated for the Anion B1 conformer of **[5-NF]**⁻

Figure S13 MO isosurfaces involved in transitions calculated for the Anion B1 conformer of **[5-NF]**⁻

Table S16 Transitions calculated for the Anion B2 conformer of **[5-NF]**⁻

Figure S14 MO isosurfaces involved in transitions calculated for the Anion B2 conformer of **[5-NF]**⁻

Table S17 Transitions calculated for the Anion B3 conformer of **[5-NF]**⁻

Figure S15 MO isosurfaces involved in transitions calculated for the Anion B3 conformer of **[5-NF]**⁻

Table S18 Transitions calculated for the Anion X conformer of **[5-NF]**⁻

4.9.7 DFT calculated frontier orbital sequences

Figure S28 Orbital sequences calculated for higher energy conformers of **[5-AF]$^+$**

Figure S29 Orbital sequences calculated for higher energy conformers of **[5-NF]$^+$**

Figure S30 Orbital sequences calculated for the Anion B1 conformer of **[5-AF]$^-$** using different functionals

Table S28 Lowest energy, highest intensity transitions calculated for the Anion B1 conformer of **[5-AF]$^-$** using different functionals

Figure S31 Orbital sequences calculated for the Anion B1 conformer of **[5-NF]$^-$** using different functionals

Table S29 Lowest energy, highest intensity transitions calculated for the Anion B1 conformer of **[5-NF]$^-$** using different functionals

Figure S32 Orbital sequences calculated for the Cation 1 conformer of **[5-AF]$^+$** using different functionals

Table S30 Lowest energy, highest intensity transitions calculated for the Cation 1 conformer of **[5-AF]$^+$** using different functionals

Figure S33 Orbital sequences calculated for the Cation 1 conformer of **[5-NF]$^+$** using different functionals

Table S31 Lowest energy, highest intensity transitions calculated for the Cation 1 conformer of **[5-NF]$^+$** using different functionals

Figure S34 Lowest energy geometries and orbital sequences calculated for the Anion B1 conformer of **[F]$^-$** and Cation 1 conformer of **[F]$^+$**

Table S32 Lowest energy, highest intensity transition calculated for the Anion B1 conformer of **[F]$^-$** and Cation 1 conformer of **[F]$^+$**

4.9.8 Calculated low frequency vibrational modes

Figure S35 Schematic depiction of low frequency vibrational modes calculated for various conformers of **[5-AF]$^-$**

Table S33 Low frequency vibrational modes calculated for various conformers of **[5-AF]$^-$**

Figure S36 Schematic depiction of low frequency vibrational modes calculated for various conformers of **[5-NF]$^-$**

Table S34 Low frequency vibrational modes calculated for various conformers of **[5-NF]$^-$**

4.9.9 References

4.9.1 Experimental procedures

[5-NF]⁻/[5-AF]⁻ and **[5-NF]⁺/[5-AF]⁺** were generated in both experimental setups (PF/tPF and IRMPD) by ESI from methanolic solutions of the respective neutrals (c=5·10⁻⁶ M) in negative and positive ion mode. For the study of the protonated forms, a small amount of formic acid (1 vol-%) was added to the sample solutions in order to increase the cation signal. The sample solutions were continuously infused by a syringe pump at a flow rate of 120 µL/h. Nitrogen as drying gas was set to a flow rate of 4 L/min at 180°C. The nebulizer pressure was set to 5 psi (345 mbar).

The femtosecond laser pulses were generated in a cryogenic ultrafast regenerative laser amplifier system delivering 50 fs pulses at ~1 kHz repetition rate (central wavelength of ca. 785 nm). The pulse train was split to pump two optical parametric oscillators of white light continuum (TOPAS-C, Light Conversion) for generating pump and probe pulses of tunable wavelength (240–2500 nm). For PF spectra only the output from one of the TOPAS-C units was utilized in a spectral range of 240 nm up to 580 nm. The PF spectra were obtained by setting the laser pulses to the according wavelengths and measuring the intensity of the parent ion and the sum of fragment ions. The fragment yield was calculated according to $F_i/(F_i+P_i)$, where F_i and P_i are the sums of the intensities of the fragment and parent ion signals, respectively, and normalized additionally by its numeric wavelength value to account for different photon energies at constant laser pulse fluence, with a typical pulse energy of ~1 µJ. For **[5-NF]⁻/[5-AF]⁻** each isolated portion of ions was irradiated by 50 laser pulses, whereas for **[5-NF]⁺/[5-AF]⁺** 150 pulses were utilized to account for a drastically reduced fragmentation yield.

For transient experiments the temporal delay between pump (510 nm, 0.3 µJ; 410 nm, 0.8 µJ) and probe pulses (1200 nm, 150 µJ) was introduced via an optical delay line. Pump and probe pulses were spatially overlapped quasi-collinearly by focusing into the center of the Paul ion trap with a lens (*f*=50 cm). The beam diameter in the ion trap was estimated to be ~1 mm using the knife-edge technique. The relative polarization of pump and probe pulses was controlled by a Berek polarization compensator in the pump path and set to the magic angle (54.7°). The initial ~1 kHz repetition rate of the laser pulses was reduced to ~330 Hz by an optical chopper. Each isolated portion of ions was irradiated by 50 pump/probe pulse pairs.

The tPF signals were recorded as extracted ion chromatograms while continuously varying the delay between the pump and probe pulses. Evaluation of the transient signals was performed as $F_i/(F_i+P_i)$, where F_i and P_i are the sums of the intensities of fragment and parent ion signals, respectively.

To evaluate the temporal resolution at a given pump/probe wavelength combination, we recorded the multiple-photon ionization signal of neutral furan in the ion trap as a function of time delay between the pump and probe pulses. The obtained signal represents an intensity cross correlation function (ccf) of the pump and probe laser pulses. The instrumental system response was then estimated from the fwhm of the resulting Gaussian-shaped photoionization signal. A typical value for the fwhm of the ccf at 510 nm (pump)/1200 nm (probe) [410 nm/1200 nm] was estimated to be ~120 fs [~130 fs]

In IRMPD experiments, the wavelength in a spectral range of 2800-3760 cm^{-1} was continuously scanned irradiating each trapped ion cloud by 2-4 laser pulses. Ion chromatograms were extracted from the mass spectra with the Bruker chromatogram software and used to calculate the IR spectra according to $F_i/(F_i+P_i)$, where F_i and P_i are the sums of the intensities of fragment and parent ion signals, respectively. For smoothing the spectra, five points averaging between adjacent data points was performed within the Origin Plot Software. A wave meter (821N-NIR, Bristol instruments) was used for IR frequency calibration.

4.9.2 Structural parameters from DFT optimized geometries
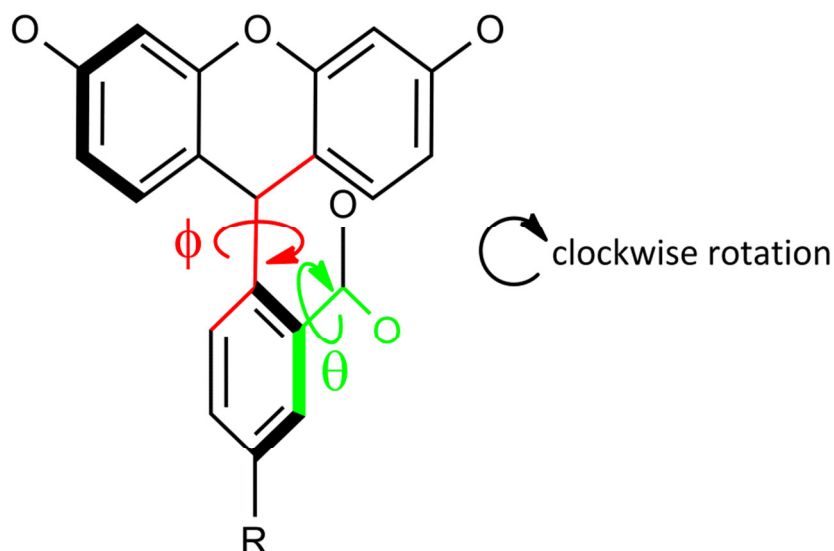
Figure S1 Schematic structure of functionalized fluorescein derivatives **[5-RF]** (R=NH$_2$, NO$_2$). The dihedral angle φ denotes the mutual orientation between the two planes that contain either the xanthene or the phenyl moieties, whereas θ denotes the orientation of the carboxylic acid group within the plane of the phenyl ring.

Table S1 Relative changes in dihedral angles $\Delta\varphi$ and $\Delta\theta$ upon geometry optimization of anions **(a)** and cations **(b)** at the DFT (ωB97XD/6-31+G(d)) level of theory, starting from θ=90° and φ=0°. Positive values of $\Delta\varphi$ and $\Delta\theta$ denote clockwise rotation around the respective C-C bond (*cf.* Figure S1), whereas negative values denote counter-clockwise rotation. Lactonic structures (Anion X') were disregarded, as the dihedral angle φ is not comparable to the angle in the non-lactone structures.

a)		Anion B1	Anion B2	Anion B3	Anion X
[5-AF]$^-$	$\Delta\varphi$ / °	-2.4	14.2	17.0	30.1
	$\Delta\theta$ / °	19.6	19.2	29.7	4.8
[5-NF]$^-$	$\Delta\varphi$ / °	3.2	-10.1	-14.4	17.7
	$\Delta\theta$ / °	-21.3	-19.8	-32.6	2.3

b)		Cation 1	Cation 2	Cation 3	Cation 4
[5-AF]$^+$	$\Delta\varphi$ / °	3.9	-20.8	-14.0	-27.4
	$\Delta\theta$ / °	1.3	-25.2	-30.8	-54.2
[5-NF]$^+$	$\Delta\varphi$ / °	3.0	-1.3	10.6	-19.1
	$\Delta\theta$ / °	0.5	-5.2	21.7	-59.4

4.9.3 Mass spectrometric data
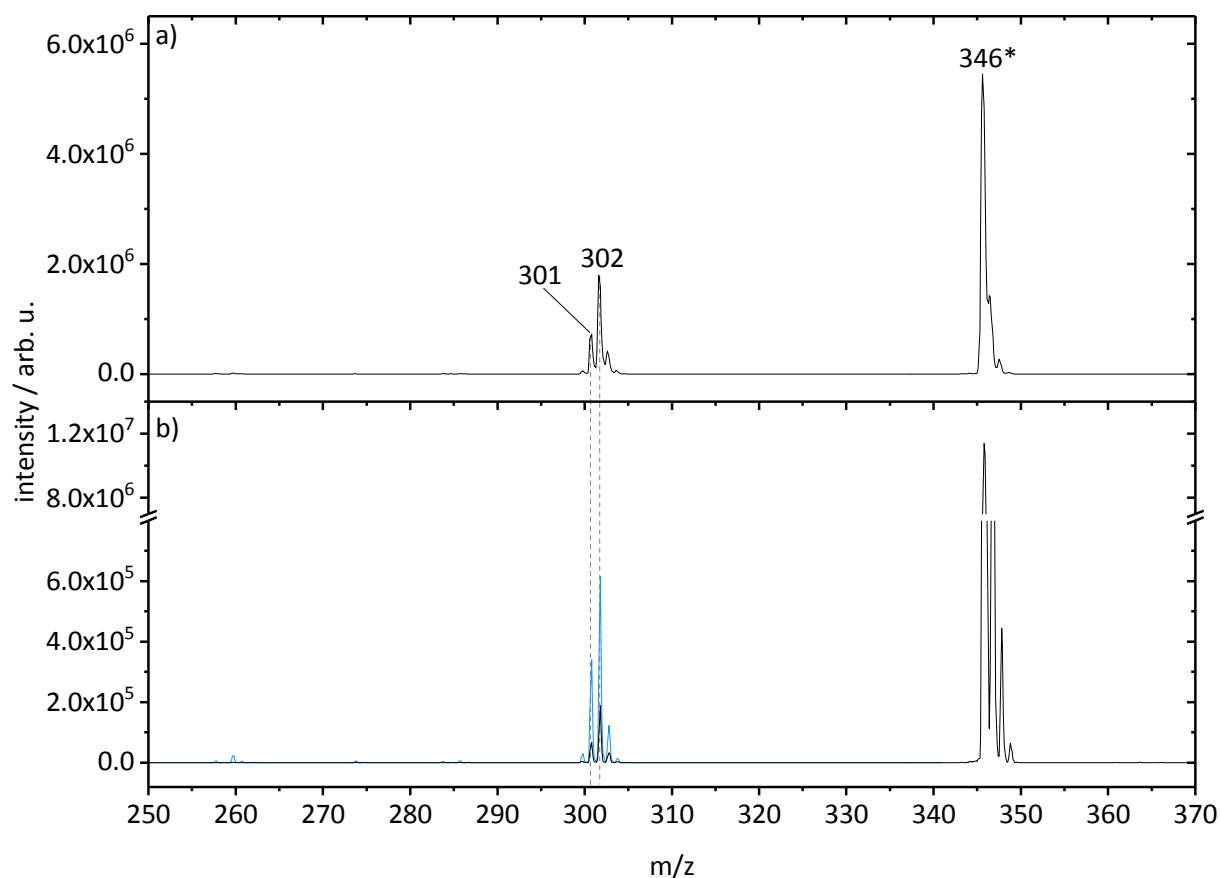
Figure S2 Mass spectrum depicting the formation of fragment ions by IRMPD **(a)**, by one-color (510 nm, 1µJ, black) and pump-probe (λ_{pump}=510 nm, 0.3 µJ; λ_{probe}=1200 nm, 120 µJ; blue) PF **(b)** of [5-AF]$^-$. Asterisk denotes parent ion signal.

Table S2 Overview over identified ion signals from CID/PF fragment mass spectra of **[5-AF]$^-$** shown in Figure S2. Numeric values denote the most abundant signal of the respective isotope pattern. Satellite signals were neglected, unless they contribute significantly to the observed isotope pattern.

m/z	mass loss / Da	assigned neutral loss
346*	-	-
302	44	$-CO_2$
301	45	$-HCO_2$

*parent ion: [5-AF]$^-$
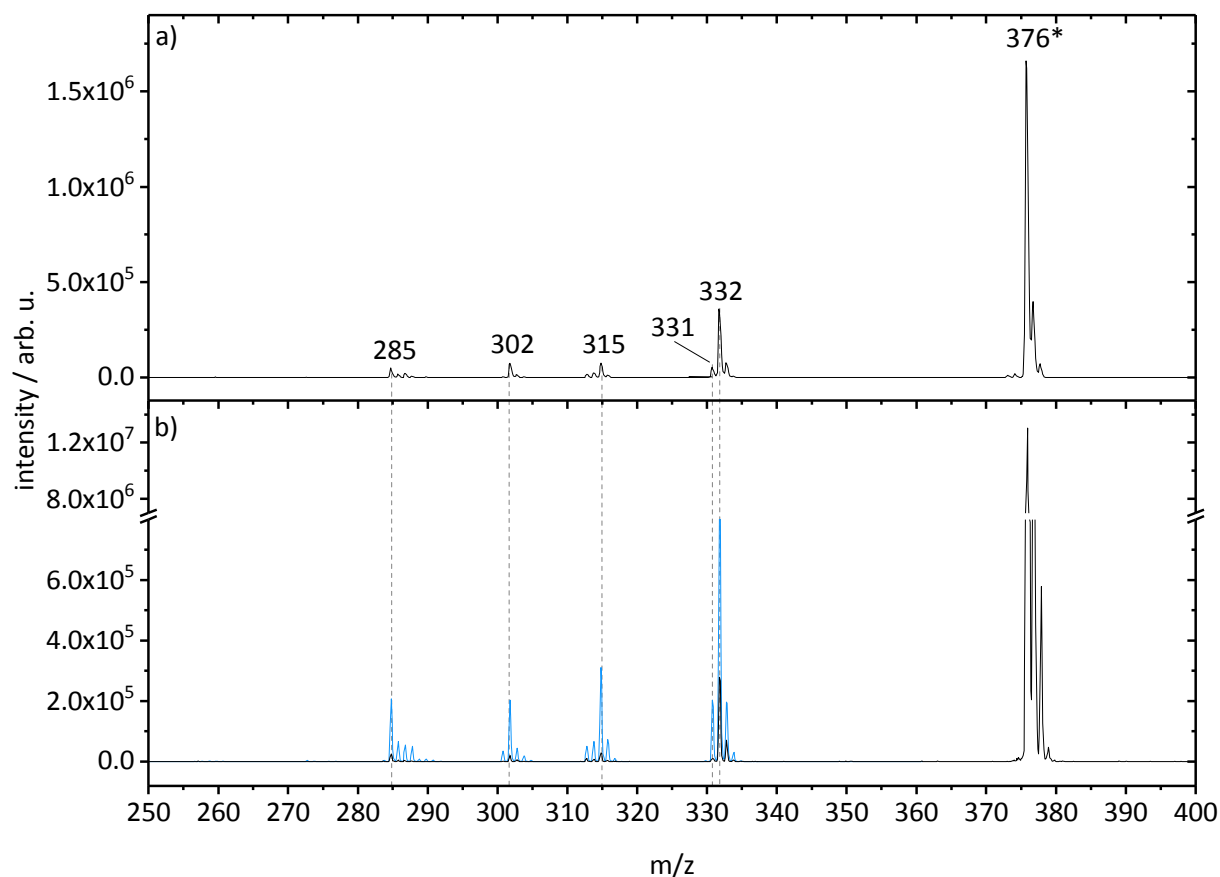
Figure S3 Mass spectrum depicting the formation of fragment ions by IRMPD **(a)** and by one-color (510 nm, 1μJ, black) and pump-probe (λ_{pump}=510 nm, 0.3 μJ; λ_{probe}=1200 nm, 120 μJ; blue) PF **(b)** of **[5-NF]**⁻. Asterisk denotes parent ion signal.

Table S3 Overview over identified ion signals from CID/PF fragment mass spectra of **[5-NF]**⁻ shown in Figure S3. Numeric values denote the most abundant signal of the respective isotope pattern. Satellite signals were neglected, unless they contribute significantly to the observed isotope pattern.

m/z	mass loss / Da	assigned neutral loss
376*	-	-
332	44	$-CO_2$
331	45	$-HCO_2$
315	61	$-CO_2,-OH$
302	74	$-CO,-NO_2/-C_2H_2,-H_2CO_2$
285	91	$-HCO_2,-NO_2$

*parent ion: [5-NF]⁻
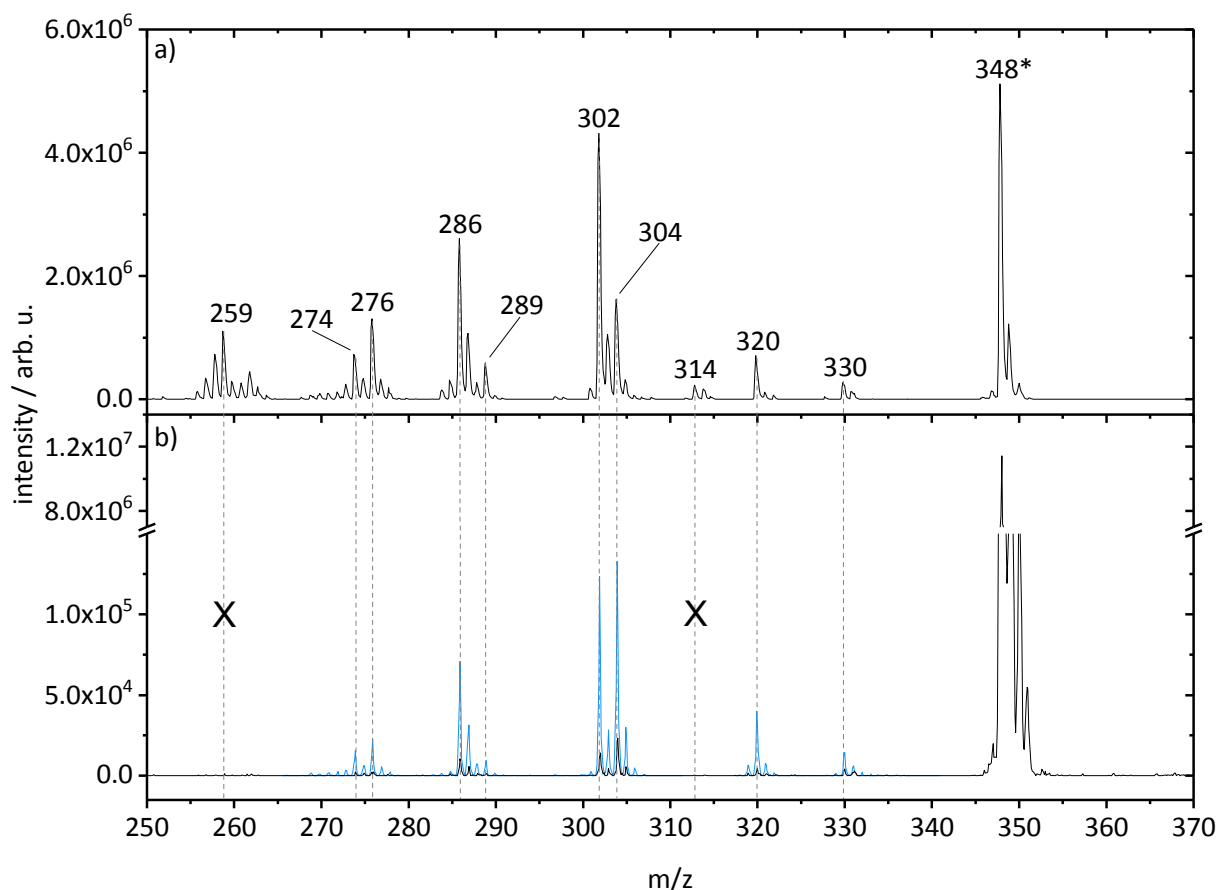
Figure S4 Mass spectrum depicting the formation of fragment ions by IRMPD **(a)** and by one-color (410 nm, 1μJ, black) and pump-probe (λ_{pump}=410 nm, 0.8 μJ; λ_{probe}=1200 nm, 120 μJ; blue) PF **(b)** of **[5-AF]⁺**. Asterisk denotes parent ion signal.

Table S4 Overview over identified ion signals from CID/PF fragment mass spectra of **[5-AF]⁺** shown in Figure S4. Numeric values denote the most abundant signal of the respective isotope pattern. Satellite signals were neglected, unless they contribute significantly to the observed isotope pattern.

| m/z	mass loss / Da	assigned neutral loss
348*	-	-
330	18	$-H_2O$
320	28	$-CO$
314	34	$-H_2O,-NH_2$
304	44	$-CO_2$
302	46	$-H_2CO_2$
289	59	$-HCO,$
286	62	$-H_2CO_2,-NH_2$
276	74	$-CO,-CO_2$
274	76	$-CO,-H_2CO_2$
256	92	$-CO,-CO_2,-H_2O$

*parent ion: [5-AF]⁺
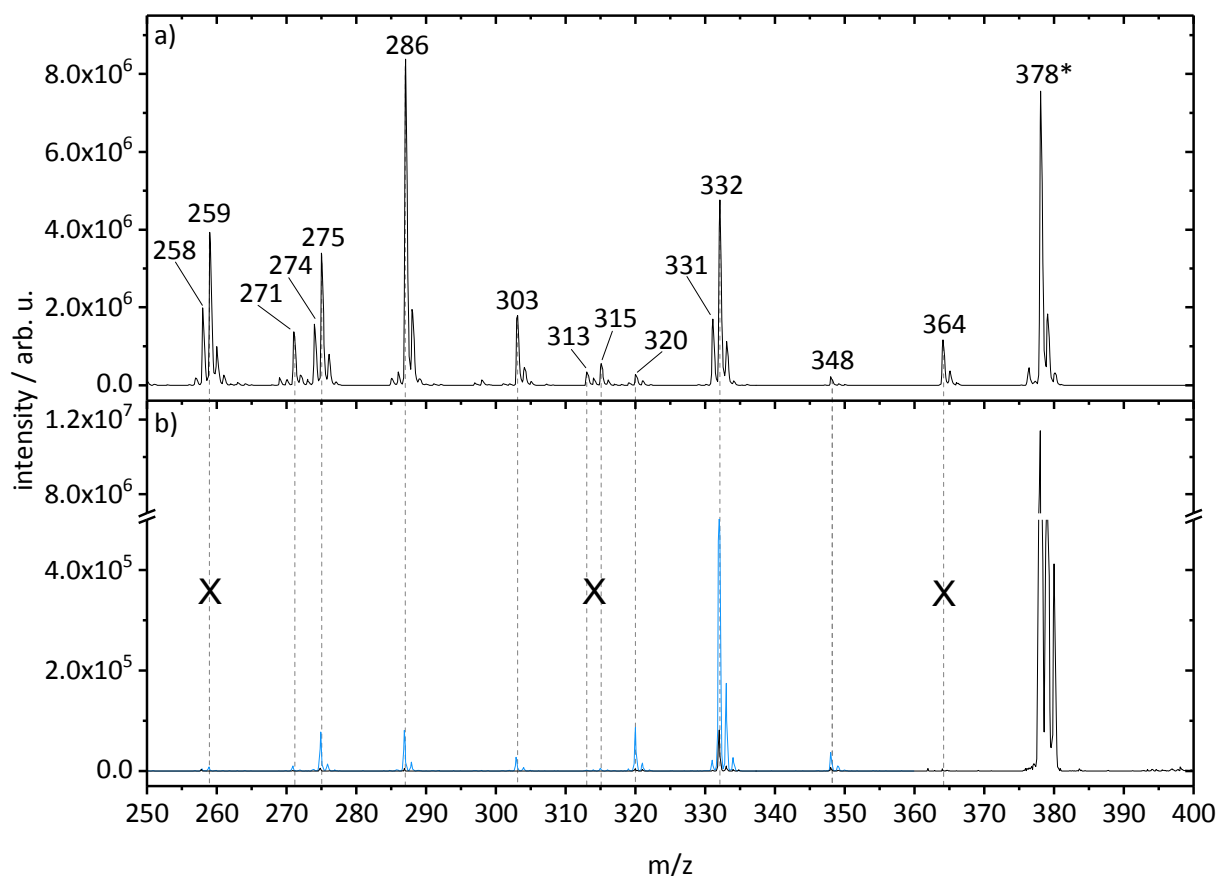
Figure S5 Mass spectrum depicting the formation of fragment ions by IRMPD **(a)** and by one-color (410 nm, 1μJ, black) and pump-probe (λ_{pump}=410 nm, 0.8 μJ; λ_{probe}=1200 nm, 120 μJ; blue) PF **(b)** of **[5-NF]⁺**. Asterisk denotes parent ion signal.

Table S5 Overview over identified ion signals from CID/PF fragment mass spectra of **[5-NF]⁺** shown in Figure S5. Numeric values denote the most abundant signal of the respective isotope pattern. Satellite signals were neglected, unless they contribute significantly to the observed isotope pattern.

ion mass / m/z	mass loss / Da	assigned neutral loss
378*	-	-
364	14	not assigned
348	-30	-NO
332	46	$-H_2CO_2$/$-NO_2$
331	47	$-NO,-OH$
320	58	$-H_2CO,-CO$
314	64	$-H_2CO_2,-H_2O$
303	75	$-HCO,-CO,-H_2O$
286	92	$-H_2CO_2,-NO_2$
275	103	$-HCO_2,-NO_2,-H_2O$
274	104	$-H_2CO_2,-NO_2-H_2O$
271	107	not assigned
259	119	not assigned
258	120	not assigned

*parent ion: [5-NF]⁺

4.9.4 DFT calculated IR frequencies

Table S6 Frequencies and intensities of IR vibrational modes calculated (DFT/ωB97XD/6-31+G(d)) for the five considered conformers of **[5-AF]$^-$**. A scaling factor of 0.95 was employed.

conformer	unscaled energy / cm^{-1}	scaled energy / cm^{-1}	IR intensity / km·mol^{-1}	mode
Anion B1	3696	3511	13	N-H$_2$ asym.
	3648	3466	506	COO-H
	3596	3416	15	N-H$_2$ sym.
Anion B2	3784	3595	82	COO-H
	3697	3512	13	N-H$_2$ sym.
	3596	3416	14	N-H$_2$ asym.
Anion B3	3777	3588	80	COO-H
	3695	3510	12	N-H$_2$ asym.
	3594	3414	13	N-H$_2$ sym.
Anion X	3842	3650	81	O-H
	3687	3503	9	N-H$_2$ asym.
	3588	3409	6	N-H$_2$ sym.
Anion X'	3846	3654	56	O-H
	3687	3503	11	N-H$_2$ asym.
	3589	3410	9	N-H$_2$ sym.

Table S7 Frequencies and intensities of IR vibrational modes calculated (DFT/ωB97XD/6-31+G(d)) for the five considered conformers of **[5-NF]$^-$**. A scaling factor of 0.95 was employed.

conformer	unscaled energy / cm^{-1}	scaled energy / cm^{-1}	IR intensity / km·mol^{-1}	mode
Anion B1	3636	3454	518	COO-H
Anion B2	3786	3597	92	COO-H
Anion B3	3777	3588	94	COO-H
Anion X	3841	3649	89	O-H
Anion X'	3844	3652	62	O-H

Table S8 Frequencies and intensities of IR vibrational modes calculated (DFT/ωB97XD/6-31+G(d)) for the four considered conformers of **[5-AF]⁺**. A scaling factor of 0.95 was employed.

conformer	unscaled energy / cm⁻¹	scaled energy / cm⁻¹	IR intensity / km·mol⁻¹	mode
Cation 1	3819	3628	28	2xO-H sym.
	3818	3627	430	2xO-H asym.
	3765	3577	144	COO-H
	3747	3560	38	N-H$_2$ asym.
	3637	3455	103	N-H$_2$ sym.
Cation 2	3817	3626	87	2xO-H sym.
	3815	3624	380	2xO-H asym.
	3763	3575	43	N-H$_2$ asym.
	3762	3574	144	COO-H
	3648	3466	162	N-H$_2$ sym.
Cation 3	3818	3627	163	2xO-H sym.
	3816	3625	300	2xO-H asym.
	3813	3622	56	COO-H
	3748	3561	40	N-H$_2$ asym.
	3638	3456	120	N-H$_2$ sym.
Cation 4	3814	3623	163	2xO-H sym.
	3812	3621	328	2xO-H asym.
	3809	3619	29	COO-H
	3763	3575	48	N-H$_2$ asym.
	3648	3466	189	N-H$_2$ sym.

Table S9 Frequencies and intensities of IR vibrational modes calculated (DFT/ωB97XD/6-31+G(d)) for the four considered conformers of **[5-NF]⁺**. A scaling factor of 0.95 was employed.

conformer	unscaled energy / cm⁻¹	scaled energy / cm⁻¹	IR intensity / km·mol⁻¹	mode
Cation 1	3816	3625	1	2xO-H sym
	3815	3624	500	2xO-H asym
	3761	3573	164	COO-H
Cation 2	3814	3623	40	2xO-H sym
	3813	3622	483	2xO-H asym
	3764	3576	133	COO-H
Cation 3	3822	3631	68	COO-H
	3816	3625	82	2xO-H sym
	3815	3625	423	2xO-H asym
Cation 4	3810	3620	212	2xO-H sym
	3810	3620	18	COO-H
	3807	3617	353	2xO-H asym

4.9.5   Photofragmentation
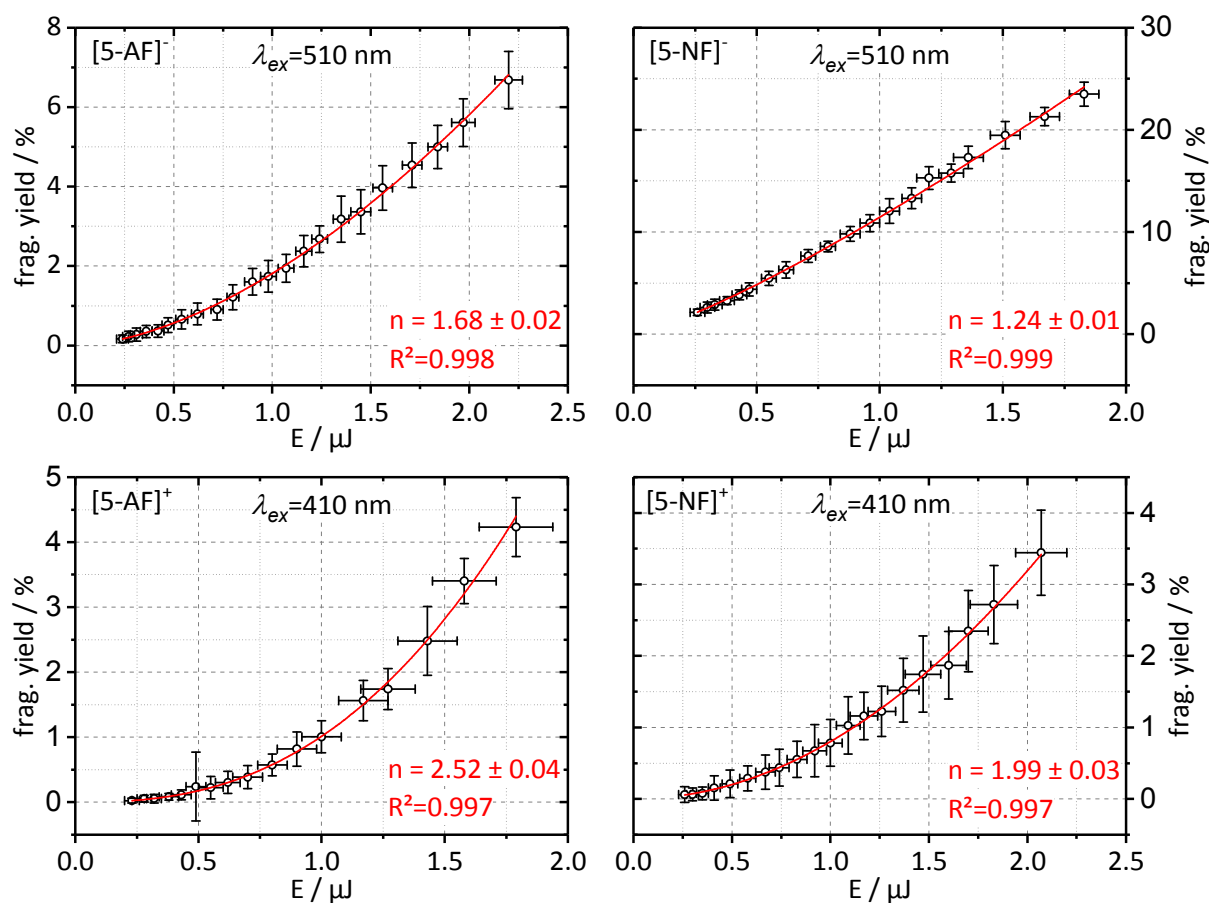
Figure S6 Pulse energy E dependent total fragmentation yield Y of **[5-AF]⁻** (top, left), **[5-NF]⁻** (top, right), **[5-AF]⁺** (bottom, left) and **[5-NF]⁺** (bottom, right) by one-color photoexcitation. Dependencies were evaluated according to $Y = A \cdot E^{n}$,[1] where n is a mean value for the number of photons absorbed to induce fragmentation and A a dimensionless fit-parameter.
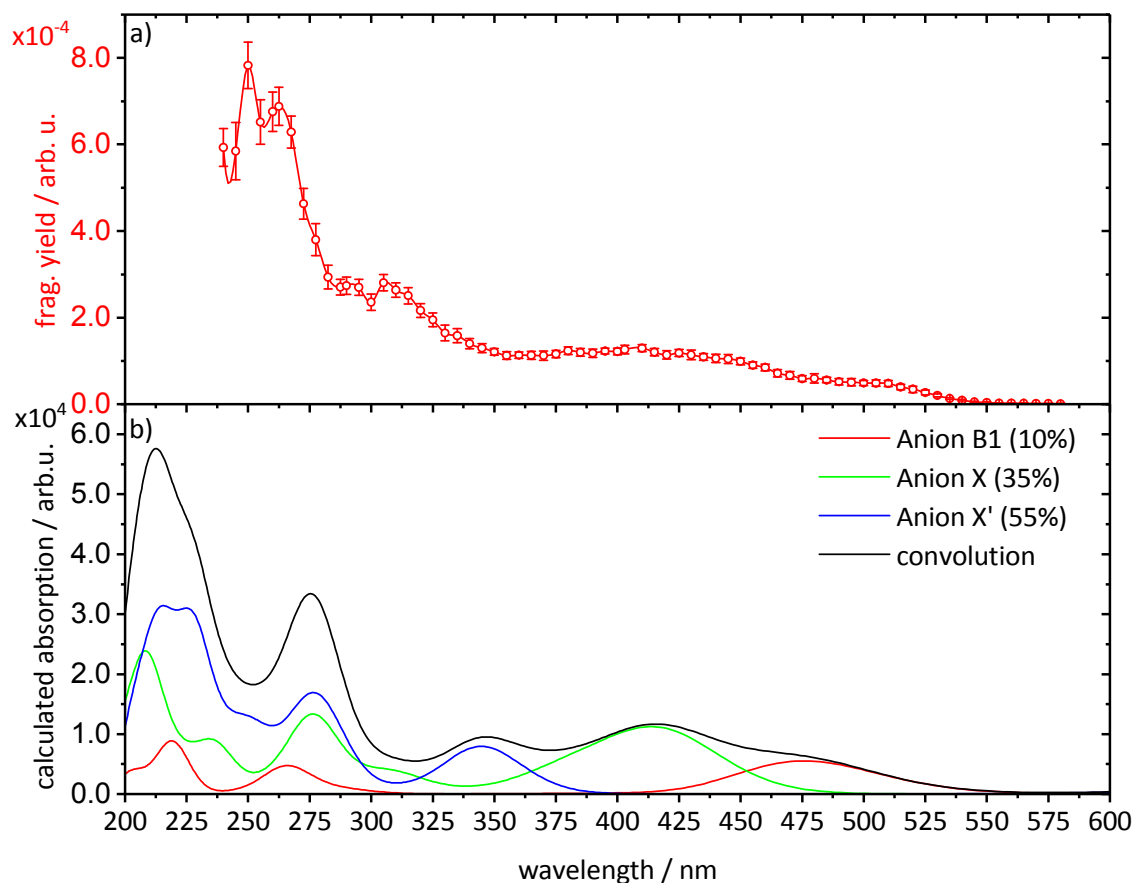
Figure S7 Comparison of the experimental PF spectrum of **[5-NF]⁻ (a)** and a theoretical absorption spectrum **(b**, black**)** obtained by convoluting the TD-DFT calculated linear absorption spectra of three conformers of **[5-NF]⁻**. Note that the weights of individual contributions (in color) to the convoluted spectrum were obtained manually so that the sum amounts to 100%. The weights do not represent the actual contributions to the ion population and are given merely for the sake of completeness.

4.9.6 TD-DFT calculated electronic transitions

Table S10 Vertical singlet transitions of **[5-AF]$^-$** (Anion B1) calculated at the ground state geometry (TD-DFT/ωB97XD/6-31+G(d)). Calculated central wavelengths λ are given together with corresponding values λ_S obtained after bathochromically shifting the transition energies by 3000 cm^{-1}. Only transitions with an oscillator strength of f>0.1 are displayed. Contributions to electronic transitions with a weight of <10 % were omitted.

state	transition	weight / %	λ / nm	λ_S / nm	f
S$_1$	HOMO→LUMO	96	419	479	0.76
S$_{13}$	HOMO-4→LUMO	71	242	261	0.12
S$_{16}$	HOMO-5→LUMO	74	238	256	0.35
S$_{29}$	HOMO-1→LUMO+3	27	209	223	0.28
S$_{30}$	HOMO-1→LUMO+3	11	209	223	0.37
S$_{32}$	HOMO-1→LUMO+3	43	204	217	0.26
S$_{33}$	HOMO-8→LUMO+1	10	202	215	0.60
	HOMO-7→LUMO+1	26			
	HOMO-6→LUMO+1	14			
	HOMO-4→LUMO+3	21			
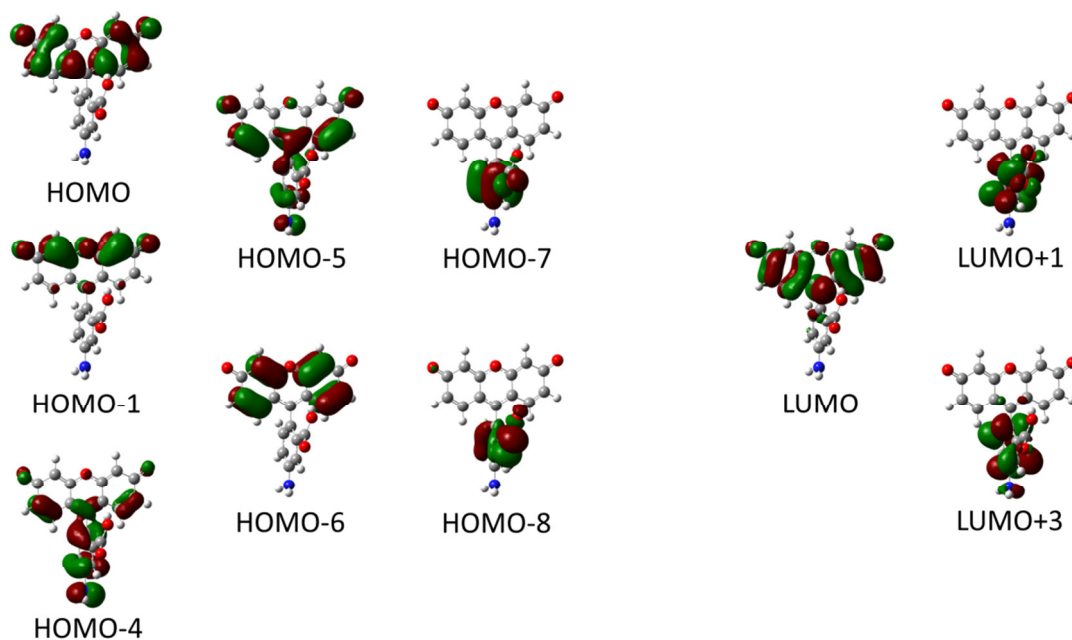
Figure S8 Molecular orbital isosurfaces of **[5-AF]$^-$** (Anion B1) with contributions to the electronic configurations, characterizing the electronic transitions listed in Table S10.

Table S11 Vertical singlet transitions of **[5-AF]⁻** (Anion B2) calculated at the ground state geometry (TD-DFT/ωB97XD/6-31+G(d)). Calculated central wavelengths λ are given together with corresponding values $λ_S$ obtained after bathochromically shifting the transition energies by 3000 cm⁻¹. Only transitions with an oscillator strength of f>0.1 are displayed. Contributions to electronic transitions with a weight of <10 % were omitted.

| state	transition	weight / %	λ / nm	$λ_S$ / nm	f
S_1	HOMO→LUMO	64	426	488	0.52
	HOMO→LUMO+1	33			
S_2	HOMO→LUMO	34	402	457	0.25
	HOMO→LUMO+1	63			
S_{14}	HOMO-5→LUMO	13	248	268	0.17
	HOMO-4→LUMO	50			
S_{17}	HOMO-5→LUMO	14	240	259	0.20
	HOMO-4→LUMO	13			
	HOMO-4→LUMO+1	45			
S_{30}	HOMO-1→LUMO+3	61	215	230	0.15
	HOMO-1→LUMO+1	17			
S_{35}	HOMO-1→LUMO+10	17	206	220	0.36
S_{36}	HOMO-1→LUMO+10	21	205	218	0.42
S_{38}	HOMO-7→LUMO	19	204	217	0.15
	HOMO-4→LUMO+3	33			
S_{42}	HOMO-5→LUMO+3	28	200	213	0.20
	HOMO-4→LUMO+3	22			
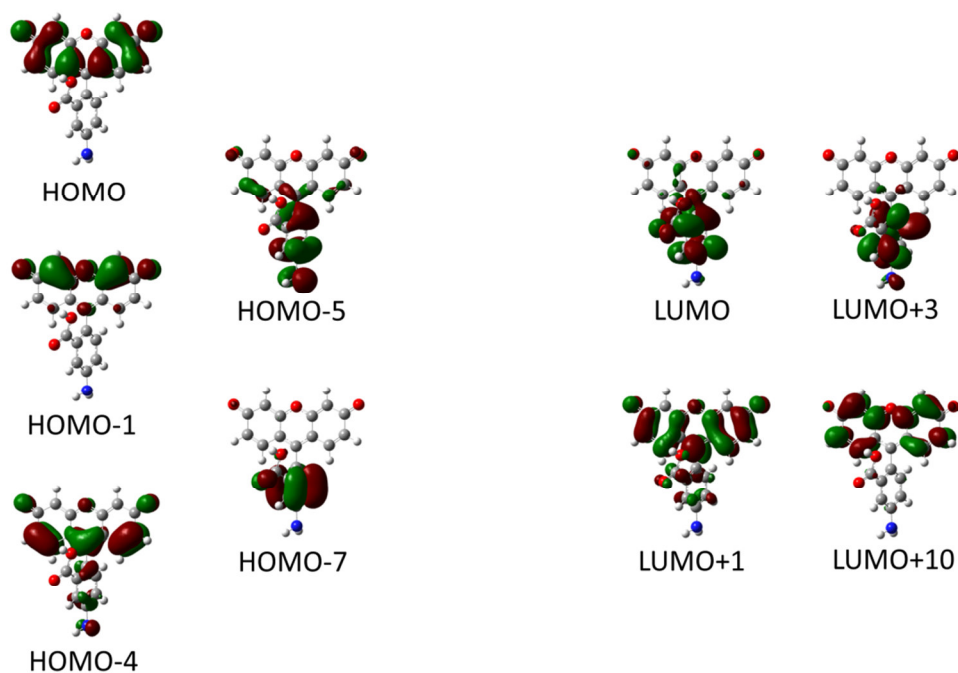
Figure S9 Molecular orbital isosurfaces of **[5-AF]⁻** (Anion B2) with contributions to the electronic configurations, characterizing the electronic transitions listed in Table S11.

Table S12 Vertical singlet transitions of **[5-AF]⁻** (Anion B3) calculated at the ground state geometry (TD-DFT/ωB97XD/6-31+G(d)). Calculated central wavelengths λ are given together with corresponding values λ_S obtained after bathochromically shifting the transition energies by 3000 cm^{-1}. Only transitions with an oscillator strength of $f>0.1$ are displayed. Contributions to electronic transitions with a weight of <10 % were omitted.

| state	transition	weight / %	λ / nm	λ_S / nm	f
S_1	HOMO→LUMO	83	433	498	0.35
	HOMO→LUMO+1	13			
S_2	HOMO→LUMO	14	408	465	0.41
	HOMO→LUMO+1	63			
S_{15}	HOMO-6→LUMO	11	246	266	0.11
	HOMO-6→LUMO+1	35			
	HOMO-4→LUMO+1	15			
S_{16}	HOMO-4→LUMO+1	40	244	263	0.28
	HOMO-4→LUMO	13			
	HOMO-4→LUMO+1	45			
S_{36}	HOMO-1→LUMO+3	26	207	221	0.57
S_{38}	HOMO-4→LUMO+3	42	205	218	0.11
S_{39}	HOMO-1→LUMO+3	15	205	218	0.14
S_{43}	HOMO-5→LUMO+3	10	201	214	0.13
S_{44}	HOMO-7→LUMO	13	200	213	0.15
	HOMO-5→LUMO+3	14			
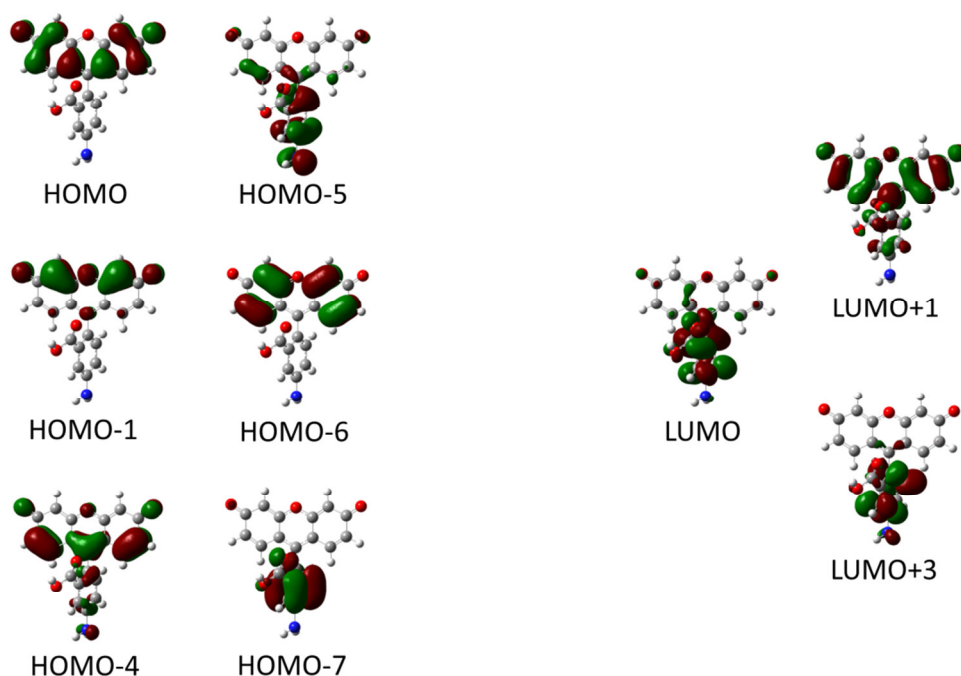
Figure S10 Molecular orbital isosurfaces of **[5-AF]⁻** (Anion B3) with contributions to the electronic configurations, characterizing the electronic transitions listed in Table S12.

Table S13 Vertical singlet transitions of **[5-AF]**⁻ (Anion X) calculated at the ground state geometry (TD-DFT/ωB97XD/6-31+G(d)). Calculated central wavelengths λ are given together with corresponding values λ_S obtained after bathochromically shifting the transition energies by 3000 cm^{-1}. Only transitions with an oscillator strength of f>0.1 are displayed. Contributions to electronic transitions with a weight of <10 % were omitted.

| state	transition	weight / %	λ / nm	λ_S / nm	f
S_1	HOMO→LUMO	91	426	488	0.42
S_2	HOMO-2→LUMO	47	341	380	0.18
	HOMO-1→LUMO	42			
S_{17}	HOMO-2→LUMO+3	13	232	249	0.10
	HOMO-2→LUMO+6	12			
S_{20}	HOMO-8→LUMO	27	225	241	0.15
	HOMO-4→LUMO+6	10			
	HOMO-3→LUMO+6	10			
S_{21}	HOMO-9→LUMO	17	223	239	0.12
	HOMO →LUMO+12	16			
S_{30}	HOMO-3→LUMO+3	13	210	224	0.11
S_{38}	HOMO-6→LUMO+3	32	200	213	0.51
	HOMO-6→LUMO+4	13			
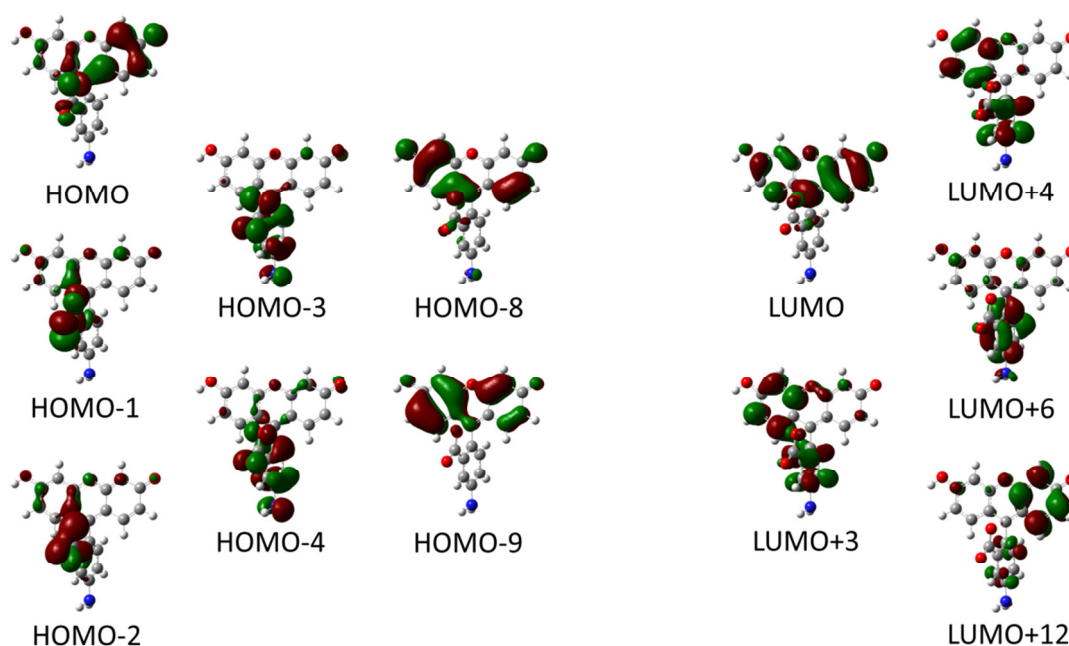
Figure S11 Molecular orbital isosurfaces of **[5-AF]**⁻ (Anion X) with contributions to the electronic configurations, characterizing the electronic transitions listed in Table S13.

Table S14 Vertical singlet transitions of **[5-AF]⁻** (Anion X') calculated at the ground state geometry (TD-DFT/ωB97XD/6-31+G(d)). Calculated central wavelengths λ are given together with corresponding values λ_S obtained after bathochromically shifting the transition energies by 3000 cm⁻¹. Only transitions with an oscillator strength of *f*>0.1 are displayed. Contributions to electronic transitions with a weight of <10 % were omitted.

| state	transition	weight / %	λ / nm	λ_S / nm	*f*
S₂	HOMO→LUMO+3 HOMO→LUMO+4	56 20	313	345	0.13
S₁₇	HOMO→LUMO+3	13	238	256	0.17
S₂₁	HOMO-2→LUMO+4 HOMO-2→LUMO+7	21 33	230	247	0.23
S₂₉	HOMO-4→LUMO HOMO-2→LUMO+4 HOMO-2→LUMO+7	30 12 20	216	231	0.21
S₃₂	HOMO-4→LUMO HOMO-2→LUMO+7	25 12	212	226	0.31
S₃₇	HOMO→LUMO+7	10	205	218	0.11
S₃₉	HOMO-1→LUMO+4	11	204	217	0.17
S₄₄	HOMO-7→LUMO HOMO-5→LUMO	10 21	201	214	0.16

Figure S12 Molecular orbital isosurfaces of **[5-AF]⁻** (Anion X') with contributions to the electronic configurations, characterizing the electronic transitions listed in Table S14.

Table S15 Vertical singlet transitions of **[5-NF]**⁻ (Anion B1) calculated at the ground state geometry (TD-DFT/ωB97XD/6-31+G(d)). Calculated central wavelengths λ are given together with corresponding values λ_S obtained after bathochromically shifting the transition energies by 3000 cm⁻¹. Only transitions with an oscillator strength of $f > 0.1$ are displayed. Contributions to electronic transitions with a weight of <10 % were omitted.

state	transition	weight / %	λ / nm	λ_S / nm	f
S$_2$	HOMO→LUMO+1	92	421	482	0.76
S$_{18}$	HOMO-7→LUMO	45	249	269	0.36
	HOMO-6→LUMO+2	15			
S$_{21}$	HOMO-8→LUMO	11	246	266	0.24
	HOMO-8→LUMO+2	17			
	HOMO-7→LUMO	16			
	HOMO-6→LUMO+2	21			
S$_{34}$	HOMO-1→LUMO+7	21	209	223	0.23
S$_{35}$	HOMO→LUMO+7	16	208	222	0.17
S$_{37}$	HOMO-1→LUMO+7	26	207	221	0.51
S$_{38}$	HOMO-8→LUMO+2	34	203	216	0.33
	HOMO-6→LUMO+2	19			
	HOMO-5→LUMO+2	27			

HOMO   HOMO-6

HOMO-1   HOMO-7

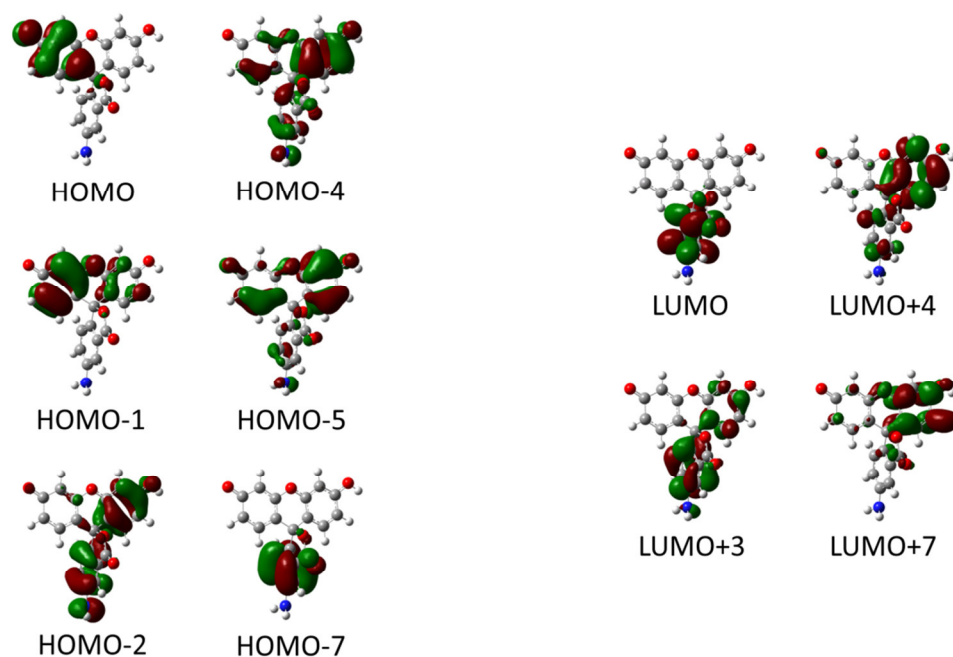HOMO-5   HOMO-8

LUMO   LUMO+2

LUMO+1   LUMO+7
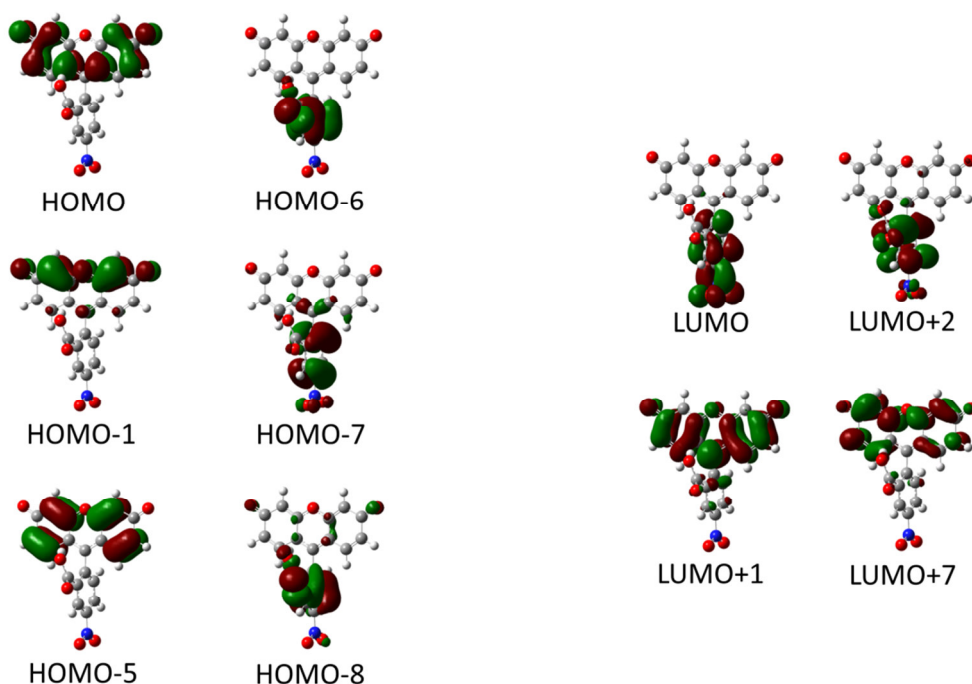
Figure S13 Molecular orbital isosurfaces of **[5-NF]**⁻ (Anion B1) with contributions to the electronic configurations, characterizing the electronic transitions listed in Table S15.

Table S16 Vertical singlet transitions of **[5-NF]⁻** (Anion B2) calculated at the ground state geometry (TD-DFT/ωB97XD/6-31+G(d)). Calculated central wavelengths λ are given together with corresponding values λ_S obtained after bathochromically shifting the transition energies by 3000 cm^{-1}. Only transitions with an oscillator strength of $f > 0.1$ are displayed. Contributions to electronic transitions with a weight of <10 % were omitted.

| state	transition	weight / %	λ / nm	λ_S / nm	f
S$_2$	HOMO→LUMO+1	83	420	481	0.12
S$_3$	HOMO→LUMO+2	88	419	479	0.64
S$_{20}$	HOMO-7→LUMO HOMO-6→LUMO	32 26	250	270	0.40
S$_{39}$	HOMO-1→LUMO+3 HOMO→LUMO+14	35 11	209	223	0.19
S$_{41}$	HOMO-10→LUMO+3 HOMO-7→LUMO+1 HOMO-6→LUMO+1	29 24 11	206	220	0.12
S$_{42}$	HOMO-1→LUMO+3 HOMO-1→LUMO+14	18 37	205	218	0.58
S$_{45}$	HOMO-10→LUMO HOMO-10→LUMO+1	22 18	202	215	0.11

Figure S14 Molecular orbital isosurfaces of **[5-NF]⁻** (Anion B2) with contributions to the electronic configurations, characterizing the electronic transitions listed in Table S16.

Table S17 Vertical singlet transitions of **[5-NF]**⁻ (Anion B3) calculated at the ground state geometry (TD-DFT/ωB97XD/6-31+G(d)). Calculated central wavelengths λ are given together with corresponding values λ_S obtained after bathochromically shifting the transition energies by 3000 cm⁻¹. Only transitions with an oscillator strength of f>0.1 are displayed. Contributions to electronic transitions with a weight of <10 % were omitted.

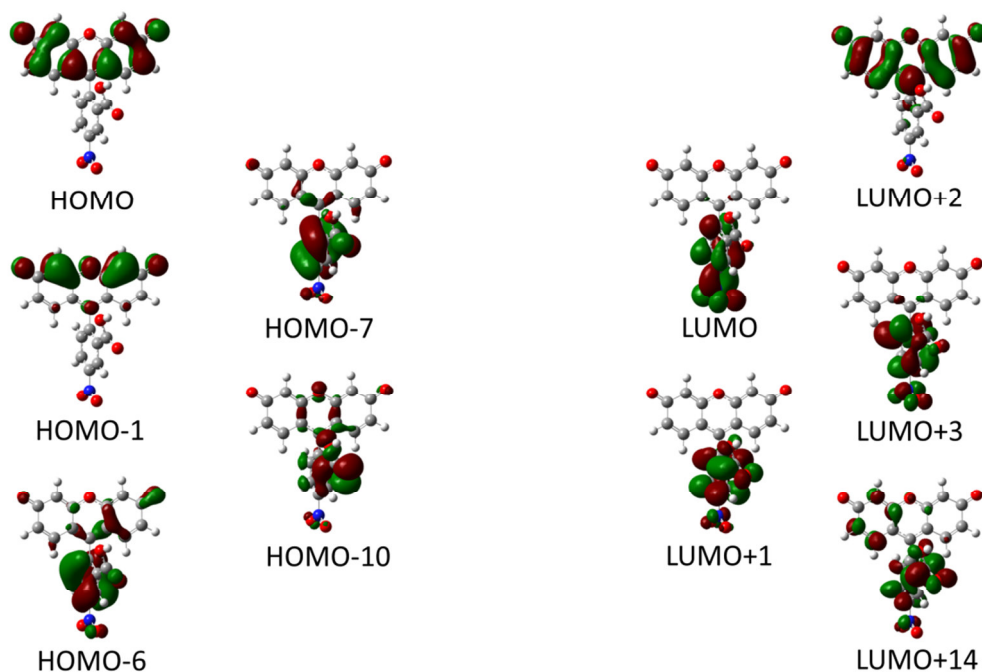| state	transition	weight / %	λ / nm	λ_S / nm	f
S₃	HOMO→LUMO+2	94	418	478	0.73
S₂₀	HOMO-6→LUMO	27	253	274	0.18
	HOMO-5→LUMO	12			
	HOMO-4→LUMO+1	12			
S₂₂	HOMO-6→LUMO	28	249	269	0.18
	HOMO-4→LUMO+1	29			
S₂₈	HOMO-4→LUMO+2	46	235	253	0.12
	HOMO-3→LUMO+1	10			
S₃₄	HOMO-5→LUMO+1	72	216	231	0.10
S₄₁	HOMO→LUMO+9	16	207	221	0.14
S₄₂	HOMO-9→LUMO	12	206	220	0.12
	HOMO-1→LUMO+9	35			
S₄₃	HOMO-9→LUMO	25	206	220	0.24
	HOMO-1→LUMO+9	14			
S₄₅	HOMO-10→LUMO+1	11	201	214	0.19
	HOMO-7→LUMO+1	22			
	HOMO-4→LUMO+3	18			
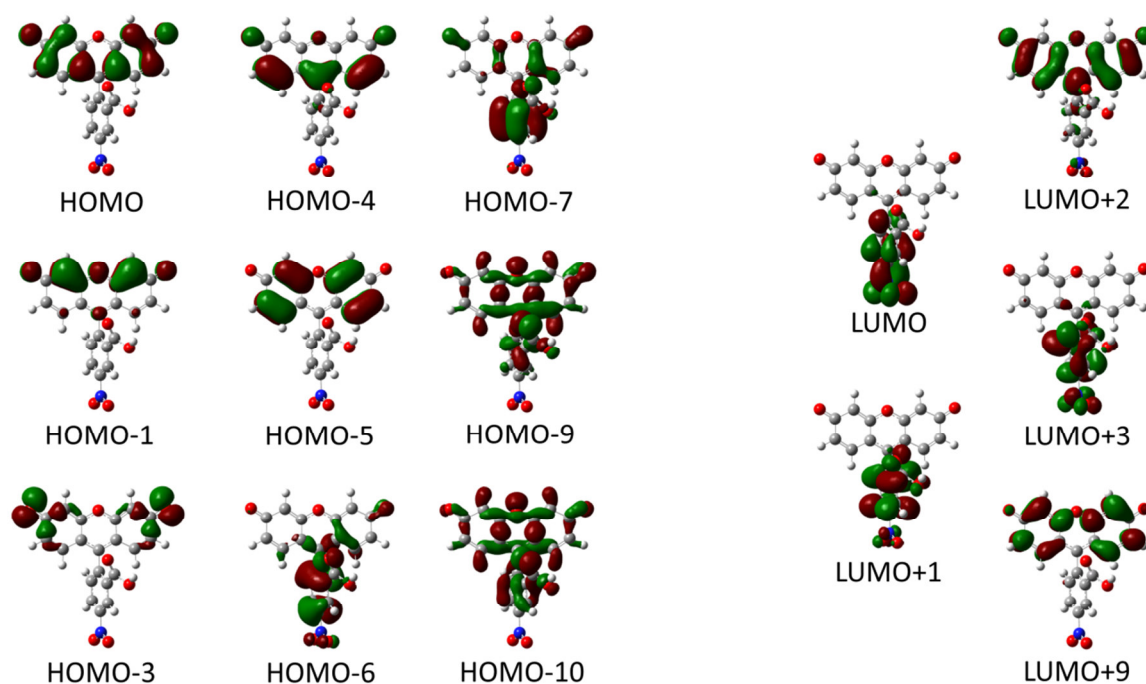
Figure S15 Molecular orbital isosurfaces of **[5-NF]**⁻ (Anion B3) with contributions to the electronic configurations, characterizing the electronic transitions listed in Table S17.

Table S18 Vertical singlet transitions of **[5-NF]⁻** (Anion X) calculated at the ground state geometry (TD-DFT/ωB97XD/6-31+G(d)). Calculated central wavelengths λ are given together with corresponding values λ_S obtained after bathochromically shifting the transition energies by 3000 cm^{-1}. Only transitions with an oscillator strength of f>0.1 are displayed. Contributions to electronic transitions with a weight of <10 % were omitted.

| state	transition	weight / %	λ / nm	λ_S / nm	f
S$_1$	HOMO→LUMO	34	376	424	0.39
	HOMO→LUMO+1	54			
S$_{16}$	HOMO-9→LUMO	35	258	280	0.45
	HOMO-7→LUMO	36			
	HOMO-6→LUMO	13			
S$_{25}$	HOMO-5→LUMO	15	222	238	0.13
S$_{35}$	HOMO-9→LUMO+2	10	206	220	0.10
	HOMO-6→LUMO+2	24			
S$_{41}$	HOMO-5→LUMO+2	12	200	213	0.12
	HOMO-5→LUMO+4	17			
	HOMO-2→LUMO+6	12			
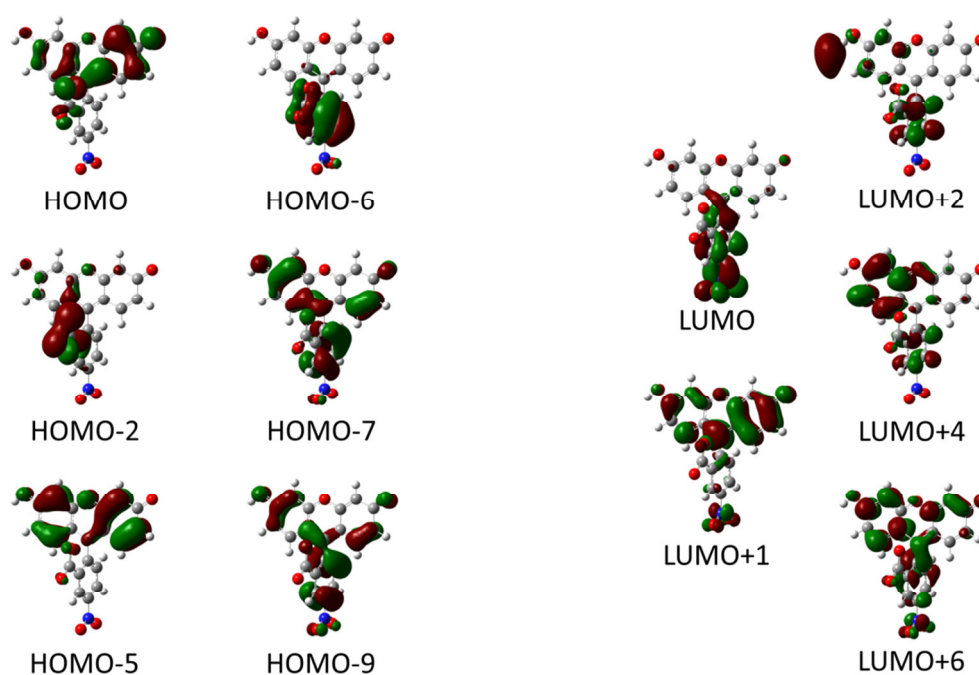
Figure S16 Molecular orbital isosurfaces of **[5-NF]⁻** (Anion X) with contributions to the electronic configurations, characterizing the electronic transitions listed in Table S18.

Table S19 Vertical singlet transitions of **[5-NF]⁻** (Anion X') calculated at the ground state geometry (TD-DFT/ωB97XD/6-31+G(d)). Calculated central wavelengths λ are given together with corresponding values λ_S obtained after bathochromically shifting the transition energies by 3000 cm⁻¹. Only transitions with an oscillator strength of f>0.1 are displayed. Contributions to electronic transitions with a weight of <10 % were omitted.

| state	transition	weight / %	λ / nm	λ_S / nm	f
S_5	HOMO→LUMO+3	78	315	348	0.19
S_{13}	HOMO-8→LUMO HOMO-3→LUMO	31 36	262	284	0.14
S_{17}	HOMO-3→LUMO+3 HOMO-2→LUMO+3	11 44	255	276	0.15
S_{23}	HOMO→LUMO+14 HOMO→LUMO+16	12 17	238	256	0.15
S_{34}	HOMO-3→LUMO+3 HOMO-3→LUMO+14	10 21	216	231	0.22
S_{36}	HOMO-4→LUMO+1 HOMO-3→LUMO+3 HOMO-2→LUMO+4	10 14 12	213	228	0.31
S_{43}	HOMO-7→LUMO+1 HOMO-4→LUMO+1 HOMO-4→LUMO+3	20 18 13	205	218	0.11
S_{46}	HOMO-8→LUMO+1 HOMO-7→LUMO+1	15 14	203	216	0.22
S_{52}	HOMO-8→LUMO+1	50	200	213	0.16

Figure S17 Molecular orbital isosurfaces of **[5-NF]⁻** (Anion X') with contributions to the electronic configurations, characterizing the electronic transitions listed in Table S19.

Table S20 Vertical singlet transitions of **[5-AF]⁺** (Cation 1) calculated at the ground state geometry (TD-DFT/ωB97XD/6-31+G(d)). Calculated central wavelengths λ are given together with corresponding values λ$_S$ obtained after bathochromically shifting the transition energies by 3000 cm^{-1}. Only transitions with an oscillator strength of $f>0.1$ are displayed. Contributions to electronic transitions with a weight of <10 % were omitted.

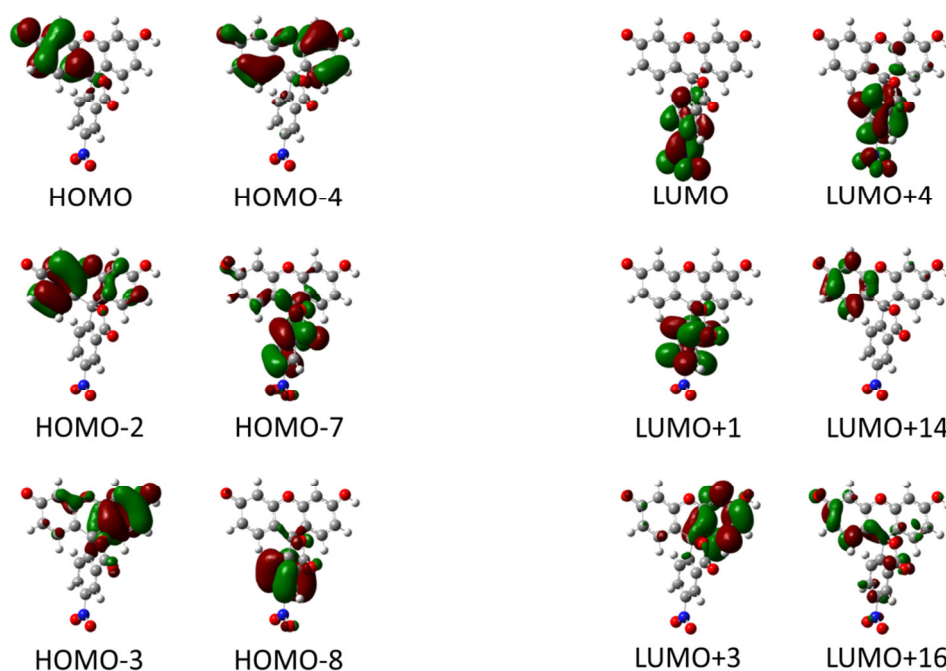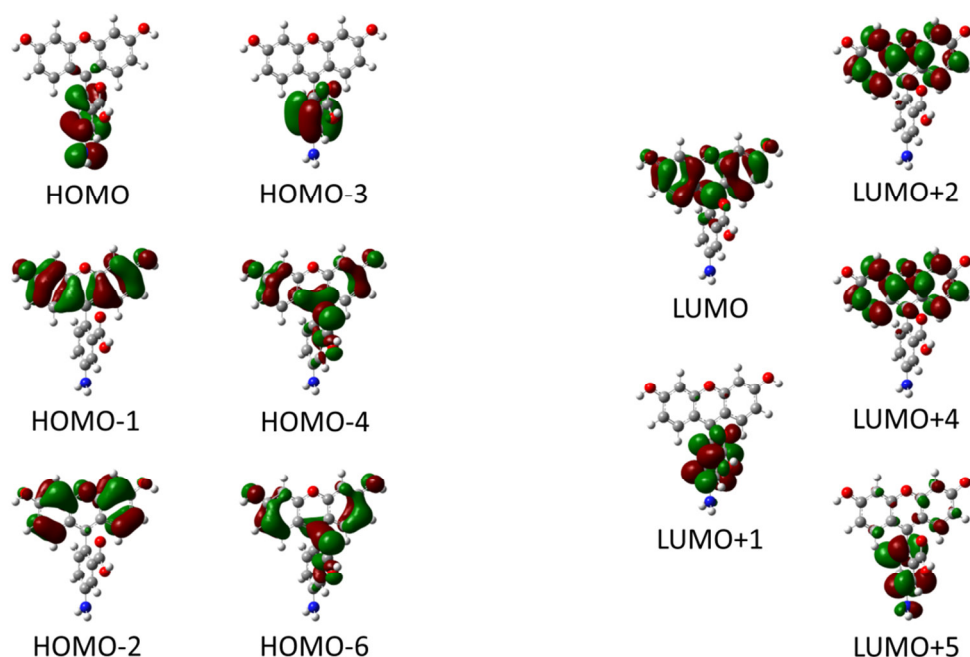| state	transition	weight / %	λ / nm	λ$_S$ / nm	f
S$_2$	HOMO-1→LUMO	94	348	389	0.58
S$_6$	HOMO-4→LUMO HOMO-1→LUMO	90 80	270	294	0.16
S$_9$	HOMO-6→LUMO HOMO-3→LUMO+1 HOMO→LUMO+5	11 18 45	238	256	0.14
S$_{10}$	HOMO-6→LUMO HOMO-1→LUMO+2	33 34	229	246	0.10
S$_{11}$	HOMO-6→LUMO HOMO-1→LUMO+1 HOMO-1→LUMO+2	38 11 28	217	232	0.28
S$_{12}$	HOMO-2→LUMO+2 HOMO-1→LUMO+4	37 37	216	231	0.31
S$_{16}$	HOMO-3→LUMO+1 HOMO→LUMO+5	32 14	205	218	0.33
S$_{20}$	HOMO-2→LUMO+2 HOMO-1→LUMO+4	39 27	200	213	0.82

Figure S18 Molecular orbital isosurfaces of **[5-AF]⁺** (Cation 1) with contributions to the electronic configurations, characterizing the electronic transitions listed in Table S20.

Table S21 Vertical singlet transitions of **[5-AF]⁺** (Cation 2) calculated at the ground state geometry (TD-DFT/ωB97XD/6-31+G(d)). Calculated central wavelengths λ are given together with corresponding values λ_S obtained after bathochromically shifting the transition energies by 3000 cm^{-1}. Only transitions with an oscillator strength of $f>0.1$ are displayed. Contributions to electronic transitions with a weight of <10 % were omitted.

| state	transition	weight / %	λ / nm	λ_S / nm	f
S$_1$	HOMO→LUMO	94	430	494	0.15
S$_2$	HOMO-1→LUMO	94	350	391	0.56
S$_8$	HOMO-5→LUMO	59	242	261	0.18
S$_{10}$	HOMO-4→LUMO	26	232	249	0.13
	HOMO-4→LUMO+1	25			
S$_{11}$	HOMO-5→LUMO	14	222	238	0.19
	HOMO-1→LUMO+1	29			
	HOMO-1→LUMO+2	23			
S$_{12}$	HOMO-2→LUMO+2	21	218	233	0.19
	HOMO-1→LUMO+2	18			
	HOMO-1→LUMO+3	10			
S$_{16}$	HOMO-3→LUMO+1	23	206	220	0.18
	HOMO-1→LUMO+2	17			
S$_{17}$	HOMO-1→LUMO+3	24	203	216	0.12
	HOMO-3→LUMO+1	11			
S$_{19}$	HOMO-2→LUMO+2	19	201	214	0.44
	HOMO-1→LUMO+1	13			
S$_{20}$	HOMO→LUMO+4	22	200	213	0.11
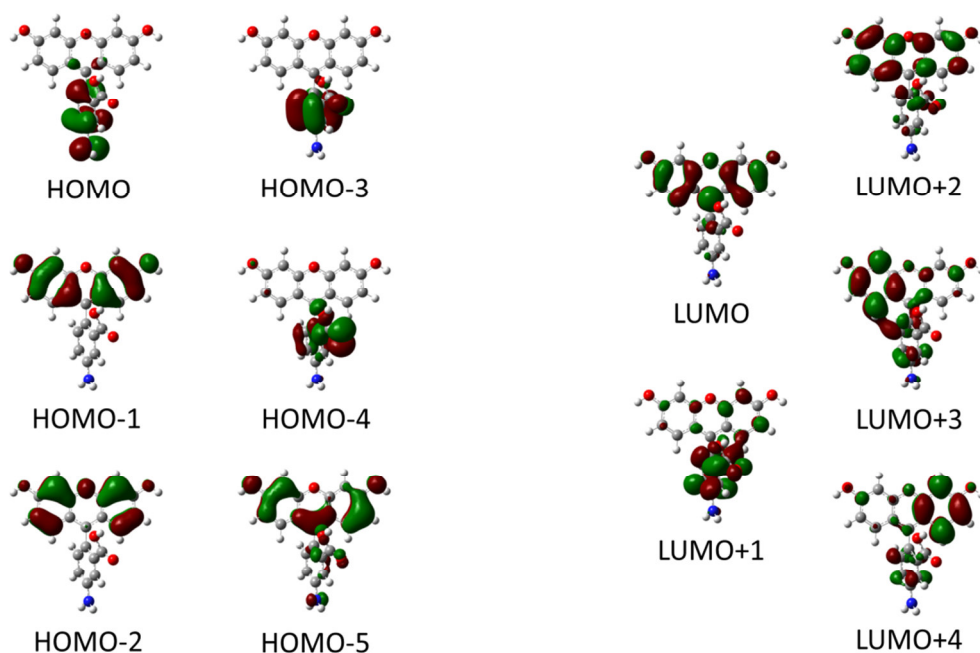
Figure S19 Molecular orbital isosurfaces of **[5-AF]⁺** (Cation 2) with contributions to the electronic configurations, characterizing the electronic transitions listed in Table S21.

Table S22 Vertical singlet transitions of **[5-AF]⁺** (Cation 3) calculated at the ground state geometry (TD-DFT/ωB97XD/6-31+G(d)). Calculated central wavelengths λ are given together with corresponding values λ_S obtained after bathochromically shifting the transition energies by 3000 cm⁻¹. Only transitions with an oscillator strength of $f>0.1$ are displayed. Contributions to electronic transitions with a weight of <10 % were omitted.

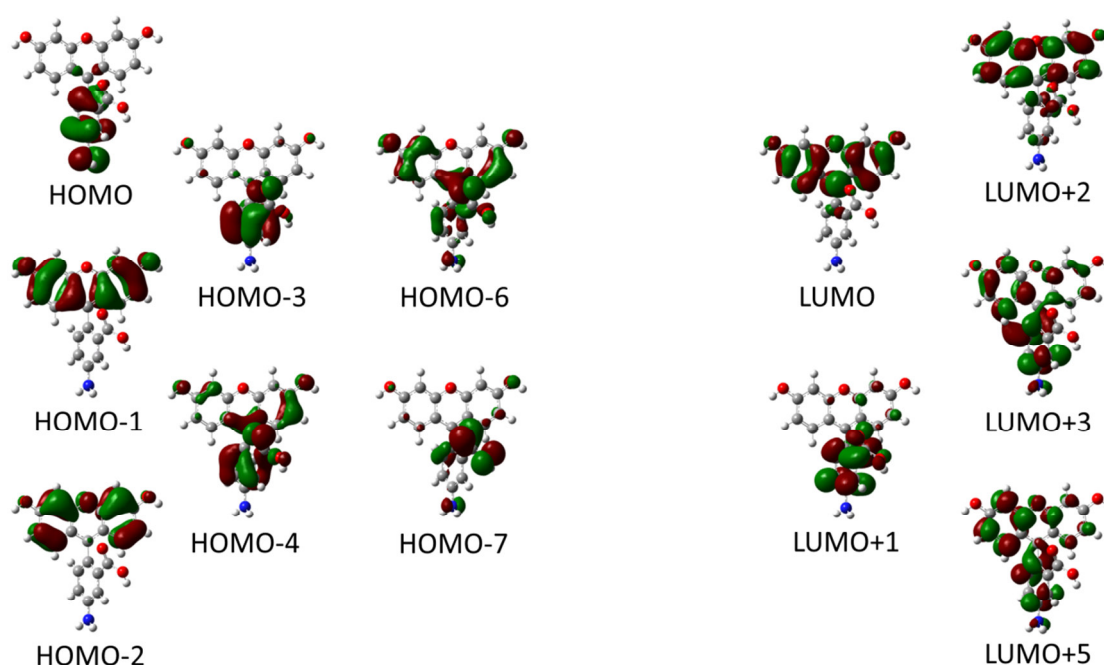| state	transition	weight / %	λ / nm	λ_S / nm	f
S_2	HOMO-1→LUMO	94	351	392	0.57
S_9	HOMO-6→LUMO	24	236	254	0.17
	HOMO→LUMO+3	27			
S_{11}	HOMO-6→LUMO	25	221	237	0.22
	HOMO-1→LUMO+1	27			
	HOMO-1→LUMO+2	21			
S_{12}	HOMO-2→LUMO+2	24	218	233	0.24
	HOMO-1→LUMO+2	17			
	HOMO-1→LUMO+5	16			
S_{14}	HOMO-2→LUMO+2	17	208	222	0.20
	HOMO-1→LUMO+1	42			
	HOMO-1→LUMO+2	25			
S_{16}	HOMO-7→LUMO	13	205	218	0.12
	HOMO→LUMO+2	52			
S_{19}	HOMO-4→LUMO+1	24	200	213	0.24
	HOMO-3→LUMO+1	30			

Figure S20 Molecular orbital isosurfaces of **[5-AF]⁺** (Cation 3) with contributions to the electronic configurations, characterizing the electronic transitions listed in Table S22.

Table S23 Vertical singlet transitions of **[5-AF]⁺** (Cation 4) calculated at the ground state geometry (TD-DFT/ωB97XD/6-31+G(d)). Calculated central wavelengths λ are given together with corresponding values λ_S obtained after bathochromically shifting the transition energies by 3000 cm⁻¹. Only transitions with an oscillator strength of $f > 0.1$ are displayed. Contributions to electronic transitions with a weight of <10 % were omitted.

| state	transition	weight / %	λ / nm	λ_S / nm	f
S_1	HOMO→LUMO	94	430	494	0.19
S_2	HOMO-2→LUMO	16	356	399	0.16
	HOMO-1→LUMO	79			
S_3	HOMO-2→LUMO	81	349	390	0.12
	HOMO-1→LUMO	16			
S_8	HOMO-6→LUMO	52	242	261	0.17
	HOMO-5→LUMO	16			
S_{10}	HOMO-4→LUMO+2	10	232	249	0.20
	HOMO→LUMO+2	11			
S_{11}	HOMO-1→LUMO+1	50	222	238	0.12
S_{12}	HOMO-2→LUMO+1	27	219	234	0.21
	HOMO-1→LUMO+2	19			
S_{18}	HOMO-8→LUMO	47	201	214	0.10
	HOMO-1→LUMO+3	17			
S_{19}	HOMO-2→LUMO+1	25	200	213	0.56
	HOMO-1→LUMO+2	17			
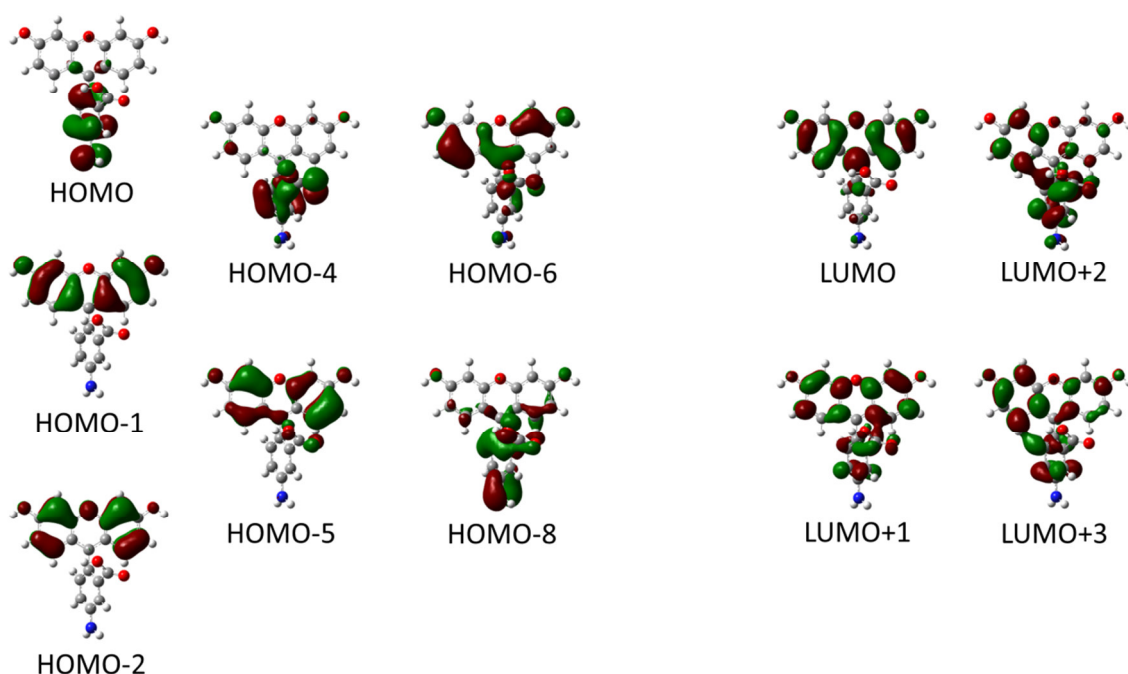
Figure S21 Molecular orbital isosurfaces of **[5-AF]⁺** (Cation 4) with contributions to the electronic configurations, characterizing the electronic transitions listed in Table S23.

Table S24 Vertical singlet transitions of **[5-NF]⁺** (Cation 1) calculated at the ground state geometry (TD-DFT/ωB97XD/6-31+G(d)). Calculated central wavelengths λ are given together with corresponding values λ_S obtained after bathochromically shifting the transition energies by 3000 cm⁻¹. Only transitions with an oscillator strength of $f > 0.1$ are displayed. Contributions to electronic transitions with a weight of <10 % were omitted.

| state	transition	weight / %	λ / nm	λ_S / nm	f
S_1	HOMO→LUMO	95	354	396	0.59
S_6	HOMO-2→LUMO	88	268	291	0.16
S_{13}	HOMO-4→LUMO	43	227	244	0.33
	HOMO→LUMO+3	27			
S_{14}	HOMO-9→LUMO	28	217	232	0.13
	HOMO→LUMO+3	25			
S_{15}	HOMO-1→LUMO+3	39	217	232	0.33
	HOMO→LUMO+5	37			
S_{20}	HOMO-5→LUMO	15	201	214	0.15
	HOMO-3→LUMO+2	21			
	HOMO→LUMO+4	20			
S_{21}	HOMO-7→LUMO+1	16	200	213	0.35
	HOMO-3→LUMO+2	28			
	HOMO→LUMO+2	21			
S_{22}	HOMO-1→LUMO+2	13	200	213	0.71
	HOMO-1→LUMO+3	31			
	HOMO→LUMO+5	28			
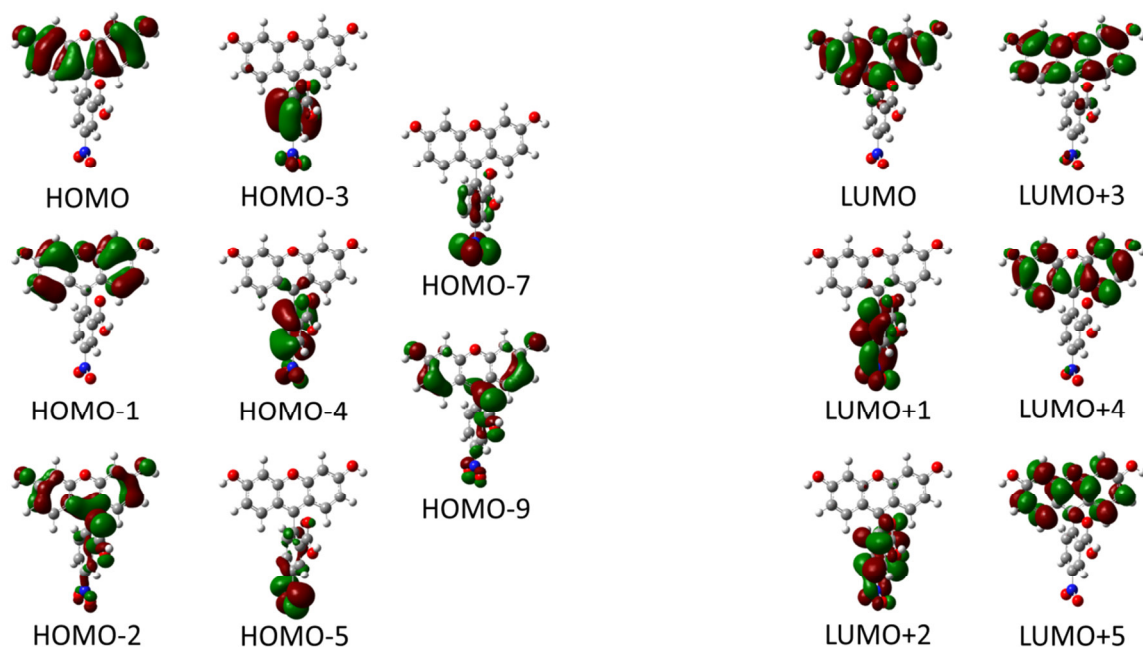
Figure S22 Molecular orbital isosurfaces of **[5-NF]⁺** (Cation 1) with contributions to the electronic configurations, characterizing the electronic transitions listed in Table S24.

Table S25 Vertical singlet transitions of **[5-NF]⁺** (Cation 2) calculated at the ground state geometry (TD-DFT/ωB97XD/6-31+G(d)). Calculated central wavelengths λ are given together with corresponding values λ_S obtained after bathochromically shifting the transition energies by 3000 cm⁻¹. Only transitions with an oscillator strength of $f>0.1$ are displayed. Contributions to electronic transitions with a weight of <10 % were omitted.

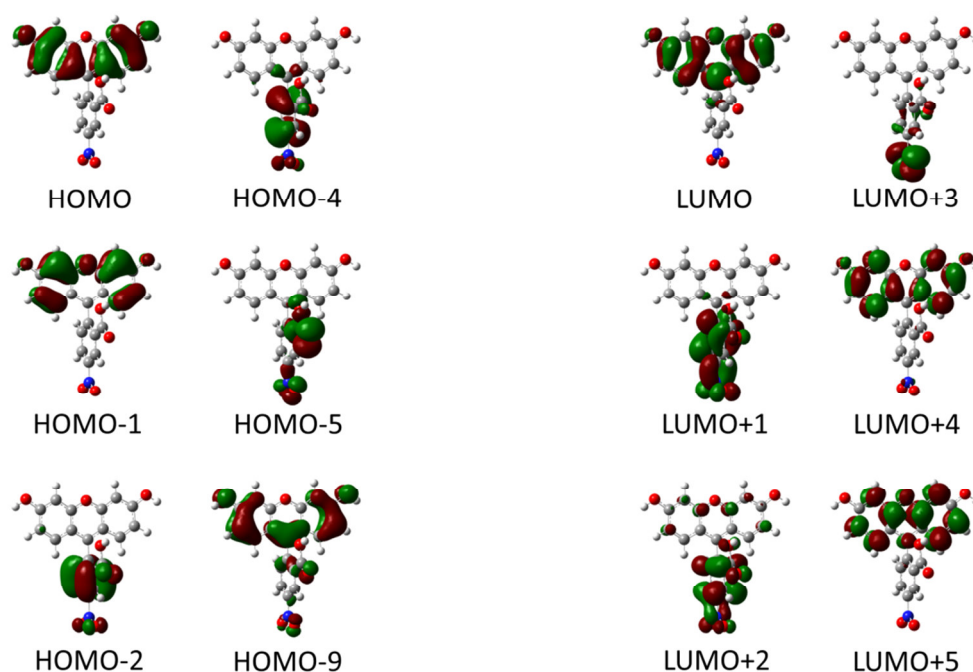| state	transition	weight / %	λ / nm	λ / nm	f
S_1	HOMO→LUMO	95	357	400	0.59
S_{10}	HOMO-9→LUMO	51	244	263	0.11
	HOMO-5→LUMO	11			
S_{12}	HOMO-4→LUMO+1	54	226	242	0.40
	HOMO→LUMO+3	16			
S_{14}	HOMO→LUMO+1	19	220	236	0.13
	HOMO→LUMO+2	10			
	HOMO→LUMO+3	32			
S_{15}	HOMO-1→LUMO+3	34	217	232	0.33
	HOMO→LUMO+5	34			
S_{22}	HOMO-4→LUMO+2	10	202	215	0.37
	HOMO-2→LUMO+1	42			
	HOMO→LUMO+4	12			
S_{23}	HOMO-1→LUMO+2	11	200	213	0.86
	HOMO-1→LUMO+3	34			
	HOMO→LUMO+5	37			

Figure S23 Molecular orbital isosurfaces of **[5-NF]⁺** (Cation 2) with contributions to the electronic configurations, characterizing the electronic transitions listed in Table S25.

Table S26 Vertical singlet transitions of **[5-NF]⁺** (Cation 3) calculated at the ground state geometry (TD-DFT/ωB97XD/6-31+G(d)). Calculated central wavelengths λ are given together with corresponding values λ_S obtained after bathochromically shifting the transition energies by 3000 cm^{-1}. Only transitions with an oscillator strength of f>0.1 are displayed. Contributions to electronic transitions with a weight of <10 % were omitted.

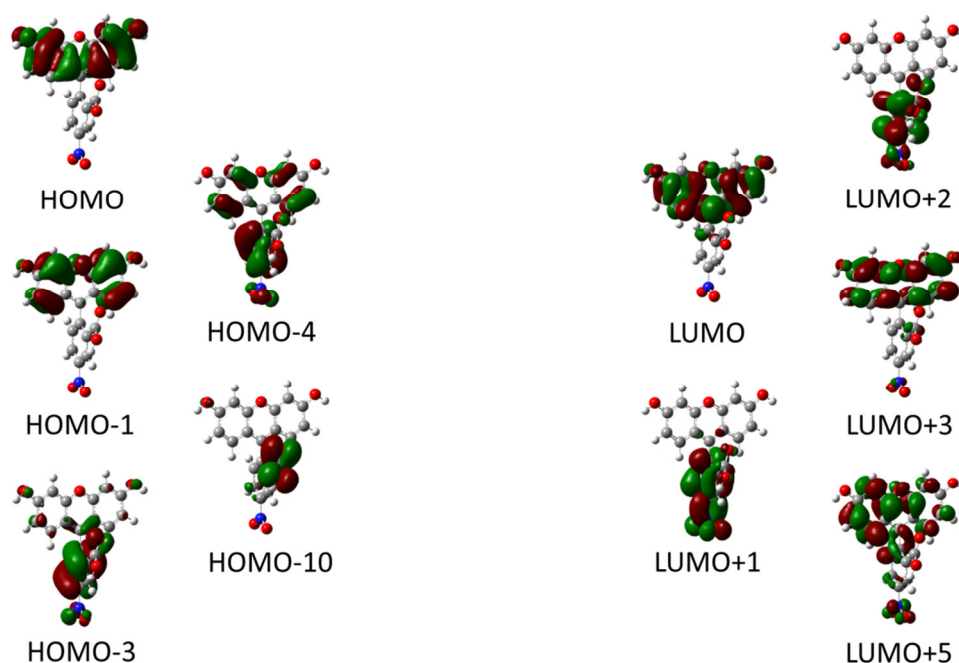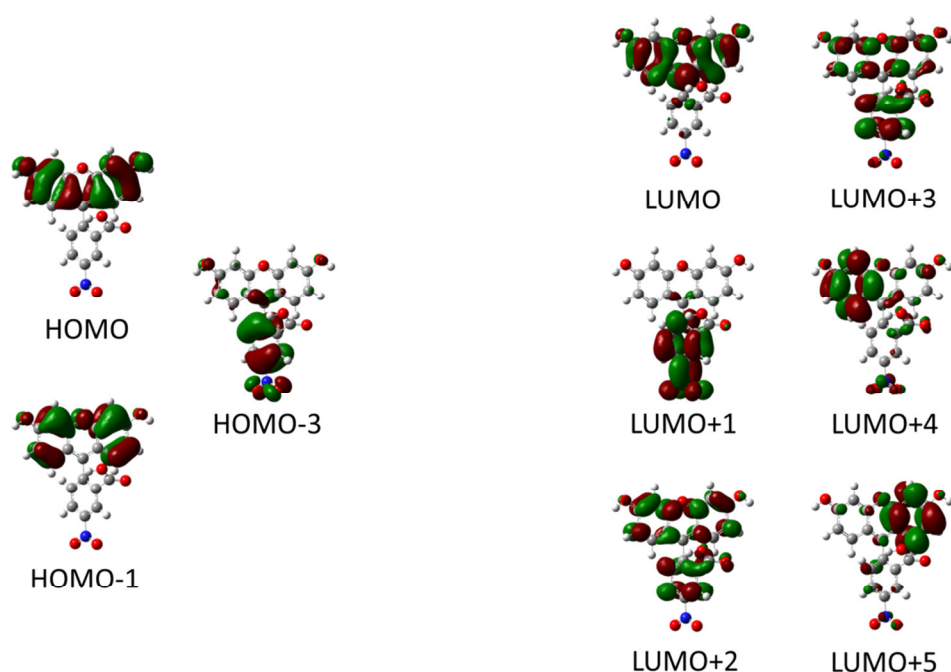| state	transition	weight / %	λ / nm	λ_S / nm	f
S$_1$	HOMO→LUMO	94	356	3.48	0.58
S$_{13}$	HOMO-4→LUMO+1	10	228	5.44	0.36
	HOMO-3→LUMO+1	37			
	HOMO→LUMO+3	21			
S$_{15}$	HOMO-1→LUMO+3	40	217	5.71	0.34
	HOMO→LUMO+5	27			
	HOMO→LUMO+3	25			
S$_{22}$	HOMO-10→LUMO	54	201	6.17	0.33
S$_{23}$	HOMO-10→LUMO	29	200	6.20	0.50
	HOMO-3→LUMO+2	11			
	HOMO-1→LUMO+2	11			
	HOMO-1→LUMO+3	11			
S$_{24}$	HOMO-3→LUMO+2	27	200	6.20	0.56
	HOMO-1→LUMO+3	13			
	HOMO→LUMO+5	10			

Figure S24 Molecular orbital isosurfaces of **[5-NF]⁺** (Cation 3) with contributions to the electronic configurations, characterizing the electronic transitions listed in Table S26.

Table S27 Vertical singlet transitions of **[5-NF]⁺** (Cation 4) calculated at the ground state geometry (TD-DFT/ωB97XD/6-31+G(d)). Calculated central wavelengths λ are given together with corresponding values λ_S obtained after bathochromically shifting the transition energies by 3000 cm⁻¹. Only transitions with an oscillator strength of $f > 0.1$ are displayed. Contributions to electronic transitions with a weight of <10 % were omitted.

state	transition	weight / %	λ / nm	λ_S / nm	f
S_1	HOMO-1→LUMO HOMO→LUMO	19 76	364	409	0.45
S_2	HOMO-1→LUMO HOMO→LUMO	78 18	357	400	0.15
S_{12}	HOMO-3→LUMO+1 HOMO→LUMO+2	13 45	226	242	0.48
S_{13}	HOMO-1→LUMO+2 HOMO→LUMO+1 HOMO→LUMO+4 HOMO→LUMO+5	17 32 15 11	222	238	0.17
S_{17}	HOMO-1→LUMO+2 HOMO-1→LUMO+3 HOMO→LUMO+1	19 10 48	213	228	0.35
S_{23}	HOMO-1→LUMO+1	68	200	213	0.18
S_{24}	HOMO-1→LUMO+2 HOMO→LUMO+5	29 29	200	213	0.60

Figure S25 Molecular orbital isosurfaces of **[5-NF]⁺** (Cation 4) with contributions to the electronic configurations, characterizing the electronic transitions listed in Table S27.

4.9.7 DFT calculated frontier orbital sequences
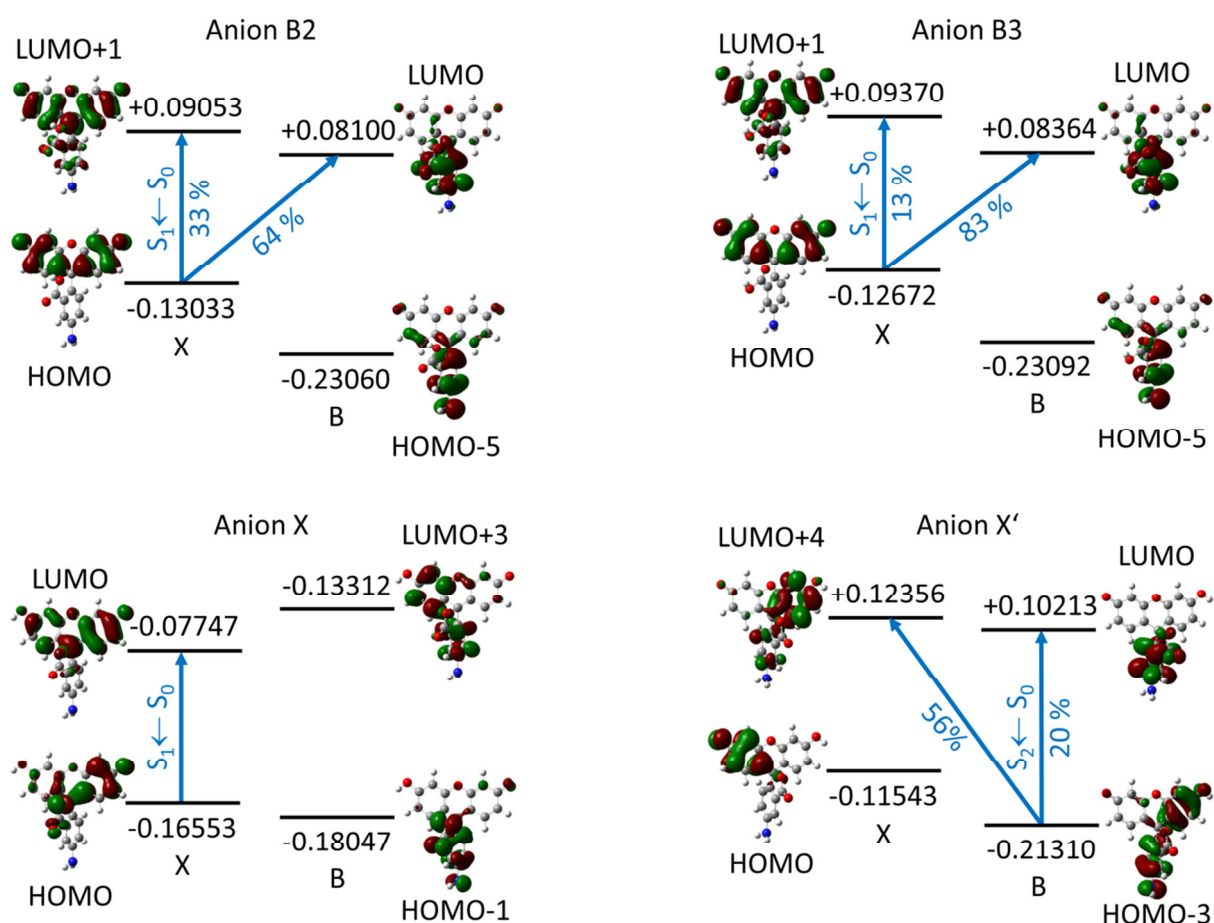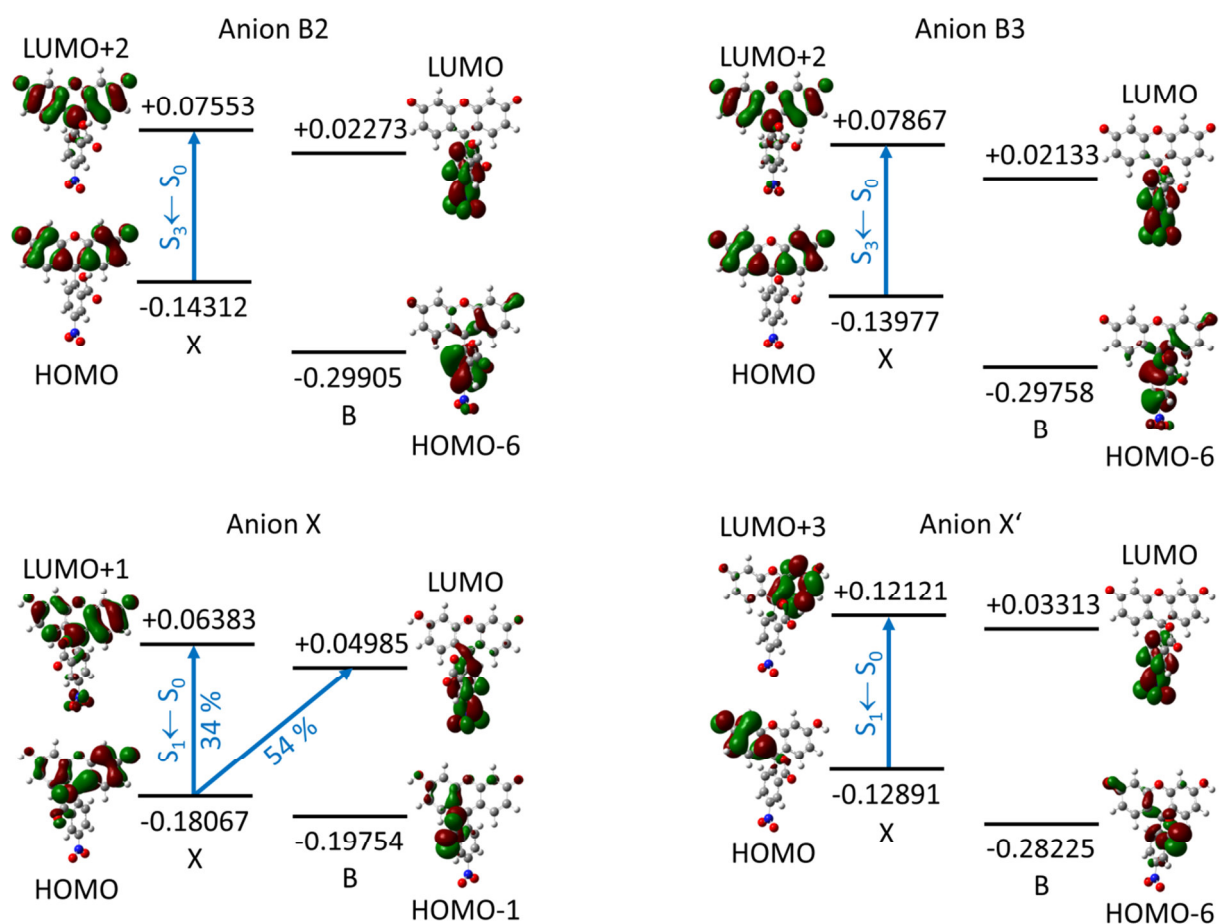

Figure S26 Sequence of highest occupied molecular orbitals (HOMO) and lowest unoccupied molecular orbitals (LUMO) centered at the xanthene (X) and benzoic acid (B) moieties calculated for the higher energy conformers of **[5-AF]**⁻. Orbital energies are given in Hartree. Blue arrow denotes the character of the respective calculated lowest energy transition most probably excited using λ_{pump}=510 nm (*cf.* Table 1).

Figure S27 Sequence of highest occupied molecular orbitals (HOMO) and lowest unoccupied molecular orbitals (LUMO) centered at the xanthene (X) and benzoic acid (B) moieties calculated for the higher energy conformers of **[5-NF]⁻**. Orbital energies are given in Hartree. Blue arrow denotes the character of the respective calculated lowest energy transition most probably excited using λ_{pump}=510 nm (*cf.* Table 2).
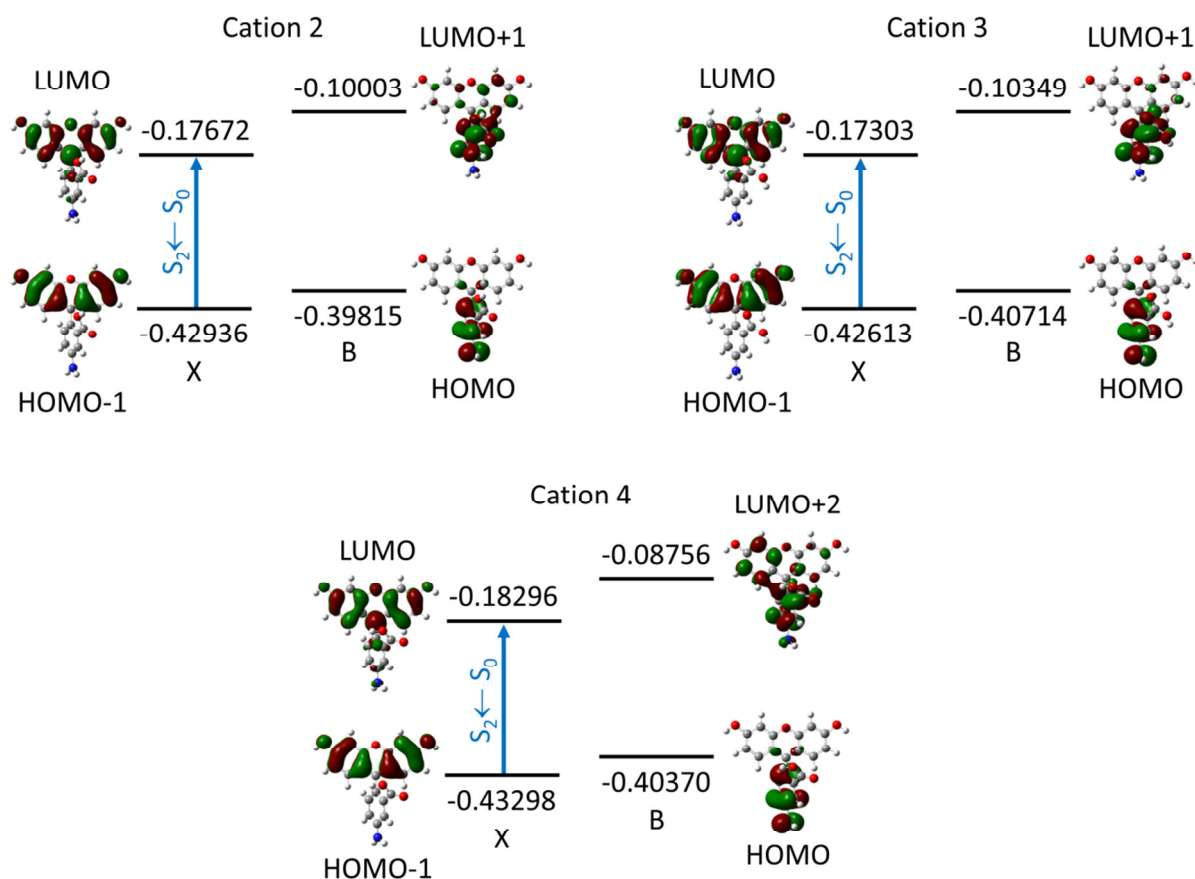
Figure S28 Sequence of highest occupied molecular orbitals (HOMO) and lowest unoccupied molecular orbitals (LUMO) centered at the xanthene (X) and benzoic acid (B) moieties calculated for the higher energy conformers of **[5-AF]⁺**. Orbital energies are given in Hartree. Blue arrow denotes the character of the respective calculated lowest energy transition most probably excited using λ_{pump}=410 nm (*cf.* Table 3).
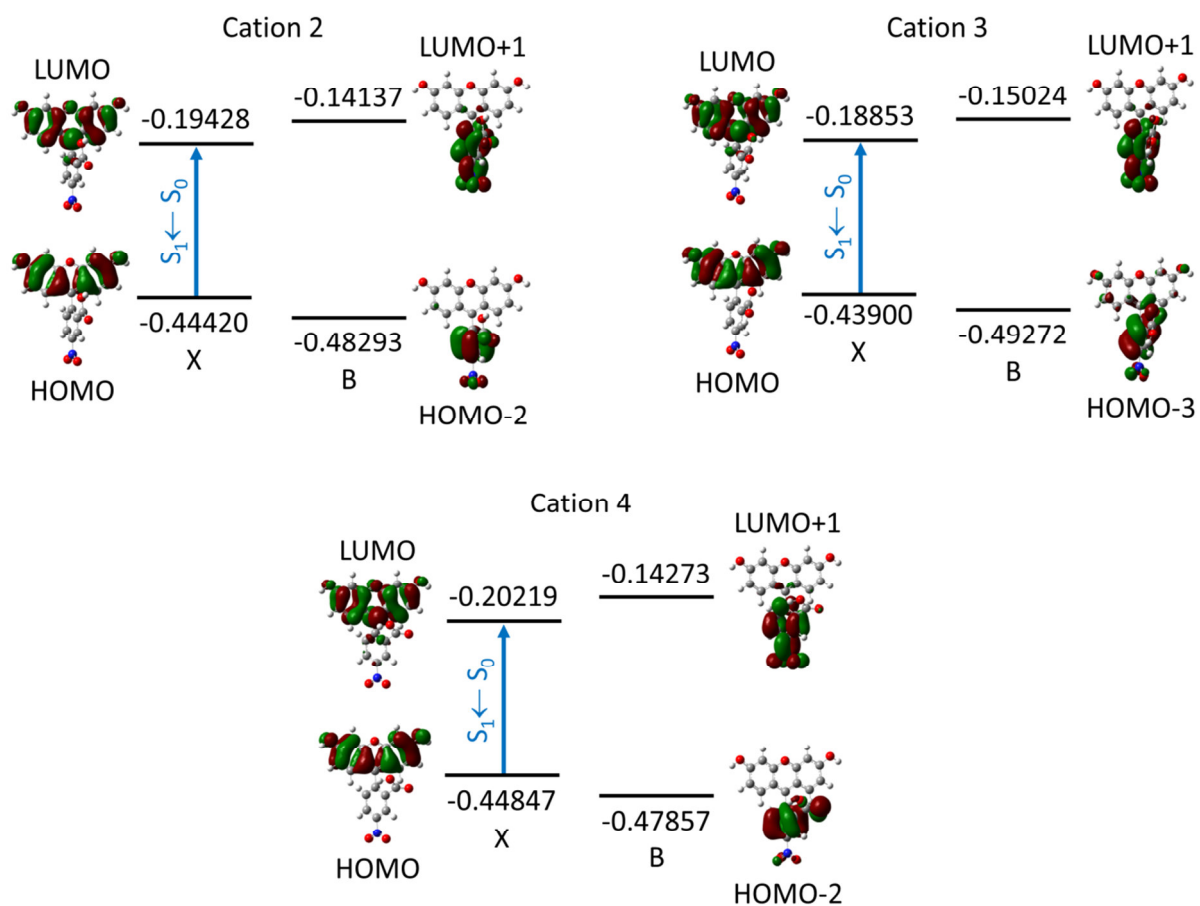
Figure S29 Sequence of highest occupied molecular orbitals (HOMO) and lowest unoccupied molecular orbitals (LUMO) centered at the xanthene (X) and benzoic acid (B) moieties calculated for the higher energy conformers of **[5-NF]⁺**. Orbital energies are given in Hartree. Blue arrow denotes the character of the respective calculated lowest energy transition most probably excited using λ_{pump}=410 nm (*cf.* Table 4).
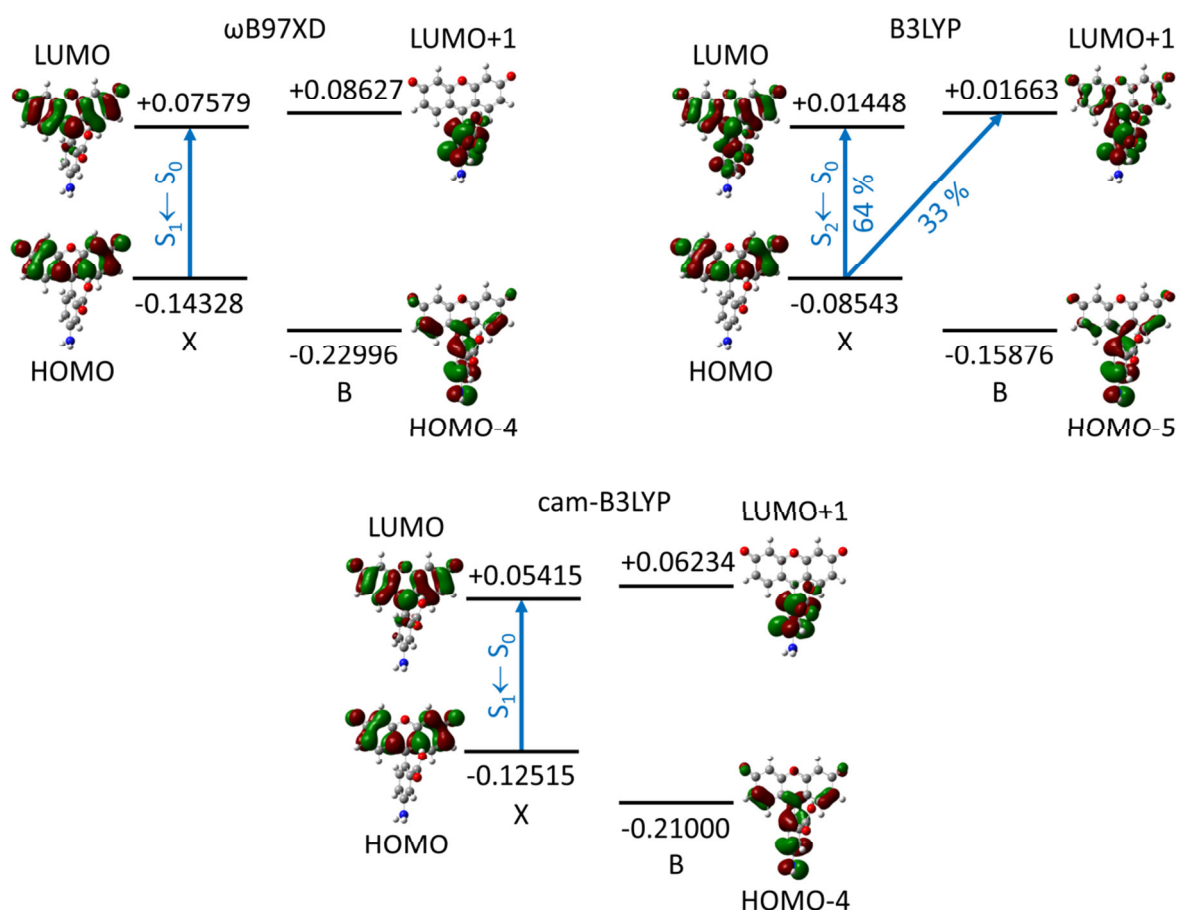
Figure S30 Sequence of highest occupied molecular orbitals (HOMO) and lowest unoccupied molecular orbitals (LUMO) centered at the xanthene (X) and benzoic acid (B) moieties calculated for the lowest energy conformers of **[5-AF]⁻** employing different hybrid functionals (ωB97XD, B3LYP and cam-B3LYP). Orbital energies are given in Hartree. Blue arrow denotes the character of the respective calculated lowest energy transition most probably excited using λ_{pump}=510 nm (*cf.* Table S28).

Table S28 Comparison of highest intensity, lowest energy transitions most probably excited using λ_{pump}=510 nm calculated for **[5-AF]⁻** (Anion B1) employing different functionals (TD-DFT/6-31+G(d)). Calculated central wavelengths λ are given together with corresponding values λ_S obtained after bathochromically shifting the transition energies by 3000 cm⁻¹. Only transitions with an oscillator strength of *f*>0.1 are displayed. Contributions to electronic transitions with a weight of <10% were omitted.

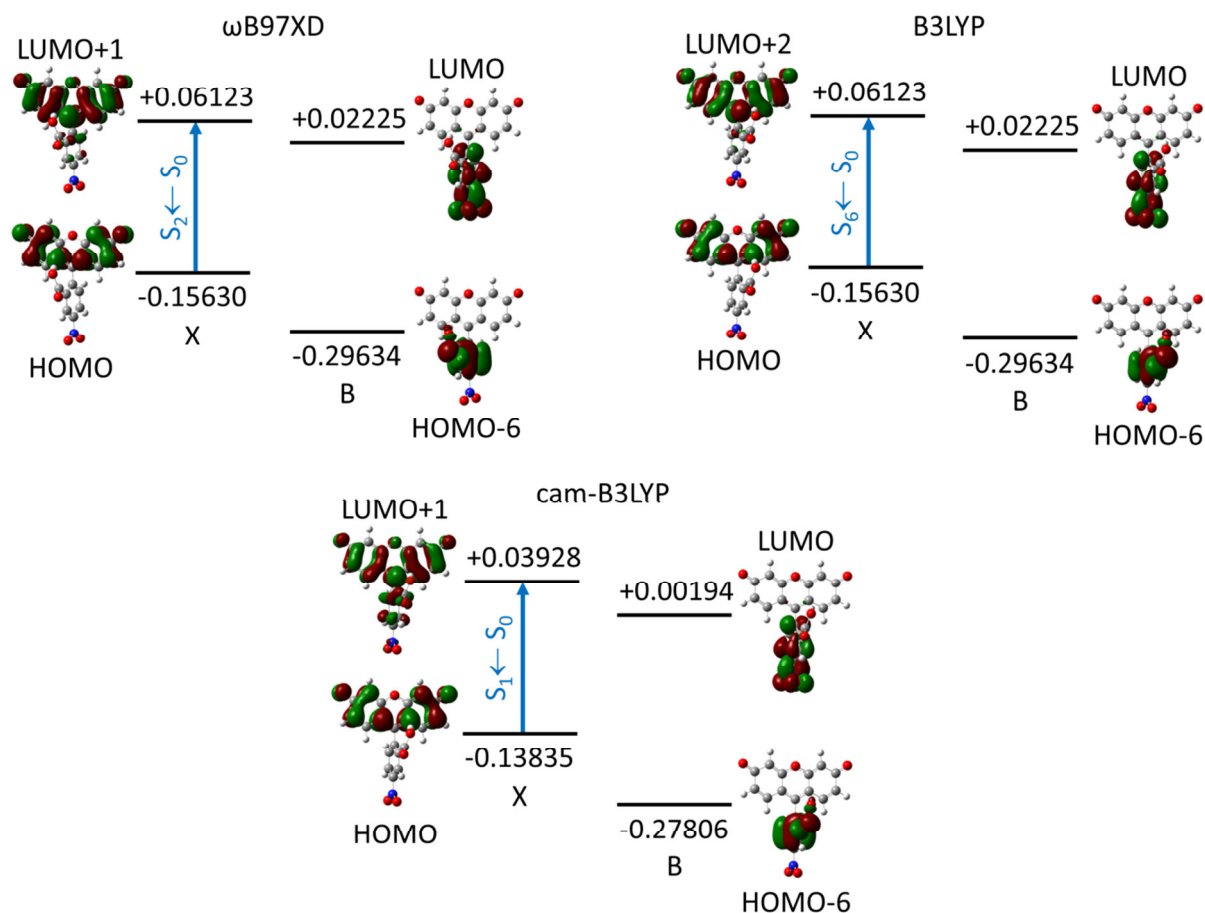| functional	state	transition (weight / %)	character	λ / nm	λ_S / nm	*f*
ωB97XD	S₁	HOMO→LUMO (96)	LE(X)	419	479	0.76
B3LYP	S₂	HOMO→LUMO (64)	LE(X)	445	514	0.62
		HOMO→LUMO (33)	CT(X→B)			
cam-B3LYP	S₁	HOMO→LUMO (96)	LE(X)	419	479	0.76

Figure S31 Sequence of highest occupied molecular orbitals (HOMO) and lowest unoccupied molecular orbitals (LUMO) centered at the xanthene (X) and benzoic acid (B) moieties calculated for the lowest energy conformers of **[5-NF]⁻** employing different hybrid functionals (ωB97XD, B3LYP and cam-B3LYP). Orbital energies are given in Hartree. Blue arrow denotes the character of the respective calculated lowest energy transition most probably excited using λ_{pump}=510 nm (*cf.* Table S29).

Table S29 Comparison of highest intensity, lowest energy transitions most probably excited using λ_{pump}=510 nm calculated for **[5-NF]⁻** (Anion B1) employing different functionals (TD-DFT/6-31+G(d)). Calculated central wavelengths λ are given together with corresponding values λ_S obtained after bathochromically shifting the transition energies by 3000 cm⁻¹. Only transitions with an oscillator strength of *f*>0.1 are displayed. Contributions to electronic transitions with a weight of <10% were omitted.

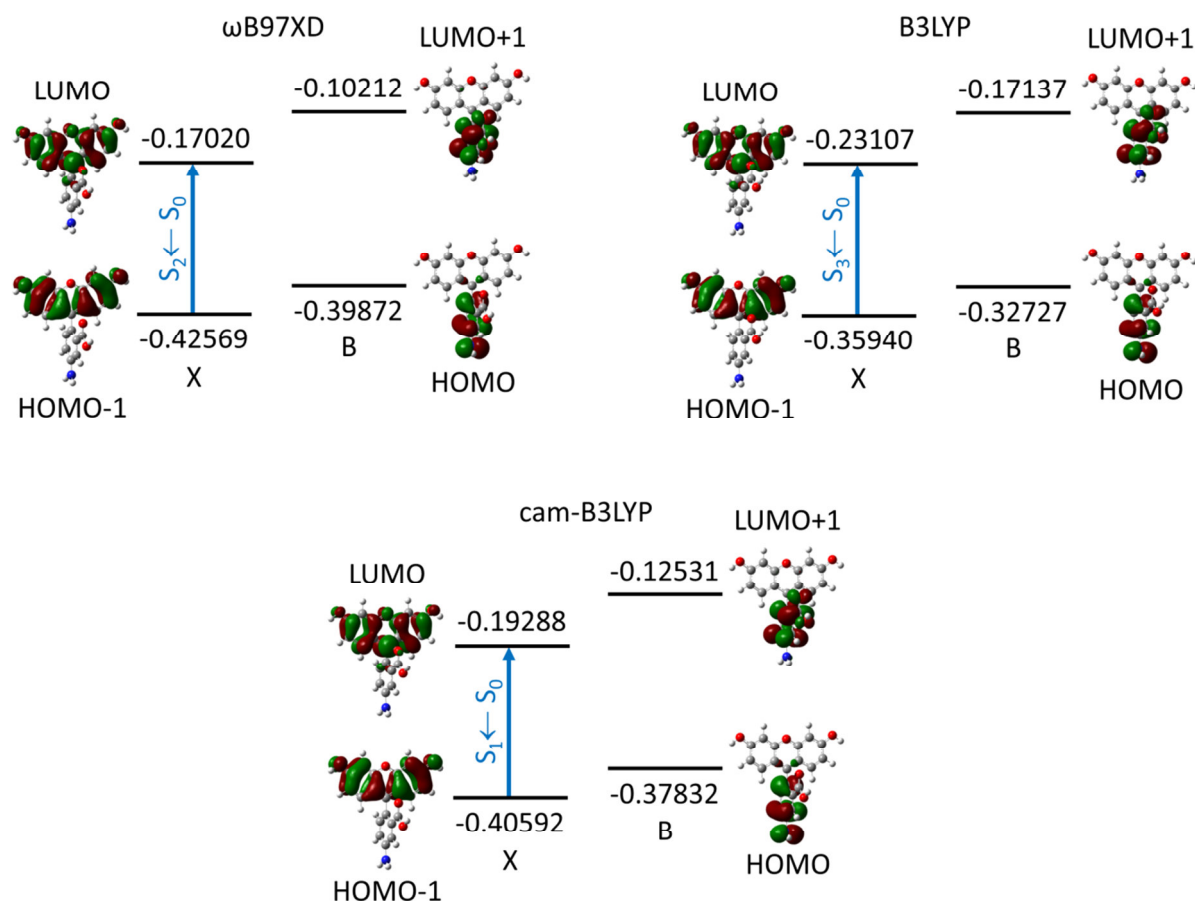| functional	state	transition (weight / %)	character	λ / nm	λ_S / nm	*f*
ωB97XD	S_2	HOMO→LUMO+1 (92)	LE(X)	421	482	0.76
B3LYP	S_6	HOMO→LUMO+2 (92)	LE(X)	445	514	0.62
cam-B3LYP	S_1	HOMO→LUMO+1 (87)	LE(X)	422	483	0.76

Figure S32 Sequence of highest occupied molecular orbitals (HOMO) and lowest unoccupied molecular orbitals (LUMO) centered at the xanthene (X) and benzoic acid (B) moieties calculated for the lowest energy conformers of **[5-AF]$^+$** employing different hybrid functionals (ωB97XD, B3LYP and cam-B3LYP). Orbital energies are given in Hartree. Blue arrow denotes the character of the respective calculated lowest energy transition most probably excited using λ_{pump}=410 nm (*cf.* Table S30).

Table S30 Comparison of highest intensity, lowest energy transitions most probably excited using λ_{pump}=410 nm calculated for **[5-AF]$^+$** (Cation 1) employing different functionals (TD-DFT/6-31+G(d)). Calculated central wavelengths λ are given together with corresponding values λ_S obtained after bathochromically shifting the transition energies by 3000 cm^{-1}. Only transitions with an oscillator strength of f>0.1 are displayed. Contributions to electronic transitions with a weight of <10% were omitted.

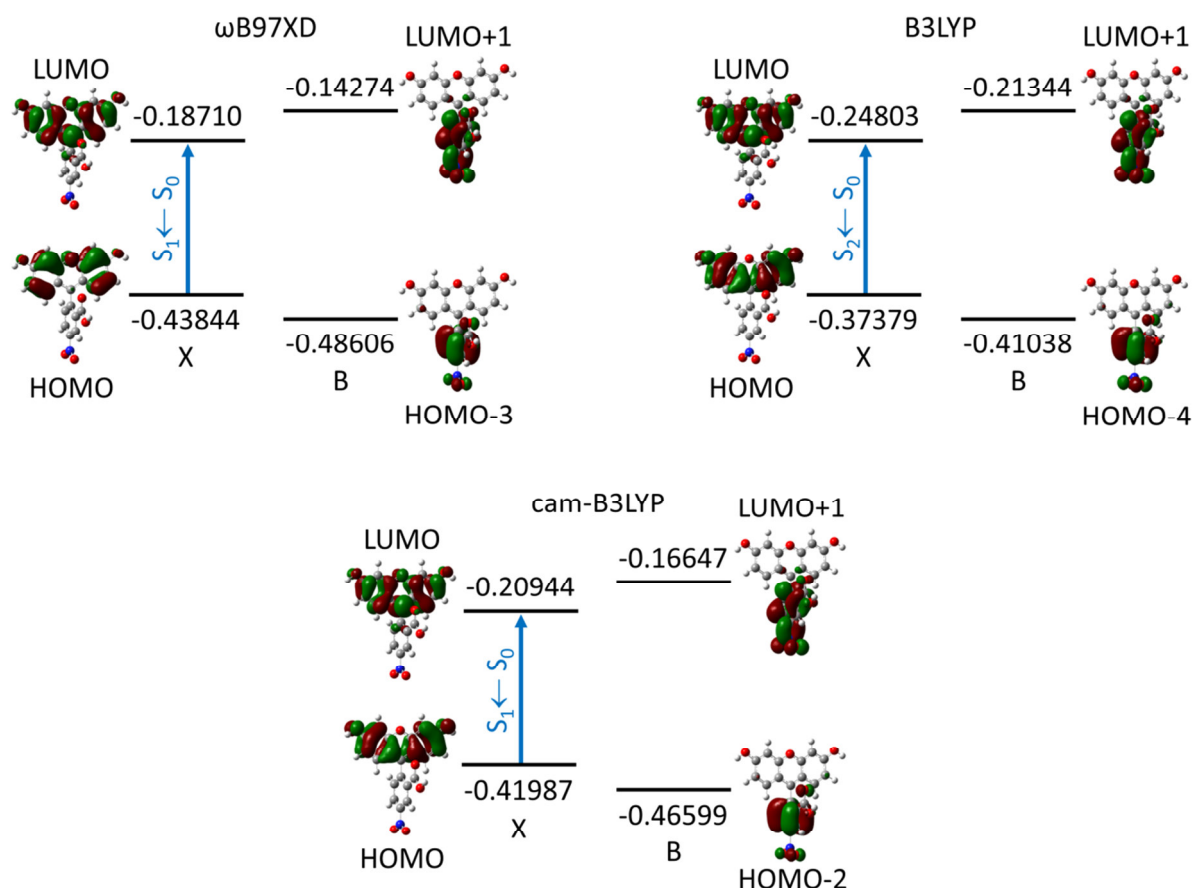| functional	state	transition (weight / %)	character	λ / nm	λ_S / nm	f
ωB97XD	S$_2$	HOMO-1→LUMO (94)	LE(X)	348	389	0.58
B3LYP	S$_3$	HOMO-1→LUMO (89)	LE(X)	380	429	0.41
cam-B3LYP	S$_1$	HOMO-1→LUMO (95)	LE(X)	350	391	0.59

Figure S33 Sequence of highest occupied molecular orbitals (HOMO) and lowest unoccupied molecular orbitals (LUMO) centered at the xanthene (X) and benzoic acid (B) moieties calculated for the lowest energy conformers of **[5-NF]+** employing different hybrid functionals (ωB97XD, B3LYP and cam-B3LYP). Orbital energies are given in Hartree. Blue arrow denotes the character of the respective calculated lowest energy transition most probably excited using λ_{pump}=410 nm (*cf.* Table S31).

Table S31 Comparison of highest intensity, lowest energy transitions most probably excited using λ_{pump}=410 nm calculated for **[5-NF]+** (Cation 1) employing different functionals (TDDFT/6-31+G(d)). Calculated central wavelengths λ are given together with corresponding values λ_S obtained after bathochromically shifting the transition energies by 3000 cm^{-1}. Only transitions with an oscillator strength of f>0.1 are displayed. Contributions to electronic transitions with a weight of <10% were omitted.

functional	state	transition (weight / %)	character	λ / nm	λ_S / nm	f
ωB97XD	S_1	HOMO→LUMO (95)	LE(X)	354	396	0.59
B3LYP	S_2	HOMO→LUMO (94)	LE(X)	385	435	0.47
cam-B3LYP	S_1	HOMO→LUMO (95)	LE(X)	357	400	0.59

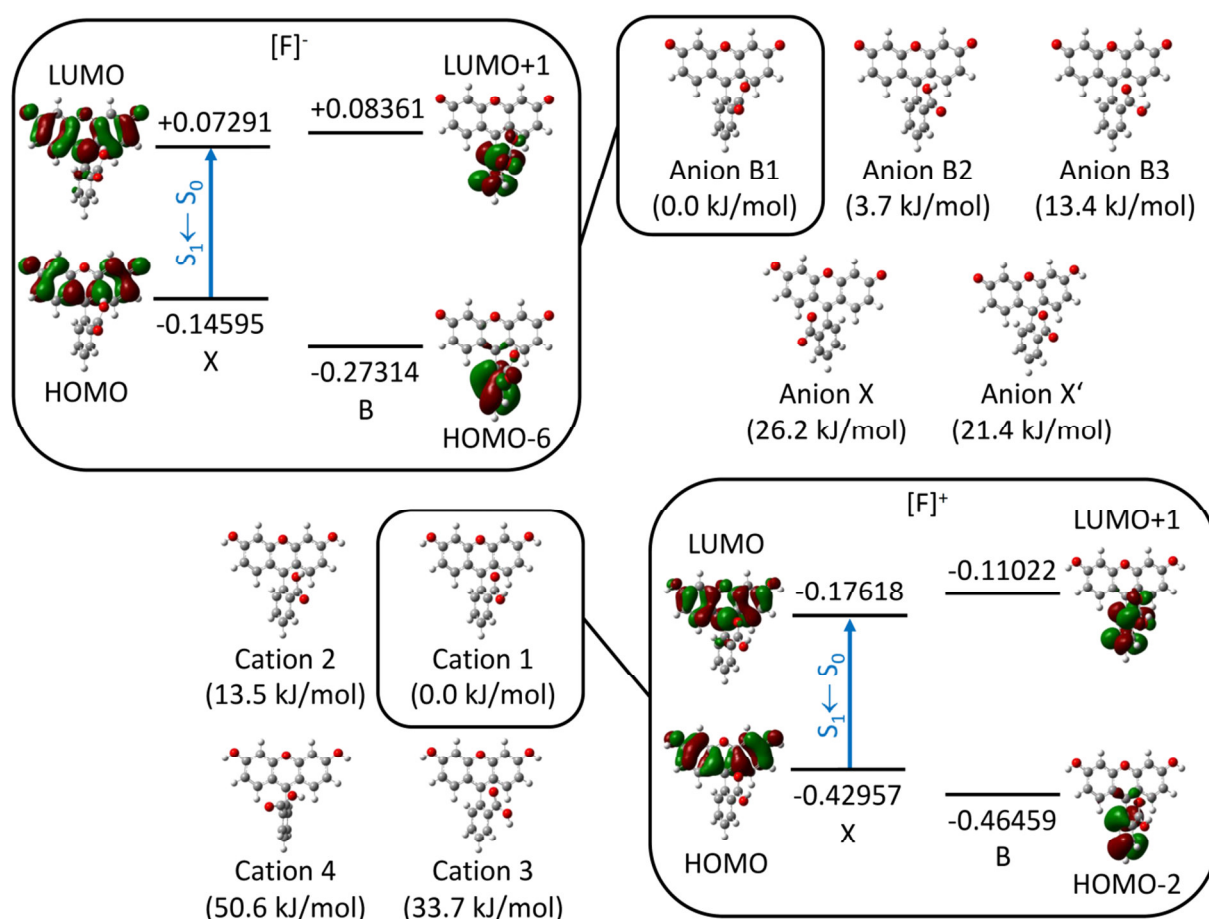**Figure S34** Lowest energy conformers of **[F]⁻** and **[F]⁺** calculated at the ωB97XD/6-31+G(d) DFT level of theory. Sequence of highest occupied molecular orbitals (HOMO) and lowest unoccupied molecular orbitals (LUMO) centered at the xanthene (X) and benzoic acid (B) moieties is only displayed examplatorily for the lowest energy conformer of **[F]⁻** (top) and **[F]⁺** (bottom). Orbital energies are given in Hartree. Blue arrow denotes the character of respective calculated lowest energy transition highest in intensity (*cf.* Table S32).

Table S32 Lowest energy vertical singlet transition calculated for the Anion B1 and Cation 1 conformer of **[F]⁻** and **[F]⁺**, respectively. TD-DFT (ωB97XD/6-31+G(d)) calculated central wavelengths λ are given together with corresponding values λ_S obtained after bathochromically shifting the transition energies by 3000 cm⁻¹. λ_{pump}=520 nm/λ_{pump}=425 nm were used in Ref. [2] for transient experiments on **[F]⁻**/**[F]⁺**.

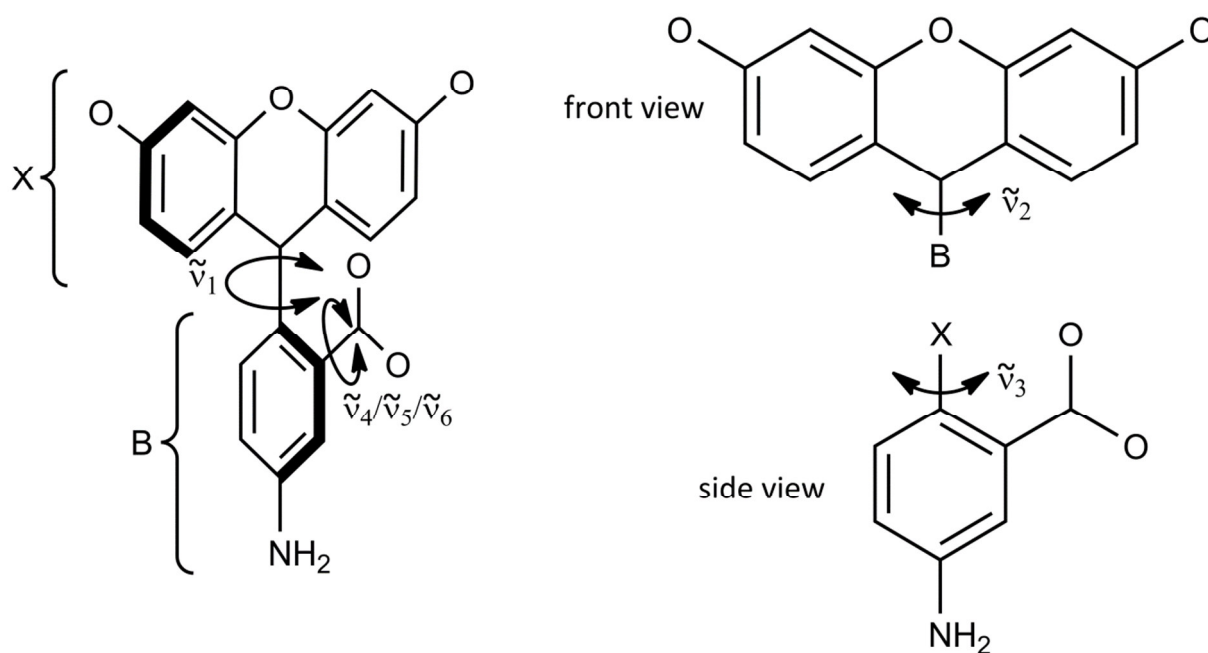|	state	transition (weight / %)	character	λ / nm	λ_S / nm	f
Anion B1	S_1	HOMO→LUMO (95%)	LE(X)	419	479	0.76
Cation 1	S_1	HOMO→LUMO (94%)	LE(X)	351	392	0.58

4.9.8 Calculated low frequency vibrational modes

Figure S35 Schematic depiction of low frequency vibrational modes (<100 cm^{-1}) in non-lactone forms of **[5-AF]$^-$**, obtained from ground state frequency calculations (*cf.* Table S33).

Table S33 Energies of low frequency vibrational modes (<100 cm^{-1}) calculated for ground state optimized geometries of the four non-lactone conformers of **[5-AF]$^-$** (DFT/ωB97XD/6-31+G(d)). Unscaled values are listed.

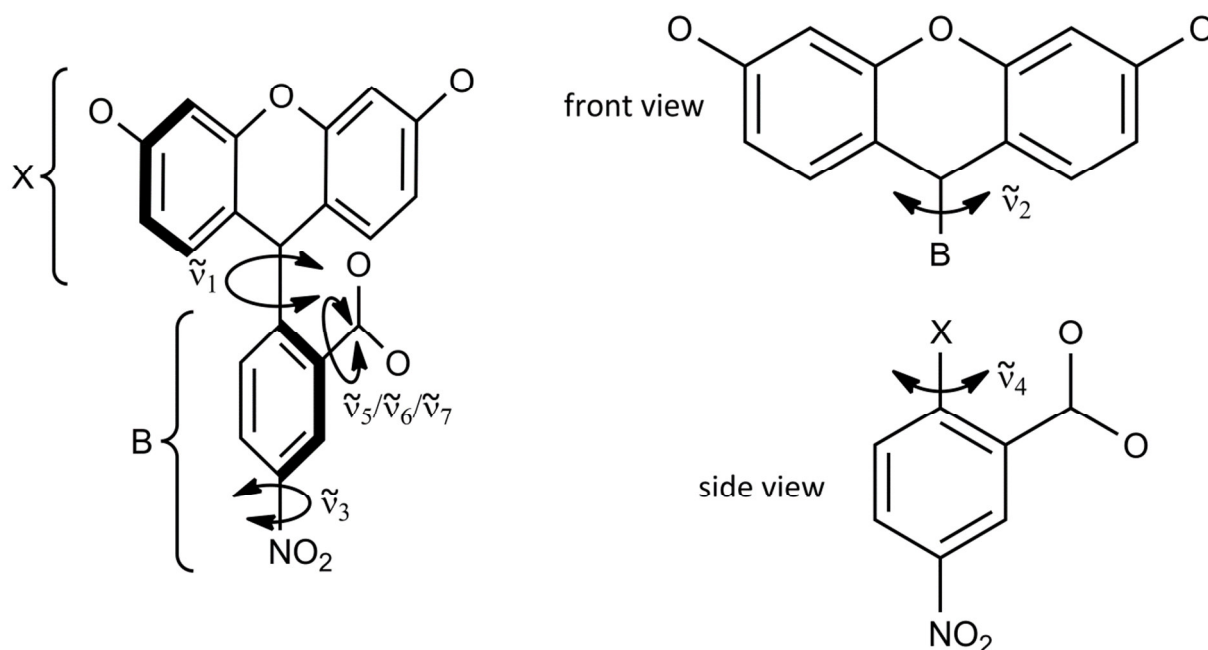| conf.	$\tilde{\nu}_1$ / cm^{-1}	$\tilde{\nu}_2$ / cm^{-1}	$\tilde{\nu}_3$ / cm^{-1}	$\tilde{\nu}_4$ / cm^{-1}	$\tilde{\nu}_5$ / cm^{-1}	$\tilde{\nu}_6$ / cm^{-1}
B1	18	39	45	57	67	86
B2	15	39	45	57	64	88
B3	15	38	47	55	63	89
X	24	41	51	57	78	98

Figure S36 Schematic depiction of low frequency vibrational modes (<100 cm^{-1}) in non-lactone forms of **[5-NF]**$^-$, obtained from ground state frequency calculations (*cf.* Table S34).

Table S34 Frequencies of low frequency vibrational modes (<100 cm^{-1}) calculated for ground state optimized geometries of the four non-lactone conformers of **[5-NF]**$^-$ (DFT/ωB97XD/6-31+G(d)). Unscaled values are listed.

conf.	$\tilde{v}_1$ / cm^{-1}	$\tilde{v}_2$ / cm^{-1}	$\tilde{v}_3$ / cm^{-1}	$\tilde{v}_4$ / cm^{-1}	$\tilde{v}_5$ / cm^{-1}	$\tilde{v}_6$ / cm^{-1}	$\tilde{v}_7$ / cm^{-1}
B1	20	30	41	44	59	71	88
B2	18	31	41	46	55	61	86
B3	17	32	41	47	55	63	86
X	24	30	41	48	56	74	96

4.9.9 References

[1] J. D. Bhawalkar, G. S. He, P. N. Prasad, "*NONLINEAR MULTIPHOTON PROCESSES IN ORGANIC AND POLYMERIC MATERIALS*", *Rep. Prog. Phys.* **1996**, 59, 1041-1070.

[2] D. Imanbaew, M. F. Gelin, C. Riehn,"*ROTATIONAL AND VIBRATIONAL DYNAMICS IN THE EXCITED ELECTRONIC STATE OF DEPROTONATED AND PROTONATED FLUORESCEIN STUDIED BY TIME-RESOLVED PHOTOFRAGMENTATION IN AN ION TRAP*", *Struct. Dyn.* **2016**, *3*, 043211.

5 A new twist to cyanine photoisomerization by ultrafast ion trap action spectroscopy

Dimitri Imanbaew[1], and Christoph Riehn[1,2]

[1]*Fachbereich Chemie, Technische Universität Kaiserslautern, Erwin-Schrödinger-Str. 52-54, 67663 Kaiserslautern, Germany*
[2]*Landesforschungszentrum OPTIMAS, Erwin-Schrödinger-Str. 46, 67663 Kaiserslautern, Germany*

5.1 Preamble

The following work has been formatted as to become a manuscript for publication. It has not been submitted, yet. Experiments, data processing and evaluation, as well as structural and energetic calculations were performed by me. The initial draft of the manuscript was written by me.

5.2 Abstract

We report on the intrinsic excited state dynamics of a cationic carbocyanine dye (3,3'-diethyloxacarbocyanine) in the gas phase. The isolated ions were investigated by femtosecond transient Vis-pump NIR-probe photofragmentation in an ion trap. The population of the S_1 excited state decays bi-exponentially, yielding two time constants on a picosecond timescale. Both time constants decrease upon excitation with pump photons of higher energy, *i.e.* upon imparting higher excess internal energies to the ions. From an Arrhenius plot of the rate constants, we estimated two energy barriers, corresponding to isomerization pathways by torsion around different C-C bonds within the polymethine backbone. Furthermore, the transient photofragmentation signal is periodically modulated, indicative of vibrational wave-packet dynamics in the S_1 excited state. The period of the wave-packet motion can be attributed to one of three low frequency vibrational modes, one of which is found to be the torsion of the C-C bridge, promoting excited state isomerization of the molecular dye.

5.3 Introduction

Energy redistribution and dissipation is a fundamental driving force in nature. Upon electronic excitation by absorption of a photon, a molecular system typically strives to release the absorbed excess energy by interaction with its environment, subduing phototoxic reactions. Fast internal conversion (IC) to the electronic ground state (S_0) is a favored relaxation process, as it leaves the molecular system in a vibrationally hot S_0 state, allowing for quick release of the stored energy to the surrounding medium. One way for efficient IC to the S_0 state involves conformational rearrangement, if the corresponding reaction coordinate couples the excited state with the S_0 state via a conical intersection. A prime example for conformational change is intramolecular torsion, such as in *e.g.* the isomerization of 11-*cis*-retinal induced by photoexcitation, which is a fundamental event in vision.[1] Understanding the underlying mechanisms behind photoisomerization is also attractive for technical applications, allowing for design of photoswitches and light-driven machines on a molecular level.[2-3] For the study on molecular photoisomerization, cyanines turned out to be an appealing system, as their photophysical properties can be easily tuned by exchange of its terminal groups or by modifying the length of the polymethine chain, bridging the end groups.[4] A chain

lengths increase, however, decreases the rigidity of the system, hence increasing the number of possible isomerization pathways by torsion around different C-C bonds within the polymethine backbone. The identification of favored isomerization pathways and the resulting isomers in solution is an ongoing endeavor, even for cyanines with short chain lengths. A drawback of condensed phase studies is thereby the impact of solvent molecules, subduing photoisomerization dynamics and additionally complicating theoretical treatment. This can be circumvented by applying gas phase techniques.

Our current study focuses on the excited state dynamics associated with the photoisomerization of the 3,3'-diethyloxacarbocyanine cation (**DOC$^+$**). This system is a symmetric carbocyanine dye, consisting of two heterocyclic terminal groups linked by a chain of three conjugated carbon atoms. From ^{1}H-NMR measurements it is known that the *trans*-**DOC$^+$** isomer is the favored conformation in solution and upon electronic excitation isomerizes about the C8-C9-bond to form the 8,9-*cis* isomer via the S$_1$ excited state (dihedral angle θ, Scheme 1).[5-6]
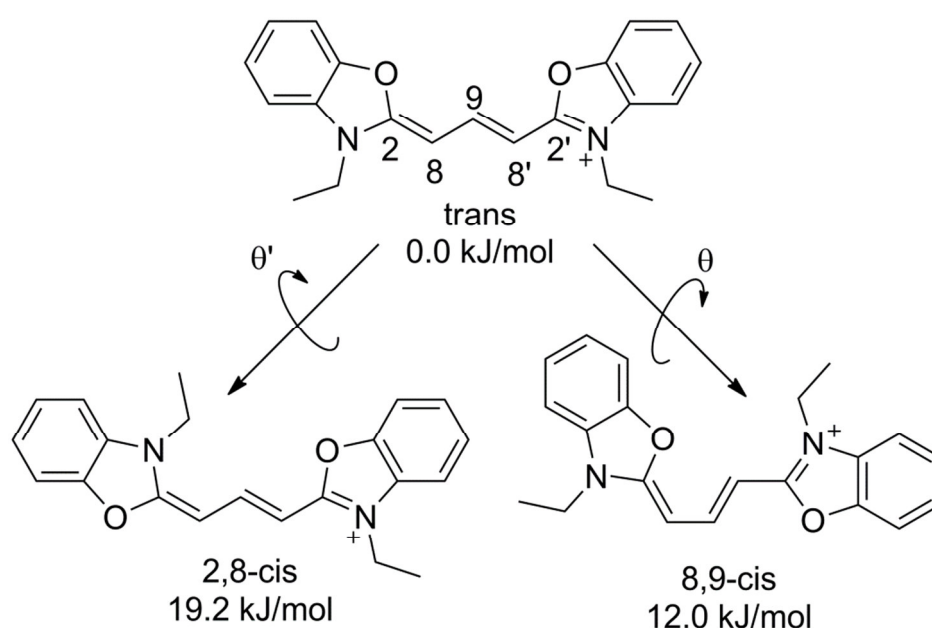
Scheme 1 Schematic structures of *trans*-, *2,8-cis*- and *8,9-cis*-**DOC$^+$**. Relative Gibbs energies were determined from B3LYP/6-31G(d) DFT geometry optimized structures.

Based on these reports, and a mainly mono-exponential excited state population decay observed in solution,[7-10] the formation of more than one isomer is typically

disregarded. However, a recent gas phase study by Adamson *et al.* on a structurally and electronically very similar cationic cyanine dye (3,3'-diethylthiacarbocyanine, DTC⁺) applying ion mobility spectrometry challenges the unequivocal identification of a single photoproduct.[11] In light of this recent report, we applied a gas phase method combining ion trap mass spectrometry with femtosecond (fs) laser spectroscopy to probe the excited state population dynamics of isolated **DOC⁺** ions by transient Vis-pump and NIR-probe photofragmentation (tPF) action spectroscopy. This study shall shed some light on the intrinsic early isomerization dynamics of **DOC⁺** and short-chain cyanine dyes in general.

5.4 Experimental setup and calculations

The iodine salt of **DOC⁺** was purchased from TCI Europe. Acetonitrile of LC-MS grade was purchased from Sigma-Aldrich and used without further purification. Steady-state PF and tPF experiments were conducted using a modified Paul-type quadrupole ion trap mass spectrometer (amaZon speed, Bruker Daltonics) in combination with a Ti:sapphire oscillator and amplifier system (Wyvern 1000™, KMLabs).[12] Briefly, **DOC⁺** was generated by electrospray ionization the iodine salt solution in acetonitrile ($c=1 \times 10^{-6}$ M) in positive ion mode. The sample solution was continuously infused by a syringe pump at a flow rate of 120 µL/h. Nitrogen as drying gas was set to a flow rate of 4 L/min at 180°C. Nebulizer pressure was set to 5 psi (345 mbar).

The fs laser pulses were generated in a cryogenic ultrafast regenerative laser amplifier system delivering 50 fs pulses at ~1 kHz repetition rate (central wavelength of ~785 nm). The pulse train was split to pump two optical parametric oscillators of white light continuum (TOPAS-C, Light Conversion) for generating pump and probe pulses of tunable wavelength (240-2500 nm). For steady state PF spectra the output from one of the TOPAS-C units was utilized in a spectral range of 350 nm up to 490 nm. The spectra were obtained by setting the laser pulses to the according wavelengths and measuring the intensity of the parent ion and the sum of fragment ions. The fragment yield was calculated according to $F_i/(F_i+P_i)$, where F_i and P_i are the sums of the intensities of fragment and parent ion signals, respectively, and normalized additionally by its numeric wavelength value to account for the different photon energies at constant laser pulse fluence, with a typical pulse intensity of ~1.5 µJ. Each isolated portion of ions was irradiated by 50 laser pulses.

For transient experiments the temporal delay between pump (405 nm, 415 nm, 430 nm, 455 nm, 465 nm, 0.5-0.7 µJ) and probe pulses (1200 nm, 120 µJ) was controlled via an optical delay line. Pump and probe pulses were spatially overlapped quasi-collinearly by focusing into the center of the Paul ion trap with a lens (f=50 cm). The beam diameter in the ion trap was estimated to be ~1 mm using the knife-edge technique. The relative polarization of pump and probe pulses was controlled by a Berek polarization compensator in the pump path and set to the magic angle (54.7°). Each isolated portion of ions was irradiated by 50 pump/probe pulse pairs.

The tPF signals were recorded as extracted ion chromatograms while continuously varying the delay between the pump and probe pulses. Evaluation of the transient signals was performed as $F_i/(F_i+P_j)$, where F_i and P_j are the sums of the intensities of fragment and parent ion signals, respectively. Fitting of the longer timescale kinetic traces was performed with Origin 2017G.

To evaluate the temporal resolution at a given pump/probe wavelength combination, we recorded the multiple-photon ionization signal of neutral furan in the ion trap as a function of time delay between the pump and probe pulses.[13] The obtained signal represents an intensity cross correlation function (ccf) of the pump and probe laser pulses. The instrumental system response was then estimated from the fwhm of the resulting Gaussian-shaped photoionization signal. For a pump+probe wavelength combination of 455 nm+1200 nm the ccf was estimated to be ~130 fs and applied in fitting of transients recorded for a shorter total pump-probe delay with an open source fitting software[14] running within the MATLAB environment.

Geometry optimization and single point energy calculations were performed using density functional theory (DFT) and time-dependent (TD-)DFT at the 6-31G(d)/B3LYP[15-16] level of theory within the Gaussian 09 program package.[17]

Steady state linear absorption spectra in acetonitrile solution (c=1·10^{-5} M) at room temperature were recorded using a Lambda 950 photospectrometer (PerkinElmer).

5.5 Results and discussion

5.5.1 Mass spectrometry and fragmentation behavior

Upon irradiation of the isolated **DOC⁺** ions with laser pulses in a wavelength range of 350-490 nm fragment products are formed (Figure 1).
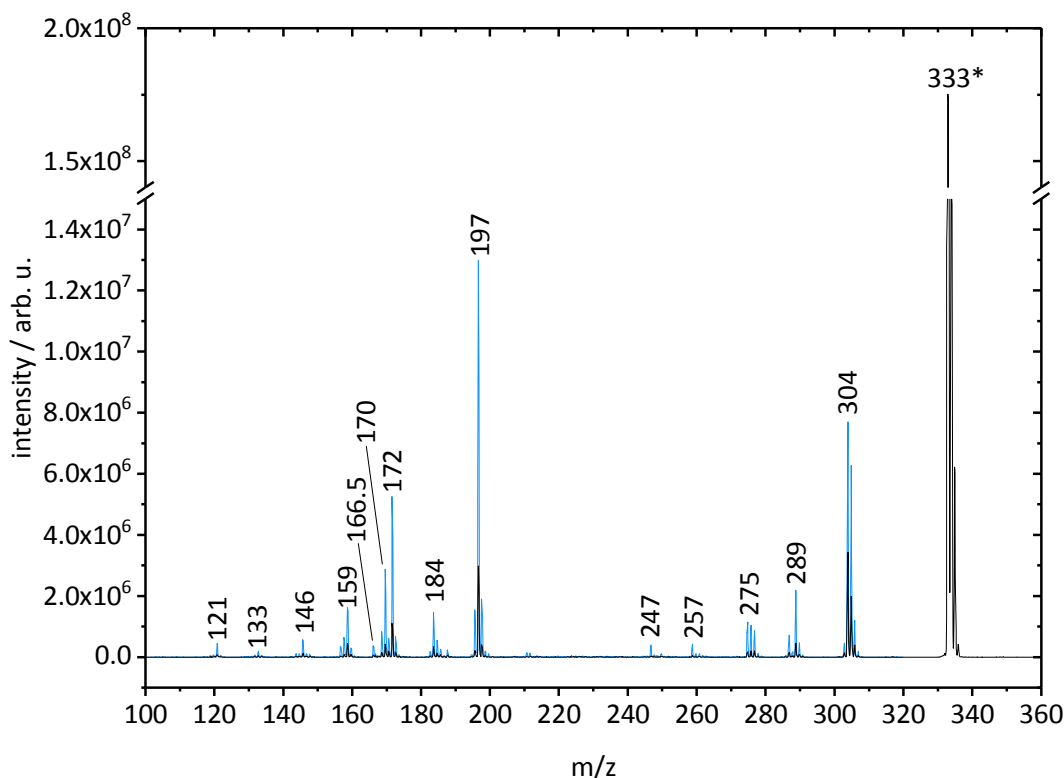

Figure 1 Mass spectrum depicting the formation of fragment ions upon photoexcitation of **DOC⁺** at λ_{ex}=455 nm. Black and blue spectra were recorded at 1.5 μJ and 3 μJ pulse energies, respectively. Asterisk denotes precursor ion signal.

The observed fragmentation behavior is quite complex, hence definite assignment to fragmentation channels remains for the most part speculative (Table S1). Nonetheless, several photoproducts could be identified, such as m/z 304 formed after the loss of an ethyl-side chain and the low-intensity product signal located at m/z 166.5 originating from electron detachment. Note that, with exception of the electron detachment channel, PF and collision induced dissociation (CID) yield similar fragment products (Figure S1), albeit at different intensity distributions of the occurring signals, with PF slightly favoring products at lower m/z ratios. The formation of lower m/z fragments thus allegedly requires higher internal activation energies, which only Vis-photoexcitation can provide.

5.5.2 Steady-state gas phase action and solution phase absorption spectra

Recording the fragmentation yield as a function of photoexcitation wavelength yields the photofragmentation (PF) action spectrum of **DOC⁺**, which is akin to the linear absorption spectrum in solution.
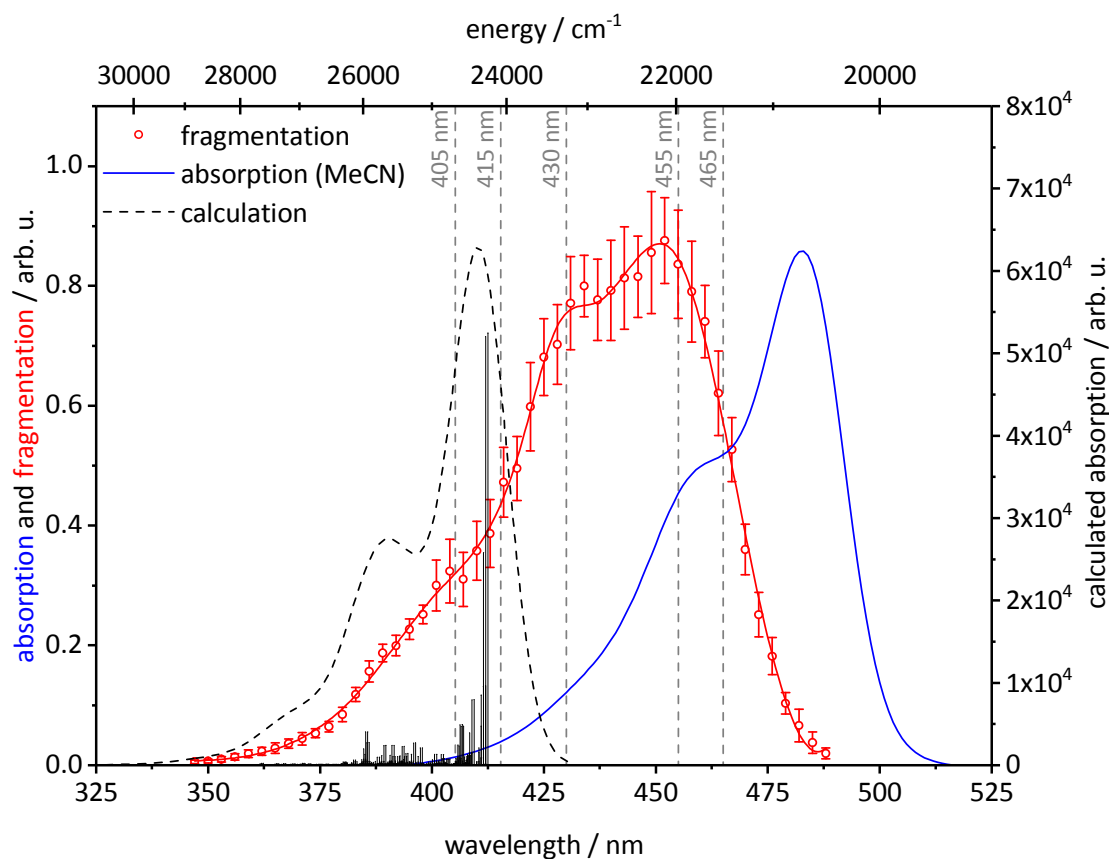

Figure 2 Linear absorption spectrum in acetonitrile (blue line), gas phase PF action spectrum (red, open circles) and calculated (vibrationally resolved) linear gas phase absorption spectrum (black, dashed line). Intensities of vibronic transitions (stick spectrum) were calculated at the (TD-)DFT/B3LYP/6-31(d) level and broadened by Gaussian functions of $400 \, \mathrm{cm}^{-1}$ fwhm to produce the (dashed) envelope. Vertical dashed lines denote pump-wavelengths in tPF experiments.

In terms of general band composition, the gas phase action spectrum (Figure 2, red open circles) compares remarkably well to the recorded linear absorption spectrum in acetonitrile solution (Figure 2, blue line), albeit being shifted hypsochromically by $\sim 1500 \, \mathrm{cm}^{-1}$, attributable to the lack of a stabilizing solvent environment. Both spectra feature absorption band progression at the respective high energy tail of the $S_1 \leftarrow S_0$ (0,0) transition located at ~ 450 nm (or ~ 480 nm in acetonitrile), typical for symmetric polymethine dyes. In literature the sub-band (~ 430 nm in PF spectrum) adjacent to the longest wavelength transition of cyanine dyes was assigned to vibronic fine structure

arising from C-C valence vibration of the polymethine chain.[18-19] The excitation of this vibronic state (0,v') in the S_1 excited state lies typically 1200-1300 cm^{-1} higher in energy with respect to a purely (0,0) electronic transition.[18-19] From our gas phase absorption spectrum we determined a spacing of $\sim$1250 cm^{-1} between the 0-0 and the adjacent 0-v' absorption band, which is in line with literature. Hence we assume vibrational fine structure being responsible for the band progression of the gas phase spectrum. Additionally, we calculated the vibrationally resolved absorption spectrum of *trans-*
DOC$^+$ by means of a DFT method implemented in the Gaussian 09 program package,[17] which determines the Franck-Condon factors for transitions between the vibronic states in the S_0 and S_1 states given the respective optimized geometries as input.[20] The theoretical spectrum reproduces the band structure quite well, further corroborating our assignment of the band structure to vibronic progression. Only the relative intensities of the (0,0) transition and the transitions to higher vibrationally excited states (0,v') in the gas phase spectrum do not match the experiment. In the gas phase spectrum the absorption band associated with the (0,0) transition has a much lower intensity then theoretically predicted, exhibiting only slightly higher signal intensity than the vibronic progression at $\sim$430 nm, which probably stems from an inherently lower fragmentation yield at higher wavelengths applying ion trap techniques.[12] This is due to fragmentation proceeding on a much longer timescale (μs-ms), most likely from a hot S_0 state after initial photoexcitation and subsequent IC, as implied by the similarity of fragmentation products by PF and CID (Figure S1). The fragmentation rate and hence the fragmentation efficiency is dictated by the amount of internal energy imparted to the molecular system upon photoexcitation. At longer wavelengths the excess energy after IC is smaller and fragmentation competes with collisional cooling with the helium buffer gas present inside the ion trap, resulting in generally lower fragmentation yields. Furthermore, one color PF requires probably the (subsequent) absorption of at least two photons (as suggested by the dependence of fragmentation yields on the pump-pulse energy; Figure S2), resulting in an overall lower excess energy at longer wavelengths and lower fragmentation due to collisional cooling.

A higher relative intensity of the vibronic sub-bands in the PF spectrum can alternatively be rationalized by a more pronounced geometry change upon excitation of the isolated ions in *vacuo*. The higher the shift of the potential well minimum of the S_1 state with respect to the S_0 minimum, the higher the intensity of the vibrational progression

associated with the respective molecular coordinate.[21] It is conceivable that the geometrical relaxation along the C-C-backbone of the polymethine bridge is unhindered in the gas phase, whereas in solution the solvent cage surrounding the molecules restricts elongation of the C-C-bonds, resulting in a smaller change in geometry and thus in a lower intensity of the vibronic progression. However, the TD-DFT optimized S_1 excited state geometries of the isolated and solvated molecules (employing the polarizable continuum conductor model, CPCM; Figure S4),[22-23] do not differ much, probably necessitating a more dedicated theoretical approach to verify our assumption.

5.5.3 Transient photofragmentation

As the absorption band of **DOC⁺** in the Vis region originates solely from excitation of different levels of vibrational modes in the S_1 excited state, it is possible to easily study the impact of excess energy on the excited state dynamics, without interference from higher lying excited states. Hence, for tPF measurements the isolated **DOC⁺** ions were pumped at various wavelengths ranging from 405 nm to 465 nm (marked in the PF action spectrum, Figure 3) and subsequently probed with higher intensity NIR pulses (1200 nm, 120 µJ). Note that a pump pulse wavelength below 405 nm or above 465 nm did not yield a two-color signal of sufficient quality, which restricted our study to this spectral range. The resulting tPF signals (for the sum of all fragments) are shown in Figure 3. All transient signals exhibit a rise on an ultrafast timescale (~200 fs) and decay back to the respective signal level at negative pump-probe delay. Signal decay could be satisfactorily modeled in all cases by a sum of two exponentials. We refrained from convoluting the exponential decay function with the ccf, as the transients do not exhibit characteristics of ultrafast decay on a sub-ps timescale. The resulting fitted lifetimes are presented in Table 1 together with the respective central pump pulse wavelengths used. Note that the transients recorded for λ_{pump}=405 nm and 415 nm (Figure 3 a and b) were recorded for a shorter total pump-probe delay (400 ps and 800 ps, respectively), but with a smaller step size between adjacent data points (1ps and 2 ps) to account for accelerated decay rates and in order to obtain more precise short timescale decay constants from fitting.
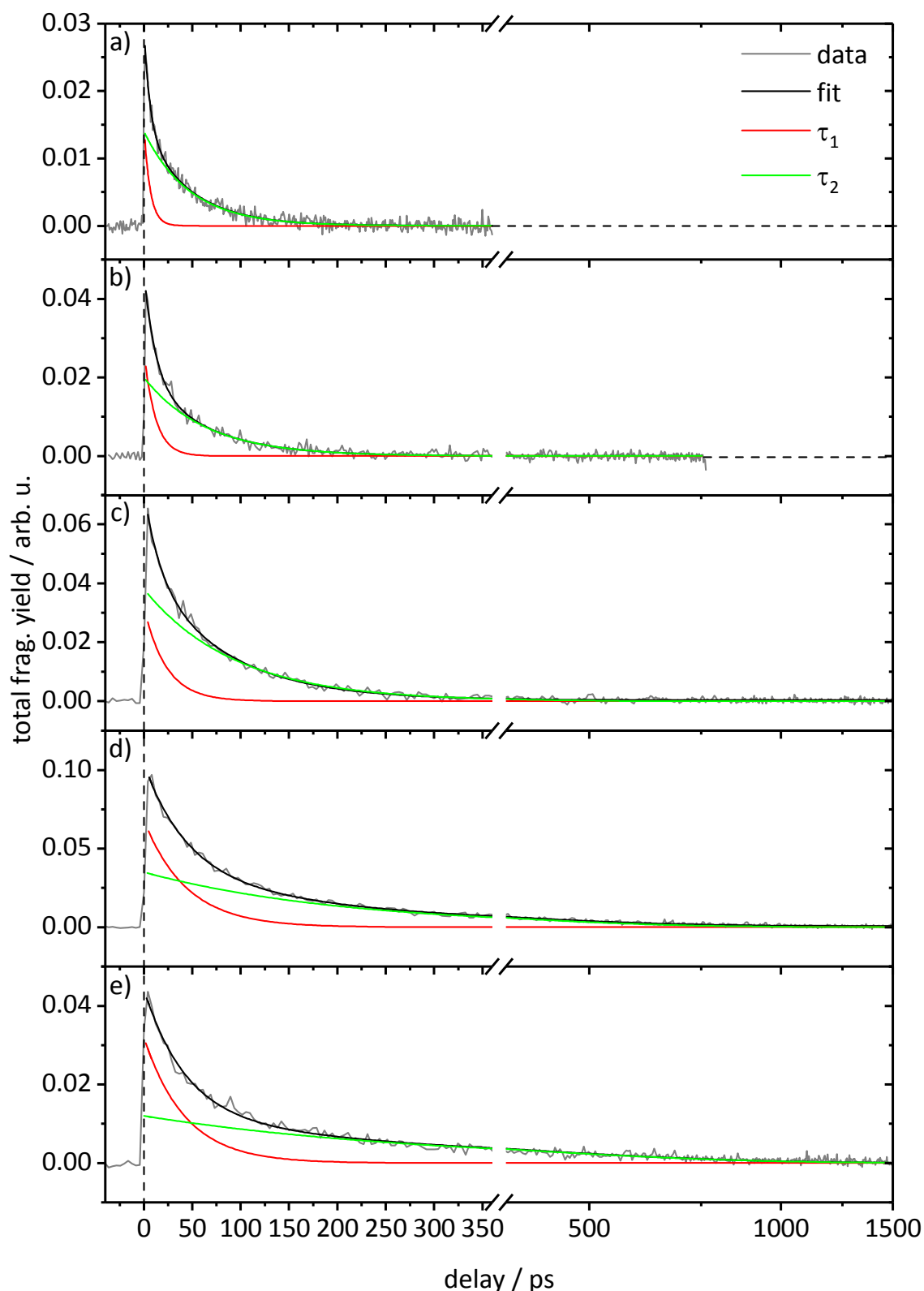
Figure 3 Total relative fragment ion yield as a function of pump-probe delay using different pump wavelengths: **(a)** 405 nm, **(b)** 415 nm, **(c)** 430 nm, **(d)** 455 nm and **(e)** 465 nm. Probe wavelength was kept the same (1200 nm). Data is shown in gray, whereas fits and fit decompositions are shown in black and color, respectively. Summary of fit parameters is given in Table 1. For the sake of clarity, fit residuals are presented separately in Figure S3.

Table 1 Fit parameters (lifetimes τ_i and decay amplitudes A_i) obtained from bi-exponential modeling of the tPF mass spectra measured using different pump wavelengths λ_{pump} (see Figure 3).

	λ_{pump} / nm	τ_1 / ps	A_1	τ_2 / ps	A_2
a)	405	6(.4)±0(.7)	0.015±0.001	47(.5)±1(.7)	0.014±0.002
b)	415	11(.8)±1(.0)	0.027±0.001	63(.9)±2(.9)	0.020±0.001
c)	430	23(.0)±2*	0.032±0.002	94(.2)±3(.6)	0.038±0.002
d)	455	44(.1)±2*	0.068±0.001	209(.7)±7(.5)	0.035±0.002
e)	465	42(.8)±2*	0.032±0.001	305(.2)±11(.4)	0.012±0.001

*) an uncertainty of ±2 is given as an upper boundary estimate, as step size is 4 ps between adjacent data points for c, d, and e.

Surprisingly, both time constants decrease with increasing photon energy, with the exception being the short decay constants τ_1 obtained for λ_{pump}=455 nm and 465 nm, which appear to be virtually of the same value. Additionally the relative amplitude ratio of the decay components (A_1 and A_2 corresponding to τ_1 and τ_2) seems to shift in favor of A_2 upon excitation with shorter pump pulse wavelengths. From these results we deduce that two competing relaxation pathways are probably responsible for the S_1 excited state population decay of **DOC+**, which proceed after overcoming an activation barrier. Furthermore, we assume that the second decay process has a slightly higher activation barrier and thus becomes more prominent using photons of higher energy. A bi-exponential excited state decay is, however, at first glance not easily rationalized, as described in the following:

In literature, **DOC+** was previously studied both theoretically[24-25] and experimentally in solution.[7-10, 26] The general model for radiationless relaxation of the S_1 excited state is believed to result from a torsional motion along the C8-C9 bond (or the equivalent C8'-C9 bond) in the conjugated backbone. This torsion promotes relaxation of the S_1 to S_0 state via a conical intersection, which is reached after overcoming an activation barrier of ~20-40 kJ/mol, estimated from liquid phase fluorescence studies in dependence on temperature and solvent.[7, 24] After IC to the S_0 state, the torsional pathway branches resulting in either the *trans-* or *cis*-isomer. The latter re-isomerizes to form the energetically favored *trans*-isomer on a millisecond timescale.[8] The model is illustrated in Figure 4 (right-side).
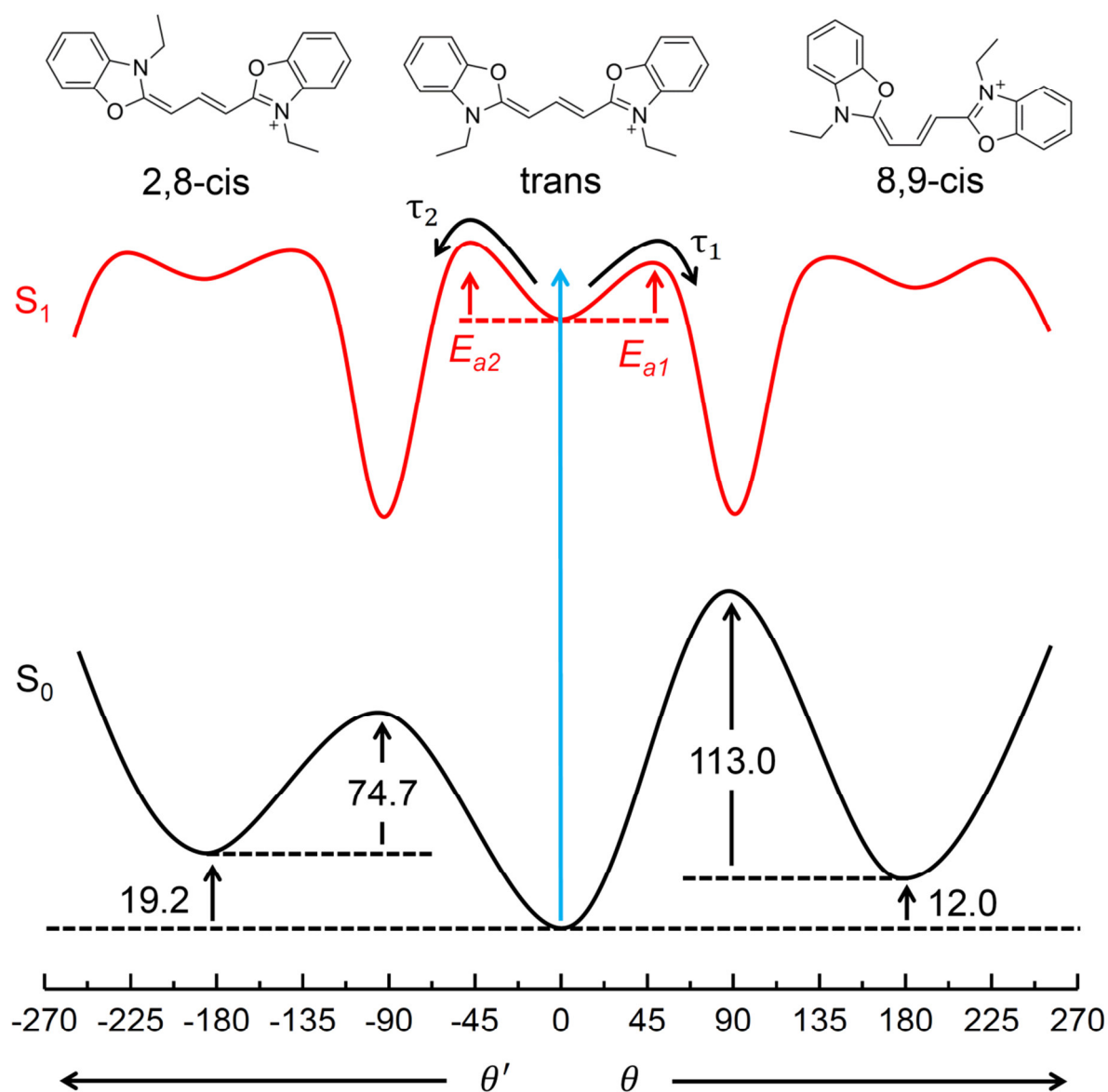
Figure 4 Schematic potential energy curves for the photoisomerization of **DOC+**. Left-side curves correspond to torsion along the 2,8 (2',8') C-C bond (θ'), whereas the right-side curves correspond to a 8,9 (8',9) C-C bond torsion (θ) to form the respective photoisomers. Heats of formation (in kJ/mol) for stationary points on the potential energy curves were obtained from B3LYP/6-31G(d) DFT calculations. Barrier heights (E_{a1}=21 kJ/mol and E_{a2}=32 kJ/mol) in the S_1 excited state were estimated from single point TD-DFT (B3LYP/6-31G(d)) calculations.

Generally, the existence of more than one photoisomer (8,9-cis) for **DOC+** (or cyanine dyes of similar chain length) in solution is dismissed, as excited state decay is mainly reported to proceed mono-exponentially[7-10] and ^{1}H-NMR studies point to only one photoproduct being formed, namely the 8,9-*cis* isomer.[5] From literature only one account is known to us in which bi-exponential fluorescence decay was observed and

tentatively assigned to the concurrent formation of two different photoisomerization products of **DOC+** (8,9-*cis* and 2,8-*cis)*.[26] In an earlier CS INDO theoretical study on **DOC+**, the S_1 excited state potential energy curve was calculated in dependence of the dihedral angles θ and θ', associated with the isomerization coordinate to form either the 8,9-*cis* or the 2,8-*cis* isomer, respectively.[25] The barrier for 8,9-cis isomerization (E_{a1}) was thereby determined to be at least 20 kJ/mol lower in energy, depending on the polarity of the solvent, in strong agreement with a favored solvent-driven relaxation along the twisting coordinate θ in solution. However, this argumentation is generally not applicable for our gas phase approach, as the excited ions are not prone to rapid thermalized under isolation. Hence relaxation may proceed via both the θ and θ' torsional coordinates, even if the latter requires slightly higher activation energies. Furthermore, recent photoisomerization studies by Adamson *et al.* on the structurally and electronically very similar cyanine dye DTC+ by ion mobility spectrometry gave evidence for the initial formation of both photoproducts, although the 2,8-*cis* population (which is deemed to be the favored isomer for DTC+ from liquid phase studies)[5] is quenched rapidly by collisions within the drift tube and hence not observed in longer timescale experiments.[11] A concurrent S_1 population decay via either isomerization coordinate thus appears to be feasible in the gas phase.

One more thing we would like to point out is the tunability of the pump wavelengths in our setup, which allowed us to impart higher internal energies upon photoexcitation to the S_1 state, trivializing the difference in barrier heights substantially. Different excitation wavelengths had obviously no influence on the order of the kinetics, always necessitating at least a bi-exponential decay model. To gain further insight into the S_1 excited state properties of **DOC+**, we estimated the isomerization barriers E_{a1} and E_{a2} from TD-DFT single point energy calculations by stepwise scanning the dihedral angle θ and θ', respectively (Figure S5). We obtained barrier heights of E_{a1}=21 kJ/mol and E_{a2}=32 kJ/mol, which are obviously to be understood as upper boundary values. Nevertheless, our theoretical calculations point to a relatively minor difference in barrier heights, making our assignment of the observed kinetics to competing 8,9-*cis* or the 2,8-*cis* isomerization processes plausible.

To further rationalize our assignment, we undertook a first attempt at estimating the activation barriers associated with either decay rate by means of a simple Arrhenius

model for a unimolecular reaction. This analysis required correlation of the excess vibrational energy in the S_1 excited state upon photon absorption and the resulting temperature of the photoexcited ions. The procedure is explained in more detail in the following section.

5.5.4 Estimation of activation barriers for trans-cis photoisomerization

To apply the Arrhenius equation, we needed to know the ion temperatures resulting from excitation at different pump photon energies, *i.e.* a correlation between the surplus of excess photon energy imparted and the corresponding rise in temperature had to be established. For this procedure, following boundary conditions had to be set:

i) Excitation at 485 nm (longest wavelength edge of the gas phase absorption spectrum, Figure 2) results in purely electronic excitation, providing no vibrational excess energy.

ii) The relative energy by excitation at shorter wavelengths than 485 nm results in complete conversion of the excess photon energy to vibrational (*i.e.* thermal energy) of the ions in the S_1 excited state. For example excitation at 455 nm≈263 kJ/mol (vs. 485 nm≈247 kJ/mol, zero excess energy) results in 16 kJ/mol excess thermal energy.

iii) The excited ions are fully thermalized upon excitation, *i.e.* the vibrational excess energy is distributed over a Boltzmann population of vibrational states.

iv) The initial temperature of the thermalized ground state ion population is estimated to be 300 K.

Based on these assumptions, we performed single point harmonic vibrational calculations at different ion temperatures (300–500 K) starting from a TD-DFT geometry optimized S_1 excited state structure of the *trans*-isomer. The thermal energy acquired from the calculation at 300 K ion temperature was set to 0 kJ/mol, *i.e.* thermal energies from calculations at higher ion temperatures are relative values and provide a correlation between the excess vibrational energy (by photoexcitation) and the resulting ion temperature (Figure 5 and Table 2).
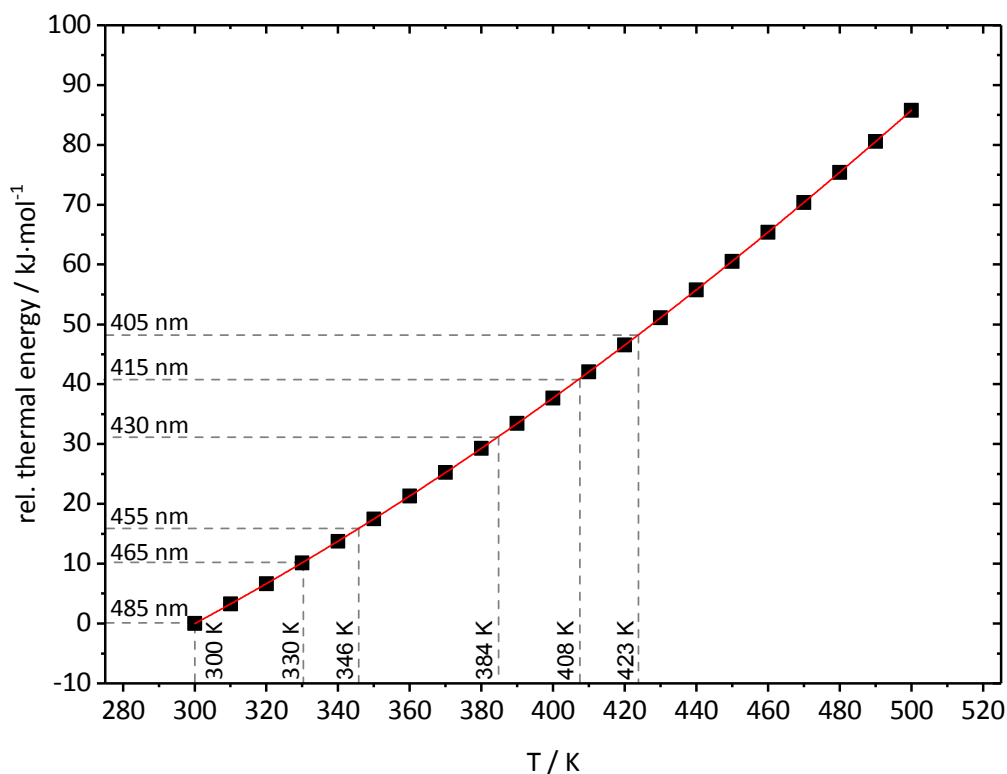
Figure 5 Relative thermal energies calculated for ion temperatures T in a range of 300-500 K, starting from a TD-DFT (B3LYP/6-31G(d)) geometry optimized S_1 excited structure of the *trans*-isomer. Data points were determined from single point harmonic vibrational calculations, whereas the red line is a Boltzmann fit.

Table 2 Central pump photon wavelengths λ_{pump}, photon energies E, relative thermal energies and the resulting ion temperatures T.

λ_{pump} / nm	photon energy E / kJ·mol^{-1}	rel. thermal energy / kJ·mol^{-1}	T / K
485	247	0	300
465	257	10	330
455	263	16	346
430	278	31	384
415	288	41	408
405	295	48	423

The resulting ion temperatures T (Table 2) and the experimental lifetimes τ_i were then used to determine the activation barriers E_{ai} according to the Arrhenius equation:

$$\ln\left(\frac{1}{\tau_i}\right) = \ln(A_i) - \frac{1}{T}\frac{E_{ai}}{R} \tag{1}$$
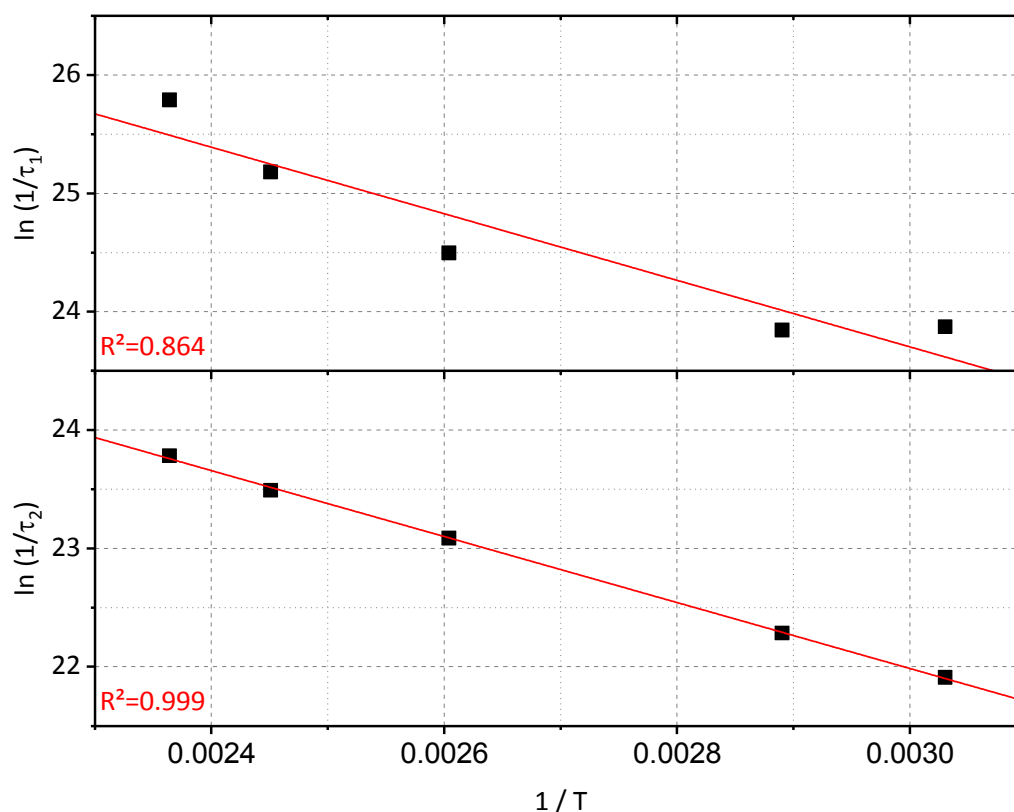
Figure 6 Arrhenius plots of the time constants from transient experiments at different pump wavelengths (Table 1) vs. the respective inverse ion temperatures (Table 2).

From the semi-logarithmic plot of the inverse lifetimes (*i.e.* rate constants) in Figure 6, it is obvious that the slower relaxation process τ_2 adheres to the Arrhenius relation remarkably well, whereas the faster process τ_1 is not in a good correlation. The slopes from linear regression are nearly identical ((-2786±540) kJ/mol and ((-2764±40) kJ/mol for τ_1 and τ_2), hence similar activation barriers for the fast and slow process are obtained, namely E_{a1}=23±5 kJ/mol and E_{a2}=23(±0.3) kJ/mol. If isomerization proceeded in a similar way along the respective twisting coordinate (θ and θ'), then we would expect a smaller value for E_{a1}, as the kinetics are much quicker. To obtain a smaller barrier, the linear fit in the Arrhenius plot should exhibit a more mellow descend, requiring the time constants τ_1 determined upon shorter

wavelength (Figure 3, a-c) pumping either to be longer or the time constants from longer wavelength pumping (Figure 3d and e) to be shorter. Although the fits given in Figure 3 are of good quality (Figure S4), we cannot exclude erroneously determined lifetimes to be the cause for a poor Arrhenius relation, as the values for τ_1 are relatively short and thus difficult to pin down precisely. It is also conceivable that isomerization to form the 8,9-*trans* isomer proceeds via a more complicated relaxation coordinate involving additional geometrical rearrangement rather than solely the rotation along the C8-C9 bond, on which our analysis was based on. Additionally, the redistribution of excess vibrational energy in the excited state may proceed on a timescale similar to the decay rates of the fast isomerization process, thus assuming a Boltzmann energy distribution over the vibrational states is more likely to produce faulty results for the faster kinetics and thus a poor Arrhenius relation, whereas slower dynamics may be less affected.

Nevertheless, the rate constants for the slower process τ_2 seem to abide the Arrhenius law and the estimated activation barrier E_{a2}=23 kJ/mol appears to be in good qualitative agreement with the theoretical value E_{a2}=32 kJ/mol we determined from single point calculations. Admittedly, our analysis was based on some drastic boundary conditions. One of these (i) required us to define a photon energy, which would result in a pure electronic excitation without additional "heating" of the excited ions. We set the energy at a photon wavelength of 485 nm ($\approx$247 kJ/mol) as a point of reference. If this zero-point is shifted, then accordingly the determined activation barriers would be different as well. However, only a shift to higher photon energies, *i.e.* lower photon wavelengths, is feasible for the analysis, as the zero-point was already set to the longest wavelength edge of the gas phase action spectrum (Figure 2). If the zero-point was set to a higher photon energy value, then the resulting activation barrier would be lower. Setting the zero-point to *e.g.* λ=465 nm ($\approx$257 kJ/mol$\hat{=}$0 kJ/mol relative thermal energy), would yield a barrier of ~18 kJ/mol. Thus the value we first determined (E_{a2}=23 kJ/mol) can be at least regarded as an upper boundary estimate for the gas phase relaxation of **DOC**$^+$ by isomerization.

5.5.5 Vibrational wave-packet dynamics in DOC⁺

Apart from ultrafast dynamics on a picosecond timescale, the tPF signal of **DOC⁺** was found to be periodically modulated, which was only recorded in good quality using a pump wavelength of 455 nm (Figure 5).
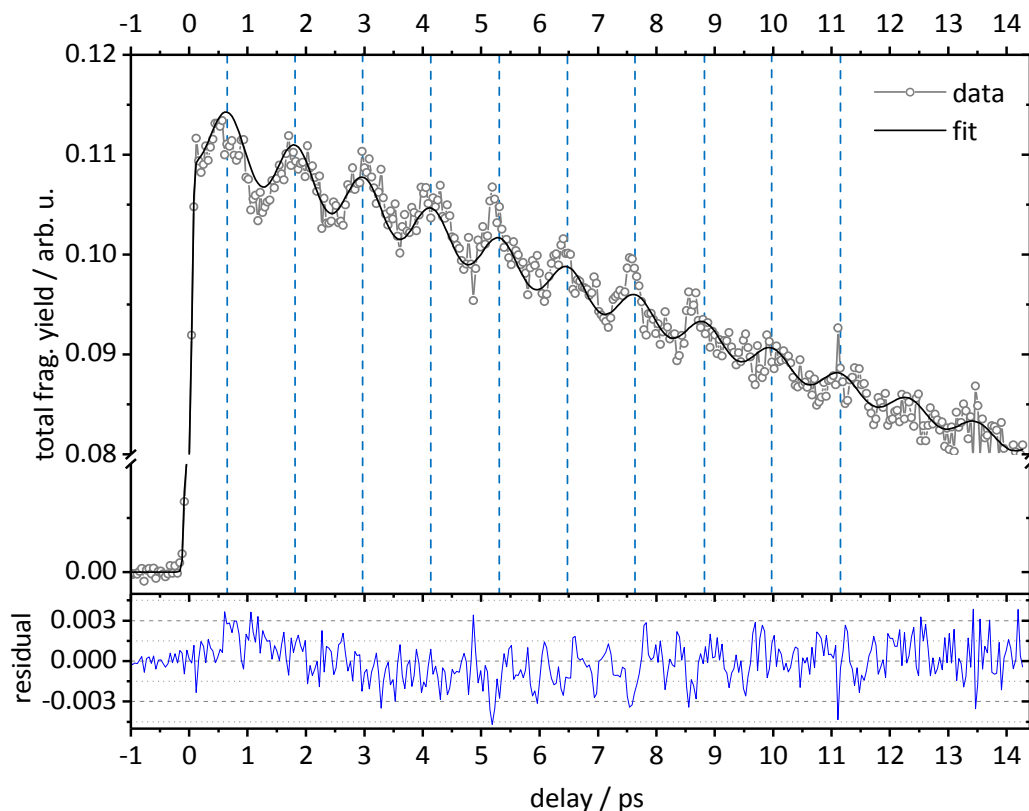

Figure 5 Modulated transient signal of **DOC⁺** obtained for λ_{pump}=455 nm and λ_{probe}=1200 nm. Data points are shown as open circles, whereas black line denotes the fitted signal based on a damped cosine function on top of an exponential decay, convoluted with the system response (ccf~130 fs)

Oscillations on top of transient signals are indicative of vibrational wave-packet motion, which is formed upon coherent excitation of several vibrational modes in the respective excited state.[27] The period of the resulting signal modulation is then dictated by energy spacing between the vibrationally excited states, *i.e.* the frequency of the vibrational mode in question.[27] The experimental tPF signal was modeled using an exponential decay modulated by a damped cosine oscillation and convoluted with the ccf function (130 fs). The period of the oscillation was determined to be ~T=1.2±0.1 ps, corresponding to a vibrational frequency of ~28±2 cm⁻¹, which is remarkably slow, given the size of the molecular system. Furthermore, the wave-packet exhibits a strikingly long lifetime, with a fitted dephasing time of ~13±3 ps. To the best of our

knowledge, only a few reports on excited state vibrational coherence associated with an isomerization coordinate in solution studies on cyanine dyes can be found in literature, but none in the gas phase. Recently, Beck *et al.* observed vibrational wave-packet dynamics for the cyanine dye Cy5 in water by transient absorption spectroscopy and assigned the excited state vibrational coherence to a mode of mixed C-C bond length alternation and twisting character.[28] Other research groups also observed wave-packet dynamics, which were attributed to a torsional or stretching vibration within the polymethine bridge.[29-33] The vibrational frequencies of these modes were, however, reported to be much higher (200-300 cm^{-1}) and additionally damped on a sub-picosecond timescale. To gain a qualitative insight into the conceivable dynamics and involved vibrational modes, we turn to the results from our harmonic vibrational calculations we performed for the S_1 excited state geometry of **DOC$^+$**, which reveal several low frequency (<100 cm^{-1}) vibrational modes (Figure S6). The three lowest energy vibrational modes have calculated vibrational frequencies of $\tilde{\nu}_1$=20.0 cm^{-1}, $\tilde{\nu}_2$=27.4 cm^{-1} and $\tilde{\nu}_3$=28.4 cm^{-1} corresponding to a torsional motion along the polymethine backbone and the in-plane and out-of-plane bending motion of the benzoxazole units, respectively. The remaining low frequency modes mainly involve torsion and bending motions of the ethane side-chains ($\tilde{\nu}_3$-$\tilde{\nu}_8$). The torsional and bending motions of the side-chains in our signal are presumably not the cause of signal modulation as these modes do not induce a change in molecular geometry, which could have a profound effect on electronic character of the system. Thus an impact on the probe pulse absorption cross section is not expected. The three modes lowest in frequency, however, should impair conjugation within the polymethine backbone and consequently affect the electronic structure of **DOC$^+$** significantly. Hence we conclude that the signal modulation we observe in our experiments can be traced back to either the torsion within the conjugated C-C chain, bending motion of the benzoxazole units with respect to each other or a combination of these modes. At this point of our study, the observation of a torsional mode should come as no surprise, with regard to the accepted mechanism for the excited state deactivation of cyanine dyes. However, it is puzzling that ours is the first reported case of wave-packet dynamics of long coherence time, which can be associated with the torsional isomerization coordinate in view of the staggering amount of experimental studies on cyanine dyes. Note that the majority of experimental studies on cyanines of various lengths were conducted in solution, in

which wave-packet dynamics may be damped rapidly, due to interaction with the solvent. Additionally, longer chain cyanines may exhibit lower activation barriers in the S_1 state,[24] promoting faster IC and thus shorter decoherence times.

5.6 Conclusion

We carried out tPF experiments on isolated **DOC$^+$** ions in an ion trap to probe its intrinsic excited state dynamics. The S_1 excited state population of **DOC$^+$** decays bi-exponentially, in contrast to solution phase studies found in literature, which mostly reported mono-exponential kinetics. Both relaxation rates decrease upon excitation with higher energy pump-photons, which is indicative of two activated processes in the S_1 excited state. In a first attempt to estimate activation barriers by means of a simple Arrhenius relation, we determined an upper boundary value of E_{a2}=23 kJ/mol associated with the slower relaxation process, which is reasonable agreement with the barrier height for the 2,8-cis photoisomerization of **DOC$^+$** determined from single point energy calculations. We furthermore observed vibrational wave-packet dynamics, manifesting themselves in a periodic modulation of the transient signal with a period of $\sim$T=1.2 ps. The corresponding vibrational frequency of $\sim$28 cm^{-1} correlates well with one of the three lowest frequency vibrational modes calculated for the S_1 excited state of **DOC$^+$**. These modes encompass twisting of the C-C polymethine backbone and the in- and out-of-plane bending of the benzoxazole terminal groups with respect to each other. The torsional motion is of particular interest, as twisting of the polymethine backbone is generally believed to promote excited state relaxation in cyanine dyes.

5.7 References

[1]   A. Wand, I. Gdor, J. Y. Zhu, M. Sheves, S. Ruhman, *"Shedding New Light on Retinal Protein Photochemistry"*, *Annu. Rev. Phys. Chem.* **2013**, *64*, 437-458.

[2]   B. K. Pathem, S. A. Claridge, Y. B. Zheng, P. S. Weiss, *"Molecular Switches and Motors on Surfaces"*, *Annu. Rev. Phys. Chem.* **2013**, *64*, 605-630.

[3]   W. R. Browne, B. L. Feringa, *"Light Switching of Molecules on Surfaces"*, *Annu. Rev. Phys. Chem.* **2009**, *60*, 407-428.

[4]   A. Mishra, R. K. Behera, P. K. Behera, B. K. Mishra, G. B. Behera, *"Cyanines during the 1990s: A Review"*, *Chem. Rev.* **2000**, *100*, 1973-2012.

[5]   S. Ghelli, G. Ponterini, *"Identification of the photoisomers of two carbocyanines by 1H NMR spectroscopy"*, *J. Mol. Struct.* **1995**, *355*, 193-200.

[6]   I. Baraldi, A. Carnevali, F. Momicchioli, G. Ponterini, *"Electronic spectra and trans—cis photoisomerism of carbocyanines. A theoretical (CS INDO CI) and experimental study"*, *Spectrochim. Acta Mol. Spectrosc.* **1993**, *49*, 471-495.

[7]   P. F. Aramendia, R. M. Negri, E. S. Roman, *"Temperature Dependence of Fluorescence and Photoisomerization in Symmetric Carbocyanines.Influence of Medium Viscosity and Molecular Structure"*, *J. Phys. Chem.* **1994**, *98*, 3165-3173.

[8]   Y. H. Meyer, M. Pittman, P. Plaza, *"Transient absorption of symmetrical carbocyanines"*, *J. Photochem. Photobiol.Chem.* **1998**, *114*, 1-21.

[9]   G. Ponterini, F. Momicchioli, *"Trans-cis photoisomerization mechanism of carbocyanines: experimental check of theoretical models"*, *Chem. Phys.* **1991**, *151*, 111-126.

[10]   L. Scaffardi, R. E. Di Paolo, R. Duchowicz, *"Simultaneous absorption and fluorescence analysis of the cyanine dye DOCI"*, *J. Photochem. Photobiol.Chem.* **1997**, *107*, 185-188.

[11]   B. D. Adamson, N. J. A. Coughlan, G. da Silva, E. J. Bieske, *"Photoisomerization Action Spectroscopy of the Carbocyanine Dye DTC+ in the Gas Phase"*, *J. Phys. Chem. A* **2013**, *117*, 13319-13325.

[12]   D. Imanbaew, Y. Nosenko, C. Kerner, K. Chevalier, F. Rupp, C. Riehn, W. R. Thiel, R. Diller, *"Excited-state dynamics of a ruthenium(II) catalyst studied by transient photofragmentation in gas phase and transient absorption in solution"*, *Chem. Phys.* **2014**, *442*, 53-61.

[13]   D. Nolting, T. Schultz, I. V. Hertel, R. Weinkauf, *"Excited state dynamics and fragmentation channels of the protonated dipeptide H2N-Leu-Trp-COOH"*, *Phys. Chem. Chem. Phys.* **2006**, *8*, 5247-5254.

[14]   S. Preus, *"DecayFit - Fluorescence Analysis Software 1.3"*.

[15]   A. D. Becke, *"Density-functional thermochemistry. III. The role of exact exchange"*, *J. Chem. Phys.* **1993**, *98*, 5648-5652.

[16]   C. Lee, W. Yang, R. G. Parr, *"Development of the Colle-Salvetti correlation-energy formula into a functional of the electron density"*, *Phys. Rev. B* **1988**, *37*, 785-789.

[17]   M. J. Frisch, G. W. Trucks, H. B. Schlegel, G. E. Scuseria, M. A. Robb, J. R. Cheeseman, G. Scalmani, V. Barone, B. Mennucci, G. A. Petersson, H. Nakatsuji, M. Caricato, X. Li, H. P. Hratchian, A. F. Izmaylov, J. Bloino, G. Zheng, J. L. Sonnenberg, M. Hada, M. Ehara, K. Toyota, R. Fukuda, J. Hasegawa, M. Ishida, T. Nakajima, Y. Honda, O. Kitao, H. Nakai, T. Vreven, J. A. Montgomery Jr., J. E. Peralta, F. Ogliaro, M. J. Bearpark, J. Heyd, E. N. Brothers, K. N. Kudin, V. N. Staroverov, R. Kobayashi, J. Normand, K. Raghavachari, A. P. Rendell, J. C. Burant, S. S. Iyengar, J. Tomasi, M. Cossi, N. Rega, N. J. Millam, M. Klene, J. E. Knox, J. B. Cross, V. Bakken, C. Adamo, J. Jaramillo, R. Gomperts, R. E. Stratmann, O. Yazyev, A. J. Austin, R. Cammi, C. Pomelli, J. W. Ochterski, R. L. Martin, K. Morokuma, V. G. Zakrzewski, G. A. Voth, P. Salvador, J. J. Dannenberg, S. Dapprich, A. D. Daniels, Ö. Farkas, J. B. Foresman, J. V. Ortiz, J. Cioslowski, D. J. Fox, Gaussian, Inc., Wallingford, CT, USA, **2009**.

[18]   W. West, A. L. Geddes, *"The Effects of Solvents and of Solid Substrates on the Visible Molecular Absorption Spectrum of Cyanine Dyes"*, *J. Phys. Chem.* **1964**, *68*, 837-847.

[19]   W. West, S. Pearce, *"The Dimeric State of Cyanine Dyes"*, *J. Phys. Chem.* **1965**, *69*, 1894-1903.

[20]   M. Dierksen, S. Grimme, *"Density functional calculations of the vibronic structure of electronic absorption spectra"*, *J. Chem. Phys.* **2004**, *120*, 3544-3554.

[21]   H. Mustroph, K. Reiner, J. Mistol, S. Ernst, D. Keil, L. Hennig, *"Relationship between the Molecular Structure of Cyanine Dyes and the Vibrational Fine Structure of their Electronic Absorption Spectra"*, *ChemPhysChem* **2009**, *10*, 835-840.

[22] M. Cossi, N. Rega, G. Scalmani, V. Barone, *"Energies, structures, and electronic properties of molecules in solution with the C-PCM solvation model"*, J. Comput. Chem. **2003**, *24*, 669-681.

[23] V. Barone, M. Cossi, *"Quantum Calculation of Molecular Energies and Energy Gradients in Solution by a Conductor Solvent Model"*, J. Phys. Chem. A **1998**, *102*, 1995-2001.

[24] J. Rodríguez, D. Scherlis, D. Estrin, P. F. Aramendía, R. M. Negri, *"AM1 Study of the Ground and Excited State Potential Energy Surfaces of Symmetric Carbocyanines"*, J. Phys. Chem. A **1997**, *101*, 6998-7006.

[25] I. Baraldi, A. Carnevali, F. Momicchioli, G. Ponterini, G. Berthier, *"Photoisomerization of 3,3'-diethyloxacarbocyanine (DOC) and 3,3'-diethylthiacarbocyanine (DTC): CS INDO CI potential energy curves for the free and solvated molecules"*, Gazz. Chim. Ital. **1996**, *126*, 211-215.

[26] J. Kabatc, J. Pączkowski, *"The photophysical and photochemical properties of the oxacarbocyanine and thiacarbocyanine dyes"*, Dyes and Pigments **2004**, *61*, 1-16.

[27] M. Gruebele, A. H. Zewail, *"Femtosecond wave packet spectroscopy: Coherences, the potential, and structural determination"*, J. Chem. Phys. **1993**, *98*, 883-902.

[28] M. M. Bishop, J. D. Roscioli, S. Ghosh, J. J. Mueller, N. C. Shepherd, W. F. Beck, *"Vibrationally Coherent Preparation of the Transition State for Photoisomerization of the Cyanine Dye Cy5 in Water"*, J Phys. Chem. B **2015**, *119*, 6905-6915.

[29] B. Dietzek, A. N. Tarnovsky, A. Yartsev, *"Visualizing overdamped wavepacket motion: Excited-state isomerization of pseudocyanine in viscous solvents"*, Chem. Phys. **2009**, *357*, 54-62.

[30] K. Misawa, T. Kobayashi, *"Wave-packet dynamics in a cyanine dye molecule excited with femtosecond chirped pulses"*, J. Chem. Phys. **2000**, *113*, 7546-7553.

[31] W. P. de Boeij, M. S. Pshenichnikov, D. A. Wiersma, *"System–Bath Correlation Function Probed by Conventional and Time-Gated Stimulated Photon Echo"*, J. Phys. Chem. **1996**, *100*, 11806-11823.

[32] B. Dietzek, B. Brüggemann, T. Pascher, A. Yartsev, *"Pump-Shaped Dump Optimal Control Reveals the Nuclear Reaction Pathway of Isomerization of a Photoexcited Cyanine Dye"*, J. Am. Chem. Soc. **2007**, *129*, 13014-13021.

[33] Z. Wei, T. Nakamura, S. Takeuchi, T. Tahara, *"Tracking of the Nuclear Wavepacket Motion in Cyanine Photoisomerization by Ultrafast Pump–Dump–Probe Spectroscopy"*, J. Am. Chem. Soc. **2011**, *133*, 8205-8210.

5.8 Supplementary material to "A new twist to cyanine photoisomerization by ultrafast ion trap action spectroscopy"

Content

5.8.1 Mass spectrometric data

Figure S1 Fragment mass spectra **DOC⁺** after PF and CID

Table S1 Identified fragment ion signals of **DOC⁺**

5.8.2 Photofragmentation

Figure S2 Pulse energy dependent fragment yields at λ_{ex}=455 nm and 430 nm

Figure S3 Fit residuals from theoretical bi-exponential modeling of the transient fragment mass signals

5.8.3 (TD-)DFT calculations

Figure S4 Bond lengths in the conjugated polymethine bridge from S_0 and S_1 geometry optimized structures of **DOC⁺** in the gas phase and acetonitrile solution

Figure S5 S_1 potential energy curve for the isomerization about the C8-C9 and C2-C8 bonds of **DOC⁺**, obtained from TD-DFT single point calculations.

Figure S6 Low frequency vibrational modes calculated for the S_1 geometry of **DOC⁺**

5.8.4 References

5.8.1 Mass spectrometric data
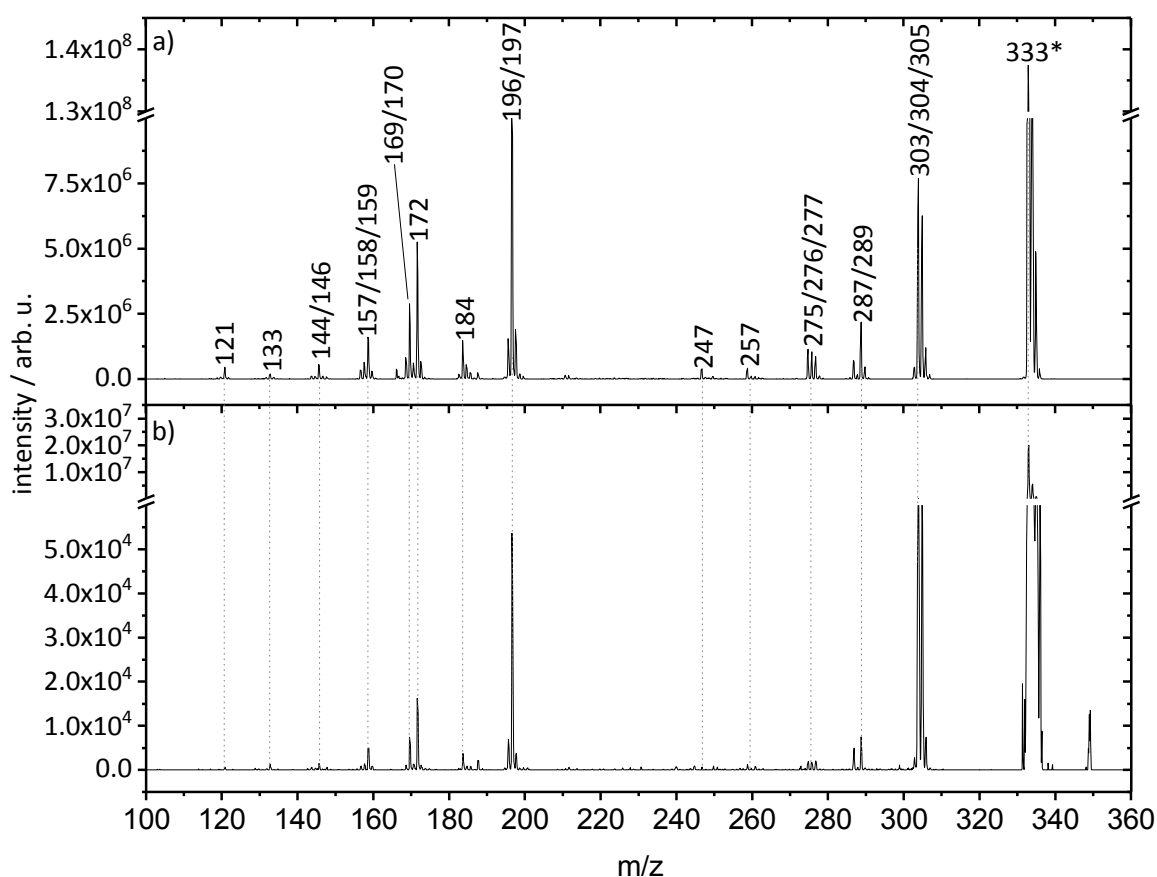
Figure S1 Fragment channel intensity distribution observed by PF **(a**; λ_{ex}=455 nm, 3 µJ**)** and CID **(b)**. Assigned fragment signals are listed in Table S1.

Table S1 Overview over observed and identified ion signals from mass spectra shown in Figure 1 and Figure S2. Numeric values denote the most abundant signal of the respective isotope pattern.

m/z	mass loss / Da	assigned neutral loss
333*)	-	-
303/304/305	30/29/28	$C_2H_6/C_2H_5/C_2H_4$
287/289	46/44	$C_2H_6+CH_4/C_2H_5+CH_3$
275/276/277	58/57/56	$2xC_2H_5/C_2H_5+C_2H_4/2xC_2H_4$
257	76	C_6H_4
247	86	not assigned
196/197	137/136	$C_8H_{10}NO/ C_8H_{11}NO$
184	149	$C_9H_{11}NO$
172	161	not assigned
169/170	164/163	not assigned
166.5	-**)	e^-
157/158/159	176/175/174	not assigned
144/146	189/187	not assigned
133	200	not assigned
121	212	not assigned

*)precursor ion signal: DOC$^+$, **)electron detachment channel

5.8.2 Photofragmentation
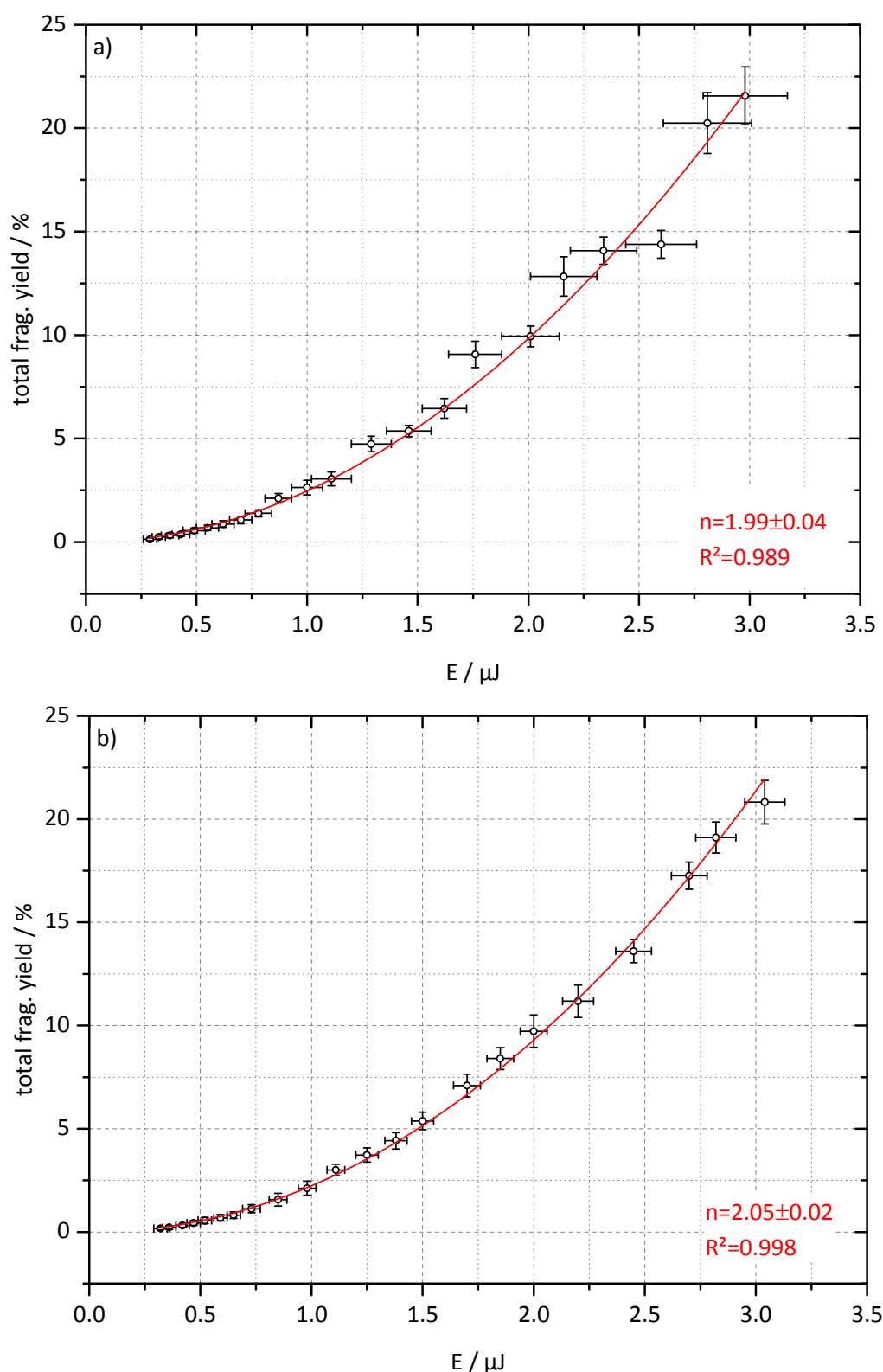
Figure S2 Pulse energy dependent E total fragmentation yield Y of **DOC$^+$** by one-color photoexcitation at λ_{ex}=455 nm **(a)** and 430 nm **(b)**. Dependencies were evaluated according to $Y = A \cdot E^n$,[1] where n is a mean value for the number of photons absorbed to induce fragmentation and A a dimensionless fit-parameter.
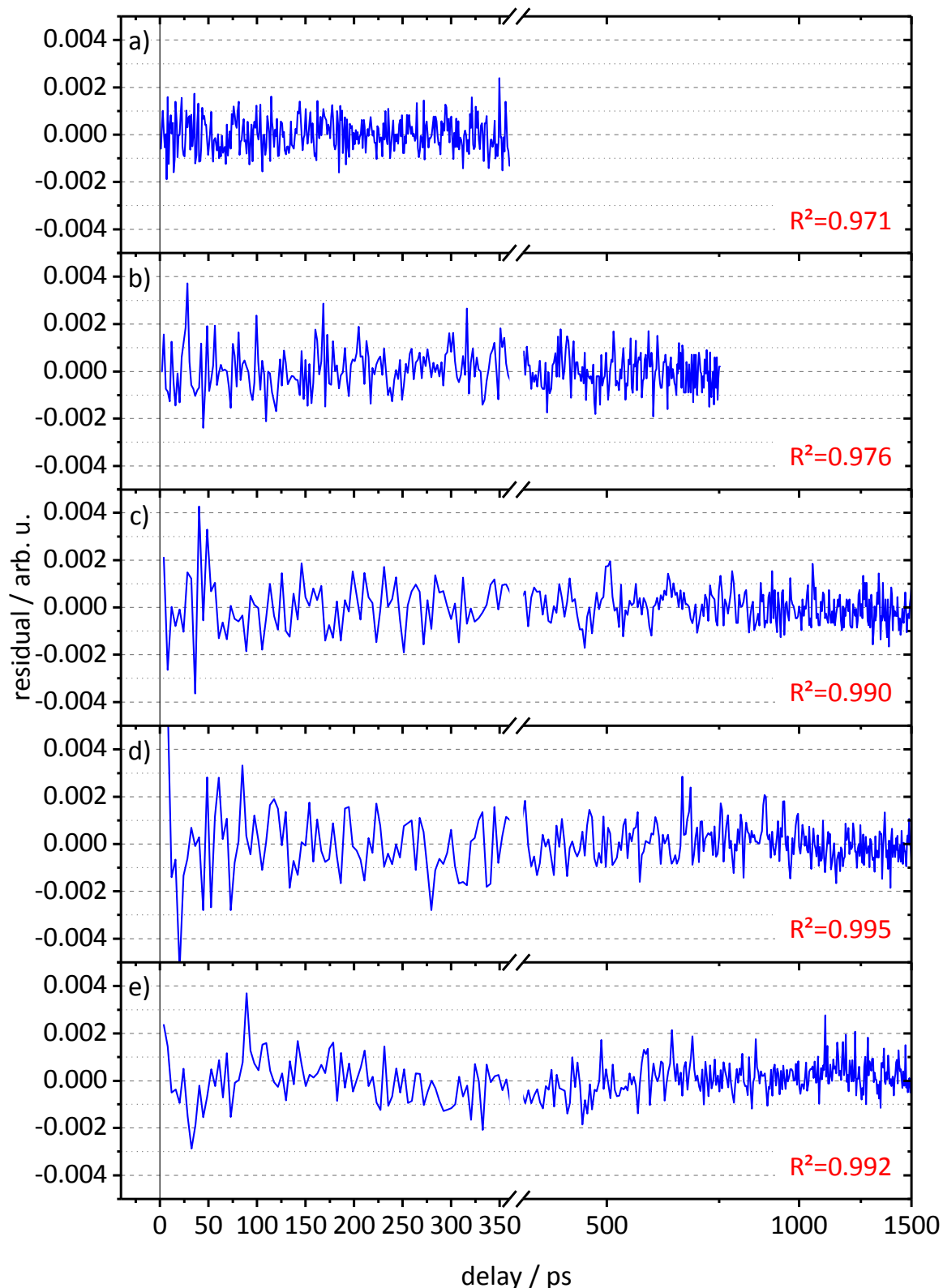
Figure S3 Fit residuals obtained from bi-exponential modeling of the transients pump-probe signals (Figure 3) measured using different pump wavelengths: **(a)** 405 nm, **(b)** 415 nm, **(c)** 430 nm, **(d)** 455 nm and **(e)** 465 nm.

5.8.3 (TD-)DFT calculations
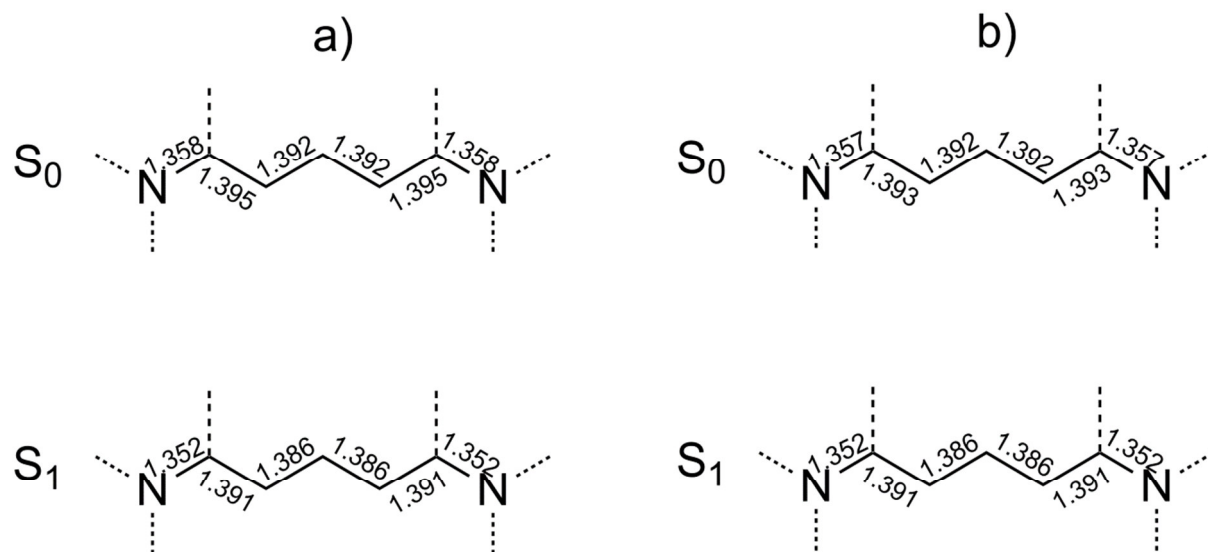
Figure S4 Bond lengths (in Å) in the conjugated bridge of **DOC⁺**, determined from (TD)-DFT geometry optimized (B3LYP/6-31G(d)) structures of the S_0 and S_1 state. Calculations were performed either for the isolated **(a)** or the solvated system **(b)** employing the polarizable continuum conductor model (CPCM, acetonitrile). The total chain length within the polymethine backbone decreases by 0.032 Å **(a)** and 0.026 Å **(b)**, respectively in the S_1 state.
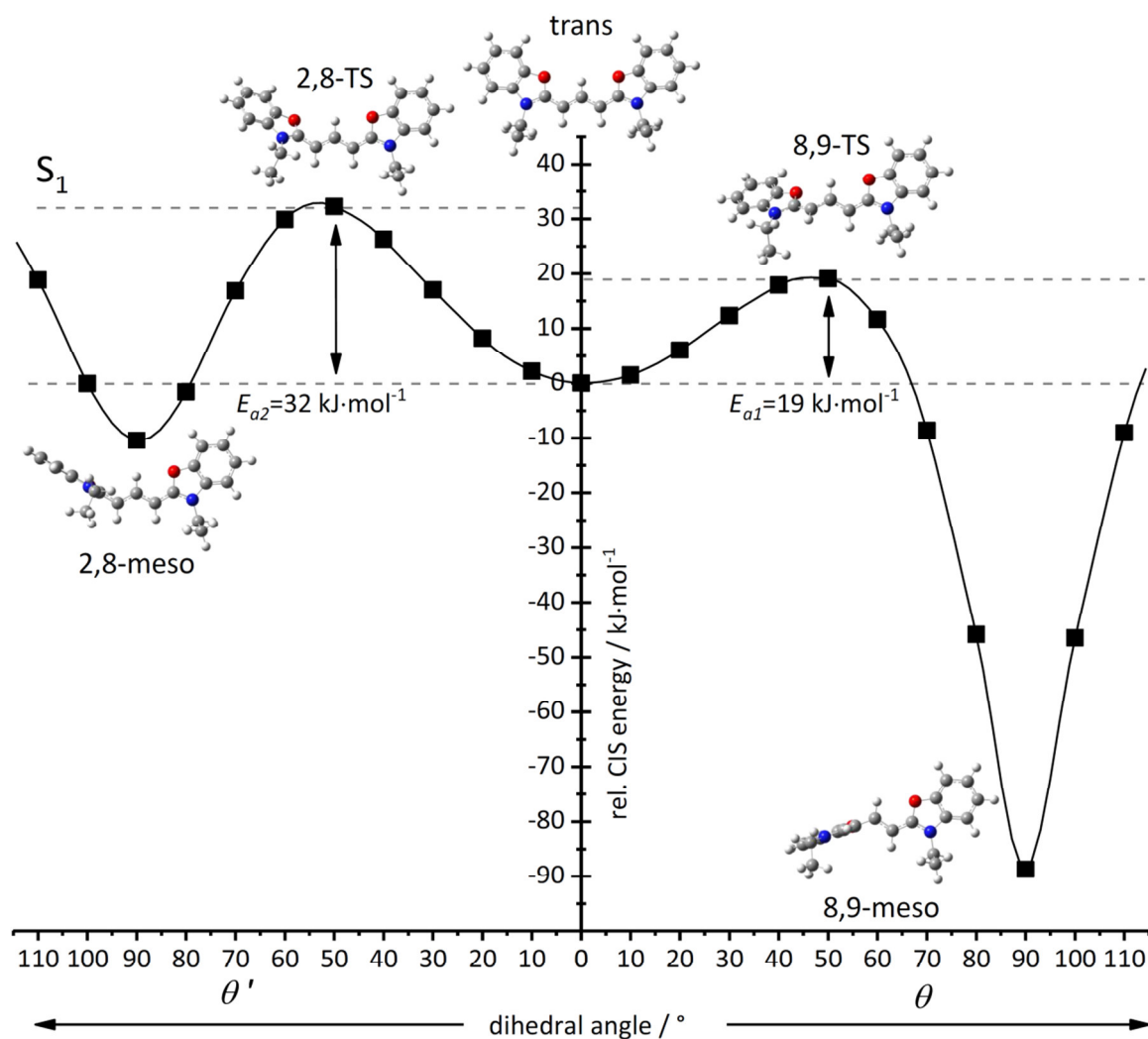
Figure S5 S_1 potential energy curve for the isomerization about the C8-C9 (right, θ) and C2-C8 (left, θ') bonds of **DOC⁺**, obtained from TD-DFT single point calculations. "TS" denotes estimated transition state geometries, whereas "meso" denotes geometries probably found at the conical intersection between the S_1 and S_0 states.

$\tilde{\nu}_1 = 20.0$ cm^{-1}

$\tilde{\nu}_2 = 27.4$ cm^{-1}

$\tilde{\nu}_3 = 28.4$ cm^{-1}

$\tilde{\nu}_4 = 51.6$ cm^{-1}

$\tilde{\nu}_5 = 53.4$ cm^{-1}

$\tilde{\nu}_6 = 68.9$ cm^{-1}

$\tilde{\nu}_7 = 78.2$ cm^{-1}

$\tilde{\nu}_8 = 84.6$ cm^{-1}
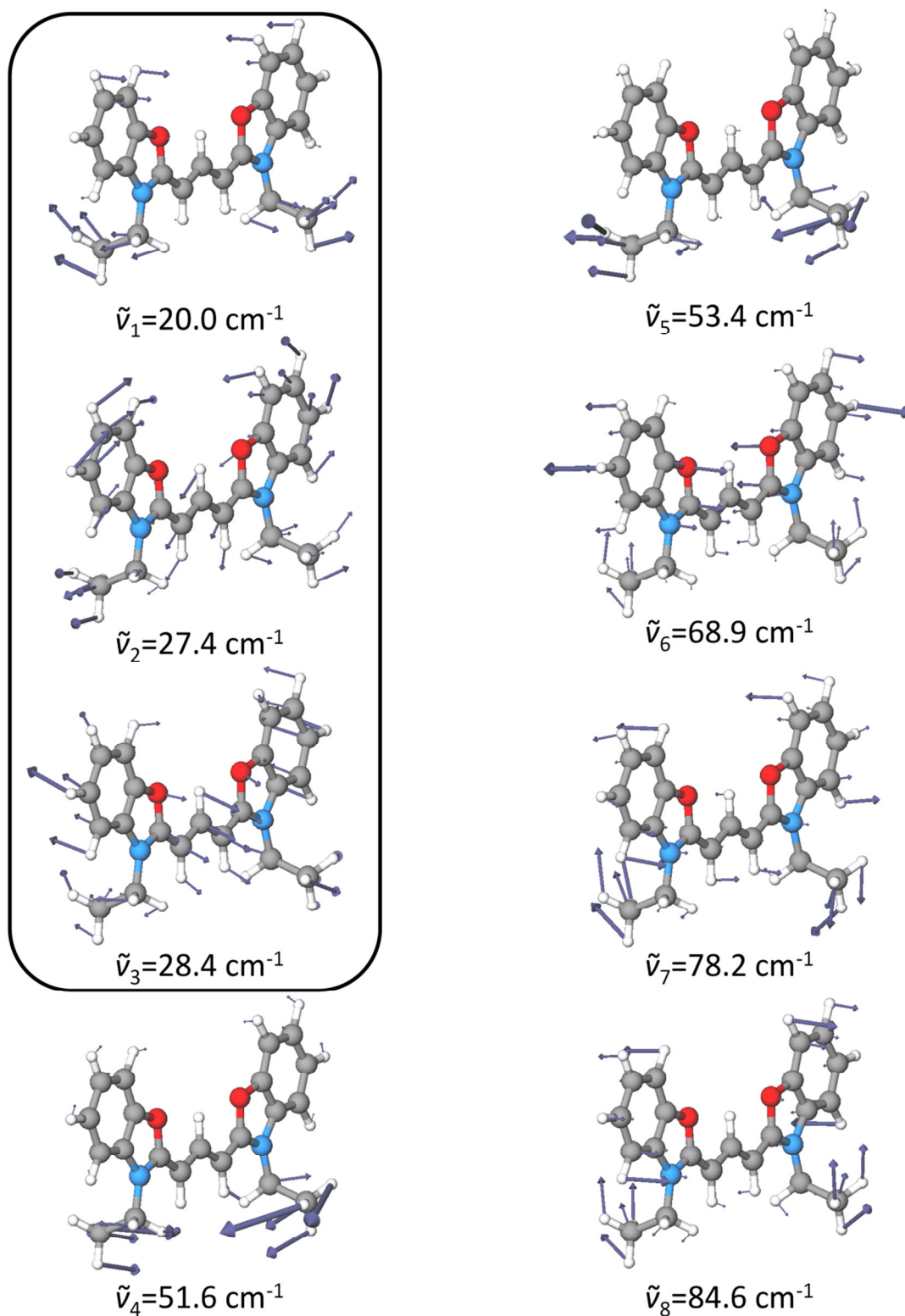
Figure S6 Eight lowest frequency vibrational modes (<100 cm^{-1}) obtained from a harmonic vibration calculation performed for *trans*-**DOC**$^+$ (TD-DFT/B3LPY/6-31G(d)) in its S$_1$ excited state geometry. Highlighted modes are probably responsible for the observed wave-packet dynamics.

5.8.4 References

[1]   J. D. Bhawalkar, G. S. He, P. N. Prasad, "*NONLINEAR MULTIPHOTON PROCESSES IN ORGANIC AND POLYMERIC MATERIALS*", *Rep. Prog. Phys.* **1996**, 59, 1041-1070.

6 Ultrafast electronic dynamics and rotational dephasing of isolated supramolecular photocatalysts in an ion trap

Dimitri Imanbaew[1], Johannes Lang[1], Maxim F. Gelin[3], Simon Kaufhold[4], Michael G. Pfeffer[4], Sven Rau[4] and Christoph Riehn[1],[2]

[1]Fachbereich Chemie, Technische Universität Kaiserslautern, Erwin-Schrödinger-Str. 52-54, 67663 Kaiserslautern, Germany

[2]Landesforschungszentrum OPTIMAS, Erwin-Schrödinger-Str. 46, 67663 Kaiserslautern, Germany

[3]Fakultät für Chemie, TU München, Lichtenbergstraße 4, 85747 Garching, Germany

[4]Anorganische Chemie I, Universität Ulm, Albert-Einstein-Allee 11, 89091 Ulm, Germany

6.1 Preamble

The chapter has been published in a shortened form in the journal *Angewandte Chemie Int. Ed*. Experimental work, data processing and evaluation, as well as structural and energetic calculations were performed by me. Samples of the complexes were provided by Sven Rau *et al.* (Universität Ulm). Simulations of the transient anisotropy data and theoretical considerations thereof were provided by Maxim F. Gelin (TU München). The initial draft of the manuscript was written by me and revised by Christoph Riehn. The shortened version, prepared as a communication, was a collaborative effort between the research groups of the TU Kaiserslautern and the Universität Ulm.

Full Reference to the publication:

6.2 Abstract

We present a gas phase study on the ultrafast dynamics of $[(^t bbpy)_2Ru(tpphz)Pt(Cl)_2]^{2+}$, **Ru-Pt**, ($^t bbpy$=4,4'-di-tert.-butyl-2,2'-bipyridin, tpphz=tetrapyrido[3,2-a:2'3'-c:3'',2''-h:2''',3'''-j]phenazine) and $[(^t bbpy)_2Ru(tpphz)Pd(Cl)_2]^{2+}$, **Ru-Pd**, by electrospray ionization mass spectrometry combined with femtosecond laser spectroscopy in an ion trap. The major fragmentation of these ions proceeds by the loss of the active metal center, *i.e.* loss of $PtCl_2$ or $PdCl_2$. Photofragmentation indicates an intrinsically higher photostability of **Ru-Pt** compared to **Ru-Pd**. The UV/Vis photofragmentation spectra for both species are found to be very similar but distinct from their absorption spectra in solution. Transient data is obtained from pump-probe time-resolved photofragmentation. The electronic states of both supramolecular catalysts decay multi-exponentially and exhibit time constants comparable to previously reported dynamics in liquid phase, supporting their assignment to intramolecular processes. The excited state life-times, however, depend on the excitation wavelength, exhibiting shorter numerical values upon longer wavelength excitation, hinting at accelerated electronic dynamics. Additionally, molecular rotational dephasing on a ~15 ps timescale is revealed for both systems from polarization dependent measurements. The obtained transient anisotropy function is simulated by the molecular orientational correlation function in dependence on the angle between pump and probe transition dipole moments. The latter is found to be aligned parallel to the long tpphz-axis of the molecules and the orientation of the former strongly dependent on the excitation wavelength. These findings strongly support the previously assumed fast electron transfer onto the tpphz bridging ligand - a key process for their photocatalytic activity towards hydrogen generation.

6.3 Introduction

The development and optimization of molecular photocatalysts for the generation of hydrogen from water is a very active area of research due to its importance for the exploration and allocation of new, non-fossil, carbon-neutral energy resources.[1] In particular, the intramolecular approach, *i.e.* the usage of supramolecular assemblies as photocatalysts, is considered to be superior to intermolecular strategies since it is not diffusion-limited with respect to initial electron transfer. Furthermore, it allows for direct structure-function optimization by means of chemical synthesis of the different

molecular subunits within one structural framework.[2-8] In principal, the layout of such an intramolecular photocatalyst consists of an antenna unit (usually a Ru^{II}-based polypyridyl photosensitizer), which absorbs strongly in the visible or near UV spectral region, and a catalytic reduction center comprised of another transition metal. The photo-center and the catalytic center are linked by means of a bridging ligand (often phenazine (phz) based). Well-known examples for this class of photocatalysts are **Ru-Pt** [(tbbpy)$_2$Ru(tpphz)Pt(Cl)$_2$]$^{2+}$, and **Ru-Pd** ([(tbbpy)$_2$Ru(tpphz)Pd(Cl)$_2$]$^{2+}$(tbbpy=4,4'-di-tert.-butyl-2,2'-bipyridin, and tpphz=tetrapyrido[3,2-a:2'3'-c:3'',2'-h:2''',3'''-j]phenazine), which are in the focus of this study (Figure 1).
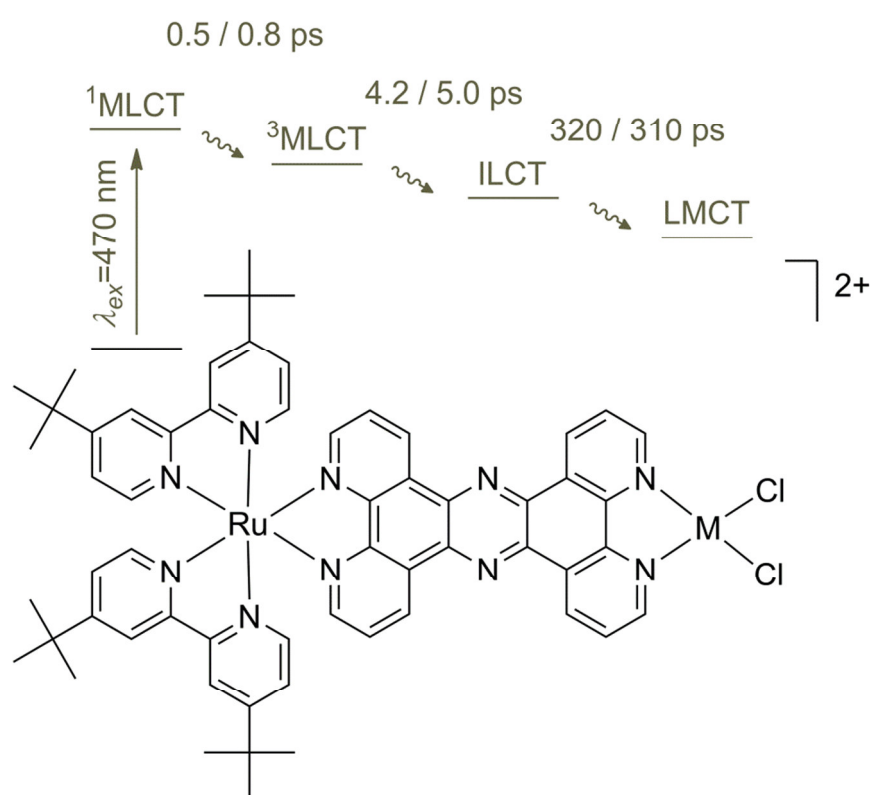
Scheme 1 Schematic structure of **Ru-M** (M=Pt, Pd) and time constants (**Ru-Pt/Ru-Pd**) of excited state dynamics from previous time-resolved studies in acetonitrile solution.[9-10]

The mode of operation of these catalysts is initiated by an electronic excitation of the Ru^{II}-photosensitizer via a ^{1}MLCT transition, which quickly transforms (<<1 ps) into a long-lived ^{3}MLCT state with primary electron localization on the polypyridyl ligands. Subsequently, an electron is transferred towards the phz bridging ligand and finally reaches the catalytic metal center at which protons are reduced to hydrogen. Additionally a sacrificial agent (triethylamine, TEA) is used to close the catalytic cycle

and recharge the photocatalyst in solution. The formation of H_2 for **Ru-M** (M=Pt, Pd) under catalytic conditions (acetonitrile/water/TEA) was proven and used to quantify its catalytic performances.[10-11] Still, many open questions remain in the details of these processes, like: how stable are the photocatalysts in solution and what are the active species? How are two protons reduced on the metal center and in which way does the recharging of the catalyst proceed? How does directed electron transfer take place and what is the influence of the solvent on this reaction?

In order to answer some of these mechanistic questions, a detailed spectroscopic investigation on the ultrafast dynamics of the excitation and charge transfer (CT) processes in solution (CH_3CN, CH_2Cl_2) was performed by femtosecond (fs) transient absorption (TA) spectroscopy.[9-10] It turned out (for **Ru-Pd**) that the observed photoexcited state decay (after excitation at 470 nm) in liquid phase can be fitted tri-exponentially to lifetimes of 0.8 ps, 5 ps and 310 ps.[9] These time constants have been assigned to the charge localization on the phenanthroline (phen) sphere of the tpphz ligand (0.8 ps), intra-ligand charge transfer (ILCT) to form a phz-centered state (5 ps) and finally electron transfer to the Pd active center (310 ps), forming a long lived excited state. Nearly identical dynamics have been reported for **Ru-Pt** in acetonitrile (0.5/4.2/320 ps),[10] however the bare **Ru** unit ($[({}^{t}bbpy)_2Ru(tpphz)]^{2+}$), without the catalytic metal center, exhibits clearly different dynamics (1.2/240 ps) and excited state spectra.[9] Additionally, coherent wave-packet motion with a vibrational frequency of ~430 cm^{-1} was observed for **Ru-Pd** and assigned, on the basis of TD-DFT calculations, to low-frequency modes of the tpphz bridging ligand corroborating the initial, fast CT onto this moiety.[12] With regard to ultrafast dynamics, *i.e.* electron transfer dynamics, in solution the differences between **Ru-Pd** and **Ru-Pt** are minor. However their overall photocatalytic performance is quite distinct. Whereas **Ru-Pd** gives a TON (turnover number) of ~234 (over 9 h, 470 nm LED),[11] for **Ru-Pt** only a TON of ~10 was obtained.[10] Furthermore, studies on the excitation wavelength dependence of the catalytic activity of **Ru-Pd** revealed higher quantum yields for hydrogen generation upon excitation at longer wavelengths,[13] and a concomitant acceleration of the electronic dynamics.[12] On the other hand, it became apparent recently that the low photostability of **Ru-Pd** leads to formation of Pd colloids, which themselves might act as

catalytically active species in solution, whereas for **Ru-Pt** no decomposition was found for a prolonged period under catalytic conditions.[10]

These results motivated us to study the intrinsic ultrafast dynamics of these supramolecular photocatalysts under strict control of charge, composition and environment, which is feasible by molecular ion trap spectroscopy in *vacuo*.[14] Despite the respectable amount of experimental and theoretical studies in solution, there are no reports on gas phase investigations for **Ru-Pd**/**-Pt** or related species. In this report we like to close this gap of knowledge by providing results obtained with electrospray ionization (ESI) ion trap mass spectrometry in combination with UV laser-induced fragmentation (PF), which additionally enables us to study ultrafast electronic dynamics by transient pump-probe photofragmentation (tPF). We report on the gas phase UV/Vis spectra and fragmentation yields by photoexcitation and collision induced dissociation (CID) of the two species. Furthermore, we discuss the observed electronic dynamics in the ion trap together with rotational dephasing obtained from TA measurements of **Ru-Pd** and **Ru-Pt** and provide implications for the direction of the ultrafast CT process.

6.4 Experimental setup and calculations

6.4.1 Materials

The doubly charged cationic complexes **Ru-Pt** and **Ru-Pd** were generated by electrospray ionization (ESI) from solutions of the corresponding salts [Ru-Pt](PF$_6$)$_2$ and [Ru-Pd](PF$_6$)$_2$ in acetonitrile. Synthesis and characterization of the complexes [Ru-Pt](PF$_6$)$_2$ and [Ru-Pd](PF$_6$)$_2$ were reported elsewhere.[10-11] Acetonitrile of HPLC gradient grade was purchased from LGC Standards GmbH.

6.4.2 ESI-MS and CID

ESI mass spectrometry was performed using a modified Paul-type quadrupole ion trap ESI mass spectrometer (amaZon Speed, Bruker Daltonics) in positive ion mode. Modifications to the ion trap allows for laser irradiation of the trapped ions. The scan range was m/z 50-1000 with a scan speed of 32.500 m/z per s (0.3 fwhm). Continuous infusion of the sample solutions (c=5·10^{-7} M) into the ESI chamber was carried out by a syringe pump at a flow rate of 120 µL/h. Nitrogen as drying gas was set to a flow rate of 3.5 L/min at 180°C. The nebulizer pressure was set to 4 psi (280 mbar) and the

electrospray needle was typically held at 4.5 kV. The pressure of helium in the ion trap is estimated to be ca. 10^{-3} mbar, resulting in ca. 10-100 collisions/ms.

6.4.3 Static and transient UV/Vis photofragmentation and anisotropy measurements

For the PF experiments the mass spectrometer was coupled with a fs laser. The fs laser pulses were generated in a Wyvern 1000™ cryogenic ultrafast regenerative laser amplifier system (KMLabs). The oscillator stage was pumped by an Opus 532 DPPS laser, whereas for the amplifier stage a frequency doubled Nd^{3+}:YAG laser (LDP-200MQG, Lee Laser) was utilized. The amplifier crystal was cryogenically cooled by a PT90 cryostat equipped with a CP950 helium compressor (Cryomech). The generated pulse train (∼4 W, 981 Hz, Δτ∼50 fs) was split in order to pump two separate optical parametric amplifiers (OPA) of white light continuum. These TOPAS-C (Light Conversion) systems were used as source of tunable radiation (240 to 2500 nm). The probe pulses (λ_{probe}=1200 nm, energy ∼60 µJ/pulse) from one of the OPAs were temporally delayed with respect to the pump pulses (λ_{pump}=440/480 nm, energy ∼1/1.5 µJ/pulse) from the other OPA using a retroreflector mounted on a single axis delay stage. Scan speed was adjusted for equidistant steps of typically 100 fs or 2 ps for a total temporal delay of 40 ps and 800 ps, respectively. The angle between the linear polarization of the pump and probe pulses was adjusted by a Berek polarization compensator, located in the OPA output beam path of the pump pulses. The pump and probe pulses were spatially overlapped and focused into the center of the Paul ion trap by a f=50 cm lens, yielding pump and probe beams of ∼1 mm in diameter. Each isolated portion of ions was irradiated by 50 pump/probe pulse pairs for transient experiments and 150 pulses for recording of one-color PF spectra. The tPF signals were recorded as extracted ion chromatograms while continuously varying the delay between the pump and probe pulses. Evaluation of the transient signals was performed by calculation of the fragment yields Y_i as $Y_i = F_i/(F_i + P_j)$, where F_i and P_j are the sums of the intensities of the fragment and parent ion signals, respectively.

The transient fragment spectra were fitted by a convolution of a sum of exponentials augmented with the system response function obtained from the laser pulse cross-correlation using a fitting software[15] based on the MINUIT optimization package[16]:

$S(t)=\Sigma_i A_i(exp(-t/\tau_i)*g(t,t_0,t_p))$ (τ_i decay time constants, t_0: time zero, t_p: fwhm of cross correlation, ccf).

PF spectra were obtained by setting the laser pulses to the according wavelengths and measuring the intensity of the parent ion and the sum of the fragment ions. The fragment yield was calculated according to $Y_i=F_i/(F_i+P_j)$, where F_i and P_j are the sums of the intensities of fragment and parent ion signals, respectively, and normalized additionally at each individually set wavelength through division by its numeric wavelength value to account for the different photon energies at constant laser pulse fluence (typical pulse energy ~1 μJ).

The ccf, as a measure of the system response function, was obtained by monitoring the multiple-photon ionization signal of furan (C_4H_2O) in the ion trap.[17] A typical value for the fwhm of the ccf at 440/480 nm (pump)/1200 nm (probe) is ~130 fs.

Polarization dependence of transient signals in the gas phase forms the basis of rotational coherence spectroscopy (RCS)[18-20] and allows for analysis of the recurrences of molecular alignment and rotational dephasing. When the probe laser pulse is applied with a varied time delay, it will map out the rotational dephasing of the original anisotropic distribution, which is based on the breadth of the populated rotational states and scales with $(B^*\cdot T)^{-1/2}$, where B^* represents a characteristic rotational constant and T the absolute temperature.

For transient anisotropy measurements the time-dependent signals were recorded at parallel ($I_\parallel(t)$) and perpendicular ($I_\perp(t)$) pump-probe polarization. The resulting transients were background corrected and normalized to unity (at ~40 ps positive time delay) and used to calculate the respective anisotropy function $r(t)$:

$$r(t) = \frac{I_\parallel(t) - I_\perp(t)}{I_\parallel(t) + 2I_\perp(t)}$$

(1)

This method of analysis was adapted from time-resolved fluorescence anisotropy (TR-FA) in solution[21-22] and has been successfully applied in previous gas phase experiments.[23-24] The anisotropy function reflects the dynamics of rotational dephasing, which contains information on the molecular structure, orientation of the transition dipole moment (TM) and temperature of the sample.

Static UV/Vis absorption spectra in acetonitrile solution ($c=1 \cdot 10^{-5}$ M) at room temperature were recorded using a Lambda 950 photospectrometer (PerkinElmer).

6.4.4 Computations

Geometry optimizations and vibrational frequency calculations for the singlet ground states of the investigated molecular species employing analytical gradient techniques were performed by density functional theory (DFT) with the Gaussian09[25] program package. The B3LYP[26-27] gradient-corrected exchange-correlation functional was used in combination with the 6-311G(d,p) basis set for C, H, N, O, Cl and the LanL2DZ[28-29] effective core potential (ECP) together with its basis set for Ru, Pt and Pd.

6.5 Results and discussion

6.5.1 ESI-MS and CID studies

The main peaks of the ESI mass spectra obtained from acetonitrile solution are located at m/z 600.0 and m/z 644.0 (most abundant mass), which corresponds to the molecular peak of the doubly charged **Ru-Pd** and **Ru-Pt** complex, respectively. The elemental composition is unequivocally assigned by the isotopic intensity patterns (Figure S1) and the charge 2+ by a 0.5 amu spacing of the mass peaks. Upon CID, which is comparable to thermal excitation, we have found the formal loss of neutral $PdCl_2$ and $PtCl_2$ to be the major fragmentation channels (80% and 60% relative yield of MCl_2 loss for **Ru-Pd** and **Ru-Pt**, respectively) followed by the subsequent loss of CH_4, C_2H_6 and $C_2H_6+CH_4$, and other additional loss channels of low intensity (Figure S2 and Table S1). CH_4, C_2H_6 and $C_2H_6+CH_4$ are probably formed by elimination from the ^{t}bbpy-ligands of the **Ru** chromophore. In general, no charge separation upon fragmentation of the doubly charged species was observed.

6.5.2 Photofragmentation: fragment channels, yields and spectra

In order to study the intrinsic response of both photocatalysts under light irradiation we performed gas phase laser-induced PF experiments in a wavelength range of 240-480 nm for the mass-selected cations of **Ru-Pd** and **Ru-Pt** in the ion trap. The types and relative yields of the occurring fragments are akin to the ones observed from CID measurements (Table S1). However, upon photoexcitation **Ru-Pd** exhibits a much

higher absolute fragmentation yield with respect to **Ru-Pt** (with all other experimental conditions constant) over the whole spectral range (up to 2-4 times larger; Figure S3). This is in agreement with the lower photostability of **Ru-Pd**, which has been reported previously for studies under catalytic conditions in solution.[10-11] DFT calculations on the energetics of the most prominent fragmentation channel (Ru-M-Cl$_2$→Ru+MCl$_2$, M=Pt, Pd) yielded a Gibbs free energy at room temperature of 216 kJ/mol for **Ru-Pt** (PtCl$_2$ calculated in singlet configuration; triplet configuration results in an energy of 250 kJ/mol) and an energy of 181 kJ/mol for **Ru-Pd**.
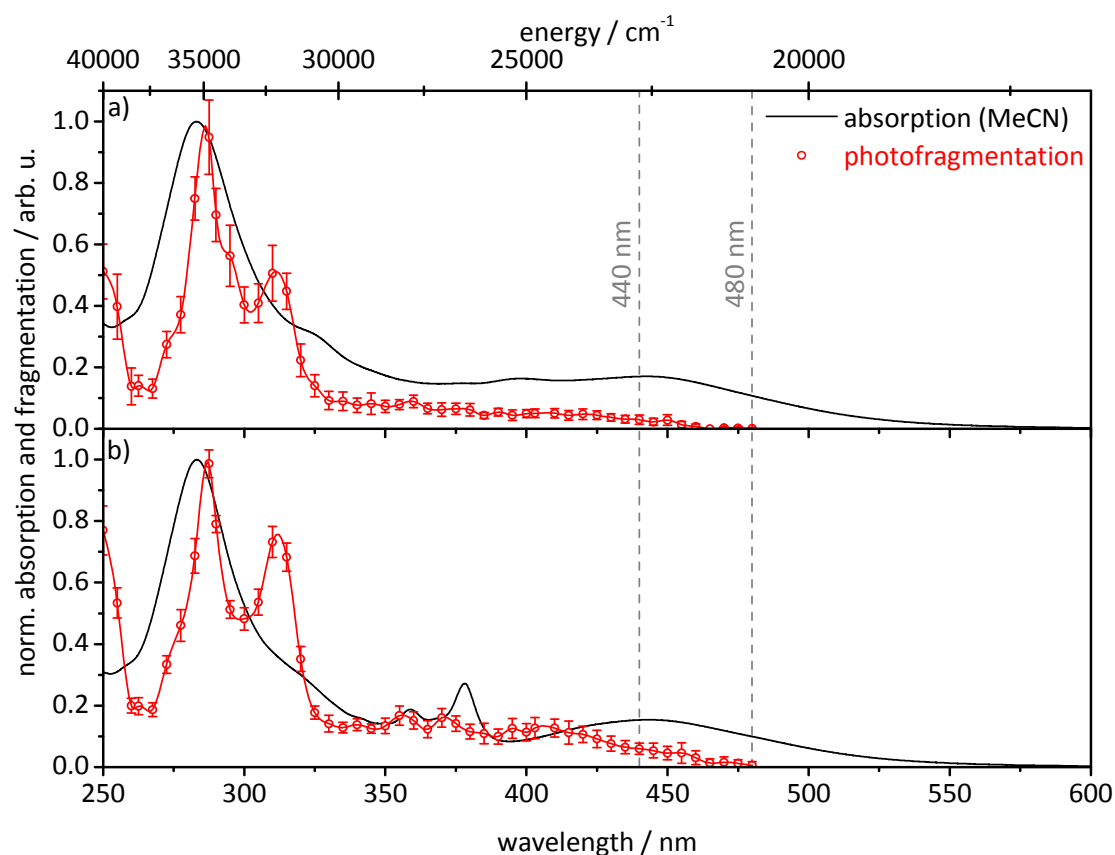
Figure 2 Normalized gas phase UV/Vis PF spectra (red) and liquid phase absorption spectra in acetonitrile (c=1·10^{-5} M) (black) of **Ru-Pt (a)** and **Ru-Pd (b)**. Pump wavelengths (440 nm and 480 nm) used in time-resolved experiments are marked by vertical dashed lines.

The recorded PF spectra for **Ru-Pd** and **Ru-Pt** compare relatively well with respect to their overall shape and structure to the corresponding UV/Vis absorption spectra in solution (Figure 2a and b). However, three differences are obvious: firstly at ~310 nm a strong absorption band is visible in the PF spectra for both compounds, while only a weak shoulder is present in the solution spectra at 320–330 nm. The band at ~310 nm can probably be assigned to a phen/tpphz centered π-π* transition, as the shoulder at

328 nm in the acetonitrile spectrum was attributed to an overlap of three transitions of $\pi_{tpphz}, d_{Pd}, n_{Cl} \rightarrow \pi^*_{tpphz}$, $d_{Pd/Pt}, n_{Cl} \rightarrow \pi^*_{tpphz}$ and $d_{Pd/Pt}, n_{Cl}, \pi_{tpphz} \rightarrow \pi^*_{tpphz}$ character.[10] Excitation of the bridging tpphz ligand may lead to a high PF yield in the gas phase, as it is positioned closer and is thus probably better coupled to the $PdCl_2/PtCl_2$ formal leaving group.

Secondly, we notice a weak and structureless CT band region (>400 nm) for both complexes in gas phase. Weak CT bands were also observed by us for other Ru^{II}-complexes and explained in terms of collisional quenching of long-lived photoexcited or highly vibrationally excited ions by the helium buffer gas in the ion trap.[14] Since the excess energy in the long wavelength range is small, the dissociation proceeds on a time scale comparable to the collision rate of the background helium (~1/(100 μs)-1/(10 μs)). Hence the quantum yield for fragmentation is reduced. Furthermore, the photon energy at 440 nm corresponds to ~272 kJ/mol, which complies with the calculated dissociation thresholds ($RuMCl_2 \rightarrow Ru + MCl_2$). Consequently, at longer wavelength excitation either only ions from the high-energy tail of the Boltzmann distribution contain enough energy for dissociation or two photons have to be absorbed prior to dissociation.[30] This is supported by the laser power dependence of the one-color PF signal (Figure S4). In the short wavelength range, *i.e.* at high photon energies, dissociation outcompetes quenching and thus the spectral shape follows more closely the UV/Vis solution spectra.

Lastly, we do not observe the narrow additional features in the PF spectrum of **Ru-Pd**, which are present in the liquid phase spectrum (350-400 nm). Based on TD-DFT calculations, this absorption band in the **Ru-Pd** spectrum was attributed to a transition of mixed $\pi_{tpphz} \rightarrow \pi^*_{tpphz}/d_{Pd} \rightarrow \pi^*_{tpphz}/n_{Cl} \rightarrow \pi^*_{tpphz}$ character.[10] A similar transition was calculated for **Ru-Pt**, however, with a bathochromic shift to 407 nm (from **Ru-Pd** to **Ru-Pt**) and a concurrent decrease in intensity, explaining the less structured solution absorption spectrum for **Ru-Pt**.[10] Due to the relatively low intensity of this band in solution, the broad spectral bandwidth of our fs pulses (~8-10 nm fwhm in a range of 350-400 nm) and the non-linear nature of the performed action spectroscopy, we do not consider the slight differences in the gas phase CT bands of **Ru-Pd** and **Ru-Pt** significant for a further interpretation.

6.5.3 Pump-probe anisotropy and excited state dynamics of Ru-Pt

The low intensity of the CT bands for **Ru-Pd** and **Ru-Pt** in the PF spectrum compared to the UV/Vis solution spectra allows for setting up a laser scheme in order to generate a two-color PF signal. The latter signal is in turn a prerequisite for recording pump-probe time-resolved PF transients. In analogy to previously published investigations on the wavelength dependent excited state dynamics of **Ru-Pd** in solution by TA spectroscopy,[12] we performed tPF measurements on both systems (**Ru-Pt** and **Ru-Pd**) by excitation at 440 nm and 480 nm, corresponding to the CT absorption band maximum (440 nm) and the long wavelength edge of the CT band (480 nm), respectively. For these measurements a low energy pump pulse (~1 μJ at 440 nm and ~1.5μJ at 480 nm) is overlapped in time and space with a probe pulse of higher intensity and longer wavelength (~60 μJ, 1200 nm) which induces a further (probably multiple-photon) excitation of the primary excited state and leads to an increase of the corresponding fragment ion signal (by a factor of ~4 for **Ru-Pt** and **Ru-Pd**). In extension of the discussion above, we like to emphasize that this increase of ion signal stems nearly exclusively from molecules primarily excited by one pump photon and that the contribution of molecules excited by two pump photons to this signal is expected to be negligible. However, it should be noted that at higher pulse energy (>60 μJ) the probe pulse alone induces fragmentation (resulting in a constant background signal level, which amounts up to ~30% of the peak fragmentation observed at zero time delay), in contrast to results of previous tPF investigations for metal-ligand complexes undertaken with our setup.[14, 31-32] This power dependence of the fragmentation signal for both complexes required a careful adjustment of the pump and probe laser intensities for the time-resolved investigations. The time delay dependence of the fragment ion yield then reflects the lifetime and dynamics of the primary excited state assuming that the subsequent electronic state, coupled to the primary one, exhibits a different, usually smaller absorption cross sections with respect to the probe laser pulse.[17, 33-35]

The transient signal of **Ru-Pt** (Figure 3; λ_{pump}=440 nm (1 μJ) and λ_{probe}=1200 nm (60 μJ)) measured at the magic angle (54.7°) exhibits an ultrafast rise at zero time delay, on the order of the estimated signal response (~130 fs), which decays within approximately 15 ps to a nearly constant level. This signal level is maintained up to a total delay of 800 ps (maximum delay of our current setup), decaying by ~7 % of the total signal

intensity. The transient could be fitted to a tri-exponential decay of τ_1=0.6±0.1 ps, τ_2=6.5±1.3 ps and τ_3>>800 ps.
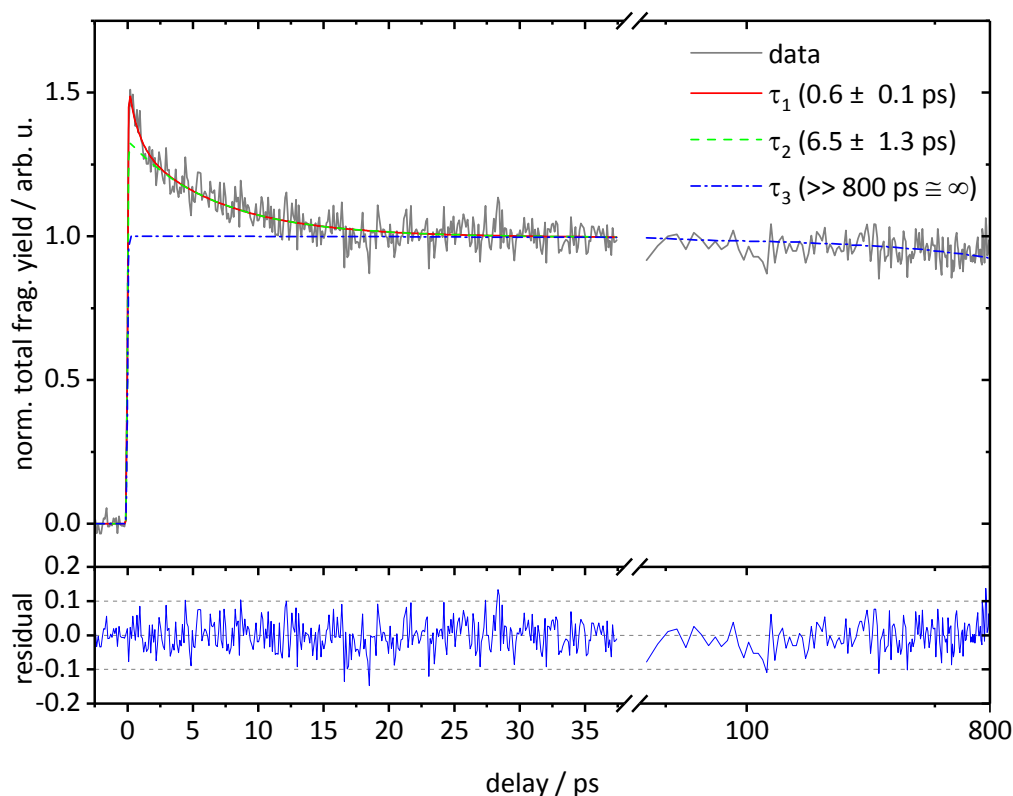

Figure 3 Normalized transient fragment ion yield of **Ru-Pt** recorded for the sum of all fragments at the magic angle; λ_{pump}=440 nm (1 µJ) and λ_{probe}=1200 nm (60 µJ). Decomposition of fit plotted.

The two shorter time constants compare relatively well to the ones obtained from TA spectroscopy (in acetonitrile: 0.5 ps, 4.2 ps and 320 ps)[10], albeit exhibiting slightly larger values. A definite value for the third component could not be determined from our data, due to its low decay amplitude and the limited delay range of our setup. From the slow decay, however, it is apparent that the lifetime in *vacuo* exceeds the lifetime of the third component from TA experiments (320 ps) by far. This time constant was attributed to a ligand-to-metal CT (LMCT) from the tpphz centered state to the Pt metal center.[10] For studies on **Ru-Pd** in solution an increase of the third decay component was observed when performing measurements in a less polar solvent (from 310 ps to 740 ps in acetonitrile and dichloromethane, respectively).[9] A deceleration of the LMCT process in dichloromethane was justified by less favorable solvation of the strongly charge separated state in the less polar solvent, reducing the driving force for LMCT. As the isolated ions are lacking a polar environment in our gas phase investigations, it is conceivable that the rate for LMCT is even slower.

For anisotropy studies the transients of **Ru-Pt** were recorded at either parallel ($I_{\parallel}(t)$) or perpendicular ($I_{\perp}(t)$) relative polarization between pump and probe laser pulses. $I_{\parallel}(t)$ (Figure 4a; cyan) exhibits a much stronger increase at shorter delay times (<15 ps) than $I_{\perp}(t)$ (Figure 4a; dark blue), which (after an initial decay within ~1-2 ps) rises to a nearly constant signal level. For delay times >15 ps the transient traces coincide. This polarization dependent behavior unambiguously points towards molecular alignment by photoexcitation and subsequent rotational dephasing.[23-24] From the experimental transients we have calculated the anisotropy function $r(t)$ for **Ru-Pt** (Fig. 4b) according to equation (1), which is related to the time-dependent correlation function of the molecular TMs for the pump and probe step, respectively.
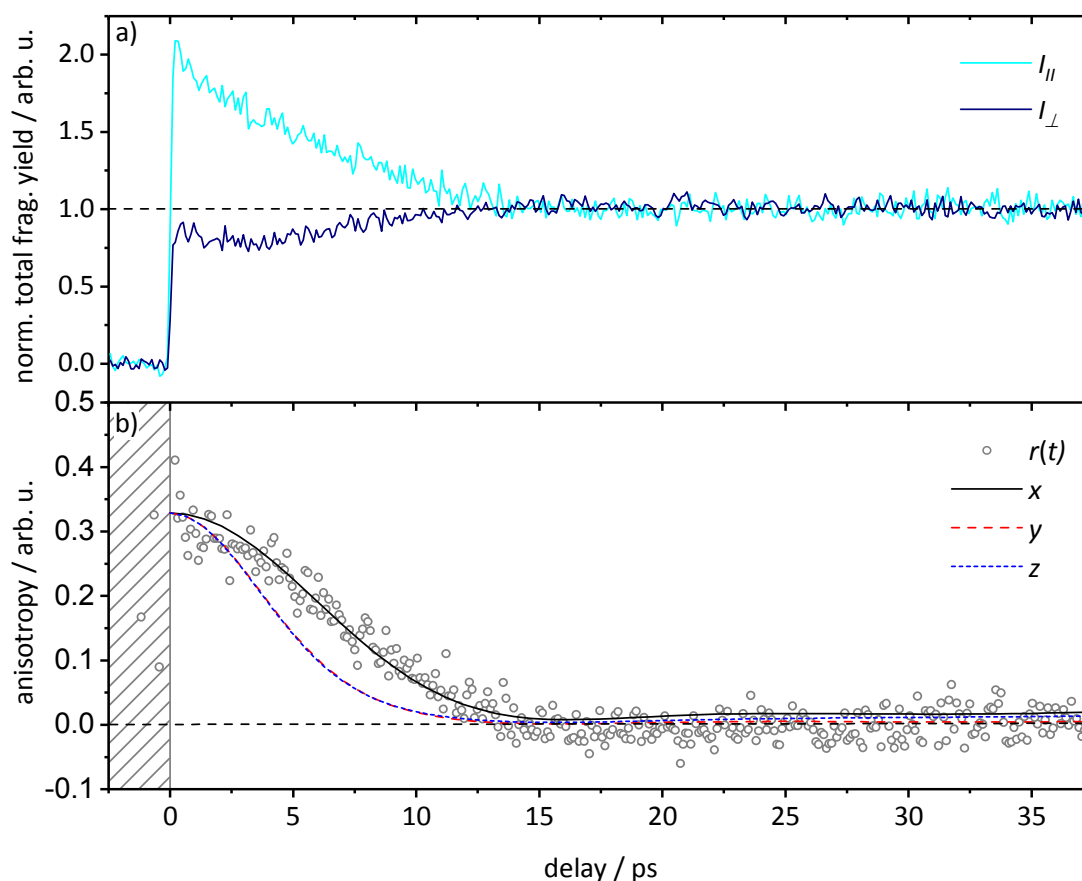
Figure 4 (a) a) Normalized transient fragment ion yield of **Ru-Pt** recorded at parallel (cyan) and perpendicular (dark blue) relative polarization of pump and probe pulses; λ_{pump}=440 nm (1 µJ) and λ_{probe}=1200 nm (60 µJ). **(b)** Anisotropy function $r(t)$ calculated from transient data shown in Figure 4a. Simulations: T=310 K, TM parallel to *x-*, *y-* or *z*-axis; rotational constants were obtained from DFT calculations (Table S2).

In TR-FA, the initial anisotropy, defined as $r(t=0)=r_0$ at time zero, gives the orientation between absorption and emission dipoles. A value of 0.4 indicates perfectly parallel

absorption and emission TMs for one-photon transitions, whereas for r_0=-0.2 the TMs are oriented perpendicularly with respect to each other.[21-22] From Figure 4b, we obtain r_0=0.31±0.04, which is a value smaller than expected for a parallel orientation of the TMs for the pump ($S_1 \leftarrow S_0$, μ_{pump}) and probe ($S_n \leftarrow S_1$, μ_{probe}) electronic transitions. Additionally, for a (1+2') excitation process we would expect r_0=+4/7≈+0.57 and r_0=2/7≈-0.29 for parallel and perpendicular mutual TM orientations, respectively.

TD-DFT calculations for **Ru-Pd** and **Ru** have shown that the broad absorption band in the wavelength region of 420–550 nm is comprised of several CT electronic transitions either from the ruthenium metal center to the bridging ligand (>500 nm) or mixed transitions involving CT to both the bridging ligand and the remaining ᵗbbpy ligands (400–450 nm).[10, 12-13, 36] Additionally, in pioneering studies it was inferred for the [$Ru^{II}(bpy)_3$]$^{2+}$ (bpy=2,2'-bipyridine) chromophore that a rapid charge localization on one ligand within 60–170 fs (depending on the solvent) follows the initially delocalized photoexcitation over three ligands. This was based on TA anisotropy measurements in solution which gave values of r_0=0.55 relaxing to 0.4.[37] This interpretation, however, was later on challenged and a more complex anisotropy decay was revealed than previously thought.[38] Recently, for heteroleptic Ru^{II}-bpy/phen complexes in acetonitrile, an ultrafast anisotropy depolarization, *i.e.* randomization of electronic excitation, was found.[39] This does not contradict the otherwise observed dynamics in the tens of ps regime for magic angle experiments considering vibrational cooling in solution. The latter slows down inter ligand electron transfer (ILET), turning it into an activated process and leads to a Boltzmann distribution for the localization of the charge on the ligands.[39-40]

Based on the results of our gas phase experiments on **Ru-Pt** and the considerations proposed in Ref. [37-39] we infer that, even if we assume an initial excitation and charge distribution over both ᵗbbpy ligands, the charge ends up eventually on the bridging ligand (tpphz)*.* Experimentally, we observe from the recorded anisotropy that on the time resolution of our setup (~130 fs) the pump laser induced CT is localized and oriented along the long axis (*x*-axis, *cf.* Figure S5) of the molecular system. As the experimental initial anisotropy has a value of 0.31, the TM of the probe absorption should also be oriented closely to this axis. In detail, we obtain an angle of 22.8° (=$arccos((5 \cdot r_0+1)/3)^{1/2}$) and 33.5° (=$arccos((3.5 \cdot r_0+1)/3)^{1/2}$) between the pump

and probe TMs for a (1+1') and (1+2') photon process, respectively. If the latter process would apply to our tPF scheme, its value of 33.5° could be interpreted as the angle between the TM for the primary ^{1}MLCT excitation ($d_{Ru} \rightarrow \pi^*_{tbbpy}$) and the TM for the excited state absorption of the quickly formed ^{3}MLCT$_{tpphz}$ state. From the calculated ground state structure of **Ru-Pt** we obtain an angle of 43.6° between the Ru-Pt and the Ru-^{t}bbpy axes projected onto the tpphz plane. A theoretical analysis of the short-time anisotropy behavior followed by simultaneous excitation of both ^{t}bbpy moieties by a pump pulse supports the above scenario (*cf. 6.8.5*). It reveals that the coherent excitation of both ^{t}bbpy-ligands may affect the anisotropy on a time scale of several hundreds of fs, which cannot be resolved in the present experiment. On a longer time scale, the effect disappears due to a fast electronic dephasing, and both ^{t}bbpy ligands contribute to the signal additively.

Additionally, from the constructed experimental $r(t)$ function (Fig. 4b) we could extract the dephasing time of the rotational coherence, as the rotational dynamics are now decoupled from the underlying population dynamics. Figure 4b implies that after ~15 ps the alignment of excited molecules is lost. As the molecular rotational motion and therefore the dephasing time depends on the rotational constants, *i.e.* moments of inertia, and the temperature T of the system, one can calculate the time for reaching the minimum anisotropy value by $\tau_{dephas}=(I_y/k_B T)^{1/2}$ (with the principal moments of inertia being $I_x \geq I_y \geq I_z$).[41] By using $I_y=9.692 \cdot 10^{-43}$ kg·m^2 (*cf.* Table S2) and T=310 K, we estimate a rotational dephasing time of $\tau_{dephas}=15.1$ ps, which agrees well with the experimental value. Analogous calculations assuming a rotation around the *z*-axis ($I_z=1.012 \cdot 10^{-42}$ kg·m^2,$\approx I_y$) and *x*-axis ($I_x=2.253 \cdot 10^{-43}$ kg·m^2) of the molecular frame yield rotational dephasing times of $\tau_{dephas}=15.4$ ps and $\tau_{dephas}=7.3$ ps, respectively.

A more detailed approach for modeling rotational dephasing dynamics is based on calculating the time-dependent rotational correlation function of the second order Legendre polynomial P_2 of the TM.[42] The molecules are treated as free rigid classical asymmetric tops at a specific temperature (here T=310 K). Given the moments of inertia and by assumption of the TM orientation along one of the molecular axes, the calculated results provide an accurate classical description of the rotational dephasing process. Some theoretical aspects of these simulations are elaborated on in *6.8.4*. The resulting correlation functions (for *x, y, z* oriented TMs) are shown in Figure 4b. It is obvious that

the simulations assuming an orientation of the TM along the *x*-axis (axis of smallest moment of inertia) are in good agreement with the experimental data. Since **Ru-Pt** (and **Ru-Pd**) represents a near prolate top with $I_x<I_y\approx I_z$ the rotational dephasing of the *x*-axis aligned TM is determined by the rotational motions along the *y*- and *z*-axis. Thus, the assigned *x*-axis (tpphz-axis) orientation of the TM strongly supports the estimation of τ_{dephas} above.

In analogy to recent reports on the wavelength dependent excited state dynamics of **Ru-Pd** in solution by TA spectroscopy, we performed tPF measurements on **Ru-Pt** by excitation at 480 nm. Note that one-color photoexcitation at 480 nm (*cf.* Figure S3) produces only a small fragmentation yield, consequently the pump-probe signal is also smaller, compared to excitation at 440 nm. Therefore, higher pump pulse energies (1.5 μJ) were used to achieve fragmentation efficiency comparable to excitation at 440 nm (1.0 μJ). Since technically the wavelength of 480 nm is close to the edge of the non-linear mixing scheme of optical parametric generator employed in this study, a lower pulse-to-pulse stability and thus smaller signal/noise is obtained for the recorded transient data. Nevertheless, we were able to obtain transients of sufficient quality for a first qualitative analysis.

Figure 5 depicts the transient signal for **Ru-Pt** recorded for a total time delay of 800 ps at the magic angle, following excitation at 480 nm, *i.e.* the red edge of the broad CT band (Figure 2). In general, the recorded transient is similar to the signal obtained by excitation at 440 nm. The tPF signal was fitted to a tri-exponential decay of $\tau_1=0.4\pm0.2$ ps, $\tau_2=4.3\pm2.7$ ps and $\tau_3\gg800$ ps, which, within experimental uncertainty, are close in value to the decay constants we obtained upon excitation at 440 nm ($\tau_1=0.6\pm0.1$ ps, $\tau_2=6.5\pm1.3$ ps and $\tau_3\gg800$ ps). However, the two fast time constants (τ_1 and τ_2) exhibit slightly smaller numeric values at longer pump pulse wavelengths. An acceleration of the initial ultrafast processes was reported by Wächtler *et al*. in a wavelength dependent study on the sub-picosecond excited state dynamics of **Ru-Pd** applying high resolution TA spectroscopy (sub-20 fs).[12] In that report, two ultrafast processes were found to describe the temporal evolution of the transient signal within the first picoseconds. Firstly, a sub-100 fs process (here denoted as τ_{W1}) ascribed to hot triplet state formation following initial population of the excited singlet state.
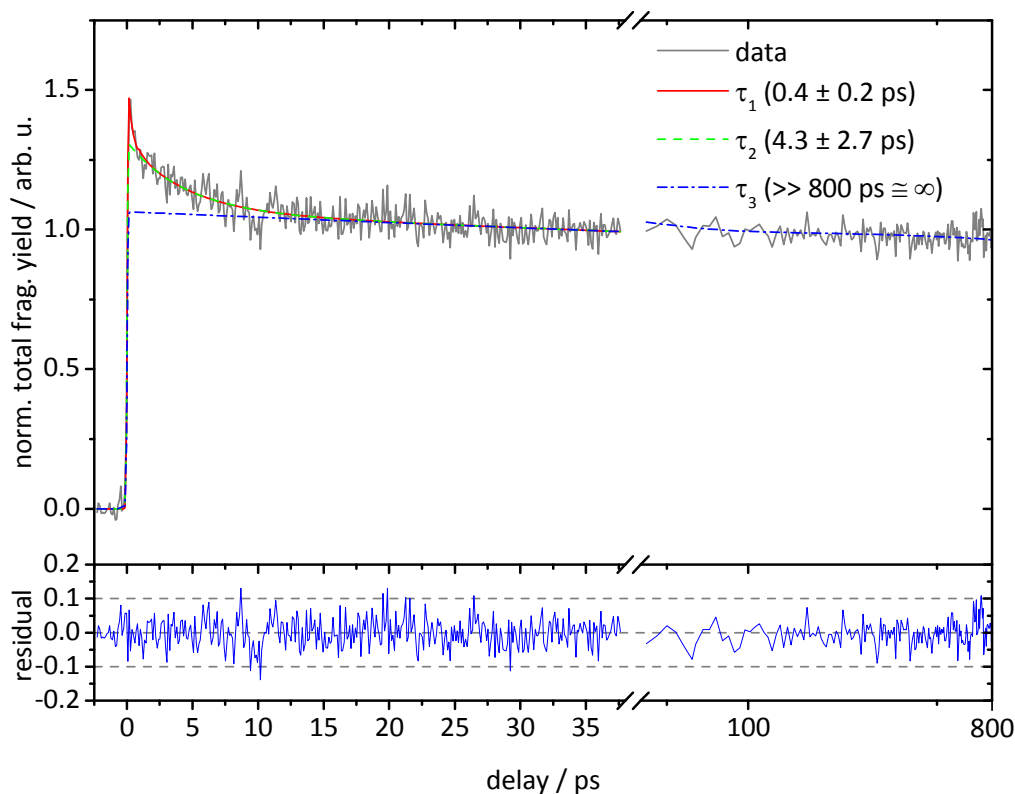
Figure 5 Normalized transient total fragment ion yield of **Ru-Pt** recorded at the magic angle; λ_{pump}=480 nm (1.5 µJ) and λ_{probe}=1200 nm (60 µJ). Decomposition of fit plotted.

Secondly, a sub-1 ps (~0.5 ps) process (here denoted as τ_{W2}) attributed to an ILCT resulting in a formation of a triplet state mainly localized on the phen moiety of the tpphz-bridging ligand. Both processes appear to speed up by excitation at longer wavelengths, dropping from τ_{W1}=85 fs to 44 fs and τ_{W2}=553 fs to 407 fs using 500 nm instead of 450 nm for pumping, and interrogating excited state evolution at 590 nm.[12] As our experimental setup lacks the required temporal resolution, we can neither detect this initial step (τ_{W1}), nor comment on any wavelength dependence of this process. The slower process (τ_{W2}) reported by Wächtler *et al.*, most likely corresponds to the shortest time constant that we have obtained from our measurements (τ_1) and for which we report a decrease in value upon longer wavelength excitation (0.4 ps vs. 0.6 ps at 480 nm vs. 440 nm). Wächtler *et al.* proposed that longer wavelength excitation in the broad CT region of **Ru-Pd** (and **Ru-Pt**) should result in population of a mainly phen-centered state, whereas for excitation at shorter wavelengths (*e.g.* 450 nm used in their experiments) a larger contribution of transitions to the ᵗbbpy ligands is expected. Thus the ultrafast process associated with the relaxation into mainly phen-localized

^{3}MLCT states (involving ILET from $d_{Ru} \rightarrow \pi^*_{tbbpy}$ ^{3}MLCT states) proceeds faster the smaller the contribution from $d_{Ru} \rightarrow \pi^*_{tbbpy}$ ^{3}MLCT states, *i.e.* the longer the excitation wavelength. Hence, we tentatively apply the same reasoning for the decrease of the first time constant obtained from our measurements. The observed decrease of the second time constant (4.3 ps vs. 6.5 ps at 480 nm vs. 440 nm), on the other hand, requires further considerations. This process was assigned to ILCT resulting in a relaxation of the phen-centered ^{3}MLCT state to a phz-localized state and is observed for both excitation wavelengths (480 nm and 440 nm). Excitation at 440 nm (with respect to 480 nm), however, provides a significant amount of excess energy to the molecular system stored in vibrational modes. This would lead to the formation of a higher vibrationally excited phen-localized ^{3}MLCT state prior to relaxation by ILCT to the phz-centered state. One may deduce from this observation that coupling between the phen-centered and the phz-centered state is worse the higher the degree of vibrational excitation of the former state. However, to prove this assumption, further theoretical studies and wavelength dependent experiments in solution are necessary to obtain values for the intermediate time constants.

For further analysis, we recorded the polarization dependent transient mass spectra. The results for **Ru-Pt** using an excitation wavelength of 480 nm are shown in Figure 6. In general the transients (Figure 6a) recorded at either parallel or perpendicular mutual polarization orientation between the pump and probe pulses show a similar behavior when exciting at 480 nm instead of 440 nm. The relative intensities, however, are slightly altered, with $I_{\parallel}(t)$ exhibiting higher and $I_{\perp}(t)$ lower signal intensities with respect to excitation at 440 nm. This results in a larger initial anisotropy value of $r(t=0)=0.40\pm0.04$ (Figure 6b), which is in line with a parallel orientation of the TMs for the pump and probe electronic transitions assuming a (1+1') absorption process. A (1+2') process, on the other hand, would result in an angle of 26.6° between the TMs in analogy to the analysis we performed for the first data set. A value of $r(t=0)=0.40$, however, would be in agreement with theoretical considerations that upon longer wavelength excitation an excited state is quickly populated, mainly centered on the bridging ligand. Hence the corresponding pump TM is also peaking along the long molecular axis (*x*-axis).
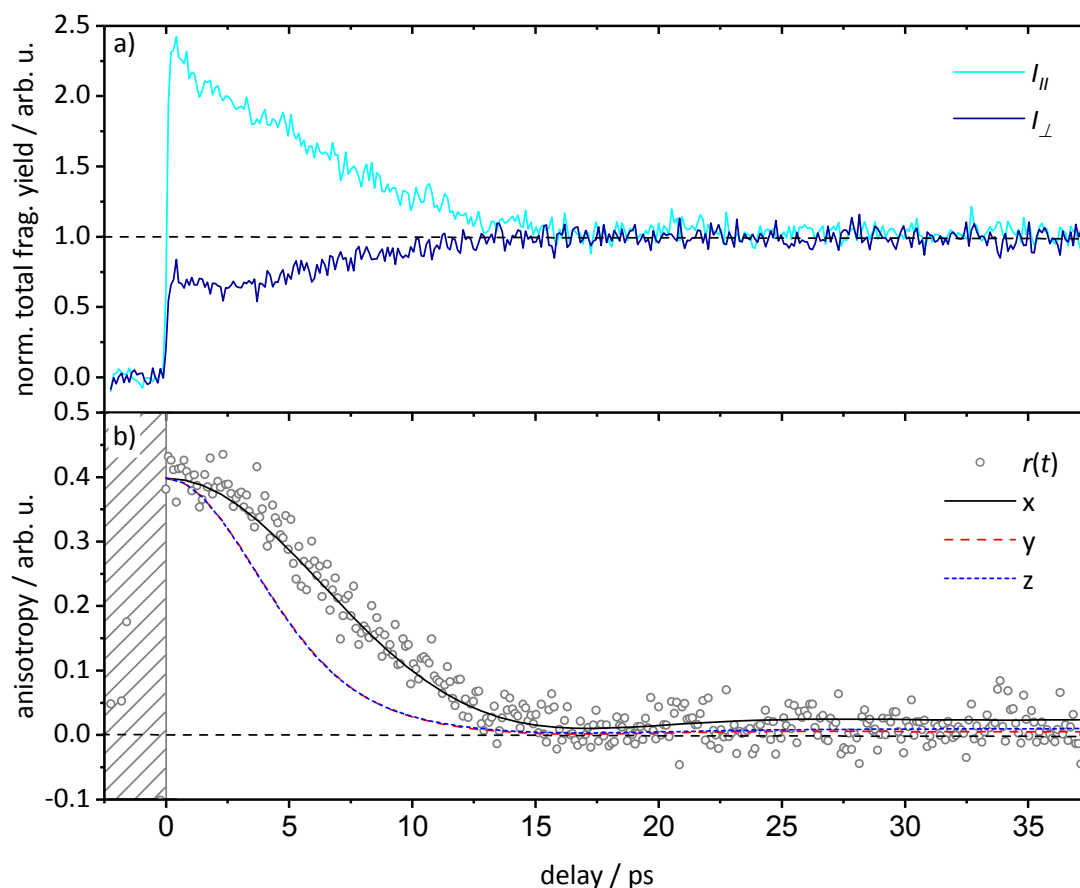
Figure 6 (a) Normalized transient total fragment ion yield of **Ru-Pt** at parallel (cyan) and perpendicular (dark blue) relative polarization of pump and probe pulses; λ_{pump}=480 nm (1.5 µJ) and λ_{probe}=1200 nm (60 µJ). **(b)** Anisotropy function $r(t)$ calculated from data of Figure 6a. Simulations: T=310 K, TM parallel to x-, y- or z-axis; rotational constants were obtained from DFT calculations (Table S2).

In summary, from our experimental data, we extracted the intrinsic excited state dynamics of **Ru-Pt** in the gas phase upon electronic excitation in the CT band at 440 nm and probing at 1200 nm. We have found spectroscopic evidence for bi-exponential picosecond kinetics (τ_1~0.6 τ_2~6.5 ps) and the ensuing formation of a long-lived state (τ_3>>800 ps). The **Ru-Pt** molecular system exhibits pronounced rotational dephasing with a time constant of τ_{dephas}~15 ps in agreement with a simulation for an angle of 22.8° (33.5°) between pump and probe TM for a 1+1' (1+2') process with a long-axis, *i.e.* tpphz-axis, polarized probe transition. Excitation at 480 nm yielded qualitatively the same results, however, the short timescale kinetics appear to accelerate (τ_1~0.4, τ_2~4.3 ps). Furthermore, the initial anisotropy determined from polarization dependent measurements amounts to $r(t=0)=r_0=0.40\pm0.04$, implying a more parallel orientation of

the pump and probe TMs, and correspondingly a more directed CT onto the bridging ligand.

6.5.4 Pump-probe anisotropy and excited state dynamics of Ru-Pd

As the absorption spectra for **Ru-Pt** and **Ru-Pd** are very similar, the same wavelengths (440 nm and 480 nm) for the pump pulses were utilized for excitation of **Ru-Pd** in our time-resolved gas phase study. Firstly, experimental results upon excitation at 440 nm are presented and discussed. Figure 7 depicts the transient signal for **Ru-Pd** recorded for a total time delay of 800 ps at the magic angle. Similar to the transient recorded for **Ru-Pt**, the signal exhibits an ultrafast rise on a timescale comparable to the estimated system response. The signal decays significantly within the first 20 ps, followed by a more pronounced decay of the long lived component by ∼45 % within 800 ps (compared to ∼7 % observed for **Ru-Pt**). The transient could be fitted to a tri-exponential decay of τ_1=0.9±0.4 ps, τ_2=6.9±2.1 ps and τ_3>>800 ps.
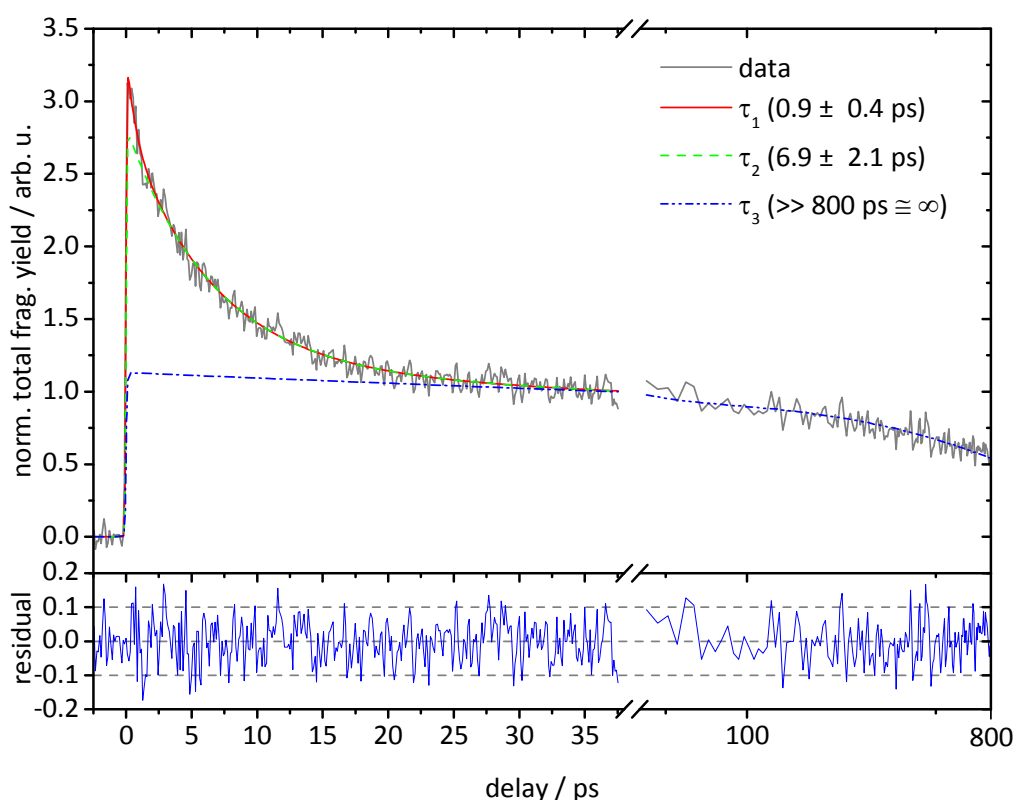
Figure 7 Normalized transient fragment ion yield of **Ru-Pt** recorded for the sum of all fragments at the magic angle; λ_{pump}=440 nm (1 μJ) and λ_{probe}=1200 nm (60 μJ). Decomposition of fit plotted.

The two shorter time constants compare relatively well to the values found for **Ru-Pd** by TA spectroscopy in acetonitrile solution (τ_1=0.8 ps and τ_1=5 ps),[9] whereas a precise value for the long time constant could not be determined from our experiments due to technical constraints in the maximum time delay. Compared to the value for τ_3 obtained from TA studies (310 ps)[9] the lifetime in *vacuo* is apparently much longer, which again may probably be attributed to the lack of solvent stabilization and thus a reduced driving force for the formation of the charge separated LMCT state, as discussed for **Ru-Pt** (*cf.* section *6.5.3*).

Comparing the transients recorded for parallel and perpendicular pump-probe polarization (Figure S8a) a strong similarity in shape is apparent, as both show a quasi-instantaneous rise and pronounced signal decay within ~15-20 ps.
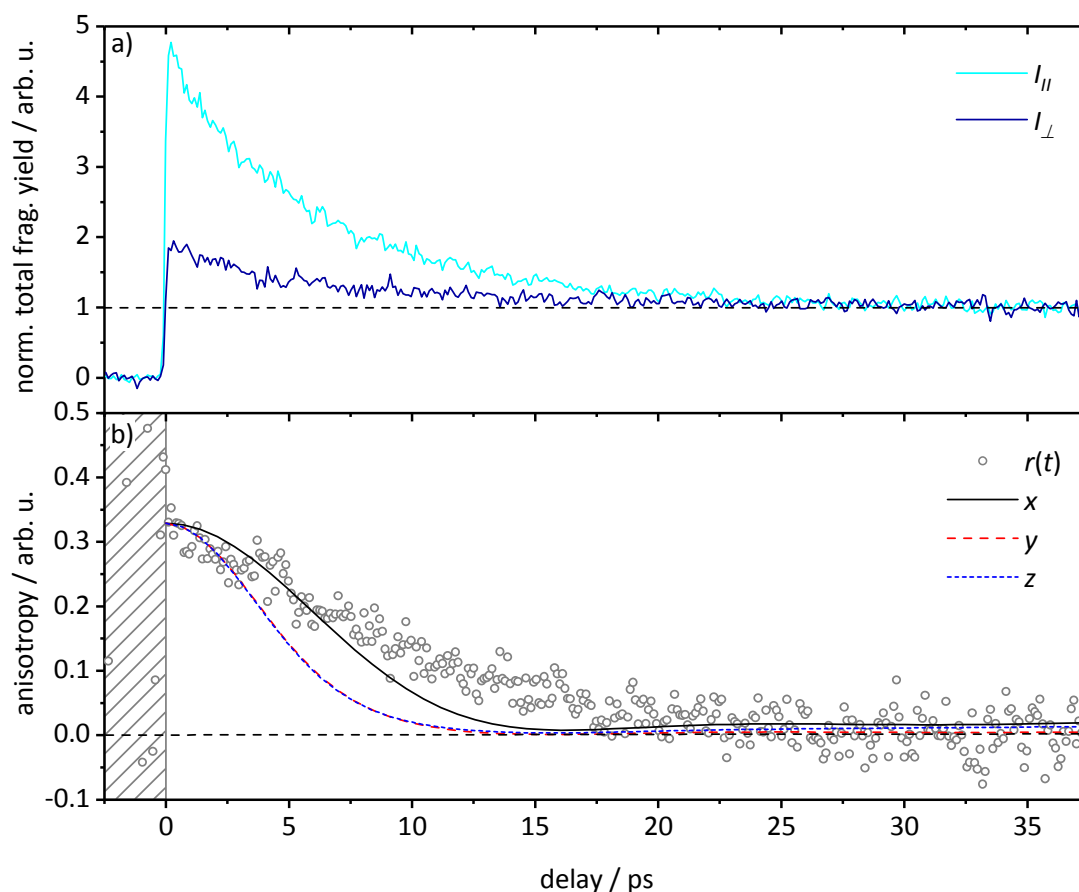
Figure 8 (a) Normalized transient fragment ion intensity of **Ru-Pd** recorded at parallel (cyan) and perpendicular (dark blue) relative polarization of pump and probe pulses; λ_{pump}=440 nm (1 μJ) and λ_{probe}=1200 nm (60 μJ). **(b)** Anisotropy function $r(t)$ calculated from transient data shown in Figure 8a. Simulations: T=310 K, TM parallel to *x*-, *y*- or *z*-axis; rotational constants were obtained from DFT calculations (Table S2).

Similar to **Ru-Pt**, the calculated anisotropy function $r(t)$ (Fig. 8b) has an initial value of $r_0=0.32\pm0.01$, however, it decays within $\sim$15-20 ps, although the calculated dephasing time ($I_y=8.341\cdot10^{-43}$ kg·m^2, T=310 K) is predicted to be slightly shorter ($\sim$14 ps) for **Ru-Pd** than for **Ru-Pt**. Additionally, we have calculated the time-dependent rotational correlation functions for **Ru-Pd** for TM orientations along the x-, y- and z-axis (Figure 8b). In contrast to **Ru-Pt**, the simulation for **Ru-Pd** assuming that the transition dipole moments are directed along the x-axis (Figure 8b, black curve; tpphz-axis) does not match the experimental data as perfectly, instead predicting faster anisotropy decay within $\sim$15 ps.

In the following we attempt to rationalize this discrepancy. We rule out collisional depolarization as it, firstly, universally decelerates anisotropy decay [43] and secondly, collisions of **Ru-Pd** with the helium buffer can anyhow be neglected on a $\sim$10 ps timescale, given the experimental conditions. On the other hand, we observed that the shape and decay time of $r(t)$ for **Ru-Pd** depends strongly on the intensity and focusing of the probe laser pulse, whereas that for **Ru-Pt** was not significantly affected. This is probably attributable to a non-linear laser intensity dependence of the probe process, which contains signal contributions from both the primary electronically excited (^{3}MLCT$_{\text{tbbpy}}$/^{3}MLCT$_{\text{phen}}$) and the ensuingly formed electronically excited state (^{3}MLCT$_{\text{tpphz}}$), as discussed in the preceding section on the dynamics of **Ru-Pt**. Specifically, not only a reduction in the absorption cross section for the probe laser pulse, but also a change in polarization dependence of the transition (*e.g.*, a switch from a parallel to a vertical transition) has to be considered. Stronger deviations at longer time delay could hence be ascribed to the formation of an electronically excited state exhibiting a different polarization dependence of the probe process. Since this change in probing depends sensitively on the level structure of higher lying electronically states, it might be specifically encountered for one photocatalyst (**Ru-Pd**) but not for the other (**Ru-Pt**). The simulation of anisotropy beyond the weak-probe limit, however, necessitates a proper generalization of the approach presented in Ref. [44].

Analogously, we performed tPF measurements on **Ru-Pd** upon excitation at 480 nm. The resulting transient signal is shown in Figure 9.
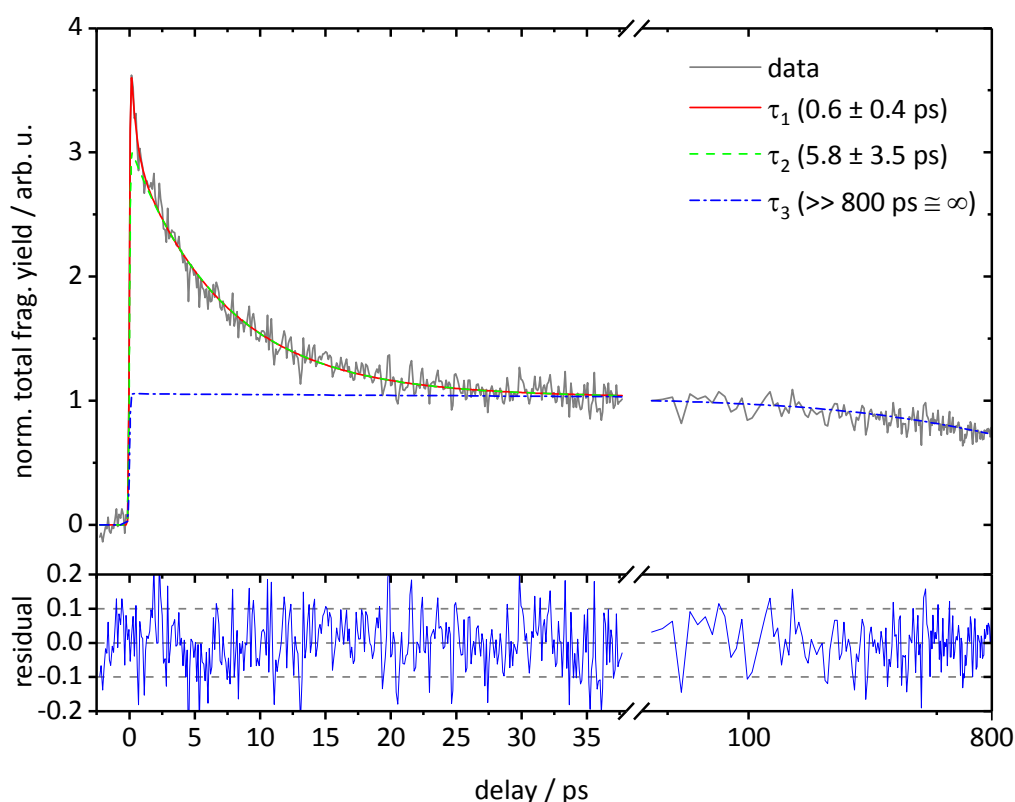

Figure 9 Normalized transient total fragment ion yield of **Ru-Pd** recorded at the magic angle; λ_{pump}=480 nm (1.5 µJ) and λ_{probe}=1200 nm (60 µJ). Decomposition of fit plotted.

The transient of **Ru-Pd** upon excitation at 480 nm resembles the signal obtained for pumping at 440 nm and furthermore could be satisfactorily fitted to a tri-exponential decay yielding three time constants: τ_1=0.6±0.4 ps, τ_2=5.8±3.5 ps and τ_3>>800 ps. In accordance to our measurements on **Ru-Pt**, the fast time constants slightly diminish upon longer wavelength pumping. Thus we believe that the same considerations (*cf.* section *6.5.3*) apply here, as well. In the following, results of our polarization dependent experiments for **Ru-Pd** using an excitation wavelength of 480 nm are presented (Figure 10).
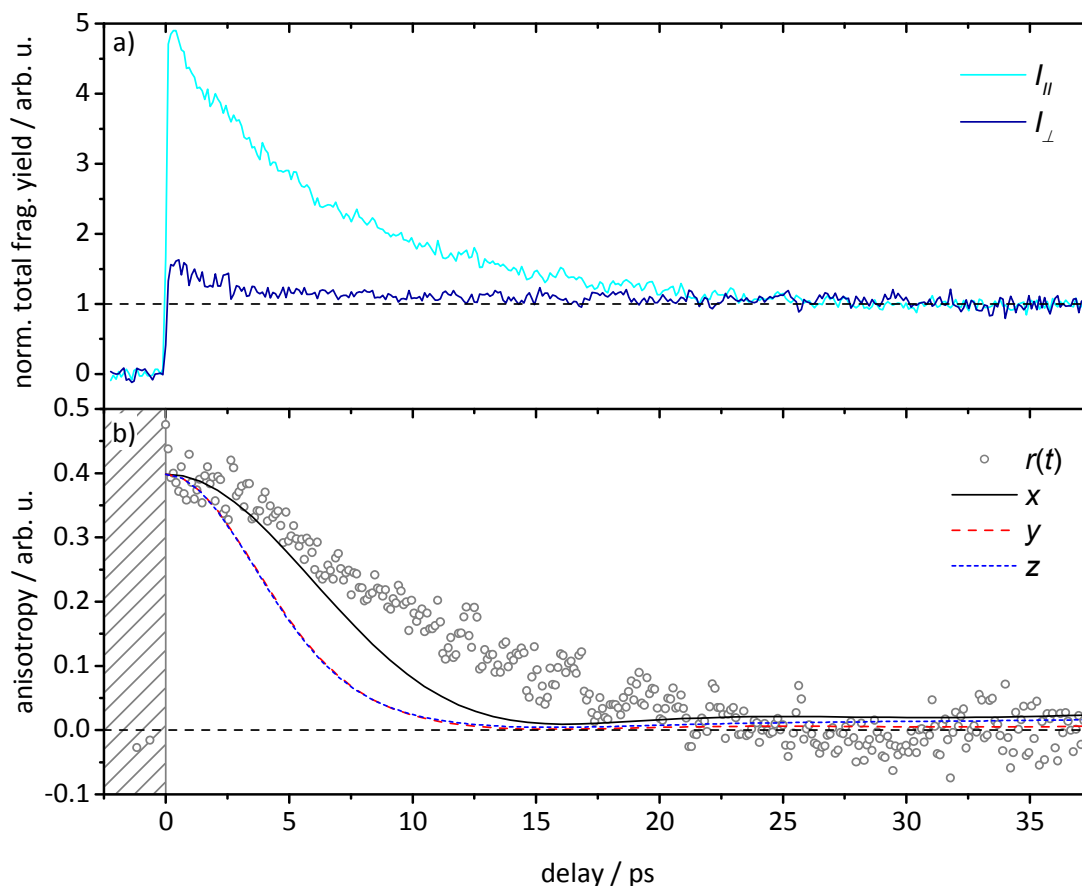
Figure 10 (a) Normalized transient total fragment ion yield of **Ru-Pd** at parallel (cyan) and perpendicular (dark blue) relative polarization of pump and probe pulses; λ_{pump}=480 nm (1.5 µJ) and λ_{probe}=1200 nm (60 µJ). **(b)** Anisotropy function r(t) calculated from data of Figure 10a. Simulations: T=310 K, TM parallel to *x*-, *y*- or *z*-axis; rotational constants were obtained from DFT calculations (Table S2).

Compared to the measurements performed using λ_{pump}=440 nm, signal intensity of $I_{\parallel}(t)$ recorded upon excitation at 480 nm is slightly higher, whereas $I_{\perp}(t)$ exhibits lower values (Figure 10a). Consequently the initial anisotropy is calculated to be higher: r_0=0.40±0.04 (Figure 10b). Strikingly, we observed the same behavior of the polarization dependent transients for **Ru-Pt** using at λ_{pump}=480 nm. Thus, the explanation can be given on the same grounds: according to TD-DFT calculations performed for **Ru-Pd** in acetonitrile, the long wavelength flank (>500 nm) of the broad CT band is dominated by a CT from the Ru^{II} metal center to the phen-part of the tpphz-bridging ligand.[10, 36] Based on our transient anisotropy simulations (Figure 10b), we infer that the probe TM is peaking along the long axis of the molecule. Thus, r_0=0.4 would imply a similar TM orientation of the pump process, in strong agreement with our assumption of a more directed electron transfer towards the Pd metal center. Again,

experimental and simulated $r(t)$ curves show deviations, thus a precise evaluation of the rotational dephasing time is not possible.

6.5.5 Summary of excited state dynamics of Ru-Pt and Ru-Pd

The time constants for the excited state electronic dynamics obtained from pump-probe tPF in an ion trap for the photocatalysts **Ru-Pt** and **Ru-Pd** are summarized in Figure 11 and listed together with previously reported values from solution experiments in Table 1.

Figure 11 Scheme summarizing ultrafast electronic dynamics of **Ru-Pt (a)** and **Ru-Pd (b)** (M=Pt, Pd) observed in gas phase tPF experiments upon excitation at λ_{pump}=440/480 nm. τ_{dephas} denotes an approximated anisotropy decay time. Orientation of the TMs for the pump and probe absorption process are illustrated as blue and red arrows, respectively. For clarity, only the most abundant neutral loss (MCl$_2$) after upon PF and CID is depicted.

Table 1 Summary of time constants obtained for **Ru-Pt (a)** and **Ru-Pd (b)** from tPF spectroscopy in the gas phase and TA spectroscopy in acetonitrile solution. Values in brackets denote decay amplitudes A_i from fitting of the respective tPF data sets.

a)	λ_{pump}/nm	τ_0/fs	τ_1/ps	τ_2/ps	τ_3/ps
tPF	440	-	0.6±0.1 (0.17)	6.5±1.3 (0.32)	>>800 (1.02)
	480	-	0.4±0.2 (0.13)	4.3±2.7 (0.25)	>>800 (1.09)
TA	470[a]	-	0.5	4.2	320

b)	λ_{pump}/nm	τ_0/fs	τ_1/ps	τ_2/ps	τ_3/ps
tPF	440	-	0.9±0.4 (0.45)	6.9±2.1 (1.81)	>>800 (1.08)
	480	-	0.6±0.4 (0.53)	5.8±3.5 (1.96)	>>800 (1.03)
TA	470[b]	-	0.8	5	310
	450[c]	85	0.55	-	-
	500[c]	44	0.41	-	-

a)Taken from Ref. [10]; b) taken from Ref. [9]; c)taken from Ref. [12]

In general, one can see from Table 1 that the dynamics of the isolated photocatalysts in gas phase are quite similar to their photophysical behavior in solution, which points to a minor influence of the solvent on the initial ultrafast dynamics (τ_1 and τ_2) and a significant impact on the slowest process (τ_3). For both systems, we have observed the relatively fast buildup of an intermediate state with a few ps lifetime, which eventually converts to a long-lived (>>800 ps) excited state. The resulting photofragments imply that energy transfer from the primary excited Ru-chromophore unit to the $PdCl_2$ or $PtCl_2$ catalytic center is eventually taking place. Thus, one could adopt the assignments put forward for the solution dynamics also to the gas phase results, namely that τ_1 is related to population transfer from the initially excited Ru^{II}-tbbpy state to the phen-sphere of the bridging tpphz-ligand. Consequently, τ_2 characterizes the subsequent ILCT from the phen- to the tpphz-sphere, which is ensued by CT (τ_3) to the respective catalytic metal center (Ru or Pt).

Some differences between ion trap and solution results have to be addressed. Firstly, the time constants τ_3 obtained from the ion trap measurements are relatively large compared with the solution results. However, the maximum adjustable time delay is ~1 ns in our setup for these measurements and the τ_3 values can only be given with a

limited precision. Thus τ_3 is to be understood as a lower boundary estimate. Moreover, from studies in solution it is obvious that changes in TA within a time window of 0.1-1 ns are relatively small.[9] Based on these observation one can assume that the differences in cross section for the probe laser in our ion trap PF experiment for the different long-lived electronic states are also minor, compromising again the accuracy of the values determined for τ_3

Secondly, the transients for **Ru-Pt** vs. **Ru-Pd** are somewhat different whereas in solution not only the absorption spectra but also the transient dynamics are nearly identical. We would ascribe the differences mainly to effects of higher lying electronic states, which are involved in the probe laser absorption process. Possibly these levels and their dynamics are more strongly influenced than the lower/first electronically excited states. The analysis of rotational dephasing dynamics is consistent with that picture.

6.6 Conclusion

We have presented for the first-time studies on the intrinsic photodynamics and fragmentation of two hydrogen evolving supramolecular photocatalysts in gas phase. The properties of both molecular systems correspond astonishingly well to their behavior in acetonitrile solution, indicating that their photoinduced key process, *i.e.* the CT towards the catalytic metal center, is taking place in isolated molecular systems as well.

Our mass spectrometric investigation revealed that the catalytically active metal centers provide the most weakly bound units in both complexes and fragment with high yield as neutral losses of $PtCl_2$ and $PdCl_2$. PF studies clearly indicate an intrinsically higher photostability of **Ru-Pt** compared to **Ru-Pd** and allowed us to record first gas phase UV/Vis spectra, which may serve as useful references for future *ab initio* calculations.

Time-resolved PF experiments on **Ru-Pd** and **Ru-Pt** yields three time constants, respectively. For both molecular systems, the two fast constants (τ_1 and τ_2) are remarkably close to the ones observed in liquid phase studies, whereas the third time constant τ_3 exhibits a larger value. The large uncertainty of the latter originates from a technical limitation of the utilized gas phase set up, as discussed. However, its value could be also a hint that CT from the bridging ligand to the metal center is impeded and

thus delayed in *vacuo*. Electron transfer to the catalytic center (Pd or Pt) results in a strongly charge separated state, which lacks a polar, stabilizing environment in the gas phase and might result in larger time-constants for the slowest CT process. The observed acceleration of the initial electronic processes (τ_1 and τ_2) upon longer wavelength excitation is in remarkable agreement with experimental studies performed in solution and complementing theoretical considerations based on TD-DFT calculations.

Furthermore, we have observed a strong dependence of the tPF signal on the mutual polarization orientation between pump and probe pulses. Polarization dependent measurements enabled us to extract a value for the initial anisotropy (r_0) and the time-dependent anisotropy function $r(t)$. The former yielded a value of 0.31 and 0.32 using an excitation wavelength of 440 nm for **Ru-Pt** and **Ru-Pd**, respectively, in agreement with excitation of a mainly ^{t}bbpy centered state and probing of tpphz localized states. Upon longer wavelength excitation (480 nm) our polarization dependent studies yield r_0=0.4, strongly supporting a more directed electron transfer toward the bridging ligand and consequently to the catalytic metal center. The respective anisotropy functions $r(t)$ were modeled by calculating the rotational correlation functions of TMs. These simulations are in good agreement with the experiments so that we infer an orientation of the probe transition dipole moments along the long axis (smallest moment of inertia) of the molecular systems, which indicates a fast charge transfer onto the tpphz-bridging ligand.

Hence, from these gas phase results of molecular alignment and rotational dephasing, the concept of an intrinsic ultrafast and directed CT in the supramolecular photocatalysts **Ru-Pd** and **Ru-Pt** is strongly supported. We finally conclude that ion trap PF experiments allow for an unprecedented insight into the stability, intrinsic spectroscopic and dynamic properties of Ru^{II}-based photocatalysts. Our studies provide a technical access to information on a molecular level with unparalleled detail. This method might contribute to the optimization of supramolecular photocatalyst performance in connection with theory-derived rational design.

Acknowledgements

6.7 References

[1]   N. Armaroli, V. Balzani, "THE FUTURE OF ENERGY SUPPLY: "CHALLENGES AND OPPORTUNITIES", *Angew. Chem. Int. Ed.* **2007**, *46*, 52-66.

[2]   Y. Halpin, M. T. Pryce, S. Rau, D. Dini, J. G. Vos ,"*RECENT PROGRESS IN THE DEVELOPMENT OF BIMETALLIC PHOTOCATALYSTS FOR HYDROGEN GENERATION*", *Dalton Trans.* **2013**, *42*, 16243-16254.

[3]   C. Chiorboli, S. Fracasso, M. Ravaglia, F. Scandola, S. Campagna, K. L. Wouters, R. Konduri, F. M. MacDonnell, "*PRIMARY PHOTOINDUCED PROCESSES IN BIMETALLIC DYADS WITH EXTENDED AROMATIC BRIDGES. TETRAAZATETRAPYRIDOPENTACENE COMPLEXES OF RUTHENIUM(II) AND OSMIUM(II)*", *Inorg. Chem.* **2005**, *44*, 8368-8378.

[4]   A. Inagaki, M. Akita, "*VISIBLE-LIGHT PROMOTED BIMETALLIC CATALYSIS*", *Coord. Chem. Rev.* **2010**, *254*, 1220-1239.

[5]   S. Rau, D. Walther, J. G. Vos, "*INSPIRED BY NATURE: LIGHT DRIVEN ORGANOMETALLIC CATALYSIS BY HETEROOLIGONUCLEAR RU(II) COMPLEXES*", *Dalton Trans.* **2007**, 915-919.

[6]   C. Kuhnt, M. Karnahl, S. Tschierlei, K. Griebenow, M. Schmitt, B. Schafer, S. Krieck, H. Gorls, S. Rau, B. Dietzek, J. Popp, "*SUBSTITUTION-CONTROLLED ULTRAFAST EXCITED-STATE PROCESSES IN RU-DPPZ-DERIVATIVES*", *Phys. Chem. Chem. Phys.* **2010**, *12*, 1357-1368.

[7]   G. Singh Bindra, M. Schulz, A. Paul, R. Groarke, S. Soman, J. L. Inglis, W. R. Browne, M. G. Pfeffer, S. Rau, B. J. MacLean, M. T. Pryce, J. G. Vos, "*THE ROLE OF BRIDGING LIGAND IN HYDROGEN GENERATION BY PHOTOCATALYTIC RU/PD ASSEMBLIES*", *Dalton Trans.* **2012**, *41*, 13050-13059.

[8]   G. W. Brudvig, J. N. H. Reek, K. Sakai, L. Spiccia, L. Sun, "*CATALYTIC SYSTEMS FOR WATER SPLITTING*", *ChemPlusChem* **2016**, *81*, 1017-1019.

[9]   S. Tschierlei, M. Presselt, C. Kuhnt, A. Yartsev, T. Pascher, V. Sundström, M. Karnahl, M. Schwalbe, B. Schäfer, S. Rau, M. Schmitt, B. Dietzek, J. Popp, "*PHOTOPHYSICS OF AN INTRAMOLECULAR HYDROGEN-EVOLVING RU–PD PHOTOCATALYST*", *Chem. Eur. J.* **2009**, *15*, 7678-7688.

[10]   M. G. Pfeffer, B. Schäfer, G. Smolentsev, J. Uhlig, E. Nazarenko, J. Guthmuller, C. Kuhnt, M. Wächtler, B. Dietzek, V. Sundström, S. Rau, "*PALLADIUM VERSUS PLATINUM: THE METAL IN THE CATALYTIC CENTER OF A MOLECULAR PHOTOCATALYST DETERMINES THE MECHANISM OF THE HYDROGEN PRODUCTION WITH VISIBLE LIGHT*", *Angew. Chem. Int. Ed.* **2015**, *54*, 5044-5048.

[11] S. Rau, B. Schäfer, D. Gleich, E. Anders, M. Rudolph, M. Friedrich, H. Görls, W. Henry, J. G. Vos, *"A Supramolecular Photocatalyst for the Production of Hydrogen and the Selective Hydrogenation of Tolane"*, Angew. Chem. Int. Ed. **2006,** *45*, 6215-6218.

[12] M. Wächtler, J. Guthmuller, S. Kupfer, M. Maiuri, D. Brida, J. Popp, S. Rau, G. Cerullo, B. Dietzek, *"Ultrafast Intramolecular Relaxation and Wave-Packet Motion in a Ruthenium-Based Supramolecular Photocatalyst"*, Chem. Eur. J. **2015**, *21*, 7668-7674.

[13] S. Tschierlei, M. Karnahl, M. Presselt, B. Dietzek, J. Guthmuller, L. González, M. Schmitt, S. Rau, J. Popp, *"Photochemical Fate: The First Step Determines Efficiency of H2 Formation with a Supramolecular Photocatalyst"*, Angew. Chem. Int. Ed. **2010**, *49*, 3981-3984.

[14] D. Imanbaew, Y. Nosenko, C. Kerner, K. Chevalier, F. Rupp, C. Riehn, W. R. Thiel, R. Diller, *"Excited-state dynamics of a ruthenium(II) catalyst studied by transient photofragmentation in gas phase and transient absorption in solution"*, Chem. Phys. **2014**, *442*, 53-61.

[15] M. Kunitski, *Fitting Program PP2Color,* Goethe University, Frankfurt, **2009**.

[16] F. James, M. Roos, *MINUIT Computer Code, Program D-506*, Cern Program Library, **1977**.

[17] D. Nolting, T. Schultz, I. V. Hertel, R. Weinkauf, *"Excited state dynamics and fragmentation channels of the protonated dipeptide H2N-Leu-Trp-COOH"*, Phys. Chem. Chem. Phys. **2006**, *8*, 5247-5254.

[18] P. M. Felker, *"Rotational coherence spectroscopy: studies of the geometries of large gas-phase species by picosecond time-domain methods"*, J. Phys. Chem. **1992**, *96*, 7844-7857.

[19] C. Riehn, *"High-resolution pump–probe rotational coherence spectroscopy – rotational constants and structure of ground and electronically excited states of large molecular systems"*, Chem. Phys. **2002**, *283*, 297-329.

[20] G. V. Hartland, L. L. Connell, P. M. Felker, *"Theory of rotational coherence spectroscopy as implemented by picosecond fluorescence depletion schemes"*, J. Chem. Phys. **1991**, *94*, 7649-7666.

[21] P. M. Felker, J. S. Baskin, A. H. Zewail, *"Rephasing of collisionless molecular rotational coherence in large molecules"*, J. Phys. Chem. **1986**, *90*, 724-728.

[22] P. M. Felker, A. H. Zewail, *"Purely rotational coherence effect and time-resolved sub-Doppler spectroscopy of large molecules. I. Theoretical"*, J. Chem. Phys. **1987**, *86*, 2460-2482.

[23] D. A. Horke, A. S. Chatterley, J. N. Bull, J. R. R. Verlet, *"Time-Resolved Photodetachment Anisotropy: Gas-Phase Rotational and Vibrational Dynamics of the Fluorescein Anion"*, J. Phys. Chem. Lett. **2015**, *6*, 189-194.

[24] D. Imanbaew, M. F. Gelin, C. Riehn, *"Rotational and vibrational dynamics in the excited electronic state of deprotonated and protonated fluorescein studied by time-resolved photofragmentation in an ion trap"*, Struct. Dyn. **2016**, *3*, 043211.

[25] M. J. Frisch, G. W. Trucks, H. B. Schlegel, G. E. Scuseria, M. A. Robb, J. R. Cheeseman, G. Scalmani, V. Barone, B. Mennucci, G. A. Petersson, H. Nakatsuji, M. Caricato, X. Li, H. P. Hratchian, A. F. Izmaylov, J. Bloino, G. Zheng, J. L. Sonnenberg, M. Hada, M. Ehara, K. Toyota, R. Fukuda, J. Hasegawa, M. Ishida, T. Nakajima, Y. Honda, O. Kitao, H. Nakai, T. Vreven, J. A. Montgomery Jr., J. E. Peralta, F. Ogliaro, M. J. Bearpark, J. Heyd, E. N. Brothers, K. N. Kudin, V. N. Staroverov, R. Kobayashi, J. Normand, K. Raghavachari, A. P. Rendell, J. C. Burant, S. S. Iyengar, J. Tomasi, M.

Cossi, N. Rega, N. J. Millam, M. Klene, J. E. Knox, J. B. Cross, V. Bakken, C. Adamo, J. Jaramillo, R. Gomperts, R. E. Stratmann, O. Yazyev, A. J. Austin, R. Cammi, C. Pomelli, J. W. Ochterski, R. L. Martin, K. Morokuma, V. G. Zakrzewski, G. A. Voth, P. Salvador, J. J. Dannenberg, S. Dapprich, A. D. Daniels, Ö. Farkas, J. B. Foresman, J. V. Ortiz, J. Cioslowski, D. J. Fox, Gaussian, Inc., Wallingford, CT, USA, **2009**.

[26]   A. D. Becke, *"Density-functional thermochemistry. III. The role of exact exchange"*, J. Chem. Phys. **1993**, *98*, 5648-5652.

[27]   C. Lee, W. Yang, R. G. Parr, *"Development of the Colle-Salvetti correlation-energy formula into a functional of the electron density"*, Phys. Rev. B **1988**, *37*, 785-789.

[28]   P. J. Hay, W. R. Wadt, *"Ab initio effective core potentials for molecular calculations. Potentials for the transition metal atoms Sc to Hg"*, J. Chem. Phys. **1985**, *82*, 270-283.

[29]   P. J. Hay, W. R. Wadt, *"Ab initio effective core potentials for molecular calculations. Potentials for K to Au including the outermost core orbitals"*, J. Chem. Phys. **1985**, *82*, 299-310.

[30]   M. W. Forbes, R. A. Jockusch, *"Gas-Phase Fluorescence Excitation and Emission Spectroscopy of Three Xanthene Dyes (Rhodamine 575, Rhodamine 590 and Rhodamine 6G) in a Quadrupole Ion Trap Mass Spectrometer"*, J. Am. Soc. Mass. Spectrom. **2011**, *22*, 93-109.

[31]   D. Imanbaew, Y. Nosenko, K. Chevalier, F. Rupp, C. Kerner, F. Breher, W. R. Thiel, R. Diller, C. Riehn, in *Ultrafast Phenomena XIX: Proceedings of the 19th International Conference, Okinawa Convention Center, Okinawa, Japan, July 7-11, 2014* (Eds.: K. Yamanouchi, S. Cundiff, R. de Vivie-Riedle, M. Kuwata-Gonokami, L. DiMauro), *Springer International Publishing, Cham*, **2015**, pp. 378-381.

[32]   S. Kruppa, F. Bäppler, Y. Nosenko, S. P. Walg, R. Diller, C. Riehn, *in International Conference on Ultrafast Phenomena*, Optical Society of America, Santa Fe, New Mexico, **2016**, p. UW4A.33.

[33]   D. Nolting, R. Weinkauf, I. V. Hertel, T. Schultz, *"Excited-State Relaxation of Protonated Adenine"*, Chem. Phys. Chem. **2007**, *8*, 751-755.

[34]   H. Kang, C. Jouvet, C. Dedonder-Lardeux, S. Martrenchard, C. Charrière, G. Grégoire, C. Desfrançois, J. P. Schermann, M. Barat, J. A. Fayeton, *"Photoinduced processes in protonated tryptamine"*, J. Chem. Phys. **2005**, *122*, 084307.

[35]   H. Kang, C. Dedonder-Lardeux, C. Jouvet, G. Grégoire, C. Desfrançois, J. P. Schermann, M. Barat, A. Fayeton, *"Control of Bond-Cleaving Reactions of Free Protonated Tryptophan Ion by Femtosecond Laser Pulses"*, J. Phys. Chem. A **2005**, *109*, 2417-2420.

[36]   J. Guthmuller, L. Gonzalez, *"Simulation of the resonance Raman intensities of a ruthenium-palladium photocatalyst by time dependent density functional theory"*, Phys. Chem. Chem. Phys. **2010**, *12*, 14812-14821.

[37]   A. T. Yeh, C. V. Shank, J. K. McCusker, *"Ultrafast Electron Localization Dynamics Following Photo-Induced Charge Transfer"*, Science **2000**, *289*, 935-938.

[38]   S. Wallin, J. Davidsson, J. Modin, L. Hammarström, *"Femtosecond Transient Absorption Anisotropy Study on $[Ru(bpy)_3]^{2+}$ and $[Ru(bpy)(py)_4]^{2+}$. Ultrafast Interligand Randomization of the MLCT State"*, J. Phys. Chem. A **2005**, *109*, 4697-4704.

[39]   C. W. Stark, W. J. Schreier, J. Lucon, E. Edwards, T. Douglas, B. Kohler, *"Interligand Electron Transfer in Heteroleptic Ruthenium(II) Complexes Occurs on Multiple Time Scales"*, J. Phys. Chem. A **2015**, *119*, 4813-4824.

[40] M.-E. Moret, I. Tavernelli, M. Chergui, U. Rothlisberger, *"Electron Localization Dynamics in the Triplet Excited State of [Ru(bpy)₃]²⁺ in Aqueous Solution"*, Chem. Eur. J. **2010**, *16*, 5889-5894.

[41] A. P. Blokhin, M. F. Gelin, E. V. Khoroshilov, I. V. Kryukov, A. V. Sharkov, *"Dynamics of optically induced anisotropy in an ensemble of asymmetric top molecules in the gas phase"*, Opt. Spectrosc. **2003**, *95*, 346-352.

[42] A. P. Blokhin, M. F. Gelin, I. I. Kalosha, S. A. Polubisok, V. A. Tolkachev, *"Polarized fluorescence of polyatomic fragments produced through photodissociation of polyatomic molecules in the gas phase"*, J. Chem. Phys. **1999**, *110*, 978-993.

[43] A. P. Blokhin, M. F. Gelin, *"Effect of the intensity of collisions on the orientational relaxation of spherical top molecules"*, Mol. Phys. **1996**, *87*, 455-468.

[44] M. F. Gelin, C. Riehn, M. Kunitski, B. Brutschy, *"Strong field effects in rotational femtosecond degenerate four-wave mixing"*, J. Chem. Phys. **2010**, *132*, 134301.

6.8 Supplementary material to "Ultrafast electronic dynamics and rotational dephasing of isolated supramolecular photocatalysts in an ion trap"

Content

6.8.1 Mass spectrometric data

Figure S1 Experimental and simulated isotopic distributions of **Ru-Pt** and **Ru-Pd**

Figure S2 Fragment ion mass signals observed by CID of **Ru-Pt** and **Ru-Pd**

Table S1 Identified fragment ion signals observed by CID and PF of **Ru-Pt** and **Ru-Pd**

6.8.2 Photofragmentation

Figure S3 Comparison of PF spectra recorded for **Ru-Pt** and **Ru-Pd**

Figure S4 Pulse energy dependent fragment yields of **Ru-Pt** and **Ru-Pd** by one-color PF using λ_{ex}=440 nm

6.8.3 (TD-)DFT calculations

Figure S5 Geometry optimized S_0 structure of **Ru-Pt** and molecular axis system

Table S2 Rotational constants and moments of inertia of **Ru-Pt** and **Ru-Pd**

6.8.4 Calculation of the orientational correlation functions of the second rank for freely rotating asymmetric top molecules

6.8.5 Anisotropy analysis of the pump-probe signal

6.8.6 References

6.8.1 Mass spectrometric data
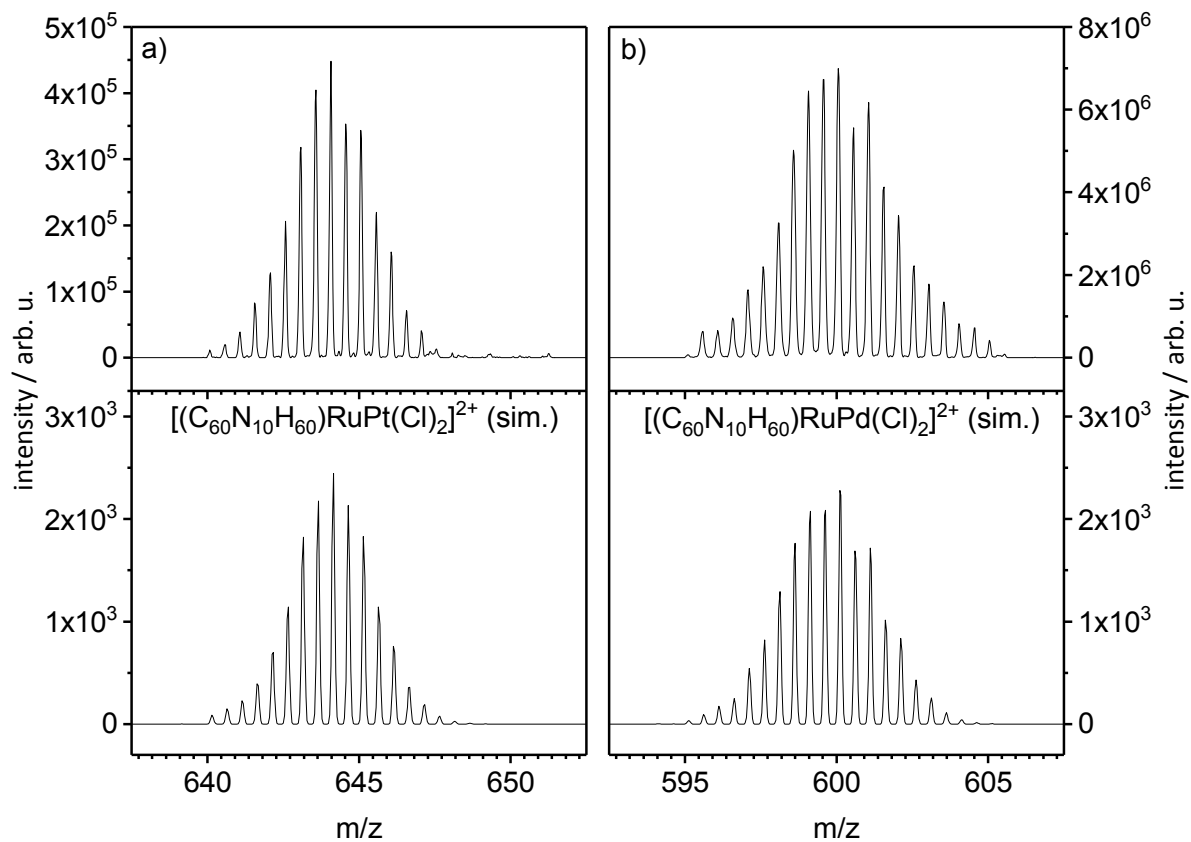
Figure S1 Isotopic distribution in the mass signals of **Ru-Pt (a)** and **Ru-Pd (b)**; respective simulated isotope pattern are shown below.
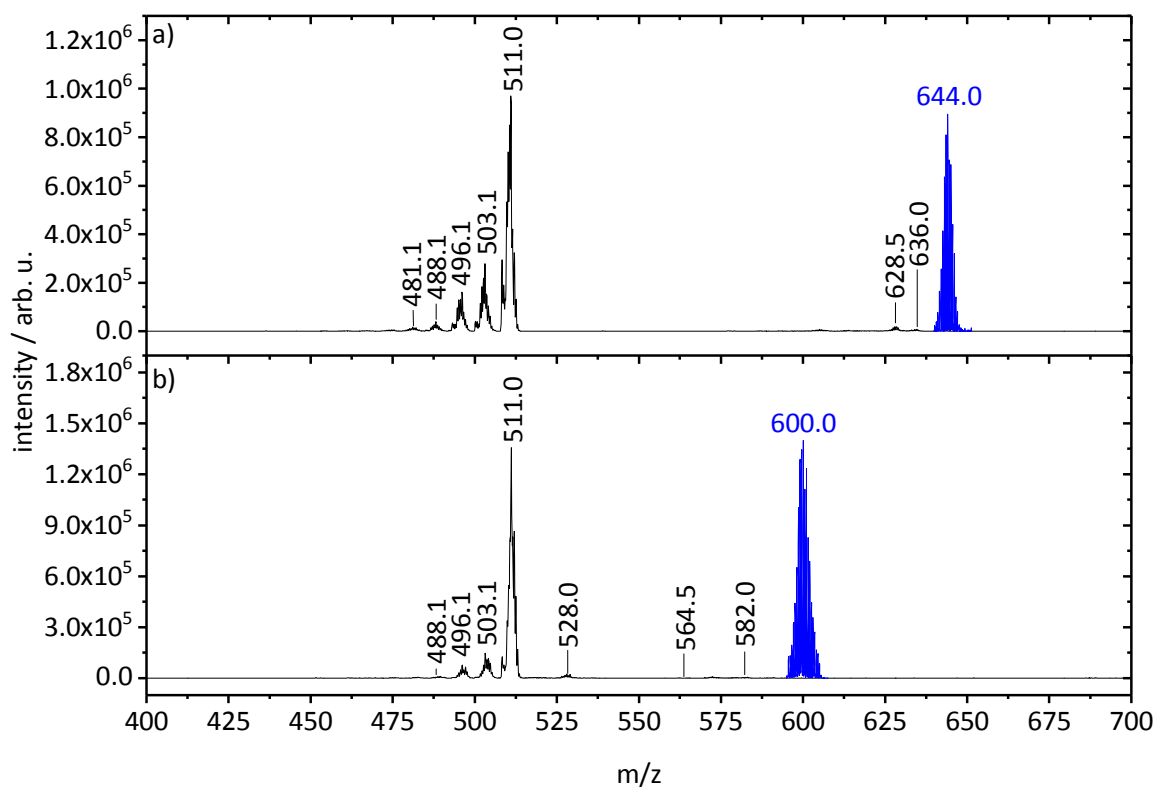
Figure S2 Mass spectrum of fragment ions formed by collision induced dissociation of **Ru-Pt (a)** and **Ru-Pd (b)**. Precursor ion signals are colored in blue. Identified fragment ion signals are listed in Table S1 and S2.

Table S1 Relative yields of fragmentation channels (by CID and PF) of **Ru-Pt (a)** and **Ru-Pd (b)**.

a)	m/z	assigned formula	loss	CID[a]/%	PF[b]/%
Ru-Pt	644.0[c]	$[(C_{60}N_{10}H_{60})RuPtCl_2]^{2+}$	-		
	636.0	$[(C_{59}N_{10}H_{56})RuPtCl_2]^{2+}$	CH_4[d]	-	0.7
	628.5	no exact assignment	C_2H_6 or $2xCH_4$[d]	1.0	0.2
	511.0	$[(C_{60}N_{10}H_{60})Ru]^{2+}$	$PtCl_2$	62.3	23.3
	503.1	$[(C_{59}N_{10}H_{60})Ru]^{2+}$	$PtCl_2/CH_4$[d]	19.7	3.9
	496.1	$[(C_{58}N_{10}H_{54})Ru]^{2+}$	$PtCl_2/C_2H_6$[d]	10.2	2.3
	488.1	$[(C_{57}N_{10}H_{50})Ru]^{2+}$	$PtCl_2/C_2H_6/CH_4$[d]	2.9	0.7
	481.1	$[(C_{56}N_{10}H_{50})Ru]^{2+}$	$PtCl_2/2xC_2H_6$[d]	2.3	0.4

b)	m/z	assigned formula	loss	CID[a]/%	PF[b]/%
Ru-Pd	600.0[c]	$[(C_{60}N_{10}H_{60})RuPdCl_2]^{2+}$	-	-	-
	582.0	no exact assignment	probably Cl*	1.0	0.4
	564.5	$[(C_{60}N_{10}H_{60})RuPd]^{2+}$	Cl_2	-	1.7
	528.0	No exact assignment	PdCl	2.8	1.3
	511.0	$[(C_{60}N_{10}H_{60})Ru]^{2+}$	$PdCl_2$	78.3	50.8
	503.1	$[(C_{59}N_{10}H_{56})Ru]^{2+}$	$PdCl_2 CH_4$[d]	10.1	4.2
	496.1	$[(C_{58}N_{10}H_{54})Ru]^{2+}$	$PdCl_2/C_2H_6$[d]	5.2	2.1
	488.1	$[(C_{57}N_{10}H_{50})Ru]^{2+}$	$PdCl_2/C_2H_6/CH_4$[d]	1.1	0.6

a) at 1.5 V (internal energy scale of the mass spectrometer), b) at λ_{ex}=290 nm (1 μJ), c) precursor ion signal (*cf.* Figure S1), d)CH_4 are C_2H_6 probably formed by elimination from the ^{t}bbpy-ligands of the Ru^{II}-chromophore

6.8.2 Photofragmentation
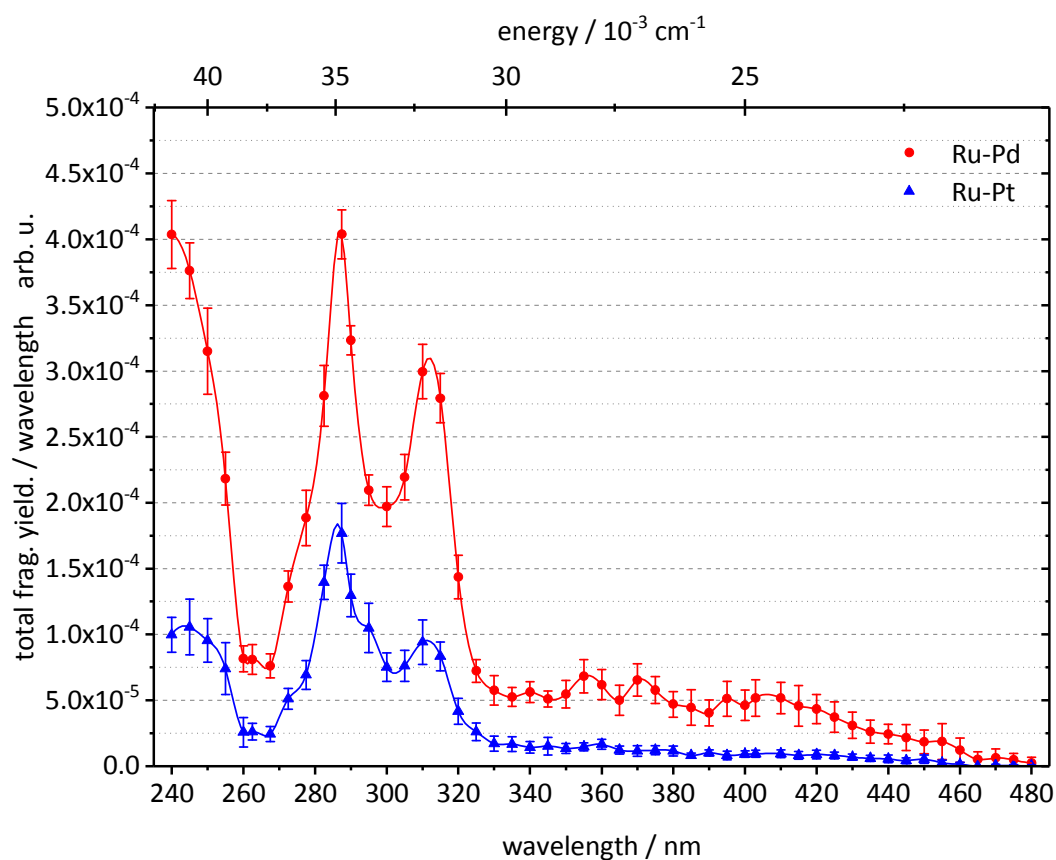
Figure S3 UV/Vis PF spectra of **Ru-Pt** (blue triangles) and **Ru-Pd** (red circles). Data points were connected using a Spline interpolation. Spectra were recorded using a laser pulse energy of 1.0 µJ and irradiating each ion cloud with 150 pulses.
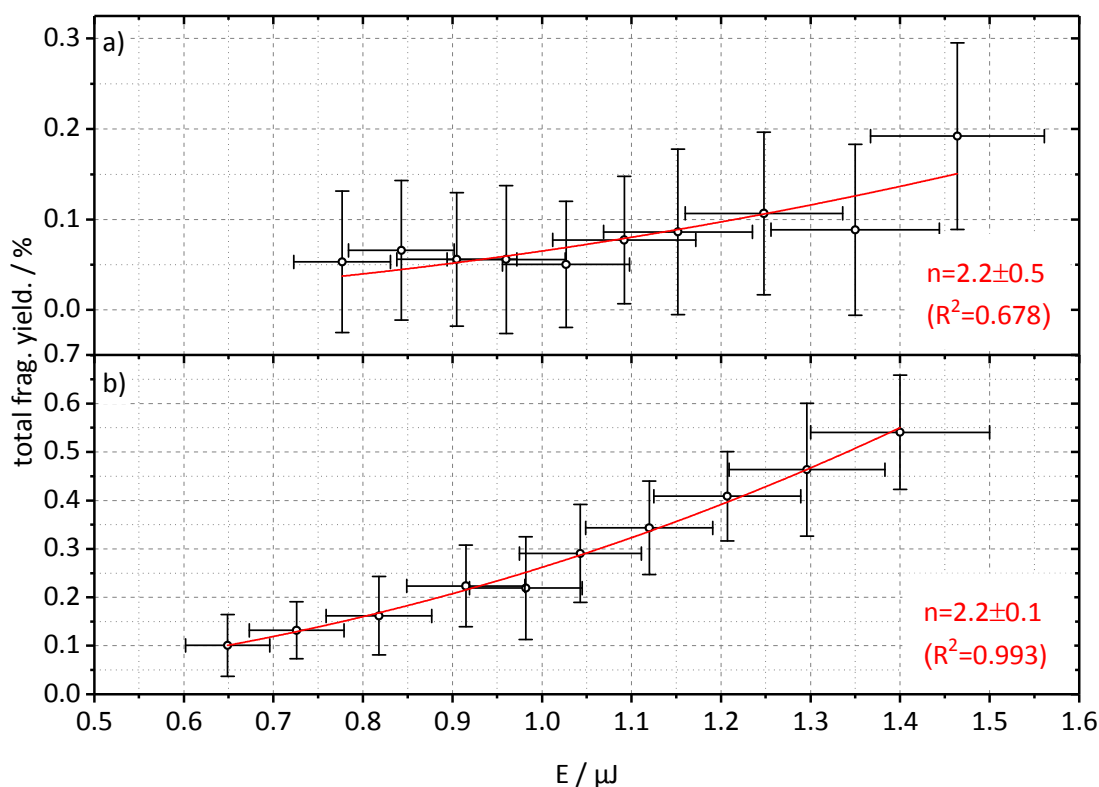
Figure S4 Pulse energy E dependent total PF yields **Y** of **Ru-Pt (a)** and **Ru-Pd (b)** by one-color photoexcitation at λ_{ex}=440 nm. Dependencies were evaluated according to $Y = A \cdot E^n$,[1] where n is a mean value for the number of photons absorbed to induce fragmentation and A a dimensionless fit-parameter.

As discussed (*cf.* section *6.5.2*), **Ru-Pd** exhibits a larger PF efficiency as **Ru-Pt**. At least two photons (λ_{ex}=440 nm) have to be absorbed to induce fragmentation in both cases. One-color (pump only) PF at the pump intensity used for transient experiments (1 µJ) is negligible (>>1 %) compared to the two color (pump-probe) signal, which amount up to 8 % and 11 % of the total ion signals of **Ru-Pt** and **Ru-Pd**, respectively. Based on this result and the value of the anisotropy function at time zero (r_0) it is reasonable to assume that the major fraction of ions contributing to the two-color (pump-probe) signal in transient experiments have absorbed only one photon by pump-pulse excitation. One-color PF at λ_{ex}=480 nm is even lower, thus pulse energy dependencies could not be evaluated.

6.8.3 DFT calculations
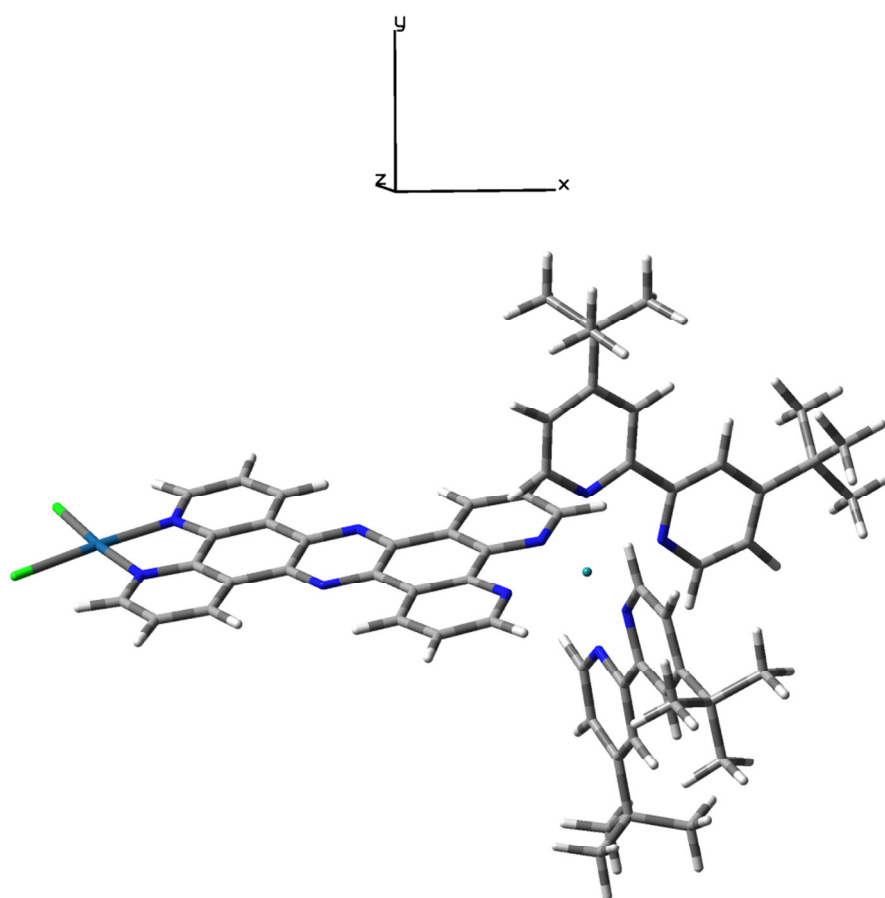
Figure S5 Geometry optimized S_0 structure of **Ru-Pt** and molecular axis system (x, y ,z; equivalent to a, b, c axes, respectively) obtained from DFT calculations (B3LYP/LanL2DZ/6-311G(d,p)). A calculation for Ru-Pd yielded a nearly identical geometry/molecular axis system and is therefore not shown.

Table S2 Rotational constants and moments of inertia of **Ru-Pt (a)** and **Ru-Pd (b)** from geometry optimized structures calculated at the (B3LYP/LanL2DZ/6-311G(d,p)) DFT level of theory.

	A/GHz	I_x/(10^{-43} kgm^2)	B/GHz	I_y/(10^{-43} kgm^2)	C/GHz	I_z/(10^{-43} kgm^2)
a)	0.0373	2.253	0.0087	9.692	0.0083	10.120
b)	0.0368	2.278	0.0101	8.341	0.0093	9.077

6.8.4 Calculation of the orientational correlation functions of the second rank for freely rotating asymmetric top molecules

For a one photon pump+one photon probe (1+1') process, the anisotropy function $r(t)$ is determined by the standard formula (S1):

$$r(t) = \frac{2}{5}\left\langle \frac{3\cos^2(\beta(t))-1}{2} \right\rangle = \frac{2}{5}\left\langle P_2(\boldsymbol{\mu}_1(0)\boldsymbol{\mu}_2(t)) \right\rangle \tag{S1}$$

For a (1+2') process, the anisotropy is given by a similar formula:

$$r(t) = \frac{4}{7}\left\langle P_2(\boldsymbol{\mu}_1(0)\boldsymbol{\mu}_2(t)) \right\rangle \tag{S2}$$

Here $\cos(\beta(t))=\boldsymbol{\mu}_1(0)\boldsymbol{\mu}_2(t)$, $\boldsymbol{\mu}_1$ and $\boldsymbol{\mu}_2$ are the unit vectors along the TMs responsible for the transitions initiated by the pump and probe pulses, $\langle ... \rangle$ stands for rotational averaging, and $P(x)=(3x^2-1)/2$ is the second order Legendre polynomial. The time dependence of $\boldsymbol{\mu}_2(t)$ results from molecular rotation. For a (1+1') process (equation (S1)), values for $r(t)$ vary from initially $r_0=r(t=0)=+0.4$ for parallel TM orientations or $r_0=-0.2$ for perpendicular TM orientations to the final stationary distribution r(t$_\text{dephas}$), where a characteristic time constant t$_\text{dephas}$ is determined by the rotational constants of the molecular system. The orientational correlation functions of equations (S1) and (S2) can explicitly be defined as follows:

$$\begin{aligned}
\left\langle P_2(\boldsymbol{\mu}_1(0)\boldsymbol{\mu}_2(t)) \right\rangle = &\, F^2_{(-2)(-2)}(t)D^2_{(-2)0}(\Omega_{\mu_a})D^{2*}_{(-2)0}(\Omega_{\mu_e}) + \\
&+ F^2_{(1)(1)}(t)D^2_{(1)0}(\Omega_{\mu_a})D^{2*}_{(1)0}(\Omega_{\mu_e}) + F^2_{(-1)(-1)}(t)D^2_{(-1)0}(\Omega_{\mu_a})D^2_{(-1)0}(\Omega_{\mu_e}) + \\
&+ F^2_{00}(t)D^2_{00}(\Omega_{\mu_a})D^2_{00}(\Omega_{\mu_e}) + F^2_{(2)(2)}(t)D^2_{(2)0}(\Omega_{\mu_a})D^2_{(2)0}(\Omega_{\mu_e}) + \\
&+ F^2_{(2)(0)}(t)(D^2_{00}(\Omega_{\mu_a})D^2_{(2)0}(\Omega_{\mu_e}) + D^2_{(2)0}(\Omega_{\mu_a})D^2_{00}(\Omega_{\mu_e}))
\end{aligned} \tag{S3}$$

Here

$$D^2_{m(\pm k)}(\Omega) = \frac{1}{\sqrt{2}}(D^2_{mk}(\Omega) \pm D^2_{m-k}(\Omega)),\ k > 0 \tag{S4}$$

are the symmetrized Wigner's D-functions, and $\Omega_{\mu_i}(\psi_{\mu_i},\theta_{\mu_i},0)$ denote the angles specifying orientations of the TMs $\boldsymbol{\mu}_1$ and $\boldsymbol{\mu}_2$ in the molecular frame.

Equation (S3) reveals that the time evolution of the orientational correlation function is governed by the six basis functions

$$F_{00}^2(t), \quad F_{(2)(2)}^2(t), \quad F_{(2)(0)}^2(t), F_{(-2)(-2)}^2(t), \quad F_{(1)(1)}^2(t), \quad F_{(-1)(-1)}^2(t) \tag{S5}$$

A convenient method of the evaluation of the basis functions (S5) has been developed in Refs. [2,3]. The method employs the action-angle representation of the rotational dynamics and yields the following explicit formulas for the quantities (S5):

$$F_{00}^{2(\Gamma_{\pm z})}(t) = 3\delta^2 \left\{ \sum_{N=-\infty}^{\infty} [(y_1 - N)^2 Q_{2N,0}^-(t) + (y_1 - 2N)^2 Q_{2N,1}^+(t)] + \right.$$
$$\left. + 6 \sum_{N=1}^{\infty} N^2 Q_{2N,0}^-(t) \right\} + F_{00}^{2(\Gamma_{\pm z})}(t \to \infty), \tag{S6}$$

$$F_{(2)(2)}^{2(\Gamma_{\pm z})}(t) = F_{(2)(2)}^{2(\Gamma_{\pm z})}(t \to \infty) + \frac{1}{\delta^2} \left\{ 6(2+\delta^2)^2 \sum_{N=1}^{\infty} N^2 Q_{2N,0}^-(t) + \right.$$
$$+ \sum_{N=-\infty}^{\infty} [(y_3(1+\delta^2) + y_4 - 2N(2+\delta^2))^2 Q_{2N,1}^+(t) +$$
$$\left. + (y_3(1+\delta^2) + y_4 - N(2+\delta^2))^2 Q_{2N,2}^-(t)] \right\} \tag{S7}$$

$$F_{(2)0}^{2(\Gamma_{\pm z})}(t) = F_{(2)0}^{2(\Gamma_{\pm z})}(t \to \infty) + \sqrt{3} \left\{ 6(2+\delta^2) \sum_{N=1}^{\infty} N^2 Q_{2N,0}^-(t) + \right.$$
$$+ \sum_{N=-\infty}^{\infty} [((y_3(1+\delta^2) + y_4 - 2N(2+\delta^2)) Q_{2N,1}^+(t) +$$
$$\left. + (y_3(1+\delta^2) + y_4 - N(2+\delta^2))^2 Q_{2N,2}^-(t)] \right\} \tag{S8}$$

$$F_{(-2)(-2)}^{2(\Gamma_{\pm z})}(t) = (1+\delta^{-2}) \left\{ 24 \sum_{N=1}^{\infty} N^2 Q_{2N,0}^+(t) + \sum_{N=-\infty}^{\infty} [(y_3 + y_4 - 4N)^2 Q_{2N,1}^-(t) + \right.$$
$$(y_3 + y_4 - 4N)^2 Q_{2N,2}^+(t) \right\} \tag{S9}$$

$$F_{(-1)(-1)}^{2(\Gamma_{\pm z})}(t) = 6 \sum_{N=0}^{\infty} (2N+1)^2 Q_{2N+1,0}^-(t) +$$
$$+ \sum_{N=-\infty}^{\infty} [(y_1 + y_4 - 2(2N+1))^2 Q_{2N+1,1}^+(t) + (y_1 + y_4 - (2N+1))^2 Q_{2N+1,2}^-(t)] \tag{S10}$$

$$F_{(1)(1)}^{2(\Gamma_{\pm z})}(t) = (1+\delta^2)\{6\sum_{N=0}^{\infty}(2N+1)^2 Q_{2N+1,0}^{+}(t) +$$

$$+\sum_{N=-\infty}^{\infty}[(y_1+y_3-2(2N+1))^2 Q_{2N+1,1}^{-}(t)+(y_1+y_3-(2N+1))^2 Q_{2N+1,2}^{+}(t)]\}. \quad (S11)$$

Here

$$F_{00}^{2(\Gamma_{\pm z})}(t\to\infty) = \frac{f_0}{2\pi}\int_{\varepsilon_0}^{1}d\varepsilon\, Kb^{-3/2}(3\varepsilon^2\frac{E}{K}-1)^2 \qquad (S12)$$

$$F_{(2)(2)}^{2(\Gamma_{\pm z})}(t\to\infty) = \frac{3f_0}{2\pi}\int_{\varepsilon_0}^{1}d\varepsilon\, K\, b^{-3/2}((2\delta^{-2}+1)(\frac{E}{K}-1)+1-\varepsilon^2)^2 \qquad (S13)$$

$$F_{(2)0}^{2(\Gamma_{\pm z})}(t\to\infty) = \frac{\sqrt{3}f_0}{2\pi}\int_{\varepsilon_0}^{1}d\varepsilon\, K\, b^{-3/2}((2\delta^{-2}+1)(\frac{E}{K}-1)+1-\varepsilon^2)(3\varepsilon^2\frac{E}{K}-1) \qquad (S14)$$

are the stationary (long-time) asymptotic values of the basis functions (S5),

$$Q_{N,n}^{\pm}(t) = \frac{f_0\pi^3}{2\delta^2}\int_{\delta/\sqrt{\delta^2+1}}^{1}d\varepsilon\frac{b^{-3/2}\varepsilon^4 q^N\exp\{2n\sigma\}}{K^3(1+q^N\exp\{2n\sigma\})^2}P_{Nn}(t), \qquad (S15)$$

$$P_{Nn}(t) = (1-\beta_{Nn}^2 t^2)\exp\{-\beta_{Nn}^2 t^2/2\}, \qquad (S16)$$

$$\beta_{Nn} = \frac{1}{I_x\sqrt{b}}[nI_y + \frac{\varepsilon I_y(I_z-I_x)(y_4-\pi N/2K)}{I_z\sqrt{1+\delta^2}}] \qquad (S17)$$

The parameters

$$f_0 = I_y\sqrt{1-\delta^2}\Big/\sqrt{I_x I_z}\ ,\delta^2 = I_z(I_x-I_y)/I_x(I_y-I_z), \qquad (S18)$$

are uniquely determined by the main moments of inertia,

$$b = I_y(I_z+\varepsilon^2(I_x-I_z))/I_x I_z, q = \exp\{-\pi K'/K\}, \qquad (S19)$$

$K = K(\lambda)$ is the complete elliptic integral of the first kind,

$$K' = K(\lambda'), \lambda' = \sqrt{1-\lambda^2} ,\qquad \text{(S20)}$$

$F(u,\lambda')$ is the elliptic integral of the second kind, $E = E(\lambda)$ is the corresponding complete integral,

$$\sigma = \frac{\pi}{2K} F(u,\lambda'), u = \operatorname{arctg}(\delta/\lambda),\qquad \text{(S21)}$$

and $y_n = \vartheta'_n(i\sigma)/\vartheta_n(i\sigma)$ where $\vartheta_n(i\sigma)$ are the Jacobi theta functions of the complex argument.

In the above formulas, time is expressed in units of the mean rotational period $\sqrt{I_y/(kT)}$, where k is the Boltzmann constant and T is a temperature.

6.8.5 Analysis of the anisotropy of the pump-probe signal

As was demonstrated by Hochstrasser *et al.*,[4] the presence of degenerate simultaneously-excited electronic levels profoundly affects anisotropy of spectroscopic signals. Below we study the influence of two bipyridine (ᵗbbpy) moieties on the anisotropy of the pump-probe signal of the present work.

Let $\boldsymbol{\mu}_1$ and $\boldsymbol{\mu}_2$ be the unit vectors along the transition dipole moments responsible for the excitation of two ᵗbbpy moieties by the pump pulse, and $\boldsymbol{\mu}_3$ be the transition dipole moment of the phenazine (phen) unit interrogated by the probe pulse. Denote the polarizations of the pump and probe pulses as (unit vectors) $\boldsymbol{e}_1$ and $\boldsymbol{e}_2$. Then the (short-time) intensity of the pump-probe signal can be written as follows:

$$I = \left\{ (\mathbf{e}_1\boldsymbol{\mu}_1)^2 A + (\mathbf{e}_1\boldsymbol{\mu}_1)^2 B + (\mathbf{e}_1\boldsymbol{\mu}_1)(\mathbf{e}_1\boldsymbol{\mu}_2)C \right\} (\mathbf{e}_2\boldsymbol{\mu}_3)^2 \qquad \text{(S22)}$$

Here the first (second) term in the parenthesis describes the pathway corresponding to a sole excitation of the first (second) ᵗbbpy moiety, while the third term describes the coherent contribution of the two moieties. The quantities A, B and C are orientationally isotropic. They depend on the carrier frequencies, durations, and the time delay between the pulses, as well as on the molecular properties. The orientational averaging in Equation (S22) can be performed as explained, e.g., in Refs. [5,6] to yield

$$r_0 = \frac{I_\parallel - I_\perp}{I_\parallel + 2I_\perp} = \frac{1}{5} \frac{(6(\boldsymbol{\mu}_1\boldsymbol{\mu}_3)^2 - 2)A + (3(\boldsymbol{\mu}_1\boldsymbol{\mu}_3)^2 - \boldsymbol{\mu}_1\boldsymbol{\mu}_2)C}{2A + \boldsymbol{\mu}_1\boldsymbol{\mu}_2 C} \tag{S23}$$

(from symmetry considerations, we set $A=B$ and $\boldsymbol{\mu}_1\boldsymbol{\mu}_3 = \boldsymbol{\mu}_2\boldsymbol{\mu}_3$).

Equation (S23) reveals two important consequences:

(i) A maximally possible coherent contribution corresponds to $C=2A$. In this case, the anisotropy is uniquely determined by the mutual geometry of the transition dipole moments:

$$r_0 = \frac{1}{5} \left[\frac{6(\boldsymbol{\mu}_1\boldsymbol{\mu}_3)^2}{1 + \boldsymbol{\mu}_1\boldsymbol{\mu}_2} - 1 \right] \tag{S24}$$

If $\boldsymbol{\mu}_1$, $\boldsymbol{\mu}_2$ and $\boldsymbol{\mu}_3$ lie all in the molecular plane (the assumption is reasonable for the present case) we can write $\boldsymbol{\mu}_1\boldsymbol{\mu}_3 = cos(\varphi)$ and $\boldsymbol{\mu}_1\boldsymbol{\mu}_2 = cos(2\varphi)$. Then, the initial anisotropy $r_0 = 0.4$, irrespective of the value of φ. Hence the anisotropy for the pump-probe signal of equation (S23) cannot exceed the standard value of 0.4.

(ii) After a short electronic dephasing time of the order of several hundreds of femtoseconds (which cannot be resolved in the present experiment) the coherent contribution in equation (S23) can be set to zero ($C=0$). Then equation (S24) reduces to

$$r_0 = 0.4 P_2(\boldsymbol{\mu}_1\boldsymbol{\mu}_3) \tag{S25}$$

,where the Legendre polynomial P_2 is defined per equation (S2).

6.8.6 References

[1] J. D. Bhawalkar, G. S. He, P. N. Prasad, "NONLINEAR MULTIPHOTON PROCESSES IN ORGANIC AND POLYMERIC MATERIALS", *Rep. Prog. Phys.* **1996**, 59, 1041-1070.

[2] A. P. Blokhin, *Izv. AN BSSR. Ser. Fiz.-Mat.* **1986**, *2*, 70-79.

[3] A. P. Blokhin, *Izv. AN BSSR. Ser. Fiz.-Mat.* **1986**, *4*, 77.

[4] K. Wynne, R. M. Hochstrasser, "ANISOTROPY AS AN ULTRAFAST PROBE OF ELECTRONIC COHERENCE IN DEGENERATE SYSTEMS EXHIBITING RAMAN SCATTERING, FLUORESCENCE, TRANSIENT ABSORPTION AND CHEMICAL REACTIONS", *J. Raman Spectrosc.* **1995**, *26*, 561-569.

[5] M. F. Gelin, W. Domcke, "SIMPLE RECIPES FOR SEPARATING EXCITED-STATE ABSORPTION AND CASCADING SIGNALS BY POLARIZATION-SENSITIVE MEASUREMENTS", *Phys. Chem. A* **1996**, *117*, 11509-11513.

[6] R. M. Hochstrasser, "TWO-DIMENSIONAL IR-SPECTROSCOPY: POLARIZATION ANISOTROPY EFFECTS", *Chem. Phys.* **2001**, *266*, 273-284.

7 UV/Vis absorption and excited state dynamics of a hydrogen-evolving photocatalyst based on an N-heterocyclic carbene/phenanthroline bridging ligand

Dimitri Imanbaew[1], Simon Kaufhold[2], Sven Rau[2] and Christoph Riehn[1],[3]

1Fachbereich Chemie, Technische Universität Kaiserslautern, Erwin-Schrödinger-Str. 52-54, 67663 Kaiserslautern, Germany

2Anorganische Chemie I, Universität Ulm, Albert-Einstein-Allee 11, 89091 Ulm, Germany

3Landesforschungszentrum OPTIMAS, Erwin-Schrödinger-Str. 46, 67663 Kaiserslautern, Germany

7.1 Preamble

The following chapter is formatted as to become a manuscript for publication and has not been submitted, yet. Experimental work, data processing and evaluation, as well as structural and energetic calculations were performed by me. Samples of the complex were provided by Sven Rau *et al.* (Universität Ulm). The initial draft of the manuscript was written by me.

7.2 Abstract

The absorption properties of a new type of heterodinuclear complex for photocatalytic hydrogen generation incorporating an N-heterocyclic carbene/phenanthroline bridging ligand have been investigated in solution and in the gas phase. Steady state absorption (action) spectra were recorded and compared to TD-DFT calculations showing good agreement with a structure in which the DMSO ligand bind to the catalytic center via the *S*-atom in *cis*-orientation to the bridge. First time-resolved investigations by transient photofragmentation action spectroscopy point to a multi-exponential decay of the excited state dynamics. The corresponding processes were assigned to a multi-step charge transfer across the electron-relaying bridge in analogy to similar photocatalytic assemblies reported in literature.

7.3 Introduction

The search for clean and sustainable energy sources is a key challenge in the ongoing endeavor to combat mankind's ever increasing need for energy and to mitigate pollution, *i.e.* emission of greenhouse gases resulting from the use of fossil fuels.[1] Hydrogen appears to be an ideal non-fossil fuel due to its storability, high energy density and the fact that combustion of hydrogen only forms water as "waste".[2-7] Elemental hydrogen is, however, not available in great quantities on earth. Thus an efficient and environmentally friendly way to produce hydrogen from renewable sources has to be developed as an alternative to today's most prominent source for hydrogen, the steam reforming of natural gas.[8] A promising approach is photolytic hydrogen generation, mimicking the light driven water cleaving in the photosynthetic process of green plants.[9] In this context, the exploration of photocatalytic concepts has gained much interest in recent past. Especially the development and evaluation of photocatalytic assemblies by linking a photosensitizer and a catalytically active site by means of bridging ligands is an active field of research.[10-13] This approach allows for optimization of each single sub-unit by structure-property-correlation derived rational design.[14] Often the molecular structure of such catalysts is based on a template first realized in 2006,[15] incorporating a Ru^{II}-polypyridyl-chromophore and a transition metal halide (such as *e.g.* PdCl$_2$ or PtCl$_2$) linked by a symmetric bi-dentate N,N-chelating ligand. In some cases, however, this binding motif yielded a less than desired stability of the

catalysts, resulting in the formation of colloidal Pt or Pd, acting as the catalytically active species.[16-18] More recently, NHC bridging ligands have gained much interest in the ongoing development of photocatalytic assemblies, exhibiting exceptional stabilizing properties.[19-23] Following this concept, a set of novel supramolecular photocatalysts for hydrogen evolution has been developed incorporating a NHC-NN-bridging ligand based on 1,3-dibenzyl-1*H*-imidazo[4,5-*f*][1,10]phenanthrolin-2-ylidene (bbip),[21, 23-24] one of which is **RubbipPt**, *i.e.* [(ᵗbbpy)₂Ru(μ-bbip)Pt(DMSO)Cl₂]²⁺ (ᵗbbpy=4,4'-di-*tert*-butyl-2,2'-bipyridine; DMSO=dimethyl sulfoxide) (Figure 1).[25]
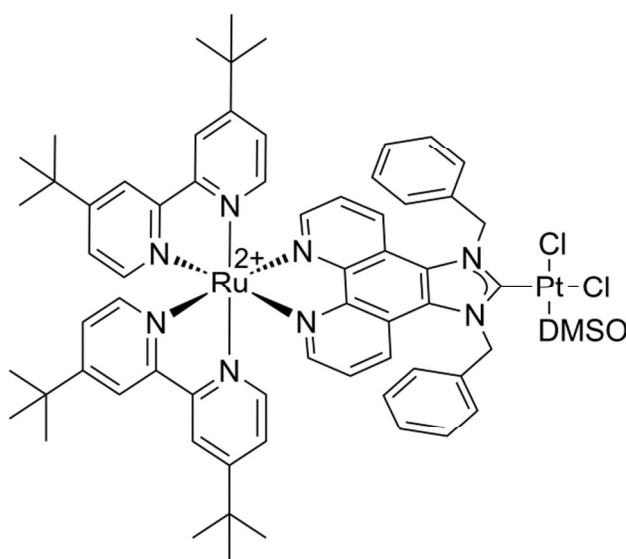
Figure 1 Schematic structure of **RubbipPt**.

The catalytic activity of **RubbipPt** has been demonstrated recently,[25] however, its photophysical properties, a vital point for any photocatalyst, remain to be fathomed by spectroscopic means. Especially time-resolved techniques are an indispensable tool for unraveling the key processes in energy/electron transfer processes. Hence, spurred by our recent experience in the investigation of analogous supramolecular catalysts[26], we applied static photofragmentation (PF) and time-resolved pump-probe photo-fragmentation (tPF) spectroscopy to probe the intrinsic (ultrafast) response of **RubbipPt** to photoexcitation in the gas phase. The gas phase PF results were compared to absorption in solution and to time-dependent (TD-)DFT calculations.

7.4 Experimental

The doubly charged cationic complex **RubbipPt** was generated by electrospray ionization from a solution of the corresponding salt [RubbipPt](PF$_6$)$_2$ in acetonitrile. Synthesis and characterization of the complex was reported elsewhere.[25] Acetonitrile of biotechnology grade (≥99.93 %) was purchased from Sigma Aldrich.

The experimental setup and procedure was reported elsewhere. [27-29] Briefly, static and time-resolved PF experiments were conducted using a modified Paul-type quadrupole ion trap mass spectrometer (amaZon speed, Bruker Daltonics) in combination with a femtosecond (fs) Ti:sapphire oscillator and amplifier system (Wyvern 1000™, KMLabs). The sample solution (1·10^{-7} M) was continuously infused by a syringe pump at a flow rate of 120 µL/h. Nitrogen as drying gas was set to a flow rate of 4 L/min at 180°C. The nebulizer pressure was set to 5 psi (345 mbar). Transient PF spectra were recorded using pump pulses of λ$_{pump}$=430/470 nm (energy ~1.5 µJ/pulse) and probe pulses of λ$_{probe}$=1200 nm (energy ~120 µJ/pulse) at ~1 kHz repetition rate resulting in 150 pump/probe pulse pairs per ion cloud. Temporal resolution was estimated from the cross-correlation function (ccf) obtained by monitoring the pump+probe multiple-photon ionization of neutral furan at a given pump-probe wavelength combination, resulting in a ccf of ~120 fs and ~130 fs for 430 nm+1200 nm and 470 nm+1200 nm, respectively.[30-31] The relative polarization of pump and probe pulses was controlled by a Berek polarization compensator in the pump path and set to the magic angle (54.7°). The tPF signals were recorded as extracted ion chromatograms while continuously varying the delay between the pump and probe pulses. Evaluation of the transient signals was performed by calculating the fragment yields Y_i as $Y_i=F_i/(F_i+P_j)$, where F_i and P_j are the sums of the intensities of fragment and parent ion signals, respectively.

Global fitting of transient kinetics was performed with Origin 9.0G applying a sum of exponentials.

Static UV/Vis absorption spectra in acetonitrile solution (c=5·10^{-6} M) at room temperature were recorded using a Lambda 950 photospectrometer (PerkinElmer).

Geometry optimizations and vibrational frequencies for the singlet ground states of the investigated molecular species employing analytical gradient techniques were performed by density functional theory (DFT) calculations with Gaussian 09[32] using the B3LYP[33-34] gradient-corrected exchange-correlation functional combined with the 6-31G(d) double-ζ basis set for C, H, N, O, S, Cl. For ruthenium (platinum) the 28-electron (60-electron) relativistic effective core potential (ECP) MWB was used with its basis set. Vertical excitation energies (250 and 300 states for calculations with and without solvent, respectively) were obtained from time-dependent DFT (TD-DFT) calculations within the adiabatic approximation employing the same functional, pseudopotential and basis set. Solvent interaction (acetonitrile, $\varepsilon=35.688$, n=1.344) and thus impact on the molecular geometry and excitation energies was taken into account by employing the polarizable continuum model (PCM) using the integral equation formalism variant (IEFPCM).[35]

7.5 Results and discussion

7.5.1 ESI-MS and CID

The peak at m/z 691 (Figure 2, most abundant mass) of the ESI mass spectrum obtained from acetonitrile solution corresponds to the molecular peak of the doubly charged **RubbipPt** complex. Performing collision induced dissociation (CID) in the trap, fragment ions are formed. The CID mass spectrum (Figure 2, Table 1) is dominated by two fragmentation products corresponding to the formal loss of HCl and DMSO (m/z 634) or $PtCl_2$, DMSO and the concomitant loss of one of the benzyl moieties (m/z 473) found in the bridging-ligand. In contrast to previous studies on two similar supramolecular catalysts, subsequent elimination of, *e.g.* CH_4 and C_2H_6, from the tbbpy-ligands was not observed.[28] Apart from the two main fragmentation channels, three fragment products of low abundance were identified, which probably result from 1) a twofold loss of HCl and the DMSO-ligand (m/z 615.5), 2) the loss of HCl, DMSO and one benzyl-moiety (m/z 588) or 3) a twofold loss of HCl, the DMSO-ligand and one benzyl-group (m/z 569.5). To form the fragment at m/z 473 higher internal energies are required, as implied by the CID amplitude dependent relative fragment ion intensities (Figure S1).
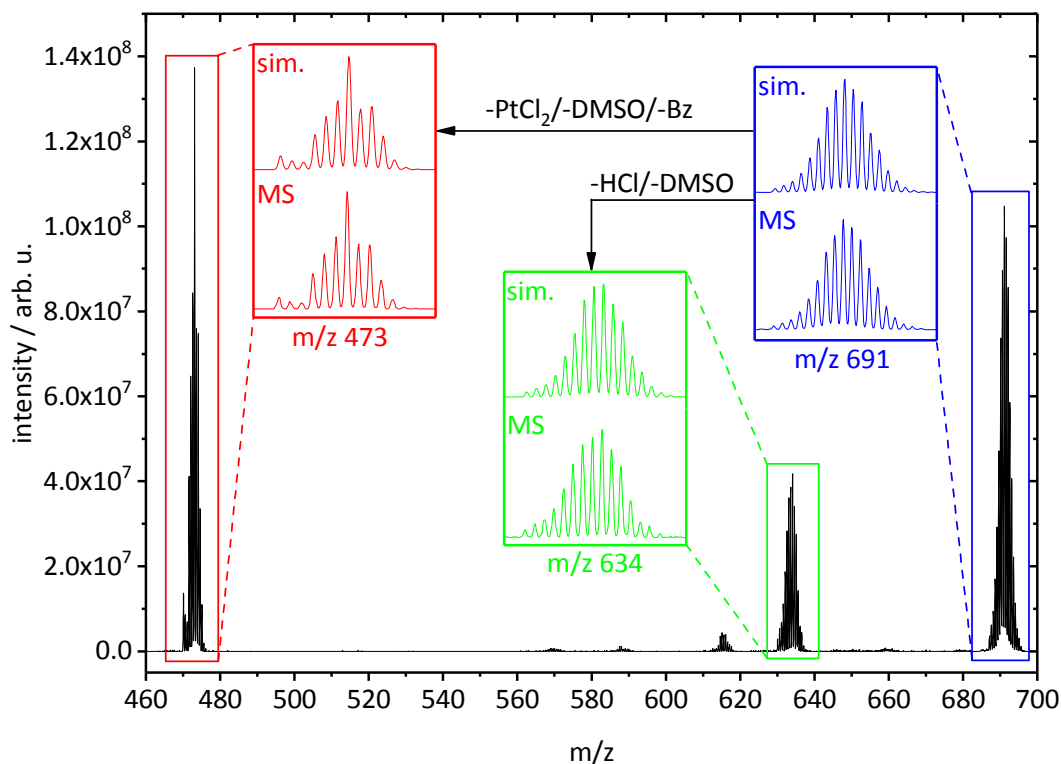
Figure 2 Fragment ion mass spectrum of **RubbipPt** applying CID. Insets show magnified experimental (bottom) and simulated isotope distributions (top) of the parent ion signal (blue, m/z 691) and the two main fragment ion signals (green, m/z 634 and red, m/z 473). Low abundance fragment signals showed no clear isotope distributions and thus were not simulated.

Table 1 Overview over identified ion signals observed in the CID fragmentation mass spectrum of **RubbipPt** (*cf.* Figure 2).

m/z	assigned formula	neutral loss
691*	$[(C_{63}H_{68}N_8)RuPtCl_2(C_2H_6SO)]^{2+}$	-
634	$[(C_{63}H_{67}N_8)RuPtCl]^{2+}$	HCl/C_2H_6SO
615.5	$[(C_{63}H_{66}N_8)RuPt]^{2+}$	$2xHCl/C_2H_6SO$
588	$[(C_{56}H_{59}N_8)RuPtCl]^{2+}$	$HCl/C_2H_6SO/C_7H_8$
569.5	$[(C_{56}H_{58}N_8)RuPt]^{2+}$	$2xHCl/C_2H_6SO/C_7H_8$
473	$[(C_{56}H_{60}N_8)Ru]^{2+}$	$PtCl_2/C_2H_6SO/C_7H_8$

*⁾precursor ion signal

7.5.2 Solution phase absorption and gas phase photofragmentation spectra

Upon laser irradiation the isolated photocatalyst ions dissociate to form product ions. In general, the types of occurring fragments are identical to the ones observed by CID (Table 1, Figure S2). However, the relative yield depends on the excitation wavelength, with excitation at shorter wavelengths resulting in the preferential formation of fragment ions at lower m/z, equivalent to our observation when applying higher

excitation amplitudes in CID experiments. In the following, the PF spectrum obtained by monitoring the fragmentation yield over a spectral range of 240-480 nm, is presented and compared to the linear absorption spectrum recorded in acetonitrile solution (Figure 3).
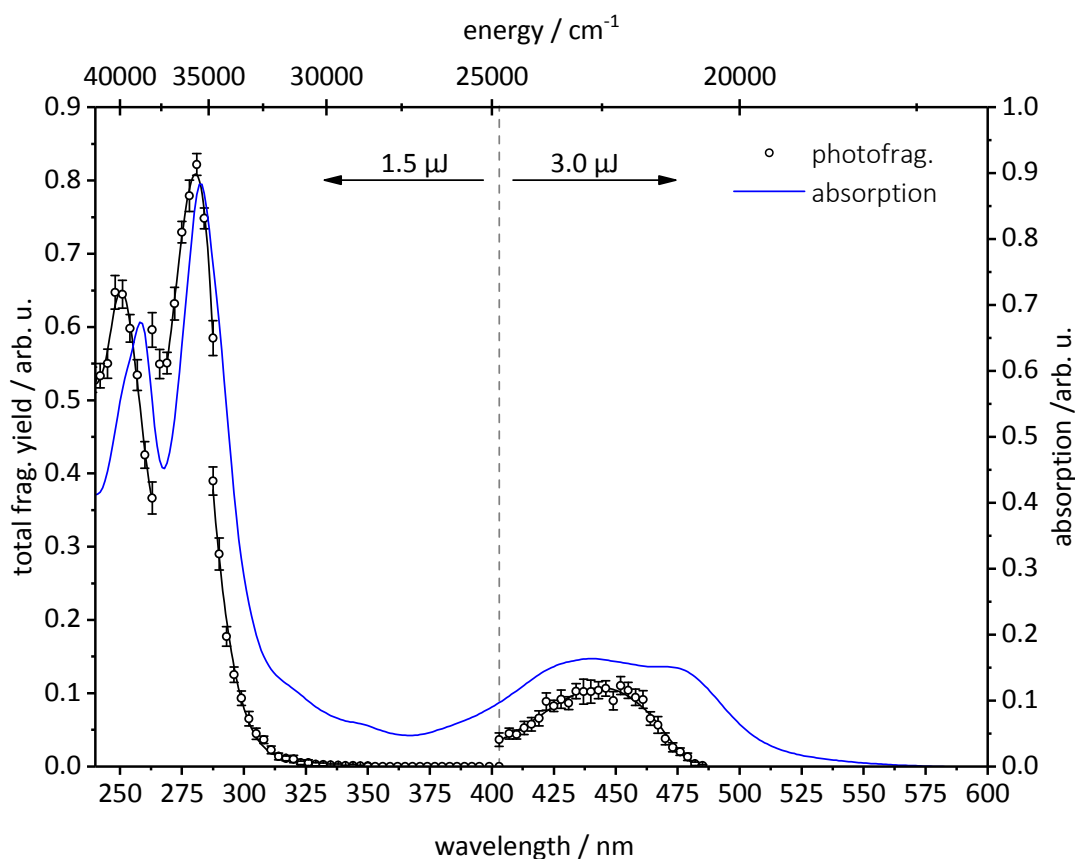
Figure 3 Gas phase UV/Vis PF spectrum (black open circles) and linear absorption spectrum of **RubbipPt** in acetonitrile solution (blue, c=5·10⁻⁶ M). Charge transfer region (400-480 nm, separated by dashed vertical line) in the PF spectrum was recorded at higher laser pulse energies (3μJ vs. 1.5 μJ for the remaining spectral range).

RubbipPt exhibits exceptionally high fragmentation in the UV region (up to 300 nm), hence the spectral shape of the gas phase action spectrum follows closely the UV/Vis solution spectrum (Figure 3), even at relatively moderate applied pulse energies (~1.5 μJ). Starting at ~290 nm, the fragmentation drops steeply to almost zero (at 325 nm) for the remaining recorded spectra range (325-480 nm). Thus we applied higher pump pulse energies (~3 μJ) to record the longest wavelength absorption band (≥400 nm). Apparently, the non-linearity of the Vis PF process (Figure S3), combined with the inherently lower absorption probability and collisional cooling with the helium buffer gas inside the trap results in low intensity absorption bands in the gas phase

action spectrum at longer wavelengths. We have previously reported on this behavior in our studies on other transition metal complexes using the same experimental setup.[28-29]

The gas phase action spectrum (Figure 3) compares remarkably well to the liquid phase absorption spectrum in acetonitrile. However, some differences have to be addressed: firstly, the intense absorption band in the higher energy UV region (at ~250 nm) is shifted hypsochromically (by ~1500 cm^{-1}) with respect to the band in solution (at ~260 nm), whereas the most intense band (at ~280 nm), present in both spectra, is mostly unaffected by the solvent. This finding probably points to some contribution of a charge transfer (CT) transition to the absorption band at ~250 nm, as a charge separated state should be stabilized in polar environments and hence shifted to lower energies with respect to a less polar environment, *i.e.* the gas phase.

Secondly, the longest wavelength absorption band (≥400 nm) in the gas phase spectrum is relatively featureless compared to the band in solution, which clearly exhibits the contribution of at least two dominating transitions centered at ~440 nm and ~480 nm (Figure S4). Lastly, this particular absorption band is much narrower in the gas phase spectrum, implying no absorption for $\lambda_{ex} \geq 480$ nm. Gas phase absorption bands should in general be narrower than in solution, being unaffected by *e.g.* collisional broadening and dipole-dipole interaction between the chromophore and the solvent. Especially CT excitations are affected by solvent interaction, as a sudden change in charge distribution in the chromophore upon electronic excitation is ensued by reorganization of the solvent shell, broadening the transition. Even without consulting our quantum chemical calculations, we can safely state that this particular absorption region (≥400 nm) is of CT($d_{Ru} \rightarrow \pi^*_{ligand}$) character, as the shape and location of the band has an uncanny resemblance to the absorption characteristics of [Ru^{II}(bpy)$_3$]$^{2+}$ (bpy=bipyridine) and various compounds using [Ru^{II}(bpy)$_3$]$^{2+}$-like chromophores as light harvesting antennae (see *e.g.* [36-37] and references therein). Hence the absorption band should be shifted to higher energies under isolation. However, this reasoning would only apply to ideal experimental conditions, excluding signal suppression by collisional quenching and non-linear signal generation, as described above. This does not apply to our experimental conditions and detection scheme. Therefore we refrain from further commenting on the shape and location of the CT absorption band we obtained with our current setup. For

high resolution gas phase UV/Vis spectra of larger transition metal complexes a dedicated experimental facility is required, ideally utilizing molecular tagging at cryo-temperatures, which enables single-photon induced dissociation action spectroscopy, as exerted by *e.g.* Weber *et al.* in their study on [Ru^{II}(bpy)$_3$]$^{2+}$.[38]

7.5.3 Geometry optimization and theoretical absorption spectra

Lacking crystallographic data, we have to rely on theoretical means to obtain reasonable molecular geometries, which will be used in concurrent excited state calculations. The tetragonal-planar coordination sphere of the catalytic Pt^{II} metal center allows for binding of up to four (mono-dentate) ligands. In the case of **RubbipPt**, two coordination sites are occupied by chlorido-ligands, leaving two sites open for binding to the NHC-bridging-ligand and one DMSO ligand (a remnant from synthesis), resulting in the coexistence of two possible stereoisomers (*cis* and *trans*). Furthermore, as an ambi-dentate ligand, DMSO can bind to Pt^{II} either via the *O*- or *S*-atom (structural isomerism). Keeping this in mind, we considered four rough structures of **RubbipPt** as starting geometries for the optimization process. The geometry optimized structures and Gibbs free energies with or without employing a solvation model (acetonitrile) are given in Figure S5.

Surprisingly, in both cases (acetonitrile and *vacuo*) the energetically lowest geometry is found to be the *trans-O* isomer, *i.e.* the DMSO ligand is bound to the Pt^{II}-center via the oxygen atom in *trans*-orientation to the bridging ligand. Typically, due to the high affinity of Pt^{II} towards sulfur, the DMSO ligand should bind to the metal by the sulfur atom.[39] Additionally, structural isomerism is deemed to be responsible for the signal pattern in the ^{1}H-NMR spectrum of **RubbipPt**, rather than stereoisomerism.[25] Furthermore, we only found reports in literature, which propose a *cis*-orientation between DMSO and NHC-ligands in platinum complexes with a coordination sphere reminiscent of **RubbipPt**.[40-45] However, without crystallographic data, at this point the binding motif of the DMSO ligand remains elusive. To further investigate the spectroscopic properties of **RubbipPt**, we calculated the liquid and gas phase vertical transition energies for all four isomers resulting from our geometry search (Figure S5).
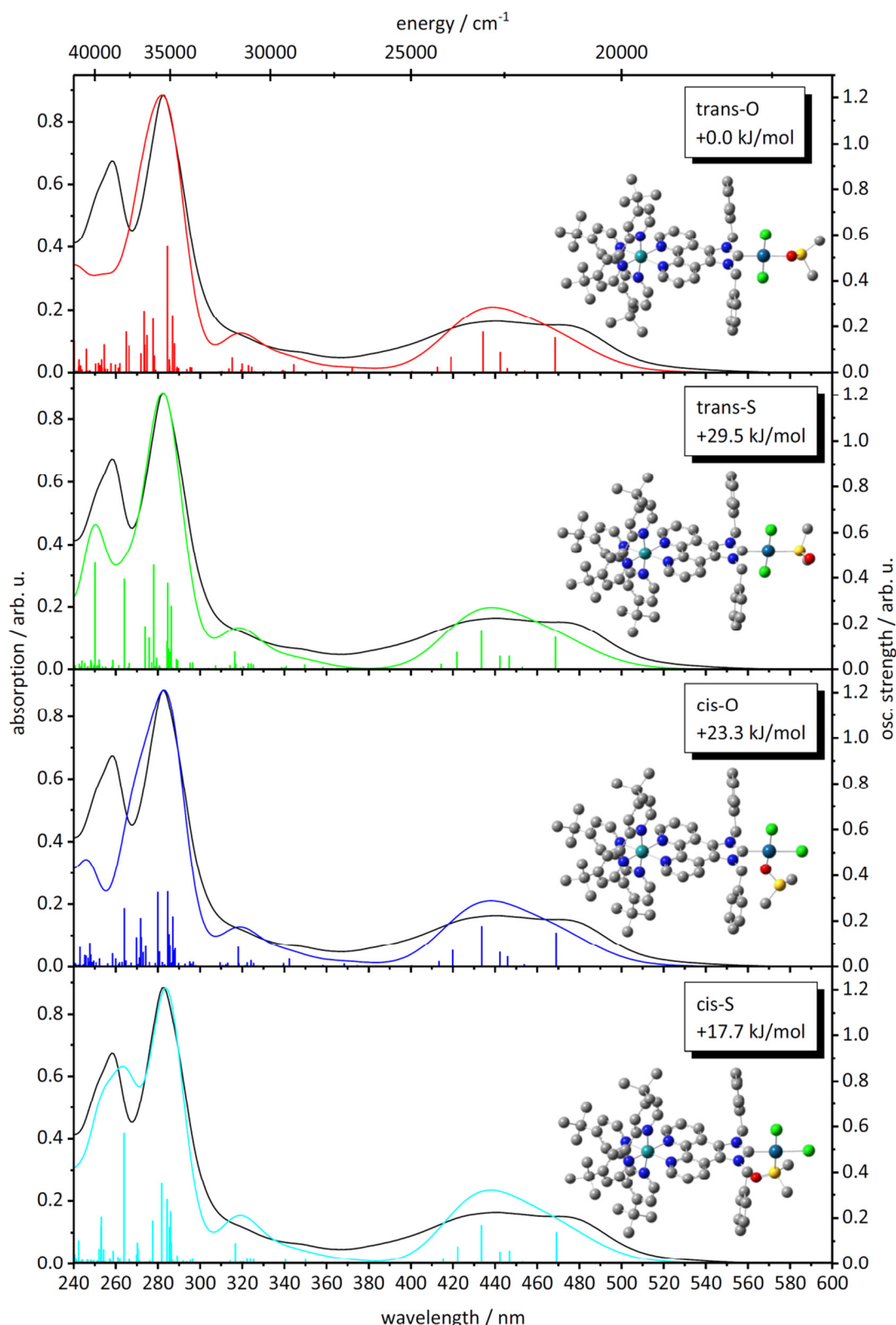
Figure 4 Linear absorption spectrum of **RubbipPt** in acetonitrile solution (black line, $5 \cdot 10^{-6}$ M). Vertical electronic transitions (colored sticks) were calculated for the four lowest lying structural isomers/stereoisomers employing a continuum model. The vertical transitions were shifted bathochromically by 1000 cm^{-1} and broadened with Gaussian functions of 2000 cm^{-1} fwhm.
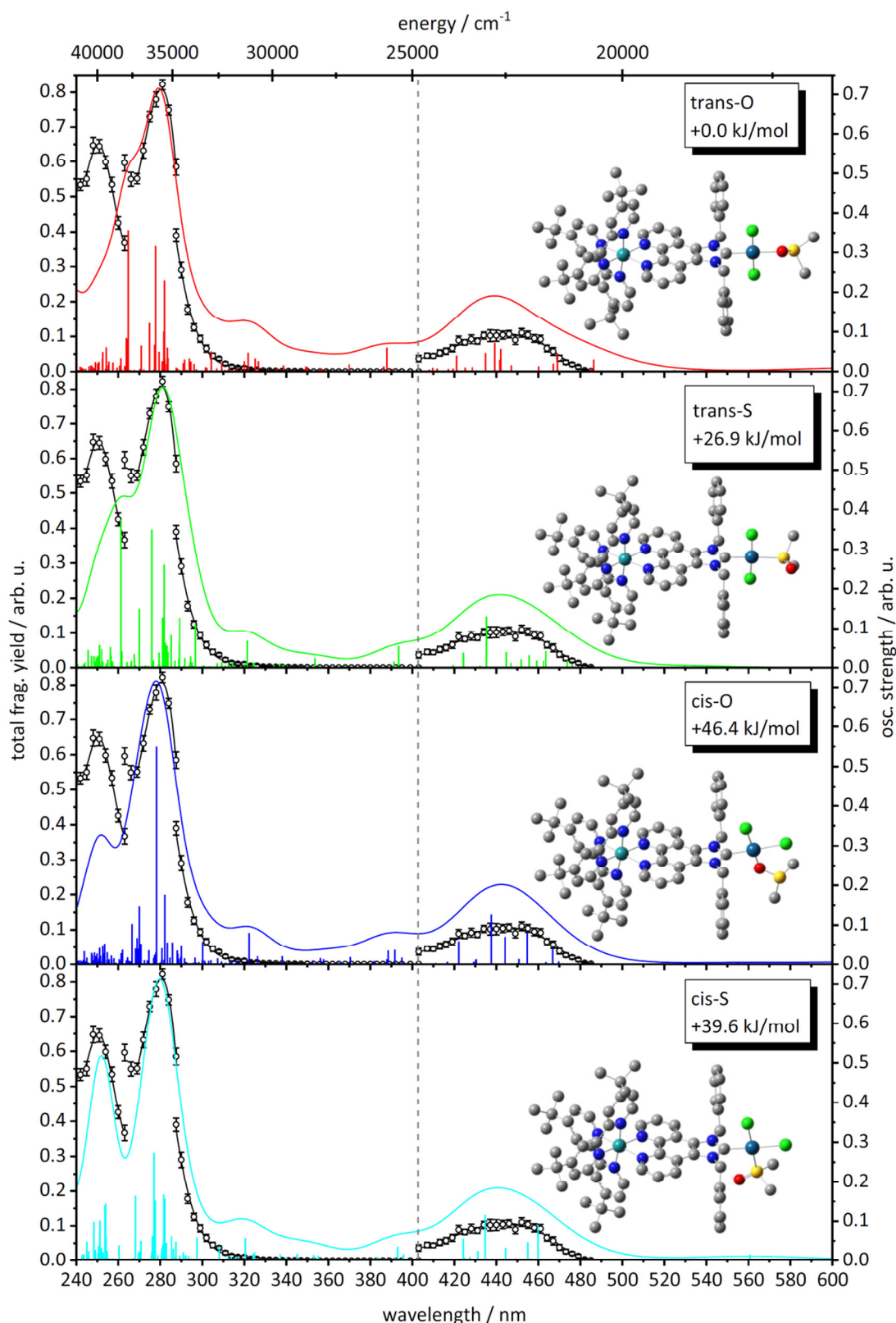
Figure 5 Gas phase UV/Vis PF spectrum of **RubbipPt** (black, open circles). Vertical electronic transitions (colored sticks) were calculated for the four lowest lying structural isomers/stereoisomers. The vertical transitions were shifted bathochromically by $1000 \, \text{cm}^{-1}$ and broadened with Gaussian function of $2000 \, \text{cm}^{-1}$ fwhm.

First we discuss the liquid phase absorption spectra. Comparing the convoluted theoretical absorption spectra calculated for the four isomers of **RubbipPt** (Figure 4), it is obvious that they are very similar in shape above 300 nm. The main difference lies within the absorption region below 300 nm, in which the experimental spectrum features two strong absorption bands centered at approximately 260 nm and 280 nm. The calculated spectrum for the *trans-O* isomer outright fails to account for the absorption band at ~250 nm, whereas the *trans-S* and *cis-O* spectrum show absorption bands at 250 nm of comparably low intensity, which may be attributed to the higher energy absorption in the experiment. The best match to the experiment is obtained for the *cis-S* geometry for which a single high intensity transition is predicted at ~263 nm, nearly coinciding with the absorption band at ~250 nm. Furthermore, the asymmetric shape (broadened shorter wavelength flank) of the band is satisfactorily reproduced.

For the calculated gas phase absorption spectra (Figure 5) a very similar behavior is observed. Neither the calculated spectra of the *S*- nor the *O*-bonded *trans*-isomer feature an additional higher frequency UV absorption band separate from the main absorption band centered at ~280 nm. From the stick spectra one can identify an intense transition at ~260 nm, however it is too close to the aggregation of transitions around ~280 nm, resulting in a shoulder in each of the convoluted spectra, instead of a separate band. The *cis-O* spectrum features a relatively low intensity absorption band close to the position of the higher energy UV absorption band in the experiment. However, in contrast to the *trans-O* and *trans-S* spectrum, this band does not originate from a singular, dominant transition, but rather from an aggregation of low intensity transitions centered at ~250 nm. Lastly, in accordance with the theoretical solution spectra, the calculated *cis-S* isomer spectrum fits the experiment best, matching the location and relative intensity of the absorption band in the PF spectrum astoundingly well.

Based on our calculations, the main absorption band at ~280 nm in both the liquid phase (*cf.* Figure S6/7 and Table S1) and gas phase spectrum (*cf.* Figure S8/9 and Table 2) of **RubbipPt** consists mainly of transitions of either ligand centered $\pi \rightarrow \pi^*$ or inter-ligand charge transfer (ILCT) character, whereas the intense UV absorption at ~250/260 nm has a significant contribution from $CT(d_{Pt} \rightarrow \pi^*_{Ligand})$ transitions, agreeing with the small solvatochromic shift we observed by comparison of the liquid phase and gas phase spectra (Figure 3). Although our assignment is mainly based on the calculations of the

cis-S isomer, as it fits the experiment the best, we should mention that the calculations for all isomers identify the band at ~280 nm to be of $\pi \rightarrow \pi^*$ or ILCT character. The contributions, intensities and positions of the CT($d_{Pt} \rightarrow \pi^*_{Ligand}$) transitions, on the other hand, depend delicately on the binding motif of the DMSO ligand, which comes as no surprise, as the respective HOMO orbitals are centered on the platinum atom and the surrounding ligand sphere. Depending on the binding motif, these transitions are shifted either closer to the $\pi \rightarrow \pi^*$/ILCT transitions thus shaping a shoulder in the calculated spectra (*e.g.* in the calculated gas phase spectrum of *trans-O* and *trans-S*) or are shifted towards higher energies and additionally exhibit lower absorption intensities, which results in weaker, albeit separate absorption features. However, the involvement of CT($d_{Pt} \rightarrow \pi^*_{Ligand}$) transitions is difficult to assess, as the respective contributions were found to be minor. Nevertheless, from these results, we infer that the most likely structure of **RubbipPt** appears to be the *cis-S* geometry, although it is not calculated to be energetically most favored isomer.

The broad absorption band ≥400 nm will be discussed in more detail in the following (Figure 6), as the CT transitions are of utmost importance for the mode of operation of an intramolecular photocatalyst. Note that we rescaled the intensities of the calculated spectra to match the experimental band maxima in this illustration.

Again we discuss the results for the liquid phase first. On closer examination of the transitions involved, the position and relative intensities do not seem to depend on the binding motif of the DMSO ligand. The absorption band structure calculated for all isomers is dominated by two intense transitions (S_5 and S_9), which are centered at ~470 nm and ~430 nm, respectively, matching the central wavelengths of the peaks from the signal decomposition analysis we performed strikingly well (Figure S4). All contributing excited states are of metal-to-ligand CT (MLCT) character involving transitions from d orbitals of the ruthenium atom to the π^* orbitals of the ^{t}bbpy- and bbip-ligands. Examplatorily, the singly-excited state configurations for the first eleven excited states (comprising the CT region) and the respective frontier orbitals are given for the *cis-S* isomer in Table 2 and Figure 8 (cf. Table S3-5 and Figure S10-12 for results obtained for the other conformers).
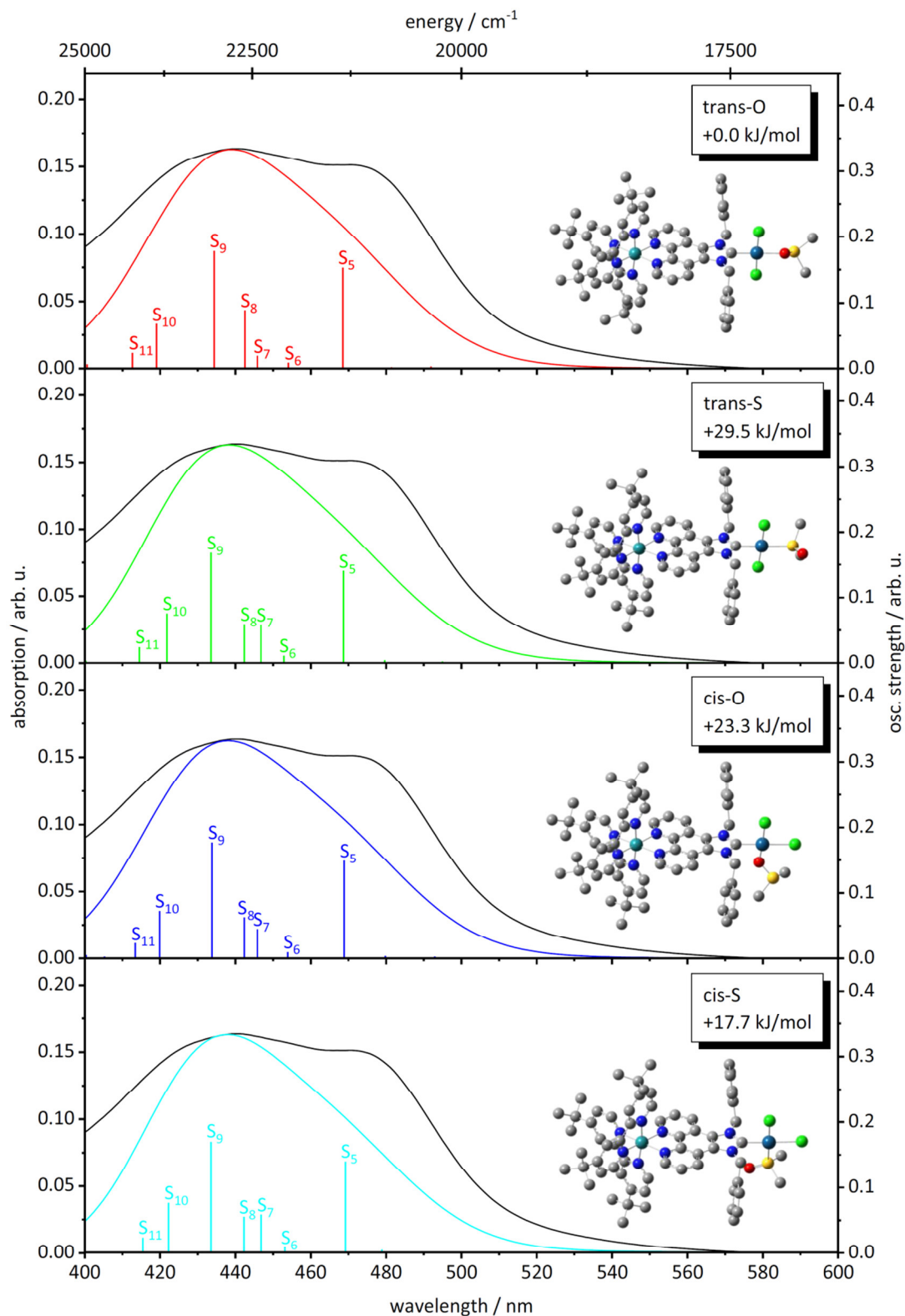
Figure 6 Magnified CT region (400-600 nm) in the solution phase absorption spectrum (black line, $5 \cdot 10^{-6}$ M) of **RubbipPt**. Computed vertical electronic transitions (colored sticks) were shifted bathochromically by 1000 cm^{-1} and scaled in intensity so that the respective absorption maxima coincide. The stick spectra were broadened by a Gaussian function of 2000 cm^{-1} fwhm.
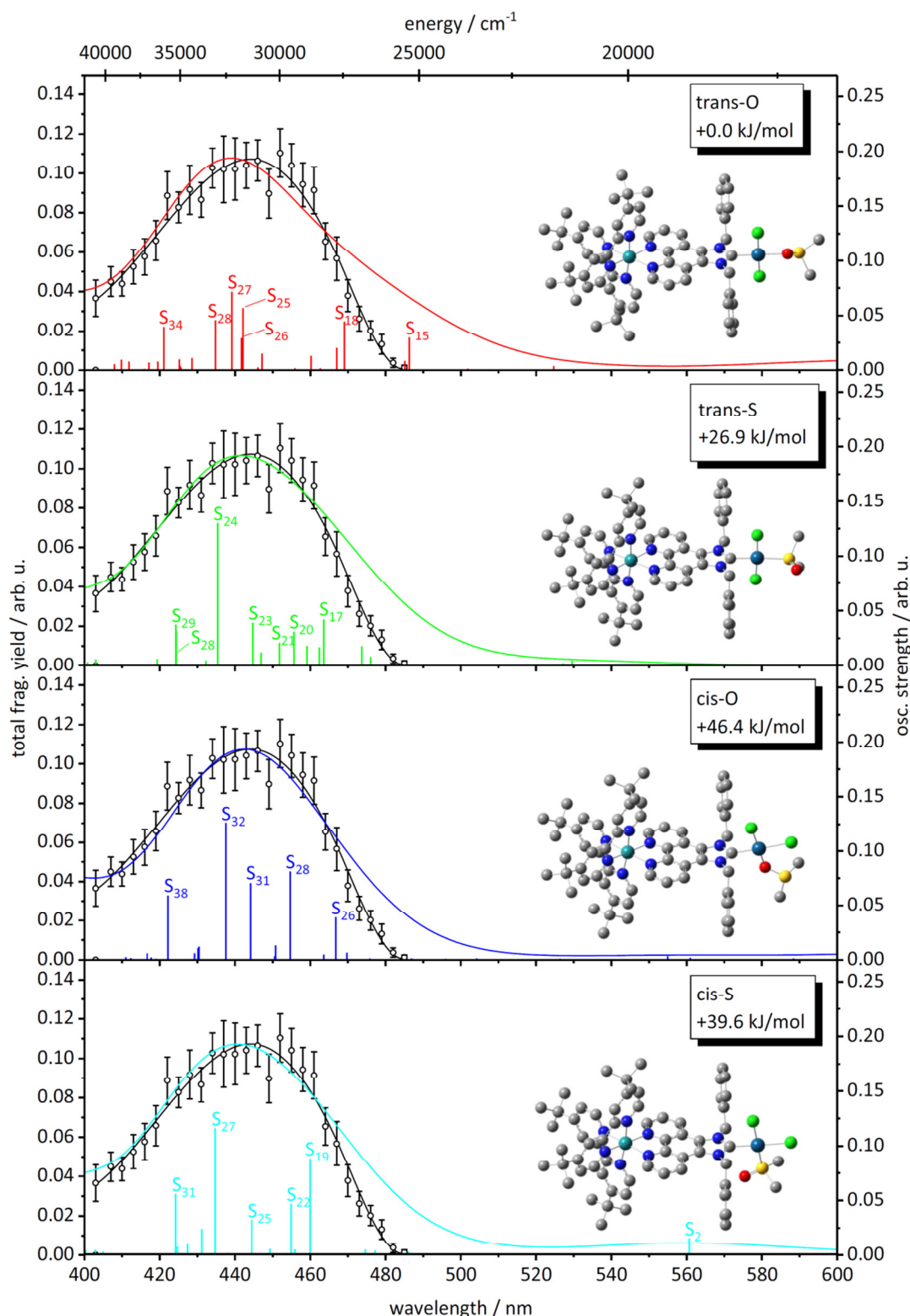
Figure 7 Magnified CT region (400-600 nm) in the gas phase PF spectrum of **RubbipPt**. Computed vertical electronic transitions (colored sticks) were shifted bathochromically by 1000 cm^{-1} and scaled in intensity so that the respective absorption maxima coincide. The stick spectra were broadened by a Gaussian function of 2000 cm^{-1} fwhm.

Table 2 Calculated liquid phase (PCM, acetonitrile) vertical excitation energies E_v, oscillator strengths f and configurations of singlet excited states S_n in the CT region of **RubbipPt** (*cis-S* isomer). Transitions were shifted bathochromically by 1000 cm^{-1}. Frontier orbital contributions to the transitions with a weight w of <10% were omitted.

| S_n	transition	$w/\%$	λ/nm	E_v/eV	f
S_1	$d_{Ru}(HOMO) \rightarrow \pi^*_{bbip}(LUMO)$	94	534	2.32	0.001
S_2	$d_{Ru}(HOMO-2) \rightarrow \pi^*_{bbip}(LUMO)$	41	495	2.50	0.002
	$d_{Ru}(HOMO-1) \rightarrow \pi^*_{bbip}(LUMO)$	52			
S_3	$d_{Ru}(HOMO) \rightarrow \pi^*_{tbbpy}(LUMO+1)$	80	487	2.55	0.001
	$d_{Ru}(HOMO) \rightarrow \pi^*_{tbbpy},\pi^*_{bbip}(LUMO+3)$	10			
S_4	$d_{Ru}(HOMO) \rightarrow \pi^*_{tbbpy}(LUMO+1)$	13	479	2.59	0.005
	$d_{Ru}(HOMO) \rightarrow \pi^*_{bbip},\pi^*_{tbbpy}(LUMO+2)$	33			
	$d_{Ru}(HOMO) \rightarrow \pi^*_{tbbpy},\pi^*_{bbip}(LUMO+3)$	45			
S_5	$d_{Ru}(HOMO-2) \rightarrow \pi^*_{bbip}(LUMO)$	41	469	2.64	0.140
	$d_{Ru}(HOMO-1) \rightarrow \pi^*_{bbip}(LUMO)$	33			
	$d_{Ru}(HOMO) \rightarrow \pi^*_{tbbpy},\pi^*_{bbip}(LUMO+3)$	17			
S_6	$d_{Ru}(HOMO-1) \rightarrow \pi^*_{tbbpy}(LUMO+1)$	70	453	2.74	0.010
S_7	$d_{Ru}(HOMO-2) \rightarrow \pi^*_{tbbpy}(LUMO+1)$	24	447	2.77	0.059
	$d_{Ru}(HOMO) \rightarrow \pi^*_{bbip},\pi^*_{tbbpy}(LUMO+2)$	39			
	$d_{Ru}(HOMO) \rightarrow \pi^*_{tbbpy},\pi^*_{bbip}(LUMO+3)$	19			
S_8	$d_{Ru}(HOMO-2) \rightarrow \pi^*_{tbbpy},\pi^*_{bbip}(LUMO+1)$	15	442	2.81	0.055
	$d_{Ru}(HOMO-2) \rightarrow \pi^*_{bbip},\pi^*_{tbbpy}(LUMO+2)$	27			
	$d_{Ru}(HOMO-2) \rightarrow \pi^*_{tbbpy},\pi^*_{bbip}(LUMO+3)$	26			
	$d_{Ru}(HOMO) \rightarrow \pi^*_{bbip},\pi^*_{tbbpy}(LUMO+2)$	13			
S_9	$d_{Ru}(HOMO-2) \rightarrow \pi^*_{tbbpy}(LUMO+1)$	33	434	2.86	0.170
	$d_{Ru}(HOMO-2) \rightarrow \pi^*_{tbbpy},\pi^*_{bbip}(LUMO+3)$	14			
	$d_{Ru}(HOMO-1) \rightarrow \pi^*_{tbbpy},\pi^*_{bbip}(LUMO+1)$	12			
	$d_{Ru}(HOMO-1) \rightarrow \pi^*_{bbip},\pi^*_{tbbpy}(LUMO+2)$	15			
	$d_{Ru}(HOMO-1) \rightarrow \pi^*_{tbbpy},\pi^*_{bbip}(LUMO+3)$	21			
S_{10}	$d_{Ru}(HOMO-2) \rightarrow \pi^*_{bbip},\pi^*_{tbbpy}(LUMO+2)$	19	422	2.94	0.077
	$d_{Ru}(HOMO-2) \rightarrow \pi^*_{tbbpy},\pi^*_{bbip}(LUMO+3)$	19			
	$d_{Ru}(HOMO-1) \rightarrow \pi^*_{bbip},\pi^*_{tbbpy}(LUMO+2)$	27			
	$d_{Ru}(HOMO-1) \rightarrow \pi^*_{tbbpy},\pi^*_{bbip}(LUMO+3)$	31			
S_{11}	$d_{Ru}(HOMO-2) \rightarrow \pi^*_{bbip},\pi^*_{tbbpy}(LUMO+2)$	38	415	2.99	0.023
	$d_{Ru}(HOMO-2) \rightarrow \pi^*_{tbbpy},\pi^*_{bbip}(LUMO+3)$	19			
	$d_{Ru}(HOMO-1) \rightarrow \pi^*_{bbip},\pi^*_{tbbpy}(LUMO+2)$	26			
	$d_{Ru}(HOMO-1) \rightarrow \pi^*_{tbbpy},\pi^*_{bbip}(LUMO+3)$	12			
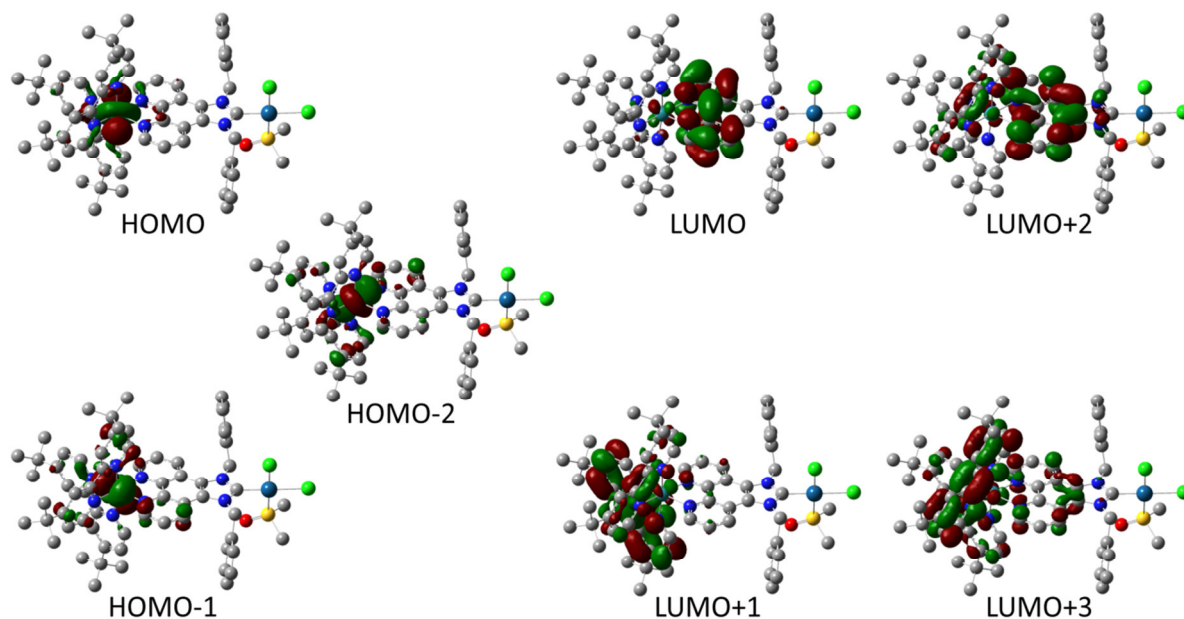
Figure 8 Isosurfaces of frontier orbitals contributing to the calculated liquid phase electronic transitions in the CT region of **RubbipPt** (*cis-S* isomer; Table 2).

Here, the lower energy transitions mainly involve CT to the phenanthroline (phen) part of the bbip ligand (*e.g.* LUMO orbital of S_5), whereas the MLCT states found at shorter wavelengths also encompass transitions to π^*-orbitals centered on the ^{t}bbpy ligands (*e.g.* LUMO+1 and LUMO+2 orbitals of S*9*). Our assignment is corroborated by a previous study combining UV/Vis and resonance Raman spectroscopy on a series of modified Rubbip-chromophores, differing by the amount of bbip-ligands. It was found that the absorption intensity ratio of the two main transitions contributing to the CT absorption band (equivalent to the signals we identified from Figure S4) depended on the number of ^{t}bbpy replaced by bbip. This resulted in an increased absorption at the longest wavelength flank and a concomitant decrease of the absorption at shorter wavelengths in the CT band with more bbip-ligands present. Additionally, excitation at longer wavelengths (476 nm vs. 456 nm) ensued in higher signal intensities of the Raman bands associated with vibrations localized on the bbip-ligand.[46] It is also worth mentioning that similar TD-DFT calculated excited states and intensity distributions in the CT region were reported for two analogous photocatalytic systems employing an identical level of theory.[16, 47-49] As the excited states of the CT absorption band apparently only involve orbitals centered on the ruthenium metal and its surrounding ligand sphere, it comes as no surprise that the binding motif of the DMSO-ligand has no

impact on the spectroscopic behavior in this spectral region, resulting in nearly identical calculated absorption spectra for all considered isomers.

The gas phase calculations, on the other hand, yield drastically different electronic transitions in the CT region. Although the LUMO frontier orbitals involved in the CT transitions are akin to the ones obtained employing a solvent model, the HOMO frontier orbitals are not centered solely on the ruthenium atom but also in part on either the platinum, chlorine atoms or on the phenyl moieties of the bridging ligand. Figure Table 3 and Figure 9 summarize the results obtained for the *cis-S* isomer (*cf.* Table S13-15 and Figure S6-8 for the other isomers).

Table 3 Calculated gas phase vertical excitation energies E_v, oscillator strengths f and configurations of singlet excited states S_n in the CT region of **RubbipPt** (*cis-S* isomer). Transitions were shifted bathochromically by 1000 cm^{-1}. For the sake of clarity, only transitions with high contribution ($f \geq 0.02$) are displayed. Frontier orbital contributions to the transitions with a weight w of <10% were omitted.

S_n	transition	w/%	λ/nm	E_v/eV	f
S_{19}	$d_{Ru},\pi_{bbip},\pi_{Ph}$(HOMO-9)$\to\pi^*_{bbip}$(LUMO)	36	460	2.70	0.088
	$d_{Ru},\pi_{bbip},\pi_{Ph}$(HOMO-9)$\to\pi^*_{tbbpy}$(LUMO+1)	13			
	d_{Ru},d_{Pt},π_{Ph}(HOMO-8)$\to\pi^*_{bbip}$(LUMO)	11			
	d_{Pt},π_{Ph}(HOMO-5)$\to\pi^*_{bbip}$(LUMO)	13			
S_{22}	d_{Ru},π_{Ph}(HOMO-10)$\to\pi^*_{tbbpy}$(LUMO+1)	10	455	2.72	0.047
	$d_{Ru},\pi_{bbip},\pi_{Ph}$(HOMO-9)$\to\pi^*_{tbbpy}$(LUMO+1)	18			
	$d_{Ru},\pi_{bbip},\pi_{Ph}$(HOMO-9)$\to\pi^*_{tbbpy}$(LUMO+2)	12			
	d_{Pt},π_{Ph}(HOMO-5)$\to\pi^*_{bbip}$(LUMO)	12			
S_{25}	d_{Ru},π_{Ph}(HOMO-11)$\to\pi^*_{tbbpy}$(LUMO+2)	22	444	2.79	0.032
	d_{Ru},π_{Ph}(HOMO-10)$\to\pi^*_{tbbpy}$(LUMO+2)	13			
	$d_{Ru},\pi_{bbip},\pi_{Ph}$(HOMO-9)$\to\pi^*_{tbbpy}$(LUMO+1)	16			
	$d_{Ru},\pi_{bbip},\pi_{Ph}$(HOMO-9)$\to\pi^*_{tbbpy}$(LUMO+2)	11			
S_{27}	d_{Ru},π_{Ph}(HOMO-11)$\to\pi^*_{tbbpy}$(LUMO+1)	24	435	2.85	0.116
	d_{Ru},π_{Ph}(HOMO-10)$\to\pi^*_{tbbpy}$(LUMO+1)	19			
	$d_{Ru},\pi_{bbip},\pi_{Ph}$(HOMO-9)$\to\pi^*_{tbbpy}$(LUMO+2)	21			
	d_{Pt},π_{Ph}(HOMO-4)$\to\pi^*_{tbbpy}$(LUMO+1)	16			
S_{31}	d_{Ru},π_{Ph}(HOMO-11)$\to\pi^*_{tbbpy}$(LUMO+2)	10	424	2.92	0.056
	d_{Ru},π_{Ph}(HOMO-10)$\to\pi^*_{tbbpy}$(LUMO+2)	11			
	d_{Ru}(HOMO-7)$\to\pi^*_{bbip}$(LUMO+3)	39			
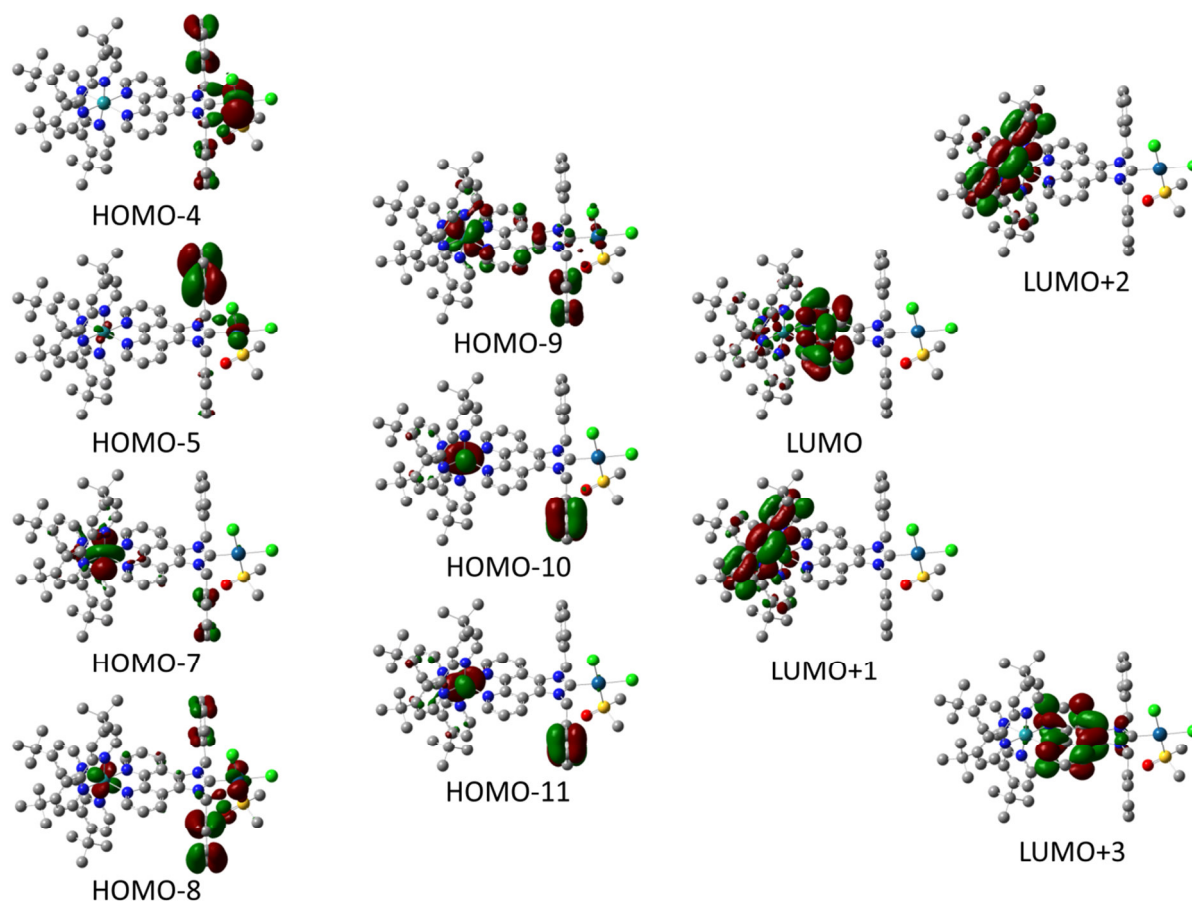
Figure 9 Isosurfaces of frontier orbitals contributing to the gas phase electronic transitions in the CT region of **RubbipPt** (*cis-S* isomer; Table 3).

Our calculations predict a strong involvement of the d_{Pt} orbitals to the lowest energy transitions in the CT region, whereas the $d_{Ru} \rightarrow \pi^*_{Ligand}$ transitions are shifted to higher energies and have in general a relatively small contribution to this absorption region, which appears to be counterintuitive, as the spectroscopic behavior of Ru^{II}-photosensitizers is well understood. This result, however, is in agreement with theoretical investigations on various transition metal-polypyridyl-complexes found in literature, pointing unanimously to the fact that TD-DFT delivers an erroneous description of the lowest energy CT transitions, if calculations were performed in vacuum, and which could only be remedied by employing a solvation model.[47, 50-54] Thus in the following discussion of our time-resolved data we will only consider results from calculations performed in liquid phase for a qualitative interpretation of our experiments.

7.5.4 Time-resolved photofragmentation

The excited state dynamics of isolated **RubbipPt** was recorded by monitoring the pump-probe delay-dependent fragment ion formation as described in *e. g.* Ref. [27-31, 55-56]. Based on previous experience with gas phase investigations on similar supramolecular catalytic assemblies[28], we decided to consult our liquid phase theoretical data for choosing appropriate excitation wavelengths rather than the gas phase TD-DFT calculations, as the latter yielded presumably erroneous results (see previous section). Hence we used pump wavelengths of either λ_{pump}=430 nm (1.5 µJ) or λ_{pump}=470 nm (1.5 µJ), which correspond to CT transitions of either mainly $d_{Ru} \rightarrow \pi^*_{tbbpy}$ or $d_{Ru} \rightarrow \pi^*_{bbip}$ character, respectively. We are very well aware that the TD-DFT calculations we performed for acetonitrile solution can be regarded as (at best) only a crude approximation for the absorption behavior expected for the isolated system. In general, the CT absorption region should be hypsochromically shifted with respect to solution. However, as already addressed, the quality of the non-linear PF signal we obtained for the CT band does not allow for estimating the extent of the hypsochromic shift. Regardless, the excited state population was created using either λ_{pump}=430 nm or 470 nm and its evolution ensuingly probed by irradiation with high intensity probe pulses in the NIR region (λ_{probe}=1200 nm, 120 µJ) resulting in a delay dependent fragmentation enhancement. As the PF mass spectrum of **RubbipPt** is dominated by two fragments (m/z 634 and 473, Figure 2), the decay of the kinetic traces monitored for the fragment channels were subjected to a global fitting routine, rather than modeling the integrated transient mass spectra. Note that the remaining fragments (m/z 615.5, 588 and 569.5, Figure 2) do not contribute significantly to the integrated transient signal and have in general a S/N too poor for fitting. Thus they have been omitted from theoretical modeling. The fragment channel dependent transients recorded for a pump pulse wavelength of λ_{pump}=430 nm and λ_{pump}=470 nm are presented in Figure 10 and 11, respectively.
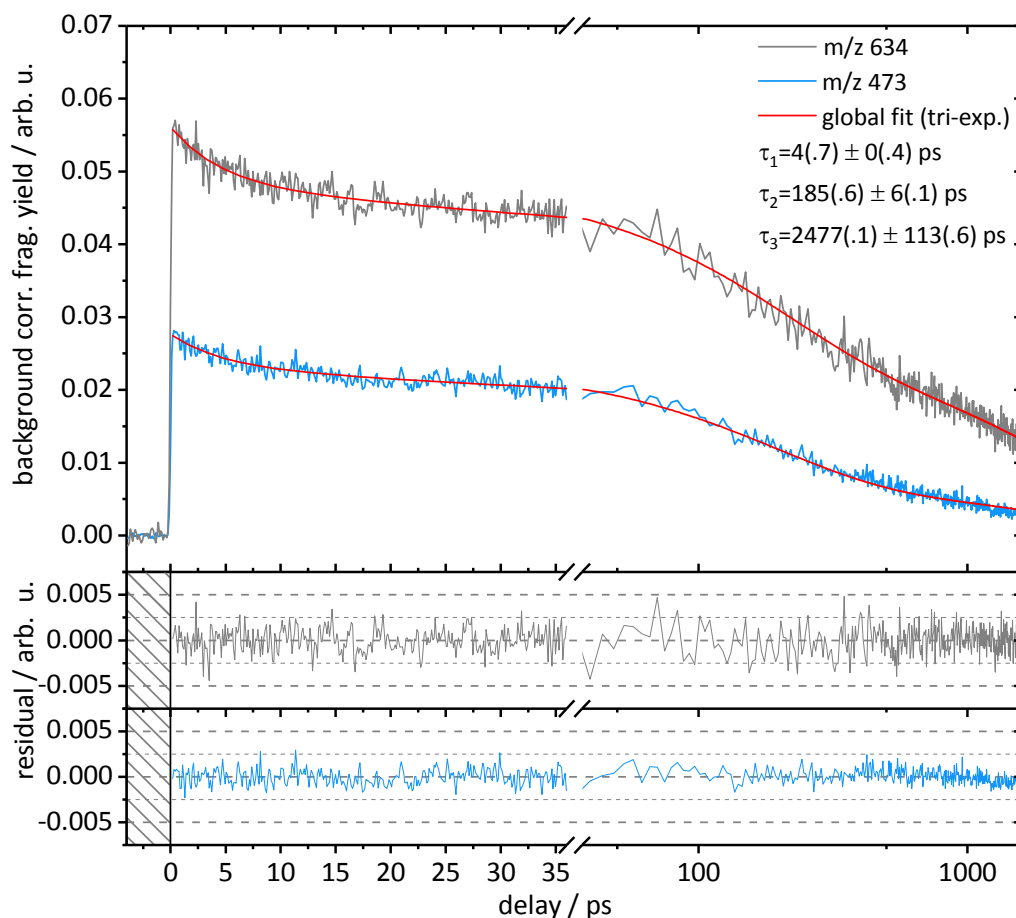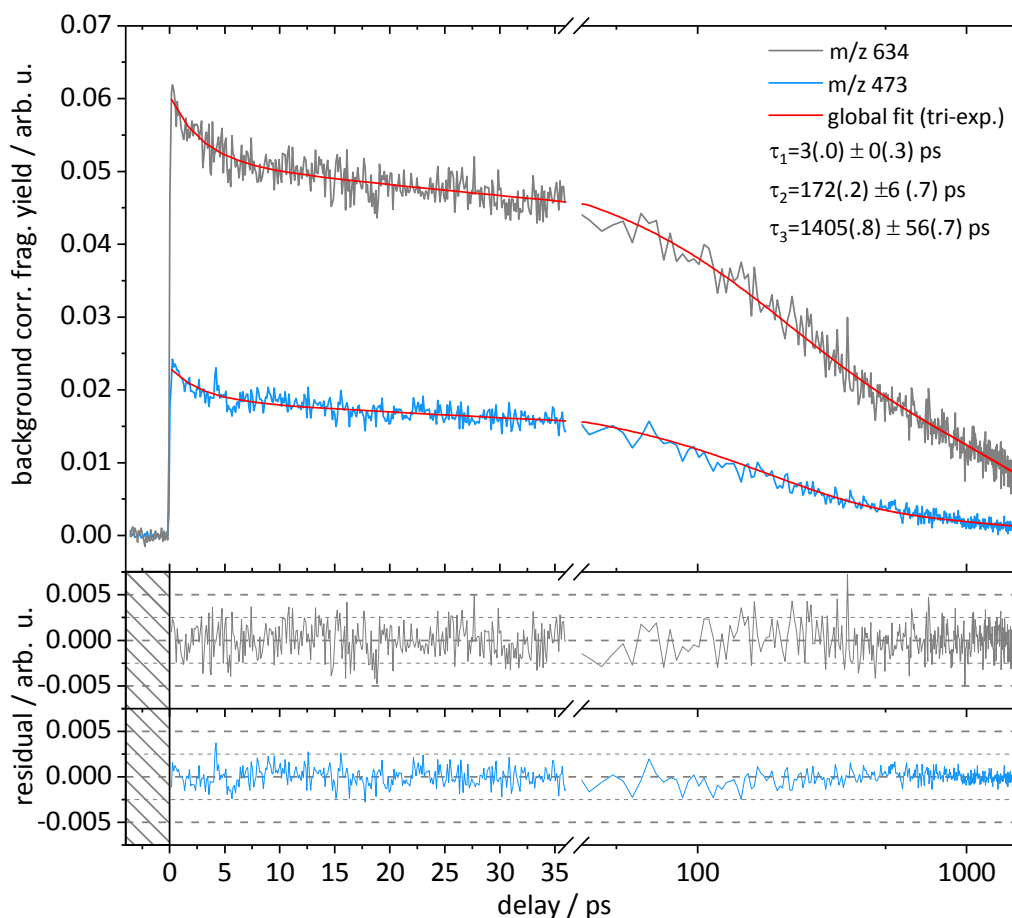
Figure 10 Transient fragment ion traces of **RubbipPt** displayed for the two most intense fragments m/z=634 (gray) and 473 (blue). The transient signals (gray) were recorded at the magic angle (54.7°) using λ_{pump}=430 nm and λ_{probe}=1200 nm. Global tri-exponential fit (red) was performed assuming shared decay kinetics (time constants τ_{1-3}) between the traces. Color coded residual signals are given below. *Cf.* Figure S17 for fit decomposition.

The transients exhibit an ultrafast rise (~200 fs) and decay multi-exponentially. Within the observed experimental limits of the total pump-probe delay (~1.6 ns) the signal decay of the two individual kinetic traces could be fitted quite satisfactorily employing a global tri-exponential decay model, yielding three shared time constants τ_1=4 ps, τ_2=185 ps and $\tau_3\approx$2.5 ns. A fit based on a bi-exponential global model is given in Figure S16. As the transient signals do not abate to the signal level at negative pump-probe delay and the numeric value of τ_3 obtained from fitting exceeds the temporal window accessible in our experiments, it should be pointed out that the value is to be understood as a lower-boundary estimate. Moreover, we cannot exclude additional steps in the electronic dynamics of **RubbipPt**, necessitating the inclusion of further decay components for a more accurate description of the transient traces.

Figure 11 Transient fragment ion traces of **RubbipPt** displayed for the two most intense fragments m/z=634 (black) and 473 (blue). The transient signals (gray) were recorded at the magic angle (54.7°) using λ_{pump}=470 nm and λ_{probe}=1200 nm. Global tri-exponential fit (red) was performed assuming shared decay kinetics (time constants τ_{1-3}) between the traces. Color coded residual signals are given below. *Cf.* Figure S19 for fit decomposition.

At first glance, the transient signals obtained upon excitation at λ_{pump}=470 nm exhibit quite similar behavior to the ones recorded using λ_{pump}=430 nm, *i.e.* rising on a sub-picosecond timescale and decaying multi-exponentially. Indeed, a global tri-exponential fit yields three shared time constants. A fit based on a bi-exponential global model is given in Figure S18. However, their numeric values are smaller (τ_1=3 ps, τ_2=172 ps and $\tau_3 \approx 1.4$ ns) than the ones obtained at λ_{pump}=430 nm (τ_1=4 ps, τ_2=185 ps and $\tau_3 \approx 2.5$ ns), indicating slightly accelerated decay kinetics upon longer wavelength excitation. We are quite confident in the decrease of τ_1 and τ_2 in value, as the transients recorded (at λ_{pump}=430 and 470 nm, respectively) are of similar quality and the fits were performed applying the same convergence criteria and boundary conditions. The massive decrease of the third constant (from $\tau_3 \approx 2.5$ to 1.4 ns), however, is questionable,

as signal decay is incomplete and small differences in the signal level at maximum delay may result in an unreasonable deviation in the fitted lifetimes. Although accurate values for τ_3 from experiments cannot be determined and compared, we cannot rule out a slight decrease of τ_3 as, qualitatively, the transients for λ_{pump}=430 nm appear to exhibit a more mellow decay at longer pump-probe delay.

Assignment of the observed kinetics to individual steps in the electronic dynamics of **RubbipPt** is, at the moment, a challenging endeavor, as further complementary spectroscopic characterization is required. Hence we have to rely on results from literature on similar supramolecular assemblies for a qualitative interpretation. Recent investigations on the Rubbip-chromophore and its corresponding heterodinuclear complexes bearing a silver, rhodium or palladium metal-center by fs transient absorption spectroscopy (TA) in acetonitrile or dichloromethane hinted at ultrafast intersystem crossing (ISC, <<150 fs for Rubbip) to a ^{3}MLCT state from the initially populated ^{1}MLCT state after excitation in the CT region (at 480 nm)[21, 46], exhibiting spectral and temporal characteristics akin to those of the well-known reference system [Ru(bpy)$_3$]$^{2+}$.[57] The ultrafast formation of a ^{3}MLCT state is furthermore corroborated by long excited state lifetimes (µs) and the susceptibility to excited state quenching by triplet oxygen. Other research groups reported similar behavior for Ru^{II}-chromophores bearing imidazophenanthrolin(ium)-ligands and their corresponding heterodinuclear metal complexes.[40, 58] If ISC does indeed proceed on such a short time scale, then we cannot detect this process, due to lack of temporal resolution.

Besides ultrafast formation of the ^{3}MLCT, no further dynamics on the sub-ns timescale were detailed, although *e.g.* Rau *et al.*[21] and Hoberg *et al.*[40] in their studies used TA setups more than capable of resolving rapid dynamics. It is tempting to ascribe the discrepancy to our present study to a difference in metal centers coordinated to the NHC-bridge (or the lack thereof). Although the complexation of a metal center to the bare photosensitizer may strongly affect the early excited-state chemistry across the electron-relaying bridge of the supramolecular complex (as showcased by *e.g.* by Rau *et al.* previously[59]), a sole exchange of the metal should not have an effect on the same order of magnitude.[16, 28] At this point it remains to be seen how this class of catalysts behaves in future solution phase investigations focusing on their early excited state dynamics.

One point of reference for assignment of the time constants we observed is our earlier study on a similar kind of photocatalysts (RutpphzM, M=Pt, Pd), in which we successfully demonstrated[28] that our gas phase approach can credibly reproduce results from solution.[16, 59] In this study we reported on two photocatalysts consisting of a ruthenium-polypyridyl sensitizer and a transition metal-chloride (PdCl$_2$ and PtCl$_2$) linked by a symmetric tetrapyrido-phenazine (tpphz) bridging ligand. In this framework, the bridge could be understood as a central phenazine (phz) unit bearing phenanthroline (phen) moieties at its ends. In agreement with the early excited state dynamics in solution phase from literature,[16] the tPF transients recorded upon excitation of the Pt-bearing compound (RutpphzPt) at the center of the CT absorption band (440 nm) could be satisfactorily modeled with a tri-exponential decay yielding time constants of τ_1=0.6 ps, τ_2=6.5 ps and additionally a time constant τ_3, which exceeded our former accessible total pump-probe delay of 800 ps. These were assigned, in accordance to processes taking place in solution, to an inter-ligand electron transfer (ILET, τ_1) within the ruthenium ligand sphere, resulting in the formation of a ^{3}MLCT state mainly centered on the phen-part of the bridge, followed by an intra-ligand CT (ILCT, τ_2) forming a phz-localized state. The ensuing reduction of the Pt-metal center by ligand-to-metal CT (LMCT) proceeds with a characteristic kinetic component of at least 800 ps. A time constant for the ultrafast ISC to a ^{3}MLCT state (<100 fs)[49] from the initially excited ^{1}MLCT state was not detected, due to insufficient temporal resolution of our experimental setup. In addition, we observed an acceleration of the first kinetic steps (τ_1 and τ_2) upon longer wavelength excitation (480 nm instead of 440 nm), in agreement with high-resolution TA spectroscopy performed for the RutpphzPd complex.[49] This effect was ascribed 1) to a lesser contribution of the ILET process to the kinetics (τ_1) related to the formation of the ^{3}MLCT$_{phen}$ state and 2) to a better coupling between a vibrationally less excited ^{3}MLCT$_{phen}$ and the ensuingly formed ^{3}MLCT$_{phz}$ state (τ_2).

Having recounted our previous results we laid out a foundation for discussing the dynamics of **RubbipPt** in our current study. The value of τ_1 we determined for **RubbipPt** (3 ps at λ_{pump}=470 nm, Figure 10b) can probably be compared to τ_1 of RutpphzPt (0.4 ps at λ_{pump}=480 nm). Keeping in mind that this process was assigned to the charge localization on the phen-moiety adjacent to the ruthenium metal-center by

ILET, the difference in values (if we assign τ_1 to the same process) can be tentatively explained by a worse coupling of the partially populated ^{t}bbpy-centered excited states and the final bbip-localized state in the case of **RubbipPt**. As a matter of fact, Rau *et al.* reported higher potentials necessary for the reduction of the phen-ligand compared to the bbip-bridge in the respective complexes, whereas the potentials associated with the reduction of the peripheral ^{t}bbpy-ligands were found to be nearly identical.[21] According to the energy gap law for radiationless transitions,[60-66] a higher energetic gap would result in worse vibronic coupling and correspondingly a slower ILCT process. Moreover, in a recent study by Reichardt *et al.* on the ultrafast electronic dynamics of a Ru^{II}-dyad bearing a pyrene (py)-functionalized imidazophenanthroline (ip) ligand (Ru^{II}-ip-py), a short time constant of 3.1 ps (in water, λ_{pump}=467 nm) was identified and assigned to the formation of an ^{3}MLCT state centered on ip.[60] Granted, the molecular system as a whole is distinctly different than **RubbipPt**, as it bears a pyrene moiety in place of a second metal center. However, in this context the immediate coordination spheres of both photosensitizers are identical and the time constants (τ_1) in remarkable mutual agreement. Additionally, upon longer wavelength excitation τ_1 becomes shorter, similar to the accelerated dynamics of in RutpphzM complexes, which was ascribed to a lesser involvement of the ancillary ^{t}bbpy ligands and thus a more directed and faster transfer to the bridge.[28, 49]. From this discussion we infer that the assignment of τ_1 to a similar process found for RutpphzM, *i.e.* the formation of the ^{3}MLCT$_{phen}$ state is justified.

Identification of the ensuing processes associated with τ_2 and τ_3, respectively, is more challenging and, admittedly, quite speculative as the similarities to our previous investigation on RutpphzM come to an end. For RutpphzM complexes, the second time constant observed both in gas phase and solution studies was much shorter (τ_2=6.5/4.3 ps vs. τ_2~185/172 ps for **RubbipPt**)[26] and assigned to the formation of a ^{3}MLCT$_{phz}$ state, *i.e.* located on the central phz unit of the bridge. τ_3, on the other hand, characterized the subsequent reduction of the catalytic metal center and proceeded with a time constant of τ_3=320 ps (310 ps) for M=Pt (Pd) in MeCN.[16, 59] In the gas phase, this process was found to be much slower (>800 ps for both M=Pt, and Pd), lacking a polar environment to stabilize the charge separated state.[26] It is conceivable that for **RubbipPt** analogous steps take place, *i.e.* first a charge localization more centered on the imidazolium part of the bridge (τ_2) succeeded by the transfer to the Pt atom (τ_3). The

much slower ILCT in the bbip bridge (τ_2=185/172 ps) compared to tpphz (τ_2=6.5 ps)[26] may be rationalized by a smaller π-system and hence a higher reduction potential. In the same vein we may justify the acceleration of τ_2 upon longer wavelength excitation by a worse coupling between a vibrationally higher excited phen centered and the imidazolium centered state. Hence, τ_3 can be tentatively assigned to an ensuing LMCT, in accordance to the timescale of τ_3 found for RutpphzM. In hindsight, this assignment is quite speculative and can be challenged easily, considering that Reichardt *et al.* in their study on the Ru[II]-ip-py dyad did not present spectroscopic evidence for charge localization on the imidazolium unit, but rather a direct transfer onto the pyrene from the [3]MLCT state delocalized on the ip-bridge within ~30 ps, strongly influenced by solvent viscosity. However, in case of the dyad, the pyrene moiety can be regarded as an extension to the π-system of the ip-bridge, whereas in RubbipPt, the metal interacts with the bridge via σ-bonding with the carbene. Hence, direct comparison of the observed dynamics is not feasible. Lastly, we want to point out, that the slow electronic dynamics compared to similar catalysts is in line with its lower photocatalytic activity, although other factors, such as the high steric demand of the benzyl groups in close vicinity to the catalytic metal center may be much more dominant in this regard.

7.6 Conclusion

We presented for the first time a study on the UV/Vis absorption properties of a novel heterodinuclear complex for photocatalytic hydrogen generation in both gas phase and solution, corroborated by TD-DFT calculations. The recorded gas phase UV/Vis action spectrum compares remarkably well to the linear liquid phase absorption spectrum from acetonitrile solution, exhibiting two distinct absorption bands in the UV and a broad CT band in the Vis region. By comparison of TD-DFT calculated linear absorption spectra to the experimental band progression in the liquid phase and gas phase spectra, the most likely structure of **RubbipPt** was found to be the *cis-S* isomer, in which the DMSO ligand binds to the platinum atom via the S atom in *cis*-orientation to the bridging ligand. Although this geometry appears to be the most prominent in structurally similar complexes found in literature, it was not calculated to be the energetically most favored geometry for **RubbipPt**. TD-DFT calculations employing a solvent model identified the CT band to be dominated by two transitions, with the lower energy transition involving mainly CT from the ruthenium metal center to the π-system of the bridging ligand,

whereas the higher energy transition encompasses CT spread over the ligand sphere of the ruthenium photosensitizer. The liquid phase calculations are in accordance to previous calculations performed for a similar type of supramolecular catalyst. Calculations on the isolated molecule, on the other hand, although in excellent agreement with the experimental PF spectrum in the UV region, fail to produce reasonable results for the lowest energy transitions in the CT region, further stressing the need for a more sophisticated theoretical approach to model the properties of low lying excited state of larger systems under isolation, which apparently TD-DFT cannot provide. The recorded transient mass spectra decayed tri-exponentially, yielding a time constant on a ns-timescale and two on a ps-timescale. Based on our calculations and by comparison of the recorded dynamics to reports found in literature, we assigned the shortest time constant to a CT transition onto the bridge. Our assignment was further corroborated by acceleration of the kinetics upon longer wavelength excitation, in agreement with a more directed electron transfer towards the catalytic metal center. The origin of the remaining two processes remains elusive at this point and begs for further complementary time-resolved investigations in solution. Nonetheless, the kinetics we reported here should set a clear framework for future studies.

Further investigations in our laboratory are on the way, exploring the impact of halide ligand exchange at the catalytic metal center on the excited state dynamics of **RubbipPt**. In a preliminary mass spectrometric and catalytic study, we found a high affinity of the Pt metal center to iodide ligands, resulting in *in situ* ligand exchange and, more excitingly, a dramatic increase in the catalytic performance of **RubbipPt**.[25] As the iodide-species could not be accessed via synthetic means, yet, our experimental setup is the only way to selectively probe its altered photodynamics.

7.7 References

[1]   N. Armaroli, V. Balzani,*"The Future of Energy Supply: Challenges and Opportunities"*, *Angew. Chem. Int. Ed.* **2007**, *46*, 52-66.

[2]   W. Lubitz, W. Tumas, *"Hydrogen: An Overview"*, *Chem. Rev.* **2007**, *107*, 3900-3903.

[3]   M. Momirlan, T. N. Veziroglu, *"The properties of hydrogen as fuel tomorrow in sustainable energy system for a cleaner planet"*, *Int. J. Hydrogen Energy* **2005**, *30*, 795-802.

[4]   P. P. Edwards, V. L. Kuznetsov, W. I. F. David, N. P. Brandon, *"Hydrogen and fuel cells: Towards a sustainable energy future"*, *Energy Policy* **2008**, *36*, 4356-4362.

[5]   I. P. Jain,*"Hydrogen the fuel for 21st century"*, *Int. J. Hydrogen Energy* **2009**, *34*, 7368-7378.

[6]   H. J. Neef, *"International overview of hydrogen and fuel cell research"*, *Energy* **2009**, *34*, 327-333.

[7]   I. Dincer, *"Environmental and sustainability aspects of hydrogen and fuel cell systems"*, *Int. J. Energy Res.* **2007**, *31*, 29-55.

[8]   J. R. Rostrup-Nielsen, *"Catalysis: Science and Technology"* (Eds.: J. R. Anderson, M. Boudart), Springer Berlin Heidelberg, Berlin, Heidelberg, **1984**, pp. 1-117.

[9]   M. D. Kärkäs, O. Verho, E. V. Johnston, B. Åkermark, *"Artificial Photosynthesis: Molecular Systems for Catalytic Water Oxidation"*, *Chem. Rev.* **2014**, *114*, 11863-12001.

[10]   E. Amouyal, *"Photochemical production of hydrogen and oxygen from water: A review and state of the art"*, *Sol. Energy Mater. Sol. Cells* **1995**, *38*, 249-276.

[11]   L. Sun, L. Hammarstrom, B. Akermark, S. Styring, *"Towards artificial photosynthesis: ruthenium-manganese chemistry for energy production"*, *Chem. Soc. Rev.* **2001**, *30*, 36-49.

[12]   A. Inagaki, M. Akita, *"Visible-light promoted bimetallic catalysis"*, *Coord. Chem. Rev.* **2010**, *254*, 1220-1239.

[13]   M. Schulz, M. Karnahl, M. Schwalbe, J. G. Vos, *"The role of the bridging ligand in photocatalytic supramolecular assemblies for the reduction of protons and carbon dioxide"*, *Coord. Chem. Rev.* **2012**, *256*, 1682-1705.

[14]   H. Ozawa, K. Sakai, *"Photo-hydrogen-evolving molecular devices driving visible-light-induced water reduction into molecular hydrogen: structure-activity relationship and reaction mechanism"*, *Chem. Commun.* **2011**, *47*, 2227-2242.

[15]   S. Rau, B. Schäfer, D. Gleich, E. Anders, M. Rudolph, M. Friedrich, H. Görls, W. Henry, J. G. Vos, *"A Supramolecular Photocatalyst for the Production of Hydrogen and the Selective Hydrogenation of Tolane"*, *Angew. Chem. Int. Ed.* **2006**, *45*, 6215-6218.

[16]   M. G. Pfeffer, B. Schäfer, G. Smolentsev, J. Uhlig, E. Nazarenko, J. Guthmuller, C. Kuhnt, M. Wächtler, B. Dietzek, V. Sundström, S. Rau, *"Palladium versus Platinum: The Metal in the Catalytic Center of a Molecular Photocatalyst Determines the Mechanism of the Hydrogen Production with Visible Light"*, *Angew. Chem. Int. Ed.* **2015**, *54*, 5044-5048.

[17]   P. Lei, M. Hedlund, R. Lomoth, H. Rensmo, O. Johansson, L. Hammarström, *"The Role of Colloid Formation in the Photoinduced H2 Production with a RuII−PdII Supramolecular Complex: A Study by GC, XPS, and TEM"*, *J. Am. Chem. Soc.* **2008**, *130*, 26-27.

[18] P. Du, J. Schneider, F. Li, W. Zhao, U. Patel, F. N. Castellano, R. Eisenberg, *"Bi- and Terpyridyl Platinum(II) Chloro Complexes: Molecular Catalysts for the Photogeneration of Hydrogen from Water or Simply Precursors for Colloidal Platinum?"*, *J. Am. Chem. Soc.* **2008**, *130*, 5056-5058.

[19] H.-J. Park, Y. K. Chung, *"Ru(II)–M(I) (M = Rh and Ir) bimetallic complexes based on a bridging ligand composed of 1,10-phenanthroline and N-heterocyclic carbene: Coordination chemistry and detection property of carbon monoxide"*, *Inorg. Chim. Acta* **2012**, *391*, 105-113.

[20] H.-J. Park, K. Kim, Y. K. Chung, *"ReI–IrI bimetallic complexes based on a bis(chelating) ligand composed of 1,10-phenanthroline and N-heterocyclic carbene: Coordination chemistry and their application for optical indicator of CO gas"*, *Inorg. Chim. Acta* **2014**, *410*, 214-220.

[21] K. Peuntinger, T. D. Pilz, R. Staehle, M. Schaub, S. Kaufhold, L. Petermann, M. Wunderlin, H. Gorls, F. W. Heinemann, J. Li, T. Drewello, J. G. Vos, D. M. Guldi, S. Rau, *"Carbene based photochemical molecular assemblies for solar driven hydrogen generation"*, *Dalton Trans.* **2014**, *43*, 13683-13695.

[22] R. Jackstell, M. Gómez Andreu, A. Frisch, K. Selvakumar, A. Zapf, H. Klein, A. Spannenberg, D. Röttger, O. Briel, R. Karch, M. Beller, *"A Highly Efficient Catalyst for the Telomerization of 1,3-Dienes with Alcohols: First Synthesis of a Monocarbenepalladium(0)–Olefin Complex"*, *Angew. Chem. Int. Ed.* **2002**, *41*, 986-989.

[23] S. Kaufhold, L. Petermann, R. Staehle, S. Rau, *"Transition metal complexes with N-heterocyclic carbene ligands: From organometallic hydrogenation reactions toward water splitting"*, *Coord. Chem. Rev.* **2015**, *304–305*, 73-87.

[24] S. Kaufhold, L. Petermann, D. Sorsche, S. Rau, *"Trojan Horse" Effect in Photocatalysis–How Anionic Silver Impurities Influence Apparent Catalytic Activity"*, *Chem. Eur. J.* **2017**, *23*, 2271-2274.

[25] S. Kaufhold, D. Imanbaew, C. Riehn, S. Rau, *"Rational in situ tuning of a supramolecular photocatalyst for hydrogen evolution"*, *submitted to Energy Environ Sci.* **2017**.

[26] D. Imanbaew, J. Lang, M. F. Gelin, S. Kaufhold, M. G. Pfeffer, S. Rau, C. Riehn, *"Pump-Probe Fragmentation Action Spectroscopy: A Powerful Tool to Unravel Light-Induced Processes in Molecular Photocatalysts"*, *Angew. Chem. Int. Ed.* **2017**, *56*, 5471-5474.

[27] D. Imanbaew, M. F. Gelin, C. Riehn, *"Rotational and vibrational dynamics in the excited electronic state of deprotonated and protonated fluorescein studied by time-resolved photofragmentation in an ion trap"*, *Struct. Dyn.* **2016**, *3*, 043211.

[28] D. Imanbaew, J. Lang, M. F. Gelin, S. Kaufhold, M. G. Pfeffer, S. Rau, C. Riehn, *"Pump-Probe Fragmentation Action Spectroscopy: A Powerful Tool to Unravel Light-Induced Processes in Molecular Photocatalysts"*, *Angew. Chem. Int. Ed.* **2017**, *56*, 5471-5474.

[29] D. Imanbaew, Y. Nosenko, C. Kerner, K. Chevalier, F. Rupp, C. Riehn, W. R. Thiel, R. Diller, *"Excited-state dynamics of a ruthenium(II) catalyst studied by transient photofragmentation in gas phase and transient absorption in solution"*, *Chem. Phys.* **2014**, *442*, 53-61.

[30] D. Nolting, T. Schultz, I. V. Hertel, R. Weinkauf, *"Excited state dynamics and fragmentation channels of the protonated dipeptide H2N-Leu-Trp-COOH"*, *Phys. Chem. Chem. Phys.* **2006**, *8*, 5247-5254.

[31] D. Nolting, R. Weinkauf, I. V. Hertel, T. Schultz, *"Excited-State Relaxation of Protonated Adenine"*, Chem. Phys. Chem. **2007**, *8*, 751-755.

[32] M. J. Frisch, G. W. Trucks, H. B. Schlegel, G. E. Scuseria, M. A. Robb, J. R. Cheeseman, G. Scalmani, V. Barone, B. Mennucci, G. A. Petersson, H. Nakatsuji, M. Caricato, X. Li, H. P. Hratchian, A. F. Izmaylov, J. Bloino, G. Zheng, J. L. Sonnenberg, M. Hada, M. Ehara, K. Toyota, R. Fukuda, J. Hasegawa, M. Ishida, T. Nakajima, Y. Honda, O. Kitao, H. Nakai, T. Vreven, J. A. Montgomery Jr., J. E. Peralta, F. Ogliaro, M. J. Bearpark, J. Heyd, E. N. Brothers, K. N. Kudin, V. N. Staroverov, R. Kobayashi, J. Normand, K. Raghavachari, A. P. Rendell, J. C. Burant, S. S. Iyengar, J. Tomasi, M. Cossi, N. Rega, N. J. Millam, M. Klene, J. E. Knox, J. B. Cross, V. Bakken, C. Adamo, J. Jaramillo, R. Gomperts, R. E. Stratmann, O. Yazyev, A. J. Austin, R. Cammi, C. Pomelli, J. W. Ochterski, R. L. Martin, K. Morokuma, V. G. Zakrzewski, G. A. Voth, P. Salvador, J. J. Dannenberg, S. Dapprich, A. D. Daniels, Ö. Farkas, J. B. Foresman, J. V. Ortiz, J. Cioslowski, D. J. Fox, Gaussian, Inc., Wallingford, CT, USA, **2009**.

[33] A. D. Becke, *"Density-functional thermochemistry. III. The role of exact exchange"*, J. Chem. Phys. **1993**, *98*, 5648-5652.

[34] C. Lee, W. Yang, R. G. Parr, *"Development of the Colle-Salvetti correlation-energy formula into a functional of the electron density"*, Phys. Rev. B **1988**, *37*, 785-789.

[35] J. Tomasi, B. Mennucci, R. Cammi, *"Quantum Mechanical Continuum Solvation Models"*, Chem. Rev. **2005**, *105*, 2999-3094.

[36] A. Maldotti, *"Photochemistry"*, The Royal Society of Chemistry, **2009**, *37*, 240-299.

[37] D. M. Roundhill, *"Photochemistry and Photophysics of Metal Complexes"*, Springer US, **1994**.

[38] S. Xu, J. E. T. Smith, J. M. Weber, *"The electronic spectrum of cryogenic ruthenium-tris-bipyridine dications in vacuo"*, J. Chem. Phys. **2016**, *145*, 024304.

[39] B. A. Sexton, N. R. Avery, T. W. Turney, *"A spectroscopic study of the coordination of dimethyl sulfoxide to a platinum (111) surface"*, Surf. Sci. **1983**, *124*, 162-174.

[40] A. A. Webster, S. K. K. Prasad, J. M. Hodgkiss, J. O. Hoberg, *"An N-heterocyclic carbene phenanthroline ligand: synthesis, multi-metal coordination and spectroscopic studies"*, Dalton Trans. **2015**, *44*, 3728-3736.

[41] J. J. Hu, F. Li, T. S. A. Hor, *"Novel Pt(II) Mono- and Biscarbene Complexes: Synthesis, Structural Characterization and Application in Hydrosilylation Catalysis"*, Organometallics **2009**, *28*, 1212-1220.

[42] C. P. Newman, R. J. Deeth, G. J. Clarkson, J. P. Rourke, *"Synthesis of Mixed NHC/L Platinum(II) Complexes: Restricted Rotation of the NHC Group"*, Organometallics **2007**, *26*, 6225-6233.

[43] E. A. Baquero, G. F. Silbestri, P. Gómez-Sal, J. C. Flores, E. de Jesús, *"Sulfonated Water-Soluble N-Heterocyclic Carbene Silver(I) Complexes: Behavior in Aqueous Medium and as NHC-Transfer Agents to Platinum(II)"*, Organometallics **2013**, *32*, 2814-2826.

[44] G. L. Petretto, M. Wang, A. Zucca, J. P. Rourke, *"Platinum(II) N-heterocyclic carbene complexes: coordination and cyclometallation"*, Dalton Trans. **2010**, *39*, 7822-7825.

[45] P. Marshall, R. L. Jenkins, W. Clegg, R. W. Harrington, S. K. Callear, S. J. Coles, I. A. Fallis, A. Dervisi, *"Chiral Ag(I) and Pt(II) complexes of ditopic NHC ligands: synthesis, structural and spectroscopic properties"*, Dalton Trans. **2012**, *41*, 12839-12846.

[46] R. Staehle, C. Reichardt, J. Popp, D. Sorsche, L. Petermann, K. Kastner, C. Streb, B. Dietzek, S. Rau, *"Ruthenium Imidazophenanthrolinium Complexes with Prolonged Excited-State Lifetimes"*, Eur. J. Inorg. Chem. **2015**, *2015*, 3932-3939.

[47]   J. Guthmuller, L. Gonzalez, *"Simulation of the resonance Raman intensities of a ruthenium-palladium photocatalyst by time dependent density functional theory"*, *Phys. Chem. Chem. Phys.* **2010**, *12*, 14812-14821.

[48]   S. Tschierlei, M. Karnahl, M. Presselt, B. Dietzek, J. Guthmuller, L. González, M. Schmitt, S. Rau, J. Popp, *"Photochemical Fate: The First Step Determines Efficiency of H2 Formation with a Supramolecular Photocatalyst"*, *Angew. Chem. Int. Ed.* **2010**, *49*, 3981-3984.

[49]   M. Wächtler, J. Guthmuller, S. Kupfer, M. Maiuri, D. Brida, J. Popp, S. Rau, G. Cerullo, B. Dietzek, *"Ultrafast Intramolecular Relaxation and Wave-Packet Motion in a Ruthenium-Based Supramolecular Photocatalyst"*, *Chem. Eur. J.* **2015**, *21*, 7668-7674.

[50]   M.-F. Charlot, A. Aukauloo, *"Highlighting the Role of the Medium in DFT Analysis of the Photophysical Properties of Ruthenium(II) Polypyridine-Type Complexes"*, *J. Phys. Chem. A* **2007**, *111*, 11661-11672.

[51]   E. R. Batista, R. L. Martin, *"On the Excited States Involved in the Luminescent Probe [Ru(bpy)$_2$dppz]$^{2+}$"*, *J. Phys. Chem. A* **2005**, *109*, 3128-3133.

[52]   S. Fantacci, F. De Angelis, A. Sgamellotti, N. Re, *"A TDDFT study of the ruthenium(II) polyazaaromatic complex [Ru(dppz)(phen)$_2$]$^{2+}$ in solution"*, *Chem. Phys. Lett.* **2004**, *396*, 43-48.

[53]   A. Vlček, S. Záliš, *"Comments on "Theoretical Studies of Ground and Excited Electronic States in a Series of Halide Rhenium(I) Bipyridine Complexes""*, *J. Phys. Chem. A* **2005**, *109*, 2991-2992.

[54]   A. Vlček Jr, S. Záliš, *"Modeling of charge-transfer transitions and excited states in d6 transition metal complexes by DFT techniques"*, *Coord. Chem. Rev.* **2007**, *251*, 258-287.

[55]   H. Kang, C. Dedonder-Lardeux, C. Jouvet, G. Grégoire, C. Desfrançois, J. P. Schermann, M. Barat, A. Fayeton, *"Control of Bond-Cleaving Reactions of Free Protonated Tryptophan Ion by Femtosecond Laser Pulses"*, *J. Phys. Chem. A* **2005**, *109*, 2417-2420.

[56]   H. Kang, C. Jouvet, C. Dedonder-Lardeux, S. Martrenchard, C. Charrière, G. Grégoire, C. Desfrançois, J. P. Schermann, M. Barat, J. A. Fayeton, *"Photoinduced processes in protonated tryptamine"*, *J. Chem. Phys.* **2005**, *122*, 084307.

[57]   N. H. Damrauer, G. Cerullo, A. Yeh, T. R. Boussie, C. V. Shank, J. K. McCusker ,*"Femtosecond Dynamics of Excited-State Evolution in [Ru(bpy)$_3$]$^{2+}$"*, *Science* **1997**, *275*, 54-57.

[58]   H.-J. Park, W. Kim, W. Choi, Y. K. Chung, *"Ruthenium(ii) complexes incorporating the bidentate ligand containing an imidazolium moiety: synthesis, characterization, and electrochemical properties and their application in a visible-light induced hydrogen-evolving system"*, *New J. Chem.* **2013**, *37*, 3174-3182.

[59]   S. Tschierlei, M. Presselt, C. Kuhnt, A. Yartsev, T. Pascher, V. Sundström, M. Karnahl, M. Schwalbe, B. Schäfer, S. Rau, M. Schmitt, B. Dietzek, J. Popp, *"Photophysics of an Intramolecular Hydrogen-Evolving Ru–Pd Photocatalyst"*, *Chem. Eur. J.* **2009**, *15*, 7678-7688.

[60]   R. Engelman, J. Jortner, *"The energy gap law for radiationless transitions in large molecules"*, *Mol. Phys.* **1970**, *18*, 145-164.

[61]   S. H. Lin, *"Energy Gap Law and Franck–Condon Factor in Radiationless Transitions"*, *J. Chem. Phys.* **1970**, *53*, 3766-3767.

[62]   J. V. Caspar, E. M. Kober, B. P. Sullivan, T. J. Meyer, *"Application of the energy gap law to the decay of charge-transfer excited states"*, *J. Am. Chem. Soc.* **1982**, *104*, 630-632.

[63]   J. V. Caspar, T. J. Meyer, *"Application of the energy gap law to nonradiative, excited-state decay"*, *J. Phys. Chem.* **1983**, *87*, 952-957.

[64]   J. V. Caspar, T. J. Meyer, *"Photochemistry of tris(2,2'-bipyridine)ruthenium(2+) ion (Ru(bpy)₃²⁺). Solvent effects"*, *J. Am. Chem. Soc.* **1983**, *105*, 5583-5590.

[65]   S. D. Cummings, R. Eisenberg, *"Tuning the Excited-State Properties of Platinum(II) Diimine Dithiolate Complexes"*, *J. Am. Chem. Soc.* **1996**, *118*, 1949-1960.

[66]   C. Reichardt, M. Pinto, M. Wächtler, M. Stephenson, S. Kupfer, T. Sainuddin, J. Guthmuller, S. A. McFarland, B. Dietzek, *"Photophysics of Ru(II) Dyads Derived from Pyrenyl-Substitued Imidazo[4,5-f][1,10]phenanthroline Ligands"*, *J. Phys. Chem. A* **2015**, *119*, 3986-3994.

7.8 Supplementary material to "UV/Vis absorption and excited state dynamics of a hydrogen-evolving photocatalyst based on an N-heterocyclic carbene/phenanthroline bridging ligand"

Content

7.8.1 Collision induced dissociation and mass spectrometric data

Figure S1 CID appearance and breakdown curves of **RubbipPt**

Figure S2 Fragment ion mass signals observed by CID and PF of **RubbipPt**

7.8.2 Photofragmentation

Figure S3 Pulse energy dependent fragmentation yields of **RubbipPt** by one-color PF using λ_{ex}=430 nm and 470 nm

7.8.3 Liquid phase UV/Vis absorption

Figure S4 Signal decomposition of the longest wavelength absorption region in the linear absorption spectrum of **RubbipPt** in acetonitrile

7.8.4 (TD-)DFT calculations

Figure S5 Geometry optimized S_0 structure of various isomers of **RubbipPt** in the gas phase and acetonitrile solution

Figure S6 Magnified experimental (*cis*-S isomer) and theoretical liquid phase (acetonitrile) absorption spectrum of **RubbipPt** in a spectral region of 240-400 nm.

Table S1 List of selected high intensity transitions (240-400 nm) calculated for the *cis-S* isomer of **RubbipPt** in acetonitrile.

Figure S7 Frontier orbitals characterizing the calculated transitions listed in Table S1.

Figure S8 Magnified experimental (*cis-S* isomer) and theoretical gas phase absorption spectrum of **RubbipPt** in a spectral region of 240-400 nm.

Table S2 List of selected high intensity transitions (240-400 nm) calculated for the *cis-S* isomer of **RubbipPt** in the gas phase.

Figure S9 Frontier orbitals characterizing the calculated transitions listed in Table S2.

Table S3 List of lowest energy electronic transitions (>400 nm) calculated for the *trans-O* isomer of **RubbipPt** in acetonitrile.

Figure S10 Frontier orbitals characterizing the calculated transitions listed in Table S3.

Table S4 List of lowest energy electronic transitions (>400 nm) calculated for the *trans-S* isomer of **RubbipPt** in acetonitrile.

Figure S11 Frontier orbitals characterizing the calculated transitions listed in Table S4.

Table S5 List of lowest energy electronic transitions (>400 nm) calculated for the *cis-O* isomer of **RubbipPt** in acetonitrile.

Figure S12 Frontier orbitals characterizing the calculated transitions listed in Table S5.

Table S6 List of lowest energy electronic transitions (240-400 nm) calculated for the *trans-O* isomer of **RubbipPt** in the gas phase.

Figure S13 Frontier orbitals characterizing the calculated transitions listed in Table S6.

Table S7 List of lowest energy electronic transitions (240-400 nm) calculated for the *trans-S* isomer of **RubbipPt** in the gas phase.

Figure S14 Frontier orbitals characterizing the calculated transitions listed in Table S7.

Table S8 List of lowest energy electronic transitions (240-400 nm) calculated for the *cis-O* isomer of **RubbipPt** in the gas phase.

Figure S15 Frontier orbitals characterizing the calculated transitions listed in Table S8.

7.8.5 Fitting

Figure S16 Bi-exponential fit of the transient signal recorded at λ_{pump}=430 nm and λ_{probe}=1200 nm

Table S17 Decomposition of tri-exponential fit used to model the transient signal recorded at λ_{pump}=430 nm and λ_{probe}=1200 nm

Figure S18 Bi-exponential fit of the transient signal recorded at λ_{pump}=470 nm and λ_{probe}=1200 nm

Table S19 Decomposition of tri-exponential fit used to model the transient signal recorded at λ_{pump}=470 nm and λ_{probe}=1200 nm

7.8.6 References

7.8.1 Collision induced dissociation

In order to initiate collision-induced dissociation (CID) a resonance excitation signal was applied to the end caps of the quadrupole ion trap (QIT) accelerating the trapped precursor ions which then undergo multiple collisions with the helium buffer gas and eventually form fragments. The helium pressure was estimated to be ~10^{-3} mbar inside the QIT. The excitation magnitude was tuned typically in the range of 0.0-1.0 arb. u., which corresponds to an internal scale of the mass spectrometer. These collisional energies (E_{Lab}) in the laboratory frame were center-of-mass (COM) transformed according to equation (S1), where m_{He} and $m_{precursor}$ are the nominal masses of helium and the precursor species, respectively.

$$E_{COM} = \left(\frac{m_{He}}{m_{He} + m_{precursor}} \right) \cdot E_{Lab} \tag{S1}$$

Relative abundances of the fragments F_i and the breakdown curve of the precursor ion signal P were calculated according to equation (S2) and (S3), respectively:

$$F_i = \left(\frac{I_i^f}{\sum_i I_i^f + I^p} \right) \tag{S2}$$

$$P = \left(\frac{I^p}{\sum_i I_i^f + I^p} \right) \tag{S3}$$

where I_i^f and I^p denote the recorded fragment and precursor ion intensities, respectively.

The relative abundance of the **RubbipPt** precursor ion and its two main fragment products in dependence of the center of mass transformed excitation amplitude applied in CID is presented in Figure S1.
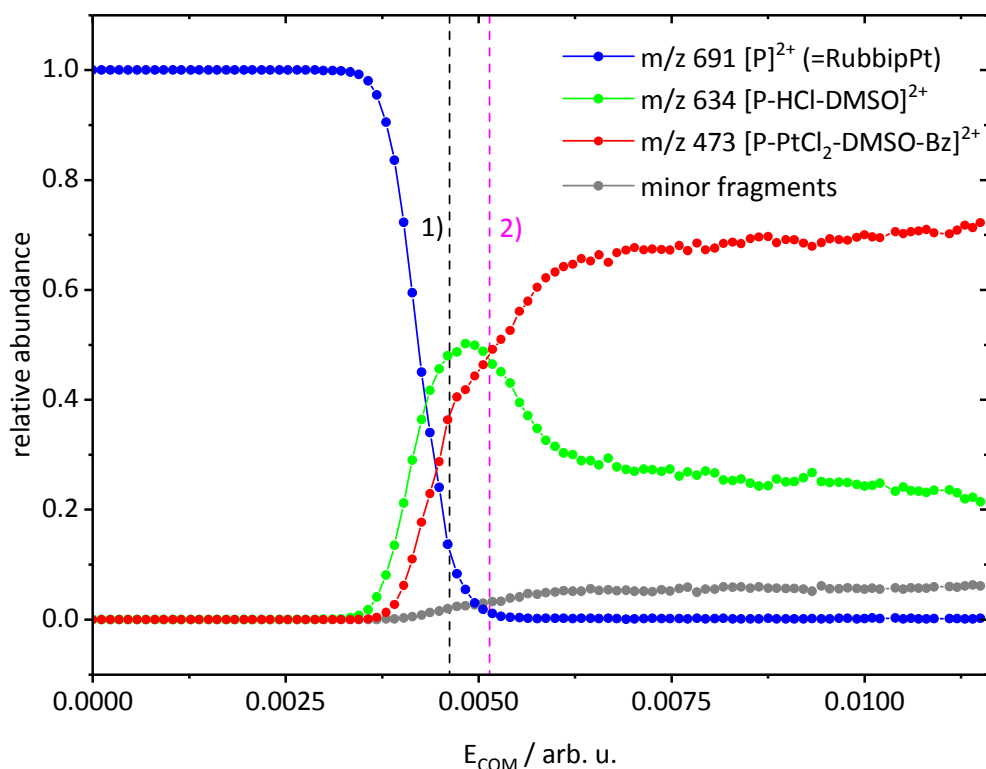
Figure S1 Relative abundance of the **RubbipPt** (blue) precursor ion and its main CID fragment products (m/z 634, green and m/z 473, red) depending on the center of mass transformed CID amplitude (E_{COM}). For clarity, contributions of minor fragment channels (m/z 615.5/588/569.5) are not shown individually.

From the recorded CID appearance curves, it is evident that for the formation of the m/z 634 fragment a lower internal energy is required. The fragment at m/z 473 first appears at slightly higher applied CID amplitudes, signifying a stronger bond between the platinum and the C atom of the NHC with respect to the platinum DMSO bond strength. For amplitudes at lower values than indicated by 1) (E_{COM}~0.0047) both fragment intensities rise in parallel, pointing to a competition between the fragment ion channels. At E_{COM}~0.0047, however, the behavior of the CID appearance curves changes. The fragment ion intensity of m/z 634 starts to decline, whereas the rise of m/z 473 exhibits a less steep slope. At amplitudes higher than indicated by 2), the imparted internal energy is sufficiently high that fragmentation to form m/z 473 outcompetes the lower fragmentation pathway.
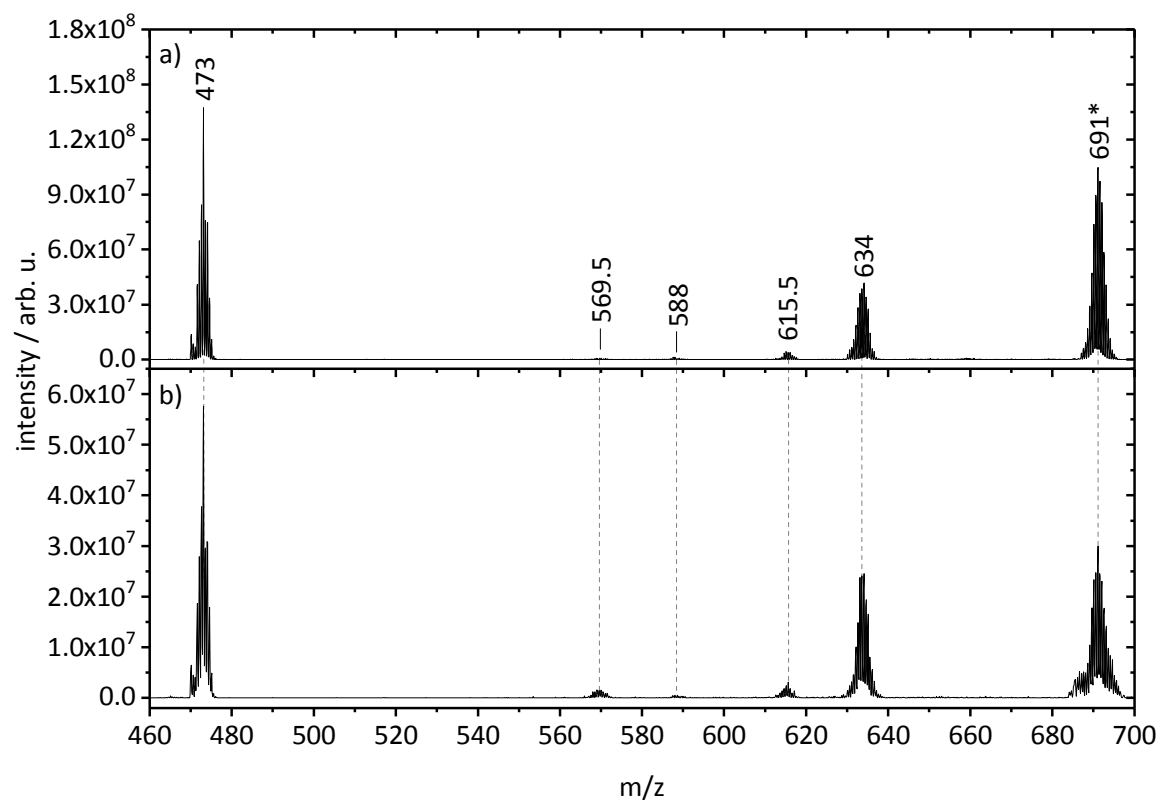
Figure S2 Mass spectra depicting fragment ion formation of **RubbipPt** by CID **(a)** and PF **(b)**. PF spectrum was recorded using λ_{ex}=270 nm (1.5 µJ) Asterisk denotes precursor ion signal. For an assignment of the occurring signals *cf.* Table 1.

7.8.2 Photofragmentation
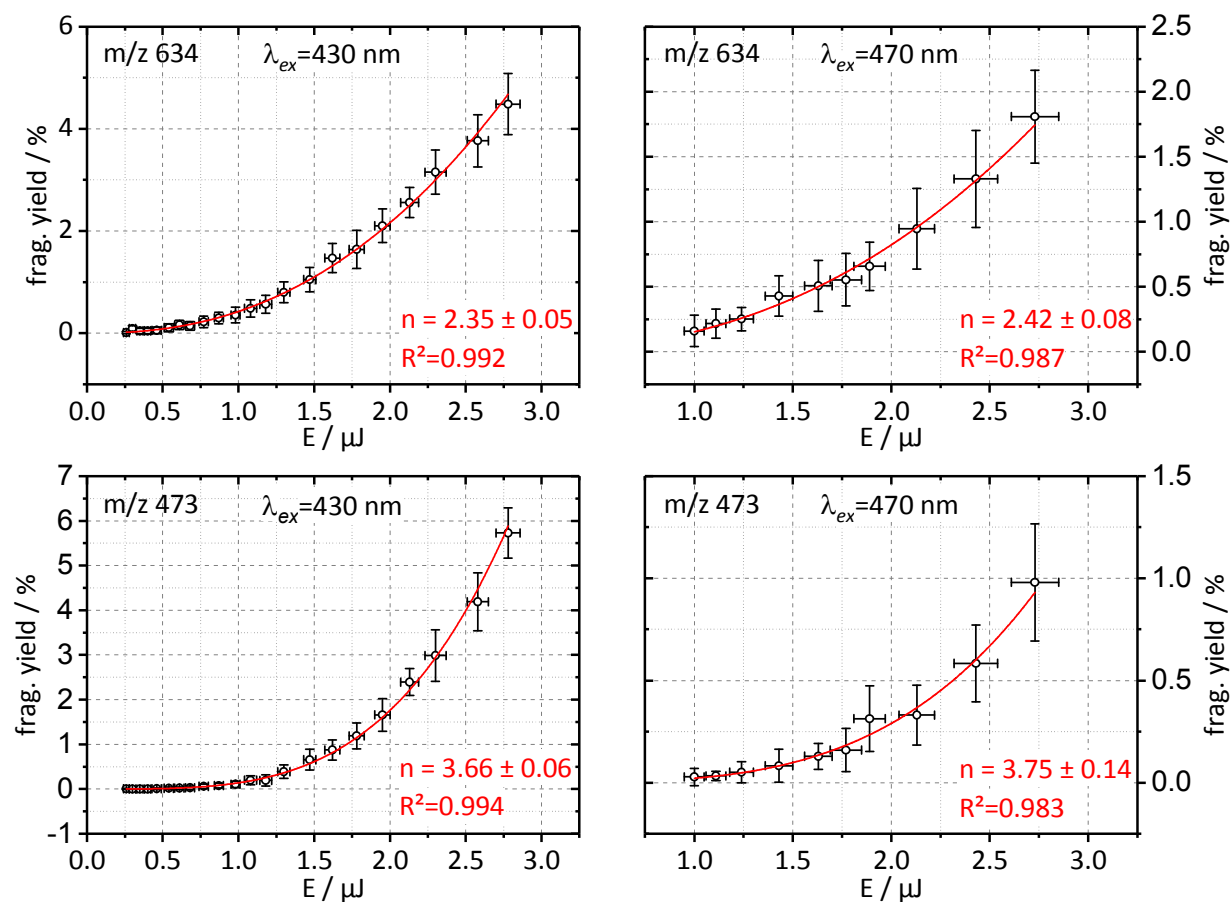
Figure S3 Pulse energy E dependent PF yield Y of **RubbipPt** by one-color photoexcitation (at λ_{ex}=430 nm and λ_{ex}=470 nm) analyzed and displayed for the two most prominent fragmentation channels (m/z 634 and m/z 473). Dependencies were evaluated according to $Y = A \cdot E^n$,[1] where n denotes a mean value for the number of photons absorbed to induce fragmentation.

7.8.3 Liquid phase UV/Vis absorption
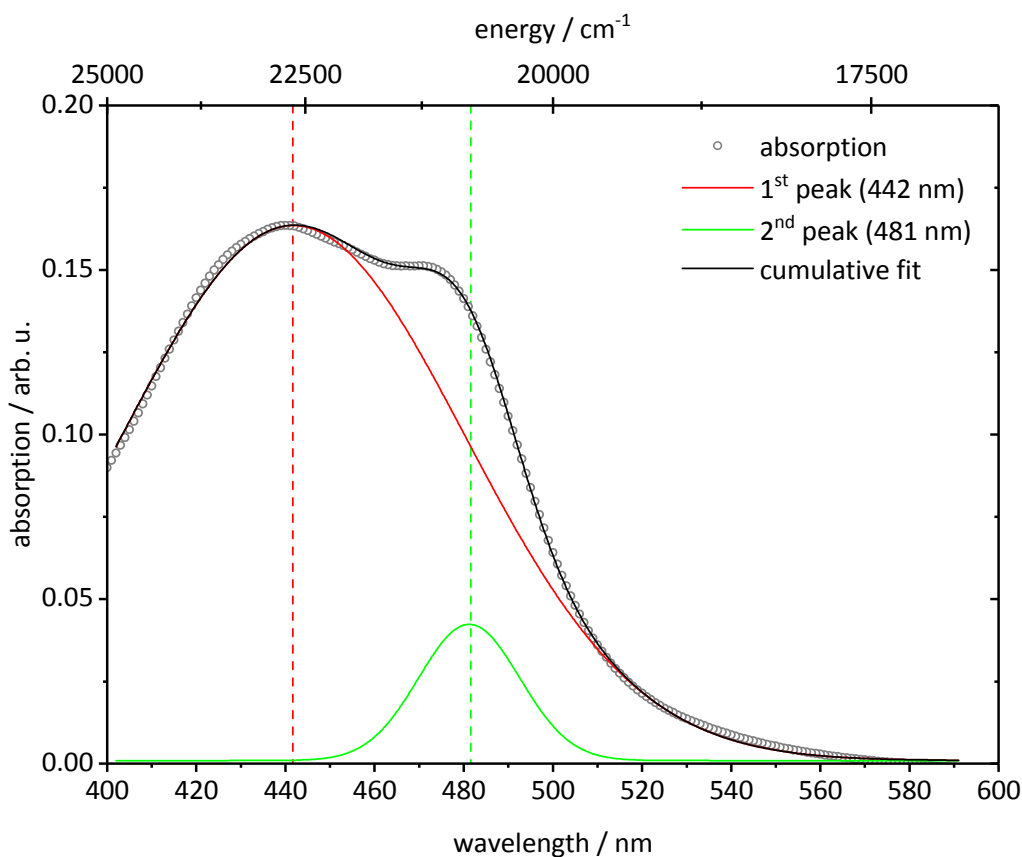
Figure S4 Signal decomposition of the longest wavelength absorption region in the linear absorption spectrum of **RubbipPt** in acetonitrile. Data points of the experimental spectrum are shown as open gray circles, whereas the individual contributing signals (red and green) and the cumulative fit (black) are shown as straight lines.

Employing a theoretical model assuming a Gaussian envelope for the individual contributions, the fitted signal matches the experimental spectrum perfectly (R^2=1.000). The individual peaks are centered at ~442 nm (red) and ~481 nm (green), respectively.

7.8.4 (TD-)DFT calculations

acetonitrile   gas phase

trans-O

+0.0 kJ/mol   +0.0 kJ/mol

trans-S

+29.5 kJ/mol   +26.9 kJ/mol

cis-O

+23.3 kJ/mol   +46.4 kJ/mol

cis-S

+17.7 kJ/mol   +39.6 kJ/mol
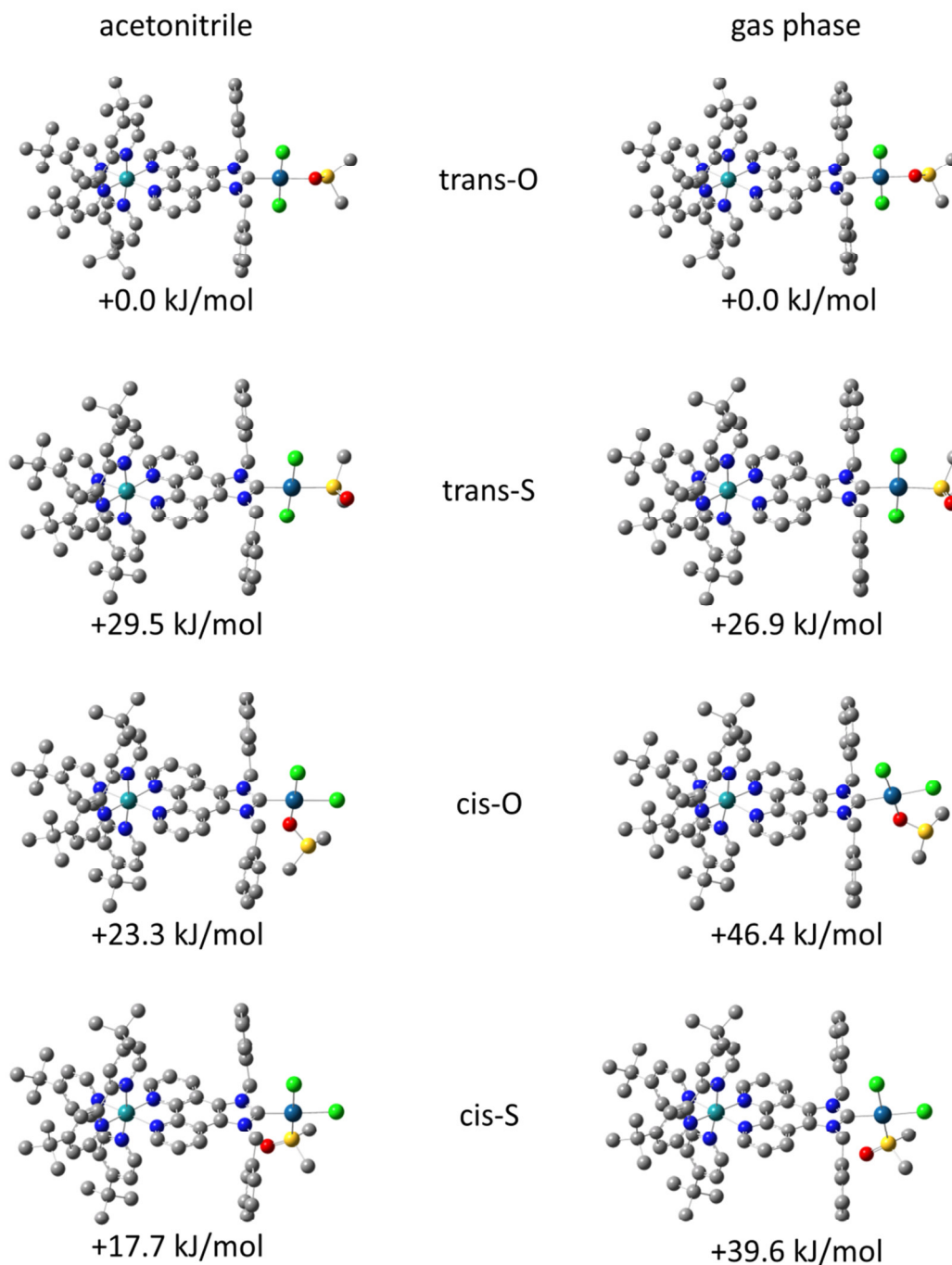
Figure S5 DFT geometry optimized structures of the four considered isomers of **RubbipPt** in acetonitrile (left) and in *vacuo* (right). Hydrogen atoms are not displayed for clarity. The relative Gibbs free energies are given along the respective structure.
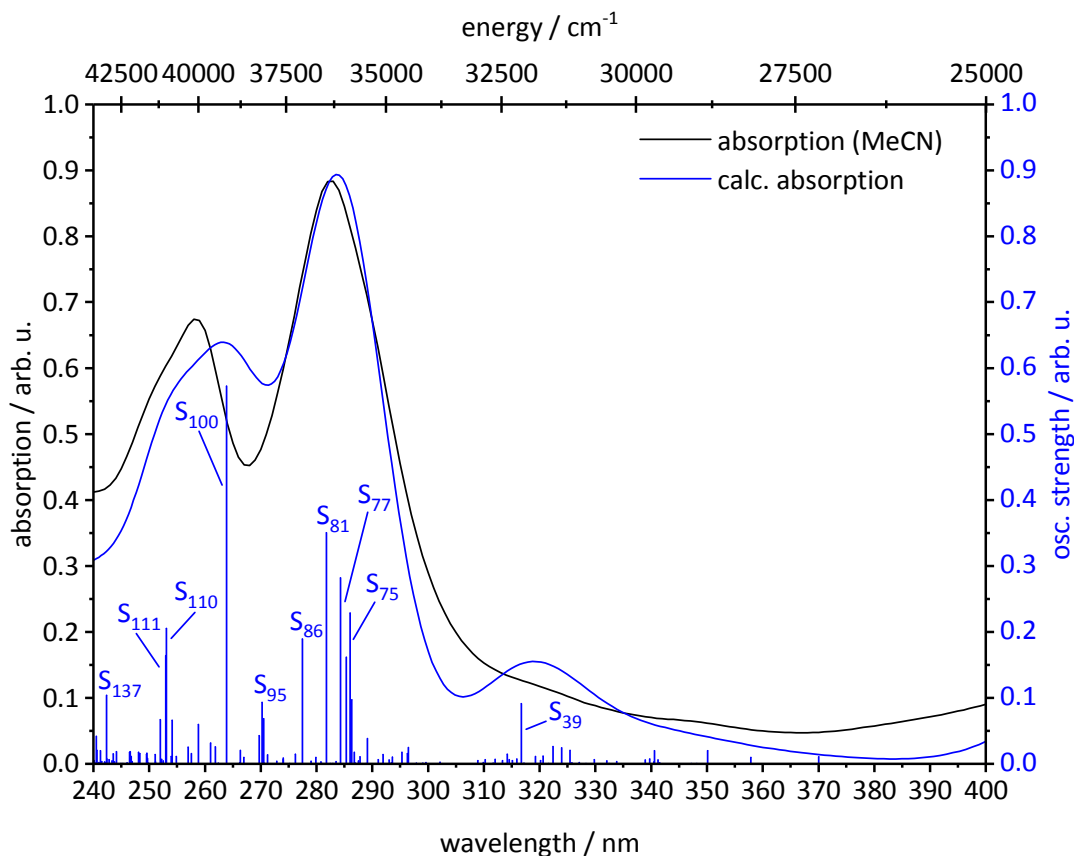
Figure S6 Magnified UV absorption region (240-400 nm) in the absorption spectrum of **RubbipPt** in acetonitrile. Computed vertical electronic transitions (blue sticks) were shifted bathochromically by 1000 cm^{-1} and scaled in intensity so that the respective absorption maxima coincide. The stick spectra were broadened by a Gaussian function of 2000 cm^{-1} fwhm. Selected highest intensity transitions S$_n$ are listed and characterized in Table S1.

Table 1 Vertical excitation energies E_v, oscillator strengths f and configurations of some selected singlet excited states S_n in a spectral region of 240-400 nm calculated for the *cis-S* isomer of **RubbipPt** in acetonitrile solution (PCM). Transitions were bathochromically shifted by 1000 cm^{-1}. Frontier orbital contributions to the transitions with a weight w of <10 % were omitted.

| S_n	transition	w/%	λ/nm	E_v/eV	f
S_{39}	d_{Ru}(HOMO-2)$\rightarrow\pi^*_{tbbpy}$(LUMO+7)	30	317	3.91	0.091
	d_{Ru}(HOMO-1)$\rightarrow\pi^*_{tbbpy},\pi^*_{bbip}$(LUMO+6)	45			
S_{75}	π_{tbbpy}(HOMO-11)$\rightarrow\pi^*_{tbbpy},\pi^*_{bbip}$(LUMO+3)	39	278	4.46	0.228
	d_{Pt},π_{Ph}(HOMO-9)$\rightarrow\pi^*_{tbbpy}$(LUMO+1)	25			
S_{77}	d_{Pt},n_{Cl},π_{Ph}(HOMO-12)$\rightarrow\pi^*_{tbbpy},\pi^*_{bbip}$(LUMO+2)	47	284	4.37	0.282
	π_{tbbpy}(HOMO-10)$\rightarrow\pi^*_{bbip},\pi^*_{tbbpy}$(LUMO+3)	15			
S_{81}	π_{bbip}(HOMO-15)$\rightarrow\pi^*_{bbip}$(LUMO)	21	282	4.40	0.350
	$d_{Pt},n_{Cl},$(HOMO-13)$\rightarrow\pi^*_{tbbpy},\pi^*_{bbip}$(LUMO+2)	27			
S_{86}	d_{Pt},n_{Cl}(HOMO-15)$\rightarrow\pi^*_{bbip}$(LUMO)	20	277	4.48	0.189
	d_{Pt},n_{Cl}(HOMO-13)$\rightarrow\pi^*_{tbbpy},\pi^*_{bbip}$(LUMO+2)	51			
S_{95}	d_{Pt},n_{Cl}(HOMO-14)$\rightarrow\pi^*_{tbbpy},\pi^*_{bbip}$(LUMO+2)	30	270	4.59	0.093
	d_{Pt},n_{Cl}(HOMO-13)$\rightarrow\pi^*_{tbbpy}$(LUMO+1)	40			
S_{100}	d_{Pt},n_{Cl}(HOMO-15)$\rightarrow\pi^*_{tbbpy},\pi^*_{bbip}$(LUMO+2)	13	264	4.70	0.573
	d_{Pt},n_{Cl},π_{bbip}(HOMO-4)$\rightarrow\pi^*_{bbip},\pi^*_{tbbpy}$(LUMO+5)	48			
S_{110}	d_{Pt},n_{Cl},π_{bbip}(HOMO-4)$\rightarrow\pi^*_{tbbpy},\pi^*_{bbip}$(LUMO+6)	33	253	4.90	0.205
	d_{Ru}(HOMO)$\rightarrow\pi_{Ph}$(LUMO+10)	17			
	d_{Ru}(HOMO)$\rightarrow\pi_{Ph}$(LUMO+11)	21			
S_{111}	d_{Pt},n_{Cl},π_{bbip}(HOMO-4)$\rightarrow\pi^*_{tbbpy},\pi^*_{bbip}$(LUMO+6)	23	253	4.90	0.164
	d_{Ru}(HOMO)$\rightarrow\pi_{Ph}$(LUMO+10)	20			
	d_{Ru}(HOMO)$\rightarrow\pi_{Ph}$(LUMO+11)	34			
S_{137}	d_{Pt},n_{Cl}(HOMO-16)$\rightarrow\pi^*_{tbbpy},\pi^*_{bbip}$(LUMO+4)	66	242	5.12	0.102
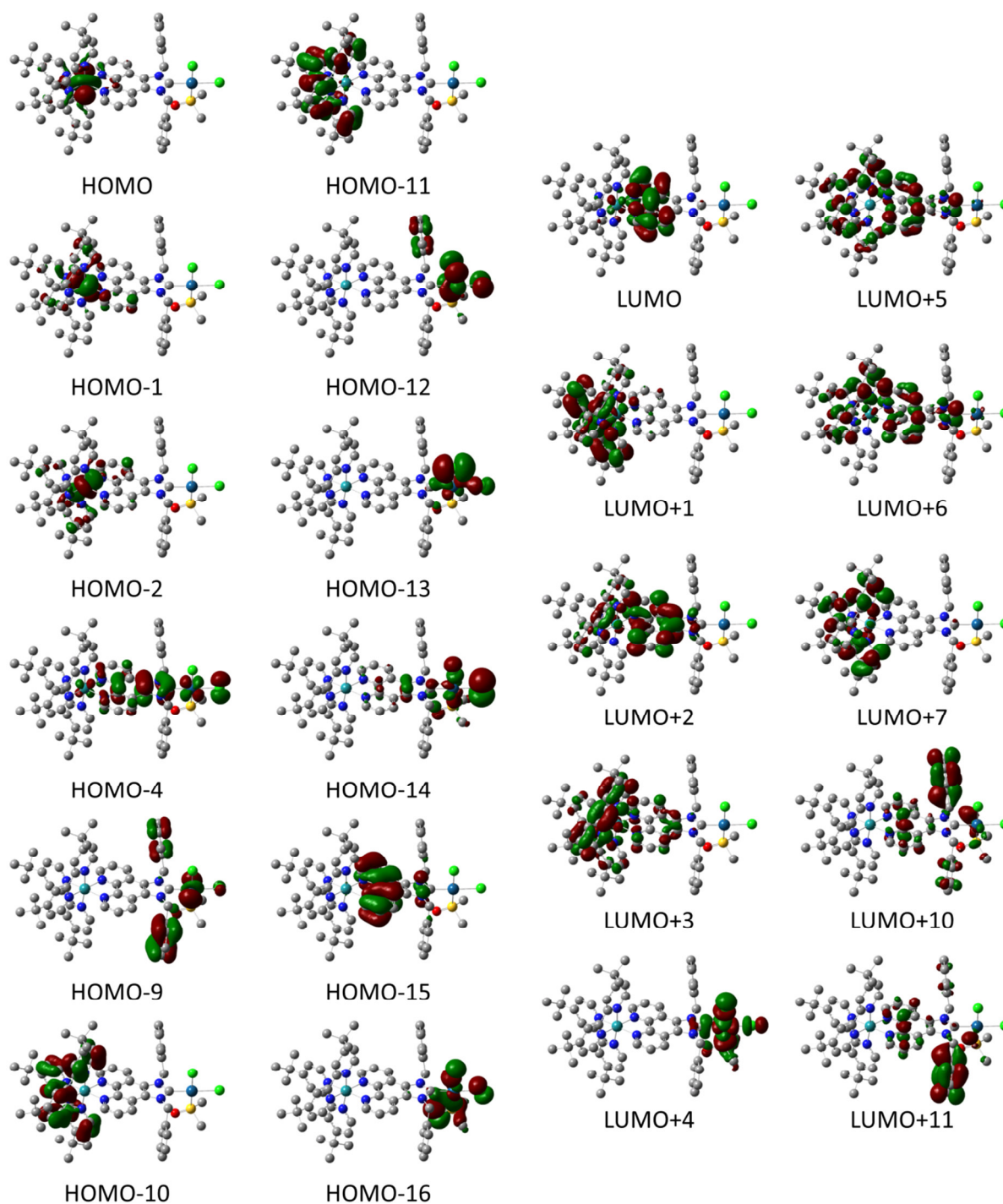
Figure 7 Frontier orbitals characterizing acetonitrile solution electronic transitions of **RubbipPt** (*cis-S*) in a spectral region of 240-400 nm (*cf.* Figure S6 and Table S1).
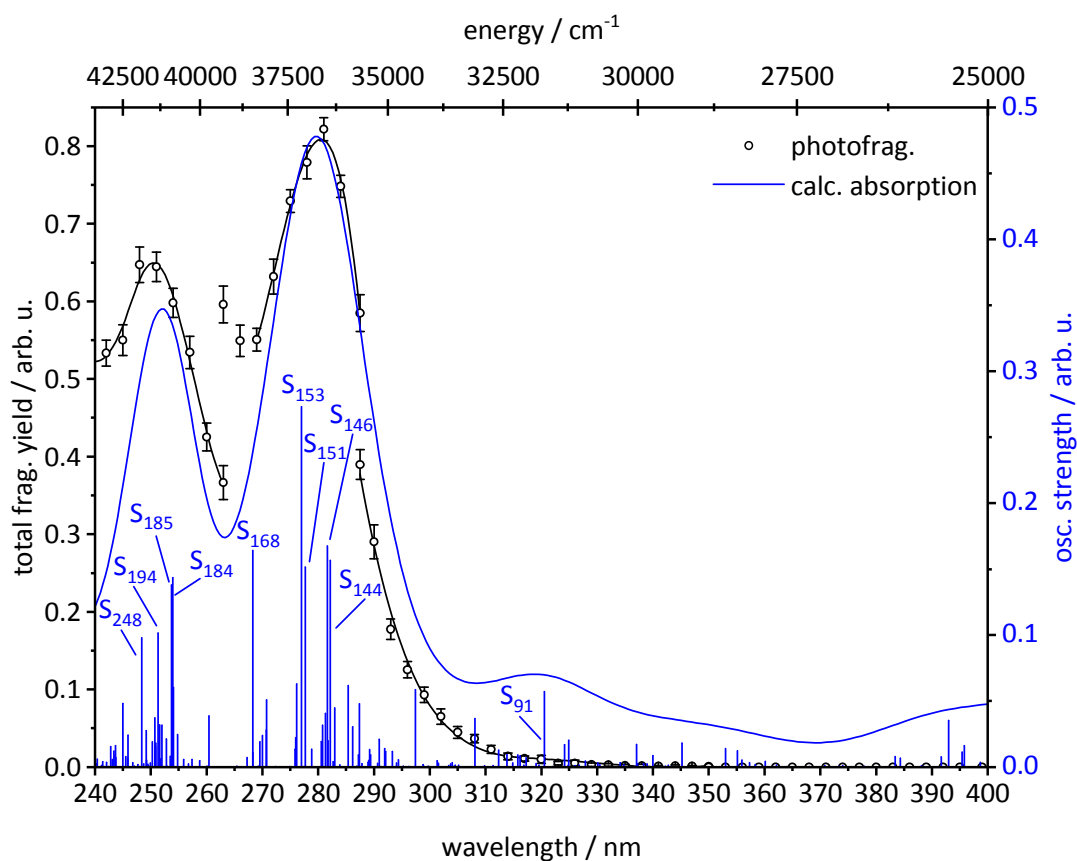
Figure S8 Magnified UV absorption region (240-400 nm) in the gas phase PF spectrum of **RubbipPt**. Computed vertical electronic transitions (blue sticks) were shifted bathochromically by 1000 cm^{-1} and scaled in intensity so that the respective absorption maxima coincide. The stick spectra were broadened by a Gaussian function of 2000 cm^{-1} fwhm. Selected highest intensity transitions S_n are listed and characterized in Table S2.

Table 2 Gas phase vertical excitation energies E_v, oscillator strengths f and configurations of some selected singlet excited states S_n in a spectral region of 240-400 nm calculated for the *cis-S* isomer of **RubbipPt**. Transitions were bathochromically shifted by 1000 cm^{-1}. Frontier orbital contributions to the transitions with a weight w of <10 % were omitted.

S_n	transition	w/%	λ/nm	E_v/eV	f
S_{91}	$d_{Ru},\pi_{bbip},\pi_{Ph}$(HOMO-9)$\rightarrow\pi^*_{tbbpy}$(LUMO+5)	39	321	3.86	0.057
	d_{Ru}(HOMO-7)$\rightarrow\pi^*_{tbbpy},\pi^*_{bbip}$(LUMO+6)	12			
S_{144}	π_{tbbpy},π_{bbip}(HOMO-19)$\rightarrow\pi^*_{tbbpy}$(LUMO+2)	28	282	4.40	0.157
S_{146}	π_{tbbpy}(HOMO-17)$\rightarrow\pi^*_{bbip}$(LUMO+2)	13	282	4.40	0.168
	$d_{Ru},d_{Pt},n_{Cl},n_{DMSO}$(HOMO-12)$\rightarrow\pi^*_{tbbpy}$(LUMO+5)	23			
S_{151}	π_{tbbpy}(HOMO-17)$\rightarrow\pi^*_{bbip}$(LUMO+2)	10			
	π_{tbbpy}(HOMO-17)$\rightarrow\pi^*_{bbip}$(LUMO+3)	50	278	4.46	0.152
	$d_{Ru},d_{Pt},n_{Cl},n_{DMSO}$(HOMO-12)$\rightarrow\pi^*_{tbbpy}$(LUMO+5)	12			
S_{153}	π_{tbbpy}(HOMO-17)$\rightarrow\pi^*_{bbip}$(LUMO+2)	11			
	π_{tbbpy}(HOMO-17)$\rightarrow\pi^*_{bbip}$(LUMO+3)	36	277	4.48	0.273
	$d_{Ru},d_{Pt},n_{Cl},n_{DMSO}$(HOMO-12)$\rightarrow\pi^*_{tbbpy}$(LUMO+5)	17			
S_{168}	d_{Ru},d_{Pt},n_{Cl}(HOMO-13)$\rightarrow\pi^*_{tbbpy}$(LUMO+4)	16	268	4.63	0.164
	d_{Ru},d_{Pt},n_{Cl}(HOMO-12)$\rightarrow\pi^*_{bbip}$(LUMO+8)	39			
S_{184}	$\pi_{tbbpy},\pi_{bbip},\pi_{Ph}$(HOMO-23)$\rightarrow\pi^*_{bbip}$(LUMO)	17	254	4.88	0.144
	d_{Ru},d_{Pt},n_{Cl}(HOMO-13)$\rightarrow\pi^*_{tbbpy},\pi^*_{bbip}$(LUMO+6)	24			
S_{185}	d_{Ru},d_{Pt},n_{Cl}(HOMO-13)$\rightarrow\pi^*_{tbbpy},\pi^*_{bbip}$(LUMO+6)	22	254	4.88	0.138
	d_{Pt},n_{Cl}(HOMO-1)$\rightarrow\pi^*_{tbbpy}$(LUMO+15)	24			
S_{194}	d_{Ru},d_{Pt},n_{Cl}(HOMO-13)$\rightarrow\pi^*_{tbbpy}$(LUMO+7)	16	251	4.94	0.102
	d_{Ru},d_{Pt},n_{Cl}(HOMO-13)$\rightarrow\pi^*_{bbip}$(LUMO+8)	33			
S_{248}	d_{Pt},n_{Cl},n_{DMSO}(HOMO-21)$\rightarrow\pi^*_{bbip}$(LUMO+2)	38	248	5.00	0.098
	d_{Pt},n_{Cl},n_{DMSO}(HOMO-21)$\rightarrow\pi^*_{bbip}$(LUMO+3)	48			
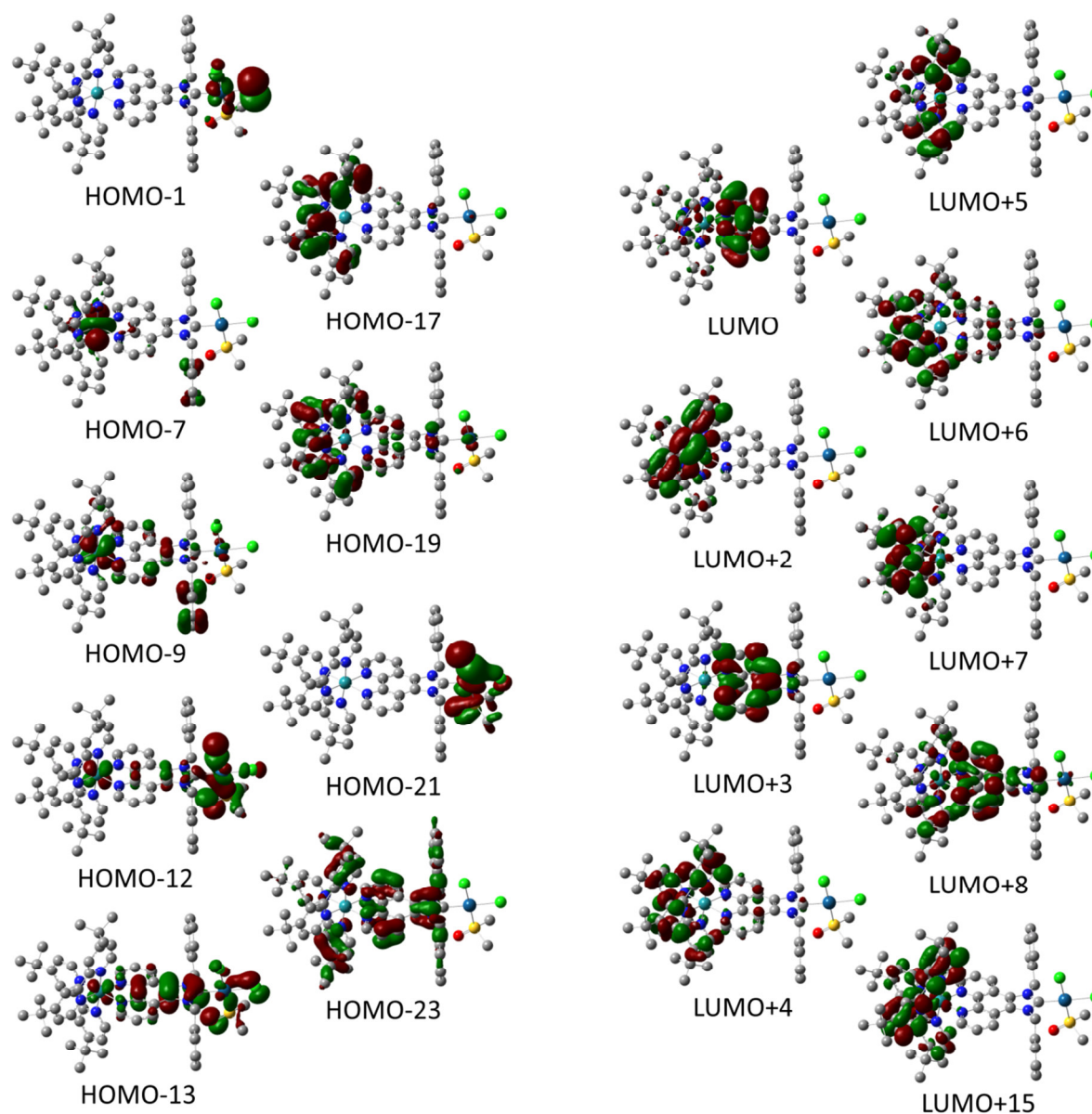
Figure 9 Frontier orbitals characterizing the gas phase electronic transitions of **RubbipPt** (*cis-S*) in a spectral region of 240-400 nm (*cf.* Figure S8 and Table S2).

Table S3 Calculated liquid phase (PCM, acetonitrile) vertical excitation energies E_v, oscillator strengths f and singlet excited state S_n configurations in the CT region of **RubbipPt** (*trans-O* isomer). Transitions were bathochromically shifted by 1000 cm^{-1}. Frontier orbital contributions to the transitions with a weight w of <10 % were omitted.

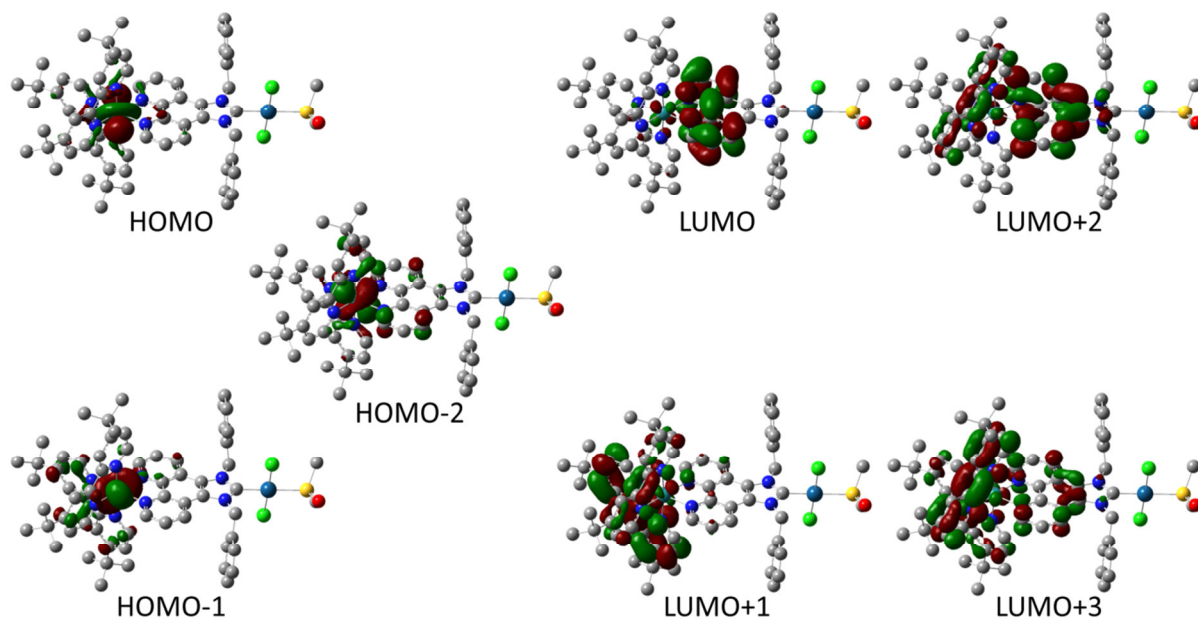| state	transition	w/%	λ/nm	E_v/eV	f
S_1	d_{Ru}(HOMO)→π^*_{bbip}(LUMO)	93	532	2.33	0.001
S_2	d_{Ru}(HOMO-2)→π^*_{bbip}(LUMO)	91	492	2.52	0.003
S_3	d_{Ru}(HOMO)→π^*_{tbbpy}(LUMO+1)	91	489	2.54	0.001
	d_{Ru}(HOMO)→π^*_{tbbpy},π^*_{bbip}(LUMO+2)	16			
S_4	d_{Ru}(HOMO)→π^*_{tbbpy}(LUMO+1)	19	481	2.58	0.002
	d_{Ru}(HOMO)→π^*_{tbbpy},π^*_{bbip}(LUMO+2)	64			
	d_{Ru}(HOMO)→π^*_{bbip},π^*_{tbbpy}(LUMO+3)	10			
S_5	d_{Ru}(HOMO-1)→π^*_{bbip}(LUMO)	80	469	2.64	0.153
	d_{Ru}(HOMO)→π^*_{bbip},π^*_{tbbpy}(LUMO+3)	15			
S_6	d_{Ru}(HOMO-2)→π^*_{tbbpy}(LUMO+1)	37	454	2.73	0.009
	d_{Ru}(HOMO-1)→π^*_{tbbpy}(LUMO+1)	30			
	d_{Ru}(HOMO-1)→π^*_{tbbpy},π^*_{bbip}(LUMO+2)	19			
S_7	d_{Ru}(HOMO-1)→π^*_{tbbpy}(LUMO+1)	29	445	2.79	0.019
	d_{Ru}(HOMO-1)→π^*_{tbbpy},π^*_{bbip}(LUMO+2)	15			
	$d_{Ru,}$(HOMO)→π^*_{bbip},π^*_{tbbpy}(LUMO+3)	32			
S_8	d_{Ru}(HOMO-2)→π^*_{tbbpy},π^*_{bbip}(LUMO+2)	35	443	2.80	0.089
	d_{Ru}(HOMO)→π^*_{tbbpy},π^*_{bbip}(LUMO+2)	11			
	d_{Ru}(HOMO)→π^*_{bbip},π^*_{tbbpy}(LUMO+3)	27			
S_9	d_{Ru}(HOMO-2)→π^*_{tbbpy}(LUMO+1)	44	434	2.86	0.178
	d_{Ru}(HOMO-1)→π^*_{tbbpy},π^*_{bbip}(LUMO+2)	31			
S_{10}	d_{Ru}(HOMO-1)→π^*_{tbbpy},π^*_{bbip}(LUMO+2)	91	419	2.96	0.068
S_{11}	d_{Ru}(HOMO-1)→π^*_{tbbpy},π^*_{bbip}(LUMO+2)	18	413	3.00	0.023
	d_{Ru}(HOMO-1)→π^*_{bbip},π^*_{tbbpy}(LUMO+3)				

Figure S10 Frontier orbitals involved in the liquid phase (PCM, acetonitrile) electronic transitions in the charge transfer region of **RubbipPt** calculated for the *trans-O* isomer (*cf.* Table S3).

Table 4 Calculated liquid phase (PCM, acetonitrile) vertical excitation energies E_v, oscillator strengths f and singlet excited state S_n configurations in the CT region of **RubbipPt** (*trans-S* isomer). Transitions were bathochromically shifted by 1000 cm^{-1}. Frontier orbital contributions to the transitions with a weight w of <10 % were omitted.

| S_n	transition	w/%	λ/nm	E_v/eV	f
S_1	d_{Ru}(HOMO)→π^*_{bbip}(LUMO)	93	535	2.31	0.001
S_2	d_{Ru}(HOMO-1)→π^*_{bbip}(LUMO)	86	495	2.50	0.002
S_3	d_{Ru}(HOMO)→π^*_{tbbpy}(LUMO+1)	78	488	2.54	0.001
	d_{Ru}(HOMO)→π^*_{tbbpy},π^*_{bbip}(LUMO+3)	11			
S_4	d_{Ru}(HOMO)→π^*_{tbbpy}(LUMO+1)	15	480	2.58	0.004
	$d_{Ru,}$(HOMO)→π^*_{bbip},π^*_{tbbpy}(LUMO+2)	37			
	d_{Ru}(HOMO)→π^*_{tbbpy},π^*_{bbip}(LUMO+3)	41			
S_5	d_{Ru}(HOMO-2)→π^*_{bbip}(LUMO)	70	469	2.64	0.141
	$d_{Ru,}$(HOMO)→π^*_{tbbpy},π^*_{bbip}(LUMO+3)	17			
S_6	d_{Ru}(HOMO-2)→π^*_{tbbpy}(LUMO+1)	45	453	2.73	0.011
	d_{Ru}(HOMO-2)→π^*_{tbbpy}(LUMO+3)	16			
	d_{Ru}(HOMO-1)→π^*_{tbbpy},π^*_{bbip}(LUMO+1)	24			
S_7	d_{Ru}(HOMO-2)→π^*_{tbbpy}(LUMO+1)	11	447	2.77	0.059
	d_{Ru}(HOMO-1)→π^*_{tbbpy},π^*_{bbip}(LUMO+1)	17			
	d_{Ru}(HOMO)→π^*_{bbip},π^*_{tbbpy}(LUMO+2)	34			
	d_{Ru}(HOMO)→π^*_{tbbpy},π^*_{bbip}(LUMO+3)	21			
S_8	d_{Ru}(HOMO-2)→π^*_{tbbpy},π^*_{bbip}(LUMO+1)	21	442	2.81	0.059
	d_{Ru}(HOMO-1)→π^*_{bbip},π^*_{tbbpy}(LUMO+2)	31			
	d_{Ru}(HOMO-1)→π^*_{tbbpy},π^*_{bbip}(LUMO+3)	19			
	d_{Ru}(HOMO)→π^*_{bbip},π^*_{tbbpy}(LUMO+2)	14			
S_9	d_{Ru}(HOMO-2)→π^*_{tbbpy}(LUMO+2)	20	433	2.86	0.168
	d_{Ru}(HOMO-2)→π^*_{tbbpy},π^*_{bbip}(LUMO+3)	32			
	d_{Ru}(HOMO-1)→π^*_{tbbpy},π^*_{bbip}(LUMO+1)	43			
S_{10}	d_{Ru}(HOMO-1)→π^*_{bbip},π^*_{tbbpy}(LUMO+2)	38	422	2.94	0.076
	d_{Ru}(HOMO-1)→π^*_{tbbpy},π^*_{bbip}(LUMO+3)	50			
S_{11}	d_{Ru}(HOMO-2)→π^*_{bbip},π^*_{tbbpy}(LUMO+2)	54	415	2.99	0.024
	d_{Ru}(HOMO-2)→π^*_{tbbpy},π^*_{bbip}(LUMO+3)	33			

Figure S11 Frontier orbitals involved in the liquid phase (PCM, acetonitrile) electronic transitions in the charge transfer region of **RubbipPt** calculated for the *trans-S* isomer (*cf.* Table S4).

Table 5 Calculated liquid phase (PCM, acetonitrile) vertical excitation energies E_v, oscillator strengths f and singlet excited state S_n configurations in the CT region of **RubbipPt** (*cis-O* isomer). Transitions were bathochromically shifted by 1000 cm^{-1}. Frontier orbital contributions to the transitions with a weight w of <10 % were omitted.

S_n	transition	w/%	λ/nm	E_v/eV	f
S_1	d_{Ru}(HOMO)$\rightarrow\pi^*_{bbip}$(LUMO)	93	533	2.33	0.001
S_2	d_{Ru}(HOMO-2)$\rightarrow\pi^*_{bbip}$(LUMO)	90	493	2.51	0.003
S_3	d_{Ru}(HOMO)$\rightarrow\pi^*_{tbbpy}$(LUMO+1)	77	490	2.53	0.001
	d_{Ru}(HOMO)$\rightarrow\pi^*_{tbbpy}$(LUMO+1)	14			
S_4	d_{Ru}(HOMO)$\rightarrow\pi^*_{tbbpy},\pi^*_{bbip}$(LUMO+2)	59	480	2.58	0.003
	d_{Ru}(HOMO)$\rightarrow\pi^*_{bbip},\pi^*_{tbbpy}$(LUMO+3)	19			
S_5	d_{Ru}(HOMO-1)$\rightarrow\pi^*_{bbip}$(LUMO)	76	469	2.64	0.149
	d_{Ru},(HOMO)$\rightarrow\pi^*_{bbip},\pi^*_{tbbpy}$(LUMO+3)	17			
	d_{Ru}(HOMO-2)$\rightarrow\pi^*_{tbbpy}$(LUMO+1)	50			
S_6	d_{Ru}(HOMO-1)$\rightarrow\pi^*_{tbbpy}$(LUMO+1)	21	454	2.73	0.009
	d_{Ru}(HOMO-1)$\rightarrow\pi^*_{tbbpy},\pi^*_{bbip}$(LUMO+2)	12			
	d_{Ru}(HOMO-1)$\rightarrow\pi^*_{tbbpy}$(LUMO+1)	23			
S_7	d_{Ru}(HOMO-1)$\rightarrow\pi^*_{tbbpy},\pi^*_{bbip}$(LUMO+2)	10	446	2.78	0.045
	d_{Ru},(HOMO)$\rightarrow\pi^*_{tbbpy},\pi^*_{bbip}$(LUMO+2)	16			
	d_{Ru},(HOMO)$\rightarrow\pi^*_{bbip},\pi^*_{tbbpy}$(LUMO+3)	36			
	d_{Ru}(HOMO-2)$\rightarrow\pi^*_{tbbpy},\pi^*_{bbip}$(LUMO+2)	26			
	d_{Ru}(HOMO-1)$\rightarrow\pi^*_{tbbpy},\pi^*_{bbip}$(LUMO+1)	12			
S_8	d_{Ru}(HOMO-1)$\rightarrow\pi^*_{tbbpy},\pi^*_{bbip}$(LUMO+2)	22	442	2.81	0.063
	d_{Ru}(HOMO)$\rightarrow\pi^*_{tbbpy},\pi^*_{bbip}$(LUMO+2)	11			
	d_{Ru}(HOMO)$\rightarrow\pi^*_{tbbpy},\pi^*_{bbip}$(LUMO+2)	11			
	d_{Ru}(HOMO-2)$\rightarrow\pi^*_{tbbpy}$(LUMO+1)	34			
S_9	d_{Ru}(HOMO-2)$\rightarrow\pi^*_{tbbpy},\pi^*_{bbip}$(LUMO+2)	14	434	2.86	0.177
	d_{Ru}(HOMO-1)$\rightarrow\pi^*_{tbbpy},\pi^*_{bbip}$(LUMO+1)	12			
S_{10}	d_{Ru}(HOMO-2)$\rightarrow\pi^*_{tbbpy},\pi^*_{bbip}$(LUMO+2)	15	420	2.95	0.072
	d_{Ru}(HOMO-2)$\rightarrow\pi^*_{bbip},\pi^*_{tbbpy}$(LUMO+3)	81			
S_{11}	d_{Ru}(HOMO-1)$\rightarrow\pi^*_{tbbpy},\pi^*_{bbip}$(LUMO+2)	30	413	3.00	0.023
	d_{Ru}(HOMO-1)$\rightarrow\pi^*_{bbip},\pi^*_{tbbpy}$(LUMO+3)	62			
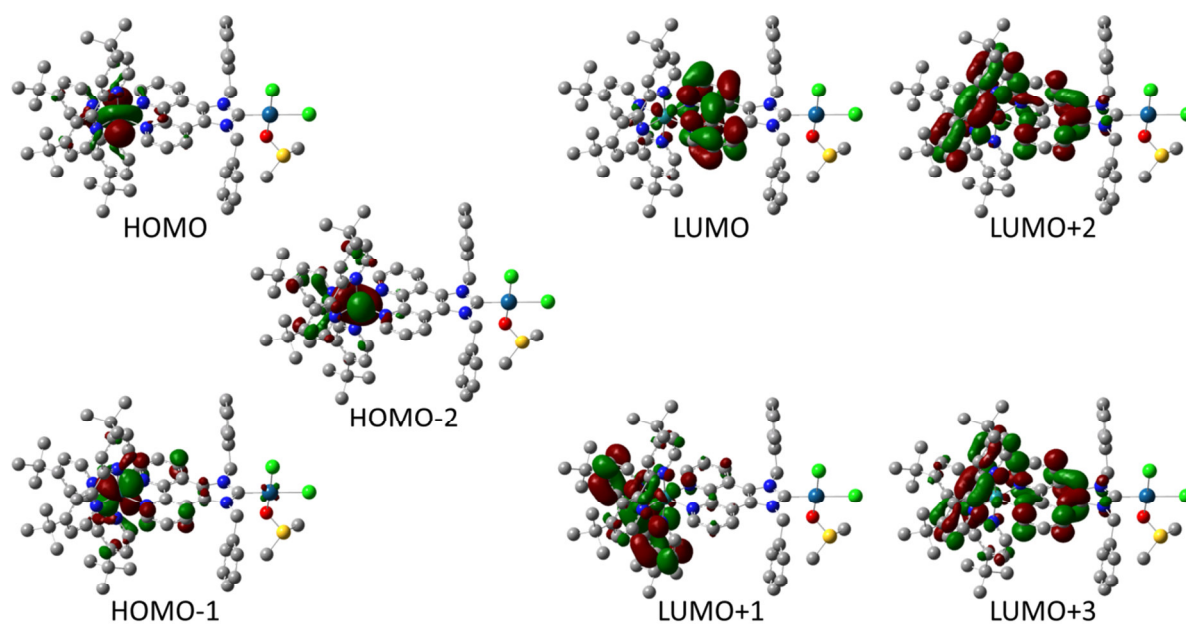
Figure S12 Frontier orbitals involved in the liquid phase (PCM, acetonitrile) electronic transitions in the charge transfer region of **RubbipPt** calculated for the *cis-O* isomer (*cf.* Table S5).

Table S6 Calculated gas phase vertical excitation energies E_v, oscillator strengths f and singlet excited state S_n configurations in the CT region of **RubbipPt** (*trans-O* isomer). Transitions were bathochromically shifted by 1000 cm^{-1}.For the sake of clarity, only transitions with high contribution ($f \geq 0.02$) are listed. Frontier orbital contributions to the transitions with a weight w of <10 % were omitted.

S_n	transition	w/%	λ/nm	E_v/eV	f
S_{15}	d_{Ru}(HOMO-8)$\rightarrow\pi^*_{tbbpy}$(LUMO+2)	12	486	2.55	0.030
	d_{Pt},n_{Cl},n_{DMSO}(HOMO-3)$\rightarrow\pi^*_{bbip},\pi^*_{tbbpy}$(LUMO)	63			
	d_{Pt},n_{Cl},n_{DMSO}(HOMO-3)$\rightarrow\pi^*_{tbbpy},\pi^*_{bbip}$(LUMO+1)	12			
S_{18}	d_{Ru},n_{Cl}(HOMO-11)$\rightarrow\pi^*_{bbip},\pi^*_{tbbpy}$(LUMO)	11	469	2.64	0.045
	π_{Ph},n_{Cl}(HOMO-4)$\rightarrow\pi^*_{bbip},\pi^*_{tbbpy}$(LUMO)	49			
S_{25}	d_{Ru},n_{Cl}(HOMO-11)$\rightarrow\pi^*_{tbbpy},\pi^*_{bbip}$(LUMO+1)	14	442	2.94	0.057
	π_{Ph}(HOMO-7)$\rightarrow\pi^*_{bbip},\pi^*_{tbbpy}$(LUMO)	24			
	d_{Pt},n_{Cl},n_{DMSO}(HOMO-3)$\rightarrow\pi^*_{tbbpy}$(LUMO+2)	16			
S_{26}	π_{Ph}(HOMO-7)$\rightarrow\pi^*_{bbip},\pi^*_{tbbpy}$(LUMO)	54	442	2.94	0.029
	π_{Ph}(HOMO-7)$\rightarrow\pi^*_{tbbpy},\pi^*_{bbip}$(LUMO+1)	12			
S_{27}	d_{Ru}(HOMO-8)$\rightarrow\pi^*_{tbbpy}$(LUMO+2)	17	439	2.82	0.072
	d_{Ru},n_{Cl}(HOMO-10)$\rightarrow\pi^*_{tbbpy},\pi^*_{bbip}$(LUMO+1)	10			
	d_{Pt},n_{Cl},n_{DMSO}(HOMO-3)$\rightarrow$(LUMO+2)	20			
S_{28}	d_{Ru},n_{Cl}(HOMO-11)$\rightarrow\pi^*_{tbbpy},\pi^*_{bbip}$(LUMO+1)	13	435	2.85	0.046
	d_{Pt},n_{Cl},n_{DMSO}(HOMO-3)$\rightarrow\pi^*_{tbbpy}$(LUMO+2)	40			
S_{34}	d_{Ru},n_{Cl}(HOMO-11)$\rightarrow\pi^*_{tbbpy}$(LUMO+2)	16	421	2.94	0.040
	d_{Ru}(HOMO-8)$\rightarrow\pi^*_{bbip}$(LUMO+3)	31			
	π_{Ph},n_{Cl}(HOMO-4)$\rightarrow\pi^*_{tbbpy}$(LUMO+2)	16			
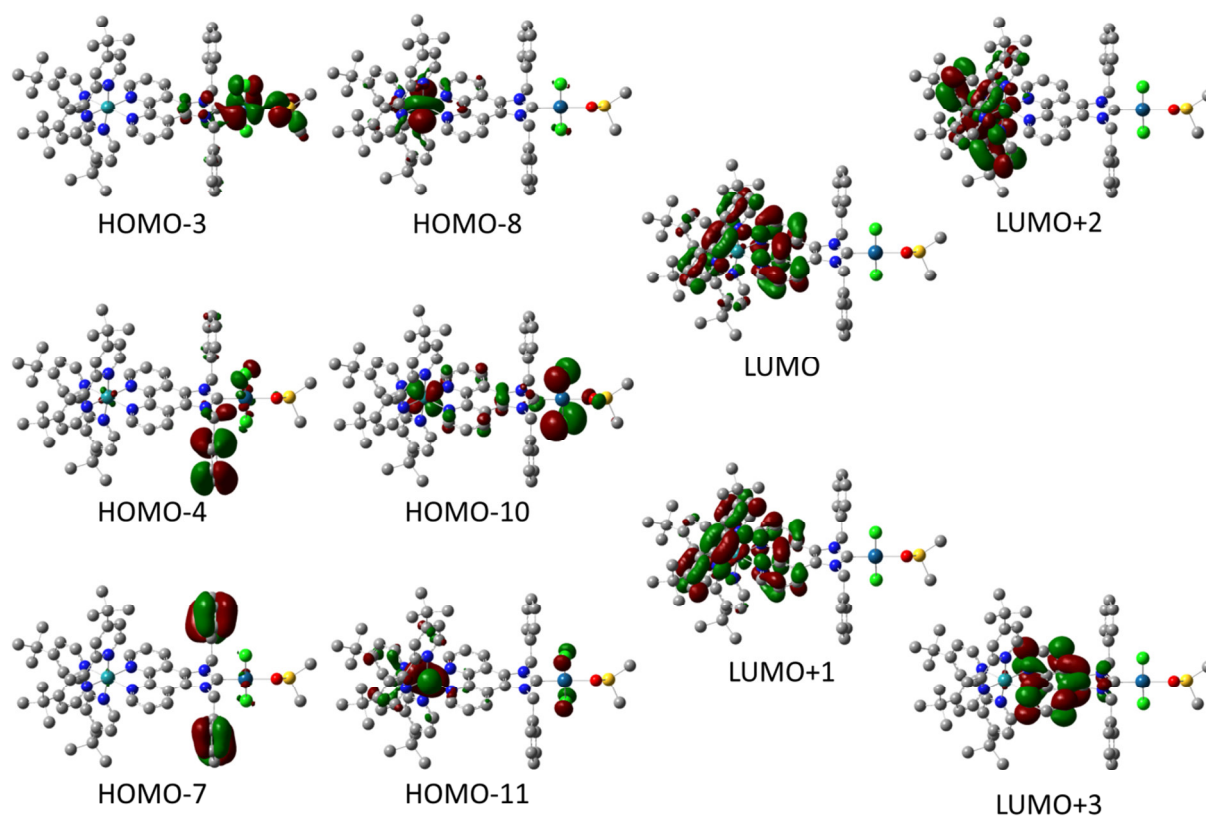
Figure 13 Frontier orbitals involved in the gas phase electronic transitions in the charge transfer region of **RubbipPt** calculated for the *trans-O* isomer (*cf.* Table S6).

Table 7 Calculated gas phase vertical excitation energies E_v, oscillator strengths f, and singlet excited state S_n configurations in the CT region of **RubbipPt** (*trans-S* isomer). Transitions were bathochromically shifted by 1000 cm^{-1}. For the sake of clarity, only transitions with high contribution ($f{\geq}0.02$) are listed. Frontier orbital contributions to the transitions with a weight w of <10 % were omitted.

| S_n	transition	w/%	λ/nm	E_v/eV	f
S_{17}	$d_{Ru},\pi_{bbip},d_{Pt},n_{Cl}$(HOMO-9)$\rightarrow\pi^*_{bbip}$(LUMO)	15	464	2.67	0.042
	$d_{Pt},\pi_{Ph},n_{Cl},n_O$(HOMO-4)$\rightarrow\pi^*_{bbip}$(LUMO)	34			
	$d_{Pt},\pi_{Ph},n_{Cl},n_O$(HOMO-3)$\rightarrow\pi^*_{bbip}$(LUMO)	14			
	d_{Pt},n_{Cl},n_O(HOMO-2)$\rightarrow\pi^*_{bbip},\pi^*_{tbbpy}$(LUMO+2)	11			
	d_{Pt},n_{Cl},n_O(HOMO-2)$\rightarrow$(LUMO+3)	11			
S_{20}	d_{Ru}(HOMO-10)$\rightarrow\pi^*_{tbbpy}$(LUMO+1)	16	456	2.72	0.030
	$d_{Ru},\pi_{bbip},d_{Pt},n_{Cl}$(HOMO-9)$\rightarrow\pi^*_{tbbpy}$(LUMO+1)	11			
	$d_{Ru},\pi_{bbip},d_{Pt},n_{Cl}$(HOMO-9)$\rightarrow\pi^*_{bbip},\pi^*_{tbbpy}$(LUMO+2)	14			
	π_{Ph}(HOMO-5)$\rightarrow\pi^*_{bbip}$(LUMO)	36			
S_{21}	$d_{Ru},\pi_{bbip},d_{Pt},n_{Cl}$(HOMO-9)$\rightarrow\pi^*_{bbip}$(LUMO)	20	452	2.74	0.021
	$d_{Ru},\pi_{bbip},d_{Pt},n_{Cl}$(HOMO-9)$\rightarrow\pi^*_{bbip},\pi^*_{tbbpy}$(LUMO+2)	10			
	π_{Ph}(HOMO-5)$\rightarrow\pi^*_{bbip}$(LUMO)	36			
S_{23}	d_{Ru}(HOMO-10)$\rightarrow\pi^*_{bbip},\pi^*_{tbbpy}$(LUMO+2)	17	445	2.79	0.039
	$d_{Ru},\pi_{bbip},d_{Pt},n_{Cl}$(HOMO-9)$\rightarrow\pi^*_{bbip}$(LUMO)	14			
	$d_{Ru},\pi_{bbip},d_{Pt},n_{Cl}$(HOMO-9)$\rightarrow\pi^*_{tbbpy}$(LUMO+1)	22			
	d_{Pt},d_{Ru},π_{Ph}(HOMO-6)$\rightarrow\pi^*_{bbip}$(LUMO)	22			
S_{24}	d_{Ru}(HOMO-10)$\rightarrow\pi^*_{tbbpy}$(LUMO+1)	46	435	2.85	0.130
	$d_{Ru},\pi_{bbip},d_{Pt},n_{Cl}$(HOMO-9)$\rightarrow\pi^*_{bbip},\pi^*_{tbbpy}$(LUMO+2)	27			
S_{28}	d_{Ru}(HOMO-10)$\rightarrow\pi^*_{bbip},\pi^*_{tbbpy}$(LUMO+2)	16	424	2.92	0.031
	d_{Ru},π_{Ph}(HOMO-8)$\rightarrow\pi^*_{bbip}$(LUMO+3)	22			
	$d_{Pt},\pi_{Ph},n_{Cl},n_O$(HOMO-3)$\rightarrow\pi^*_{bbip},\pi^*_{tbbpy}$(LUMO+2)	34			
	$d_{Pt},\pi_{Ph},n_{Cl},n_O$(HOMO-3)$\rightarrow\pi^*_{bbip}$(LUMO+3)	10			
S_{29}	d_{Ru}(HOMO-10)$\rightarrow\pi^*_{bbip},\pi^*_{tbbpy}$(LUMO+2)	12	424	2.92	0.037
	d_{Ru},π_{Ph}(HOMO-8)$\rightarrow\pi^*_{bbip}$(LUMO+3)	15			
	$d_{Pt},\pi_{Ph},n_{Cl},n_O$(HOMO-4)$\rightarrow\pi^*_{bbip}$(LUMO+3)	11			
	$d_{Pt},\pi_{Ph},n_{Cl},n_O$(HOMO-3)$\rightarrow\pi^*_{bbip},\pi^*_{tbbpy}$(LUMO+2)	12			
	$d_{Pt},\pi_{Ph},n_{Cl},n_O$(HOMO-3)$\rightarrow\pi^*_{bbip}$(LUMO+3)	35			
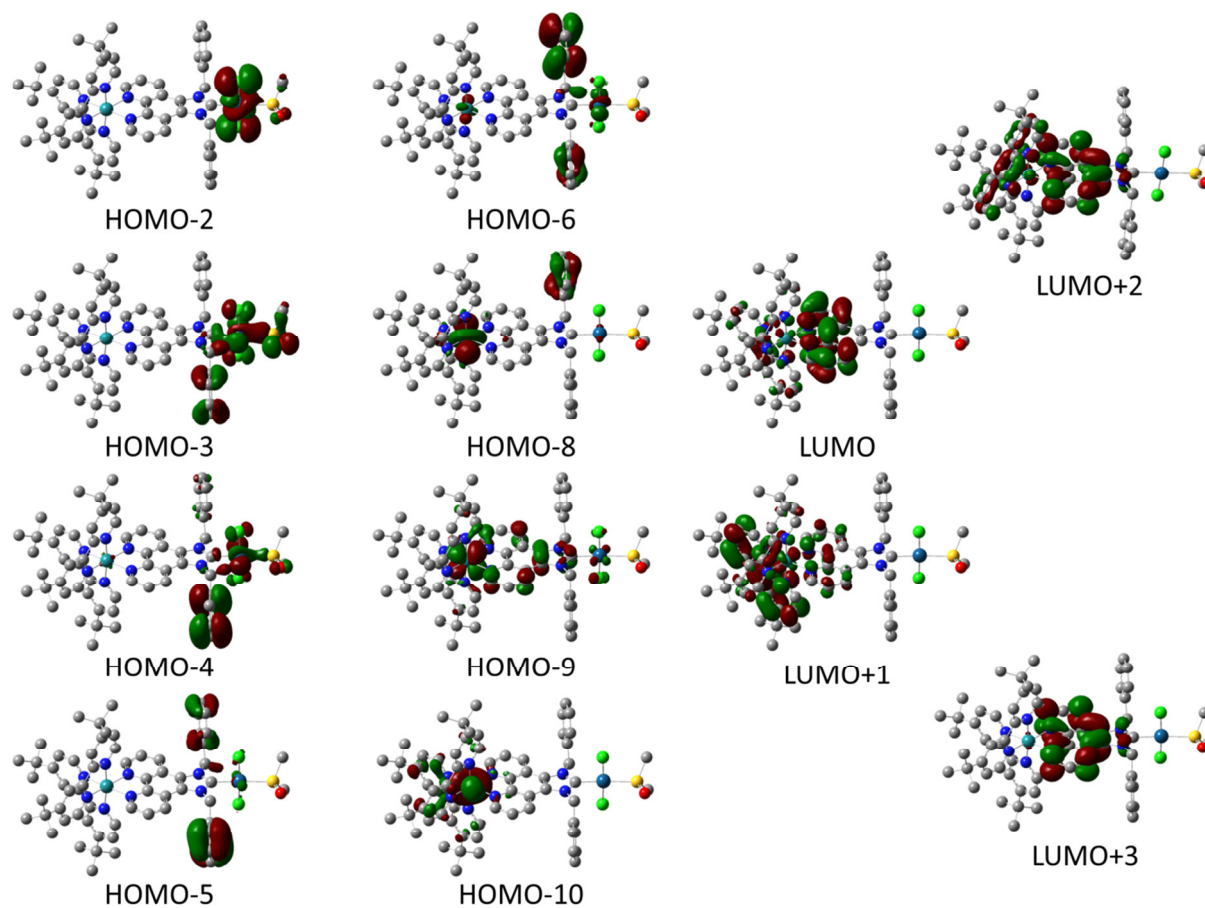
Figure S14 Frontier orbitals involved in the gas phase electronic transitions in the charge transfer region of **RubbipPt** calculated for the *trans-S* isomer (*cf.* Table S7).

Table 8 Calculated gas phase vertical excitation energies E_v, oscillator strengths f and singlet excited state S_n configurations in the CT region of **RubbipPt** (*cis-O* isomer). Transitions were bathochromically shifted by 1000 cm^{-1}. For the sake of clarity, only transitions with high contribution ($f \geq 0.02$) are listed. Frontier orbital contributions to the transitions with a weight w of <10 % were omitted.

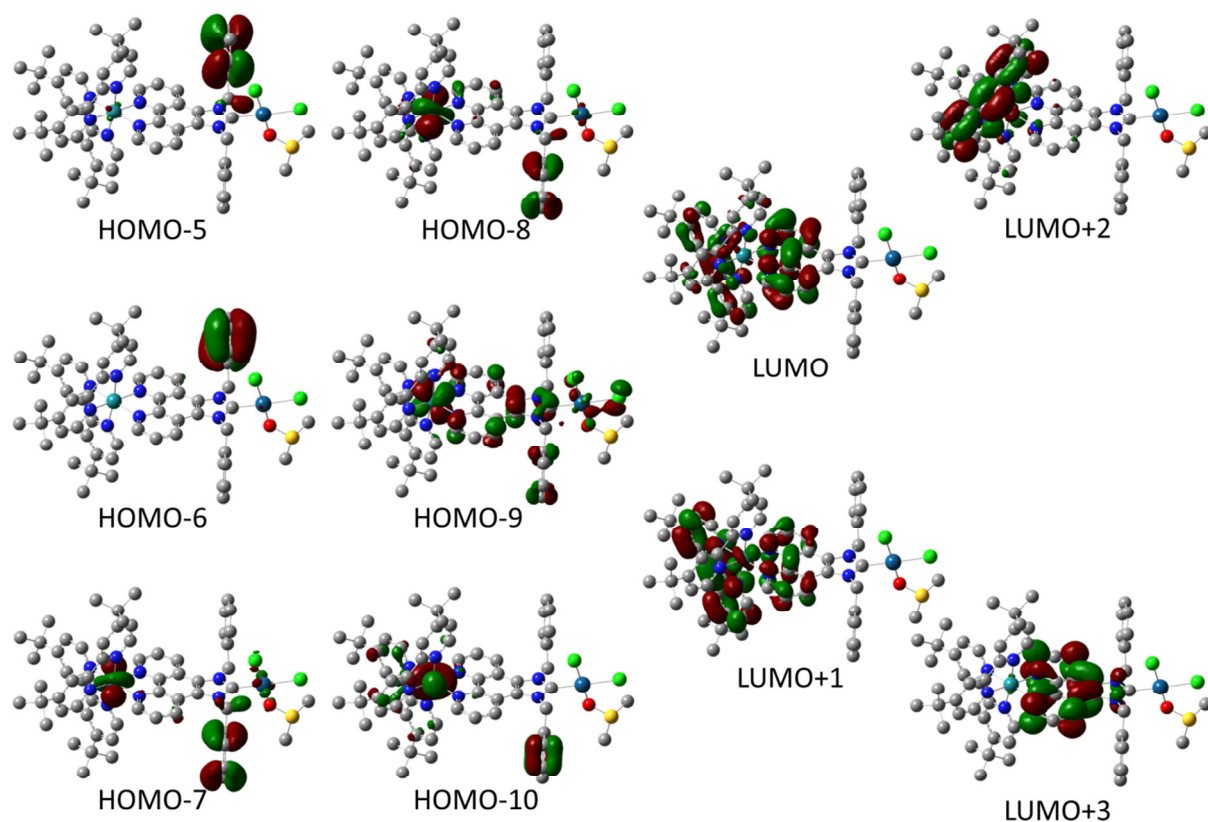| S_n	transition	w/%	λ/nm	E_v/eV	f
S_{26}	d_{Ru},π_{Ph}(HOMO-10)$\rightarrow\pi^*_{bbip},\pi^*_{tbbpy}$(LUMO)	11	467	2.65	0.039
	π_{Ph}(HOMO-5)$\rightarrow\pi^*_{bbip},\pi^*_{tbbpy}$(LUMO)	55			
	π_{Ph}(HOMO-5)$\rightarrow\pi^*_{tbbpy},\pi^*_{bbip}$(LUMO+1)	10			
S_{28}	d_{Ru},π_{Ph}(HOMO-10)$\rightarrow\pi^*_{bbip},\pi^*_{tbbpy}$(LUMO)	12	455	2.72	0.081
	$d_{Ru},\pi_{bbip},\pi_{Ph},d_{Pt},n_{Cl}$(HOMO-9)$\rightarrow\pi^*_{bbip},\pi^*_{tbbpy}$(LUMO)	18			
	π_{Ph}(HOMO-6)$\rightarrow\pi^*_{bbip},\pi^*_{tbbpy}$(LUMO)	22			
S_{31}	d_{Ru},π_{Ph}(HOMO-10)$\rightarrow\pi^*_{tbbpy}$(LUMO+2)	24	444	2.79	0.070
	$d_{Ru},\pi_{bbip},\pi_{Ph},n_{Cl}$(HOMO-9)$\rightarrow\pi^*_{tbbpy},\pi^*_{bbip}$(LUMO+1)	15			
	$d_{Ru},\pi_{bbip},\pi_{Ph},n_{Cl}$(HOMO-9)$\rightarrow\pi^*_{tbbpy}$(LUMO+2)	18			
S_{32}	d_{Ru},π_{Ph}(HOMO-10)$\rightarrow\pi^*_{tbbpy},\pi^*_{bbip}$(LUMO+1)	31	438	2.83	0.126
	$d_{Ru},\pi_{bbip},\pi_{Ph},d_{Pt},n_{Cl}$(HOMO-9)$\rightarrow\pi^*_{tbbpy}$(LUMO+2)	18			
S_{38}	d_{Ru},π_{Ph}(HOMO-10)$\rightarrow\pi^*_{tbbpy}$(LUMO+2)	22	422	2.94	0.059
	d_{Ru},π_{Ph}(HOMO-8)$\rightarrow\pi^*_{bbip}$(LUMO+3)	23			
	d_{Ru},π_{Ph}(HOMO-7)$\rightarrow\pi^*_{bbip}$(LUMO+3)	19			

Figure S15 Frontier orbitals involved in the gas phase electronic transitions in the charge transfer region of **RubbipPt** calculated for the *cis-O* isomer (*cf.* Table S8).
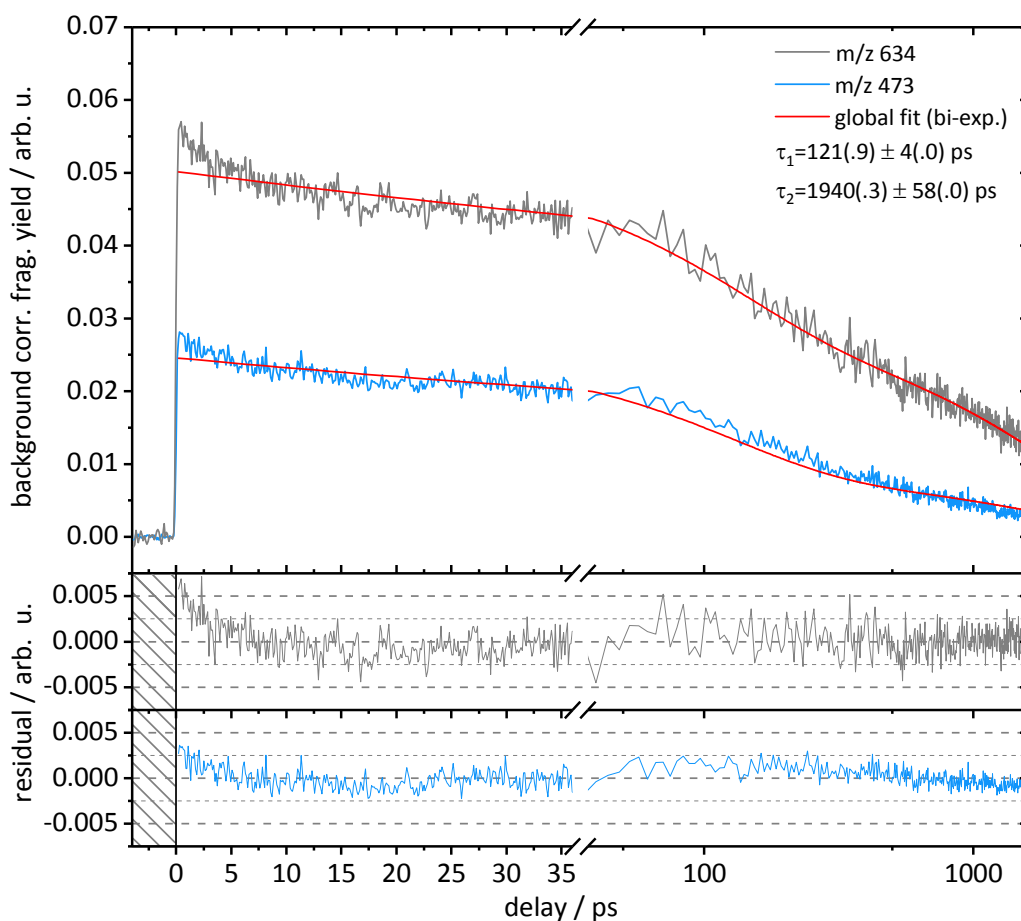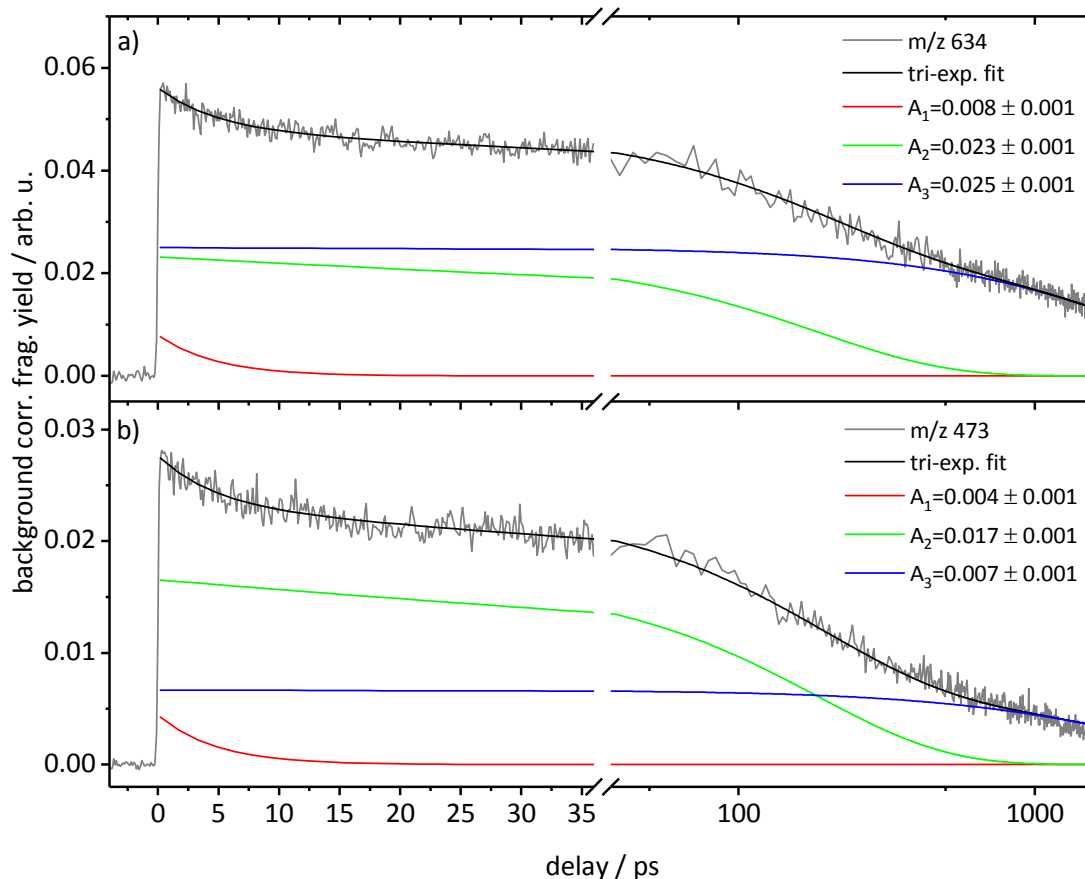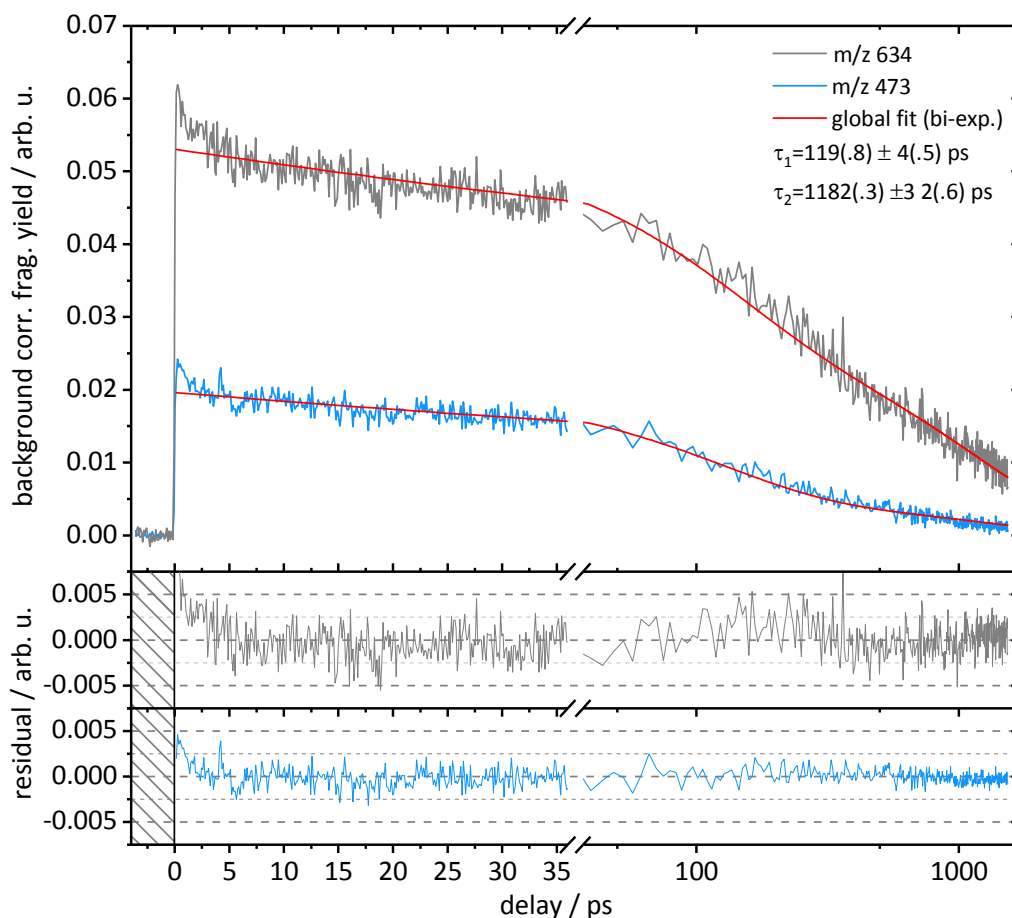
7.8.5 Fitting

Figure S16 Transient fragment ion traces of **RubbipPt** displayed for the two most intense fragments m/z 634 (black) and 473 (dark cyan). The transient signals (gray) were recorded at the magic angle (54.7°) using λ_{pump}=430 nm and λ_{probe}=1200 nm. Global bi-exponential fit (red) was performed assuming shared decay kinetics (time constants $\tau_{1\&2}$) between the traces. Color coded residual signals are given below. Fit decomposition was not performed, due to a poor match of the applied decay model.

Figure S17 Transient fragment ion traces of **RubbipPt** displayed for the two most intense fragments m/z 634 **(a)** and 473 **(b)**. The transient signals (gray) were recorded at the magic angle (54.7°) using λ_{pump}=430 nm and λ_{probe}=1200 nm. Global tri-exponential fit (black) was performed assuming shared decay kinetics (τ_1=4 ps, τ_1=185 ps and τ_3≈2.5 ns) between individual traces. Fit decomposition is presented as colored traces and given along the respective decay amplitudes A_i.

Figure S18 Transient fragment ion traces of **RubbipPt** displayed for the two most intense fragments m/z 634 (black) and 473 (dark cyan). The transient signals (gray) were recorded at the magic angle (54.7°) using λ_{pump}=470 nm and λ_{probe}=1200 nm. Global bi-exponential fit (red) was performed assuming shared decay kinetics (time constants $\tau_{1\&2}$) between the traces. Color coded residual signals are given below. Fit decomposition was not performed, due to a poor match of the applied decay model.
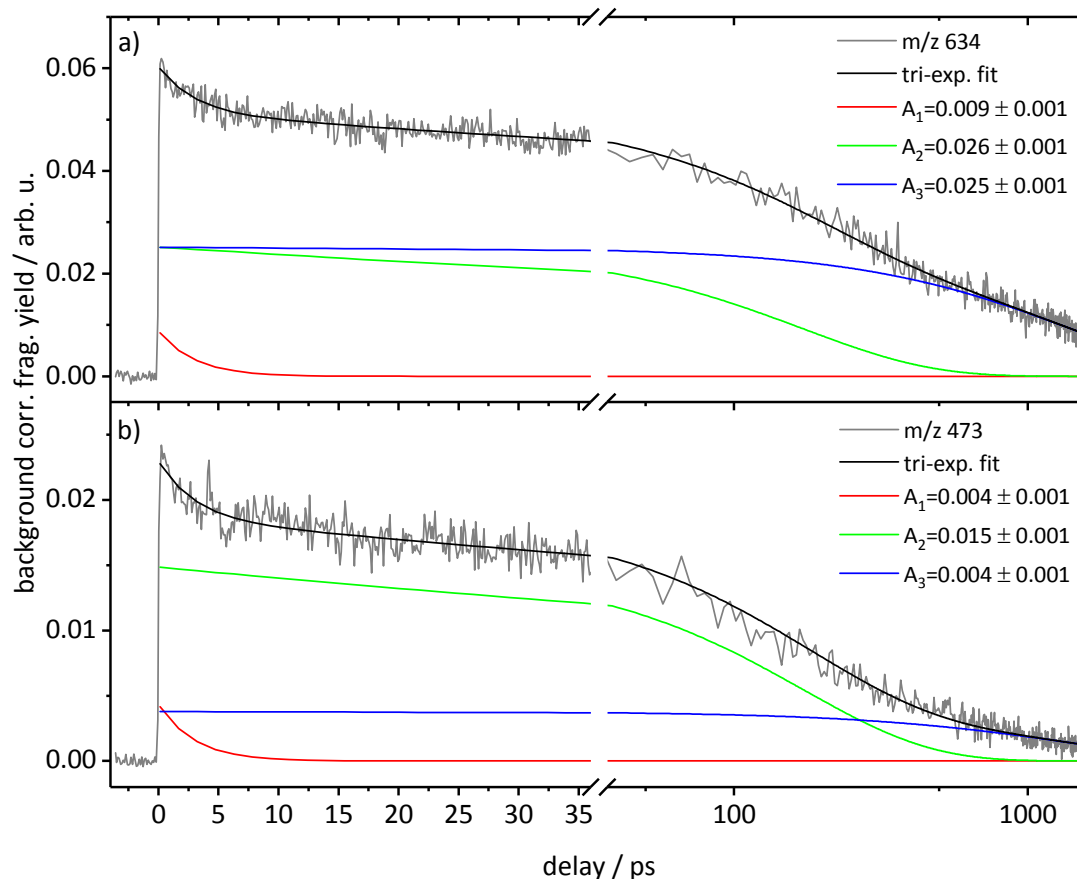
Figure S19 Transient fragment ion traces of **RubbipPt** displayed for the two most intense fragments m/z 634 **(a)** and 473 **(b)**. The transient signals (gray) were recorded at the magic angle (54.7°) using λ_{pump}=470 nm and λ_{probe}=1200 nm. Global tri-exponential fit (black) was performed assuming shared decay kinetics (τ_1=3 ps, τ_1=172 ps and $\tau_3\approx$1.4 ns) between individual traces. Fit decomposition is presented as colored traces and given along the respective decay amplitudes A_i.

7.8.6 References

[1] J. D. Bhawalkar, G. S. He, P. N. Prasad, "*NONLINEAR MULTIPHOTON PROCESSES IN ORGANIC AND POLYMERIC MATERIALS*", *Rep. Prog. Phys.* **1996**, 59, 1041-1070.

8 Rational *in situ* tuning of a supramolecular photocatalyst for hydrogen evolution

Simon Kaufhold[1], Dimitri Imanbaew[2], Christoph Riehn[2],[3] and Sven Rau[1]

[1]Anorganische Chemie I, Universität Ulm, Albert-Einstein-Allee 11, 89091 Ulm, Germany

[2]Fachbereich Chemie, Technische Universität Kaiserslautern, Erwin-Schrödinger-Str. 52-54, 67663 Kaiserslautern, Germany

[3]Landesforschungszentrum OPTIMAS, Erwin-Schrödinger-Str. 46, 67663 Kaiserslautern, Germany

8.1 Preamble

The following chapter has been submitted to the journal *Energy and Environmental Science.* The manuscript is currently under review and contains unpublished data. Thus, a reprint of the manuscript is not shown. The results therein are part of the PhD thesis of Simon Kaufhold (Universität Ulm). Experimental work involving synthesis, characterization and catalytic performance evaluation was performed by Simon Kaufhold. The manuscript was mainly prepared by Sven Rau and Simon Kaufhold. My contribution to the publication encompassed mass spectrometric measurements to verify the postulated *in situ* ligand exchange reaction, as well as theoretical calculations and identification of the occurring intermediate ion signals. Additionally, I helped revising the manuscript.

9 Summary and Outlook

This thesis encompasses investigations on the gas phase absorption properties and ultrafast electronic dynamics of several (functionalized) fluorescein derivatives, a carbocyanine dye and heterodinuclear transition complexes for photocatalytic hydrogen evolution. Several experimental and theoretical methods were employed: mass spectrometry, steady state liquid phase and gas phase absorption action spectroscopy, time-resolved pump-probe photofragmentation and infrared multiple-photon dissociation spectroscopy. Experimental results were corroborated by identification of minimum energy structures and transition states, as well as vertical electronic transition calculations by means of (time-dependent) density functional theory.

Polarization dependent transient photofragmentation experiments on the monoanionic (**[FL-H]⁻**) and cationic (**[FL+H]⁺**) forms of unsubstituted fluorescein were performed to probe the respective excited state, vibrational and rotational dynamics. For **[FL-H]⁻** pronounced vibrational wave-packet motion was observed, which is connected to the relaxation of the dihedral angle between the benzoic acid and xanthene units in the electronically excited state. For **[FL+H]⁺** no signature of vibrational wave-packet formation was detected, which was ascribed to the lack of a relaxation coordinate akin to the one found for **[FL-H]⁻**. This assumption was corroborated by single point DFT calculations. The polarization dependence of the transients signals for **[FL-H]⁻** was found to be weak, whereas for **[FL+H]⁺** a strong polarization dependence of the transient traces was observed, from which the time-resolved anisotropy function could be determined. The observed rotational dephasing was interpreted by the loss of anisotropy of an **[FL+H]⁺** ion ensemble at room temperature. The dephasing of the corresponding rotational wave-packet was successfully simulated by the time-resolved orientational correlation function, which furthermore allowed the assignment of the probe process to a two photon transition with the respective transition dipole moment aligned parallel to the xanthene unit. This study was published as a paper in the journal *Structural Dynamics*.

An extensive spectroscopic gas phase and theoretical study was conducted on the monoanionic and cationic forms of two fluorescein derivatives, functionalized with either an electron withdrawing nitro- (**[5-NF]**$^{-/+}$) or an electron donating amino-group (**[5-AF]**$^{-/+}$) at the benzoic acid ring. Infrared multiple-photon dissociation spectra were recorded in a spectral range characteristic for the O-H stretching vibration, which revealed the coexistence of tautomers in the case of the anionic nitro derivative, whereas for the amino-derivative only one tautomer (carboxylate) is deemed to contribute to the gas phase population. The cationic ion populations, on the other hand, consist of several rotamers, differing in the orientation of the carboxylic OH-group. However, only geometries in which the proton at the carboxylic acid group point towards the xanthene ring are significantly stabilized by long-range interaction with the π-system of the xanthene and are thus expected to contribute to the ion population. Steady-state UV/Vis absorption action spectra were recorded. The spectra of the cations are in good agreement with TD-DFT calculated linear absorption spectra. The spectra recorded for the anions on the other hand were not in accordance with theory, in particular for the weak long wavelength spectroscopic features, which are probably suppressed by collisional quenching - a possible drawback of the experimental setup. Excited state dynamics following a localized excitation of the xanthene chromophore exhibited remarkable dependence on the nature of the substituent (amino/nitro), as well as on the charge state. Experimental evidence for excited state dynamics on a fs- and ps-timescale was only obtained for **[5-AF]**$^+$ and **[5-NF]**$^-$, and attributed to excited state quenching by photoinduced electron transfer (PeT). The sequence of frontier orbitals from DFT calculations were in remarkable accordance with this assumption, only enabling d(onor)-PeT for **[5-NF]**$^-$ and a(cceptor)-PeT for **[5-AF]**$^+$. Additionally, the transient fragment mass signals of the anions were found to be periodically modulated, indicative of vibrational wave-packet dynamics. However, in contrast to the modulation observed for the unsubstituted fluorescein monoanion, the modulation is much more complex, requiring at least two damped sine functions of different frequencies for theoretical modeling. From the period of the modulation, two frequencies could be extracted, pointing to the concurrent coherent excitation of at least two vibrational modes in the excited states of **[5-NF]**$^-$ and **[5-AF]**$^-$. Based on vibrational frequency calculations for the ground state geometries of **[5-NF]**$^-$ and **[5-AF]**$^-$, the vibrational modes are tentatively assigned to the torsion of the benzoic acid moiety with respect to

the xanthene ring and a rocking motion of the former vs. the latter within the plane of the xanthene ring.

Time-resolved photofragmentation experiments on isolated 3,3'-diethyloxacarbo-cyanine (**DOC⁺**) ions were carried out in a quadrupole ion trap to investigate its intrinsic excited state and photoisomerization dynamics. The S_1 excited state population of **DOC⁺** decays bi-exponentially and the corresponding lifetimes were found to be dependent on the pump photon energy, decreasing with increasing excess energy, indicative of two competing, activated processes in the S_1 excited state. An upper boundary value could be determined for the activation barrier of the slower process (E_{a2}=23 kJ/mol) by means of a simple Arrhenius relation. The estimated barrier height is in fair agreement with the value determined from single point TD-DFT calculations (E_{a2}=31 kJ/mol). Additionally, vibrational wave-packet dynamics were observed by a periodic modulation of the transient signal with a period of T=1.2 ps, corresponding to a vibrational frequency of ~30 cm^{-1}. From vibrational frequency calculations performed for the S_1 excited state of **DOC⁺**, three low frequency modes were identified, which are deemed to be responsible for wave-packet formation. These modes involve torsional motions and in- and out-of-plane bending of the benzoxazole end groups with respect to each other. The observation of a torsional motion is of particular interest, as the twisting around the C-C bonds within the polymethine backbone promotes excited state deactivation by this specific isomerization coordinate.

The intrinsic photodynamics and fragmentation of two hydrogen generating supramolecular photocatalysts **Ru-Pt** and **Ru-Pd** ([(ᵗbbpy)₂Ru(tpphz)M(Cl)₂]²⁺ M=Pt, Pd; ᵗbbpy=4,4'-di-tert.-butyl-2,2'-bipyridin, tpphz=tetrapyrido[3,2-a:2'3'-c:3'',2''-h:2''',3'''-j]phenazine) were investigated in the gas phase. The properties of both molecular systems correspond astonishingly well to their behavior in acetonitrile solution, indicating that their photoinduced key process, *i.e.* the charge transfer towards the catalytic metal center, is taking place in isolated molecular systems as well. Mass spectrometric investigations revealed for both complexes that the catalytically active metal centers provide the most weakly bound units in the complexes and fragment with high yield as neutral losses of $PtCl_2$ and $PdCl_2$. Photofragmentation studies clearly indicate an intrinsically higher photostability of **Ru-Pt** compared to **Ru-Pd** and resulted

in the first gas phase UV/Vis spectra for both species that serve as highly useful references for future *ab initio* calculations. Time-resolved photofragmentation experiments on **Ru-Pd** and **Ru-Pt** yielded three time constants, respectively. For both molecular systems, two fast constants were found (τ_1 and τ_2), which are remarkably close to the ones observed in liquid phase studies, whereas the third time constant τ_3 exhibits a larger value. The large uncertainty of the latter originates in a technical limitation of the utilized delay stage set up. However, its larger value could be also a hint that the charge transfer from the bridging ligand to the metal center is hindered and thus delayed in *vacuo*, due to lack of stabilization of the final strongly charge separated state. Additionally, the kinetics were found to be dependent on the pump-photon wavelength, decreasing at longer wavelength excitation. This is in agreement with the assumption that upon long wavelength excitation, an excited state is quickly populated, which is centered mainly on the bridging ligand, thus facilitating electron transfer towards the catalytic metal center Furthermore, polarization dependent transient studies were performed for both catalysts, from which the initial anisotropy and the time-dependent anisotropy function were determined and simulated by the time-resolved orientational correlation function. The former yielded a value of 0.31 and 0.32 at an excitation wavelength of 440 nm for **Ru-Pt** and **Ru-Pd**, respectively, and a value of 0.4 using a longer pump wavelength (480 nm), strongly supporting a directed electron transfer towards the bridge, which is more pronounced upon longer wavelenght excitation. These ion trap photofragmentation experiments allowed for valuable insights into intrinsic spectroscopic and dynamic properties and stability of Ru^{II}-based photocatalysts and might contribute to the optimization of supramolecular photocatalyst performance in connection with theory-derived rational design. The results were published as a paper in the journal *Angewandte Chemie International Edition.*

The UV/Vis absorption properties of a novel heterodinuclear complex **RubbipPt** (^{t}bbpy)$_2$Ru(μ-bbip)Pt(DMSO)Cl$_2$]$^{2+}$, ^{t}bbpy=4,4'-di-*tert*-butyl-2,2'-bipyridine, bbip=1,3-dibenzyl-1*H*-imidazo[4,5-*f*][1,10]phenanthrolin-2-ylidene, DMSO=dimethyl sulfoxide) for photocatalytic hydrogen generation were studied in gas phase and solution. Lacking crystallographic data for this complex, the molecular structure was identified by comparison of the experimental spectra to the theoretical TD-DFT linear absorption

spectra. The spectrum calculated for the *cis-S* geometry, in which the DMSO ligand binds to the platinum atom via the S atom in *cis*-orientation to the bridging ligand, is in remarkable agreement with the experiment. TD-DFT calculations employing a solvent model identified the absorption band in the charge transfer region to be dominated by two transitions, with the lower energy transition involving mainly charge transfer from the ruthenium metal center to the π-system of the bridging ligand, whereas the higher energy transition encompasses charge transfer spread over the ligand sphere of the ruthenium photosensitizer. The liquid phase calculations are in accordance to previous calculations performed for a similar type of supramolecular catalyst. Calculations on the isolated molecule, on the other hand, although in excellent agreement with the experimental photofragmentation spectrum in the UV region, failed to produce reasonable results for the lowest energy transitions in the charge transfer region, further stressing the need for a more sophisticated theoretical approach to model the properties of low lying excited state of larger systems under isolation, which apparently TD-DFT cannot provide. The recorded transient mass spectra decayed tri-exponentially, yielding a time constant on a ns-timescale and two on a ps-timescale. The shortest time constant was assigned to a charge transfer transition onto the bridge, corroborated by acceleration of the kinetics upon longer wavelength excitation, in agreement with a more directed electron transfer towards the catalytic metal center. The origin of the remaining two processes remains elusive at this point and requires further complementary time-resolved investigations in solution. Nonetheless, the kinetics should provide a valuable point of reference for future studies.

A novel supramolecular catalyst **RubbipPt** ([(^{t}bbpy)$_2$Ru(μ-bbip)Pt(DMSO)Cl$_2$]$^{2+}$, ^{t}bbpy=4,4'-di-*tert*-butyl-2,2'-bipyridine, DMSO=dimethyl sulfoxide, bbip=1,3-dibenzyl-1*H*-imidazo[4,5-*f*][1,10]phenanthrolin-2-ylidene) for hydrogen generation was developed and characterized by S. Kaufhold (Universität Ulm). Performance was found to be low under standard catalytic conditions. However, the admixture of an iodide salt (TBAI, tetrabutylammonium iodide) boosted the performance dramatically, which was ascribed to an *in-situ* ligand exchange (Cl$^-$ vs. I$^-$) and thus to a putatively increased electron density at the catalytic platinum metal center. Other halide salts (TBAX, X=F, Cl, and Br) had a negligible effect. *In situ* ligand exchange after admixture of TBAI was monitored by mass spectrometry. Two product signals evolved in time from the parent ion signal [(^{t}bbpy)$_2$Ru(μ-bbip)Pt(Cl)(OMe)]$^{2+}$ (in methanol), which were identified to

originate from single ligand exchange ([(^{t}bbpy)$_2$Ru(μ-bbip)Pt(DMSO)(Cl)I]$^{2+}$) and double ligand exchange ([(^{t}bbpy)$_2$Ru(μ-bbip)Pt(DMSO)I$_2$]$^{2+}$). The latter signal rose dramatically in intensity by adding larger amounts of TBAI. Additionally, natural population analysis (NPA) was performed for the parent ion and for several conceivable product ions, which may be formed by *in situ* ligand exchange (Cl vs. X, X=F, Br, I, OMe). The highest electron population in the Pt(5dz^2) orbital was found for [(^{t}bbpy)$_2$Ru(μ-bbip)Pt(DMSO)I$_2$]$^{2+}$, in qualitative agreement with its improved catalytic performance. This study provided more insight into the structure-property-correlation of supramolecular photocatalytic assemblies and is expected to contribute to the optimization of supramolecular photocatalyst performance in connection with theory-derived rational design. The results were submitted as a paper to the journal *Energy & Environmental Science*.

In summary, several experimental methods were applied to study the intrinsic excited state properties of organic dye molecules and supramolecular catalysts under isolation. DFT and TD-DFT calculations allowed the identification of gas phase structures of the investigated compounds and helped characterizing the absorption bands observed in experimental IRMPD and UV/Vis photofragmentation spectra. In conclusion, the applied technique of femtosecond transient photofragmentation in an ion trap proves to be very valuable for the analysis of ultrafast molecular vibrational and rotational dynamics, and electronically excited states of ionic dye molecules and larger photocatalytic systems under isolated conditions. It is complementary to other time-resolved liquid phase and gas phase methods and provides valuable insight into the intrinsic, early excited state dynamics of metal complexes and organic compounds alike.

10 Zusammenfassung und Ausblick

Diese Arbeit umfasst die Untersuchungen von optischen Eigenschaften und elektronischer Ultrakurzzeit-Dynamik in der Gasphase an mehreren (funktionalisierten) Fluorescein-Derivaten, an einem Carbocyaninfarbstoff und an heterodinuklearen Übergangsmetall-Komplexen zur photokatalytischen Wasserstofferzeugung. Es wurden mehrere experimentelle und theoretische Methoden verwendet: Massenspektrometrie, stationäre Flüssigphasen-Absorptionsspektroskopie und Gasphasen-Konsequenz-Spektroskopie, zeitaufgelöste Pump-Probe Photofragmentations- und Infrarot-Multiphotonen-Dissoziations-Spektroskopie. Die experimentellen Ergebnisse wurden unterstützt durch die theoretische Bestimmung von energieminimierten, molekularen Strukturen und Übergangszuständen sowie durch Berechnung von vertikalen elektronischen Übergängen mittels (zeitabhängiger) Dichtefunktionaltheorie (DFT/TD-DFT).

Polarisationsabhängige transiente Photofragmentations-Experimente wurden an monoanionischem (**[FL-H]**⁻) und kationischem (**[FL+H]**⁺), unsubstituiertem Fluorescein durchgeführt, um dessen Schwingungs- und Rotationsdynamik im angeregten Zustand zu untersuchen. Für **[FL-H]**⁻ wurde ausgeprägte Schwingungswellenpaketbewegung beobachtet, die mit der Relaxation des Diederwinkels zwischen der Benzoesäure- und Xanthen-Untereinheiten im elektronisch angeregten Zustand einhergeht. Für **[FL+H]**⁺ wurde keine Schwingungskohärenz beobachtet und dies dem Fehlen einer Relaxationskoordinate, ähnlich der des **[FL-H]**⁻ zugeordnet. Diese Vermutung wurde durch Single-Point-DFT-Berechnungen unterstützt. Die transienten Signale von **[FL-H]**⁻ zeigten nur eine geringe Polarisationsabhängigkeit, wohingegen für **[FL+H]**⁺ eine stark ausgeprägte Polarisationsabhängigkeit der transienten Signale beobachtet wurde. Daraus konnte die zeitabhängige Anisotropie-Funktion ermittelt werden. Die beobachtete Rotations-Dephasierung wurde dabei als ein Verlust der Anisotropie eines **[FL+H]**⁺ Ionenensembles bei Raumtemperatur gedeutet. Die Dephasierung des entsprechenden Rotationswellenpakets konnte erfolgreich mittels zeitabhängiger Rotationskorrelationsfunktionen simuliert werden, wodurch der Probe-Prozess einem Zwei-Photonenübergang zugeschrieben werden konnte, dessen Übergangsdipolmoment

parallel zur langen Achse der Xanthen-Einheit ausgerichtet ist. Die Untersuchungen wurden als Paper im Journal *Structural Dynamics* veröffentlicht.

Es wurde eine umfangreiche spektroskopische und theoretische Gasphasen-Studie an monoanionischen und kationischen Formen von zwei Fluorescein-Derivaten durchgeführt, die zum einen eine elektronenziehende Nitro- (**[5-NF]$^{-/+}$**) oder zum anderen eine elektronenschiebende Aminogruppe (**[5-AF]$^{-/+}$**) am Benzoesäurering tragen. Infrarot-Multiphotonen-Dissoziations-Spektren wurden in einem für die OH-Streckschwingung charakteristischen Spektralbereich aufgezeichnet, die für das Anion des Nitroderivates die Koexistenz von Tautomeren belegten, wohingegen für das Anion des Aminoderivates die Ionenpopulation in der Gasphase vermutlich nur aus einem Tautomer (Carboxylat) besteht. Die Population der Kationen setzt sich hingegen aus mehreren Rotameren zusammen, die sich lediglich in der Stellung der carboxylischen OH-Gruppe unterscheiden. Aus der Studie folgt, dass nur diejenigen Strukturen energetisch begünstigt sind, in denen das Proton der Carbonsäuregruppe auf den Xanthenring gerichtet ist, womöglich bedingt durch eine langreichweitige Wechselwirkung mit dem π-System des Xanthens. Nur solche Geometrien tragen daher vermutlich zur Ionenpopulation in der Ionen-Falle bei. Es wurden wellenlängenabhängige UV/Vis-Konsequenzspektren aufgezeichnet. Die Spektren der Kationen sind im guten Einklang mit mittels TD-DFT berechneten linearen Absorptionsspektren. Die Spektren der Anionen zeigen keine Ähnlichkeit mit den Ergebnissen aus theoretischen Rechnungen, insbesonders für die schwach ausgeprägten Banden im langwelligen Absorptionsbereich. Dies liegt vermutlich an einer stoßinduzierten Unterdrückung des Fragmentationsprozesses - ein Nachteil der verwendeten experimentellen Methode. Die elektronische Dynamik nach lokaler elektronischer Anregung des Xanthen-Chromophors zeigte eine bemerkenswerte Abhängigkeit von der Art des Substituenten (Amino-/Nitro-) sowie vom Ladungszustand. Experimentelle Hinweise auf schnelle elektronische Dynamik auf einer fs- und ps-Zeitskala wurden allerdings nur für **[5-AF]$^+$** und **[5-NF]$^-$** beobachtet. Dies wurde auf die Desaktivierung des entsprechenden angeregten Zustandes mittels photoinduziertem Elektronentransfers (PeT) zurückgeführt Die Abfolge der Grenzorbitale aus DFT-Berechnungen stimmt mit dieser Annahme in bemerkenswerter Weise überein, wobei nur ein D(onor)-PeT für **[5-NF]$^-$** und ein A(kzeptor)-PeT für **[5-**

AF]⁺ möglich erscheint. Zudem sind die transienten Fragment-Massensignale der Anionen periodisch moduliert, was auf Schwingungswellenpaket-Dynamik im angeregten Zustand hinweist. Im Gegensatz zu der für das unsubstituierte Fluorescein-Monoanion beobachteten Modulation, ist die hier beobachtete Signalmodulation deutlich komplexer und erfordert mindestens zwei gedämpfte Sinusfunktionen unterschiedlicher Frequenz für eine überzeugende theoretische Beschreibung. Aus den Perioden der überlagerten Modulationen konnten zweifellos zwei Frequenzen ermittelt werden, was auf die gleichzeitige kohärente Anregung von mindestens zwei Schwingungsmoden in den angeregten Zuständen von **[5-NF]⁻** und **[5-AF]⁻** hinweist. Anhand der Schwingungsfrequenzen, berechnet für die Grundzustandgeometrien von **[5-NF]⁻** und **[5-AF]⁻**, wird nun angenommen, dass diese Schwingungsmoden des Wellenpakets im angeregten Zustand die Torsion der Benzoesäure gegenüber dem Xanthenring und die Knick-Schwingung des Benzoesäurerings innerhalb der Xanthen-Ebene enhalten.

Es wurden zeitaufgelöste Photofragmentations Experimente an isolierten 3,3'-Diethyloxacarbocyanin-Ionen (**DOC⁺**) in einer Quadrupol-Ionenfalle durchgeführt, um deren intrinsische Dynamik im angeregten Zustand und die Dynamik des Photoisomerisierungs-Prozesses zu untersuchen. Die Population im angeregten Zustand (S$_1$) von **DOC⁺** zerfällt bi-exponentiell; die entsprechenden Lebensdauern sind dabei abhängig von der Pump-Photonenenergie (Wellenlänge) und nehmen mit zunehmender Überschussenergie ab, was auf zwei aktivierte Prozesse im angeregten Zustand schließen lässt. Eine Obergrenze für die Aktivierungsbarriere (E_{a2}=23 kJ/mol) des langsameren Prozesses konnte mittels einer einfachen Arrhenius-Beziehung abgeschätzt werden. Diese ist in guter Übereinstimmung mit dem Wert, der aus Single-Point-TD-DFT-Rechnungen erhalten wurde (E_{a2}=31 kJ/mol). Zusätzlich wurde Schwingungswellenpaketdynamik beobachtet, die in einer periodischen Modulation des transienten Signals mit einer Periode von T=1.2 ps beobachtbar ist, was einer Schwingungsfrequenz von ~30 cm^{-1} entspricht. Mittels Berechnungen der Schwingungsfrequenzen für den S$_1$-angeregten Zustand von **DOC⁺**, wurden drei niederfrequente Schwingungsmoden identifiziert, die für die Ausbildung des Wellenpakets in Frage kommen. Diese Schwingungsmoden umfassen Torsionsbewegungen und die Biegung der Benzoxazol-Endgruppen in und aus der

Cyanin-Ebene heraus. Die Beobachtung einer Torsionsschwingung ist von besonderem Interesse, da die Drehung um die C-C-Bindungen innerhalb des Polymethin-Rückgrats die Desaktiverung des angeregten Zustandes über diese Koordinate ermöglicht.

Die intrinsische Photodynamik und das Fragmentationsverhalten von zwei Wasserstoff-erzeugenden supramolekularen Photokatalysatoren **Ru-Pt** und **Ru-Pd** ([(tbbpy)$_2$Ru (tpphz)M(Cl)$_2$]$^{2+}$ M=Pt, Pd; tbbpy=4,4'-di-tert.-butyl-2,2'-bipyridin, tpphz=tetrapyrido [3,2-a:2'3'-c:3'',2''-h:2''',3'''-j]phenazin) wurde erstmals in der Gasphase untersucht. Das Verhalten beider molekularen Systeme ist in guter Übereinstimmung mit dem in Lösung (Acetonitril), was darauf hindeutet, dass die photoinduzierten Schlüsselprozesse, d.h. der schrittweise Ladungstransfer in Richtung des katalytischen Metallzentrums, analog in den isolierten Systemen stattfindet. Massenspektrometrische Untersuchungen zeigten für beide Komplexe, dass die katalytisch aktiven Metallzentren die Schwachstelle im Molekül sind, somit Fragment-Ionen größtenteils aus dem Verlust von PtCl$_2$ und PdCl$_2$ resultieren. Photofragmentations-Untersuchungen an **Ru-Pt** und **Ru-Pd** zeigten, dass ersterer Komplex eine intrinsisch höhere Photostabilität aufweist. Zudem wurden erste Gasphasen-UV/Vis-Spektren für beide Spezies aufgezeichnet, die als nützliche Bezugspunkte für zukünftige *ab initio* Berechnungen dienen können. Zeitaufgelöste Photofragmentations-Experimente an **Ru-Pd** und **Ru-Pt** lieferten jeweils drei Zeitkonstanten. Für beide molekularen Systeme wurden zwei kurze Lebensdauern ermittelt (τ_1 und τ_2), die auf bemerkenswerter Weise den Werten aus Flüssigphasen-Untersuchungen ähneln. Die dritte Zeitkonstante τ_3 ist hingegen weitaus länger. Die große Abweichung im letzteren Wert ergibt sich möglicherweise aus einer technischen Einschränkung des verwendeten experimentellen Aufbaus. Allerdings könnte der größere Wert auch ein Hinweis darauf sein, dass der Ladungstransfer über den Brückenliganden zum Metallzentrum im Vakuum verzögert stattfindet, da der resultierende stark ladungsgetrennte Zustandes in der Gasphase nicht stabilisiert werden kann. Zusätzlich wurde festgestellt, dass die Dynamik von der Pump-Wellenlänge abhängt, d.h. bei Anregung mit Licht etwas längerer Wellenlänge (480 nm) beschleunigt wird. Dies stimmt mit der Annahme überein, dass bei Anregung mit Licht längerer Wellenlänge ein angeregter Zustand besetzt wird, der hauptsächlich auf dem Brückenliganden zentriert ist und somit der Elektronentransfer in Richtung des katalytischen Metallzentrums begünstigt wird. Weiterhin wurden für beide

Katalysatoren polarisationsabhängige transiente Untersuchungen durchgeführt. Daraus konnten die Anfangsanisotropie und die zeitabhängige Anisotropie-Funktion bestimmt werden, die auf Grundlage der zeitabhängigen Rotationskorrelationsfunktion simuliert wurde. Bei einer Anregungswellenlänge von 440 nm nahm die Anfangsanisotropie einen Wert von ~0.3 (für **Ru-Pt** und **Ru-Pd**) an, wohingegen bei Verwendung größerer Pumpwellenlängen (480 nm) ein Wert von ~0.4 ermittelt wurde. Dies deutet auf einen gerichteten Elektronentransfer in Richtung der Brücke hin, welcher bei größerer Wellenlänge verstärkt wird. Mittels Ionenfallen-Photofragmentations-Spektroskopie konnten wertvolle Einblicke in die intrinsischen spektroskopischen und dynamischen Eigenschaften von Ru^{II}-basierten Photokatalysatoren sowie deren Stabilität erhalten werden, die dazu beitragen könnten die Leistungsfähigkeit solcher supramolekularer Photokatalysatoren in Zukunft weiter zu optimieren. Die Ergebnisse wurden als Paper im Journal *Angewandte Chemie International Edition* veröffentlicht.

Die UV/Vis-Absorptionseigenschaften eines neuartigen heterodinuklearen Komplexes **RubbipPt** ([(^{t}bbpy)$_2$Ru(μ-bbip)Pt(DMSO)Cl$_2$]$^{2+}$, ^{t}bbpy=4,4'-Di-tert-butyl-2,2'-bipyridin, bbip =1,3-dibenzyl-1H-imidazo[4,5-f][1,10]phenanthrolin-2-yliden, DMSO=Dimethyl-sulfoxid) für photokatalytische Wasserstofferzeugung wurde in Gasphase und in Lösung untersucht. Angesichts fehlender kristallographischer Daten für diesen Komplex konnte die molekulare Struktur nur durch Vergleich der experimentellen mit theoretischen Absorptionsspektren identifiziert werden. Das für die *cis-S*-Geometrie berechnete Spektrum, bei dem der DMSO-Ligand *cis*-ständig zum Brückenliganden über das *S*-Atom an das Platinatom bindet, stimmt sehr gut mit den experimentellen Spektren überein. TD-DFT-Berechnungen unter Verwendung eines Lösemittelmodells ergaben, dass der spektrale Charge-Transfer-Bereich (>400 nm) im Wesentlichen von zwei Übergängen dominiert wird. Der niederenergetische Übergang besteht dabei hauptsächlich aus einem Ladungstransfer vom Ruthenium-Metallzentrum zum π-System des verbrückenden Liganden, wohingegen der höherenergetische Übergang den Ladungstransfer über die gesamte Liganden-Sphäre des Ruthenium-Photo-sensibilisators beinhaltet. Die Berechnungen in Flüssigphase sind im Einklang mit früheren theoretischen Studien an ähnlichen supramolekularen Katalysatoren. TD-DFT Rechnungen am isolierten Molekül hingegen lieferten keine nachvollziehbaren Ergebnisse für die langwelligsten Übergänge im Charge-Transfer-Bereich, wohingegen

der berechnete UV-Bereich im exzellenten Einklang mit dem experimentellen Photofragmentations Spektrum steht. Dieser Befund offenbart die Notwendigkeit zur Verwendung anspruchsvollerer theoretischer Methoden für die Modellierung niedrig liegender angeregter Zustände in supramolekularen, isolierten Systemen, da hierfür TD-DFT offensichtlich nicht mehr ausreicht. Die aufgezeichneten transienten Photofragmentations-Signale zeigten einen tri-exponentiellen Zerfall, woraus eine Zeitkonstante auf ns-Zeitskala und zwei auf der ps-Zeitskala bestimmt wurden. Die kürzeste Zeitkonstante wurde dem Charge-Transfer-Übergang auf den Brückenliganden zugeordnet. Die Zuordnung wurde durch eine Beschleunigung der elektronischen Dynamik nach Anregung mit Pulsen längerer Wellenlänge bekräftigt, in Einklang mit einem gerichteten Elektronentransfer in Richtung des katalytischen Metallzentrums. Der Ursprung der verbleibenden zwei Prozesse ist zum gegenwärtigen Punkt der Forschung nicht zuzuordnen und erfordert weitere komplementäre, zeitaufgelöste Untersuchungen in Lösung. Dennoch stellt die beobachtete Kinetik einen wertvollen Bezugspunkt für zukünftige Studien dar.

Ein neuartiger supramolekularer Katalysator **RubbipPt** ([(^{t}bbpy)$_2$Ru (μ-bbip)Pt(DMSO)Cl$_2$]$^{2+}$, ^{t}bbpy=4,4'-Di-tert-butyl-2,2'-bipyridin, DMSO=Dimethylsulfoxid, bbip=1,3-Dibenzyl-1H-imidazo[4,5-f][1,10]phen-anthrolin-2-yliden) zur Wasserstoff-erzeugung wurde von S. Kaufhold (Universität Ulm) entwickelt und charakterisiert. Dessen Wirksamkeit ist jedoch gering unter den üblichen katalytischen Bedingungen. Durch Zusatz eines Iodid-Salzes (TBAI, Tetrabutyl-ammoniumiodid) wurde die katalytische Leistung jedoch dramatisch erhöht, was auf einen *in situ* Ligandenaustausch (Cl$^-$ vs. I$^-$) zurückgeführt wurde. Diese geht vermutlich mit einer höheren Elektronendichte am katalytischen Platin-Metallzentrum einher. Der Zusatz anderer Halogenidsalze (TBAX, X=F, Cl und Br) hatte nur einen vernachlässigbar kleinen Effekt. Der *in situ* erfolgte Ligandenaustausch nach Zusatz von TBAI wurde massenspektrometrisch verfolgt. Es bildeten sich zeitgleich zwei Produktsignale aus dem Mutterionensignal [(^{t}bbpy)$_2$Ru(μ-bbip)Pt(Cl)(OMe)]$^{2+}$ (in Methanol), die anhand ihrer Isotopenmuster identifiziert und einem einfachen ([(^{t}bbpy)$_2$Ru(μ-bbip)Pt(Cl)I]$^{2+}$) und doppelten ([(^{t}bbpy)$_2$Ru(μ-bbip) PtI2]$^{2+}$) Ligandenaustausch zugeordnet wurden. Die Signalintensität des letzteren Produkts nahm bei Zusatz größerer Mengen TBAI drastisch zu. Zusätzlich wurden mittels DFT, Populationsanalysen (NPA) für das

Mutterion und für mehrere denkbare Austauschprodukte durchgeführt, die aus einem möglichen *in situ* Ligandenaustausch (Cl vs. X, X=F, Br, I, OMe) hervorgehen können. Die höchste Elektronendichte im Pt($5dz^2$) Orbital wurde für [(^{t}bbpy)$_2$Ru(μ-bbip)PtI$_2$]$^{2+}$ ermittelt, in qualitativer Übereinstimmung mit dessen verbesserten katalytischer Aktivität. Diese Studie liefert einen faszinierenden Einblick in die Struktur-Eigenschaft-Beziehung supramolekularer, photokatalytischer Systeme und sollte einen wertvollen Beitrag leisten zur Optimierung der Wirksamkeit supramolekularer Photokatalysatoren auf Grundlage theoretischer Konzepte. Die Ergebnisse sind Teil der Doktorarbeit von S. Kaufhold (Universität Ulm) und wurden zusätzlich als Communication im Journal *Energy & Environmental Science* eingereicht.

Abschließend lässt sich zusammenfassen, dass eine Vielzahl bekannter und ebenfalls neuer experimenteller Methoden angewendet wurde, um die intrinsischen Eigenschaften elektronisch angeregter Zustände von isolierten organischen Farbstoffmolekülen und supramolekularen Katalysatoren zu untersuchen. DFT- und TD-DFT-Berechnungen dienten der Identifizierung von Gasphasenstrukturen der untersuchten Systeme und der Charakterisierung von Absorptionsbanden, die in experimentellen IRMPD- und UV/Vis-Photofragmentations Spektren beobachtet wurden. Die hier erstmalig intensiv angewendete transiente Femtosekunden Photofragmentation in einer Ionen-Falle erweist sich als eine äußert wertvolle Methode zur Untersuchung ultraschneller molekularer Schwingungs- und Rotationsdynamiken sowie der Dynamik elektronisch angeregter Zustände von ionischen Farbstoffmolekülen und größeren photokatalytischen Systemen unter isolierten Bedingungen. Sie ist komplementär zu anderen zeitaufgelösten Flüssigphasen- und Gasphasen Methoden und wird sicherlich auch weiterhin wertvolle Einblicke in die ultraschnelle Dynamik elektronisch angeregter Zustände von Metallkomplexen sowie organischer Verbindungen liefern.

List of Publications

"EXCITED-STATE DYNAMICS OF A RUTHENIUM(II) CATALYST STUDIED BY TRANSIENT PHOTOFRAGMENTATION IN GAS PHASE AND TRANSIENT ABSORPTION IN SOLUTION"

D. Imanbaew, Y. Nosenko, C. Kerner, K. Chevalier, F. Rupp, C. Riehn, W. R. Thiel, R. Diller

Chem. Phys. **2014**, *442*, 53-61

http://doi.org/10.1016/j.chemphys.2014.03.005

"EXCITED-STATE DYNAMICS OF CATALYTICALLY ACTIVE TRANSITION METAL COMPLEXES STUDIED BY TRANSIENT PHOTOFRAGMENTATION IN GAS PHASE AND TRANSIENT ABSORPTION IN SOLUTION"

D. Imanbaew, Y. Nosenko, K. Chevalier, F. Rupp, C. Kerner, F. Breher, W. R. Thiel, R. Diller, C. Riehn

Ultrafast Phenomena XIX: Proceedings of the 19th International Conference, Okinawa Convention Center, Okinawa, Japan, July 7-11, 2014 (Eds.: K. Yamanouchi, S. Cundiff, R. de Vivie-Riedle, M. Kuwata-Gonokami, L. DiMauro), Springer International Publishing, Cham, **2015**, pp. 378-381

http://dx.doi.org/10.1007/978-3-319-13242-6_92

"ROTATIONAL AND VIBRATIONAL DYNAMICS IN THE EXCITED ELECTRONIC STATE OF DEPROTONATED AND PROTONATED FLUORESCEIN STUDIED BY TIME-RESOLVED PHOTOFRAGMENTATION IN AN ION TRAP"

D. Imanbaew, M. F. Gelin, C. Riehn

Struct. Dyn. **2016**, *3*, 043211.

http://dx.doi.org/10.1063/1.4953367

"PUMP-PROBE FRAGMENTATION ACTION SPECTROSCOPY: A POWERFUL TOOL TO UNRAVEL LIGHT-INDUCED PROCESSES IN MOLECULAR PHOTOCATALYSTS"

D. Imanbaew, J. Lang, M. F. Gelin, S. Kaufhold, M. G. Pfeffer, S. Rau, C. Riehn

Angew. Chem. Int. Ed. **2017**, *56*, 5471-5474.

http://dx.doi.org/ 10.1002/anie.201612302

Danksagung

Herrn PD Dr. Christoph Riehn möchte ich für die Betreuung, die unbeschwerte Zusammenarbeit und den mir eingeräumten Freiraum während meiner Promotion danken. Besonders die langen Konversationen und tiefgreifende Diskussionen über verschiedenste Themen werden meine Beine in guter Erinnerung behalten.

Herrn Prof. Dr. Gereon Niedner-Schatteburg danke ich für die freundliche Aufnahme in den AK GNS, die Übernahme des Zweitgutachtens und die Möglichkeit unter der Betreuung von PD Dr. Christoph Riehn in der „Femto-Zweigstelle" meine Promotion durchführen zu können.

Herrn Prof. Dr. Werner Thiel danke ich für die Übernahme des Prüfungs-kommissionsvorsitzes und die gute Kooperation.

Herrn Prof. Dr. Markus Gerhards und dem gesamten AK Gerhards danke ich für das freundliche Arbeitsumfeld und die gegenseitige Hilfsbereitschaft unter den Physiko-Chemikern im 5ten Stock des Fachbereichs Chemie.

Meinem Mitarbeiter in der Femto-Gruppe Sebastian Kruppa danke ich für die gute Zusammenarbeit. Besonders danke ich jedoch Dr. Yevgeniy Nosenko für die Einführung in die Laserphysik, seine unermessliche Geduld und Diskussionsbereitschaft. Ich hoffe, dass seine pragmatische und ruhige Arbeitsweise etwas auf mich abgefärbt hat.

Den Absolventen „alter Schule" aus dem AK GNS Dr. Lars Barzen, Dr. Fabian Menges, Dr. Christine Merkert, Dr. Jennifer Meyer und Dr. Matthias Tombers danke ich für die gemeinsame Zeit und die Einführung in die wissenschaftliche Arbeitsweise. Dr. Christian Kerner (AK Thiel) verdanke ich den guten Kontakt zum AK Thiel und meinen unerschöpflichen Vorrat an trockenem Acetonitril. Dr. Yvonne Schmitt (AK Gerhards) danke ich für die erstklassige Betreuung und die nette Zeit während meiner Praktika im Fluoreszenzlabor.

Lebenslauf

Name: Dimitri Imanbaew

Akademischer Werdegang

Okt 2013 – Juli 2017   TU Kaiserslautern, Kaiserslautern

Doktorand im Fachbereich Physikalische Chemie im Arbeitskreis von Prof. Dr. G. Niedner-Schatteburg unter Betreuung von PD Dr. C Riehn

Okt 2008 – Okt 2013   TU Kaiserslautern, Kaiserslautern

Studiengang in Fachrichtung Chemie

Abschluss: Diplom (1.0)

Sep 1998 – Juli 2007   Kepler Gymnasium, Weiden i. d. Opf.

Abschluss: Abitur (1.5)

Sep 1994 – Juli 1998   Gerhardinger Grundschule, Weiden i. d. Opf.

Eidesstattliche Erklärung

Hiermit erkläre ich, Dipl.-Chem. Dimitri Imanbaew, dass ich die vorliegende Arbeit gemäß der Promotionsordnung des Fachbereichs Chemie der Technischen Universität Kaiserslautern selbstständig und ohne Benutzung anderer als der angegebenen Quellen und Hilfsmittel verfasst habe.

Kaiserslautern, den _____

_____

Dimitri Imanbaew